AFRL-ML-WP-TR-1999-4179

DEVELOPMENT OF THE ELECTROCHEMICAL FATIGUE SENSOR FOR IMPROVED DURABILITY ASSESSMENT OF MILITARY AIRCRAFT—PHASE 1

S.J. HUDAK, JR.
M.A. MILLER
G.A. CRAGNOLINO   SOUTHWEST RESEARCH INSTITUTE
D.S. DUNN
P.C. McKEIGHAN
R.H. HILL, JR.

C. LAIRD
Y. LI
J.J. DeLUCCIA   UNIVERSITY OF PENNSYLVANIA
S.A. KASSAM
J. WANG
M. WANG
D. LEES

J.W. GOODMAN   TENSIODYNE SCIENTIFIC CORPORATION
R.M. BERNSTEIN

AUGUST 1999

FINAL REPORT FOR 02/25/1997 – 02/25/1999

APPROVED FOR PUBLIC RELEASE; DISTRIBUTION UNLIMITED

MATERIALS AND MANUFACTURING DIRECTORATE
AIR FORCE RESEARCH LABORATORY
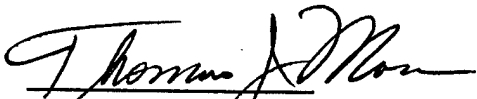AIR FORCE MATERIEL COMMAND
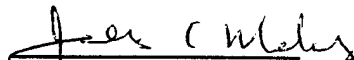WRIGHT-PATTERSON AIR FORCE BASE OH 45433-7750

NOTICE

WHEN GOVERNMENT DRAWINGS, SPECIFICATIONS, OR OTHER DATA ARE USED FOR ANY PURPOSE OTHER THAN IN CONNECTION WITH A DEFINITELY GOVERNMENT-RELATED PROCUREMENT, THE UNITED STATES GOVERNMENT INCURS NO RESPONSIBILITY OR ANY OBLIGATION WHATSOEVER. THE FACT THAT THE GOVERNMENT MAY HAVE FORMULATED OR IN ANY WAY SUPPLIED THE SAID DRAWINGS, SPECIFICATIONS, OR OTHER DATA, IS NOT TO BE REGARDED BY IMPLICATION OR OTHERWISE IN ANY MANNER CONSTRUED, AS LICENSING THE HOLDER OR ANY OTHER PERSON OR CORPORATION, OR AS CONVEYING ANY RIGHTS OR PERMISSION TO MANUFACTURE, USE, OR SELL ANY PATENTED INVENTION THAT MAY IN ANY WAY BE RELATED THERETO.

THIS REPORT IS RELEASABLE TO THE NATIONAL TECHNICAL INFORMATION SERVICE (NTIS). AT NTIS, IT WILL BE AVAILABLE TO THE GENERAL PUBLIC, INCLUDING FOREIGN NATIONS.

THIS TECHNICAL REPORT HAS BEEN REVIEWED AND IS APPROVED FOR PUBLICATION.

THOMAS J. MORAN, Project Engineer
Nondestructive Evaluations Branch
Metals, Ceramics & NDE Division

JAMES C. MALAS, Chief
Nondestructive Evaluations Branch
Metals, Ceramics & NDE Division

GERALD J. PETRAK, Assistant Chief
Metals, Ceramics & NDE Division
Materials & Manufacturing Directorate

IF YOUR ADDRESS HAS CHANGED, IF YOU WISH TO BE REMOVED FROM OUR MAILING LIST, OR IF THE ADDRESSEE IS NO LONGER EMPLOYED BY YOUR ORGANIZATION, PLEASE NOTIFY, AFRL/MLLP, WRIGHT-PATTERSON AFB, OH 45433-7817 AT (937) 255-9819 TO HELP US MAINTAIN A CURRENT MAILING LIST.

COPIES OF THIS REPORT SHOULD NOT BE RETURNED UNLESS RETURN IS REQUIRED BY SECURITY CONSIDERATIONS, CONTRACTUAL OBLIGATIONS, OR NOTICE ON A SPECIFIC DOCUMENT.

REPORT DOCUMENTATION PAGE

Form Approved
OMB No. 0704-0188

Public reporting burden for this collection of information is estimated to average 1 hour per response, including the time for reviewing instructions, searching existing data sources, gathering and maintaining the data needed, and completing and reviewing the collection of information. Send comments regarding this burden estimate or any other aspect of this collection of information, including suggestions for reducing this burden, to Washington Headquarters Services, Directorate for Information Operations and Reports, 1215 Jefferson Davis Highway, Suite 1204, Arlington, VA 22202-4302, and to the Office of Management and Budget, Paperwork Reduction Project (0704-0188), Washington, DC 20503.

1. AGENCY USE ONLY *(Leave blank)*	2. REPORT DATE	3. REPORT TYPE AND DATES COVERED
	AUGUST 1999	FINAL REPORT FOR 02/25/1997 - 02/25/1999

4. TITLE AND SUBTITLE
DEVELOPMENT OF THE ELECTROCHEMICAL FATIGUE SENSOR FOR
IMPROVED DURABILITY ASSESSMENT OF MILITARY AIRCRAFT—PHASE 1

5. FUNDING NUMBERS
C   F41608-96-D-0108
PE   63112
PR   3153
TA   40
WU   FJ

6. AUTHOR(S)
S.J. Hudak, Jr., M.A. Miller, G.A. Cragnolino, D.S. Dunn, P.C. McKeighan,
R.H. Hill, Jr., C. Laird, Y. Li, J.J. DeLuccia, S.A. Kassam, J. Wang, D. Lees,
J.W. Goodman, R.M. Bernstein

7. PERFORMING ORGANIZATION NAME(S) AND ADDRESS(ES)
SOUTHWEST RESEARCH INSTITUTE
P.O. DRAWER 28510
SAN ANTONIO, TX 78228-0510

8. PERFORMING ORGANIZATION REPORT NUMBER

18-8784-1

9. SPONSORING/MONITORING AGENCY NAME(S) AND ADDRESS(ES)
MATERIALS AND MANUFACTURING DIRECTORATE
AIR FORCE RESEARCH LABORATORY
AIR FORCE MATERIEL COMMAND
WRIGHT-PATTERSON AFB, OH 45433-7750
POC: THOMAS J. MORAN, AFRL/MLLP, 937-255-9800

10. SPONSORING/MONITORING AGENCY REPORT NUMBER

AFRL-ML-WP-TR-1999-4179

11. SUPPLEMENTARY NOTES

12a. DISTRIBUTION AVAILABILITY STATEMENT

APPROVED FOR PUBLIC RELEASE, DISTRIBUTION UNLIMITED.

12b. DISTRIBUTION CODE

13. ABSTRACT *(Maximum 200 words)*

The Electrochemical Fatigue Sensor (EFS) concept, initially developed by the University of Pennsylvania, has the potential to provide information on the early stages of fatigue damage in structural materials. Consequently, its applicability to inspection of military aircraft is being assessed in a multi-phased program. Phase 1, reported here, established the feasibility of EFS for aircraft applications. EFS measurements were shown to change systematically as fatigue damage accumulated in aluminum alloy 7075-T73511, 4130 steel, and titanium alloy Ti-6Al-4V. The EFS electrolyte was demonstrated to be benign to these aircraft alloys. Fatigue microcracks on bare metal specimens were detected as small as 75 μm in surface length. EFS measurements were also shown to be feasible on primer-coated aluminum alloys, although with decreased sensitivity compared to uncoated material. Measurements on aluminum alloy with both primer and top-coat were problematic due to the high electrical impedance of these coatings. The feasibility of making EFS measurements: a) with small sensors (5 ml of electrolyte and 1.5 cm^2 footprint), and b) within the electromagnetic background noise typical of aircraft hangars was also demonstrated. A companion technology, Electrochemical Impedance Spectroscopy (EIS), was adapted for detection of fatigue damage in aluminum alloy 7075. Unlike EFS, EIS does not require the structure to be loaded since it perturbs the material electrically, instead of mechanically. However, EIS is in other respects less mature than EFS, and its application to steel and titanium-alloys remains problematic.

14. SUBJECT TERMS
Electrochemical, Fatigue Sensor, Durability, Damage Tolerance, Nondestructive Inspection, Aircraft, Turbine Engines.

15. NUMBER OF PAGES
487

16. PRICE CODE

17. SECURITY CLASSIFICATION OF REPORT	18. SECURITY CLASSIFICATION OF THIS PAGE	19. SECURITY CLASSIFICATION OF ABSTRACT	20. LIMITATION OF ABSTRACT
UNCLASSIFIED	UNCLASSIFIED	UNCLASSIFIED	SAR

Standard Form 298 (Rev. 2-89) (EG)
Prescribed by ANSI Std. 239.18
Designed using Perform Pro, WHS/DIOR, Oct 94

TABLE OF CONTENTS

TABLE OF CONTENTS (CONTINUED)

TABLE OF CONTENTS (CONTINUED)

TABLE OF CONTENTS (CONTINUED)

TABLE OF CONTENTS (CONTINUED)

LIST OF FIGURES

LIST OF FIGURES (Continued)

LIST OF FIGURES (Continued)

LIST OF FIGURES (Continued)

LIST OF FIGURES (Continued)

LIST OF FIGURES (Continued)

LIST OF TABLES

LIST OF TABLES (Continued)

ACKNOWLEDGMENTS

EXECUTIVE SUMMARY

Engineering materials derive their corrosion resistance from the presence of stable oxide films on their surfaces that serve as barriers to reactions with chemically aggressive environments. During cyclic loading the fatigue process causes strain localization at the microscopic level that eventually causes the materials' protective films to breakdown. This process of mechanical depassivation exposes fresh, highly reactive metal that leads to local dissolution followed by rapid reformation of the passive film. Since this dissolution and repassivation process is electrochemical in nature it gives rise to a transient current. In previous studies, researchers at the University of Pennsylvania demonstrated that measurement of this transient current could be employed as an Electrochemical Fatigue Sensor (EFS) to assess the state of fatigue damage in a material. The objective of the present program was to assess the feasibility of employing EFS to quantify the early stages of fatigue damage in military aircraft materials—both prior to and after the onset of cracking. Establishing such a technology could lead to improvements in the availability and safety of aging military aircraft by enhancing the detectability and predictability of fatigue damage, while lowering the cost of inspection, maintenance, and repair.

Using a systematic experimental and analytical approach many of the technical hurdles to establishing the feasibility of the EFS as a practical inspection tool have been overcome in the present program. The underlying phenomenon was demonstrated for a range of aircraft alloys including aluminum alloy 7075-T73511, 4130 steel and titanium alloy Ti-6Al-4V. EFS current transients were shown to change in a systematic and characteristic manner as fatigue damage accumulated in these materials throughout their fatigue lives. Using these characteristic responses, fatigue microcracking in the size range of 70 to 75 μm was detected and improvements on this minimum detectable crack size are believed to be possible. Moreover, these measurements were accomplished with an electrolyte that was demonstrated to be benign to the three aircraft alloys investigated.

The potential of a companion technology, electrochemical impedance spectroscopy (EIS), for detection of fatigue cracking was also demonstrated in the aluminum alloy. EIS senses fatigue damage indirectly through an increase in the nascent reactivity of the fatigue-damaged surface. Although EIS is a less mature technology than EFS, it has the attractive feature that measurements can be made without the need to load the structure, since the material is perturbed electrically instead of mechanically as in the case of EFS. However, the use of EIS was found to be problematic for the steel and Ti-alloy examined because of the rapid repassivation kinetics in these alloys, consequently, considerably more work is needed to resolve this problem.

Both EFS and EIS were capable of detecting fatigue damage through the porous primer coating used on aluminum alloy aircraft components, although the sensitivity was found to be decreased somewhat compared to measurements on uncoated material. Measurements on aluminum alloy with both primer and top coat were found to be more problematic due to the high electrical impedance of this coating. However, preliminary results indicate that useful measurements may be possible on aged coating due to the presence of cracks and other defects in the coatings.

The feasibility of making EFS measurements with small sensors having 5 ml of electrolyte and contact areas on 1.5 cm^2 was also demonstrated, as well as the feasibility of making EFS measurements within the electromagnetic background noise typical of aircraft hangars.

The remaining technical challenges to further development of EFS as an inspection tool are specific to the particular mode of application of this technology. Four potential modes of application are envisioned: 1) Mode 1:Laboratory tool for characterizing and understanding the evolution of fatigue damage in aerospace alloys tested in well-controlled laboratory experiments; 2) Mode 2: Tool for monitoring fatigue damage evolution in full-scale testing—either of critical components or the entire aircraft; 3) Mode 3: Fatigue sensor for periodic in-service inspection of aircraft components during overhaul; and 4) Mode 4: In-flight fatigue sensor for continuous or periodic monitoring of fatigue damage evolution at fatigue critical locations in aircraft. Presently EFS is sufficiently mature for Mode 1 laboratory application and close to being used in Mode 2 component or aircraft testing applications. However, there are presently five remaining technical challenges that need to be overcome for EFS to be employed in Modes 3 and 4 as periodic or continuous in-service inspection tools, respectively.

(1)   Although consistent trends have been demonstrated between EFS current response and fatigue microcrack nucleation and growth, there is a need to develop these trends into fully quantifiable relationships that can be used to assess the state of fatigue damage with the reliability needed to make run/repair/retire decisions on aircraft components. A primary technical challenge to achieving this goal is to develop methods to either eliminate or compensate for the settling-in transients that often occur on initial application, or periodic reapplication, of the EFS probe due to time-dependent changes in the nature of the surface film, particularly on aluminum alloys.

(2)   Utilizing the EFS technology as an in-service monitor of evolving fatigue damage has a number of distinct advantages—for example, the structure would be self-loaded in a manner consistent with the evolving fatigue damage, and continuous measurements would result in more rigorous and reliable fatigue assessments. However, in order to apply the EFS as an in-service monitor, a more complete understanding and quantification of fatigue damage accumulation under complex, aircraft spectrum loading needs to be developed, including methods to account for frequency (*i.e.*, strain-rate) effects.

(3)   Widespread application of EFS will require it to be suitable for most, if not all, of the known fatigue critical location on aircraft. Such widespread application will require the EFS to provide information relevant to inaccessible sites where the sensor cannot be placed in direct contact with the surface on which fatigue damage nucleates. Such information can conceivably be acquired by sensing cracks indirectly through their attendant crack-tip plasticity, or by remotely sensing expected increases in net section stress as the crack grows. The development of a solution to this problem will likely require a coordinated experimental-analytical approach.

(4)   Although the present work has demonstrated the benign nature of the EFS electrolyte, practical application of the sensor will likely require measurements to be made in situations

where more aggressive service environments may be present. In particular, this can occur where chlorides or other contaminants can cause chemical depassivation within crevices and other occluded regions that are common at fatigue critical locations on aircraft. Thus, the capability of EFS to assess fatigue damage in the presence of such background electrochemical "noise" from localized corrosion needs to be systematically examined.

(5)   Widespread application of EFS to the periodic assessment of fatigue damage in aircraft may be practically limited by the need to load the structure in order to activate the EFS response. Mechanical loading may not always be technically or economically feasible. One alternative is the previously mentioned application of EFS as an in-service monitor—in which case the problems associated with signal interpretation under spectrum loading will need to be resolved. The EIS technology represents another alternative. Although EIS measurements are widely used to study chemical breakdown of passivity in coated specimens in the absence of cyclic deformation, the application of this technology to the assessment of fatigue damage is relatively new and will require time and resources to mature.

1.0 INTRODUCTION

The San Antonio Air Logistics Center supports a number of aging aircraft including the T-38, F-5, T-37, and C-5. Since metal fatigue often controls the inspection, maintenance, repair/replacement, and safety of flight of such aging aircraft, it is important to develop innovative methods for improved assessment of fatigue damage in these aircraft. The overall objective of this program is to improve the United States Air Force's (USAF) capability to perform fatigue durability assessments of military aircraft, including both airframes and engines, through the application of Electrochemical Fatigue Sensor (EFS) technology. As described below, EFS involves a device and technology initially developed at the University of Pennsylvania, and currently licensed to Tensiodyne Scientific Corporation, which has the potential to provide information on the early stages of fatigue damage in structural materials.

The specific objective of the current Phase 1 program being reported here was to establish the feasibility of applying the EFS device to military aircraft alloys and structures in order to quantify the early stages of fatigue damage—both prior to and after the onset of cracking—without specific knowledge of the previous loading/stress history. The alloys and the structural components to be considered as part of this program are typical of military fighter and transport aircraft such as the T-38 and C-5, respectively, as well as engines which are known to be susceptible to High Cycle Fatigue (HCF). The eventual benefit of establishing such a technology would be to improve the availability and safety of aging aircraft by enhancing the detectability and predictability of fatigue damage, while also lowering the cost of inspection, maintenance, and repair. For example, the ability to better characterize and understand early fatigue damage could lead to economic benefits by lengthening the times to initial inspection thereby reducing both inspection cost and aircraft downtime.

1.1 Background

Based on studies of electrochemical-mechanical interactions [1.1-1.3], an electrochemical device was invented to measure fatigue damage in a structure without requiring information

concerning the history of the structure [1.4]. This device is called the Electrochemical Fatigue Sensor (EFS), and it operates on the following principle: a three-electrode cell is fitted to a structure, the fatigue status of which is desired to be determined at the point where the cell is attached. The material of the structure at the point of cell attachment is arranged to be an electrode of the cell, usually the anode. A controlled electrochemical reaction is established in the cell by means of a potentiostat and the cell current (the transient current) is measured while the structure undergoes fatigue loading. The variation in applied stress causes variation in the transient current which depends on the nature of the load cycle and the current state of fatigue damage. Consequently, the current transient changes systematically as the fatigue damage develops. When such a device is suitably chosen and calibrated for the material of interest, its transient current response can be used to determine the status of fatigue in the structure.

An example of transient current behavior for a ductile metal specimen undergoing fatigue is shown schematically in Figure 1-1. Figure 1-1(a) indicates that the specimen is experiencing a sinusoidal load/strain cycle. Figure 1-1(b) shows that for each cycle, the transient current often exhibits two peaks and two valleys, a pair being associated with each tensile and compressive reversal. Such a transient current shows that fatigue microplasticity occurs in both tension and compression. Early in life the amplitude of the variable transient current is small; this behavior is shown schematically in Figure 1-1(c) where the recorder speed has been slowed down to allow the pen to sweep out a signal band, the height of which is the amplitude of the current transient. As fatigue damage accumulates, the amplitude of the transient current increases as shown in Figure 1-1(b) and (c) reflecting the increased damage. After a small crack initiates, its presence can be detected by the occurrence of an additional peak (the crack peak) which occurs at the start of the tensile reversal. Thus, the EFS can also respond to the plasticity associated with crack growth. As the crack grows, the amplitude of the crack peak increases, providing a measure of the crack size and growth rate.

The technical studies performed to date and described in references [1.1-1.7] indicated that the EFS holds promise for application to military aircraft. As the past work unfolded, there were concerns over a variety of technical obstacles: (a) the possibility that the background current associated with elastic deformation in aluminum alloys and steels may be too high in

relation to the interesting fatigue-related signals, (b) difficulty in finding the optimum electrolyte and reference-electrode geometries, (c) information loss during application of complex load-cycling, and (d) concerns that specific metals may not provide adequate signals.

In many respects, the modern adaptation of EFS was found to be at a more advanced state of development than originally thought. In fact, the formulation of the technical plan for the present program contributed to an enhanced level of understanding of the essential physics and phenomenological similarity between EFS and two other well-established materials characterization techniques, namely, electrochemical impedance spectroscopy (EIS) [1.5-1.7] and its mechanical analog electrochemical-mechanical impedance spectroscopy (EMIS) [1.8]. For the purpose of introduction, it is instructive to describe briefly, in very general terms, the relationship between EIS and EMIS.

The overall objective of these techniques is to measure the response of a system to an applied, frequency- and amplitude-dependent perturbation under carefully controlled electrochemical conditions. As these are cause-and-effect measurements, a transfer function (*i.e.*, output over input) can be defined for each case in terms of an impedance. The perturbation used in EIS is a small amplitude, cyclic electric field (*i.e.*, current or voltage) with a transfer function corresponding to a true, frequency-dependent impedance ($Z(\omega)=E/I$). Such a perturbation is useful in probing the charge transfer and ion mobility response of the system. In EMIS the perturbation is a cyclic, mechanical load, and the response of the system is measured as a cyclic current or voltage under controlled potentiostatic conditions. This sort of perturbation probes the electrochemical response of a material system to a mechanical load that causes structural changes (*e.g.*, dislocation motion, persistent slip or crack formation, and crack growth). Consequently, it was recognized that the EFS method could possibly be further developed and applied in this program as a special case of EMIS and EIS, which share common elements of the experimental setup and apparatus.
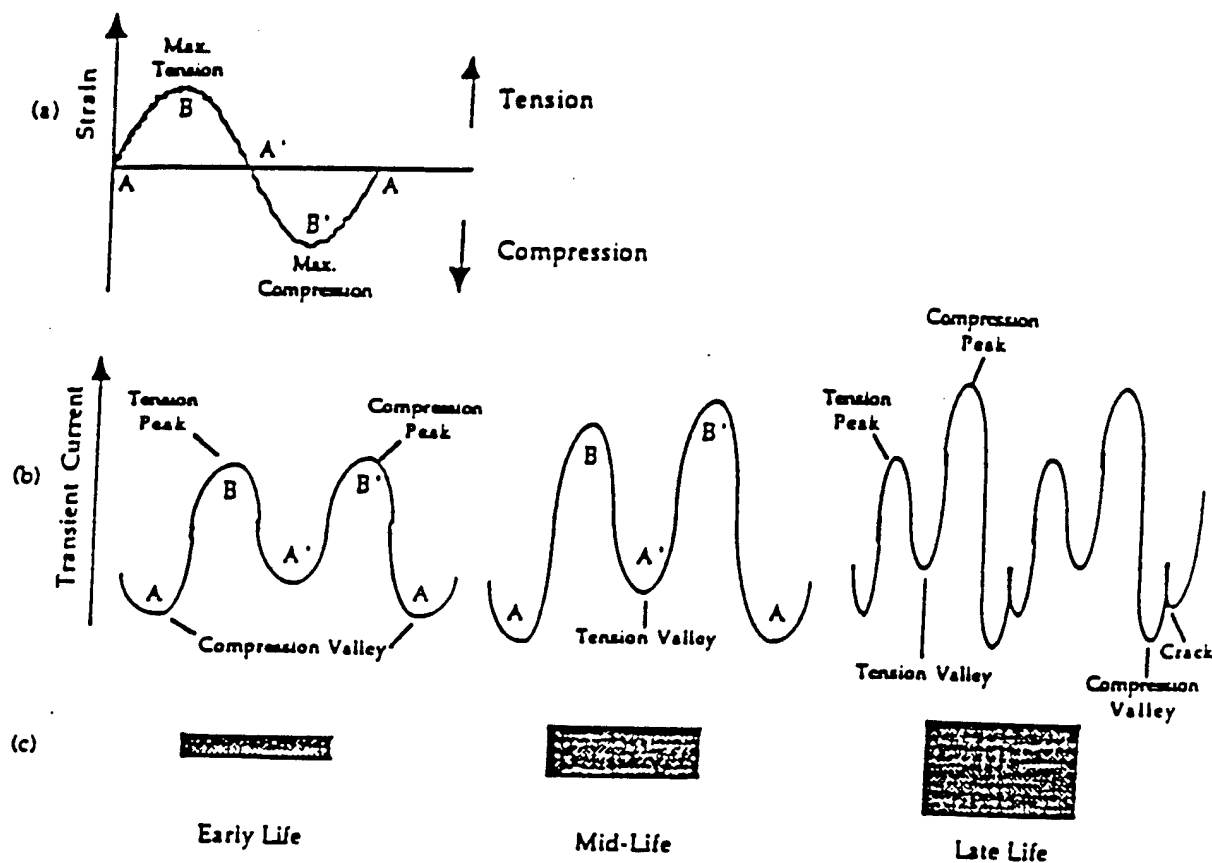
Figure 1-1. Transient current behavior is shown schematically for cyclic deformation applied to a specimen as life is consumed: (a) fatigue strain cycle; (b) transient current waveforms; and (c) transient current behavior recorded on a chart recorder at low chart speed.

EIS has been extensively used in recent years in electrochemistry and corrosion science to study transport of reactive species in aqueous or solid electrolytes, adsorption of reactive species on conductive and semiconductive surfaces and charge transfer interfacial reactions [1.9-1.11]. By using instruments such as a Frequency Response Analyzer (FRA) or methods based on lock-in amplifiers, it is possible to measure the impedance of a medium and interface over a wide frequency range by applying a small amplitude, sinusoidal voltage (or current) perturbation to obtain the corresponding current (or voltage) response. The impedance, defined for a linear electric system as a transfer function between the response and the input, can be readily determined in terms of a complex (real and imaginary) vector.

The present program provided for the first time an opportunity to systematically test theories in the relaxation phenomenon of materials when approached from the common metric of an impedance transfer function. A unified perspective of the EFS, EIS, and EMIS technologies

based on this common metric was expected to contribute significantly to the further development and augmentation of EFS as an enabling sensor technology for noninvasive fatigue damage assessment of aircraft structures. From a practical viewpoint, the primary advantage of EIS as the basis of an inspection technology would be the elimination of the need to mechanically load the component/structure (as is presently required by EFS) in order to assess the present state of fatigue damage.

1.2   Research Team

The current program was conducted using a team of researchers in order to benefit from the unique and complementary skills from several organizations including Southwest Research Institute (SwRI), the University of Pennsylvania (Penn), and Tensiodyne Scientific Corporation (TSC).

SwRI was responsible for the overall program management, including direction and coordination of the subcontracts with Penn and TSC. SwRI also contributed expertise in sensor development, aircraft coatings technology, electrochemical impedance spectroscopy, fatigue and damage tolerance testing, and aircraft engineering.

Penn, the inventor and patent holder of the EIS technology, contributed valuable experience gained in developing the electrochemical fatigue sensor, as well as expertise in cyclic deformation of engineering materials, mechanical-electrochemical interactions and related corrosion technology, and signal processing.

TSC, the worldwide exclusive licensee of the EFS technology, provided over ten years of experience in developing novel fatigue sensors. TSC also supported and monitored the technical output of the program and used this information in conjunction with economic data to assess the feasibility of fully deploying the EFS technology from both practical and financial perspectives.

1.3   Program Overview

As initially conceived, the overall program was organized into three distinct phases—addressing feasibility, development, and validation. Although the current program is limited to an assessment of feasibility (Phase 1), all three phases are briefly outlined below since this broad view is useful for understanding the work which has been completed thus far and reported herein.

Phase 1 - Feasibility: Establish the feasibility of EFS and related technology as a military aircraft fatigue sensor by addressing the fundamental and practical limitations of the technology using both theory and experiment. In this phase, all experiments were limited to the laboratory using simplified/idealized specimens thereby enabling a large number of conditions and variables to be examined.

Phase 2 - Development: Formulate methods and generate specific data needed to transition the EFS and related technology from the laboratory to field application. Included in this effort will be the design and construction of a breadboard EFS system which will be delivered to the Air Force Research Laboratory (AFRL). The Phase 2 effort has been recently initiated.

Phase 3 - Validation: Verify the utility of the technology for field measurements through component simulation testing, and selected field application to a T-38 aircraft. Included in this phase would also be recommendations for full deployment of the technology. Phase 3 has not been funded at this point.

The current Phase 1 effort reported here was organized into ten distinct but interrelated technical subphases, each of which was designed to address a technical challenge associated with transitioning the EFS and related technology from a laboratory measurement to a viable sensor for early detection of fatigue damage. Each of these subphases is briefly described below and its relation to the report sections is also indicated:

Subphase 1: Electrolyte Optimization — formulate suitable liquid and gel electrolytes which are stable, non-corrosive, and non-invasive (Section 3).

Subphase 2: Surface Effects — characterize the effect of newly formulated electrolyte on fatigue surface morphology to ensure that enhanced fatigue damage does not result from corrosion-fatigue due to the presence of the electrolyte (Section 3).

Subphase 3: Electrode Optimization — develop optimum electrodes based on consideration of size/geometry, stability, accuracy, sensitivity, and ruggedness. Also, integrate results of Subphases 1 through 3 into a first-generation EFS sensor (Sections 4 and 8).

Subphase 4: Initial Alloy Tests — characterize baseline mechanical properties and transient current responses under straining for an aluminum alloy, titanium alloy, and steel representative of military aircraft materials (Sections 2 and 5).

Subphase 5: Electrical Isolation — Establish background noise levels associated with aircraft inspections in a depot and assess the feasibility of electrically isolating EFS/EIS measurements on large structures and components representative of military aircraft (Section 9).

Subphase 6: Surface Coatings — assess feasibility and develop means of performing EFS/EIS measurements on coated materials (Sections 5 and 6).

Subphase 7: General Relationships — assess feasibility of developing generalized relationships among EFS/EIS responses and the extent of fatigue over an appropriate range of key fatigue loading variables (Section 5 and 6).

Subphase 8: Elastic versus Plastic Cyclic Deformation — separate EFS responses under elastic versus plastic deformation and establish the theoretical sensitivity limitations of the measurements (Section 5).

Subphase 9: Spectrum Fatigue Loading — assess feasibility of interpreting EFS measurements as a function of extent of fatigue damage generated under typical aircraft spectrum loading (Section 9).

Subphase 10: Economic Assessment — assess the economic feasibility of the application of EFS to fatigue damage measurement on military aircraft (Section 10).

1.4   References

1.1   Li, Y.F., Farrington, G.C., and Laird, C., "Cyclic Response-Electrochemical Interaction in Mono and Polycrystalline AISI 316L Stainless Steel in H_2SO_4 Solution, Part I," *Acta Metall. Mater.*, 41 (1993) 693-708.

1.2   Li, Y.F., Farrington, G.C., and Laird, C., "Cyclic Response-Electrochemical Interaction in Mono and Polycrystalline AISI 316L Stainless Steel in H_2SO_4 Solution, Part II," *Acta Metall. Mater*, 41 (1993) 709-721.

1.3   Li, Y.F., Farrington, G.C., and Laird, C., "Cyclic Response-Electrochemical Interaction in Mono and Polycrystalline AISI 316L Stainless Steel in H_2SO_4 Solution, Part III," *Acta Metall. Mater.*, 41 (1993) 723-37.

1.4   Patent: Methods and Devices for Electrochemically Determining Metal Fatigue Status, Serial No. 08/022, 560, Y.F. Li and C. Laird, 1993.

1.5   Gabrielli, C., "Identification of Electrochemical Processes by Frequency Response Analysis," Technical Report No. 004/83. Solartron Instruments, Farnborough, U.K.

1.6   MacDonald, D. D. and McKubre, M.C.H., "Impedance Measurements in Electrochemical Systems," **Modern Aspects of Electrochemistry**, J.O.M. Bockis, B. E. Conway, and R. E. White (Eds.), Plenum Press, NY, Vol. 14, pp. 61-150, 1982.

1.7   Staehle, R. W., "Stress Corrosion Cracking of the Fe-Co-Ni Alloy System," **Theory of Stress Corrosion Cracking in Alloys**, J. C. Scully (Ed.), NATO, Brussels, pp. 223-288, 1971.

1.8   Eiselstein, L. E., McKubre, M.C.H., and Caligiuri, R. D., "Electrical and Mechanical Impedance of Crack Growth," Final Report by SRI, Office of Naval Research.

1.9   Roelandt, A. and Vereeken, J., *Surface Technology*, 9, pp. 347-349, 1979.

1.10   Roelandt, A. and Vereeken, J., "Materials Science Forum," **Electrochemical Methods in Corrosion Research**, M. D. Prat (ed.), Trans. Tech. Publications, Switzerland, Vol. 8, pp. 225-232, 1986.

1.11   Fox, W. C. and Miller, M. A., "An Osseous Implant for Studies of Biomaterials Using an In Vivo Electrochemical Transducer," *J. Biomed. Mat. Res.*, 27, 1993.

2.0 MATERIALS, SPECIMENS AND BASELINE PROPERTIES

The purpose of this section is to detail the material used, describe the fatigue test specimens, and provide an assessment of the baseline fatigue properties. The goal of quantifying the baseline fatigue properties is to provide a measure of the fatigue performance of the materials, make an assessment of lab-to-lab variability and compare with data from handbooks for the materials considered. Additional detail is provided concerning the coatings used for the materials, the fatigue test methodologies, and the data recording process.

2.1 Materials

2.1.1 Relevance of Material Selections

At the outset of this program, the goal was to confine material choices to a range that could be used to appropriately assess the overall performance of the EFS methodology applied to the complete aircraft structure. Specifically, the materials should be representative of the USAF range of equipment with special attention paid to the material requirements of the Proven Aircraft Directorate at Kelly AFB.

When focusing on the structural integrity of airframe and engine components, three obvious material choices are steel, aluminum and titanium. In order to further narrow the choices, typical structural components on the T-38 were examined. The range of fatigue critical locations (FCLs) examined resulted in the selection of extruded 7075 aluminum alloy and 4130 steel. These choices were based on the structure for the upper cockpit longeron and dorsal longeron of the T-38. It should also be noted that the majority of the life limiting fatigue critical locations on the wing of the T-38 are also manufactured from 7075 aluminum (albeit in a plate form). A titanium alloy was also selected that was characteristic of rotating elements commonly found in engine components.

2.1.2 Alloys, Product Forms and Processing

A description of these three materials is included in Table 2-1. The 7075-T73511 aluminum bar extrusions were ordered and delivered in a ready-to-test form. The extruded bars were randomly selected from stock and hence could have come from different lots. Since the material was supplied in the required temper, no further processing was subsequently required. However, the steel and titanium required further processing after initial delivery to achieve the required tempers.

The cold finished 4130 steel order was of aerospace grade and normalized before delivery. Prior to heat treating, the yield and tensile strengths of the normalized steel were 717 MPa and 745 MPa, respectively. The heat treatment processing applied to the 4130 steel is consistent with that applied to the dorsal longeron of the T-38. Heat treating was performed by Texas Heat Treatment (Round Rock, TX) as per MIL-H-6875 with an ultimate strength target of 1034-1172 MPa. The heat treating was performed with all the material in a single lot and using pieces of stock approximately 0.61 meters long. Confining all of the material to one furnace load mitigated heat-to-heat issues that can sometimes impact property variability.

The heat treatment applied to the Ti-6Al-4V alloy material was derived from standard practice in the aircraft engine community. Specifically, the alloy was solutionized at 938°C for 30 minutes in argon gas and fan cooled to below 93°C. It was then aged at 704°C for 2 hours in argon gas and fan cooled to below 93°C. All processing was performed in vacuum by Titanium Industries, Inc. (Grand Prairie, TX) and the material length during all thermal processing was limited to 1.2 meter.

2.1.3 Tensile Properties

Once all materials were fully processed, blanks were cut and shipped to a contractor for tensile testing. The goal of the tensile testing was to determine baseline strength level as well as to ensure consistent properties along the length of the material and across the width of the aluminum and steel bars. A summary of the results of the tensile properties is given in Table 2-2. The data from each of the tensile tests are tabulated and provided in Appendix AA.

The observed strength levels for the titanium and steel after heat treating were consistent with original specifications. A comparison between the values in Table 2-2 and the allowables in MIL-HNDK-5G [2.1] indicate that all materials are within specification. Furthermore, the tensile test data in Appendix AA indicate no discernible variation either along the length of the product or, for the case of the aluminum and steel, across the width of the bars.

2.2   Material Coatings

A total of 31 aluminum alloy (Al-7075) specimens were chemically processed and coated for fatigue sensor investigations under the experimental plan of this program. Maintenance personnel and facilities located at Randolph AFB, San Antonio, TX, for T-38/T-37 aircraft painting operations were employed to prepare the coated specimens.

Among all coated specimens, thirteen were chemically treated to remove surface adherends and subsequently spray painted with a primer coating (MIL P 23377G Type 1 Class C). The remaining eighteen were chemically treated and subsequently spray painted with the primer coating and a top coat (MIL C 85285 Type 1). These procedures were conducted in accordance with acceptable standards established for the maintenance of military aircraft materials of this type and, therefore, result in an adequate representation, other than age, of an aircraft painted surface to which the experimental technique might be applied. The compositional specifications of these coatings are summarized in Table 2-3.

In each case, the gage section plus one-half inch of the shank beyond both ends of the start of each radius was coated with either the primer or the primer plus top coat. This coverage ensured that the electrolyte of the EFS electrochemical cell made contact only with the coated region of the specimen once the specimen and cell were affixed to the fatigue apparatus. In this sense, the coated fatigue specimens were tested in an identical manner to all of the uncoated specimens. The basic methodologies employed will be described in further detail in Section 2.3.

2.3 Fatigue Testing Methods, Specimens and Recorded Data

Since the function of the EFS is to determine fatigue damage in a material and detect the earliest crack initiation stage, the primary experimental method employed was fatigue cycling smooth specimens. However, testing was also performed using notched specimens so as to model the stress concentration typically encountered with riveted airframe.

A limited amount of testing was also performed using cracked, fracture mechanics specimens to more fully understand the effect of the EFS electrolyte on the fatigue. Since these tests are not crack nucleation experiments, they are described in more detail in a subsequent chapter of this report.

2.3.1 *Fatigue Testing Smooth and Circumferentially Notched Specimens*

Fatigue testing was performed at both SwRI and Penn. In general, the experimental methods used in both laboratories were derived from the relevant ASTM E466[1] test practice [2.2] for load control, fatigue testing. Additional issues, more fully discussed in the E606[2] test practice [2.2], were also used. In fact, a limited number of strain-control tests were selectively performed. However, the vast majority of the experiments were load-control tests. Typical test setups at SwRI and Penn are shown in Figures 2-1 and 2-2, respectively.

Special consideration was paid to ensuring the load train alignment was within the required 5% allowable bending specification. Alignment was monitored with strain gaged specimens. For the tests with a positive load ratio (also termed R-ratio and defined by the ratio of minimum load to maximum load), a universal joint was inserted in the load train to further minimize bending.

The majority of the fatigue tests were run continuously with the specimen loaded until failure (defined in all cases as separation of the specimen into two halves). However, a number of the tests were interrupted prior to failure to assess damage state. Other specimens were

---

[1] "E466-96: Standard Practice for Conducting Force Controlled Constant Amplitude Axial Fatigue Tests of Metallic Components"
[2] "E606-92: Standard Practice for Strain-Controlled Fatigue Testing"

subjected to changing conditions throughout the entire test. The extensive fatigue testing included in this work assessed a wide range of different variables that included

- control mode (strain or load),
- coatings (primer only, primer plus topcoat),
- environment (lab air, EFS, water),
- form of EFS environment (liquid, gel)
- type of EFS environment (aluminum or steel solutions),
- electrochemical variables (electrode type, current control),
- frequency and load ratio,
- stress level (fixed or changed), and,
- variable amplitude loading (random, simple overloads, blocked spectra).

Coordinating testing efforts between two labs required some level of standardization. For instance, a standard specimen numbering scheme was adopted, as described in Appendix AA.

Specimen drawings for the different smooth and notched fatigue specimens are shown in Figures 2-3 to 2-5. The specimen used by SwRI (Figure 2-3) had a nominal gage length of 10.5 mm and diameter of 5.1 mm. One end of the specimen was threaded whereas the other end was smooth and mechanically clamped with friction loading. Long shanks were left on the specimen to allow for positioning the electrochemical cell as shown in Figure 2-1. The Penn specimen in Figure 2-4 had a similar diameter and gage length but was considerably shorter due to a different corrosion cell arrangement. Both ends of the specimen were fixed in threaded fasteners. Penn also performed some testing using a flat bar specimen geometry (see Section 8.4 for details).

The notched fatigue specimen shown in Figure 2-5 was identical to the SwRI smooth specimen except that it had a 0.635 mm radius circumferential notch machined into the center of the gage length. This notch, as well as the reduced sections of all of the fatigue specimens, had stringent surface finish requirements of 16 RMS or better. Only machining vendors with specialized low-stress grinding capability were allowed to manufacture specimens.

2.3.2 Fatigue Crack Growth Testing

The fatigue crack growth testing described in Section 3.7 was performed in the spirit of the ASTM E647[3] standard test method [2.2]. A standard compact-tension specimen shown in Figure 2-6 was used for this testing. This specimen had a width of 50.8 mm and thickness of 6.35 mm. The cut-out on the front face of the specimen provided additional clearance to attach a CMOD gage for non-visually monitoring crack length.

A SwRI-developed, specialized environmental setup schematically illustrated in Figure 2-7 was employed to perform corrosion fatigue tests on the pin-loaded, compact-tension specimen. This technique uses neoprene seals to insure that no leakage occurs through the loading pin holes. The environments studied during the crack growth testing included deionized water, EFS electrolyte at open circuit potential and aerospace-standard, dye penetrant.

2.3.3 Other Experimental Apparatus

During testing at both Penn and SwRI, numerous types of standard and hybrid data acquisition systems were used to measure the data signals generated. For instance, during some of the variable load amplitude work performed at SwRI, a high-speed digital storage oscilloscope was used to trigger and record data. Similarly, each laboratory used closed-loop, servohydraulic controllers to perform the variable amplitude testing and insure accurate loading of the specimens.

Although the purpose of this section is not to provide the extensive detail required to address the different electrochemical setups used for EFS monitoring, it is useful to briefly address the similar features characteristic of the Penn and SwRI data acquisition systems. The electrochemical testing at each lab used different types of potentiostats to provide a controlled potential at the specimen surface. The purpose of the electrochemical monitoring systems was to provide continuous recording of current transients occurring in the specimens during the fatigue cycling. In addition to providing data suitable for off-line, post-test analysis, the systems were also designed to provide continuous, graphical assessments of the observed behavior.

---

[3] "E647-95a: Standard Test Method for Measurement of Fatigue Crack Growth Rates"

The fatigue test setup at SwRI was electrically isolated by including non-conductive couplings in the load train. Conversely, the majority of Penn fatigue tests were performed in a non-isolated system with no provision to eliminate electrical current paths through the loading train. Previous experimental work performed at Penn had shown that electrical isolation was a non-issue in the Penn test facility due to the method by which their potentiostat was grounded.

Both SwRI and Penn developed their own LabView-based, data acquisition systems suitable for recording and displaying data. The primary reason for each lab developing their own system was to insure flexibility and local support of the code. The LabView systems are relatively complex; they continually evolved through use. They gained new capability depending upon the requirements of each different researcher using the systems.

A sample display from the computer screen of the SwRI system is depicted in Figure 2-8. Three channels of input data are recorded and displayed graphically. These channels include applied load and displacement from the servohydraulic controller and transient current from the potentiostat. Options are available to illustrate the data as a function of time as well as to plot each of the signals against each other.

Data recording was triggered from the TTL pulse emitted from the function generator applying the load signal. Although the data is read continuously into a buffer, only "snapshots" of the signals are recorded to an external data file. The cyclic interval between recordings is a parameter that the user can change, depending upon how the signals change and evolve during the conduct of the test. Once a test is complete, a number of sequential data files are recorded that can then be sequentially viewed in a "playback" mode to more fully understand and quantify the electrochemical response of the specimen during the test.

2.4 Baseline Fatigue Properties

The purpose of this section is to present the baseline fatigue data generated on the three materials. An extensive number of fatigue tests on smooth specimens were performed during this project. The tests involved a wide range of variables and conditions, as detailed in

Tables A-4 to A-6 in Appendix AA. A summary of the testing is provided in Table 2-4 illustrating the range of loading variables and environments.

2.4.1 Development of Baseline Fatigue Test Dataset

The exploratory nature of much of the testing involved in this program complicated development of the baseline fatigue performance dataset. A significant number of the fatigue tests documented in Tables A-4 to A-6 involved mixed conditions employed to understand the impact of variables on the EFS response of the materials. Consequently, developing the baseline fatigue test dataset required censoring the complete matrix of tests to exclude the evaluations focusing on basic material behavior. In particular, the criteria used to omit data included:

- coated samples,
- any test identified with mixed conditions,
- non-constant stress range or tests with a questionable stress range,
- variable amplitude loading,
- failures outside the gage length of the specimen,
- strain control tests,
- interrupted or uncompleted tests, and,
- other tests with questionable data (e.g. uncertain cycle counts or other unknowns).

Applying these criteria resulted in exclusion of approximately 25% of the overall collection of data. Even though these tests were not included in the baseline dataset, they are nevertheless valuable in terms of understanding how different variables impact EFS response, and they are examined in detail later in this report.

The primary loading variables in the baseline tests were load magnitude and load ratio. Data are provided for all three materials and the two predominant load ratios (R=-1 and R=0.05) in Figures 2-9 to 2-14. The data are represented by so-called S-N plots in which fatigue lives are shown plotted against the maximum applied stress. These plots also differentiate as to the specific laboratory performing the test and the environment used.

2.4.2 Comparison of Baseline Data to Handbook Data

It is important to examine whether the baseline data obtained for the aluminum, steel and titanium material were consistent with that available from standard sources of fatigue data.

However, when comparing fatigue test data, it is crucial to insure that the material, temper and product form are all the same. The most robust, directly comparable dataset is 4130 data from reference [2.1]. A normalized comparison is provided in Figure 2-15 between these handbook data and the results generated at SwRI and Penn. However, the 4130 handbook data are from an alloy with an ultimate tensile strength of 1241 MPa (versus 1096 MPa for the alloy tested herein). The trend line shown in Figure 2-15 represents the best fit of the handbook data.

The fatigue test data generated at Penn and SwRI generally compared well to the handbook data as well as the trend line. The measured lives of the handbook data were somewhat less than observed herein, with the greatest differences observed in the low stress, longest life regime. The differences between these datasets are further explored in Figure 2-16. In this plot, the datapoints in Figure 2-5 are compared directly to the values expected from the trend line. A life ratio of unity indicates perfect agreement. Upper and lower bounds of ±1 decade of life ratio are also provided in Figure 2-16 bracketing the response observed when the trend line is compared to the handbook data.

The majority of the data generated herein lies in a narrower scatter band than the literature data. In fact, with the exception of the two lowest stress tests, all of the data lies within one decade of life difference (implying variability on the order of 10x). Given the typical scatter usually observed in such fatigue test results and the slight strength differences, the handbook data and the baseline data from this work are not believed to be significantly different.

In general, the fatigue behaviors of aluminum and titanium are especially sensitive to product form, production method, thickness and temper. As such, relevant handbook datasets with sufficient robustness for adequate comparison are quite limited. Nevertheless, Figure 2-17 provides a basic comparison for the R=0.05 baseline datasets and a band relevant for the handbook data observed for both aluminum and titanium (from References [2.1] and [2.3]). Excellent agreement is observed between the handbook bands for both materials and the baseline datasets.

2.4.3 Inter-laboratory Comparison of Baseline Data

Testing was performed by both labs for all three materials at R=-1. However, the only directly comparable data for all materials is that tested in EFS solution. Although the optimum comparison would be in air, no data exists under replicate testing conditions to provide this assessment. Hence the only lab-to-lab comparison can be made for the EFS environment fatigue test results in Figures 2-9, 2-11 and 2-13.

The EFS electrolyte environment itself should not influence any conclusions regarding inter-laboratory variability. In fact, it is not uncommon to perform inter-laboratory assessments of fatigue crack propagation behavior (*e.g.*, crack growth) using high-humid air conditions to insure that differences in relative humidity between laboratories do not impact the assessment of variability.

The similarity between the Penn and SwRI data is clearest for aluminum in Figure 2-9. There does not appear to be any definitive, systematic bias in these. Conversely, no definitive conclusion can be drawn for the titanium data in Figure 2-13 due to the limited available data. In the mid-range life regime, the data appears comparable whereas at longer lives the Penn data appear to exhibit greater lives. Finally, the fatigue test data from the steel material in Figure 2-11 can be used to conclude that no apparent systematic bias exists between Penn and SwRI generated results. The similarity can also be inferred by examining the life ratio data presented in Figure 2-16.

2.4.4 Summary

The baseline fatigue performance agrees well with the limited data obtained for these materials from handbooks. Furthermore, no apparent inter-laboratory bias appears evident in the fatigue test data based upon replicate testing conditions. Although these comparisons were limited to certain conditions and did not apply to the full range of variables examined, they were sufficiently robust to confidently conclude that the fatigue testing methodologies used by both laboratories are sound and equivalent.

The primary reason for comparing the baseline fatigue data to the literature and assessing inter-laboratory variation was to illustrate that the methods used at both SwRI and Penn did not

introduce any measurable bias into the complete dataset. Presumably if a bias existed, it could imply that conclusions drawn from the fatigue testing in the specific context of EFS performance would be limited. The similarity observed between the handbook fatigue data and that generated herein suggests that the methods used evaluated typical material behavior. Furthermore, the lack of any definitive inter-laboratory variability suggests that results generated can be compared independent of the specific laboratory performing the work. As such, this broadens possible EFS performance comparisons and allows for a larger range of assessment.

2.5 References

2.1 *Military Handbook: Metallic Materials and Elements for Aerospace Structure*, MIL-HNDK-5G, Department of Defense, vol. 1-3, November 1994.

2.2 *1998 Annual Book of ASTM Standards*, Section 3: Metals Test Methods and Analytical Procedures, vol. 3.01, Metals – Mechanical Testing, American Society for Testing and Materials, West Conshohocken, PA, 1998.

2.3 Henry, Scott D., *Fatigue Data Book: Light Structural Alloys*, ASM International, Materials Park, OH, 1995.

Table 2-1. Description of the Material Used During All Phases of Experimental Testing.

Material Type	Material Identifier	Product Form	Processing or Heat Treatment (HT) Specification	Product Section, mm	Total Quantity (length each)
Aluminum	7075-T73511	extruded bar	QQ-A-200/11	31.8 x 102	7 bars (3.7 m)
Steel	4130	cold drawn bar	MIL-H-6875	12.7 x 127	7 bars (3.7 m)
Titanium	Ti-6Al-4V	round bar	AMS4928 (special HT)	16.0 diam	24 bars (1.3 m)

Table 2-2. Measured Tensile Properties for the Three Different Materials After Heat Treating.

Material Type	Material Identifier	Yield Strength MPa	Tensile Strength MPa	Percent Elongation	Percent Reduction of Area	Young's Modulus, GPa
Aluminum	7075-T73511	444	514	14.4	34.1	66.9
Steel	4130	1029	1093	18.7	62.5	203
Titanium	Ti-6Al-4V	893	959	17.1	52.0	107

Table 2-3. Description of the Coatings Used During Some of the Fatigue Testing.

Specification	Primer	Top Coat
Military Specification	MIL P 23377G	MIL C 85285
Type	I (Standard Pigment)	I (Standard Pigment)
Class	C ($SrCrO_4$ – Based Inhibitor)	-
Color	Green (Natural Inhibitor)	White (FED-STD-595-Color 17925)
General Composition	Epoxy, High Solids	Aliphatic Polyurethane, High Solids
Base Resin	Epoxy	Pigmented, Polyester
Curing Agent	Polyamide and/or Amine	Aliphatic Isocyanate

Table 2-4. Range of Conditions Examined in the Smooth Specimen Fatigue Tests (numbers of tests and percentage of total is shown).

Matl ID	No. of tests	Performed by		R-ratio Condition				Environmental Condition			
		SwRI	Penn	-1	0.05	0.5	other	air	EFS	mixed	other
Alum	177	107 (60%)	70 (40%)	125 (71%)	45 (25%)	5	2	44 (25%)	119 (67%)	7	7
Steel	116	52 (45%)	64 (55%)	86 (74%)	28 (24%)	1	1	40 (34%)	68 (59%)	1	7
Ti	45	33 (73%)	12 (26%)	21 (47%)	22 (48%)	2	-	22 (49%)	19 (42%)	-	4
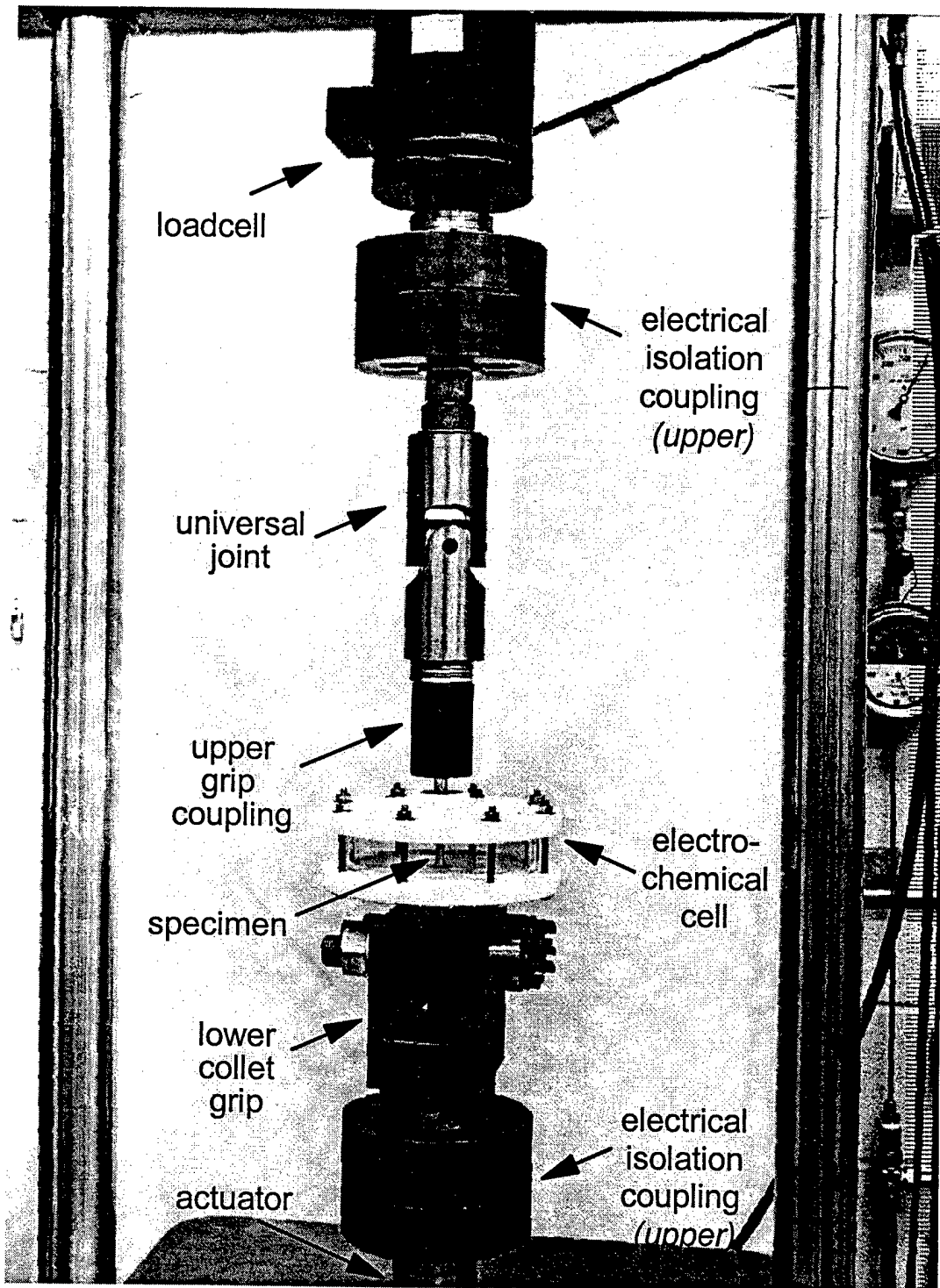
Figure 2-1. Photograph of a SwRI fatigue specimen showing grips and fixtures.

(a)

(b)
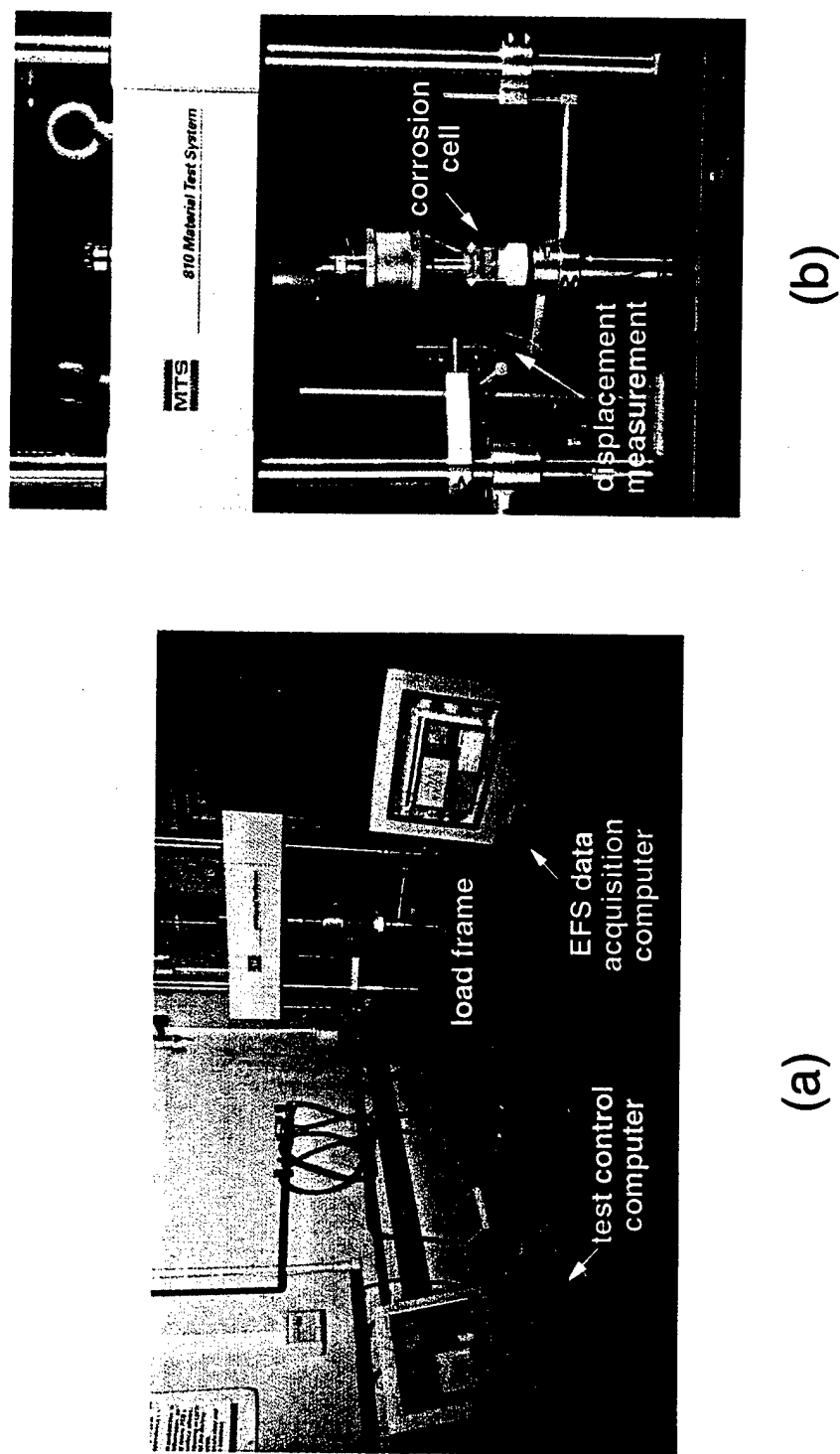
Figure 2-2. Photograph of (a) the overall Penn setup with instrumentation and (b) detailed view of the corrosion cell test apparatus.

Be sure to maintain specimen ID numbers marked on specimen and included on packaging

7.500

threaded end,
1/2 - 20UNF - 2A

0.425" 0.001
diam

0.200 " 0.001
diam

0.750
radius /C\

gage
length /A\

specimen
shank /A\

1.250

1.633

3.278

0.414

grip area

2.000

3.413

3.808

**Mark specimen identification number
on OD of shank with permanent marker**

NOTES:

/A\ shank diameter concentric with
gage diameter to 0.005.

/B\ Use low stress machining procedure
(16 RMS finish required).

/C\ Do not undercut radii.

Drawn:	P. C. McKeighan			S R I Southwest Research Institute	
Date:	8 April 1997			San Antonio, Texas	
		Tolerances (inches)		Title	
Matl: various	Basic Dimension	Decimals	Frac-tions	Uniaxial Cylindrical Fatigue Specimen (EFS Application)	
		2 place	3 place		
Finish: 16 RMS	under 6	±0.01	±0.005	±1/32	Drawing Number	06-8784_cyl.fatig	Scale *** none ***
	6-24 incl	±0.03	±0.010	±1/16		
Qty N/A Reqd:	over 24	±0.06	±0.015	±1/6	Filename c:\pcm\drawings\misc\efs.fat3.pre	Sheet 1 of 1
	angles	±0° 30'		±1° 0'		

Figure 2-3. Specimen design used for smooth specimen fatigue testing at SwRI (dimensions in inches where 1 inch=25.4 mm).
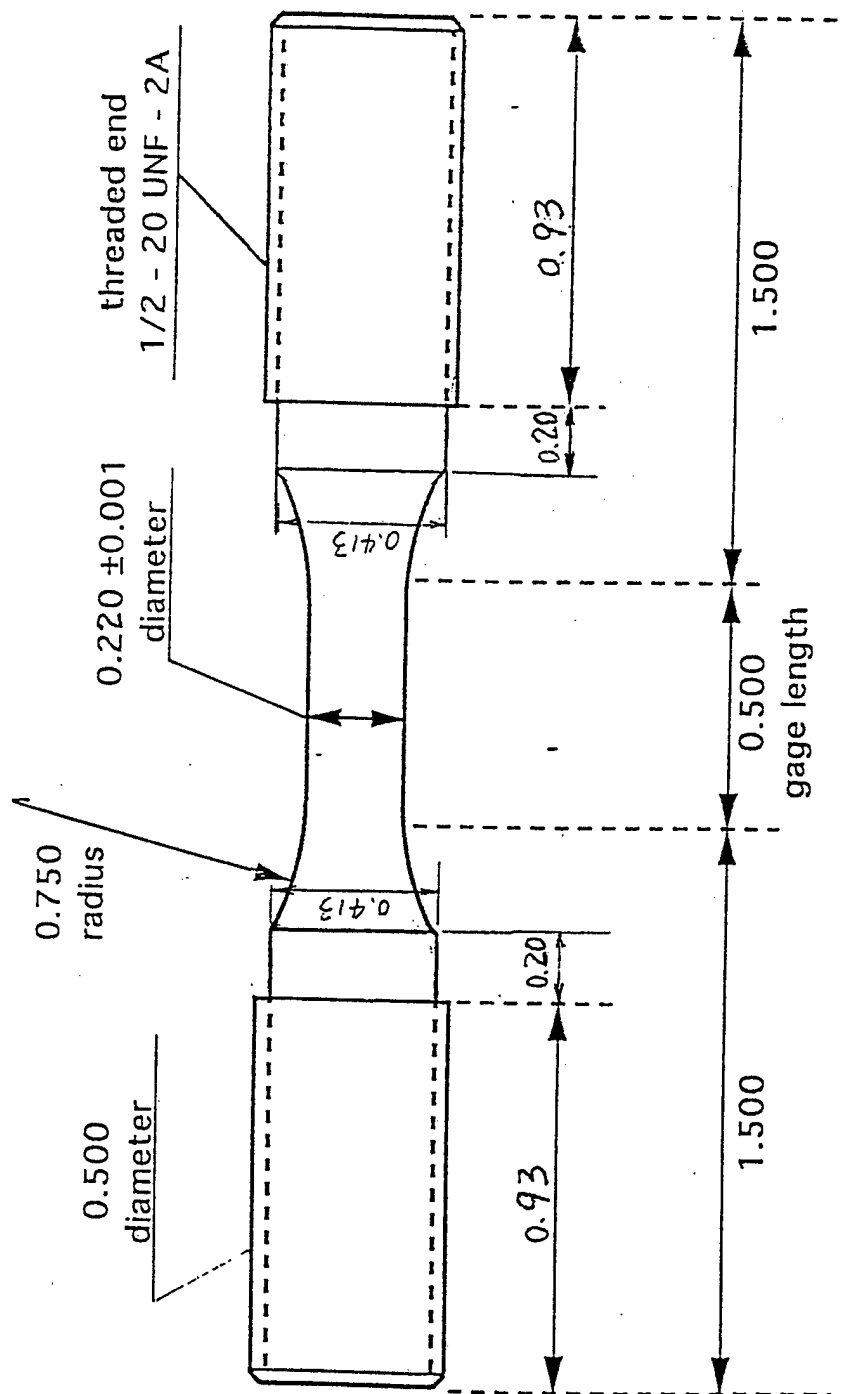
Figure 2-4. Specimen design used for smooth specimen fatigue testing at Penn (dimensions in inches where 1 inch=25.4 mm).
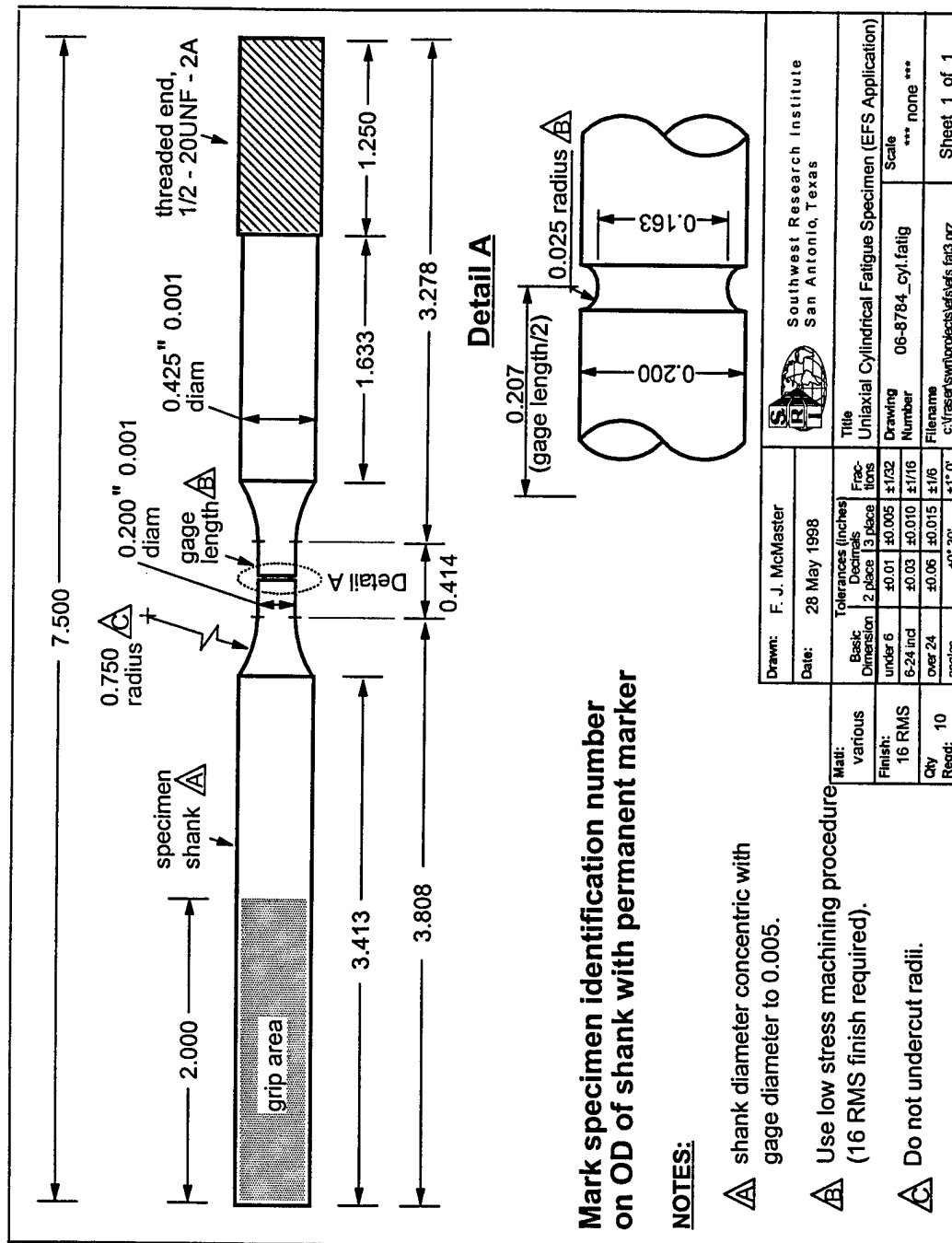
Figure 2-5. Specimen design used for notched specimen fatigue testing at SwRI (dimensions in inches where 1 inch=25.4 mm).

0.503/0.505 diam ream thru (2)

Stamp specimen ID

2.400

1.200

0.550

0.550

1.200

front face

2.000

0.500

0.350

0.250

A   A

Section -AA-

Material	Number of Specs	Specimen ID's
7075-T73511 extrusion	8	AJ-56C1-FPM to -56C2-FPM
		AJ-59C1-FPM to -59C2-FPM
		AJ-62C1-FPM to -62C2-FPM
		AJ-64C1-FPM to -64C2-FPM
4130 steel (UTS = 160ksi)	5	SA-17C-FPM
		SA-19C-FPM
		SA-22C-FPM
		SA-25C-FPM
		SA-28C-FPM

0.005 - 0.012 wide EDM notch

EDM   notch

front face

0.375

1.100

Drawn:	F. J. McMaster			SRI	Southwest Research Institute
Date:	13 May 1998				San Antonio, Texas

Matl: various	Tolerances (inches)			Title	
	Basic Dimension	Decimals 2 place | 3 place	Frac- tions	1 T Plan Shape Fatigue Crack Growth Specimen	
Finish: 32 rms	under 6	±0.01 | ±0.005	±1/32	Drawing Number 06-8784-1TCT-FCG)	Scale *** none ***
	6-24 incl	±0.03 | ±0.010	±1/16		
Qty Reqd: various	over 24	±0.06 | ±0.015	±1/6	Filename c:\fraser\swri\projects\efs\ct_fcg.prz	Sheet 1 of 1
	angles	±0° 30'	±1° 0'		

Figure 2-6. Specimen design used for the fatigue crack growth testing performed at SwRI (dimensions in inches where 1 inch=25.4 mm).

Compact Specimen

Plastic Bag

Clevis Pin

Loading Pin

Steel Washer

Neoprene Washer

Steel Bushing (Free fit in specimen hole)

Clevis Pin
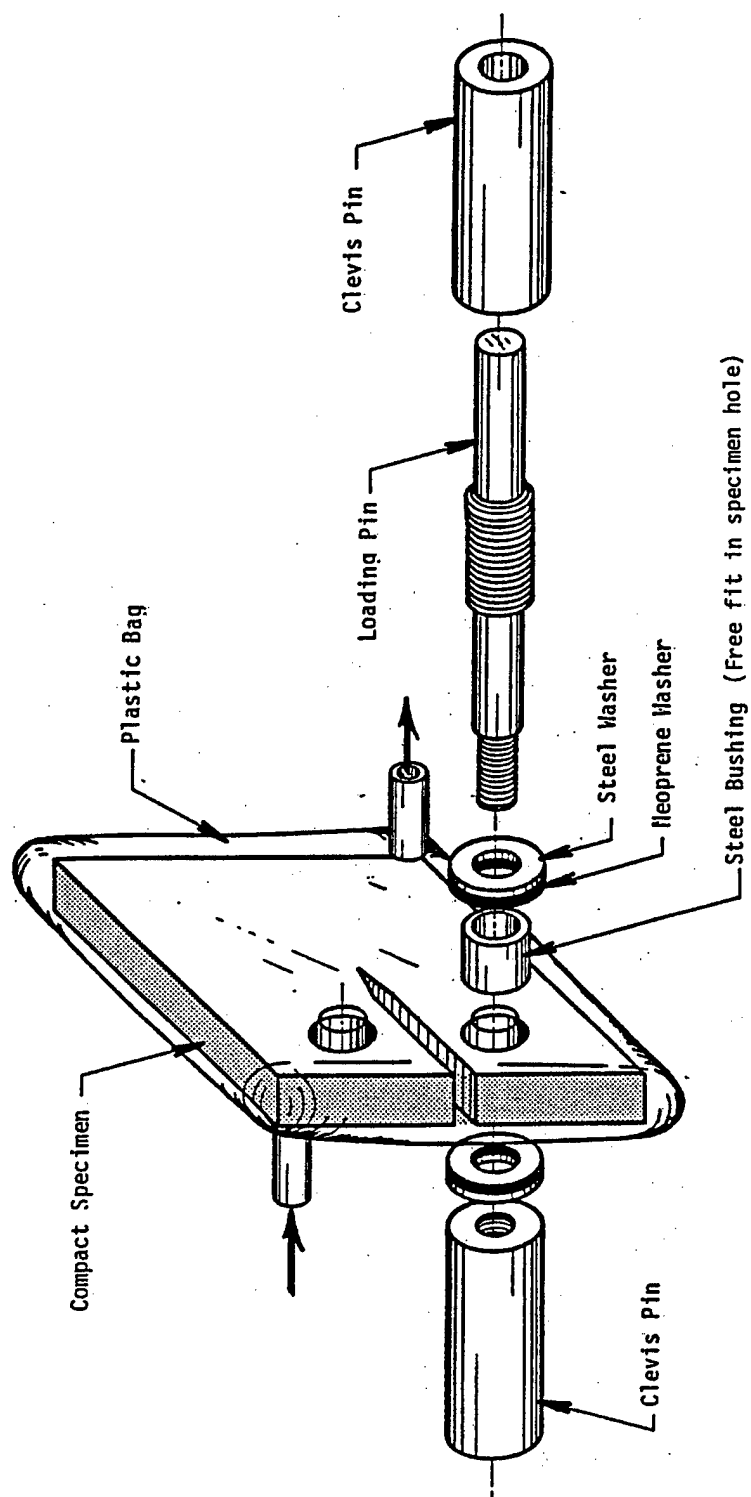
Figure 2-7. Schematic of the sealing method used to perform corrosion fatigue crack growth tests on a pin-loaded, C(T) specimen.
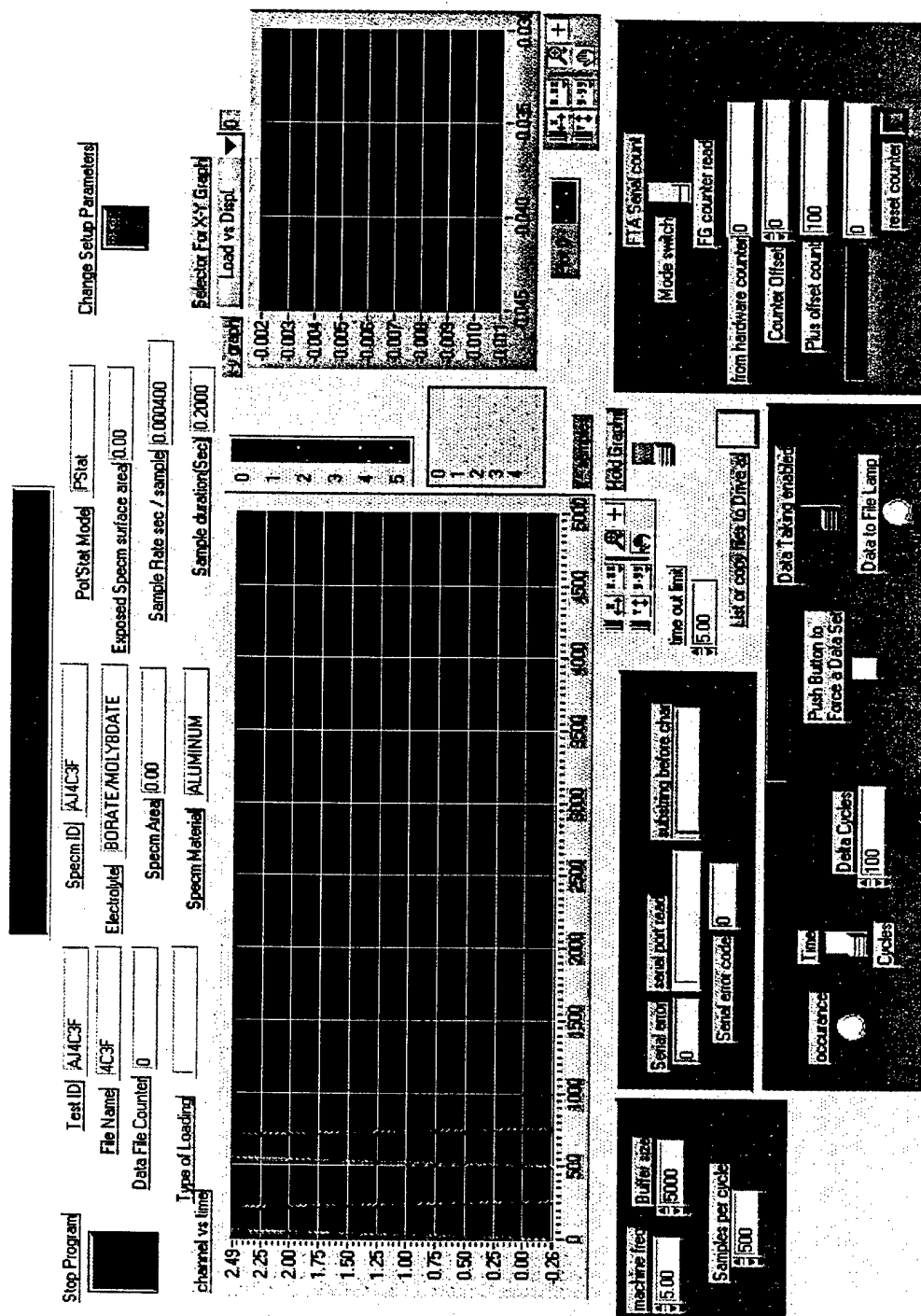
Figure 2-8. Sample LabView configured data acquisition screen illustrating range of recording options available.
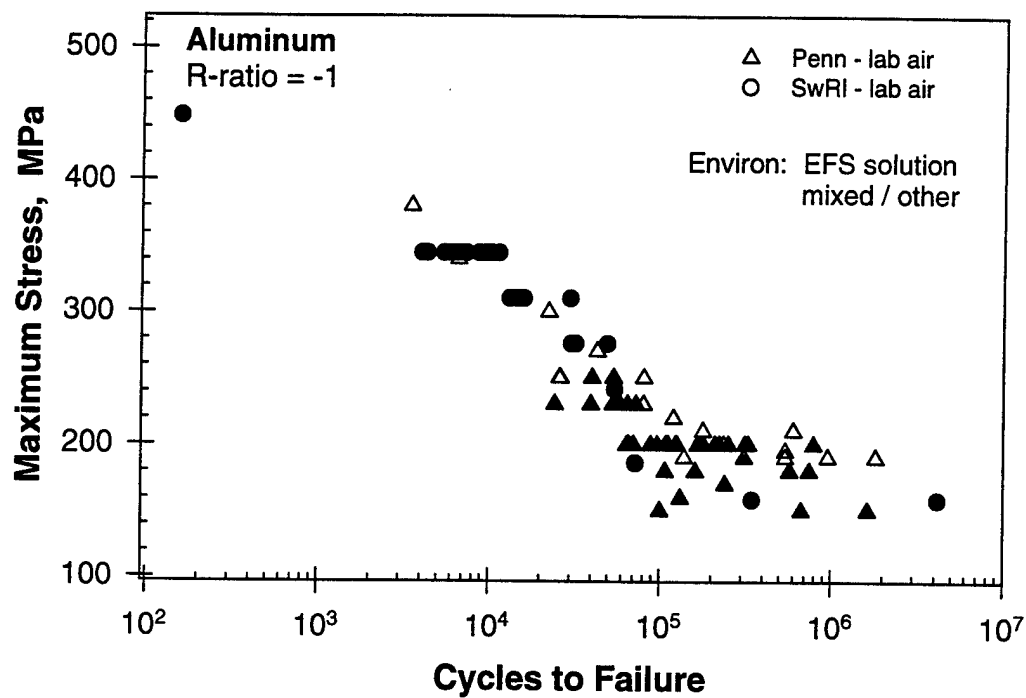
Figure 2-9. Smooth specimen fatigue data for 7075-T73511 at R = -1, generated at both Penn and SwRI
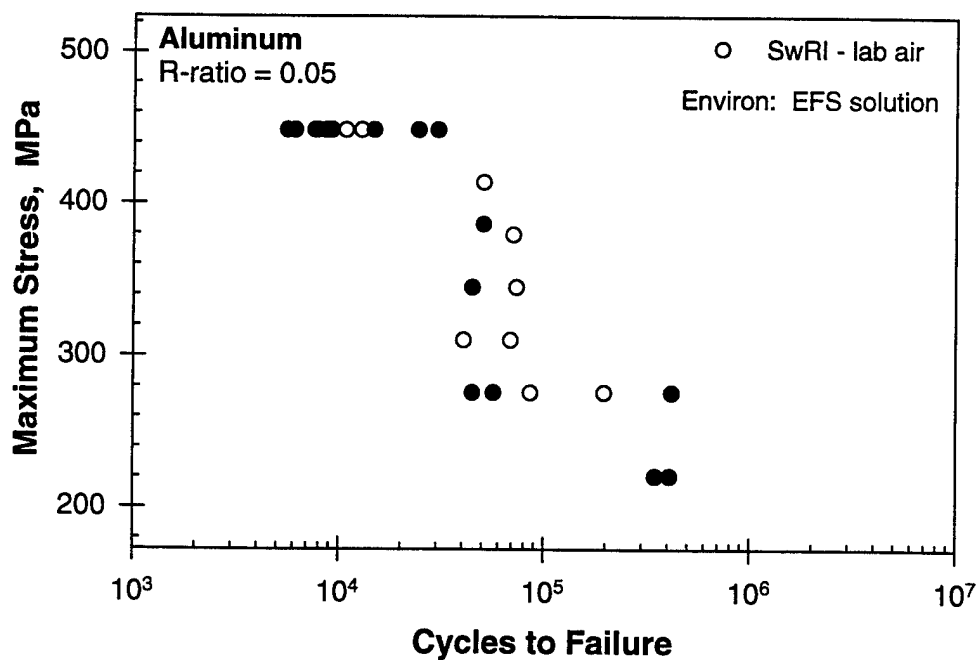
Figure 2-10. Smooth specimen fatigue data for 7075-T73511 at R=0.05, generated at SwRI.
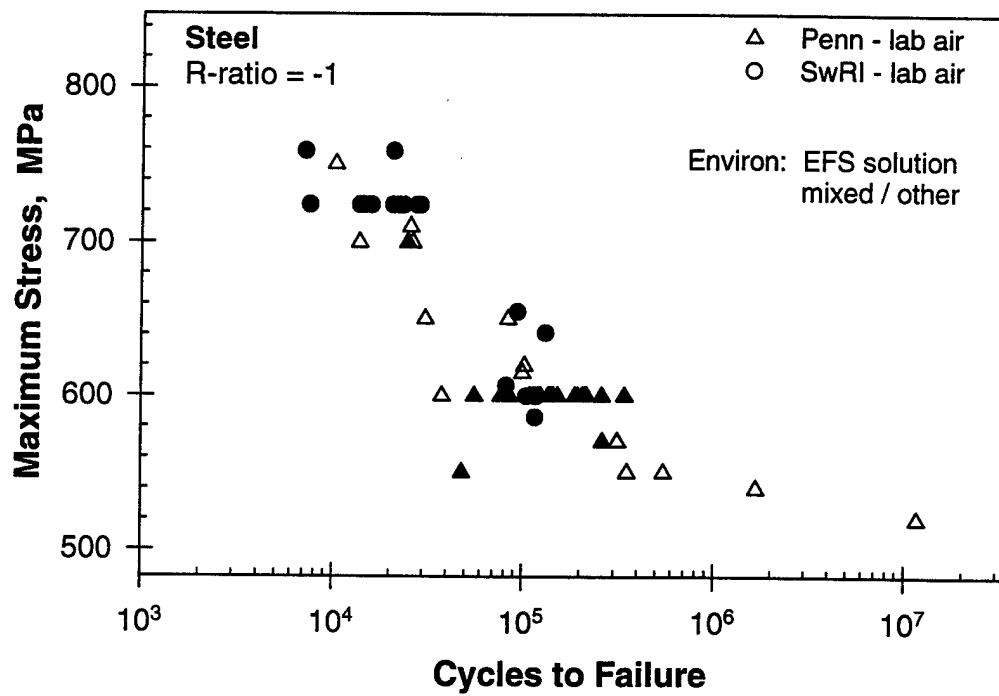
Figure 2-11. Smooth specimen fatigue data for 4130 at R = -1.
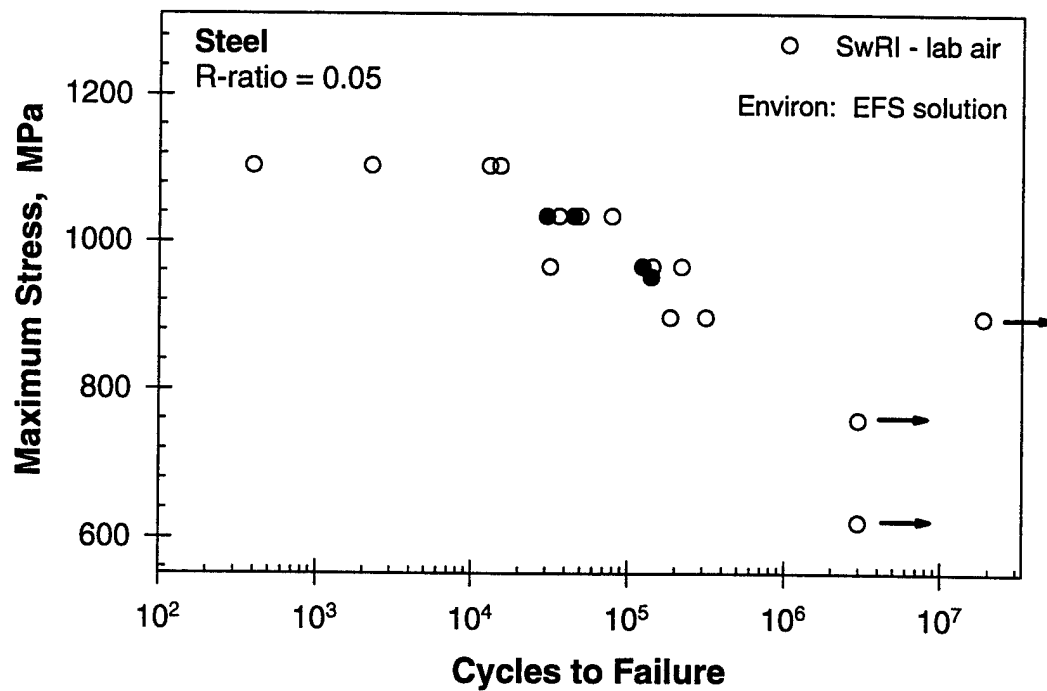
Figure 2-12. Smooth specimen fatigue data for 4130 at R=0.05.
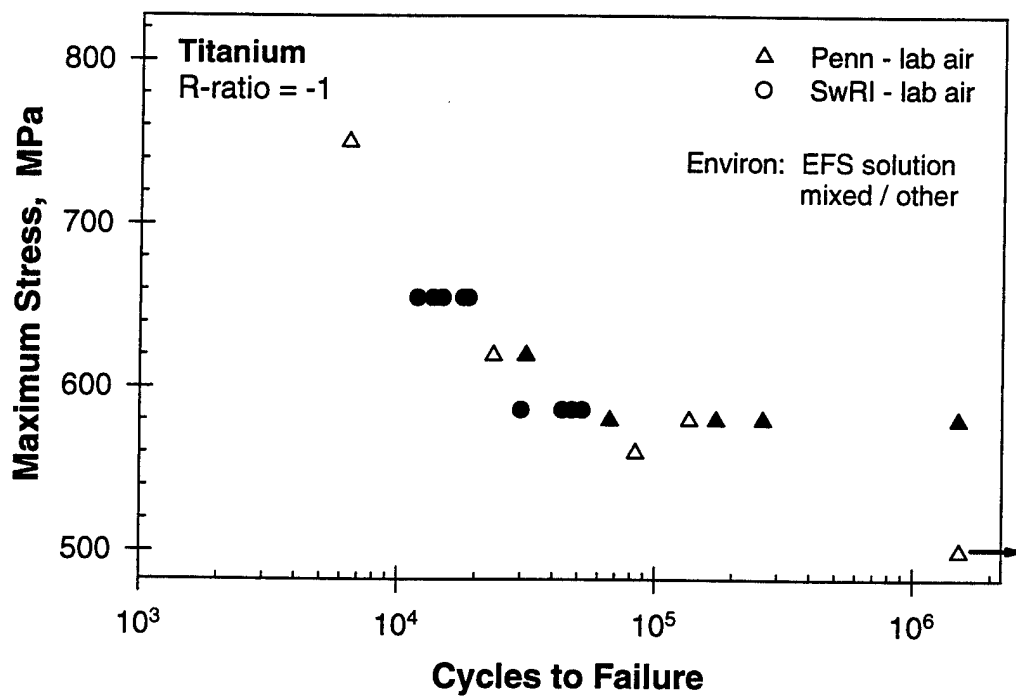
Figure 2-13. Smooth specimen fatigue data for Ti-6Al-4V at R = -1.
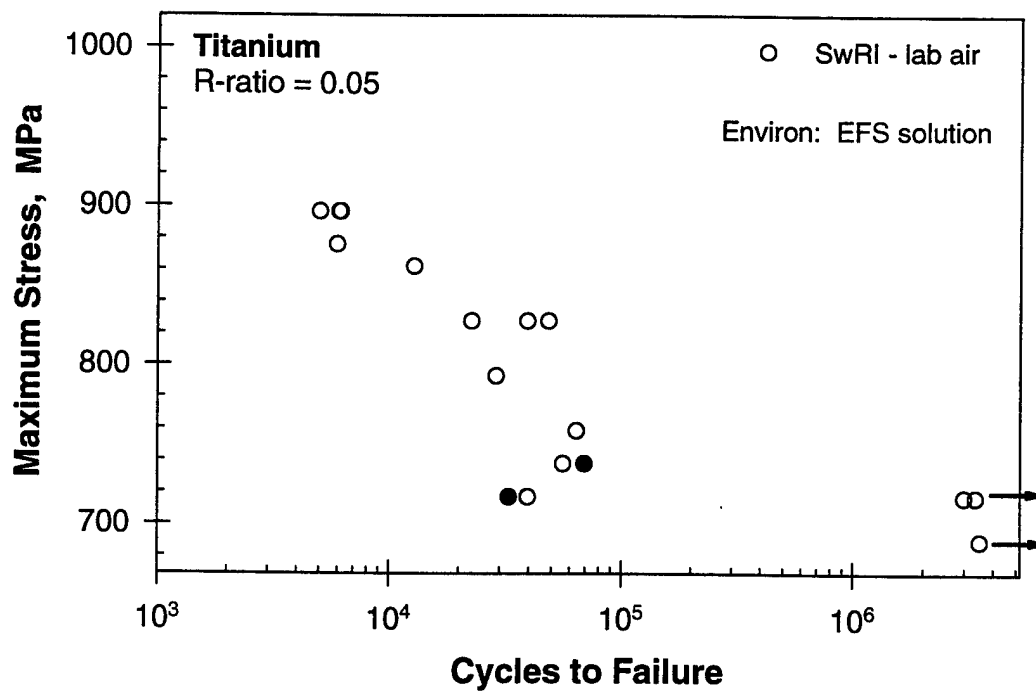
Figure 2-14. Smooth specimen fatigue data for Ti-6Al-4V at R=0.05.
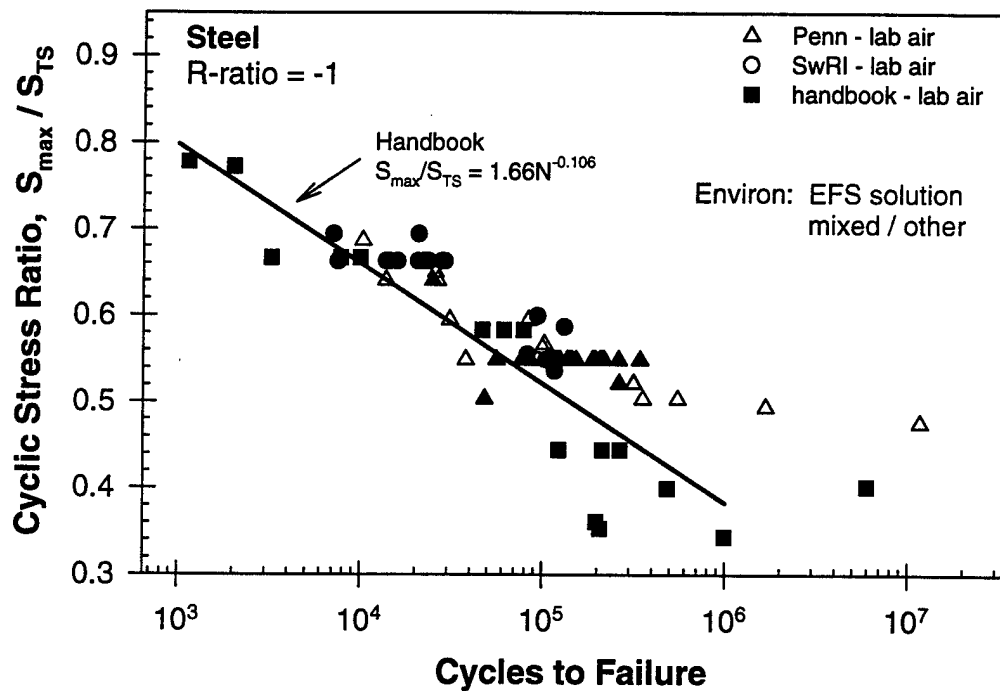
Figure 2-15. Comparison of fatigue test results for steel with values from a handbook.
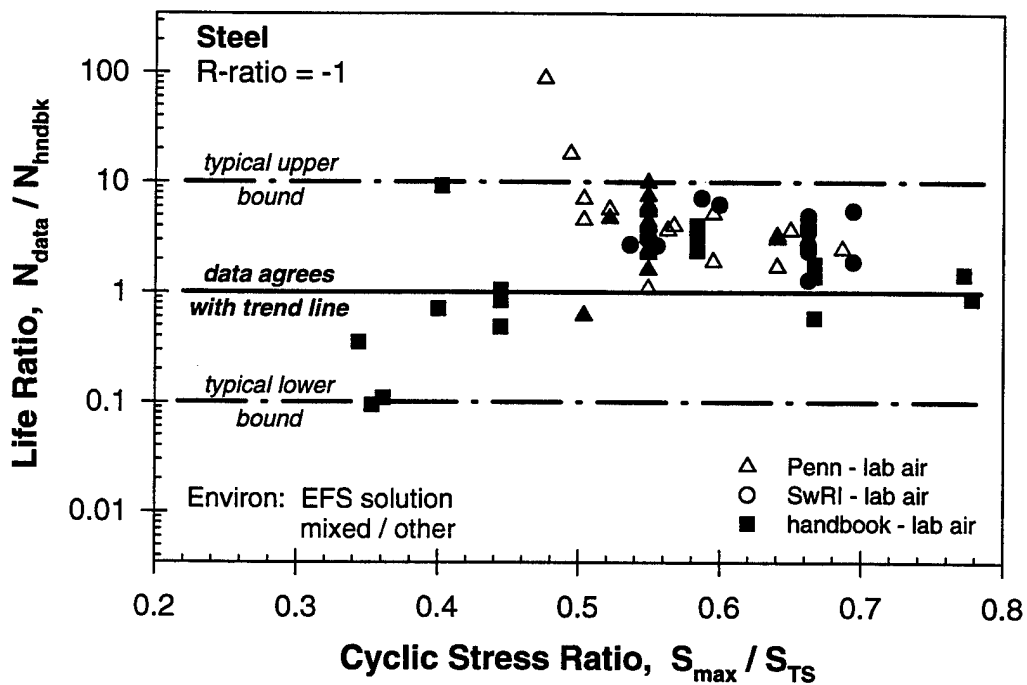
Figure 2-16. Total life differences between data and a trend line derived from the handbook data.
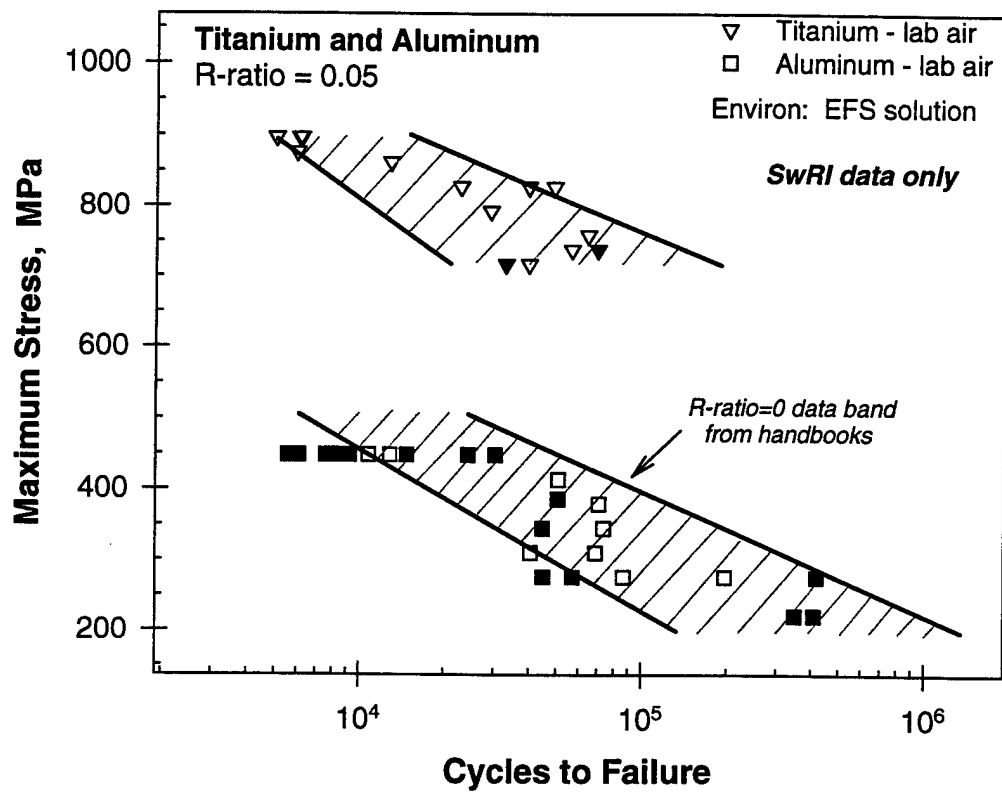
Figure 2-17. Comparison of fatigue test results from aluminum and steel with handbook data.

3.0 ELECTROLYTE OPTIMIZATION

3.1 Objective and Approach

Since the overall program objective is to improve the USAF's ability to perform durability assessments of aircraft, it follows that the electrolyte used in the EFS to make these assessments must not degrade the durability or damage tolerance of these aircraft. The nature of the electrolyte is critically important since the aircraft alloys chosen for study (high strength aluminum, high strength steel, and titanium) can be susceptible to environmental cracking (stress corrosion cracking and corrosion fatigue in certain environments) [3.1, 3.2, 3.3].

The specific objectives were as follows:

1) Develop electrolyte(s) that will:

   - render the alloys passive when unstrained, but sufficiently active when strained to provide adequate current signals for EFS measurements,

   - be benign to the substrates of the aircraft and not cause any degradative effects, and

   - be capable of incorporation into a useful gel that precludes the inconvenience of working with a liquid electrolyte on the aircraft.

2) Develop procedures that would facilitate:

   - the application of EFS using the gelled electrolyte on aircraft structural components,

   - the after-test removal of any residual gelled electrolyte from the aircraft components including crevices.

The approach to achieving the above objectives was as follows. Since the EFS operates while electrochemically polarizing the alloys within their passive regions (0.3 to 0.5 volts v. SCE electrode), the electrolytes chosen should be mildly oxidizing (free of reducing anions) and within a pH region to preclude corrosion. These criteria led to candidate electrolyte formulations that were tested for general corrosion, pitting corrosion, miniscus (crevice) corrosion, potentiodynamic anodic polarization, and effects on fatigue lives of the alloys studied.

Candidate electrolyte formulations were then incorporated in commercially available gelling agents. Anticipating the use of one or two candidate gelled electrolytes, application and removal procedures utilizing a portable, ruggedized cell suitable for field use [see Section 8] is planned. The removal procedure will be based on existing techniques for removal of electrolytes from aircraft, *i.e.*, sea water, as described in the tri-service "509" manual [3.4].

3.2 Liquid Electrolyte Formulations

Initial formulations were made on the basis of the two airframe alloys: aluminum and steel, with emphasis on the more corrosion-prone aluminum alloy. The important thermodynamic tool, the Pourbaix diagram, was used for both steel and aluminum and provided a starting point for the chemical formulations. These equilibrium diagrams of electrochemical potential vs. pH for pure metals exposed to aqueous systems are cataloged in an atlas [3.5]. Pourbaix plots show regions of stability for corrosion, passivity, and immunity for the specific metal in question. Figures 3-1, 3-2, and 3-3 are the simplified published diagrams for aluminum, iron, and titanium, respectively. Based on this thermodynamic information, candidate electrolyte compositions and their pH values were selected and are shown in Table 3-1.

3.2.1 Corrosion Testing

A common method of assessing a metal's corrosion resistance is to perform in situ weight loss measurements as a result of exposing the metal to the electrolyte in question for a given period of time. This is particularly useful if the metal/electrolyte combination results in uniform, general corrosion of the surface.

In the case of aluminum and titanium, localized corrosion in the form of pitting occurs (if it occurs at all) in aqueous electrolytes so that traditionally derived corrosion rates derived from weight loss measurements such as the surface penetration rate, millimeters per year (mm/yr) are not meaningful. The weight loss measurements taken in this study for aluminum and titanium are thus useful as indicators of the material's susceptibility, but cannot provide true surface penetration rates.

The generally accepted formula to calculate weight loss in mm/yr was employed [3.6]:

$$r = \frac{87.6W}{DAT} \qquad (3.1)$$

where r is in mm/yr; W is the weight loss in mg.; D is the density of the metal in g/cubic centimeter; A is the exposed surface area in square centimeters; and T is the exposure time in hours. Weight loss results on each of the three alloys of interest are summarized below.

3.2.1.1 Aluminum: Coupons measuring 1 in. x 1 in. x ¼ in. were polished to a 600 grit finish on all sides and then weighed to the accuracy of 1/10 mg. These were then immersed erect in approximately 500 ml of electrolyte in a beaker open to air for ten days. They were then removed, cleaned, and re-weighed to determine a corrosion rate. Four replicate specimens per condition were tested. Average corrosion rates from these tests are summarized in Table 3-2.

Three electrolyte compositions were chosen for aluminum weight loss tests. From Table 3-1, they are compositions (1), (3), and (6).

The large improvement in pitting resistance of electrolyte (6) prompted adjustments to its pH. The sodium di-borate content was lowered to achieve a neutral pH, resulting in electrolyte (8) of Table 3-1, which is the interim choice for the aluminum alloy.

3.2.1.2 Steel: As with aluminum specimens, coupons of steel, measuring 1 in. x 1 in. x ¼ in., were polished to a 600 grit finish on all sides and then weighed to the accuracy of 1/10 mg. These were then immersed erect in approximately 500 ml of electrolyte in a beaker open to air for specified times. They were then removed, cleaned, and re-weighed to determine a corrosion rate. Four replicate specimens per condition were tested. Average corrosion rates from these tests are summarized in Table 3-3.

The electrolyte chosen for exposure of steel (number (7) of Table 3-1) is a boric acid/borate solution with a passivity reinforcer, sodium molybdate, adjusted to a pH of 8.4.

3.2.1.3 Titanium: A 3/4 inch diameter bar of 6Al - 4V titanium alloy was cut into 1/4 inch wafers for in situ corrosion testing. The same preparation procedure was employed with these samples as per the steel and aluminum preparations. Duplicate specimens were exposed to electrolyte (7), the steel electrolyte, for 7 days with no weight loss or pitting corrosion occurring.

A second set of duplicate specimens were exposed to electrolyte (7) for 29 days with no measurable weight loss or pitting noted. Another set of duplicate specimens were exposed to electrolyte (8), the aluminum electrolyte for 7 days again with no weight loss or pitting noted. The titanium alloy appeared impervious to the steel and aluminum electrolytes.

3.2.2 Anodic Polarization Testing of Liquid Electrolytes

Polarization is generally described as the change in reversible electrochemical potentials of an electrode in an electrolyte when current is allowed in the system. Since the alloys of this study must be polarized at potentials within their passive regions in order for the EFS to be operative, anodic polarization scans over a range of potentials were used to study the important parameters affecting the formation and stability of passive films on the alloys in the specific electrolytes. In order to define anodic polarization of an active-passive alloy, *i.e.*, the alloys of this study, a potentiostatic polarization procedure is required. The potentiostat imposes a fixed potential on the alloy and the resulting current (the dependent variable) is recorded. When this procedure is allowed over a range of potentials from below the open circuit potential of the alloy in the electrolyte to a final positive (active) value, usually at or above the anodic breakdown potential for water, an anodic polarization plot results. This polarization plot now defines a voltage range over which the alloy is passive and the ensuing current extant when the alloy is potentiostatically held within that region. The magnitude of this current also provides an indication of the material's corrosion propensity in the particular electrolyte.

3.2.2.1 Anodic Polarization of Aluminum Alloy: Figure 3-4 shows a polarization scan cycle for the 7075 T-73 aluminum alloy in electrolyte (8) of Table 3-1. The voltages were imposed at a rate of 10 millivots/second starting at a cathodic potential of -1.5v to the anodic potential of +1.2v and then allowed to return to -1.5v to complete a cycle. The area of exposure for all polarization tests was 1.5 square centimeters. The electrolyte during the test was open to air. All potentials (voltages) in this study are referred to the standard saturated calomel electrode (SCE). Figure 3-4 shows the initial formation of a well defined passive region from +0.2v to over +1.0 v. An important factor noted on all anodic polarization scans of this alloy/electrolyte combination is the absence of a lowered pitting potential which would be evident in the return scan trace intersecting the forward trace at some lower potential within the passive region. No such intersection occurs. Thus, polarization data as manifested by Figure 3-4, as well as the

favorable in situ corrosion data, endorses the choice of electrolyte (8) for EFS measurements on the aluminum alloy.

3.2.2.2 Anodic Polarization of Steel: Figure 3-5 shows a polarization scan cycle for the 4130 steel in electrolyte (7) of Table 3-1 (pH = 8.4). The voltages were imposed at a rate of 10 millivolts per second starting at a cathodic potential -1.1v to the anodic potential of +1.25v and then allowed to return to -1.1v to complete the cycle. Figure 3-5 shows a well-defined passive region extending from -0.2v to +1.0v. An absence of a lowered pitting potential was again noted on all polarization runs for this steel/electrolyte combination. Thus, polarization data as manifested by Figure 3-5, as well as the favorable in situ corrosion data, endorses the choice of electrolyte (7) for EFS measurements on the 4130 steel.

3.2.2.3 Anodic Polarization of Steel: Figure 3-6 shows a polarization scan for the titanium alloy in electrolyte (7) of Table 3-1 (pH = 8.4). The voltages were imposed at a rate of 10 millivolts/second starting at a cathodic potential of -1.2v to the anodic potential of +1.25v and then allowed to return to -1.2v to complete the cycle. From Figure 3-6, we note two passive regions; one spanning from the open circuit voltage -0.7v to +0.1v at a current of 10-5.1 amps per square centimeter; the other from +0.5v to the cut off voltage of +1.25v at a current of 10-4.5 amps per square centimeter. These current values are well within the region of protective passivity and as for the steel and the aluminum alloy, allows for an appropriate applied EFS potential. An absence of a lowered pitting potential was again noted on all polarization runs for this titanium/electrolyte combination. Thus, polarization data as manifested by Figure 3-6, as well as the favorable in situ corrosion data; i.e., no weight loss, endorses the choice of electrolyte (7) for EFS measurements on the titanium alloy.

3.2.2.4 Corrosion Testing at a Passive Potential with Crevice Effects: In order to determine the extent of corrosion, if any, that would occur on the wetted surface of the steel and aluminum alloys while exposed to a typical EFS passive potential, duplicate samples of each were tested in their respective chosen electrolytes at an imposed passive potential of +0.3v (vs. saturated calomel electrode) and the passive current noted. Each 1"x1"x1/4" specimen was partially immersed in the electrolyte.

The unwetted portion was connected to an electrical lead to the polarization circuit. The experimental set-up is shown in Figure 3-7. Both aluminum and steel were tested in this fashion; the aluminum exposed to electrolyte (8) of Table 3-1, hereafter referred to as the aluminum electrolyte and the steel exposed to electrolyte (7) of Table 3-1, hereafter referred to as the steel electrolyte. After one week of exposure, the samples were cleaned and examined for pitting corrosion. For both the steel and the aluminum, the wetted areas of the samples were free of pits. All samples exhibited what is known as a meniscus effect. That is, corrosion pits occurred at and just above the immersion line. The meniscus in this case is defined as the boundary or junction between the substrate (metal), electrolyte (liquid), and air. Depending on the surface energy of the substrate at this junction, localized differences in oxygen concentration in the electrolyte occur resulting in differential aeration corrosion cells. This phenomenon is the basis for what is known as crevice corrosion.

In order to minimize the meniscus effect and assess the crevice phenomenon in a configuration closer to what is contemplated as the wetted area of a prototype EFS cell, an area of 1.5 square centimeters enveloped by an elastomeric "O" ring provided electrolytic access to the metallic substrate. This is the same configuration for the wetted areas used in all the anodic polarization scans of this work. After five days of exposure at a constant potential of +0.3v, no evidence of pitting was noted, and there was no crevice corrosion caused by a meniscus effect in both steel and aluminum. It was possible, however, to see where the "O" ring pressed against the metal by noting a difference in discoloration where wetting occurred. This encouraging result allowed continued experimentation with the higher pH steel electrolyte serving both the 4130 steel as well as the unscathed Ti-6Al-4V titanium alloy and the neutral pH electrolyte serving the 7075-T73511 aluminum alloy.

3.3   Formulation of Gelled Electrolytes

3.3.1   CAB-O -SIL Gelled Electrolytes

The first gelling agent examined was CAB-O-SIL, a product of the Cabot Corporation which is made up of aggregates of fumed silica. When the particles of silica are dispersed in an aqueous liquid, the isolated hydroxyl groups at the surface of the particles cause hydrogen bonding with other particles, creating a three-dimensional exoskeleton that traps the liquid, in this case the electrolyte(s). Depending on the concentration of the aggregate, the temperature,

the mixing conditions, and the chemistry of the electrolyte, gels of varying viscosity and clarity are obtained.

3.3.1.1 CAB-O-SIL Formulation and Testing: Procedures were established for creating a gel containing the steel/titanium electrolyte and the aluminum electrolyte. The procedure for the steel electrolyte consisted of dispersing 9.0 weight percent CAB-O-SIL in the electrolyte and stirring for 4 minutes at a paddle speed of 500 rpm at room temperature. The only difference in gelling the aluminum electrolyte was a slightly lower (8. 5 weight percent) amount of CAB-O-SIL.

3.3.1.2 In Situ (Weight loss) Corrosion Testing: The procedure used for this testing is as described in Section 3.2.1.1. Duplicate specimens of steel and aluminum were totally immersed in their respective gelled electrolytes for a period of eleven days. For the steel samples, there was no weight loss or discernible pitting when examined at 30 magnifications (30X). The aluminum samples exhibited a small amount of pit nuclei on each. One aluminum sample sustained a weight loss of just 0.5 milligrams, which translates to a corrosion rate of 0.02 mm/year. The other sample actually showed a weight gain.

3.3.1.3 Properties of the CAB-O-SIL Gelled Electrolytes: Both gelled electrolytes (for steel and aluminum) were optically opaque due to differences in the electrolyte's and the CAB-O-SIL's indices of refraction. Gels with acceptable viscosity exhibited no change in pH before and immediately after gellation. Electrolytic conductivity and the ability to maintain passivity when anodically polarized were also maintained after gellation. An insurmountable problem with the CAB-O-SIL gels is that they "dry out" (become hardened) when exposed in an open beaker to laboratory air within two hours. This problem prompted a search for another gelling agent.

3.3.2 Laponite Gelled Electrolytes

Laponite is a synthetic material that closely resembles the natural clay mineral hectorite in structure and composition. It is a layered hydrous magnesium silicate that is free of natural clay impurities. Laponite is synthesized under controlled conditions. At a typical use level of 0.5 to 2.0% by weight Laponite dispersed in the liquid constituent to be gelled (in this case the electrolytes) will produce a clear gel with thixotropic rheology.

Having a clay-type structure, Laponite separates into many tiny platelets. During its dispersion in an aqueous medium, an electrical double layer forms around the platelets. Depending on the electrolytic strength of the aqueous medium, *i.e.*, presence of cations and anions, the double layer is affected so that attraction between the platelets becomes possible. This results in platelet bonding that forms a " house of cards" structure capable of holding and maintaining the electrolyte in a gelled state. There are two grades of Laponite pertinent to this study. The standard grade is termed RD. The sol grade, termed RDS, has a greater tolerance for strong electrolytes. Laponite will function over a pH range of 3 to 13.

3.3.2.1 Laponite Formulation and Testing: It was determined that the strength of the electrolytes would require some RDS grade Laponite. The RDS grade contains 6% Tetra sodium pyro phosphate which acts to keep the highly cationic active electrolytes from completely overcoming the negatively charged platelets. Numerous experiments led to an optimum formulation of 3.75% by weight Laponite (50% RD; 50% RDS), balance steel electrolyte solution. As the materials are being mixed, the solution is stirred for 30 to 45 minutes. An optimized gel forms within 24 hours. The gelled steel electrolyte is clear and much more stable than that made from CAB-O-SIL. When exposed to air the gel loses about half its volume to evaporation of water molecules over a period of 3 days. Drying and cracking will occur within a one week period. If properly sealed, the gel would maintain its properties indefinitely, *i.e.*, thixotropic rheology, clarity and electrolytic conductivity.

Similar experiments were carried out with the aluminum electrolyte with much less success. This can be attributed to the lower pH of aluminum electrolyte.

3.3.2.2 Testing of Steel in the Gelled Steel Electrolyte

3.3.2.2.1 Corrosion and Polarization Testing: Weight loss experiments, as previously described, were performed on two steel samples totally and continuously exposed to the gel for ten days. No discernible weight loss was noted (weighed to 0.1 of a milligram). This exposure produced no pitting or other forms of localized corrosion. Steel specimens were anodically polarized, using the previously described methods, in the gelled electrolyte. Figure 3-8, a semi-log, cyclic polarization plot, shows the variation in electrochemical current with imposed potentials starting from a cathodic potential of -0.6 volts to an anodic potential of +1.5 volts and return. The scan

rate was 1.0 millivolt per second and the exposed area was 1.5 square centimeters. The well-defined passive region and the absence of a lowered pitting potential indicates the gelled electrolyte's capability to develop and maintain passivity in the required range of EFS measurements.

It was concluded that the gelled steel electrolyte does not present a corrosion or a passivity problem for steel. It was therefore assessed as a candidate for the prototype EFS cell by measuring its effect on fatigue life and its ability to manifest an appropriate EFS current response.

3.3.2.2.2 EFS Current Measurements Using Gelled Steel Electrolyte: Two steel specimens were tested at 600 MPa and 0.5 Hz. Each was made part of a three electrode electrochemical cell, as previously described, so that EFS current measurements could be made during cyclic loading using the gelled electrolyte. The current vs. stress behavior as cyclically manifested exhibited no discernible differences from those obtained in the liquid electrolyte. Thus, it is concluded that the Laponite gelled electrolyte will function electrochemically in making EFS measurements on steel with the caveat that it not be dried out.

3.4   Effect of Electrolytes (Liquid and Gelled) on Fatigue Resistance (S-N)

As previously mentioned, the benignity of the electrolyte is critically important since the aircraft alloys chosen for study—high strength aluminum, high strength steel, and titanium—are susceptible to environmental cracking (stress corrosion cracking and corrosion fatigue) [3.1, 3.2, 3.3]. This prompted experiments to assess the effects, if any, that the chosen electrolytes, *i.e.*, for steel/titanium and for aluminum, would have on the fatigue life of the alloys as determined by constant amplitude stress vs. cycles to failure (S-N) experiments on smooth, round bar specimens.

3.4.1   Effects of Liquid Environments on the Fatigue Resistance of 4130 Steel

Figure 3-9 depicts the S-N response of quenched and tempered 4130 steel when tested in the following: air, bracketed by dotted curves; ordinary tap water at two stress levels, open triangles; and in the previously described solution designated steel electrolyte at four stress levels. It can be seen that what might be considered seemingly benign tap water, substantially

shortens the fatigue life over that tested in air at the two stress levels. It is important to note that the steel, when tested in the steel electrolyte, does not show a decrease in fatigue life over that tested in air. This is not surprising since the electrolyte was formulated to minimize surface effects such as corrosion or pitting of the steel. Multiple tests were conducted at 600 MPa in the electrolyte since this is the stress level chosen for many of the EFS measurements on this steel.

3.4.2 Effects of Gelled Electrolyte on the Fatigue Resistance of 4130 Steel

Figure 3-10 depicts the S-N behavior of the steel when fatigued and simultaneously enveloped in the gelled steel electrolyte at the 600 MPa stress level as compared to fatigue in air. As is seen, exposure to the gel does not appear to affect the fatigue life of the steel at that stress level. This is not unexpected since static exposure to the gelled electrolyte produced no corrosion or pitting of the steel (see Section 3.3.2.2.1).

3.4.3 Effects of Liquid and Gelled Steel Electrolyte on the Fatigue Resistance of Titanium Alloy, 6AL-4V

The S-N response of the titanium alloy when tested in air, liquid "steel" electrolyte, and gelled "steel" electrolyte is shown in Figure 3-11. The lack of any surface effects on the titanium when statically exposed to the steel electrolyte (see Sections 3.2.1.1.3 and 3.2.2.3) is extended to its fatigue behavior in the liquid electrolyte. This behavior is due to the inherently impervious nature of the oxide film on the surface of the titanium alloy. Figure 3-11 shows the titanium alloy to be virtually unaffected by exposure to the gelled steel electrolyte at the stress level tested, 580 MPa.[*] It is interesting to note that a titanium specimen exposed to the gelled steel electrolyte under variable amplitude fatigue loading at a higher frequency (2 Hz.), was unbroken after sustaining 1.36 million cycles.

3.4.4 Effects of Liquid Environments on the Fatigue Resistance of 7075-T73 Aluminum Alloy

Figure 3-12 depicts the S-N behavior of the aluminum alloy when fatigued and simultaneously exposed to the formulated liquid aluminum electrolyte or to tap water, both as

---

[*] It should be noted that the smooth curve for fatigue in air is based on a limited number of tests, the statistics of which are discussed elsewhere in this report

compared to fatigue in air. As noted above for steel, tap water is seen to have a deleterious effect on the fatigue life of the aluminum alloy. This is believed to be caused/aided by a hydrogen embrittlement mechanism in this alloy [3.7, 3.8, 3.9].

Although the effect of the aluminum electrolyte was not as detrimental as that caused by the tap water, fatigue lives fell within the scatterband for fatigue in air. The previously mentioned slight pitting the aluminum experiences in this electrolyte is still a cause for concern. It should be emphasized that the aluminum alloy of this study, 7075-T73, is of commercial quality and as such contains unwanted iron and manganese inclusions that will serve as sites for pit nucleation in any aqueous medium. This concern and the inability to achieve an acceptable gel with the lower pH electrolyte (see section 3.3.2.1), prompted an evaluation of the aluminum alloy in the successfully established gelled steel electrolyte of higher pH, as described in 3.6.

The question of whether or not the electrolyte has depreciated the fatigue life of the 7075-T73 alloy, at long lives (Figure 3-12), is complicated to answer. To prove whether or not there is an environmental effect, it would be necessary to perform a rigorous statistical analysis, and the difficulties and expense of doing so in relation to the life distributions that occur in air and in electrolyte are described in detail in the Appendix BB. Pending the outcome of such an analysis, it is necessary to rely on engineering judgment, and it would appear on this basis that there is in fact a small environmental effect. This conclusion has been modified by a discovery following the termination of the subject contractual period. When a gel form of the electrolyte was used on the 7075-T73 alloy, for purposes of performing a continuous EFS test, a globule of foreign matter was observed at the tip of the reference electrode after the fatigue life ended. Analysis of this matter by SEM/EDS revealed that chloride ions originating from the KCl salt bridge of the reference electrode had been leaking into the liquid electrolyte used as the medium in the EFS tests. The major reason for the leak was that a head of 15 cms had been consistently applied to the calomel electrode to insure electrical continuity, but this had also induced a small mass transfer, hitherto undetected, because the matter was distributed in the liquid electrolyte. Repeat tests were then performed at long life, using zero head on the reference electrode. No electrical anomalies were observed but all the fatigue lives became considerably longer and nicely straddled the life scatterband for tests in air. On the basis of engineering judgement, the conclusion is that the long life results shown in Figure 3-12 were slightly depreciated by the

influx of chloride ion, but absent this impurity, the effect of the electrolytic environment is no more damaging than that of laboratory air.

3.5 Influence of EFS Electrolyte on Fatigue Crack Growth

Certain aqueous environments are known to accelerate the rate of fatigue crack growth in aircraft materials [3.10, 3.11]. Thus, the objective of this effort was to assess the potential influence of the EFS electrolyte on fatigue crack growth in aircraft materials in general, and T-38 materials in particular. This was accomplished by performing fatigue crack growth experiments on pre-cracked fracture mechanics specimens of both 4130 steel and 7075 aluminum alloy exposed to the EFS electrolyte, as well as a number of other environments to which aircraft are commonly exposed—air, water, and dye penetrant used to inspect aircraft. These experiments were designed to complement the S-N fatigue testing described in Section 3.4. Fracture mechanics crack growth results often exhibit less data scatter than S-N data and thus may provide a clearer assessment of the influence of the EFS electrolyte on the fatigue behavior of aircraft materials. Moreover, such results are consistent with the present USAF practice of managing aircraft using damage tolerance concepts and periodic in-service inspection.

The EFS environment was examined under the "freely-corroding", open circuit condition—that is, without an applied electrochemical potential. The "freely-corroding" condition was designed to simulate the effect of residual electrolyte that might remain behind following an inspection. This "freely-corroding" condition is believed to be more detrimental than the controlled potentials within the passive range that would be employed during EFS inspections; thus, this condition is expected to represent a worst-case scenario with respect to enhancement of fatigue crack growth in aircraft structure. Comparison experiments were also performed in air environments having various moisture levels, as well as in distilled water in order to simulate the presence of rainwater and condensation—environments to which aircraft are commonly exposed. Experiments were also performed in dye penetrant solution since this fluid is widely used in inspection of aircraft components.

Experiments in the above environments were performed at relatively low cyclic frequencies in order to ensure adequate time for interaction between the environments and the material at the crack tip. The optimum test frequency generally represents a compromise

between permitting a maximum environmental effect and completing the testing in a reasonable period of time. This optimum frequency was selected based on a review of environmentally-enhanced fatigue crack growth data from the literature on similar material-environment systems. For example, Figure 3-13 provides a summary of results for various steels exposed to seawater [3.10]. Note that the environmentally-enhanced fatigue crack growth (da/dN) is inversely related to cyclic frequency, and at very low frequencies a plateau is achieved, below which further decreases in frequency cause little or no increase in growth rates. Analogous results for 2024 and 7075 Al exposed to humid air at different values of relative humidity are shown in Figure 3-14 [3.11]. These data also exhibit an inverse relationship between da/dN and cyclic frequency, similar to that demonstrated for steel in Figure 3-13. However, the data in Figure 3-14 also show that frequency-dependent environmental effects in aluminum alloys are markedly sensitive to moisture level, as well as alloy composition.

The data in Figures 3-13 and 3-14 indicate that significant enhancement in fatigue crack growth rates can occur at a cyclic frequency of 0.5 Hz for both steels and aluminum alloys exposed to aqueous environments. Consequently, 0.5 Hz was chosen for the initial experiments conducted in this portion of the study. Supplemental experiments were subsequently performed at 0.05 Hz in 7075-T73511 aluminum when only modest environmentally-enhanced fatigue crack growth rates were observed in this material at the higher frequency of 0.5 Hz. The need to adjust the frequency is not surprising since the precise magnitude of environmentally-enhanced fatigue crack growth is specific to both the material and the environment.

3.5.1 Design of Fatigue Crack Growth Experiments

The crack growth experiments performed in the various environments are listed in Table 3-4. As indicated in Table 3-4, the results in lab air and dry air were generated at 5.0 Hz to intentionally suppress environmental effects since both of these environments were considered baseline conditions. In contrast, tests in the environments of interest were performed at either 0.5 or 0.05 Hz to facilitate environmental interaction.

To maximize the amount of information obtained, each test was performed in two segments. The first segment was performed in air under decreasing stress intensity (K-decreasing) conditions, whereas the second segment was performed in the environment of

interest under K-increasing conditions. This procedure minimized the number of cycles (and thus, crack length and test time) required to assess a given ΔK regime, thereby enabling a comparison of several environments on the same specimen. These K-controlled experiments were conducted using a computer-controlled, servo-hydraulic test system that continually adjusted the applied load based on the instantaneous crack size, as determined from the elastic compliance of the specimen [3.12, 3.13]. Supplemental experiments performed under constant-ΔK conditions were conducted in similar fashion. These constant-ΔK experiments were more practical at the lower frequency of 0.05 Hz; they also provided a more precise measurement of da/dN that enabled an improved comparison of subtle differences in environmental effects in the 7075 aluminum alloy.

The above crack growth experiments were conducted in accord with ASTM E647 [3.14] using the following normalized K-gradients ($C = 1/K \ dK/da$):

K-increasing tests: $C = +3 \ \text{in.}^{-1}$

K-decreasing tests: $C = -3 \ \text{in.}^{-1}$

Constant-ΔK tests: $C = 0$

All experiments were performed using compact-type C(T) fracture mechanics specimens having a width of 51 mm (2 in.) and a thickness of 6.35 mm (0.25 in.). Figure 3-15 shows the test specimen in the experimental set-up. As can be seen, loads were applied to the specimen using a pin-and-clevis arrangement, and a clip gage was attached to the front face of the specimen to measure the crack opening displacement. Measurements of the applied load and crack opening displacement were used as the feedback signals to the computer to compute the crack length, and thus control the K-gradient by automatically adjusting the applied load throughout the test. As shown in Figure 3-15, the test environments were contained around the specimen in a sealed plastic bag.

3.5.2 Fatigue Crack Growth in 4130 Steel

The measured fatigue crack growth rates in 4130 steel exposed to lab air and to EFS electrolyte are plotted as a function of the applied stress intensity factor range (ΔK) in Figure 3-16. As is apparent, no significant differences were observed between these two environments.

Any minor differences between the data sets in Figure 3-16 are well within typical experimental scatter for fatigue crack growth rate testing [3.15]. Thus, with respect to fatigue crack growth in 4130 steel, the EFS electrolyte is no more damaging than air—an environment to which aircraft are commonly exposed.

The aforementioned results in air and EFS electrolyte are compared in Figure 3-17 with fatigue crack growth data in both de-ionized (DI) water and dye penetrant fluid (Sherwin Inc. RC-50). This comparison clearly shows that the EFS environment is less damaging than either DI water, which was designed to be generally representative of rain water, or dye penetrant, which is commonly used to inspect aircraft. The lower growth rates in the EFS environment are likely the result of the molybdate species added to the EFS electrolyte as corrosion inhibitors. It should also be noted that actual rainwater, which can be acidic due to pollutants, or contain chlorides due to carry-over from sea-cost environments, may actually be more damaging than the DI water environment used in the current experiments. Thus, a comparison of the EFS environment with actual rainwater would likely make the EFS environment look comparatively better than indicated by the data in Figure 3-17. (However, the practicalities associated with testing in "representative" rainwater are problematic.) Nevertheless, the results demonstrate that the EFS electrolyte can actually be viewed as having beneficial effects with respect to environmentally enhanced fatigue crack growth in steel.

3.5.3   Fatigue Crack Growth in 7075 Aluminum

The measured fatigue crack growth rates in 7075 aluminum alloy exposed to air and to EFS electrolyte are shown in Figure 3-18. As in the case of steel, the fatigue crack growth rates were found to be the same in both of these environments, thereby indicating that the EFS electrolyte is no worse than air. However, as shown in Figure 3-19, initial fatigue crack growth rate testing in 7075 aluminum at 0.5Hz also indicated little difference between lab air (at a relative humidity of 60%) and water environment. Since relative humidity levels on the order of 60% can sometimes cause capillary condensation within the crack and associated environmental effects, subsequent baseline testing was performed in dry air conditions. The dry air conditions were achieved by adding desiccant to the environmental enclosure resulting in relative humidity levels of 5% or less. However, further assessment of these results indicated little difference between dry air and lab air conditions. Consequently, questions arose about whether or not the

cyclic frequency of 0.5 Hz was slow enough to allow significant environmental effects in this alloy.

Although results in Figure 3-19 exhibit some environmental enhancement compared to vacuum, it was decided that additional testing at a slower frequency were warranted in the aluminum alloy to provide a more rigorous assessment of possible detrimental effects due to the presence of the EFS electrolyte on aircraft structure.

Supplemental experiments on 7075 aluminum were performed at a slower frequency of 0.05 Hz in the above three environments, as well as in dye penetrant. As described in the previous section, these experiments were performed under constant-ΔK conditions for expediency. The results in Figure 3-20 exhibit a slight enhancement in crack growth rates, compared to air, in both DI water and EFS electrolyte, while the crack growth rate in the dye penetrant environment is significantly higher than that observed in any of the other environments. A summary of these results is provided in Figure 3-21 where it can be seen that on average the water and EFS electrolyte data exhibit a 9% to 10% crack growth rate increase compared to air, while the dye penetrant data are about 33% faster than those in air. Although these data exhibit environmental effects at this slow frequency, it should be pointed out that all of these differences are relatively small and would be difficult to discern in the more traditional da/dN vs. ΔK curve previously shown in Figures 3-18 and 3-19. Nevertheless, the data once again show that no unusual detrimental effects on fatigue crack growth are expected to occur due the presence of EFS electrolyte since the EFS data are equivalent to those in water, and better than those in dye penetrant—two environments to which aircraft are commonly exposed.

3.6   Feasibility of Using the Gelled Steel Electrolyte For Aluminum

Although the pH of the steel electrolyte is higher than that for the aluminum, 8.4 instead of 6.9, this would only be beneficial for a condition of general corrosion on a pure aluminum substrate. Since localized corrosion in the form of pitting and/or miniscus corrosion is of concern here, the gelled solution with the higher pH was tested on the aluminum alloy.

3-16

3.6.1 Total Immersion and Alternate Immersion Testing, Aluminum in Gelled Steel Electrolyte

Size and surface preparation of test coupons was as previously described. Six aluminum coupons were completely immersed in the gelled steel electrolyte for one week. Minimal weight loss was noted, yielding a calculated average corrosion rate of 0.045 mm/yr. Microscopic examination revealed only a few scattered pit nuclei on three of the six coupons. This is most likely a consequence of the aforementioned inclusions in the commercial alloy.

In order to assess the effect of the gel drying out on the surface of the aluminum and hence becoming more concentrated in the interim, an alternate immersion test was devised. The test consisted of totally immersing the coupons in the gel for four hours and then removing them and allowing air drying for twenty hours. This daily cycle was repeated five times on the six aforementioned coupons that were totally immersed. Although alternate immersion testing in aluminum alloys in liquid environments is considered more severe, there was no weight loss by any of the six coupons after the five cycles. Additionally, no new pit nuclei formed and the preexisting pit nuclei did not grow.

3.6.2 Anodic Polarization of Aluminum in Gelled Steel Electrolyte

As previously described in Section 3.2.2, anodic polarization response defines a metal's passivity from voltage range and current standpoints. Figure 3-22 shows a cyclic anodic polarization plot for the aluminum alloy in the gelled steel electrolyte. The plot shows a passive region from -0.2 volt to +1.0 volt. This provides a sufficiently stable region over which EFS measurements can be made. The absence of a decreased pitting potential is again noted.

3.6.3 Effect of Gelled Steel Electrolyte on the Fatigue Resistance of Aluminum

Constant amplitude fatigue tests have been performed on the aluminum alloy at the stress level of 200 MPa immersed in the gelled steel electrolyte with no loss in fatigue life as compared to fatigue in air. Figure 3-23 shows the effect.

3.7 Procedure for Application and Removal of Gelled Electrolyte From Aircraft Surfaces

It should be noted that the gelled steel electrolyte, hereafter known as the gelled electrolyte, has been successfully used in EFS studies utilizing both two and three electrodes on round bar steel, aluminum and titanium specimens (studies described in Section 5 of this report). The gelled electrolyte has also been incorporated in a Teflon prototype EFS cell designed for use on flat specimens. Sucessful EFS signals were achieved with a two-electrode system and the gelled electrolyte in the prototype cell (details described in Section 8 of this report).

As previously described, the Laponite gel used in formulating the gelled electrolyte demonstrates thixotropic behavior. This thixotropy minimizes the possibility that the gelled electrolyte will seep into crevices or other occluded areas on the aircraft during or after EFS testing. In the event that the gel needs to be removed, the emergency procedures outlined in the DoD Tri-Service Technical Manual, "Aircraft Weapons Systems Cleaning and Corrosion Control," will be used [3.16]. The procedure involves flushing the area with copious amounts of fresh water; if needed, the use of a detergent, appropriately diluted MIL-C 43616; followed by fresh water flushing to remove the detergent; and finally aerosol spraying of the water displacing corrosion preventive compound MIL-C 81309. This is a proven and effective procedure for removing pollutants and corrosives from aircraft surfaces. Thus, it follows that application and removal of a two-electrode prototype using the gelled electrolyte will easily transition to on-aircraft use.

3.8 Summary

An electrolyte, number (7) of Table 3-1, has met the three objectives of this study as outlined in Section 3.1.1, *i.e.*, it must:

- be sufficiently active to provide adequate current signals for EFS measurements on the alloys as they appear on the aircraft,
- be benign to the substrates of the aircraft and not cause any degradative effects, and
- be capable of incorporation into a useful gel that precludes the inconvenience of working with a liquid electrolyte on the aircraft.

The additional benefit of having one gelled electrolyte serve for the three aircraft test alloys (steel, aluminum, and titanium) has been achieved.

The gelled electrolyte conceived and developed in this study has also been shown to function in the EFS prototype (application and removal), and thus its use for aircraft is positively anticipated.

3.9 References

3.1   DeLuccia, J. J., "The Corrosion of Aging Aircraft and its Consequences," Proceedings of AIAA 32nd Structures, Dynamics, and Materials Conference, AIAA-91-0953-CP p. 1667 (1991).

3.2   Wanhill, R. J. H., "Environmental Effects on Fatigue of Aluminum and Titanium Alloys," AGARD Report N⁰· 659, AGARD-NATO (1977).

3.3   Wei, R. P., *Engineering Fracture Mechanics*, Vol. 1, p. 633 (1970).

3.4   *Tri-Service Technical Manual*, "Aircraft Weapons Systems Cleaning and Corrosion Control," NAVAIR 01-1A-509, T.O. 1-1-691, TM 1-1500-344-23 sections 9-5, 9-7, 1 January (1992).

3.5   Pourbaix, M., "Atlas of Electrochemical Equilibria in Aqueous Solutions," Pergamon Press, New York (1966).

3.6   Jones, D. A., *Principles and Prevention of Corrosion*, Macmillan Press, New York (1992).

3.7   Gest, R. J. and Troiano, A. R., "Stress Corrosion and Hydrogen Embrittlement in an Aluminum Alloy," *Corrosion-NACE* **30** (8) p. 274 (1974).

3.8   Duquette, D. J., "Mechanisms of Corrosion Fatigue in Aluminum Alloys," *Environment Sensitive Fracture of Metals and Alloys*, Office of Naval Research, Arlington, VA, p. 1 (July 1987).

3.9   Jacko, R. J. and Duquette, D. J., *Met. Trans*, 8A, pp. 1821-1927 (1977).

3.10   Burnside, O. H. and Hudak, S. J., Jr.,"Long-Term Corrosion Fatigue of Welded Marine Steels," in *Proceedings of the Ship Structure Symposium '84* SY-20, The Society of Naval Architects and Marine Engineers, New York, NY, pp. 139-157, 1984.

3.11   Wei, R. P., "Some Aspects of Environment-Enhanced Fatigue-Crack Growth," Engineering Fracture Mechanics, Vol. 1, pp. 633-651, 1970.

3.12 Saxena, A. and Hudak, S. J., Jr., "Review and Extension of Compliance Information for Common Crack Growth Specimens," *International Journal of Fracture*, Vol. 15, No. 5, pp. 453-468, 1978.

3.13 Saxena, A., Hudak, S. J., Jr., Donald, J. K., and Schmidt, D. W., "Computer-Controlled Decreasing Stress Intensity Techniques for Low Rate Fatigue Crack Growth Testing," *Journal of Testing and Evaluation*, JTEVA, Vol. 6, No. 3, pp. 167-174, May 1978.

3.14 ASTM E-647, "Standard Method for Measurement of Fatigue Crack Growth Rates," Annual Book of ASTM Standards, Vol. 03.01, 1998.

3.15 Clark, W. G., Jr. and Hudak, S. J., Jr., "Variability in Fatigue Crack Growth Rate Testing," *Journal of Testing and Evaluation*, JTEVA, Vol. 3, No. 6, pp. 454-476, 1975.

3.16 *Tri-Service Technical Manual*, "Aircraft Weapons Systems Cleaning and Corrosion Control," NAVAIR 01-1A-509, T.O. 1-1-691, TM 1-1500-344-23 section 9-7-1, 1 January (1992).

Table 3-1. Compositions and pH of Candidate Liquid Electrolytes Tested

Compositions (7) and (8) chosen as interim electrolytes for steel and aluminum, respectively.

	PH
(1) 0.25M Na2SO4	5.7
(2) 0.25M Na2SO4 + 0.05M Na2MoO4	9.2
(3) 0.25M Na2SO4 + 0.01M Na2MoO4	6.5
(4) 0.1M Na2HPO4	9.2
(5) 0.3M H3BO3 + 0.03M Na2B4O7	7.4
(6) 0.3M H3BO3 + 0.03M Na2B4O7*10H2O + 0.06M Na2MoO4	7.8
(7) 0.3M H3BO3 + 0.075M Na2B4O7*10H2O + 0.06M Na2MoO4	8.4
(8) 0.3M H3BO3 + 0.005M Na2B4O7*10H2O + 0.06M Na2MoO4	6.9

Table 3-2. Aluminum Alloy 7075 - T73 Corrosion Test Results

Electrolyte	Corrosion Rate, mm/yr*	Surface Condition
(1)	3.24 E – 02	random pitting, solution clouding
(3)	1.19 E – 02	less pitting / clouding than electrolyte(1)
(6)	1.41 E – 02	slight pitting on 3 of 4 specimens, no solution clouding

* NOTE: Corrosion resistance rates of 0.02 - 0.01mm/yr are considered excellent [3.6]

Table 3-3. 4130 Steel Corrosion Test Results

Time of Test	Corrosion Rate, mm/yr	Surface Appearance
10 days	8.78 E – 04	~20 pits on one edge of one specimen (out of four)
20 days	1.95 E - 03	no change

Table 3-4. Conditions Tested During the FCG Assessments at an R-ratio of 0.5

Material	Specimen ID	Freq, Hz	Environ	Test Type
Steel	SA28CFPM	5.0 0.5	lab air DI water	K-decreasing K-increasing
	SA19CFPM	5.0 0.5	dry air EFS electrolyte[†]	K-decreasing K-increasing
	SA17CFPM	5.0 0.5	dry air dye penetrant	K-decreasing K-increasing
Aluminium	AJ64C2FPM	5.0 0.5	lab air DI water	K-decreasing K-increasing
	AJ56C1FPM	5.0 0.5	dry air DI water	K-decreasing K-increasing
	AJ56C2FPM	5.0 0.5	dry air EFS electrolyte[†]	K-decreasing K-increasing
	AJ62C2FPM	5.0 0.05 0.05	dry air DI water EFS electrolyte[†]	Constant-ΔK
	AJ59C2FPM	5.0 0.05 0.05	dry air EFS electrolyte[†] DI water	Constant-ΔK
	AJ64C1FPM	5.0 0.05	dry air dye penetrant	Constant-ΔK

[†] The EFS electrolyte employed was that initially formulated for steel, but eventually recommended for use with aluminum and titanium alloys as well (electrolyte #7 in Table 3-1).
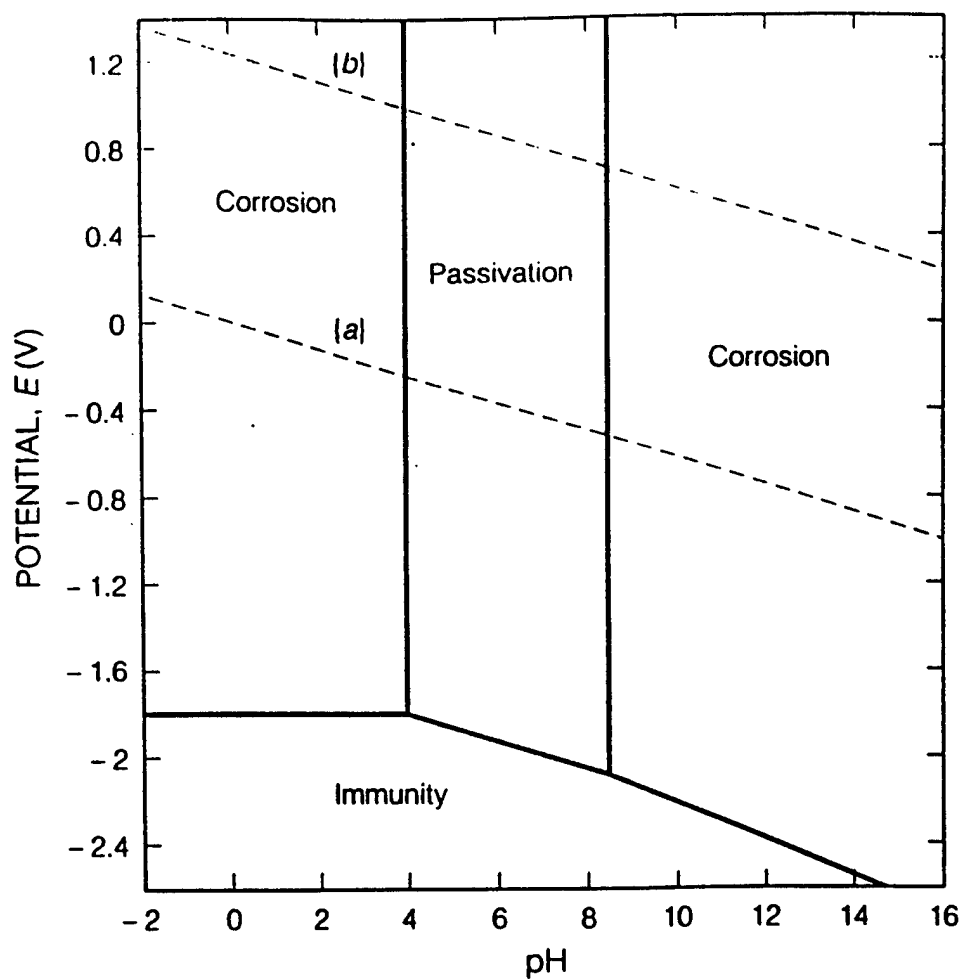
Figure 3-1. Pourbaix diagram for aluminum. All dissolved species at activities of 10^{-6} gram – equivalents/liter. All potentials v. normal hydrogen electrode. Ref. [3.5]
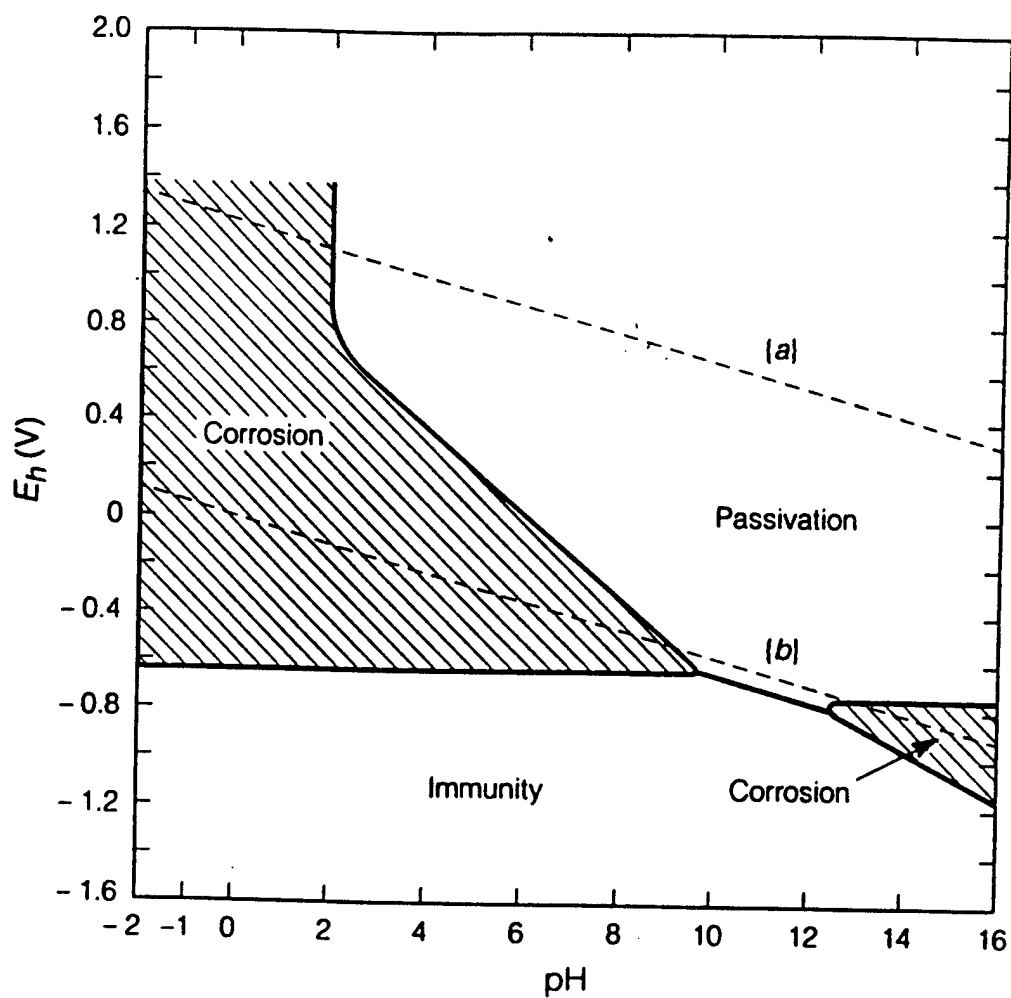
Figure 3-2. Pourbaix diagram for iron. All dissolved species at activities of 10^{-6} gram – equivalents/liter. All potentials v. normal hydrogen electrode. Ref. [3.5]
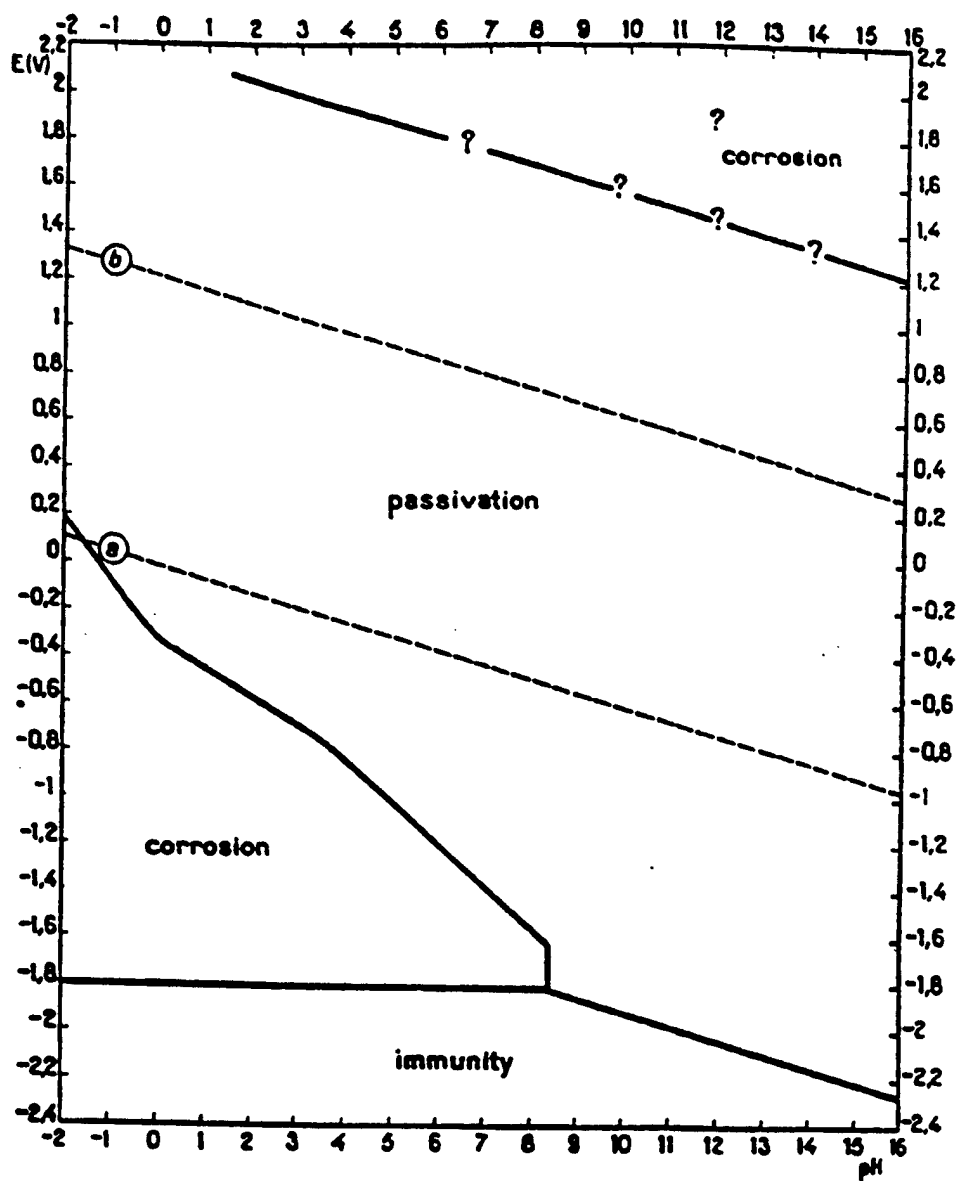
Figure 3-3. Pourbaix diagram for titanium. All dissolved species at activities of 10^{-6} gram – equivalents/liter. All potentials v. normal hydrogen electrode. Ref. [3.5]
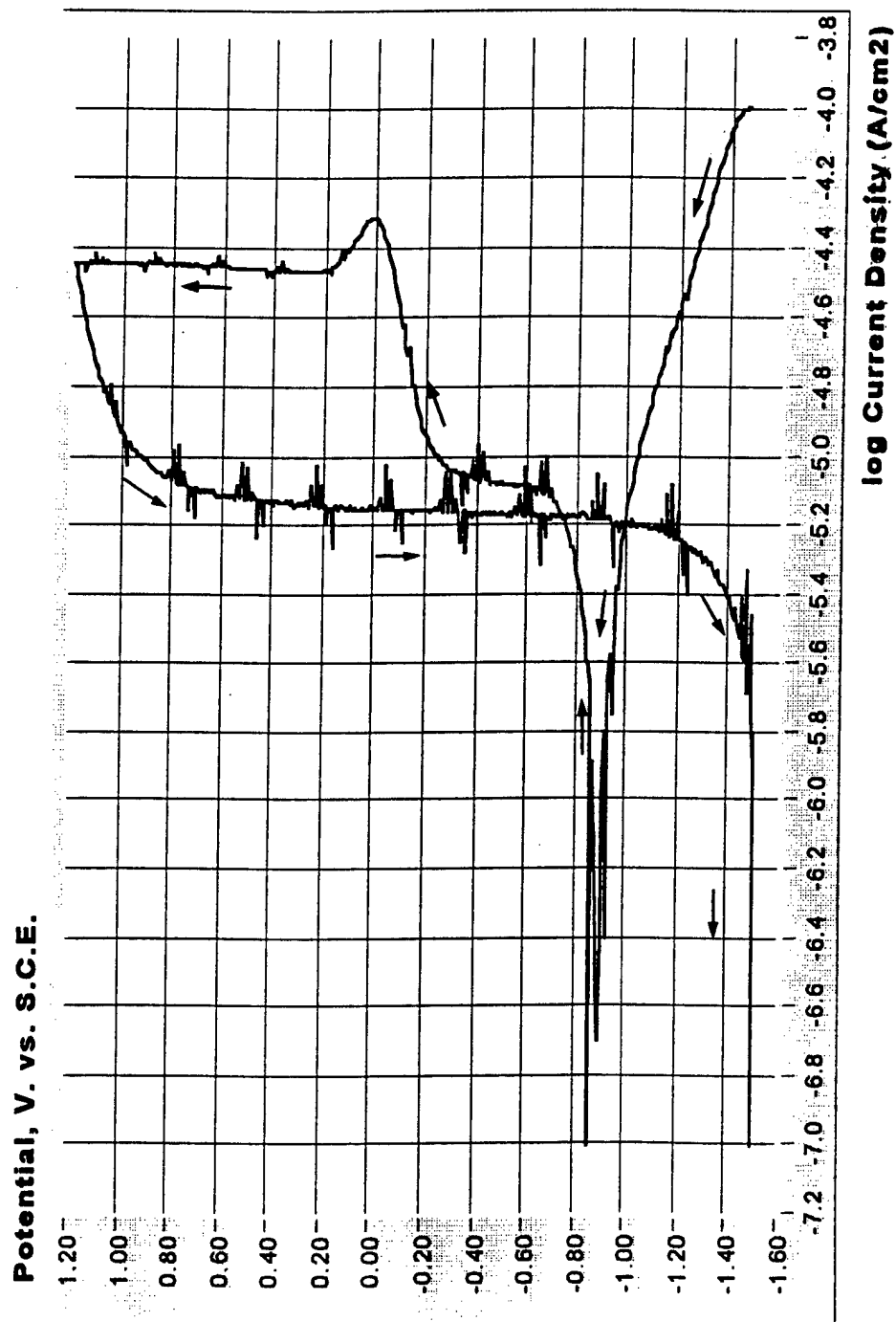
Figure 3-4. Anodic polarization cycle for aluminum alloy 7075-T73 in 0.3M H3B03 + 0.005M Na2B407. 10H2O + 0.06M Na2MoO4. 2H2O (10 mV/sec Scan Rate)
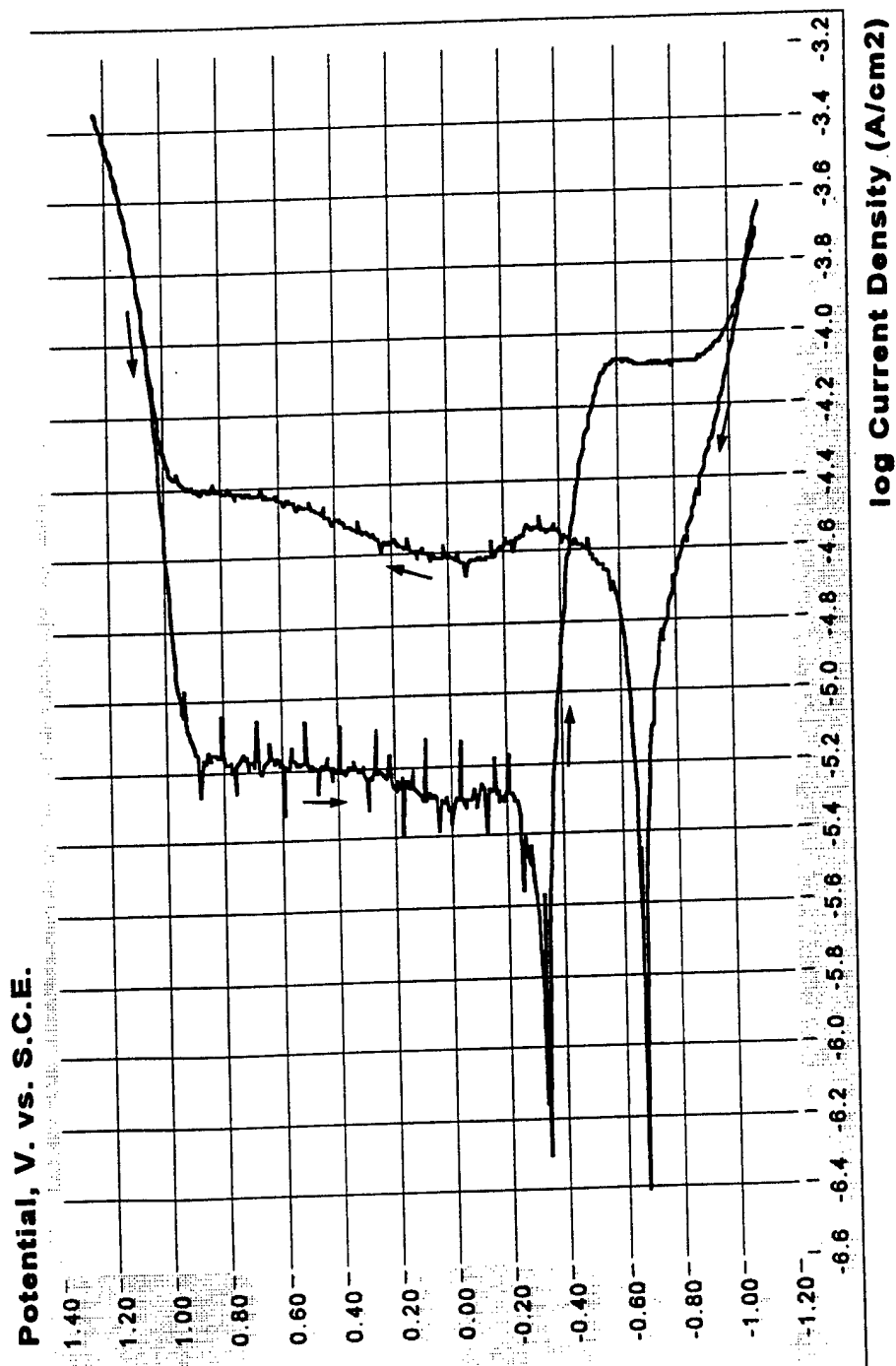
Figure 3-5. Anodic polarization cycle for 4130 steel in 0.3M h3BO3 + 0.075M Na2B4O7. 10H2O + 0.06M Na2MoO4. 2H2O (10 mV/sec Scan Rate)
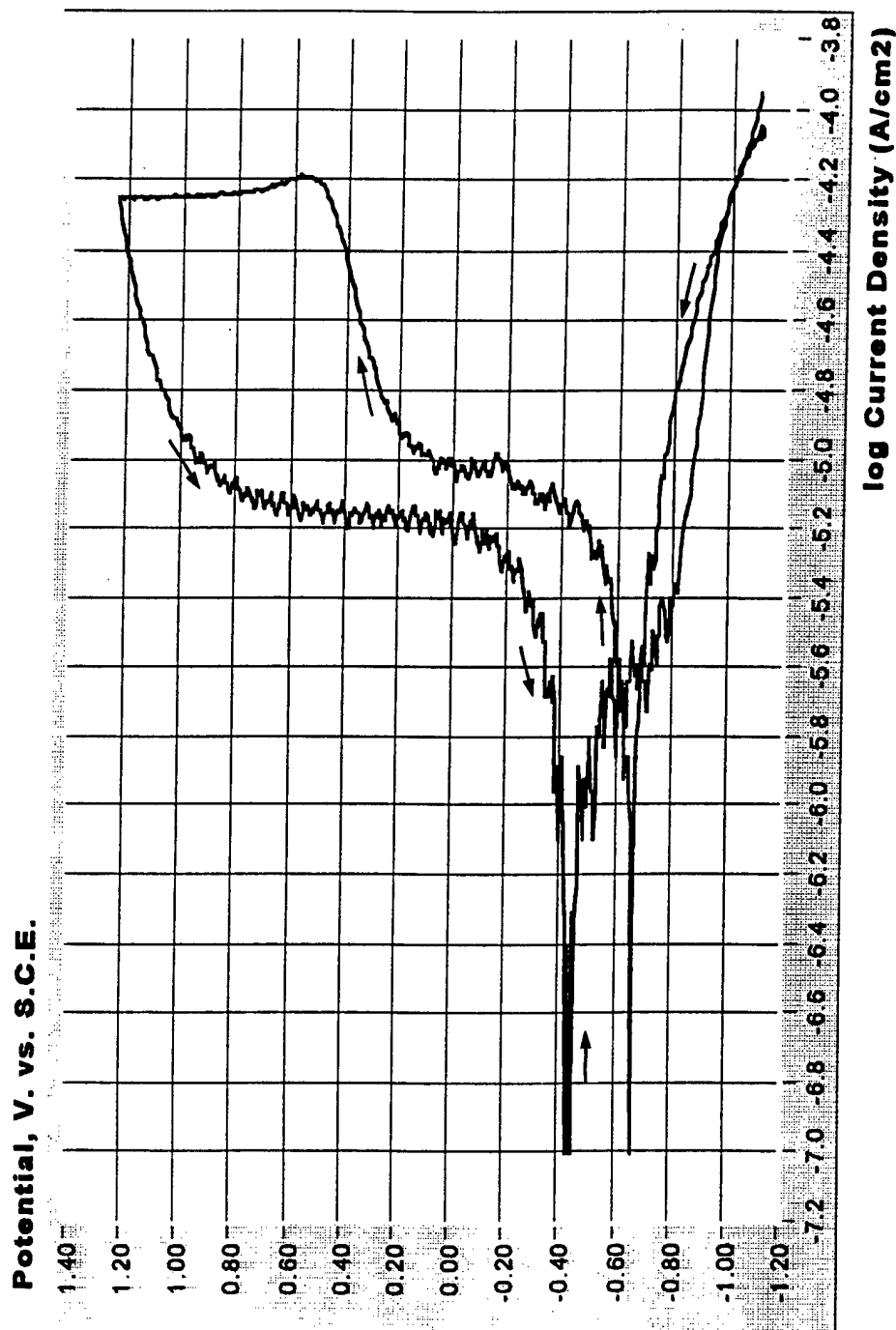
Figure 3-6. Anodic polarization cycle for 6Al-4V titanium alloy in 0.3M H3B03 + 0.075M Na2B407. 10H2O + 0.06M Na2MoO4. 2H2O (10 mV/sec Scan Rate)
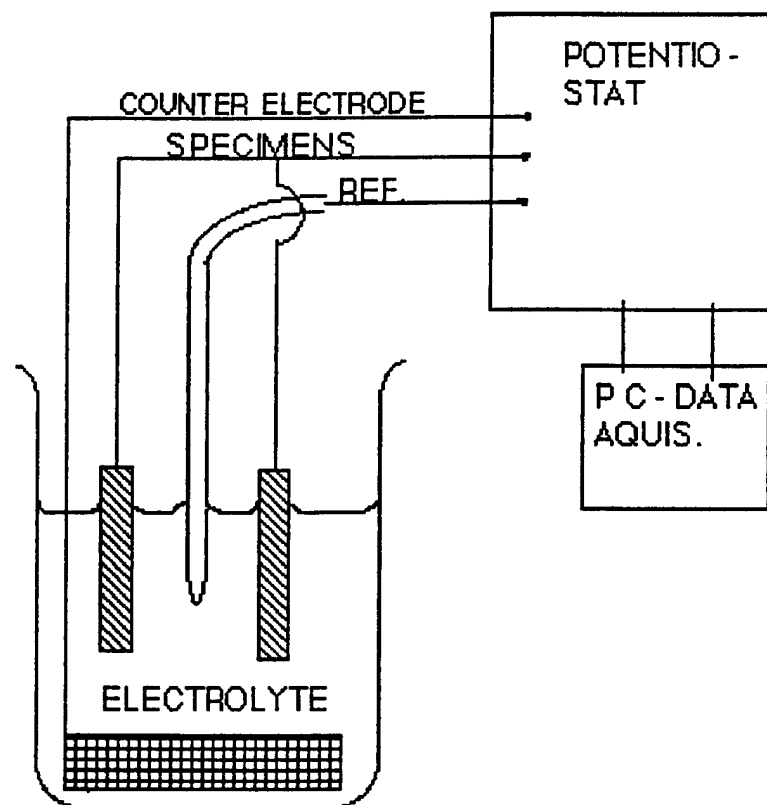
Figure 3-7. Corrosion testing at an applied constant passive potential.
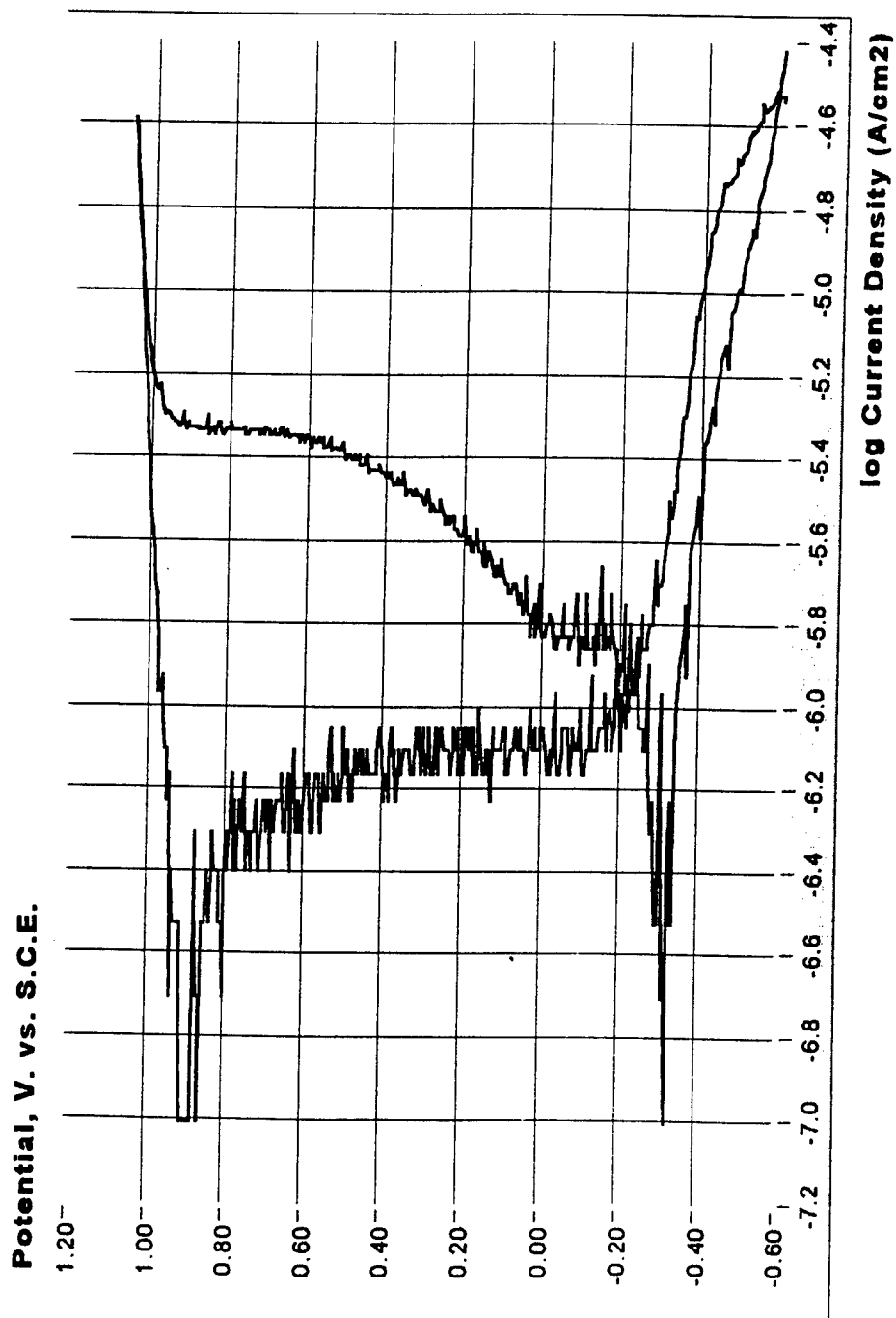
Figure 3-8. Anodic polarization cycle for 4130 steel in a gelled electrolyte of 0.3M H3BO3 + 0.075M Na2B4O7. 10H2O + 0.06M Na2MoO4. 2H2O (1 mV/sec Scan Rate)
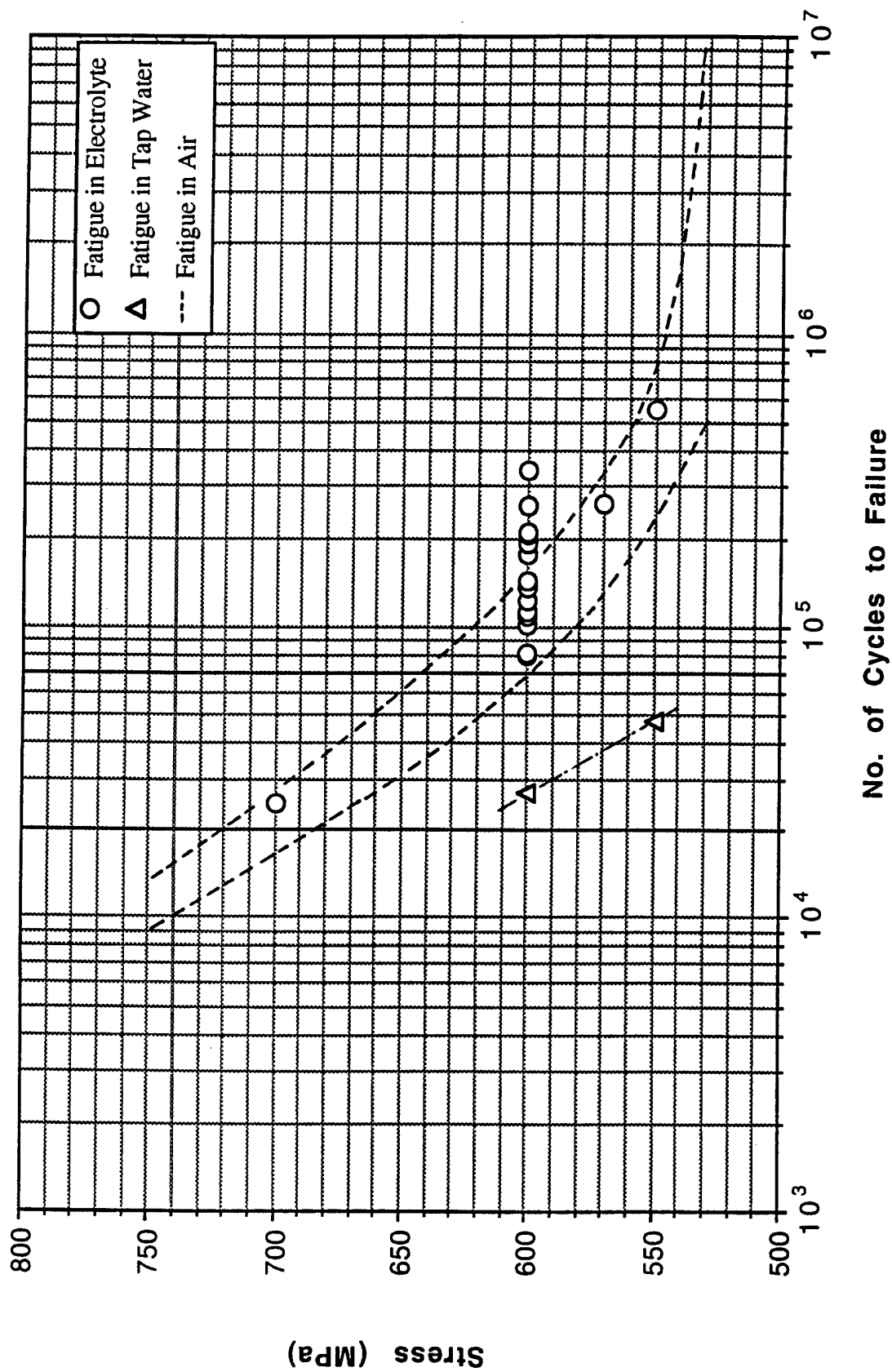
Figure 3-9. Stress vs. number of cycles to failure, R=-1, 0.5 Hz for 4130 quenched and tempered steel in air, tap water, and liquid steel electrolyte.
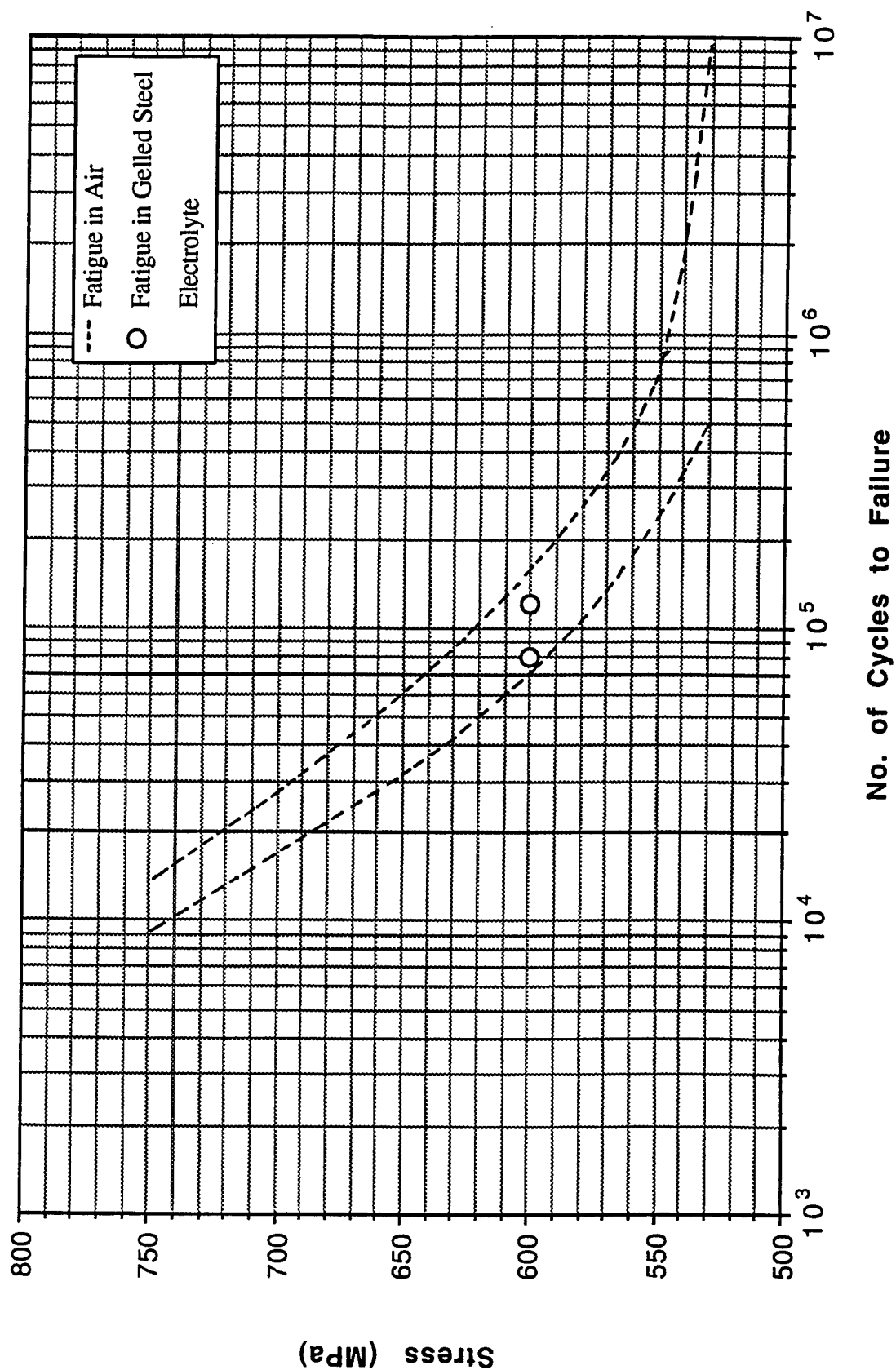
Figure 3-10. Stress vs. number of cycles to failure, R=-1, 0.5 Hz for 4130 quenched and tempered steel in air, and in gelled steel electrolyte.
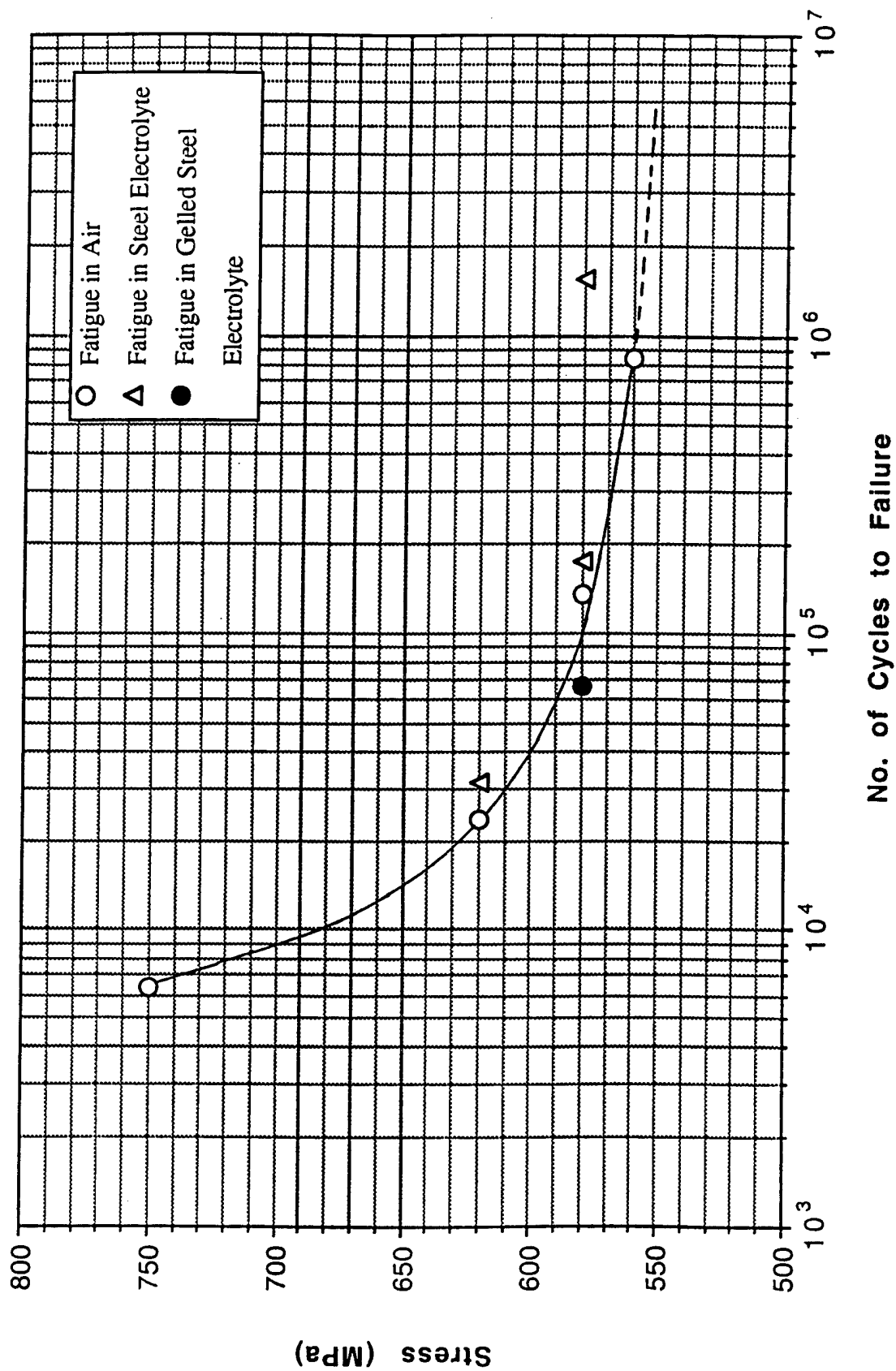
Figure 3-11. Stress vs. number of cycles to failure, R=-1, 0.5 Hz for titanium 6 Al-4V in air; liquid steel electrolyte; and gelled steel electrolyte.
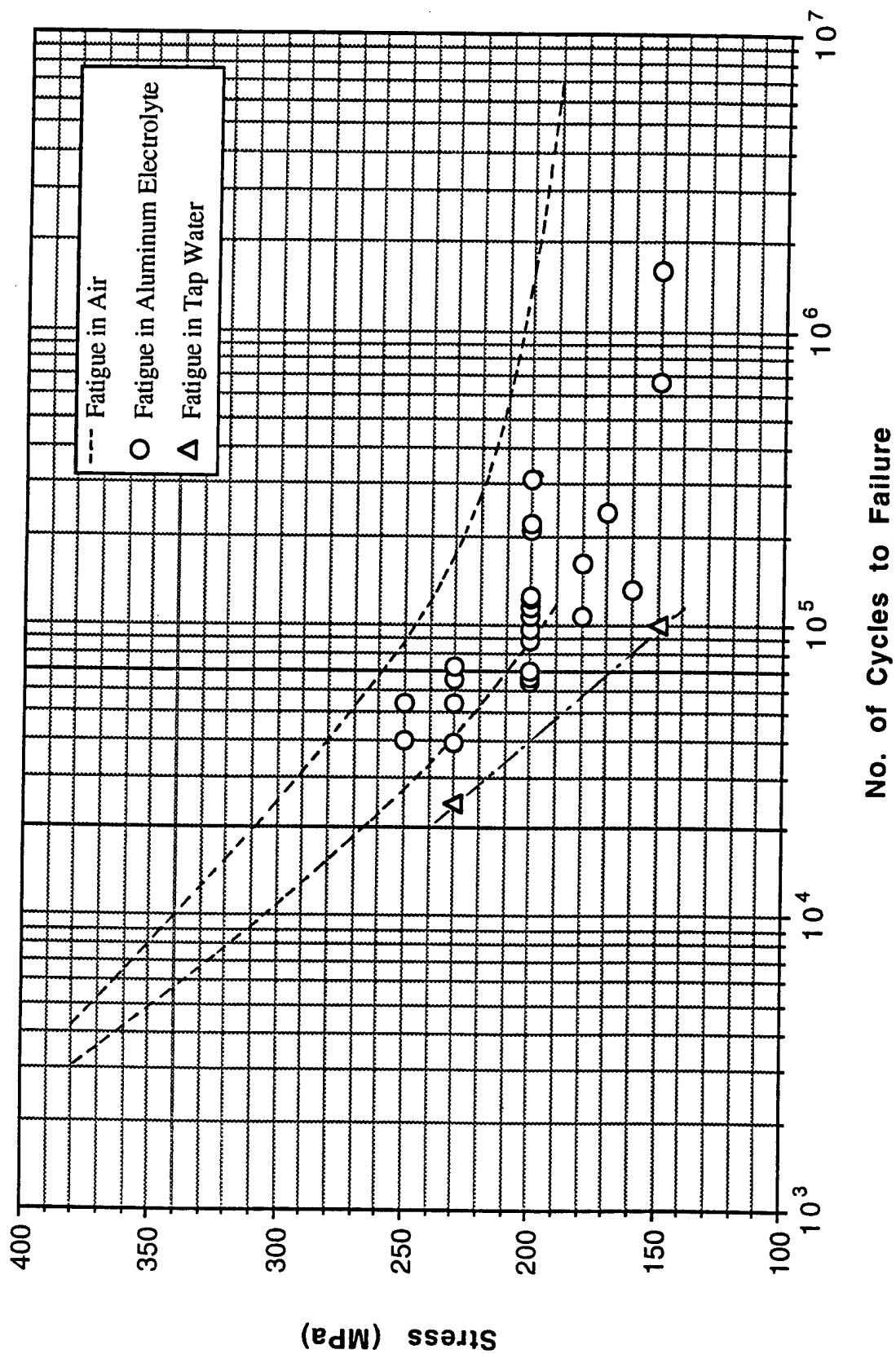
Figure 3-12. Stress vs. number of cycles to failure, R=-1, 0.5 Hz for 7075-T73 aluminum alloy in air; liquid aluminum electrolyte; and tap water.
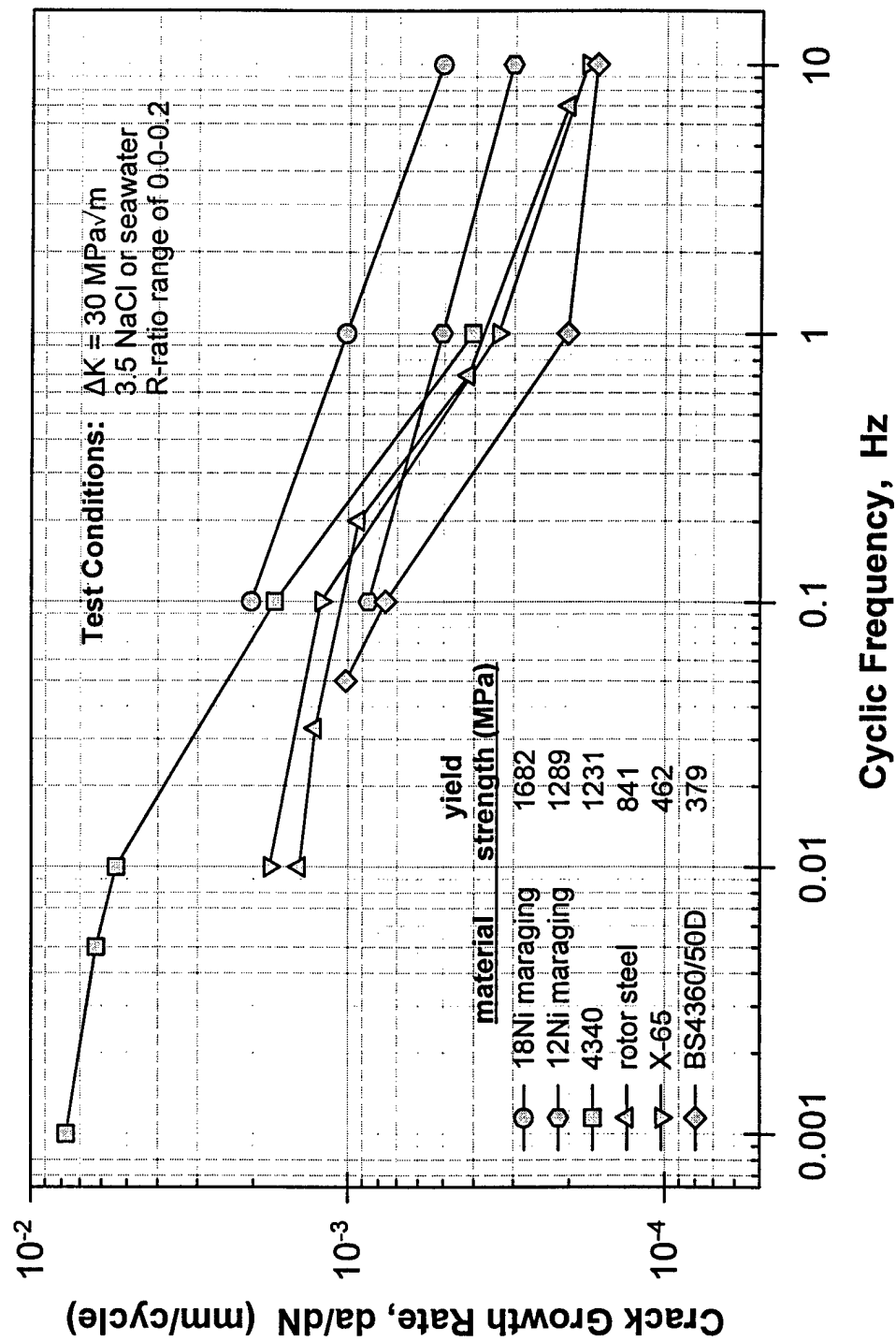
Figure 3-13. Influence of frequency on environmental crack growth in 3.5% NaCl or seawater for a variety of different steels [3.10].
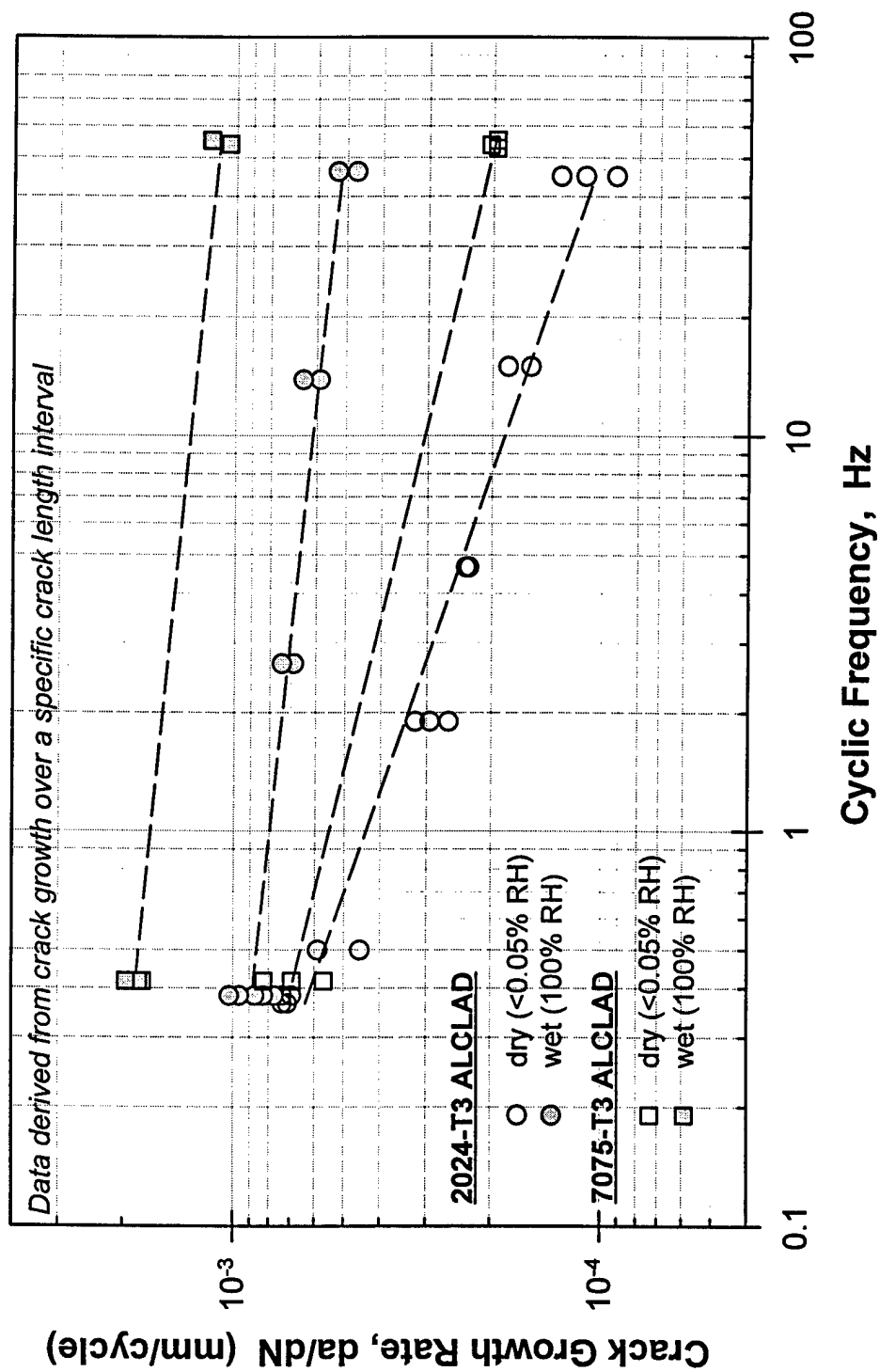
Figure 3-14. Influence of frequency on environmental crack growth in dry and wet air for a two structural aluminum alloys [3.11].
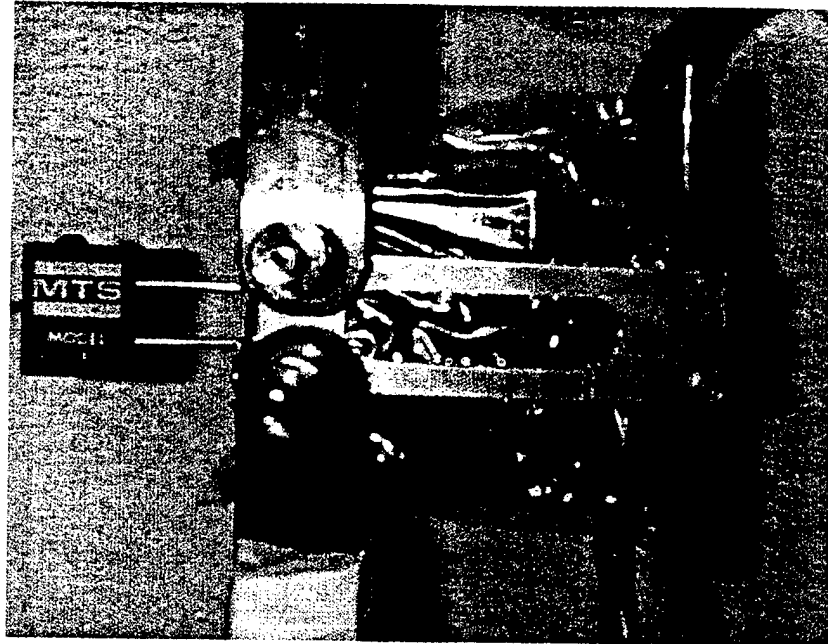
Figure 3-15. Photograph of the environmental fatigue crack growth setup.
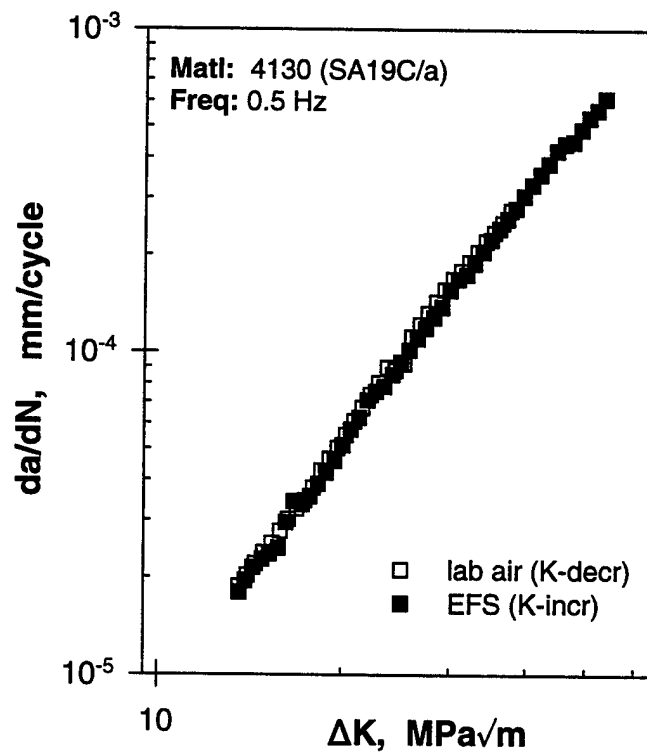
Figure 3-16. EFS and lab air environment for 4130 steel.
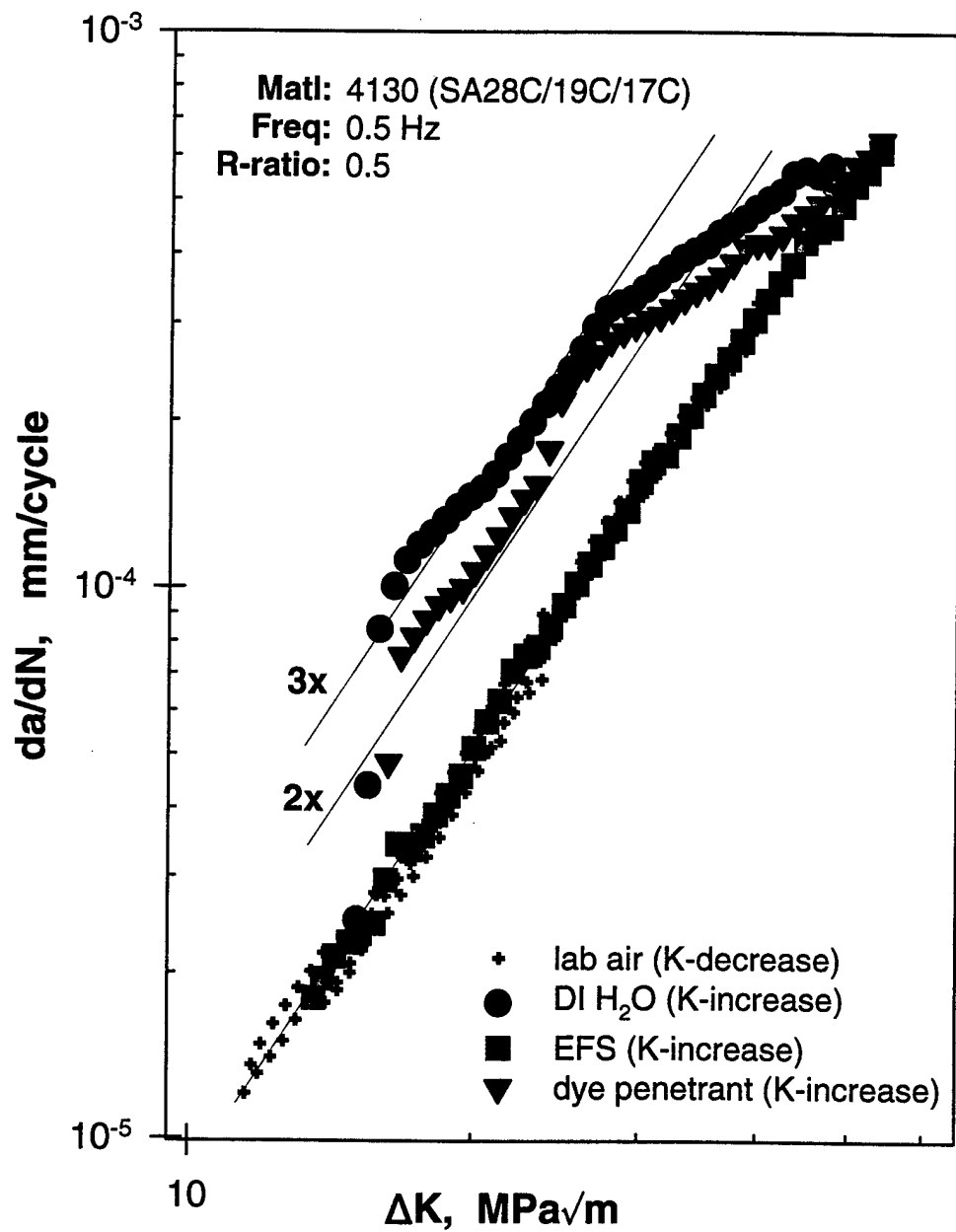
Figure 3-17. Comparison between lab air, water, EFS electrolyte and dye penetrant for 4130 steel.
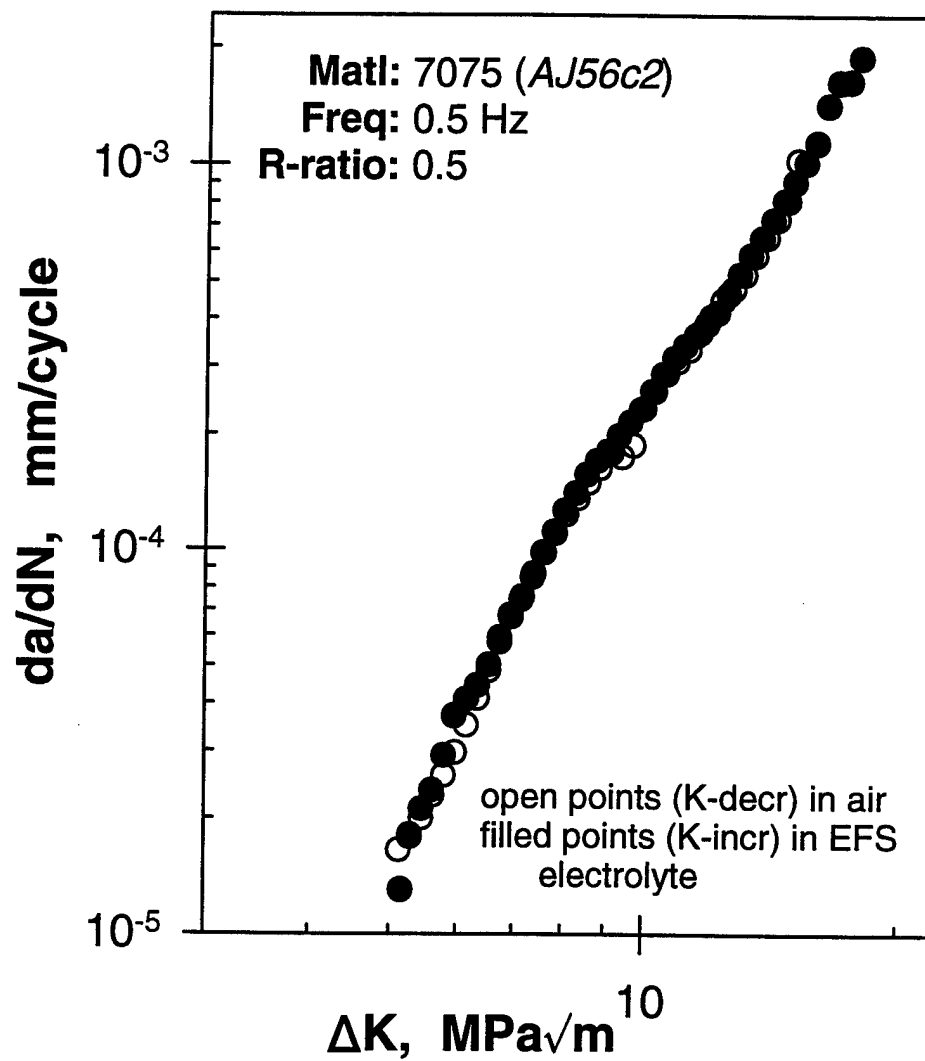
Figure 3-18. Fatigue crack growth behavior of aluminum in air and EFS electrolyte.
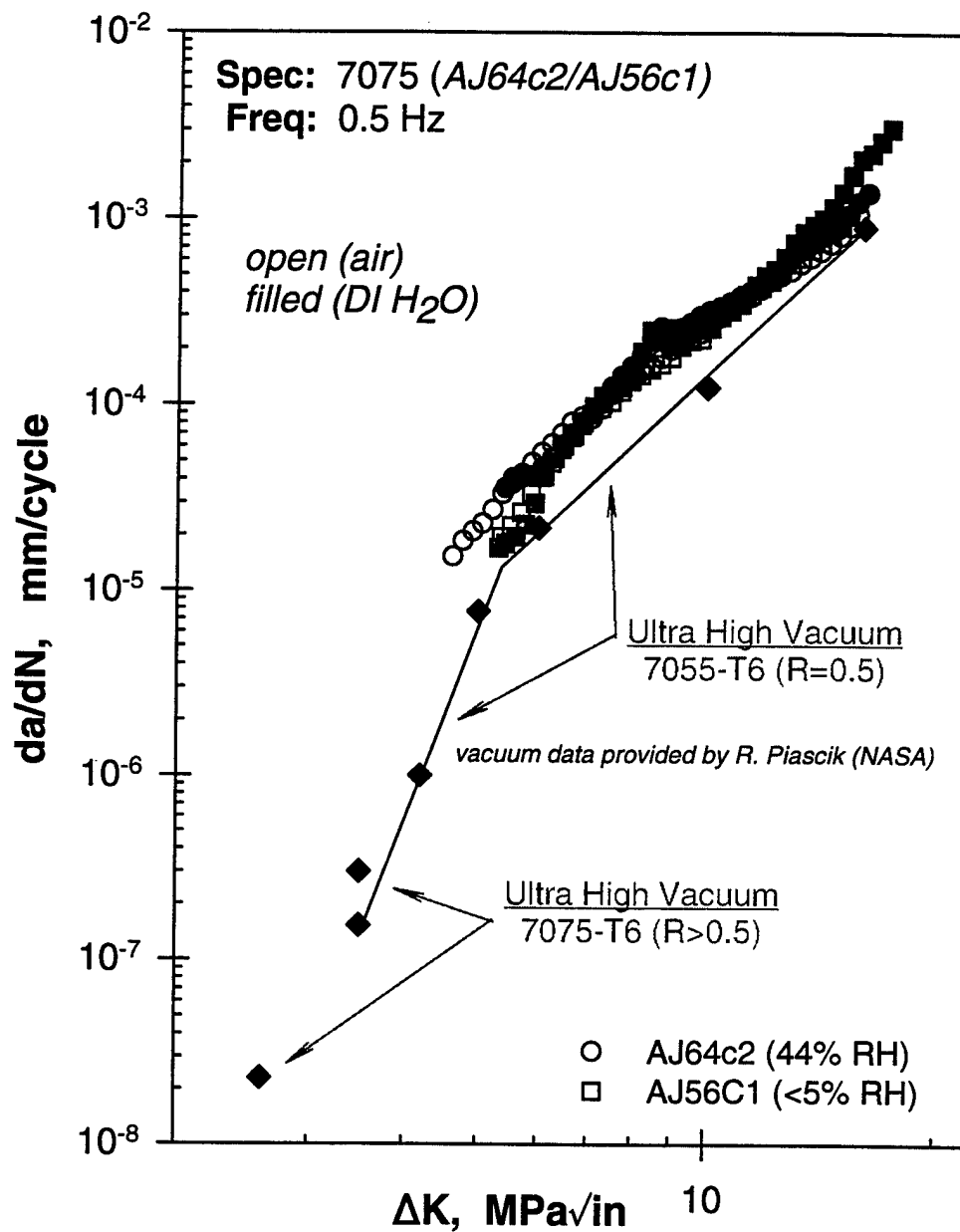
Figure 3-19. Comparison between FCG rates in air and water at 0.5 Hz and vacuum data for 7xxx aluminum alloys.
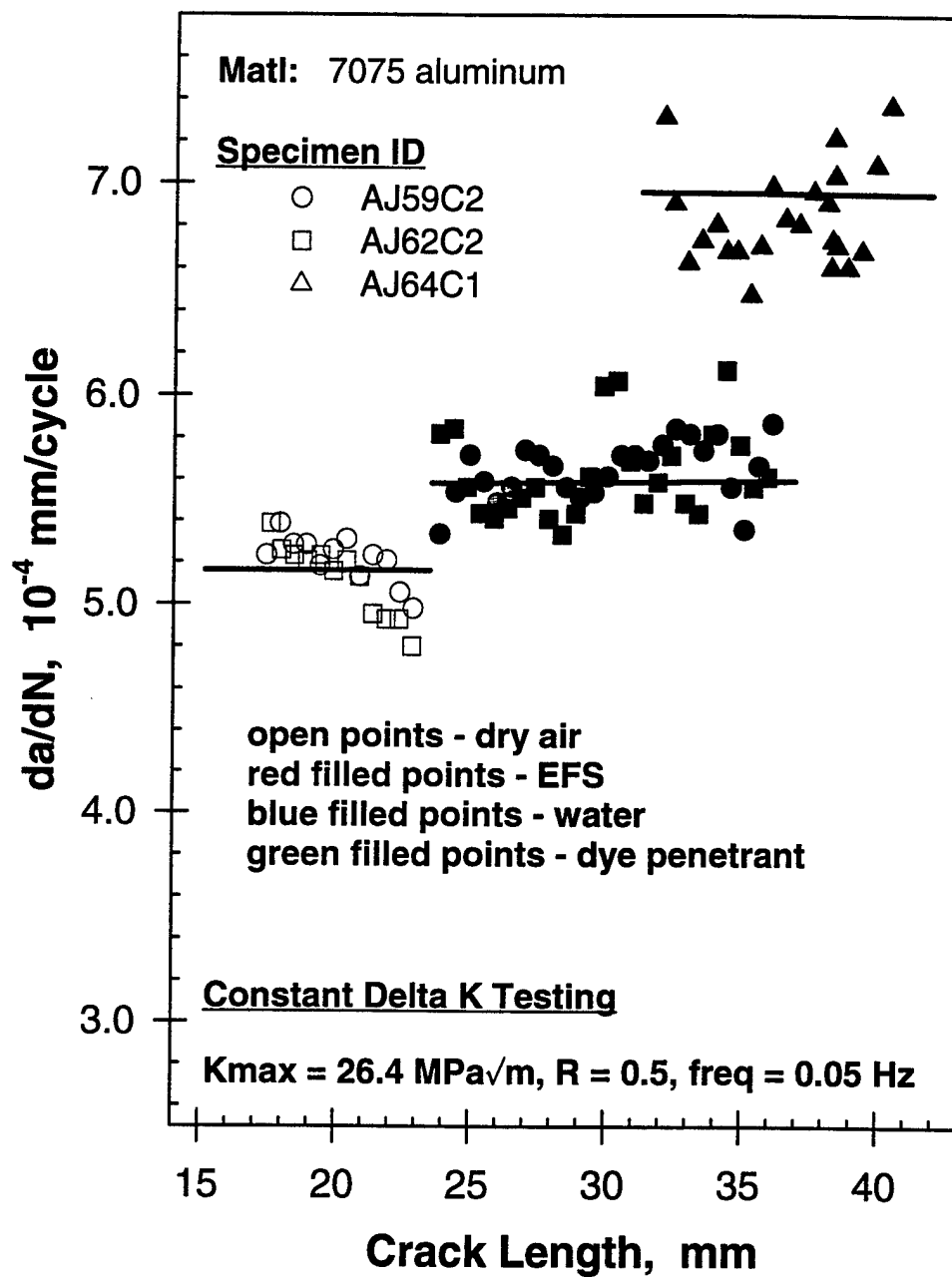
Figure 3-20. Constant-ΔK FCG tests for aluminum in various environments performed at 0.05 Hz and an R-ratio of 0.5.
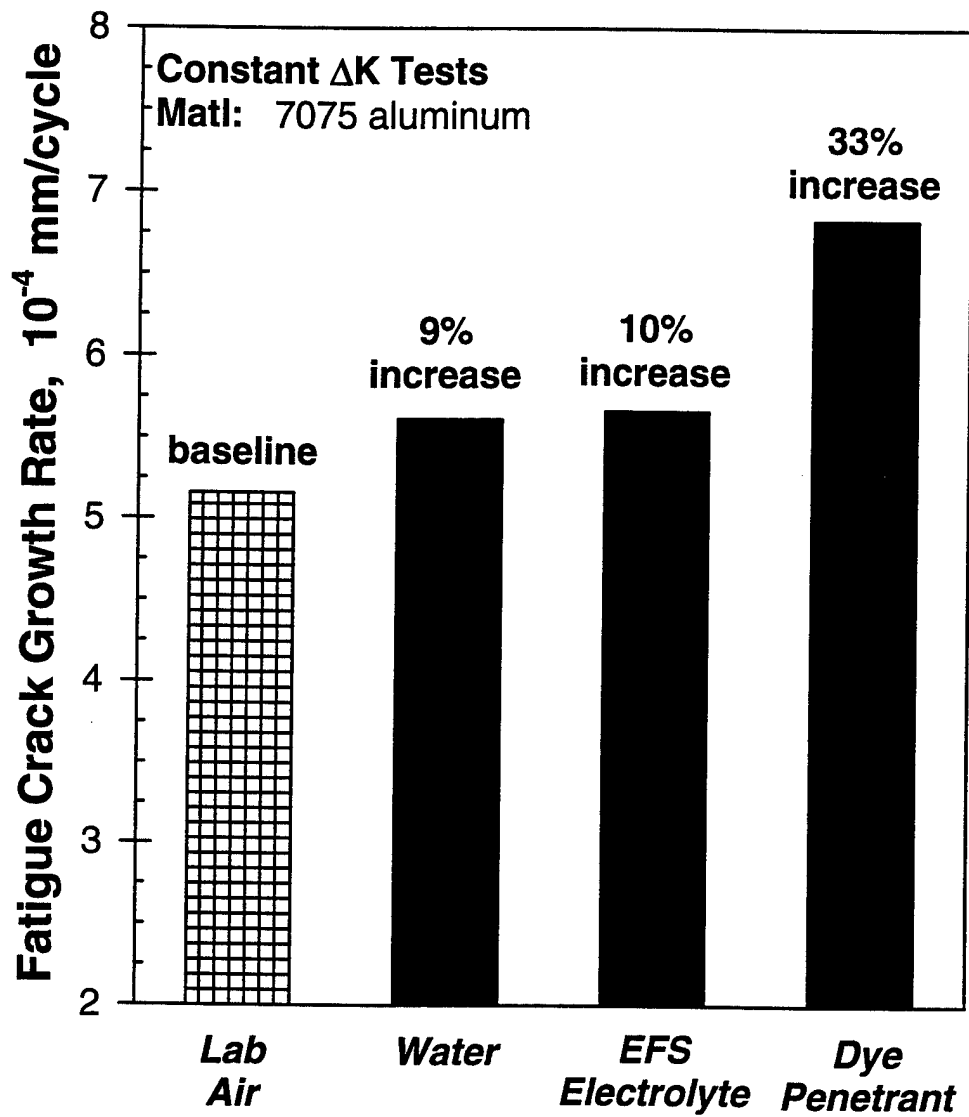
Figure 3-21. Comparion between crack growth rates obtained during constant-ΔK tests for aluminum in various environments performed at 0.05 Hz.
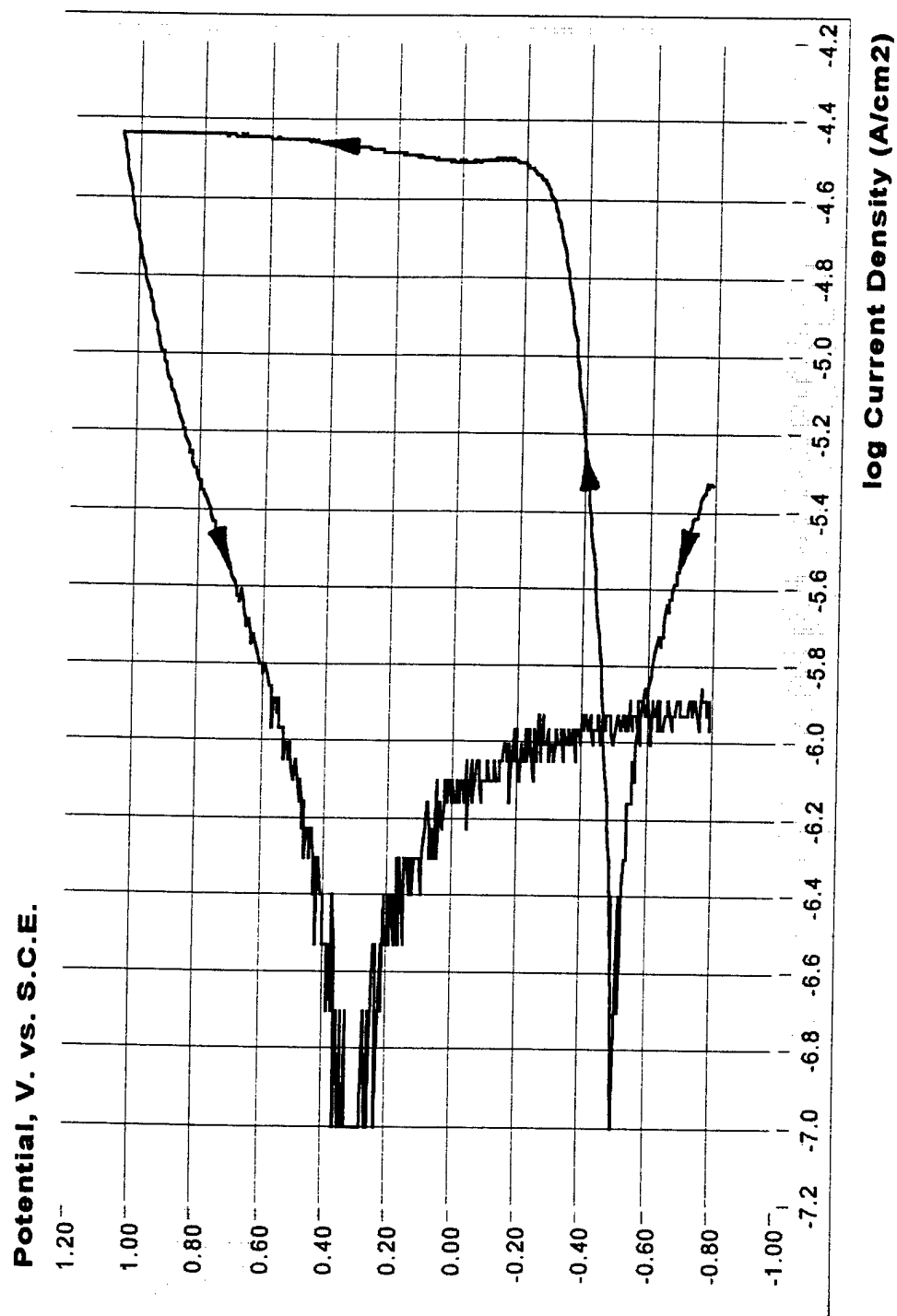
Figure 3-22. Anodic polarization cycle for aluminum alloy 7075-T73 in a gelled steel electrolyte; 0.3M H3BO3 + 0.075M Na2B4O7. 10H2O + 0.06M Na2MoO4. 2H2O. (Scan Rate: 5mV/sec)
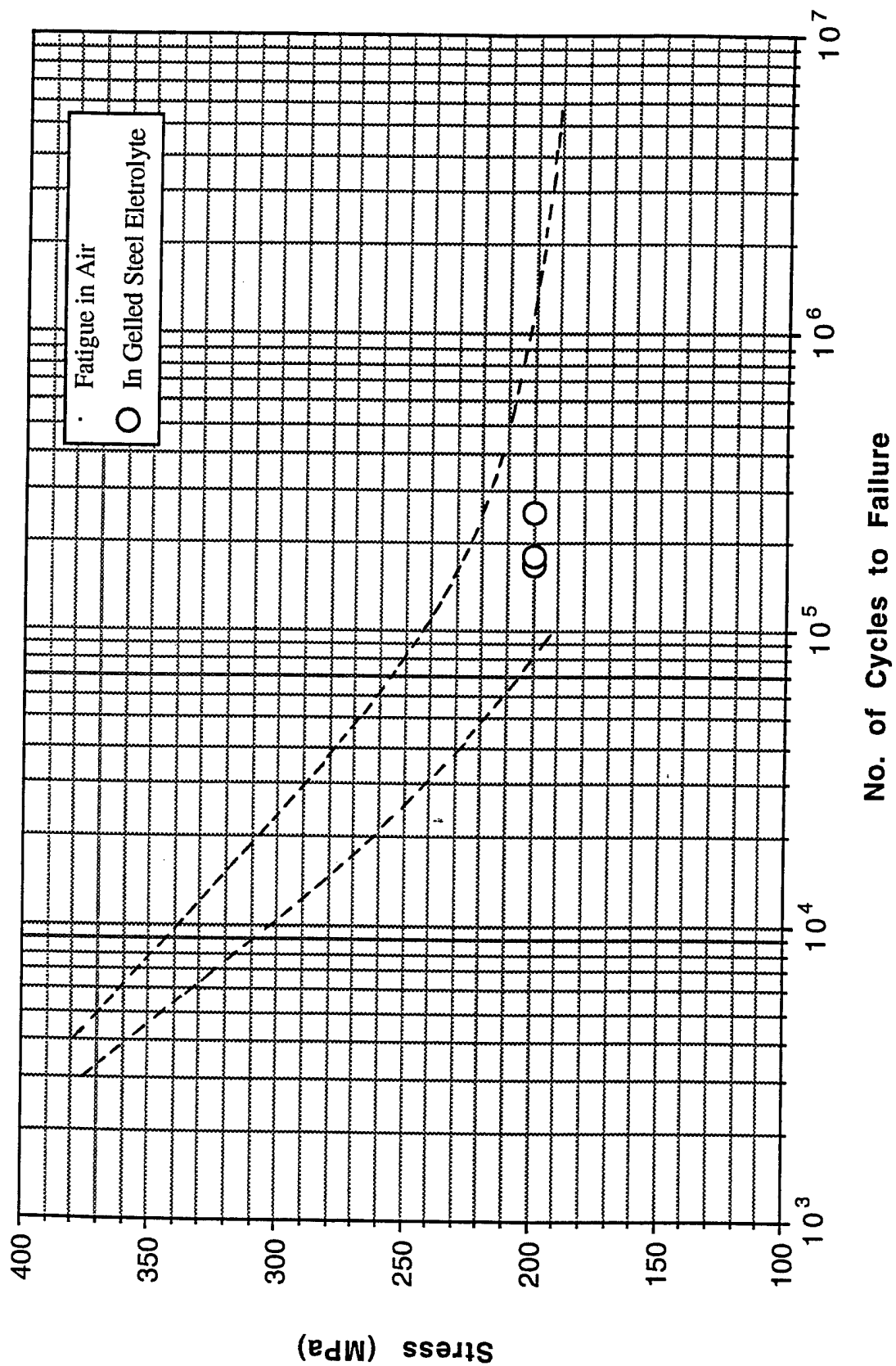
Figure 3-23. Stress vs. number of cycles to failure, R=-1 for 7075-T73 aluminum alloy in gelled steel electrolyte.

4.0 ELECTRODE OPTIMIZATION:

4.1 Objective and Approach:

The basis for the electrochemical fatigue sensor rises from original experiments utilizing a three-electrode system driven by an electronic potentiostat to appropriately polarize (passivate) the metal under study. It is the objective of this effort to simplify the EFS by developing a workable two-electrode system which will

- function with existing and newly developed electronic potentiostats; and ultimately,

- function to inherently provide the necessary polarizing potential and the associated current to the metal under study so that EFS measurements are driven without the use of an electronic potentiostat.

4.2 Development of an Electronically Driven, Two Electrode System

As previously stated, the objective of electrode development in this study is to maintain the aircraft surface, whether coated or uncoated, at a passive potential that enables measurable signals of electrochemically generated currents as a result of cyclic, mechanical loading. Electronic potentiostats function to maintain the potential of a working electrode, in this case the aircraft surface, at a chosen value as measured against a standard reference electrode, *e.g.*, saturated calomel. A third electrode or counter electrode is included in the circuit to provide or receive the necessary charge to the working electrode. When the working electrode is polarized in the passive region, a low corrosion current (~microamps/sq. cm.) is realized. It is this current which is monitored for changes brought about by surface effects as a result of cyclic mechanical loading (*e.g.*, film rupture) that constitutes an EFS signal. The standard three-electrode system as it applies to EFS measurements is shown in Figure 4-1. In order to simplify the circuit, experiments were performed without the use of the calomel reference electrode and its attendant liquid junction/salt bridge glass ware. The platinum counter or auxiliary electrode is now required not only to provide the necessary charge from the potentiostat but to do so at a maintained passive potential on the surface of the working electrode. This circuit is described as

a potentiostatic zero resistance ammeter which allows for the continuous measurement of the required current. A full description is given in reference [4.1.]

4.2.1 Electrode Selection

A major requirement for the second electrode in an electronically driven two-electrode system is chemical as well as electrochemical stability. The logical choice is platinum since it serves as the electrode in the universal standard hydrogen electrode against which all electrochemical potentials are referred. The secondary standard saturated calomel electrode's potential value is measured against hydrogen as its benchmark. Platinum exhibits the requisite non-polarizing behavior, *i.e.*, stability over wide ranges of imposed potentials as well as chemical inertness. Brief consideration was given to silver as the second electrode in this study since its cost is less than platinum. A few successful experiments were realized with silver but its use was abandoned since its inertness cannot be guaranteed under expected conditions (its tendency to tarnish in industrial atmospheres). Successful use of platinum in the two electrode, electronically driven (potentiostat) system is has proven acceptable for EFS measurements on steel in both liquid and gelled electrolytes as described in Section 5.4.1.1. Thus, the preferred auxiliary or counter electrode in the electronically driven two-electrode system for EFS measurements is platinum, usually in the form of wire mesh to assure sufficient surface area.

4.3   Development of a Self-Driven Two-Electrode System

A self driven, two-electrode system with the second driver or power electrode providing the appropriate electrochemical potential in the passive region to the working metal electrode, would greatly simplify and ruggedize the hardware for EFS measurements. The driver electrode, unlike platinum in the electronically-driven, two-electrode system, would now serve a triple purpose. Hence, the driver electrode would effectively replace the potentiostat, the calomel reference electrode (including the salt bridge), and the platinum counter electrode.

A non-polarizing electrode with a stable electrochemical potential sufficiently noble to the aircraft alloys of this study might be used to impose the necessary passivity to these alloys enabling EFS measurements without the use of the typical two- or three-electrode potentiostated

circuit. Reversible metal/metal oxide systems extant could be explored for this purpose. A nickel-nickel oxide (Ni/NiO) system was a likely candidate for such a system based on:

- a body of knowledge exists on this electrode as it applies to a similarly polarized electrochemical device to detect and quantify embrittling hydrogen—*i.e.,* the "barnacle electrode," in high strength steels [4.2, 4.3], and
- Ni / NiO is commercially available and inexpensive.

Ni/NiO electrodes have long been used as cathodes in ambient temperature power systems. The electrode consists of a nickel metal substrate with a layer of hydrated nickel oxide deposited on the surface. The resulting potential for the electrode in neutral or alkaline aqueous solutions is thermodynamically stable (non-polarizing) and is thus capable of imposing its own half-cell potential on the surface of metal anodes; in this case, the aircraft alloys. A variety of compounds consisting of nickel, oxygen, and hydrogen have been claimed as a result of charge and discharge of nickel "oxide" electrodes. X-ray diffraction measurements indicate that β-NiOOH and $Ni(OH)_2$ exist under ordinary charge-discharge conditions [4.4]. Since the currents in the EFS scheme of measurements are of the order of microamps, it is anticipated that the discharge of the Ni/NiO electrode will not be problematical in the expected time frames (weeks). Nickel-cadmium power systems maintain their power output over a time frame of months [4.5].

4.3.1 Electrochemical Potential and Stability of Ni/NiO

Commercially available Ni/NiO electrode material was obtained [4.6], and its reversible potential was measured vs. saturated calomel in both the steel and aluminum liquid electrolytes (Electrolytes 7 and 8 in Table 3-1) using a high impedance electrometer. For the first thirty hours, the potential drifted approximately one tenth of a volt, stabilizing at 0.5 volts in the steel electrolyte, where it remained steady for one week. The same effect was noted with the aluminum electrolyte with stabilization occurring at 0.55 volts. The measured potential transient prior to stabilizing is consistent with excess capacity associated with the initial discharge of freshly charged, new Ni/NiO plates which are known to require 48 hours of self discharge before stabilizing [4.7]. Thus, it appears that new or freshly charged Ni/NiO electrodes will require a settling-in treatment of at least thirty hours in the appropriate electrolyte prior to use.

4.3.2 Electrochemical Potential Stability of Ni/Ni O in the Presence of Current

In order to assess the electrode's stability with current in the system, a three-electrode circuit was employed with a potentiostat used to measure the potential of the Ni/NiO vs. calomel when galvanostatic currents were imposed between the Ni/NiO and a platinum counter electrode. The galvanostatic currents imposed ranged from 1 micro amp to 0.2 milliamps. These measurements were taken in both the steel and aluminum electrolytes with pHs of 8.4 and 7.0, respectively, over an electrode area of approximately six square centimeters. The potentials of 0.50 v. and 0.55 v. for the steel and aluminum electrolytes, respectively, remained constant for imposed currents of up to 30 microamps. Currents greater than 30 microamps resulted in significant potential drift. Thus, with electrochemical system currents below this value, as is the case with EFS measurements, the Ni/NiO electrode is expected to yield a stable, non-polarized potential on the surface of the working electrodes.

4.3.3 Imposed Passive Potentials by Ni/NiO on Aluminum and Steel

In order for Ni/NiO to be effective as the driving electrode in a two-electrode EFS measuring system, it must impose stable potentials within the passive regions of both the steel and aluminum alloys of this study for appropriate lengths of time. In order to monitor this potential, the experimental set-up depicted in Figure 4-2 was employed. The surface potential of the steel or aluminum alloy is monitored even as each of them is short circuited to the Ni/NiO electrode. The coupling of the electrode to the steel or aluminum results in an electrochemical system where the half-cell potential of the metal (anode) polarizes to the half-cell potential of the "stable" Ni/NiO electrode within the passive region of each metal. A single experiment was performed on both steel and aluminum in their respective liquid electrolytes, and one experiment on steel in its gelled electrolyte. The results are shown in the table below.

Table 4-1. Electrochemical Effects of Coupling Steel and Aluminum to an Ni/NiO Electrode Absent an Electronic Driver (No Potentiostat).

	POTENTIAL volts v. SCE Liquid / Gel	SYSTEM CURRENT micro amps/sq. cm. Liquid / Gel
STEEL	0.475 / 0.475	0.2 / 0.05 – 0.1
ALUMINUM	0.485	0.5

The data of Table 4-1 were obtained from the experiment depicted in Figure 4-2 after a settling-in period of 30 minutes. The exposed areas of the steel and aluminum working electrodes as well as the area of the Ni/NiO driver were approximately 10 square centimeters. The potentials noted for both the steel and the aluminum held steady for at least one week (for steel both in liquid and in gelled electrolyte). The very low system currents is indicative of both the steel and aluminum existing in their respective passive zones. The potentials of 0.475 v. and 0.485 v. vs SCE, verifies this passivity as is noted previously in the anodic polarization plots for aluminum and steel (Figures 3-4 and 3-5). Thus, this experiment lends great encouragement for the future use of Ni/NiO as a driving electrode for EFS measurements.

4.3.3.1 Corrosion of Substrates Polarized by Ni/NiO Electrodes: It was necessary to ascertain the effect of the electrode's imposed polarization potential on the corrosion tendency of the working electrodes, e.g., steel and aluminum. Corrosion inspections for pitting and weight loss experiments (details of which are given in Section 3) were performed on both aluminum and steel coupled to Ni/NiO in the requisite electrolytes, including the gelled steel electrolyte, for a period of two weeks for steel and 10 days for aluminum specimens. Both the steel and aluminum tests showed no sign of pitting or weight loss, indicating that both metals are held in their passive, inactive state while coupled to the Ni/NiO electrode. Thus, it is concluded that the natural potential imposed on the surfaces of the alloys tested by the commercial Ni/NiO electrode provides the requisite passivity without any surface degradation such as general or pitting corrosion.

4.3.3.2 Size Effects of Ni/NiO Electrodes: Since the Ni/NiO electrode maintains a half cell potential which naturally imparts a desired voltage on the alloys of this study when coupled and immersed in the appropriate electrolytes, there must exist some finite time of discharge for various anode to cathode area ratios. The discharge reaction in aqueous solutions is believed to be the following [4.8]:

$$NiOOH + H_2O + e \longrightarrow Ni(OH)_2 + (OH)^- \tag{4.1}$$

Thus, the reduction of nickel oxyhydroxide to nickel hydroxide is finite and as such depends on the amount of surface area available. Preliminary experiments were performed to determine

suitable driver-electrode-to-working-electrode surface areas (cathode-to-anode area ratios). It was found that if the Ni/NiO surface area was roughly equal to that of the working electrode, the electrochemical parameters assuring the required passivity was achieved for at least one week. This was shown to be true for steel in both liquid and gelled electrolytes and for aluminum in its liquid electrolyte. Thus, any prototype two-electrode EFS cell design that uses Ni/NiO as its power electrode should incorporate same with a surface area greater than or equal to the size of the exposed working electrode. It is anticipated that exposed areas of the EFS on actual aircraft will be of the order of several square centimeters. This is a realistic surface area for a Ni/NiO driving electrode in an EFS cell.

4.3.4 EFS Behavior with Ni/NiO as the Driving (Power) Electrode

Having established the stability and the electrochemical suitability of Ni/NiO in a static sense, EFS experiments were performed on steel round bar specimens exposed to liquid steel electrolyte. The use of a two-electrode EFS system with the second electrode acting as a driver greatly simplifies the measuring circuit by eliminating the need for a potentiostat and its attendant complexities. The simplified circuit schematic is shown in Figure 4-3, which employs an electrometer, capable of measuring small current signals with appropriate outputs for data acquisition. Three EFS experiments were performed, the results of which are shown in Table 5-17 and further discussed in Section 5.4.7. Although results were not optimal, the characteristic EFS response was clearly obtained during the fatigue and the onset of cracking processes. There remains a considerable amount of experimental work to be done in optimizing the driving two-electrode system before it can be routinely used in electrochemical fatigue sensing measurements, not the least of which is improved signal processing techniques.

The work thus far performed shows the feasibility of such a system and lends great encouragement to its ultimate success.

4.4 Summary

The objective of this effort to simplify the EFS by developing a workable two-electrode system has been met for an electronically driven EFS measuring system. The system described

as a potentiostatic zero resistance ammeter using platinum mesh as the second electrode and a gelled electrolyte is now state-of-the-art EFS technology.

Great progress has also been made in achieving a two-electrode system that functions to inherently provide the necessary passive potentials to the metals under study enabling EFS measurements without the use of an electronic potentiostat. The initial successes with Ni/NiO represents a major step to this end and bodes well for the ultimate adaptation of an EFS system for field use.

4.5   References

4.1   Jones, D. A., "Principles and Prevention of Corrosion," Macmillan Publishing Company, section 6.3.2, p. 180 (1992).

4.2   Berman, D. A., Beck, W., and DeLuccia, J. J., "The Determination of Hydrogen in High Strength Steel Structures by an Electrochemical Technique," in *Hydrogen in Metals*, I. M. Bernstein and A. W. Thompson, eds., American Society for Metals, p. 595 (1974).

4.3   DeLuccia, J. J., and Berman, D. A., "An Electrochemical Technique to Measure Diffusable Hydrogen in Metals (Barnacle Electrode)," ASTM-STP 727, p. 256 (1981).

4.4   Jasinski, R., *High Energy Batteries*, Plenum Press, N. Y., p.81 (1967).

4.5   Ibid, p. 237

4.6   Puglisi, V., Director of Technology, Energizer Power Systems

4.7   Jasinski, R., *High Energy Batteries*, Plenum Press, N. Y., p. 81 (1967).

4.8   Motupally, S. et al., *J. Electrochem. Soc.*, 145, $N^{\underline{o}}$ 1, p. 34 (1998).
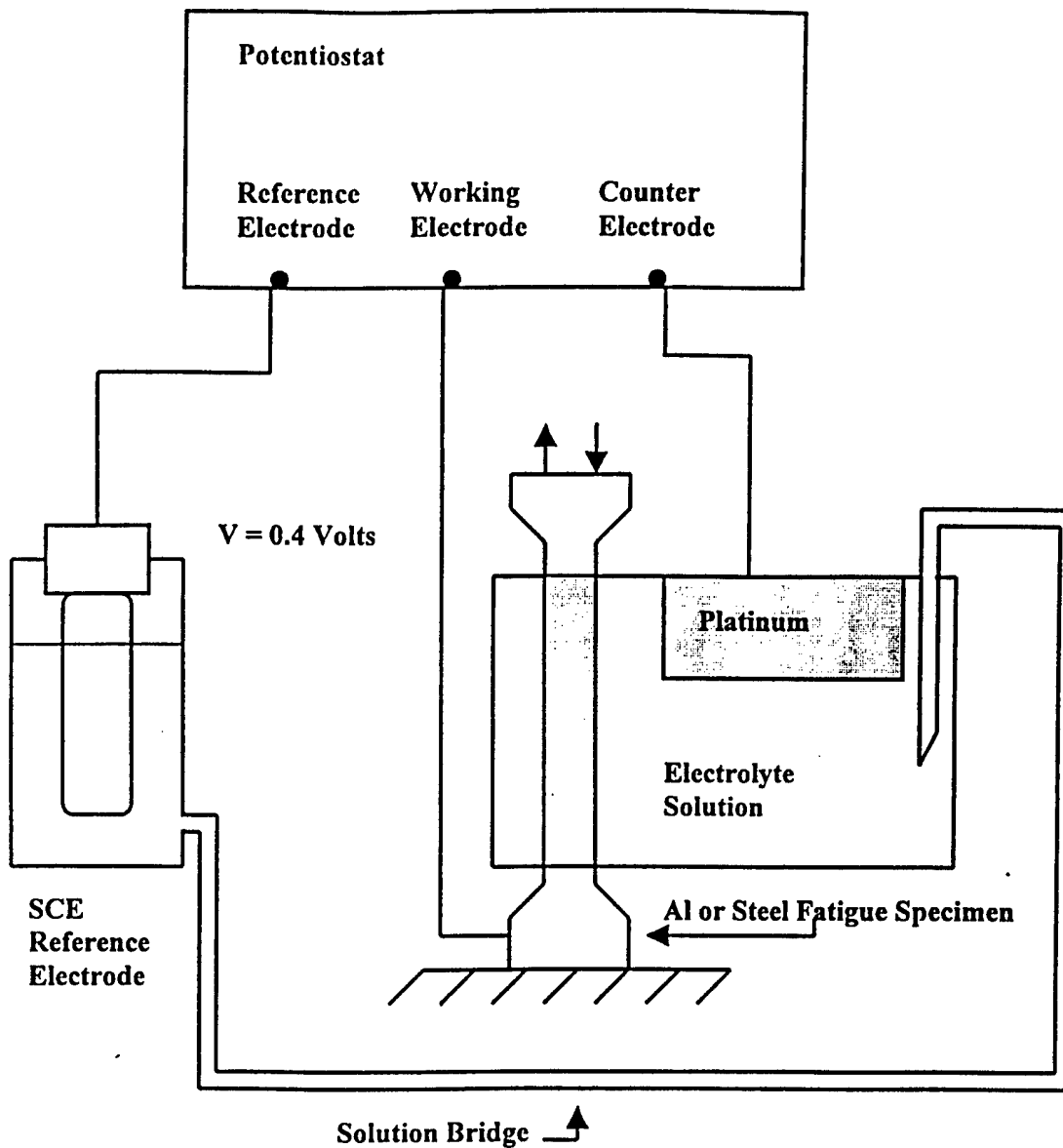
Figure 4-1. Typical three-electrode, electronically driven, EFS measuring circuit. Data acquisition system not shown.
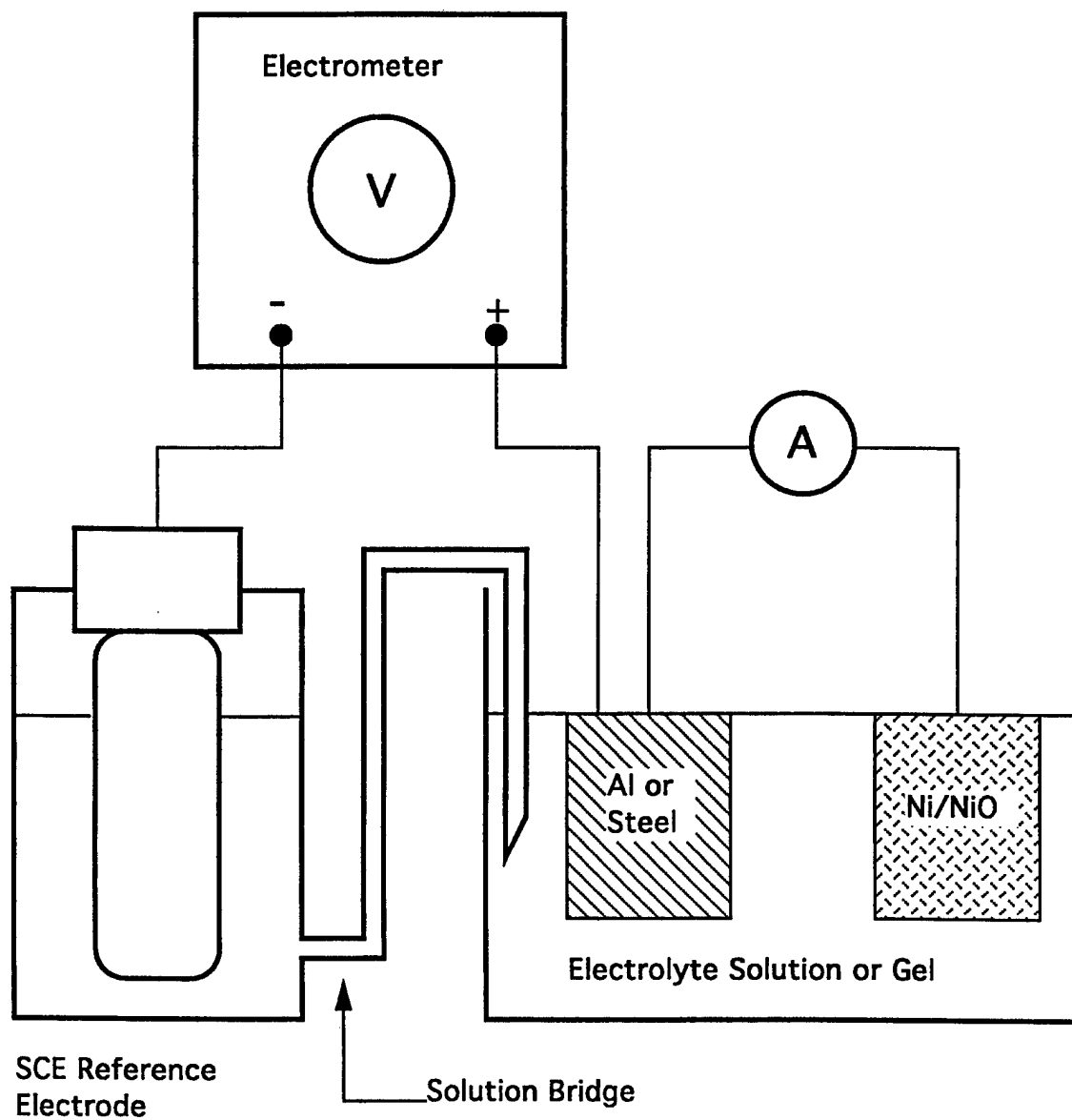
Figure 4-2. Experimental circuit to determine imposed potential and system current as a result of coupling a working electrode to a Ni/NiO driver electrode.
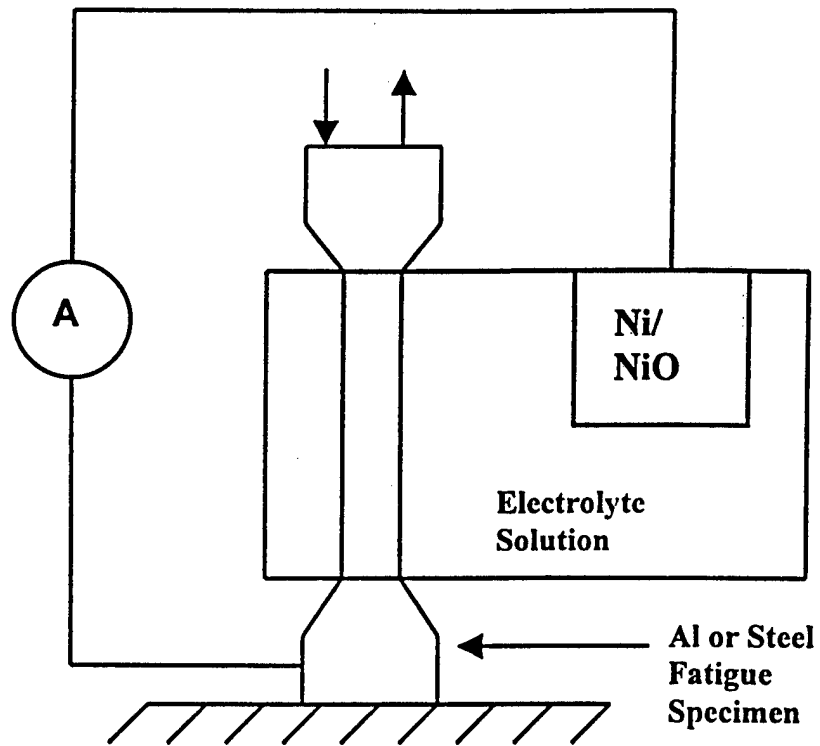
Figure 4-3. Simplified two-electrode EFS measuring circuit utilizing Ni/NiO as the driving (power) electrode. Data acquisition system not shown.

5.0 ELECTROCHEMICAL LABORATORY MEASUREMENTS

5.1 Objective and Approach

Since previous development work on the EFS had shown that the transient current of a three-electrode system could respond to both a stress cycle and the extent of the fatigue damage produced by many reversals of stress, it was necessary to show that such behavior would apply to the types of high strength materials used in aircraft construction and specifically that of the T-38. Previous work, for example [5.1–5.3], had dealt with ductile materials in which localized slip behavior developed early in life and cracks also initiated relatively early in life. Localized slip and cracking tends to develop later in the lives of high strength material.

Also, limited ranges of life had been explored in previous work, and effort had been focused on short life. Since damage develops early in life at high strains, the EFS was exposed to more rapid and extensive changes in fatigue damage than would occur at longer lives. Furthermore, all cycling had been carried out under fully-reversed conditions of cyclic strain (R= -1) and at the rather low frequencies (around 1 Hz) customarily used for high strain cycling. Although such frequencies are observed in aircraft performance during operational maneuvers, it was necessary to explore EFS response over a wider range of frequencies, applied stress, and loading ratios.

Still another issue relates to the surface condition of the material. In laboratory tests, specimen surfaces are usually highly polished and bare (*i.e.,* uncoated). In contrast, commercial surfaces are used in a wide range of finished conditions and are usually coated with metallic or organic coatings or combinations of coatings. Whether or not the EFS would perform satisfactorily through commercial finishes is an important practical issue, because application would be more difficult and expensive if the surface finish had to be removed before testing (and replaced afterwards). Moreover, mechanical removal of the finish could alter the state of the fatigue damage which usually (but not always) is concentrated at the surface.

Furthermore, the great majority of previous EFS research has been performed in liquid electrolytes. While such electrolytes are convenient to use in the laboratory, they are undesirable in the workplace due to the possibilities of accidental spillage, seepage into crevices, difficulty of post testing cleanup and the difficulty of handling. Therefore, as reported in Sections 3 and 4, a large effort was expended in developing suitably formulated gels, which would avoid the inconveniences of liquids in the workplace. Even if gels can be developed which are suitable for their chemical behavior, it is necessary to establish that their performance will be satisfactory from the physics aspects when applied in the EFS.

So far [5.1–5.3], specimens explored by the EFS have been tested, in the majority of experiments, for the whole of life under electrochemical control. Such exposures would be typical of service conditions if EFS would be used for continuous monitoring in aircraft structures. However, it is also envisaged that periodic testing would be used to track the development of fatigue damage. When a three electrode cell (or some variant thereof) is applied to a metal surface, time-dependent chemical changes occur and such conditioning (especially if passivation is desired) will possibly influence the EFS behavior and the capacity of the instrument to detect fatigue damage. It is necessary, therefore, to determine how "settling in" occurs and the kinetics of the process. It is also necessary to establish whether the EFS will respond faithfully to the state of the fatigue damage if it has developed in an environment different from that of the EFS.

The onset of cracking in fatigue is usually detected by the EFS through the occurrence of a crack peak in the transient current. In early work [5.1–5.3], a small crack was detected in polycrystalline 316L stainless steel by its demonstration as a crack peak. The minimum crack size detectable in high strength materials and particularly the high strength aircraft materials applied in the T-38 needs to be established.

In light of the above needs, the work summarized in this task was conducted to provide additional fundamental and applied information on EFS behavior, with the objective of exploring the following properties, variables and testing protocols:

1. EFS behavior of T-38 airframe materials, viz., 4130 steel in the quenched and tempered condition, 7075-T731 and titanium alloy Ti-6Al-4V (see properties in Section 2);

2. EFS response in liquid and gel electrolytes;

3. EFS behavior under a wide-range of applied cyclic stresses and fatigue lives;

4. EFS behavior as influenced by load ratio (R);

5. EFS behavior as affected by cyclic frequency, especially at frequencies greater than 1Hz;

6. EFS behavior in intermittent, as opposed to continuous, immersion in electrolyte;

7. EFS behavior in bare metal and coated specimens.

The experimental approach taken to investigate the problems listed above was to employ laboratory tests of the type used in previous work [5.1–5.3], namely with the whole specimen immersed in electrolyte, as if an electrochemical test was being performed, and with the cell set up as a standard three electrode cell and using conventional reference electrodes (usually the calomel electrode for the electrolytes and salt bridges used here). However, as reported in Sections 3 and 4, effort was directed to optimizing the cell and electrode design. This provided the opportunity to explore EFS behavior in two- (rather than three-) electrode cells, with and without the application of the potentiostat to control the electrochemical behavior.

Further, in previous work [5.1–5.3], an electrically isolated electrochemical system was used, to avoid interference from or to the electrohydraulic machine being used to cycle the specimen, as well as to insure the validity of the electrochemical results, since the transient current is usually very small and its measurement is demanding. In this respect, Penn and SwRI took different experimental approaches in light of their different program responsibilities: SwRI continued with the use of an isolated electrochemical system. Penn initiated their testing program using an isolated system but subsequently explored and developed different types of potentiostats to do away with the need for electrical isolation. This was done for the practical reason that eventual application of the EFS technology to aircraft cannot reasonably be performed using isolated electrochemical systems and effort had to be directed to this problem in the long run whatever the outcome of the research developments. SwRI had the responsibility of looking at the larger scale aspects of isolation in the aircraft environment which freed them from

the need to deal with the potentiostat problem (Section 9). Also, from the SwRI interest in EIS (Section 6), they were constrained to use commercial potentiostats having a wider range of capabilities—particularly, higher frequency response. In the results section that follows, the data reported by Penn were all gathered from the non-isolated system, while all SwRI results were obtained using electrically isolated specimens.

There is another aspect in which Penn and SwRI took different approaches. Penn emphasized the investigation of long fatigue lives, and SwRI short ones. Since the mechanics and kinetics of damage differ for these different conditions, the two groups employed different techniques and software. Accordingly, SwRI results are reported in Section 5.2, and Penn's in a separate section, Section 5.3.

Since the EFS results are available as electrical perturbations of a carrier signal associated with the stress cycle, a generous opportunity is presented for data processing. For this reason, all the results were acquired through PC data acquisition systems using LabView software. Major efforts were needed to integrate the acquisition requirements of electrohydraulic testing in combination with electrochemical results. Special programs were created to process the data and to conduct routine manipulations on a day-to-day basis. However, an electronic connection was also established at Penn between the EFS systems and the more powerful computers of the Electrical Engineering Department to pursue more sophisticated lines of signal processing. Initially the data were too noisy and variable for development reasons to permit the most advanced processing to be employed. However, as the potentiostat systems were improved, the opportunities for advanced processing also improved and results of these efforts are reported in Section 5.4.

5.2   EFS Laboratory Measurements at SwRI

5.2.1   *Experimental Procedures*

Fatigue tests at SwRI with simultaneous measurement of potentiostatic current transients were conducted in the test cell shown in Figure 5-1. The cell was constructed using a glass cylinder (15.2 cm in diameter and 3.8 cm in height) with the top and bottom lids made of polytetrafluoroethylene (PTFE). A neoprene o-ring and a PTFE nut provided a tight seal around

the specimen at the bottom of the cell. No o-ring was used at the top lid to avoid friction with the specimen during cyclic loading. Two semicircularly bent, thin sheets of platinum (only one is shown in Figure 5-1) were used as a counterelectrode located around the specimen to provide an even distribution of current. A saturated calomel electrode (SCE) was used as reference and a Luggin capillary with a porous silica tip connected the electrolyte in the cell with the SCE.

Tests were conducted using a Solartron 1287 potentiostat to control the potential applied to the specimen. Applied potentials were checked periodically during the testing program using a Keithley Model 614 electrometer. Cyclic loading was accomplished using a MTS 810 servohydraulic test machine. The potential and current analog output signals from the potentiostat and the load and displacement outputs from the MTS were input into a Pentium computer with an 8 channel, 16 bit National Instruments A/D data acquisition board. The LabView 4.1 software was used to collect, manage, and display (in a monitor screen) the cyclic load and transient current data. Two complete experimental set-ups including the servohydraulic testing machine, potentiostat, and data acquisition system were used in the testing program at SwRI. A detailed view of the test cell and the load train is shown in Figure 2-1. The universal joint shown in Figure 2-1 was only used in preliminary tests but eliminated in further testing. It is important to emphasize, as noted in Figure 2-1, that the specimen was electrically isolated from the load frame through a specially designed coupling. The purpose of the electrical isolation was to avoid ground loops and the concurrent development of spurious signals because the optimum potentiostat operation (higher signal to noise ratio) occurs when the specimen is only connected to ground via the potentiostat.

Tests were conducted following a well-established procedure to minimize variability in the data. Specimens were mechanically polished down to 600 grit SiC paper prior to being placed in the cell. The cell with the specimen in place was then installed in the servohydraulic machine using a specially designed collet grip at the lower end of the specimen and a threaded joint at the upper end. The cell, which was open to the atmosphere, and the Luggin capillary were filled with approximately 500 mL of the test solution. As described in Section 3.0, the following solutions were used in the tests:

7075 T-7351 Al alloy: 0.3 M $H_3BO_3 + 0.005$ M $Na_2B_4O_7 + 0.06$ M Na_2MoO_4; pH = 6.9
4130 Steel: 0.3 M $H_3BO_3 + 0.075$ M $Na_2B_4O_7 + 0.06$ M Na_2MoO_4; pH = 8.4
Ti-6Al-4V alloy: 0.3 M $H_3BO_3 + 0.075$ M $Na_2B_4O_7 + 0.06$ M Na_2MoO_4; pH = 8.4

After attaining a stable open circuit potential in the air saturated solution, the desired potential was applied and cyclic loading was initiated after approximately one hour when a steady state current was reached. In all tests, cyclic loading was performed under stress control. No attempt was made to measure the strain response in the gage length of the specimen. However, as noted above the displacement of the collet grip was monitored.

Most of the tests were conducted until failure occurred. The fractured portions of the specimens were washed and dried, and preserved for further examination, if needed. In selected tests, however, cyclic loading was interrupted before failure and the specimen was removed from the cell for optical examination to detect incipient cracks corresponding to the occurrence of specific patterns in the EFS signal.

5.2.2 EFS Signal Processing and Analysis

The objective of this activity was to extract EFS signal features that can be related to the evolution of fatigue damage. The approach adopted was the development of a computer program for processing the EFS signal to facilitate further analysis of features that are characteristic of different stages in the fatigue life of the aircraft alloys examined.

5.2.2.1 Development of EFS Data Scanning Program

A quick-look data analysis program was developed using the LabView® 5.0 software to provide an efficient tool for analyzing the changes of the EFS signal during the entire fatigue life. Figure 5-2 shows a typical screen of the program exhibiting five fatigue cycles of the load signal as an output of the servohydraulic machine and the filtered EFS current. The program provides single-scan and auto-scan modes for reviewing the EFS data.

As shown in Figure 5-2, the upper part of the screen displays information on the specimen, the number of cycles and the corresponding data file, and the test loading conditions. The lower part of the screen presents information on the power spectral analysis of the transient

current (using Fast Fourier Transform) and provides the values of parameters arising from signal processing as discussed below.

5.2.2.2 Design of a Digital Low-pass FIR Filter

A 10 Hz analog low-pass filter is used in the Solartron 1287 potentiostat to eliminate interference resulting mainly from the 60 Hz frequency of the AC voltage supply line. However, high frequency noise still exists in the EFS signal. This noise affects the programmed extraction of features from the EFS signal that may indicate the initiation and growth of fatigue cracks during a cyclic loading test. Therefore, a digital low-pass FIR filter was designed to remove the high frequency (> 20 Hz) noise from the EFS signal collected in the data files. Figure 5-3 illustrates the frequency characteristics of the digital filter. A flat top low-pass filter was used to minimize the frequency distortion from 0 to 5 Hz while a FIR filter was used to retain the phase of the EFS signal. This filter attenuates the signal level approximately 10.8 dB as shown in Figure 5-3. The phase and shape of the EFS signal are, however, preserved without changes in a particular sampling period despite the filtering of the signal. This assures that the analysis of the waveform evolution during the test is not affected even though the signal is attenuated.

5.2.2.3 Frequency Domain Analysis

The frequency spectrum of each segment of the EFS current signal during the fatigue life was analyzed using digital Fourier transform with the Hanning window (the Hanning window is used to reduce the artifacts caused by performing Fourier transform on finite length data). The relative magnitude of each frequency component of the transient current was plotted against the number of fatigue cycles for DC, 1, 2, 3, 4 and 5 Hz, as shown in Figure 5-4. The plot is useful to evaluate the changes in the various frequency components of the EFS signal during the course of the fatigue life.

5.2.2.4 Time Domain Analysis

The EFS signal exhibited waveforms that can be related to the tensile and compressive portions of the loading cycles during the fatigue test and were identified as T- and C-peaks respectively. The change of a T-peak to a C-peak or the opposite can be related to the fatigue life. To investigate the change from a T-peak to a C-peak, a bent-point detection algorithm was

developed to locate the peaks and valleys of the EFS signal. By comparing the EFS signal peaks with the peaks and valleys in the load signal, it is possible to differentiate T-peaks from C-peaks. A T-peak was defined as that corresponding to the tensile component of the load cycle (peaks marked with ● in Figure 5-2). A C-peak was defined as that corresponding to the compressive part of the load cycle (peaks marked with ■ in Figure 5-2). After separating the T-peaks and the C-peaks, the following features were extracted to characterize both waveforms:

1) Base – the minimum value (valley) of the waveform
2) Range – the difference between peak and valley of the waveform
3) Area – the total area under the waveform
4) Rise time – the slope of the rising edge of the waveform
5) Fall or decay time – the slope of the falling edge of the waveform
6) Width – the half-magnitude width (HMW) of the waveform
7) Spike – the difference between the peak of a spike and the valley of the waveform

In Figure 5-2, the base, range, area, rise time, fall time, and width of the T- and C-peaks are shown in the lower part of the screen for the cycle number listed at the top. Using these waveform features, it was found that the T- and C-peaks changed differently for the various materials during the course of the fatigue test. However, regardless of the material and test conditions, the T-peak eventually starts to dominate the whole EFS signal when the specimen is approaching failure. Figure 5-5 shows an example of the changes in the range of the T- and C-peak for 4130 Steel whereas Figure 5-6 illustrates the changes in the rise time for the T- and C-peaks during the same fatigue test. More detailed analyses of these features and their relationship to fatigue life are presented in Sections 5.4 and 5.5.

The emergence of current spikes in the EFS signal appears to be related to the initiation and growth of fatigue cracks during a cyclic loading test. Two methods were used to detect the spikes in the EFS signal. In one method a spike is detected indirectly by monitoring the change in the rise-time of a T- or C-peak. By examining the EFS signal, it was found that a spike often starts at the rising edge of a T- or C-peak. Figure 5-6 shows that the rise-time of the C-peaks

5-8

started to decrease abruptly at around 20,000 cycles. Concurrently, a spike was observed to emerge from the rising edge of the C-peak at the same cycle number.

A more direct method of detecting the current spikes is by using the bent-point detection algorithm. Figure 5-7 shows a view of the screen for the test of a 7075 Al specimen in which the detection of spikes (marked with ■) on the rising edge of the T-peaks is indicated. The amplitude of the spike is displayed in the lower right part of the screen. Changes in the spike amplitude during a fatigue test are plotted in Figure 5-8. In this example, it is shown that the spikes emerge from the rising part of the T-peak after about 4,500 cycles of fatigue life, for a specimen which failed after 6,000 cycles.

5.2.3 *EFS Response in Uncoated Materials*

5.2.3.1 General EFS Response of Bare7075 Aluminum Alloy

The transient current response of 7075 Al alloy to cyclic loading at a frequency of 1 Hz is shown, as a function of the percentage of fatigue life as a generalized damage parameter, for the periods early and late in life in Figures 5-9a and b. The plots correspond to a specimen tested at 345 MPa (50 ksi) and R $=$ -1, under an applied potential of 0.3 V_{SCE}, that failed after 11,387 cycles. The evolution of the current signal with fatigue life is clearly seen. The occurrence of current peaks associated with the tensile (T) and compressive (C) portions of the loading cycle is characteristic of the early life (Figure 5-9a), while late in life (Figure 5-9b) a more complex pattern develops. The emergence of a small peak in the rising part of the T-peak current, shown at 88.3% life in Figure 5-9b appears as a distinctive indication of fatigue damage, prior to the significant increase in the T-peak current associated with the sustained fatigue crack propagation that precedes failure. The baseline passive current density was approximately 2 A/cm^2 during most of the life but started to increase at a life percentage above 44 %.

The qualitative analysis of the main features in the variation of the EFS signal with fatigue life presented above improved significantly when the signal was analyzed as discussed in Section 5.3. Figure 5-10 shows, as a typical example, the filtered transient current at 15, 32, 70, 85, and $\approx$100 % of the fatigue life for an specimen that failed in 7,178 cycles under similar experimental conditions as above. The most important features in the different stages of fatigue

life can be described as follows. There is an initial stage in which the T- and C-current peaks coexisted with the T- peak being greater than the C- peak (Figure 5-10b). This stage was followed at about 15 % life by a relatively prolonged stage in which the amplitude of the T- and C-peaks are comparable, as shown in Figure 5-10c. The third stage was characterized by the development of a spike in the rising portion of the T-peak, which occurred in this case (Figure 5-10d) at about 70% of the fatigue life, while the C-peak was decreasing in amplitude. In the final stage preceding failure, the amplitude of the T-peak increased significantly and dominated the whole waveform (Figure 5-10e), accompanied by a significant increase in the mean current and the associated charge (Figure 5-10f), until final fracture occurred.

Variations of significant parameters used to characterize the EFS signal pattern, as described in Section 5.2.2, are shown in Figures 5-11 and 5-12, as well as in Figure 5-8 for the test discussed above. Figure 5-11 shows the significant increase in the amplitude of the T-peak that occurred at about 5,000 cycles, with a concurrent decrease in the amplitude of the C-peak. At about the same percentage of life, the electric charge (or area) associated with the T-peak also increased, as shown in Figure 5-12. However, the earliest indication of fatigue damage was provided by the occurrence and increase of the current spike in the rising portion of the T-peak that appeared at about 4,500 cycles (63 % life) as indicated in Figure 5-7.

Another specimen tested under the same cyclic loading conditions exhibited a similar EFS response. This specimen failed after 9,623 cycles and the current spike in the rising portion of the T-peak appeared at about 6,000 cycles (63 % life). The results of the tests discussed in this section clearly reveal the reproducibility of the EFS signal, including the specific features that yield information on the progressive development of fatigue damage.

5.2.3.2 General EFS Response of 4130 Steel

The transient current response of 4130 steel to cyclic loading at a frequency of 1 Hz is plotted in Figures 5-13a, b, and c using the percentage of fatigue life as a generalized damage parameter. The plots correspond to a specimen tested at 724 MPa (105 ksi) and R = -1, under an applied potential of 0.4 V_{SCE}, that failed after 22,850 cycles. As seen in Figures 5-13a, a current peak associated with the C portion of the loading cycle is a characteristic occurrence over a large

fraction of the life, while a more complex pattern develops later. The emergence of a small peak in the rising portion of the C-current peak, shown at 79.9% life in Figure 5-13b, appears as a distinctive indication of fatigue damage, prior to the significant increase in the T-current peak associated with the sustained crack propagation that precedes failure (Figure 5-13c). The baseline passive current density was approximately one order of magnitude lower than in the case of the Al alloy indicating good passive behavior in the electrolyte. This passivity is also reflected in the cathodic current transients (negative values) observed just after the compressive peak of the loading cycle (Figure 5-13a and b) that become fully anodic at the end of fatigue life (Figure 5-13c).

A more detailed analysis of the main features in the evolution of the EFS signal during fatigue life was conducted with the approach discussed in Section 5.2.2. Figure 5-14 shows the filtered transient current at 58, 72, 81, 94, 98 and ≈100 % of the fatigue life for a specimen that failed in 27,641 cycles under similar experimental conditions as above, with the exception of the potential which was 0.5 V_{SCE}. The most important features in the different stages of fatigue life can be described as follows. There is a long, initial stage (Figure 5-14b) in which the C-current peak dominates the EFS response. In a few cases, particularly at high maximum stresses, this stage is preceded by a brief stage in which a T-peak coexists with the C-peak. This long stage is followed at about 70 % life by a stage in which a T-peak emerges from the rising portion of the C-peak, as shown in Figure 5-14c. In the final stage preceding failure (Figures 5-14d, e, and f), the amplitude of the T-peak increases significantly and dominates the whole waveform, accompanied by the almost complete disappearance of the C-peak near failure (Figure 5-14g).

Examples of the variations of significant parameters used to characterize the EFS signal pattern, as described in Section 5.2.2, are shown in Figures 5-15 and 5-16. Figure 5-15 shows the significant increase in the amplitude of the T-peak that occurs at about 24,700 cycles (90 % life), with a concurrent decrease in the amplitude of the C-peak. At about 25,870 cycles a crack was clearly visible with the naked eye in the middle of the gage section. However, the earliest indication of fatigue damage was provided by the occurrence and increase of the current spike in the rising portion of the C-peak that appears at about 20,000 cycles (72 % life), as shown in Figure 5-14c. This feature is associated with a significant drop in the C-peak rise time, as shown in Figure 5-16. In addition, drops in the C-peak width and in the C-peak decay time

(Figure 5-17) are clearly distinguishable in the filtered EFS signal at about the same life percentage. It should be noted that the abrupt peak and the corresponding drop observed at about 18,000 cycles in Figures 5-15 and 5-16, respectively, were due to a transitory electrical anomaly during the test. In other tests no such similar type of fast transient in the C-peak amplitude was observed during the analogous portion of the fatigue life.

In another test, conducted under the same experimental conditions, the fatigue life was 21,804 cycles. The same early indications of fatigue damage were found in the analysis of the filtered current for this test. At about 14,500 cycles (67% life) significant drops in the C-peak rise time, C-peak decay time, and C-peak width were observed in plots similar to those of Figures 5-16 and 5-17. The T-peak amplitude and the T-peak area that represent the current and the electric charge associated with the tensile component of the stress cycle only started to increase significantly at about 18,750 cycles (86 % life).

5.2.3.3 General EFS Response of Ti-6Al-4V Alloy

The transient current response of Ti-6Al-4V Al alloy to cyclic loading at a frequency of 1 Hz is shown, using the percentage of fatigue life as a generalized damage parameter, for the period early and late in life in Figure 5-18a and b. The plots correspond to a specimen tested at 565 MPa (82 ksi) and R = -1, under an applied potential of 0.4 V_{SCE}, that failed after 46,901 cycles. Despite the fact that the EFS signal is noisier than in the previous examples, the evolution of the current signal with fatigue life is clearly seen. The occurrence of current peaks associated with the tensile (T) and compressive (C) portions of the loading cycle is characteristic of the early life with a progressive decrease of the C-peak between 4.2 and 78.8 % life (Figure 5-18a). At life percentages greater than 89 %, a significant increase in the amplitude of the T-peak is evident in Figure 5-18b. However, the EFS signal for Ti-6Al-4V alloy exhibited less obvious features than those observed for 7075 Al alloy and 4130 steel. The baseline passive current density was similar to that of 4130 steel indicating good passive behavior in this alloy also.

The analysis of the EFS signal as discussed in Section 5.2.2 reveals four stages of fatigue life for a specimen tested at 655 MPa (95 ksi), R = -1, and 1 Hz, under an applied potential of 0.5 V_{SCE}. The specimen failed after 11,888 cycles. Figure 5-19b shows an example of the filtered

transient current at 2.5 % life. It is seen that in the initial stage the T- and C-peak coexist, but the amplitude of the T-peak is greater than that of the C-peak. In the second stage that extends over a long period of fatigue life from about 5 % to above 57% (Figure 5-19c), the T-peak gradually dominates the whole peak and exhibits a shift in the peak location. The third stage is characterized by a rather abrupt narrowing of the upper portion of the T-peak, as shown in Figure 5-19d for 80 % fatigue life. In the final stage the whole T-waveform becomes wider and the amplitude of the T-peak increases substantially, as shown in Figure 5-19e, until failure occurs.

Examples of the variations of significant parameters used to characterize the EFS signal pattern, as described in Section 5.2.2, are shown for the test discussed above in Figures 5-20 through 5-22. Figure 5-20 shows the significant increase in the amplitude of the T-peak that occurs as the end of the fatigue life is approached. However, the increase in both this parameter and the electric charge (or area) of the T- peak takes place gradually above 80 % life, as shown in Figure 5-21. Others indicators of change in the EFS signal, such as a drop in the rise time of the T-peak or an increase in its decay time, appear very late in life (> 90%). In the case of Ti-6A-4V alloy the decrease in the width of the T-peak appears to be the most sensitive indicator of fatigue damage, presumably triggered by the nucleation and growth of fatigue cracks, combined with the rapid repassivation kinetics characteristic of this alloy. As shown in Figure 5-22, the abrupt decrease in the width of the T-peak occurs at about 9,400 cycles corresponding to 80 % of the fatigue life.

The EFS signal exhibited the same patterns in two other tests conducted under equivalent experiment conditions, with the single exception that in one test the applied potential was 0.4 V_{SCE} and in the other 0.5 V_{SCE}. In the first case failure occurred after 14,847 cycles and in the second one after 18,691 cycles. In both cases all the features of the EFS signal were similar and, in particular, the decrease in the width of the T-peak occurred after 11,560 and 13,650 cycles, corresponding to 78 % and 73% fatigue life, respectively.

5.2.3.4 Effect of Maximum Stress on EFS Response

At constant R ratio and frequency, the value of the maximum stress affects the amplitude of the EFS signal. In the case of 7075 Al, a decrease of 10 % in the maximum stress from 345 MPa (50 ksi) to 310 MPa (45 ksi) decreased the amplitude of the T-peak by about 40 % at R = −1 and 1 Hz. Nevertheless, although attenuated, all the important features of the EFS signal can be detected, in particular, the occurrence of the current spike in the rising portion of the T-peak. Results of these tests are summarized in Table 5-1. The increase in the percentage of life at which damage is initially detectable in these experiments is consistent with the general observation in fatigue testing that crack nucleation occurs later in life as the total life increases.

For 4130 steel a decrease of the maximum stress from 724 MPa (105 ksi) to 600 MPa (87 ksi) reduced the amplitude of the C-peak by about 30 % at R = −1 and 1 Hz, as summarized in Table 5-2. However, no appreciable difference was noted by increasing the maximum stress to 760 MPa (110 ksi). As in the case of 7075 Al, all the important features of the EFS signal were detected at the lower maximum stress. As expected, the drop in the C-peak rise time that seems to be related to the initiation and growth of fatigue cracks occurred later in life at lower maximum stress. The drop was observed at about 104,000 cycles for a specimen that failed in 117,471 cycles representing 89 % fatigue life. For several specimens tested at 724 MPa (105 ksi) in which the fatigue life ranged from 21,700 to 28,500 cycles, the drop in the C-peak rise time occurred between 68 % and 79 % of the fatigue life.

5.2.3.5 Effect of Mean Stress

The effect of mean stress in the EFS signal was evaluated indirectly through the variation of the R-ratio at a constant maximum stress. Tests were conducted at a selected maximum stress using R values of −1, 0.05, and 0.5. Under such conditions, the main effect in terms of the EFS signal arises from the decrease in the cyclic stress amplitude and, as a consequence, results in a decrease in the amplitude of the EFS signal. The effect was particularly noticeable at R = 0.5, where the amplitude of the cyclic stress is reduced by 75 %, as compared to R = -1, and the EFS signal-to-noise ratio was significantly reduced. The results of specific tests are summarized in Table 5-3. Unfortunately, the signal to noise ratio was so low in tests at R = 0.05 and 0.5 that the spike in the rising portion of the T-peak was not easily detected by the program described in

Section 3.2.2. As a consequence the increase in the amplitude or the area of the T-peak was used as criterion for the detection of fatigue damage.

5.2.3.6 Effect of Frequency

The effect of cyclic loading frequency for 7075 Al alloy was evaluated at two values of maximum stress for $R = -1$, as summarized in Table 5-4. The amplitude of the T-peak is lower at the higher frequency, decreasing from 3.7 A at 1 Hz to 1.3 A at 5 Hz during most of the fatigue life for the tests at 345 MPa and from 1.8 A to 0.7 A at 276 MPa. The effect of frequency on the characteristic features of the EFS signal, presumably related to the occurrence of fatigue cracks, is also shown in Table 5-4.

Contrary to the case of 7075 Al, increasing the frequency for 4130 Steel tested at 724 MPa, $R = -1$, and 0.5 V_{SCE} increases the amplitude of the C-peak during most of the fatigue life from 0.6 A at 1 Hz to 4.2 A at 5 Hz, both values as the mean of three tests. The results of these tests are summarized in Table 5-5. The last two rows include data of tests in which the specimens were removed from the cell following the interruption of the cyclic loading (see Section 5.2.5 for a detailed discussion of these tests). Therefore, the fatigue life percentages for these specimens are not included in the last column. However, it is useful to show that the increase in frequency does not significantly affect the number of cycles at which the occurrence of distinctive EFS features is an indication of fatigue damage, as can be noted for specimen SE343C2F.

In the case of Ti-6Al-4V alloy the loading frequency had a minor effect on the amplitude of the T-peak. Nevertheless, the T-peak amplitude decreased with increasing frequency as in the case of 7075 alloy. The mean current for two tests at 655 MPa, $R = -1$, and 1Hz at 0.5 V_{SCE}, was 4.5 A but decreased to 3.3 A under identical conditions with a frequency increase to 5Hz. The results in terms of the features of the EFS signal are summarized in Table 5-6.

It can be concluded from these tests that although increasing frequency may decrease the amplitude of the current response (i.e., for 7075 Al and, in a minor proportion, for Ti-6Al-4V alloy), it does not have a measurable influence on the percentage of life at which fatigue damage is initially detected.

5.2.3.7 EFS Response in Gel Electrolyte

Two tests were conducted on 7075 Al alloy at 345 MPa (50 ksi), R = -1, and 1 Hz using the gel electrolyte at an applied potential of 0.3 V_{SCE}. The specimens failed in 7,202 and 10,160 cycles. The pattern of the EFS signal was essentially similar to that reported for specimens tested under equivalent experimental conditions in the liquid electrolyte, in particular the amplitude of both the T- and C- peaks. Even though the initial baseline current density was similar to that measured in the other tests, the signal-to-noise ratio was lower. The first of these tests was particularly noisy, but in the second one there was a significant improvement in the signal-to-noise ratio. Nevertheless, it was difficult to detect the current spike in the rising portion of the T-peak that was observed in equivalent tests conducted in the liquid electrolyte at about 70% fatigue life.

Contrary to the observations noted above, the comparison of data obtained at the University of Pennsylvania and presented in Section 5.3.3.7 corresponding to testing of 4130 steel in the aqueous and gel electrolytes respectively, reveals the opposite effect. The EFS signal obtained in the aqueous electrolyte, once fatigue cracks are initiated and detected through the increase in the current amplitude, exhibits more noise than that in the gel.

5.2.3.8 Effect of Applied Potential on EFS Response

The effect of applied potential was evaluated in the case of 7075 Al alloy, and in a more limited fashion for 4130 Steel and Ti-6Al-4V alloy. Two specimens of 7075 Al alloy tested under the same cyclic loading conditions as those described in Section 5.2.3.4 [345 MPa (50 ksi), R = -1, 1 Hz] but under applied potentials of 0.4 and 0.5 V_{SCE}, exhibited a similar EFS response to that observed on the specimen polarized to 0.3 V_{SCE}. These specimens failed after 5,836 and 10,391 cycles respectively. Despite the relatively large difference in the number of cycles to failure between the two specimens, the current spike in the rising portion of the T-peak appeared at about 68% of the fatigue life for that tested at 0.4 V_{SCE} and at 60% for that tested at 0.5 $V_{SCE.}$. Even for a specimen tested at an applied potential of 0.0 V_{SCE}, which failed in 6,511 cycles, a relatively well defined EFS signal was obtained. In this case the current spike in the rising portion of the T-peak emerged at about 4,300 cycles which corresponded to 66 % fatigue life. In all these tests the initial baseline current before cyclic loading ranged between 4.0 and 8.7 A,

indicating that over that wide range of potentials (0.0 to 0.5 V_{SCE}) the passive current is practically independent of potential. The observations are summarized in Table 5-7.

As described in Sections 5.2.3.5 and 5.2.3.6, variations of about 100 mV in the applied potential for 4130 steel and Ti-6Al-4V alloy did not introduce noticeable variations in the EFS signal. This behavior indicates that the same EFS features are developed in the passive region over a reasonable range of potentials ($\approx$100 mV) above 0.4 V_{SCE}. As a result, the same parameters can be used to assess the development of fatigue damage over this range of potentials.

5.2.4   EFS Response of Coated 7075 Al Alloy

5.2.4.1 EFS Response of Primer Coated 7075 Al Alloy

Two primer coated specimens were tested at 345 MPa (50 ksi), R = −1, and 1 Hz under an applied potential of 0.3 V_{SCE}, to compare the EFS signal with that of uncoated specimens. Failure in these specimens occurred at 8,725 and 11,161 cycles, values that are within the range of variation found for the cycles to failure of uncoated specimens. These results suggest that the presence of the coating had no effect on the fatigue life. However, during the initial stages of the fatigue life, the signal-to-noise ratio was relatively low as a result of the low EFS currents caused by the relatively high electrical impedance of the primer. It should be noted that the presence of the primer, although it is a porous coating, reduces the initial baseline current by more than an order of magnitude. Currents lower than 0.4 μm were measured compared with values of about 4 μm or more for the uncoated specimens.

As an example, Figure 5-23 shows the filtered transient current at 22, 79, 86, and almost 100% of the fatigue life for the specimen that failed in 8,725 cycles. A relatively noisy signal in which the T- and P- peaks are still distinguishable is shown in Figure 5-23b, corresponding to 22% life. However, the EFS signal was too noisy up to about 79% life to reveal the initial emergence of the current spike in the rising portion of the T-peak that in uncoated specimens seems to be associated with the occurrence of cracks. The EFS signal in Figure 5-23c, corresponding to 79% life, exhibited a shoulder in the T-peak rather than the current spike that emerges at 70% life for the uncoated specimens, as a comparison with Figure 5-10d reveals. However, at higher life percentages, as seen by comparing Figures 5-23d and 5-23e with Figures

5-10e and 5-10f, the features of the EFS signal are almost identical for uncoated and primer coated specimens. These observations indicate that despite the presence of a relatively high impedance coating, the formation of cracks and the associated fatigue damage can be detected in the primer coated specimens, albeit with some delay.

Similar results were obtained when a primer coated specimen was tested under equivalent cyclic loading conditions but under an applied potential of 0.4 V_{SCE}. Failure occurred in 10,828 cycles. Additional tests were conducted on primer coated samples at 310MPa (45 ksi), R = -1, and 1 Hz and, using three R ratios (-1, 0.05, and 0.5), at 276 MPa (40 ksi) and 5 Hz. In these four tests, the applied potential was 0.3 V_{SCE}. As observed at the highest maximum stresses, the EFS signal in the initial part of the fatigue life was found to be noisy, precluding the detection of early features that can be associated with fatigue damage and the occurrence of cracks. However, at life percentages higher than 80 %, presumably as a result of the degradation of the primer and the consequent decrease in the overall impedance, the EFS signal becomes comparable to that detected under similar cycling loading conditions on uncoated specimens. The most important observations resulting from these tests are summarized in Table 5-8.

5.2.4.2 EFS Response of Primer Plus Top Coated 7075 Al Alloy

Two primer plus top coated specimens were tested at 345 MPa (50 ksi), R = -1, and 1 Hz under an applied potential of 0.3 V_{SCE}, to compare the EFS signal with those of uncoated and primer coated specimens. Failure in these specimens occurred at 10,672 and 12,383 cycles, values which are within the range of variation found for the cycles to failure of uncoated specimens, although displaced towards the upper end of that range. These results suggest that the presence of the coating had no appreciable effect on the fatigue life. However, during the initial stages of the fatigue life, the signal-to-noise ratio of the EFS signal was extremely low due as a result of the low currents caused by the high electrical impedance of the coating.

The EFS signal was found to be too noisy up to about 80% of life to detect any feature that might indicate the occurrence of cracks. However, at higher life percentages, the features of the EFS signal were almost identical to those of uncoated and primer coated specimens. In particular, the increase in the amplitude of the T-peak was clearly noticeable as well as the

concurrent increases in its area, indicating the increase of the electrical charge associated with the growth of fatigue cracks leading to failure. These observations indicate that despite the presence of a high impedance coating, the fatigue damage associated with significant crack growth can be detected in the primer plus top coated specimens.

Similar results were obtained when a primer plus top coated specimen was tested under equivalent cyclic loading conditions but under an applied potential of 0.4 V_{SCE}. Failure occurred in 7,680 cycles. Additional tests were conducted on primer coated samples at 310 MPa (45 ksi), and 1 Hz and, using three R ratios (-1, 0.05, and 0.5), at 276 MPa (40 ksi) and 5 Hz. In these four tests, the applied potential was 0.3 V_{SCE}. The EFS signal in the initial part of the fatigue life was found to be noisy, precluding the detection of early features that could be associated with the occurrence of cracks. Nevertheless, at life percentages ranging from 82 to 95%, the EFS signal became comparable to that observed on uncoated specimens. Under such conditions, cracks were visible on the gage section of the specimens. The most relevant results obtained in these tests are summarized in Table 5-9.

5.2.5 EFS Detectable Crack Size

A series of tests were conducted in which cyclic loading was interrupted at a certain estimated percentage of the fatigue life and the specimens were removed from the cell for optical examination. The purpose of these tests was to examine the surface of the specimens at a sufficiently high magnification to detect any sign of fatigue damage, in particular the presence of incipient fatigue cracks, and relate these observations to specific features of the EFS signal. These specimens and the testing conditions are listed in Table 5-10. The estimated percentage of life range for the number of cycles at which each test was interrupted (last column in Table 5-10) was calculated by subtracting or adding the standard deviation from the mean value of the cycles to failure for all tests conducted under identical cyclic loading conditions.

Cycling loading of the AF58C2AF specimen was interrupted when a spike in the T-peak, started to increase significantly as shown in Figure 5-10(d). Figure 5-24 shows the EFS signal at 12,000 cycles, prior to the increase in the T-peak, and Figure 5-25 exhibits the signal obtained at about 13,000 cycles, just before the interruption of the test. After removing the specimen from

the cell, visual examination revealed the presence of a rather long crack on the specimen surface, as shown in Figure 5-26. The specimen was then pulled to failure after cutting with a diamond saw most of the cross sectional area corresponding to the position of the crack to avoid damaging the fracture surface. The fractograph shown in Figure 5-27 reveals the topographic features, thumb-nail shape, and dimensions of the fatigue crack. In an attempt to detect smaller cracks, cyclic loading of specimens AF35C3F and AF19C3F was interrupted when the EFS signal exhibited features usually observed just before the emergence of the spike in the T-peak. The specimens were then examined optically, even using fluorescent penetrating dye, but no cracks were detected on the gage length surface. Unfortunately, machining and polishing marks affected the level of resolution of the microscopic examination.

In the case of 4130 steel, cyclic loading for specimen SE343C2F was interrupted when the current spike in the rising portion of the C-peak, as shown in Figure 5-14d, became comparable with the C-peak. This feature occurred at about 23,000 cycles. A long crack (approximately 1.8 mm in length) was detected in the center of the gage section when the specimen was removed from the cell and visually examined. Specimen SE350C3F was then removed earlier in the fatigue life, at the first indication of the development of the current spike, as shown in the plot of the EFS signal obtained at 15,000 cycles (Figure 5-28). However, the detection of the current spike in the rising portion of the C-peak depends on the level of filtering of the EFS signal. When additional filtering was incorporated in the software to facilitate the signal processing described in Section 5.2.2, the small spike became undetectable due to the smoothness of the EFS signal, as illustrated in Figure 5-29. Detection of cracks by optical examination was difficult in this specimen even with the use of fluorescent penetrating dye. For this reason, the specimen was heat tinted (by heating in air at temperatures about 350°C to oxidize and mark any exposed surface) and fractured in order to distinguish the fatigue crack from the ductile fracture surface. Figure 5-30 shows the appearance of three small crack nuclei ($\approx$ 75 μm in size) along the edge of the fracture surface.

From these experiments it can be concluded that some features of the EFS signal when sufficiently developed and identifiable, such as the current spike in the rising portion of the T-peak for 7075 Al alloy and the T-peak emerging in the rising portion of the C-peak for 4130 steel, are related to the occurrence of fatigue microcracks. To improve the correlation of the EFS

signal with the very early stages of microcrack nucleation, special preparation of the specimen surface (e.g., electropolishing) would be required to facilitate microscopic observation.

5.3   EFS Laboratory Measurements at Penn

5.3.1   EFS Experimental Procedures

The EFS studies conducted at Penn employed a conventional specimen with a cylindrical gauge section, surrounded by an appropriate electrolyte contained in a three-electrode cell. Most of the EFS experiments were performed with this apparatus or a modification of it. Some of the work required a more "applied" type of research specimen for which a rectangular bar configuration was chosen. Electrohydraulic testing machines were used exclusively for studying the electrochemical/mechanical interaction because they offer the most flexible means of test control and data acquisition. Finally, special means were used to acquire and combine the mechanical signals from the machines, such as the stress and strain waveforms, and the electrochemical signals produced by the specimen/electrolyte interaction. Details concerning these experimental components are as follows:

Figure 5-31 shows the configuration for the specimen with cylindrical gauge section used in the majority of the tests, and for all the materials. The specimens were machined by Cincinnati Testing Laboratories using "stress-free" machining techniques. Figure 5-32 shows the design of the flat bar specimen used for the 4130 steel sample when it was desired to attach an EFS to the specimen. Some of the flat specimens were prepared with a hole in the middle of the gauge section, as indicated in the figure, while others did not have such a hole.

Surface preparation for fatigue testing of the as-machined specimen involved the following procedures: The specimen was first mechanically polished, using grade 600, 1200, and 2000 emery papers sequentially. Finally, the specimen was ultrasonically cleaned in acetone.

Fatigue tests were performed on three hydraulic machines: an MTS machine of an older model (MTS 810.21 System), an Instron machine (Model 1331), and a new MTS machine (MTS 810 TestStar II System) with digital capability for designing arbitrary test waveforms.

Most of the tests were conducted under simple sinusoidal load control with a stress ratio R of –1, while other waveforms and control modes were also used for a limited number of tests, such as: 1) a stress ratio of 0 for the flat specimen tests, 2) strain control tests, and 3) variable-amplitude loading tests. The variable-amplitude loading tests were conducted using the new MTS machine, with interconnected sinusoidal waveforms of different amplitudes (see Figures 5-33 and 5-34 for the two waveforms employed).

Figure 5-35 shows the configuration of the testing frame of the fatigue machine used for most of the tests. Some early tests were performed in the horizontal mode as described in Ref. [5.4]. However, this mode can be clumsy because the machine has to be upright for entering the specimen in the Wood's metal grips. For the permanently upright machine, the center part consists of a load cell, a special grip, an environmental cell with specimen, and an actuator. Other attachments include an anti-rotation holder, and an extensometer mounted on the exterior, rather than on the gauge section, of the specimen.

Figure 5-36 shows the environmental cell used for most of the tests. The base of the cell is made of Teflon, and the wall is Plexiglas. Inside the wall, there is a groove for the counter electrode. Near the top of the wall, there are two holes, one is for the outlet of the counter electrode, and the other is for inserting a reference electrode. When a specimen was mounted in the machine, the two-threaded ends (shoulders) were covered by Teflon caps for insulation purpose. All the gaps at the joints were sealed with wax to prevent leakage. This cell has a capacity of 50 ml. Smaller cells (5 ml capacity) were also used for special tests.

5.3.2   EFS Signal Processing At Penn

In order to acquire and analyze experimental data digitally and conveniently, a LabView graphic-programming language was used to develop various kinds of data acquisition software and analysis software.

5.3.2.1 Data Acquisition Software Developed at Penn

Data acquisition (DAQ) software was developed in such a way that experimental data (stress, strain, current, and applied voltage) can be displayed on the computer screen almost instantly. Meanwhile, selected sets of data can be stored into the hard disk automatically.

The information displayed on the screen consisted of hysteresis loops and transient current. For the latter, the DAQ software has a built-in fast Fourier transform (FFT) function. Therefore, the current curve displayed on the screen can be in the form of waveform, Fourier spectrum, or even the elastic and plastic parts of the EFS current. The EFS current associated with the elastic strain can be out of phase with the stress/strain cycle, but has the same frequency [5.1–5.4]. Since the EFS current associated with plastic strain develops during tensile and compressive stress peaks, its frequency is double that of the stress cycle [5.1–5.4]. Therefore, Fourier analysis of the total current signal automatically identifies these currents and their connection with the fatigue damage. This is the method by which the currents were identified and computed. At later stages of life, when cracking occurs, the current spikes associated with cracking produce higher order harmonics in the Fourier spectrum.

During any test, a set of data was saved in hard disk every 100 cycles. Each set of data consists of 640 data points for each signal, corresponding to five consecutive cycles. By doing so, a good resolution was achieved in both the time domain (waveform) and the frequency domain (FFT).

5.3.2.2 Data Analysis Software Developed at Penn

Special software was developed for data analysis by using LabView. For EFS applications, the transient current can provide information about fatigue damage in several forms. The current waveform provides information for individual cycles, such as the number of current peaks within a cycle, and the nature and the magnitude of the peaks. FFT analysis for each cycle reveals detailed information about each harmonic contained in the current data, as noted above.

EFS data contains contributions from different processes, such as 1) the basic electrochemical reaction which occurs on the specimen surface when no mechanical loading is applied; 2) the current associated with elastic deformation; and 3) the current associated with plastic deformation. Therefore, it is useful to distinguish these components.

The total current can be divided into components by Fourier analysis:

$$I_t = i_0 + i_1 + i_2 + \ldots\ldots = i_0 + i_1 + \sum_{j=2} i_j$$

where i_0 is the DC part and is called the base current, i_{base}; i_1 is the current associated with elastic deformation, $i_{elastic}$; since a sinusoidal stress was used for mechanical excitation, i_1 is also sinusoidal. The rest of the current, *i.e.*, $i > i_1$ is considered the current associated with plastic deformation, $i_{plastic}$. Occasionally, a single term, i_2, was used to describe the current associated with plastic deformation, $i_{plastic}$. For example, in the DAQ software, one piece of information displayed on the screen is the peak value of i_2 as a function of number of cycles, which was used to monitor the crack nucleation and propagation behavior. Elaboration concerning the nomenclature of these different current components is necessary, as follows: the DC component of the signal i_{base} is subtracted from the so-called peak values of i_1 or i_2, and these quantities therefore represent the amplitudes of the AC components superimposed on i_{base}. The term "peak current" is used repeatedly throughout the present section (and others) and is intended to be understood in terms of the above definition.

Another parameter derived from FFT is the phase factor of the i_1 component, which was measured against the applied stress signal. The value of the phase factor is given not in the unit of degrees, but rather is measured in terms of the period of the stress cycle, in the range from -0.5 to 0.5. By using this unit, it is convenient to compare the results obtained for different frequencies.

Furthermore, EFS monitoring happens in a period of time or cycles. Therefore, it is desired to organize the analytical results in a historic fashion, *i.e.*, how the values of the base current, the amplitude of the $i_{elastic}$ and $i_{plastic}$ components, and the phase factor develop with time and with respect to special events occurring in the life of the specimen.

All the aspects mentioned above have been taken care of by the analysis software. The following example shows how this analysis was used. A steel specimen S-50 was tested in solution for about 200,000 cycles. Figures 5-37a and 5-37b indicate the variations of the peak values ($i_{elastic}$, $i_{plastic}$, i_{base}) against the number of cycles. Figure 5-37c shows the relationship between phase factor and the number of cycles. From these curves, one can easily pick out when

the cracking started, and how these parameters change with the fatigue process. On the other hand, Figure 5-37d and 5-37e give a visual impression of how the transient current changes within one or a few cycles as the life of the specimen is consumed. In each of the figures, a sinusoidal curve is included, which corresponds to the applied stress. By using this arrangement, the transient current variation due to cycling can be revealed in terms of peak position and phase factor. The attention of the reader is especially directed to Figures 5-37d and 37e. In Figure 5-37d, the EFS current is seen to increase as cycles accumulate, as would be expected of a technique intended to measure the development of fatigue damage. However, in Figure 5-37e, where waveforms are provided over a fairly narrow range of cycles, from 150,100 to 150,800, the transient current actually decreases, tempting the reader to believe that the cycles for the waveforms have been mislabeled. This is not so. Figures 5-37a to c show the occurrence of "instabilities" in the transient currents. Figure 5-37e shows the waveforms during an instability when the currents are in decay, probably caused by repassivation. It is unknown whether the instabilities are produced by uneven rates of crack advance, when the cracks are small. (For interpretation of these results, see Section 5.3.3)

5.3.3 EFS Response In Bare Uncoated Materials

5.3.3.1 General EFS Response on Bare 4130 Steel

Typical EFS results for steel are shown above (Figure 5-37a to 37e) with respect to the definitions of the parameters of interest. As noted in Section 5.3.2.2, the total transient current can be analyzed into that associated with elastic behavior and that associated with plastic deformation, whether or not it is connected with precracking behavior or cracking itself. As shown in Figure 5-37a and 37b, which applies to a steel specimen which failed in nearly 200,000 cycles, the base current is initially high as the passive condition was established, and the transient current varies between 0.15 and 0.2 μ A/cm2. However, the base current rapidly falls, in the specimen illustrated in less than 1000 cycles (the cyclic frequency, as can be seen in Figure 5-37d and 37e, was 0.5 Hz), as passivity develops and stabilizes at a low current. The current associated with plastic strain also falls to a low value. Since damage develops very slowly in this hardened steel, little variation in the plastic current transient is observed for nearly

75% of life. This observation is consistent with many observations concerning the kinetics of damage formation in hardened steels [5.5–5.8].

Figures 5-37a to 37c show plots of the peak value of the parameter per cycle as a function of elapsed cycles. The cycle-by-cycle waveforms at different life intervals are shown in Figure 5-37d and 37e. Consistent with the results for the peak values, little change occurs in the waveform during the first three quarters of life. However, at about 150,000 cycles, the current waveform, which has roughly the same shape as the stress signal (this test was run under stress control), develops a bump on the tensile side of the sinewave shoulder. We believe that this behavior indicates cracking, which in turn causes repeated episodes of passivity breakdown and re-establishment, seen as sharp peaks in the plastic current as well as the base current (Figure 5-37a and 37b) which responds to the electrochemical condition of the specimen surface. As cracking develops further, the crack peak on the tensile shoulder of the plastic current continues to grow and the overall current amplitude increases. We conclude, therefore, that the EFS transient current response in this steel faithfully follows the damage mechanism and kinetics.

Signal processing of the data acquired allows the phase shift in the components of the transient current to be measured and recorded. A plot of this parameter, defined in Section 5.3.2.2 also indicates the onset of cracking, as shown in Figure 5-37c. Note that the phase shift remains constant (after some variation at the very beginning of life) at around −0.30 for most of the life, when cracks have either not yet formed or are still too small to affect the cyclic plasticity. However, once cracking begins, then this parameter shows major variation and burst behavior associated with temporary interruptions in passivity. Thus this parameter could also be used as a damage indicator.

Results for repeat tests on the 4130 steel, all cycled at 0.5 Hz and 600 MPa under stress control are shown in Table 5-11. The lives of these specimens ranged from a low of 108,900 to a high of 259,800 cycles, and exhibit normal scatter. The EFS results showed that cracking could be detected at from 63 to 84% of life also consistent with the scatter. Note that elastic, plastic, and base currents are listed in Table 5-11. It will be seen from Figures 5-37 and 5-38 that these currents vary considerably throughout life, as noted above. For comparison purposes, in Table 5-11 and subsequently in this section, when such currents are reported, the specific values

listed correspond to 50% of life, or the long quiescent period occupying the early- and mid-regions of life. Detailed results for another specimen, S-42, shown in Figure 5-38, are of great interest. These results were obtained with a two-electrode cell and a somewhat different voltage, not with the traditional three-electrode cell used to obtain the results for Figure 5-37. However, the results are closely similar to those shown in Figure 5-37a to 37e, and indicate good reproducibility of the response and the same series of damage connected indications, for the different electrode configuration. Since the two electrode system is much easier to install and maintain, we view the results of Figure 5-38 as very encouraging. There is yet another point of interest connected with the results of Table 5-11: a counter electrode of silver was used for specimens S–25 instead of the normal platinum (for reasons of economy). In spite of this difference, the results were still satisfactory. In general, however, we would not recommend using metals other than platinum for this purpose because it could introduce unforeseen complications. Also, in service, the amount of platinum used per cell could be quite small.

The results shown in Table 5-11 and Figures 5-37 and 5-38 are representative of the reproducibility observed in tests performed under equivalent conditions of fatiguing and performing EFS measurements. The results are regarded as highly reproducible within the limits of fatigue scatter. Many direct comparisons of EFS data gathered under similar conditions can be seen in Reference [5.9].

5.3.3.2 General EFS Response on Bare Aluminum Alloy 7075-T731

Typical EFS response for aluminum alloy, tested continually in liquid electrolyte, with a frequency of 0.5 Hz, and under stress control at stress amplitude 200 MPa, showing the same parameters as defined for steel, are shown in Figure 5-39, for the specimen identified as a-b 72. It will be noted that the behavior is somewhat different from that for steel. The current density is initially high in the first few dozens of cycles. We interpret this behavior as associated with initial cyclic plasticity, the production of slip lines, active electrochemical effects with the production of fresh surface and the subsequent decay of the current as the surface passivates.

However, after the immediate sharp peak on start-up and the subsequent current decline, the current then gradually increases as cycles accumulate, rising to a maximum at around

15,000 cycles and again slowly decaying until about 70,000 cycles. This behavior is associated with gradual changes in the surface condition, more than with the effects of cycling because we are able to reproduce it with respect to time, at lower kinetics, in the absence of cycling. Note in Figure 5-39c that the phase shift remains steady at around 0.5 period while the gradual current changes occur. The behavior indicates, we believe, the long term development of the passive film which takes about 10 hr to complete (at least while cycling is performed). After passivation is complete the current drops and ultimately the phase shift goes to zero because of cracking. Thus, the phase shift is a very good indicator of that part of the fatigue damage associated with cracking. Once cracking develops, again fairly late in life, instabilities appear in association with the temporary breakdown of passivation and repassivation, just as in steel.

Unlike steel, which does not show the double peak per cycle observed previously in ductile metals when the cycle-by-cycle waveform is viewed, aluminum does show a double peak at the amplitude chosen for illustration. This behavior is shown in Figure 5-39d. The double peak behavior is interesting: at less than a thousand cycles, the tensile current peak is larger than the compressive peak (note the current trace recorded at 700 cycles in Figure 5-39d); by the time 1700 cycles were reached, the amplitude of the tensile peak had declined to that of the compressive peak but thereafter both the background current and the compressive peak gain in strength (e.g., 3000 cycles). As passivation develops in full strength, the compressive peak remains larger than the tensile peak (see Figure 5-39e - waveform at 68,000 cycles). The sudden start in the reduction of the phase shift (Figure 5-39c) suggests that cracking began at 70,000 cycles and a crack peak is clearly evident in the trace at 78,000 cycles shown in Figure 5-39e. As the life became exhausted to the point of complete failure at 96,400 cycles, the current increased considerably. Note in Figure 5-39a and 39b, it goes off-scale long before final fracture. In association with this behavior the tensile peak becomes increasingly dominant in the transient current and a significant crack peak is seen (Figure 5-39e).

For specimens of aluminum alloy cycled at the same amplitude, the EFS response was found to be extremely uniform. This result, for four specimens all cycled at 200 MPa, is shown in Table 5-12. The specimen lives ranged from 64,000 to 126,000 cycles and cracking is indicated as securely established in the 80 - 90% range of life. In fact, this judgement, as can be seen from Figure 5-39, is extremely conservative, and a much earlier indication of cracking (by

about 10%) can be interpreted from the phase shift behavior. As a further demonstration of reproducibility, see the record of waveforms for specimen A-b 105 shown in Figure 5-40a and 40b. Table 5-12 lists the "cracking cycles" for this specimen as 114,000 and indeed the waveform shows a well-established crack peak in Figure 5-40b, but a smaller peak is also evident in the trace for 112,000 cycles.

The EFS thus gives sensitive indications of fatigue damage and the response corresponds closely with late-life crack initiation in strong aluminum alloys observed by replication techniques in early work [5.10, 5.11]. Note that crack propagation in these smooth, small-diameter fatigue specimens is very rapid under stress control because the stress intensity increases rapidly with crack growth. We anticipate that, in aircraft structures, because of their size and the boundary conditions, this rapid increase will be minimal. There should therefore be plenty of opportunity to detect small cracks. The present results are thus extremely encouraging in supporting the feasibility of using the EFS to detect and measure fatigue damage under service conditions.

5.3.3.3 General EFS Response on Bare Titanium Alloy Ti - 6Al - 4V

Since the titanium alloy of interest, like 7075-T731 and 4130 steel, is also strong, as an aircraft material, and is therefore generally fatigue resistant, as well as being a good passivator, it would be expected that its EFS response should be rather similar to those of the other alloys. This expectation was supported by the EFS results as can be seen in Figure 5-41a to 41d. However, in general, the variation of the EFS parameters is smoother. Thus, for the high strain specimen exemplified (life to failure 31,300 cycles), the peak currents declined from a higher initial value as passivity developed, stabilized into the long quiescent mid-life region, and then increased smoothly as cracking developed. The abrupt instabilities observed in steel and aluminum were not observed for this titanium alloy. We attribute the difference to the strong passivation tendency of this metal. Another difference from steel and aluminum can be observed in the cycle-by-cycle waveforms, again attributable to the differing passivation tendencies of the metals. The tensile peak is dominant in titanium and considerably asymmetric, showing a faster rate of decline on the compressive side of the peak than the rate on the build-up. The crack peak

occurred rather late in life, at 86% (see Table 5-13), but the phase shift parameter gave an earlier indication, Figure 5-41c, at about 21,000 cycles or 67% of life.

Further comparisons of the EFS response of the steel, aluminum and titanium alloys of interest are shown in Table 5-14 (the data for the three alloys are averaged for common stresses). In steel, the dominant contribution to the transient current is the elastic component reflecting general electrochemical action throughout the surface exposed to electrolyte and excited by the action of the stress (the current variation is low if the stress variation is low). This component is much lower in aluminum and titanium. The base current for aluminum is high, however, but low in the other two alloys. The phase shift parameters are different for all three. Crack detection seems to be easier in steel than for the other two, although the variation of the phase shift parameter is significant for all three in terms of giving cracking indications. It remains to be seen for interrupted tests whether or not the phase shift parameter will be useful in this respect since the baseline datum readily provided in a continuously exposed specimen may not be available during intermittent tests. Results for interrupted tests are reported in Section 5.3.3.6.

5.3.3.4 Dependence of EFS Response on Fatigue Life – Uncoated Specimens

Since early work had focused on high strain tests and short lives, in which cracking tends to develop early in life and thereby to give dramatic variations in the EFS response, it was of concern to determine how the response depends on fatigue life, and especially long life, which is of most concern in military aircraft. Results directed to this issue were obtained for aluminum 7075-T731 alloy and 4130 steel

A summary of results for aluminum specimens, covering lives in the finite life region from 45,800 to 611,000, is given in Table 5-15. It is encouraging to find that the overall trend in the evolution of the current transients is not much affected by the stress level. For most of the finite life regime, both the elastic and plastic peak currents are not affected and the base current appears constant. Note that, for stresses in the range of 160 to 250 MPa, the plastic current for the 50% point in life is constant at about 0.03 to 0.044 $\mu A/cm^2$. Only at the lowest stresses and longest lives (150 MPa) is there much change: all current values are very low. The phase factor

(which applies in the midlife regime) appears reduced at the highest stresses (230 and 250 MPa) but otherwise remains constant. Also the crack detectability, the very conservative judgement commented upon above, remains constant in the range of 80 to 90% of life.

Results for steel, shown in Table 5-16, indicate behavior similar to that for aluminum. Although the results are fewer, they cover an equally wide range of lives, and the lowest stress employed for the steel was not much above the fatigue limit. There does not seem to be much effect of stress level on the current values at 50% of life. Those for the longest lived specimen, S-41, may seem a little high, but we are not convinced on this point. It should be noted that test S-41 was a fairly early test, in which a different and less developed potentiostat was used. We attribute the difference to the choice of potentiostat. Another point of remark concerns the slightly reduced phase factor for the specimen broken at the highest stress which, at a value of −0.27, we consider to be significantly different from the value of -0.30 observed for specimens broken at longer life.

Based on the results for aluminum and steel, and the similarity observed in the EFS response of titanium, for the limited number of tests performed, to that of the other metals, we predict that the stress effect will not be significant for titanium either. Therefore, we conclude for the three metals that the present and previous results observed at high cyclic strains will carry to longer lives and that the application of EFS is feasible for longer lives.

5.3.3.5 EFS Response as a Function of Frequency -- Uncoated Specimens

Since fatigue occurs over a wide range of frequency, it would be desirable to determine EFS response over a wide range of this variable. However, as the tests were performed in the laboratory, there was a need to examine the EFS responses and the mechanical response by means of the same data acquisition system, so that the signals could be compared. Filters required to remove noise from the electrochemical circuits before input to the data acquisition system limited the frequency range over which the specimens could be tested. Tests in which EFS response was recorded were therefore mainly carried out at 0.5 or 1 Hz. To investigate the frequency effect, the limited range of 2 to 5 Hz was used. Both steel and aluminum 7075-T731 were studied.

The effect of frequency was studied by cycling different specimens to failure under the same mechanical and electrochemical conditions except that different frequencies were used for each specimen. No attempt was made to vary the frequency in cycling bouts for a single specimen although such an experiment might prove interesting. The usual scatter in fatigue life was observed for the specimens cycled at different constant frequencies, and no clear effect of frequency on life was detectable. However, the differences in EFS response were considerable for the different specimens and are described as follows.

Examples of the current waveforms which occurred in steel as a function of cycles and frequency are shown in Figure 5-42a to 42c, for three different specimens, in comparison to the sinusoidal stress cycles applied to the specimens (± 600 MPa, R = -1). EFS measurements and life data for these three specimens are listed in Table 5-17. The waveforms have been selected as representative from points early in life to late in life. As noted in Section 5.3.3.1, the EFS response for steel consists of a singly peaked current cycle shifted in phase with respect to the stress cycle. As damage develops, at a frequency of 2 Hz (Figure 5-42a), the current displays a shoulder on the tensile side of the current wave and the shoulder subsequently grows into a pronounced crack peak. At 3.5 Hz (Figure 5-42b), the same behavior applies but the crack peak is not so pronounced. At 5 Hz (Figure 5-42c), the deviations from the sinusoidal form are suppressed and the changes in the waveform are more gradual.

In analyzing the frequency response of the EFS, it is necessary to take into account certain details of the data acquisition system. In particular, since the potentiostat is equipped with an internal filter for signal conditioning, the phase factor of the current signal will be affected to some extent depending on the cyclic frequency. Therefore, a correction for this effect may be necessary when considering the frequency response of the EFS. The filter in the potentiostat is a one-stage low-pass type with a high cut-off frequency of 10 Hz. For the frequency region adopted in the EFS tests here (0.5 to 5 Hz), the time delay caused by the filter to a sinusoidal signal is about 0.02 sec. with a little variation depending on the cyclic frequency. As shown in Table 5-18, such a time delay is negligible for 0.5 Hz (changing the phase factor by only 1%). However, it cannot be ignored for a testing frequency of 5 Hz (10% error).

Therefore, the results shown in Tables 5-17 and 5-19 (for aluminum) have been corrected according to the test frequency.

An interpretive summary of the frequency effect as revealed by the results in the three steel specimens illustrated in Figure 5-42 is provided in Table 5-17. We note that, with an increase in frequency, there occurs: 1) a delay in the phase shift, that is, the shift increases in the negative direction, 2) an increase in the base current, and 3) an increase in the elastic current. However, the plastic current was not affected significantly. Thus, the signal to background ratio is reduced as the frequency increases and damage detection becomes more difficult. Note in the table that the column providing the cycles of crack detection progresses to higher percentages as frequency increases. At 5 Hz, the point of crack detection is discerned from the change in sign of the phase shift in the constantly sinusoidal waveform rather than from the appearance of a shoulder on the wave. Note that there is a leftward drift in the maximum location between the records for 105,000 and 108,000.

Similar recordings obtained for aluminum alloy at the same three frequencies as used for steel are shown in Figure 5-43a to 43c, along with a data Table 5-19. The waveforms correspond to rather late stages of life. In all of them, the doubly peaked current cycle becomes increasingly asymmetric and oriented to the tensile reversal as damage develops. However, the detailed manner in which this behavior occurs is frequency dependent, with distinct differences. As frequency increased, there was a systematic change in the phase shift. However, the elastic current and the base current peaks were not significantly affected, and the plastic current did not change much until a frequency of 5 Hz was applied when it decreased markedly, probably because the rate of the plastic deformation began to outstrip the kinetics of the electrochemical reactions. The stability of this response had the effect of maintaining the crack detection capability (cf Table 5-19 with Table 5-15). Note that the point of crack detection, as a percentage of the total life, remained in the high 80's to low 90's.

5.3.3.6 EFS Behavior During Intermittent Exposures To Electrolyte

Since the maintenance of EFS cells can be expected to be demanding and expensive if attempts are ever made to monitor continuously with the tool during any fatigue life, periodic

testing during the life of a structure would be more cost effective. It is interesting to determine, therefore, how the EFS will behave during intermittent specimen exposures, at various points throughout life, for small percentages of the life. Accordingly tests were conducted in which specimens were intermittently cycled in air and in EFS electrolyte, with the EFS operated to reveal the state of the fatigue damage. Results of such tests obtained on steel and aluminum are reported as follows:

Table 5-20 summarizes the behavior of three tests for steel in which the specimens were fatigued both in air and in the EFS cell, intermittently. Also provided for purposes of comparison are average results for tests in which the specimens were continuously immersed in EFS environment throughout life. The test for specimen S-18 was performed by first fatiguing in air for 70,000 cycles and then completing the test (82,500 cycles) with the EFS in operation. The test for S-46 was initiated by setting up the cell, cycling at 0.5 Hz at a stress of 600 MPa, and allowing the surface film to become established in about 5000 cycles. The tests were then interrupted, the cell emptied of electrolyte, the specimens flushed and cleaned, and the cycling resumed in laboratory air. To increase productivity, the cycling in air was performed at 8 Hz. After about 20% of the expected life was expended (it was assumed that the intermittent exposures to the EFS would have no effect on life), the tests were again interrupted, the cells refilled with electrolyte, and cycling was resumed in the EFS at 0.5 Hz for 4,400 cycles. Recleaning of the specimen and fatiguing in air was again resumed thereafter. At just under 50% of life, the test was interrupted once again to expose the specimen to the electrolyte and cycling was continued to failure during operation of the EFS. During this final bout of cycling, the EFS read the fatigue damage and, as shown in Table 5-20, gave warning of fatigue cracking around the 90% mark. The test procedure for S-20 involved making frequent alternations between testing in air and in solution.

Figure 5-44a to 44d shows the detailed current, phase shift and waveform behaviors, for a typical steel specimen, S-46, during life. The points shown in Figure 5-44a to 44c represent EFS results. The intermittent bouts of cycling in air are shown as straight lines connecting groups of EFS results. The results show that several thousand cycles are required at each EFS exposure to re-establish the appropriate surface film condition. The current associated with cyclic loading does not vary much at each restart, but the changes in the base current are large

(see Figure 5-44b). This figure shows that the base current increases by six times on the restart in the EFS, indicating that any surface condition developed in a previous exposure to the EFS is not inherited intact in a subsequent exposure. "Settling-in" thus seems to require the re-development of the regular EFS surface condition. It is interesting to note, however, that the phase shift (Figure 5-44c) does not vary on restart, but as usual, changes markedly as cracking develops. In spite of the settling-in process, the phase shift usefully informs whether cracks are, or are not, present at the stage of the fatigue process sensed.

An important difference for EFS results in the intermittently exposed tests is that the current instabilities that develop when cracking begins are not nearly so pronounced as they are during continuous exposure to the EFS. Also the appearance of the crack peak (see Fig. 5-44d) seems to be delayed in the life (see also Table 5-20). The reader will note that, for S-46, no interruption of a test in air and sensing with the EFS was accomplished when cracks were present in the specimen. It may not be obvious that this is a difficult experiment to perform in smooth specimens cycled under stress control. The problem is fatigue scatter. In this hardened material, the crack propagation phase of the fatigue life in smooth specimens is a small fraction of the total life and much less than the variation in life due to scatter. While the specimen is fatiguing in air, there is no indication of the progress of the fatigue and the experimenter has to guess the suitable point to interrupt the test. If he is too conservative he will interrupt the test before cracking has begun. If he is too bold, the specimen will fail during the small fraction of life in which the cracking is occurring and he will fail to catch it. Fortunately, this will not be a problem in actual structures, which are usually larger and in which the stress intensity does not increase rapidly as the crack propagates, as it does in a smooth specimen tested under load control.

To overcome the problem of interrupting the test infrequently and arbitrarily in the hope of catching "interesting" fatigue damage, the test on S-20 was run with frequent interruptions. The history of this specimen is shown in Table 5-21, listing the number of cycles in which the specimen was exposed to EFS electrolyte and to air. Thus, it started life with 2000 cycles in the EFS cell. It then had 62,300 cycles in air before going back into solution for 800 cycles. Then it had another 15,000 cycles in air, and so on, for a total of 19 episodes of EFS testing during its life. The EFS current responses and phase shift behavior for this specimen is shown in Figure 5-45a and 45b. The same convention as used for Figure 5-44, that is, using open points to indicate

the bouts of EFS cycling, is also used here. Note that the large increase that is observed in the current after a bout of air cycling seems only to occur if the air exposure is long. For the shorter intervals used in the later stages of the fatigue life, the increase does not occur. Moreover, the EFS follows the damage development just as it does in continual exposure to the electrolyte, irrespective of whether a crack is present or not. This is a most encouraging and important result.

Results for tests on aluminum specimens subjected to intermittent immersion, of the two types used for steel, are summarized in Table 5-22 and compared to the average behavior for specimens continuously immersed in EFS electrolyte. Three specimens were run in air first and finished in the EFS. Different frequencies were used for the air-cycling but a frequency of 0.5 Hz was always used for EFS operations. For these specimens, there appears to be little difference, if any, in the EFS response as compared to that in the continuously exposed specimens. The first indication of cracking may again occur somewhat later in life for intermittent immersion, but it is not clear if the difference is statistically significant for aluminum alloy.

In addition, Table 5-22 shows that two specimens were run with frequent evaluations by the EFS between bouts of air-cycling. As reported above for steel, this approach can be helpful in interrupting a test when the specimen contains a crack. Typical behavior for one of them, A-b82, for which the detailed history is shown in Table 5-23, is shown in Figure 5-46a to 46c with the same convention as used for steel to discriminate the air-cycling and the EFS-cycling. Consistent with the slow settling-in shown by the EFS in continuously exposed aluminum specimens, these also were slow to reach the stable surface configuration. However, there appears to be a memory of the film formation which allows the behavior from the previous bout of EFS to be inherited by the next. All three reported currents, elastic, plastic and base, steadily increase with cycle accumulation, and the phase shift trends towards 0.5, at least until cracking occurs when the usual drop in the phase shift and the rapid increase of the EFS currents also occur. Again, like behavior in steel, there is a tendency for cracking to be detected later in life. Note that one test interruption was obtained when a crack was just present. The EFS response appears to have performed appropriately but more investigation of this aspect is necessary.

While there is a clear need for more results to be gathered in the context of test interruptions, the present results show no evidence of adverse life effects from test interruptions and intermittent exposures of the subject materials to the EFS. Much development work remains to be done with regard to accelerating the settling-in period, but overall the results reported above are considered encouraging for eventual, successful development of the EFS.

5.3.3.7 EFS Behavior in Gel Electrolyte

As noted in Section 3, it was considered essential for practical reasons to convert the liquid electrolyte into gel form, with the hope that operation of the EFS with a gel electrolyte would not adversely affect its performance and might even improve it. For example, in early stages of development, it was found that use of a gel electrolyte had the effect of suppressing noise in the transient current, probably by eliminating convection currents that occur in an EFS with liquid electrolyte. We report here EFS results of tests on military aircraft materials, the steel and titanium alloy of interest, using the gel form of the electrolyte developed for steel.

A comparison of behavior in liquid electrolyte, expressed as the average for several tests, with that in gel based on laponite is shown for four steel specimens in Table 5-24. It is exciting to find no significant difference in behavior, for the summarized parameters, between the two versions of the electrolyte. Further results supporting this conclusion are shown in Figure 5-47a to 47c; this figure shows the behavior of the various transient and base currents as well as the phase shift behavior throughout life for steel specimen S-54 which, like many of the specimens reported in Sections 5.3.2 and 5.3.3.1 for liquid electrolyte, was cycled at 600 MPa. The reader is encouraged to compare the results shown in Figure 5-47 with those of Figure 5-48. The overall trends are essentially the same and the resolution for crack detection is also similar. A clear difference in the two sets of results is that the instabilities which indicate passivity breakdown as well as damage phenomena tend to be quieter in the gel as compared to the liquid form.

The EFS behavior of the subject titanium alloy when cycled in the same gel, previously identified as being suitable for this metal when the electrolyte is in liquid form, has also been studied. A summary and comparison of the same type as reported above for steel is shown in

Table 5-25. In this comparison, a stress of 580 MPa was used in the stress controlled tests but an additional variable was introduced: frequency. For directly comparable conditions, the EFS behavior in the two electrolyte versions is essentially identical. Moreover, when the frequency is increased, the cycle dependent currents, which depend on the strain rate, also increase and the phase shift decreases, in line with behavior in steel.

We conclude, therefore, that there are no adverse effects of testing in the gel form of the electrolytes for the reported subject materials and the feasibility of converting EFS application to gel electrolyte has been established.

5.3.3.8 Comparison of Fatigue Behavior in Stress and Strain Control and of the Effect of the EFS Sensor Chamber Size

Performing fatigue tests in stress control has certain advantages for EFS investigation. Absence of an extensometer across the gauge length of the specimen allows the test to be run in a vertical orientation, for which most electrohydraulic machines are configured. Only one machine at Penn can be operated in a horizontal orientation. Further, absence of an extensometer permits greater freedom in the fixturing of the EFS sensor hardware. For these reasons most of the tests run during the present program were run in stress control. However, strain control tests have the advantage that, after the crack has been initiated, the increase in stress intensity with crack depth is minimal.* Therefore, the specimen can be expected to spend more of its life in crack propagation, which can be helpful in tests where it is desired to explore EFS response to crack propagation. Accordingly, tests were designed to be run in strain control, after they had been initiated in stress control and the strain behavior of the specimen had been established. It remained to be seen whether or not differences in life periods caused by variations in crack propagation rates could be detected against the background of fatigue scatter and the fact that crack initiation occurs late in the lives of the hardened metals of interest here. Therefore, tests were performed on the steel only.

---

* In this regard, strain control is also more representative of regions of stress concentration (notches) in aircraft components where fatigue damage usually occurs.

Another issue of concern involves the size of the EFS chamber. If the EFS is to be applied to real structures, it can be anticipated that there will be geometrical constraints and the need for placing sensors in small spaces must be considered. Accordingly, the volume of electrolyte available to the EFS was also investigated.

Two approaches to performing strain control tests were attempted. In the first, the standard jig used at Penn for strain monitoring was employed. This jig uses the type of extensometer regularly employed on gauge lengths but attached to hardware connected to the actuator and the load frame. This type of jig thus experiences the elastic strains of many components in the load train as well as that of the specimen and is recognized to be problematic for purposes of strain control. Tests identified as S-2, S-43 and 4130-3 were run in this mode. In order to improve the mode of strain control, while still performing tests in a vertically oriented machine, a new jig was configured in which the extensometer was attached across the shoulders of the specimen, but was located outside the EFS cell. Tests run in this mode are identified as 4130-6 and S-8.

With regard to the size of the sensor and the volume of electrolyte that it contains, the behavior of the regular EFS cell used for most of the Penn tests was compared to that of the smaller sensor designed for application to flat specimens containing stress concentrations. The volume of electrolyte in the regular cell is 50 ml, that of the smaller cell 5 or 6 ml, depending on the apparatus details. For exploring the effect of the cell size the variant having a volume of 5 - 6 ml was selected.

Results showing the effect of these variables are tabulated in Table 5-26. From these measurements, which apply to intermediate life, it is apparent that strain cycling (or the approximation of strain cycling used here) has little effect on life which can be discriminated from scatter (Compare with the results of Table 5-11 obtained under stress control at the same stress). In spite of the inadequacy of the strain control, the sensitivity of crack detection has increased for some tests. Overall, one can say, for this strong steel, prolongation of life by strain cycling does not appear significant, at least as far as convenience in obtaining EFS results is

concerned, but this conclusion might well be modified if the tests were properly controlled in strain with an extensometer attached to the gauge section.

Table 5-26 also shows results obtained for the small size of sensor. It is most encouraging to find that the observed behavior appears to differ not at all from that of the large cell. Further support for this finding can be seen in the standard transient and base current plots, as well as in the phase shift plot and the wave traces as a function of life expended, for steel specimen 4130-3, shown in Figure 5-48a to 48d. The behavior observed in the large cell is mirrored here with good reproducibility. A further point of satisfaction is that this cell is typical of one that might be used in testing a military aircraft; the results demonstrate that the laboratory result can be reproduced in a practical EFS sensor.

5.3.3.9 EFS Behavior with a Driver Ni/NiO Electrode

As part of the effort in optimizing the EFS electrode, reported in Chapter 4, preliminary attempts were made to test commercially available Ni/NiO immersed in the chosen electrolyte, as both the counter electrode and as the driver electrode. Such an apparatus could possibly dispense with the potentiostat and simplify the EFS data acquisition process by allowing the cell current to be recorded, much as was done previously with the Barnacle electrode for analyzing the hydrogen content of steel. Therefore, three tests were performed on steel using a driver electrode of Ni/NiO after it had been tested for benignity in its interaction with the subject alloys, immersed in the liquid form of their electrolytes.

The EFS and fatigue results of these tests are shown in Table 5-27 along with the average of the results conducted with a potentiostat in the three-electrode mode. It will be noted that there was considerable variation in the various currents observed and in the measured phase shifts. Also, the Ni/NiO results were not as sensitive in detecting fatigue cracking as the potentiostated form of the EFS. Nevertheless the Ni/NiO driver worked in the EFS mode. We regard these results as encouraging, because they represent preliminary results and we have had little opportunity to develop the Ni/NiO driver in this context. The results warrant expending more effort on the complete development of the Ni/NiO driver electrode.

5.3.4 EFS Response of Coated Materials

Since the EFS measures the microscopic condition of the surface of the structure as it is affected by the loading, it would be undesirable to alter the surface mechanically or chemically before or during application of the EFS. Most structural surfaces are coated. It is necessary, therefore to deal with the issue of whether or not to remove the coating before applying the EFS. The most desirable approach would be not to remove the coating. Accordingly, EFS tests were performed on aluminum specimens which were coated according to the regular procedures used in painting conventional aircraft surfaces. Generally, on interior surfaces, a primer is used; on the exterior, the same primer is used and it is finished with a topcoat to represent the exterior of the aircraft. Specimens were prepared with either primer alone to exemplify the interior or with both primer and top coat. Both of these types of specimen were tested. Details of the painting are provided in Section 2.2. It is necessary to know that, before the specimens were painted, they were machined by stress free machining and the gauge surfaces were polished through the emery grades to a 1200 finish, with the emery scratches being oriented in the longitudinal direction. Details of the EFS results from tested specimens are reported as follows.

A total of five coated aluminum specimens were tested at a stress amplitude of 200 MPa (R = -1) under stress control and with continual exposure to EFS interrogation. Their fatigue and EFS behavior are summarized in Table 5-18 and compared with average behavior (top line of Table 5-28) for specimens in the uncoated condition. With regard to coatings and their identification, T indicates the top coated finish and P the primed specimens. The behaviors of the two top-coated specimens were quite different from any other specimen studied in the present program. In A-b71, the coat was intact and strongly insulating. Very little EFS current could penetrate the coating and there were no indications of cracking, even when we were sure that the specimen contained a significant crack. It appears that the top coat is sufficiently rubbery to bridge the crack and to provide a strong barrier to the interrogating electrolyte. We believe the observed behavior will be typical of a new coating.

In aircraft which have been in service for months or years we believe that few top coats will be fully intact. Accordingly, on specimen A-b10, we made a small scratch on the gauge section of the specimen so as to breach the top coat, and then performed a fatigue test with it,

using the EFS to measure damage development continuously. Figure 5-49a and 49b shows the transient current and phase shift behaviors, respectively, of this specimen. The transient current is very low initially but the EFS signals become very active at the mid-life region, and cracking is indicated particularly early in life, perhaps because there was a stress concentration introduced by the scratch that initiated the fatal crack. However, the personnel were not convinced that significant mechanical damage had been done to the specimen in the scratching operation. Interestingly enough, this specimen had a particularly long life within the scatter band. The results indicate that the EFS can be extremely sensitive to fatigue damage when a coating is present that serves to suppress the background current.

The EFS and fatigue behaviors of the primed aluminum specimens, summarized in Table 5-28, appear much more similar to those of uncoated specimens. We note, however, that the EFS transients are reduced somewhat but the signal to background behavior is enhanced and crack detection can be made earlier in life based on certain of the signals recorded. The details of the EFS behavior are shown in Figure 5-50, specifically for specimen A-b69. The extended variation of the "elastic" current at the beginning of life indicates the usual changes in the surface films and also that the prime coat is being penetrated by the electrochemical reactions. Interestingly, the phase shift behavior is significantly affected (Figure 5-50c) and the crack peak, when it develops (Figure 5-50d) is strongly pronounced. The phase shift does not show the large change of magnitude observed in uncoated specimens, but rather a great increase in instability, indicating fatigue damage. These results demonstrate that it is feasible to employ the EFS on painted surfaces, especially on the interior primed surfaces of military aircraft, and possibly on top-coated surfaces if these are aged and cracked.

Also shown in Table 5-28 are results for tests on primed specimens in which the frequency was varied. The transient current increased significantly at the highest frequency, 5 Hz, used on the 7075 alloy, but the crack detectability was not affected. Note that cracking was indicated at about 70% of life irrespective of frequency. More work is needed over a wider range of frequency, especially at higher frequencies.

5.3.5 Preliminary Results on Minimum Crack Size Detection

An important property of any tool for non-destructive evaluation of fatigue damage is its response to cracks of different sizes. The EFS offers the valuable property that it can potentially detect damage prior to the onset of cracking because it responds to the mechanisms of pre-initiation, to varying degrees depending on the metal, and its metallurgical state, *i.e.*, on both its chemistry and its strength/hardness. Generally, more ductile metals, which show pronounced forms of strain localization, give better pre-cracking information concerning damage with the EFS than harder, brittle metals. Whatever the case, however, the EFS detects the presence of cracks and it is necessary to demonstrate the limits of crack detectability with the tool. Preliminary attempts to measure the minimum detectable crack size were carried out, using the steel of interest here as the vehicle.

Experiments were performed as follows. Steel specimens were entered into the EFS cell and cycled at 600 MPa while the data acquisition system recorded the EFS responses. After cracking indications were recorded, but before they had developed extensively, the test was interrupted, the specimen dismounted from the machine and a search was made of the gauge section for cracks using optical microscopy and the SEM in order to detect the indicated crack(s). Certainly no such crack was detectable by the naked eye. Initially, the specimens were studied with their surfaces prepared by the standard preparation technique developed early in the program, namely a wet/dry emery finish to 1200 grit. In four specimens studied, in which we knew that there were cracks, we could find cracks in the size range of 130 to 170 microns in only two of them, in spite of persistent efforts with the SEM at high magnification. Part of the difficulty of finding the cracks was that they were small, but more importantly, the 1200 grit surface finish was sufficient to hide them. Another factor was that the electrohydraulic machine was programmed to complete a cycle from the compression reversal, and therefore any crack present would be squeezed shut, making it more difficult to find.

A more certain technique of finding a crack, especially when it is small, is to interrupt a test periodically and replicate the surface on each occasion. Then, after a crack has become obvious so as to identify the fatal crack, it is possible to follow its development on the replicas back to its initiation. This method, while effective, is extremely tedious and becomes doubly so

when the specimen is being interrogated by the EFS. Thus, at each interruption, it is necessary to clean and dry the specimen before taking the replica. Nevertheless, a steel specimen, code numbered st210-50, was polished to a mechanical finish superior to that of the regular grit finish, cycled at 600 MPa while under interrogation by the EFS and subjected to periodic replication. In light of the tedious nature of the experiment, only a few interruptions were made. The effect of two of them before the onset of cracking can be seen in the "plastic" current versus cycles record of this specimen shown in Figure 5-51. The dips at cycles 15,000 and 46,000 in the more or less constant current that precedes cracking in this steel are associated with the restart changes in the electrochemical response after an interruption. Optical micrographs of the gold-shadowed replicas recorded after the marked instabilities noticeable in Figure 5-51 and which indicate cracking are shown in Figure 5-52. These test interruptions and replications were performed at 56,000 and 84,000 cycles. Figure 5-51 shows that the specimen was rapidly approaching the end of its life in the mid 80 thousands of cycles because the plastic current increased exponentially.

The two views of the cracks shown in Figure 5-52 demonstrate that a crack of the order of 100 microns can be detected readily in this material subject to the applied fatigue conditions. Note that the test was not interrupted at the first sign of cracking but only after the experimentalist was convinced that a crack was present. Therefore, it is clear that improved performance will be possible in the subject aircraft materials. We view the present results as highly promising.

5.4   Advanced Signal Processing of EFS Response

Since EFS signals are complex and have been determined to be filled with information concerning cyclic behavior and fatigue damage, it seems prudent to explore the possibilities of advanced signal processing techniques. Successful application of these techniques to EFS data processing promises to produce economies in the application of the technique, as well as making the tool more readily available to a wider user base, because it could well reduce the need for input and interpretation by highly skilled personnel. Accordingly the Information and Communications section at Penn was encouraged to examine the latent possibilities of the EFS system in this direction. At first, application of advanced signal processing to EFS measurements was found difficult because the potentiostats initially employed were noisy and

fatigue tests were often interrupted for experimental purposes. The signal perturbations thus introduced made it difficult for the computer to recognize the valuable signals. However, when ad hoc potentiostats were constructed, improved, and applied to EFS measurements, reliable signals became available. Several signal processing techniques have been found to be of potential value in classifying the fatigue damage of aircraft metal samples tested with the EFS. This section documents these signal processing techniques and applies them to the EFS data selected from the sections above.

5.4.1 Two-Dimensional Measurement Display

One aim was to show the whole damage history of a fatigue specimen, as read by the EFS, on a single page. Accordingly a graphical technique was developed. It will be noted that full information concerning damage is visible in the waveform plots shown in preceding subsections and in fact several such waveforms, identified by their cycle counts, can be displayed in a single figure to show the development of their fatigue damage (see, for example, Figure 5-40a and b). One could alternatively show such measurements and indeed every waveform recorded, by making a plot of cycles versus time, and then drawing a family of straight lines on the plot, the intensity of which is determined by the magnitude of the total EFS current in the positive direction. An example of this plot for aluminum specimen A-b 105, the object of interest in Figure 5-40, is shown in Figure 5-53a. (See Table 5-12 for the fatigue and EFS conditions for this specimen). The family of lines is drawn parallel to the time axis and they are so dense that they map out black and white regions of shading on the plot. Dark regions correspond to current peaks and white regions to current minima. Note from Figure 5-40 that EFS waveforms corresponding to 4 stress cycles are plotted and there are EFS T-peaks and C-peaks for each. Usually the C-peak is dominant. Accordingly, in Figure 5-53 there are four dense dark bands representing those peaks. The T-peaks, of lesser current, appear as less dark bands parallel to the bands for the C-peaks. After the crack(s) initiate the C-peak disappears, the crack peak appears as a subsidiary dark band adjacent to the T-peak and finally the T-peak becomes dominant as the fatal crack grows.

A similar type of two dimensional representation, an EFS map, of the EFS and damage behavior of steel specimen S-42, the testing details of which can be obtained from Table 5-11, is shown in Figure 5-54a. The corresponding waveforms of this specimen can be seen in Figure 5-

38e and f. Unlike aluminum which has T-peaks and C-peaks, only one dominant peak appears for steel under the fatigue conditions which apply here. Therefore there are only as many dark bands as there are cycles in Figure 5-54a, although another vestigial peak can be made out adjacent to the dominant peak. This vestigial peak eventually develops into the dominant crack peak in the latest stages of life. At a glance, then, the whole damage history of the specimen can be absorbed by the observer.

As noted in Section 5.3.2, fast Fourier transforms (FFT) were routinely obtained of the current waveforms, as the EFS measurements were recorded. The FFT can also be represented as a map with respect to life and the corresponding maps for the aluminum and steel specimens discussed above are shown in Figures 5-53b and 5-54b, respectively. In thus analyzing and displaying the frequency behavior of the current signals, the main spectral components of both the aluminum and steel samples are seen to lie at 0.5 and 1 Hz (the cyclic loading frequency was 0.5 Hz). At a quick estimate, the 0.5 and 1 Hz components for aluminum are roughly equal, for most of the life, until cracking develops when spectral components at 1.5 and 2 Hz gain strength. In steel, on the other hand, the 1 Hz component appears weak at the outset of life but gains strength later and the higher harmonics are more complex than those of aluminum.

A more quantitative approach to treating the FFT data can be obtained by computing the power in the various spectral components. Graphs of "Percentage of Total Power in FFT of Current" for the aluminum and steel specimens A-b 105 and S-42 are shown in Figures 5-55 and 5-56, respectively, specifically for the frequencies of 0.5 and 1 Hz. For the aluminum specimen, the percentage of power at 0.5 Hz shows a clear trend of decreasing for most of its fatigue life, while the percentage of power at 1 Hz increases. For the steel specimen (Figure 5-56), the percentages of power for both the 0.5 and 1 Hz frequencies remain stable for approximately two-thirds of its fatigue life, and then the percentage of power decreases at 0.5 Hz and increases at 1 Hz, although with a significant amount of variance. This variance, as noted previously, is caused by the exposure and repassivation of new metal surface from cracking and associated plasticity, which in turn causes abrupt increases and decreases in the amplitude of the output current.

The method of two-dimensional display can also be applied to EFS measurements obtained from specimens subjected to variable loading, including both changes in stress amplitude and frequency. The effect of varying stress inputs can be seen in Figure 5-57 for aluminum specimen A-T51 and Figure 5-58 for steel specimen S-47. The aluminum specimen was subjected to the Penn 3 low - 1 high sequence described in Section 7.3 and the steel specimen to the Penn alternating low-high sequence also described in that section. The testing details and EFS responses of these specimens can be read from Tables 7-4 and 7-5.

In order to correlate the stress inputs against the EFS maps of 5-57 and 5-58, the stress signals of the aluminum and steel specimens are shown in Figures 5-59a and 59b, respectively. Note that the time scales, given in seconds, of the maps and the signals correspond exactly. The fatigue behavior of these specimens, as revealed in the maps, is interesting. For example, in aluminum, there is a strong T-peak for the high tensile excursion even early in life, followed by a strong C-peak as expected for the high amplitude compression. The next T-peak, for the first of the three low amplitude cycles, is also strong, reflecting the large tensile reversal from the high compression amplitude. Note the decline of the C-peaks as cracking develops and the instabilities associated with the high tension amplitude.

It will be recalled that the EFS current is recorded for several cycles each 100 cycles of life. For the steel specimen, Figure 5-58, the specific cycles recorded for the high and low amplitudes interchanged periodically through life, giving rise to the pattern of alternations visible in the map. When cracking was established, the dominant T-peak naturally was associated with the high amplitude cycle.

The b parts of Figures 5-57 and 5-58 show the FFT (also in map form) for the EFS maps as a function of life expended. Although the harmonics are more complex than those observed in constant amplitude cycling, the same pattern is observed of an increase in the intensity of higher harmonics as damage develops late in life. This result offers encouragement that the EFS will be effective in assessing damage in more complex service stress histories. EFS maps do not require that the stress cycles be recorded and their use could eliminate the need to use strain gauges, a considerable convenience in applying the EFS.

5.4.2 Correlation and Bispectral Index

A standard method of investigating the relationship between two signals, x and y, say, is to calculate their correlation, which is a measure of their similarity, and can be defined as:

$$C = \frac{x \cdot y}{(x \cdot x)(y \cdot y)}$$

where x and y are defined as normalized zero mean data vectors. In the matter of interest, the correlation between the input stress signal [the fatigue cycle] and the output current signal, the total EFS current, that is, the sum of the alternating elastic and plastic currents, is calculated over the life of the specimens. Figures 5-60 and 5-61 show the graphs "A-B 105: Correlation between Current and Stress" and "S-42: Correlation between Current and Stress" and how the correlation values change over the fatigue lives of these two aluminum and steel specimens, respectively. The changes in the correlation values are caused mostly by phase shifts between the input stress and the measured EFS current, although there is also a contribution from changes in the waveform shape of the current signal. The aluminum specimen shows an approximately linear increase in correlation over most of its fatigue life, with an abrupt increase towards the end of its life. The steel sample shows a stable correlation value for approximately two thirds of its fatigue life, and then an increasing trend, with some variance, for the remainder of its life. Again, we believe that this variance is due to the exposure and repassivation of the steel surface from cracking. The correlation behavior seems to faithfully reflect the gradual development of fatigue damage during the bulk of the lives of these hardened materials, followed by accelerated damage development in the final stages.

Bispectral analysis can be used to determine the amount of phase coupling between two frequencies in a complex signal. In particular, we have examined the phase coupling between the two main spectral components of specimens subjected to constant amplitude cycling at a frequency of 0.5 Hz., namely the 0.5 and 1 Hz components. The bispectrum is defined by:

$$M (u, v) = X(u) X(v) X (u + v)$$

where u and v are the desired frequency components in radians. Figures 5-62 and 5-63, respectively, show the graphs for the identified aluminum and steel specimens. These graphs show the bispectral index for the two main frequency components (0.5 and 1.0 Hz) in the EFS output currents of the specimens. Not surprisingly, because the 0.5 Hz component is connected to the current associated with the elastic strain through the stress input, the indices tend to show the same behavior as the correlation. That is, aluminum specimen A-b 105 shows an approximately linear increase in the bispectral index over most of its fatigue life, with an abrupt increase towards the end of its life. The steel specimen S-42 shows a stable bispectral index for approximately two-thirds of its fatigue life, and then an increasing trend with some variance for the remainder of its life.

Finally, the last technique investigated is time-domain waveform analysis. This method examines quantitatively how the output current signal changes over time with respect to the relative heights and locations of its peaks and valleys, behavior which can be qualitatively assessed by eye from the waveform plots shown previously. So far, aluminum samples which have been examined show the well known EFS trend of having peaks at both positive and negative stress input values (T-peaks and C-peaks), changing towards having only a peak at the tensile stress input as the growing fatal crack asserts its effect. Comparative measures of the relative current peak values show clear trends indicating how the fatigue life of the specimen is expended.

5.4.3 Concluding Remarks on Advanced Signal Processing

The signal processing techniques that have been described (percentage of total FFT power at specific frequencies, correlation, bispectral analysis, and time-domain waveform analysis) appear to relate to the physics of the fatigue damaging processes and therefore can be used to generate inputs to a feature classifier or a neural network. At present, because of the time taken to overcome experimental difficulties in gathering reliable EFS measurements in the opening stages of the program, efforts in this direction are still preliminary. The main challenge is to find normalized feature sets for different metal/alloy types that can provide reliable fatigue life estimation regardless of varying structure/specimen parameters (size, shape, input stress, frequency, *etc*). In Phase 2, we plan to continue investigation into other classification techniques

to identify the fatigue damage of a metal specimen given a finite number of cycles of the EFS output current.

5.5 References

5.1   Li, Y. F., Farrington, G. C., and Laird, C., *Acta Metall. Mater.*, **41** (1993) 693

5.2   Li, Y. F., Farrington, G. C., and Laird, C., *Ibid*, **41** (1993) 709

5.3   Li, Y. F., Farrington, G. C., and Laird, C., *Ibid*, **41** (1993) 723

5.4   Li, Y. F., *Ph.D. Thesis*, University of Pennsylvania, 1991

5.5   Boettner, R. C., Laird C., and McEvily, A. J., *Trans. AIME*, **223** (1965) 379

5.6   Henry, M., G. E. Research Laboratories, Schenectady, NY, private communication, 1992

5.7   Laird, C., and Duquette, D. J., in *Corrosion Fatigue*, Eds. O. J. Devereux, A. J. McEvily, and R. W. Staehle, NACE, pp. 87-117, 1972

5.8   Starke, E. A., and Lütjering, G., in *Fatigue and Microstructure*, Am. Soc. Metals, 1979, pp. 205-244.

5.9   Lees, D., MS Thesis on Advanced Signal Processing of EFS Results, University of Pennsylvania, 1998.

5.10 James, P., Ph.D. Thesis, University of Cambridge, 1961

5.11 Forsyth, P. J. E., *Phil. Mag.*, **2** (1957) 437

Table 5-1. Effect of Maximum Stress on Features of EFS Signal for 7075 Al Alloy Tested at R = -1 and 1 Hz.

Specimen ID	Max Stress (MPa)	Max Stress (ksi)	Cycles to Failure	Current spike in T-peak	Percentage of Fatigue Life
AH4C3F	345	50	7,178	4,500	62
AC58CF	345	50	11,387	7,100	63
AF65C3F	310	45	14,622	10,200	70
AH12C3F	276	40	49,252	42,300	86

Table 5-2. Effect of Maximum Stress on Features of EFS Signal for 4130 Steel Tested at R = -1 and 1 Hz.

Specimen ID	Max Stress (MPa)	Max Stress (ksi)	Cycles To Failure	Drop in C-peak rise time	Percentage of Fatigue Life
SM335C4F	758	110	20,673	14,000	68
SM335C1F	724	105	21,804	14,400	66
SI343C3F	724	105	23,426	17,670	75
SE335C1F	724	105	27,641	19,670	72
SM350C4F	724	105	28,741	22,730	79
SB220C2F	724	105	22,850	16,430	72
SI335C4F	655	95	93,452	85,000	91
SM350C1F	641	93	130,791	124,000	95
SC459C3F	600	87	117,471	103,570	88

Table 5-3. Effect of R-Ratio on Features of EFS Signal for 7075 Al Alloy.

Specimen ID	Max Stress (MPa)	R Ratio	Cycles to Failure	Feature in EFS Signal	Percentage of Fatigue Life
AF65C2AF	345	-1	9,623	6,000 [a]	63
AF50C3F	345	0.05	44,639	36,000 [b]	81
AJ35C2BF	345	0.5	57,095	50,200 [c]	88
AF43C2AF	276	-1	32,067	22,000 [c]	69
AF27C2AF	276	0.05	56,995	51,000 [c]	89
AF12C2BF	276	0.5	416,310	391,300 [c]	94

Feature: a) Increase in width of T-peak; b) Increase in T-peak decay time; c) Increase in T-peak amplitude

Table 5-4. Effect of Loading Frequency on EFS Signal for 7075 Al Alloy.

Specimen ID	Stress (Mpa)	Frequency (Hz)	Cycles to Failure	Feature in EFS Signal	Percentage of Fatigue Life
AH4C3F	345	1	7,178	4,500 [a]	63
AF65C2AF	345	5	9,623	6,000 [a, c]	63
AH12C3F	276	1	49,252	42,300 [a]	86
AF43C2F	276	5	32,067	22,000 [b]	69

Feature: a) Current spike in T-peak; b) Increase in T-peak amplitude: c) Increase in T-peak width

Table 5-5. Effect of Loading Frequency on EFS Signal for 4130 Steel.

Specimen ID	Frequency (Hz)	Cycles to Failure	Drop in C-peak decay time	Drop in C-peak rise time	Percentage of Fatigue Life
SM350C4F	1	28,741	22,300	22,700	79
SM335C1F	1	21,804	14,400	14,500	67
SE335C1F	1	27,641	20,000	19,900	72
SI343C3F	5	23,426	20,000	20,000	85
SE343C2F	5	23,000 [a]	22,100	21,800	—
SE350C3F	5	15,000 [a]	—	—	—

a) interrupted test

Table 5-6. Effect of Loading Frequency on EFS Signal for Ti-6Al-4V Alloy.

Specimen ID	Frequency (Hz)	Cycles to Failure	Drop T-peak width	Percentage of Fatigue Life
TV19CF	1	11,888	9,550	80
TW41CF	1	14,847	11,560	78
TW19CF	5	17,843	13,300	75

Table 5-7. Effect of Applied Potential on EFS Signal for 7075 Al alloy.

Specimen	Potential (V_{SCE})	Cycles to Failure	Spike in T-peak	Percentage of Fatigue Life
AH35C3F	0.0	6,511	4,300	66
AH4C3F	0.3	7,178	4,500	63
AH65C1F	0.4	5,836	4,000	68
AH12C2AF	0.5	10,391	6,250	60

Table 5-8. Effect of Several Variables on EFS Signal of Primer Coated 7075 Al Alloy.

Specimen	Stress (MPa)	R	Frequency (Hz)	Potential (V_{SCE})	Cycles to Failure	Amplitude T-peak	Life Percent
AH50C2AF	345	-1	1	0.3	8,725	7,000	80
AH27C1F	345	-1	1	0.4	10,828	—	—
AH35C2BF	310	-1	1	0.3	26,788	22,000	82
AH27C2BF	276	-1	5	0.3	67,331	61,600.	91
AH58C2BF	276	.05	5	0.3	92,918	81,200	87
AH65C3F	276	0.5	5	0.3	3,445,038	—	—
AH27C2AF	241	-1	5	0.3	66,817	60,600	91

Table 5-9. Effect of Several Variables on EFS Signal of Primer plus Top Coated 7075 Al Alloy

Specimen	Stress (MPa)	R	Frequency (Hz)	Potential (V_{SCE})	Cycles to Failure	Amplitude T-peak	Life Percent
AH35C2AF	345	-1	1	0.3	10,672	8,700	82
AH19C2AF	345	-1	1	0.3	12,383	10,000	82
AH19C2BF	345	-1	1	0.4	7,680	7,100	92
AH50C1F	310	-1	1	0.3	29,828	28,800	97
AH4C2AF	276	-1	5	0.3	22,200	21,140.	95
AH4C2BF	276	.05	5	0.3	172,214	168,200	98
AH43C2AF	276	0.5	5	0.3	1,275,000[a]	—	—
AH12C2BF	241	-1	5	0.3	109,798	106,600	97

a) test interrupted before occurrence of specific feature in the EFS signal

Table 5-10. Experimental Conditions for Interrupted Tests

Alloy	Specimen	Stress (Mpa)	R	Frequency (Hz)	Potential (V_{SCE})	Interruption (Cycles)	Estimated Life (%)
7075	AF19C3F	310	-1	5	0.3	6,500	20–40
7075	AF35C3F	310	-1	1	0.3	8,345	30–60
7075	AF58C2AF	310	-1	1	0.3	13,000	40–80
130	SE350C3F	724	-1	5	0.5	15,000	40–80
4130	SE343C2F	724	-1	5	0.5	23,000	40–80

Table 5-11. **Fatigue Conditions and Behavior, and EFS Response of 4130 Steel Cycled in Electrolyte at a Frequency of 0.5 Hz.**

Specimen ID	Stress (MPa)	Potential (Volt)	Life (cycle)	CIAC*	% of life	Plastic current	Elastic current	Base current	Phase factor
S-53	600	0.5	123,400	104,000	84.3	0.01	0.09	0.06	-0.29
S-9	600	0.5	108,900			0.017	0.081	0.08	-0.29
S-50	600	0.4	209,600	150,000	71.6	0.01	0.16	0.01	-0.3
S-42	600	0.4	193,800	122,000	63.0	0.008	0.12	0.017	-0.3
S-25	600	0.525	259,800	210,000	80.8	0.004	0.035	0.03	-0.3
Average			196,600	146,500	75	0.01	0.1	0.04	-0.3

All current unit = $\mu A/cm^2$

* CIAC = Crack Indication at Cycle

For test on sample S-25, a 2-electrode system with a silver counter electrode was used, the current value seems very low, when compared to other tests.

Table 5-12. **Fatigue Conditions and Behavior, and EFS Response of Aluminum Alloy 7075 Cycled in Electrolyte at a Frequency of 0.5 Hz.**

Specimen ID	Stress (MPa)	Potential (Volt)	Life (cycle)	CIAC	% of life	Plastic current	Elastic current	Base current	Phase factor
A-t87	200	0.5	64,200	56,000	87.2	0.033	0.03	0.84	0.49
A-t78	200	0.3	65,600	58,000	88.4	0.03	0.025	0.8	0.5
A-b72	200	0.4	96,400	80,000	83.0	0.05	0.04	1.5	0.5
A-b105	200	0.35	125,800	114,000	90.6	0.05	0.06	1.6	0.5
Average			88,000	77,000	87.3	0.04	0.038	1.19	0.5

All current unit = $\mu A/cm^2$
* CIAC = Crack Indication at Cycle.

Table 5-13. **Fatigue Conditions and Behavior, and EFS Response of Ti-6Al-4V Cycled in Electrolyte at a Frequency of 0.5 Hz.**

Specimen ID	Stress (MPa)	Potential (Volt)	Life (cycle)	CIAC	% of life	Plastic current	Elastic current	Base current	Phase factor
Ti-12	620	0.6	31,300	27,000	86.3	0.025	0.07	0.05	0.25
Ti-21	580	0.6	176,000	172,000	97.7	0.02	0.06	0.05	0.25

All current unit = $\mu A/cm^2$
* CIAC = Crack Indication at Cycle.

Table 5-14 Comparison of EFS Response of Aircraft Alloys Cycled at a Frequency of 0.5 HZ Under Sinusoidal Stress Control.

Specimen Material	Stress (MPa)	% of life	Plastic current	Elastic current	Base current	Phase factor
Al-7075	200	86	0.03	0.025	0.75	0.46
Steel 4130	600	77	0.016	0.12	0.05	-0.3
Ti-6-4	580	92	0.022	0.07	0.04	0.24

All current unit = $\mu A/cm^2$

Table 5-15. EFS Response of Aluminum 7075 in Relation to Stress Amplitude and Fatigue Life.

Specimen ID	Stress (MPa)	Life (cycle)	CIAC	% of life	Plastic current	Elastic current	Base current	Phase factor
A-t75	250	53,700	45,800	85.3	0.03	0.02	1	0.425
Average	230	58,800	52,800	89.6	0.044	0.024	1	0.42
Average	200	88,000	77,000	87.3	0.04	0.038	1.19	0.5
Average	180	134,000	108,000	79.4	0.035	0.035	1.25	0.48
A-b33	160	131,700	110,000	83.5	0.03	0.027	1.2	0.48
A-t73	150	671,200	611,000	91	0.004	0.006	0.25	0.48

All current unit = $\mu A/cm^2$
* CIAC = Crack Indication at Cycle.

Table 5-16. EFS Response of 4130 Steel in Relation to Stress Amplitude and Fatigue Life.

Specimen ID	Stress (MPa)	Life (cycle)	CIAC	% of life	Plastic current	Elastic current	Base current	Phase factor
S-41	550	531,800	400,000	75.2	0.04	0.14	0.2	-0.3
Average	600	196,600	146,500	75	0.01	0.1	0.04	-0.3
4130-5	700	24,700	19,700	80	0.02	0.15	0.25	-0.27

All current unit = $\mu A/cm^2$
* CIAC = Crack Indication at Cycle.

Table 5-17. Effect of Cyclic Frequency on the EFS Response of 4130 Steel.

Specimen ID	Freq. (Hz)	Stress (MPa)	Life (cycle)	CIAC	% of life	Plastic current	Elastic current	Base current	Measured Phase	Corrected Phase
Average	0.5	600	196,600	146,500	75	0.01	0.1	0.04	-0.3	-0.29
S-19	2	600	216,100	185,000	85.6	0.007	0.44	0.04	-0.37	-0.33
4130-8	3.5	600	55,700	47,000	84.4	0.015	0.75	0.12	-0.45	-0.38
S-40	5	600	116,000	108,000	93.1	0.003	0.7	0.4	-0.54	-0.44

All current unit = $\mu A/cm^2$
* CIAC = Crack Indication at Cycle.

Table 5-18. Phase Shift Correction Required from Signal Conditioning Unit.

Testing Frequency	Period (second)	Correction Number (Period)
0.5	2	0.01
2	0.5	0.04
3.5	0.29	0.07
5	0.2	0.1

Table 5-19. Effect of Cyclic Frequency on the EFS Response of Al 7075.

Specimen ID	Freq. (Hz)	Stress (MPa)	Life (cycle)	CIAC	% of life	Plastic current	Elastic current	Base current	Measured Phase	Corrected Phase
Average	0.5	200	88,000	77,000	87.3	0.04	0.038	1.19	0.5	0.51
A-t85	2	200	210,200	192,500	91.6	0.045	0.05	1.25	0.35	0.39
A-b36	3.5	200	123,400	106,000	85.9	0.05	0.05	1.2	0.25	0.32
A-b94	5	200	314,800	290,000	92.1	0.007	0.03	1.2	0.1	0.2

All current unit = $\mu A/cm^2$
* CIAC = Crack Indication at Cycle.

Table 5-20. Comparison of EFS Behavior in 4130 Steel Continually and Intermittently Exposed to Electrolyte.

Type of Test	Specimen ID	Freq. (Hz)	Stress (MPa)	Cycles in air	Cycles in Solution	CIAC	% of life	Plastic current	Elastic current	Base current	Phase Factor
Continuous		0.5	600		196,600	146,500	75	0.01	0.1	0.04	-0.3
Air+Solution	S-18	8/0.5	600	70,000	82,500	140,000	91.8	0.006	0.125	0.03	-0.29
Interrupt	S-46	0.5	600		182,800	170,000	90	0.0075	0.17	0.03	-0.29
Interrupt	S-20	0.5	600		157,900	151,000	95.6	0.02	0.14	0.1	-0.28

All current unit = μA/cm^2

* CIAC = Crack Indication at Cycle.

Table 5-21. Electrolyte Exposure History for Steel Specimen S-20 Intermittently Subjected to EFS Testing.

Solution in at or before # of cycle	Solution out At or after # of cycle	# of Cycles in Solution	Then # of Cycles in Air
1	2,000	2,000	62,200
64,200	65,000	800	15,000
80,000	80,500	500	4,900
85,400	86,000	600	6,000
92,000	92,500	500	5,000
97,500	98,000	500	5,500
103,500	104,500	1,000	3,000
107,500	108,000	500	2,500
110,500	111,000	500	2,000
113,000	113,500	500	2,500
116,000	116,500	500	2,000
118,500	119,000	500	6,000
125,000	125,500	500	4,500
130,000	130,500	500	3,500
134,000	134,500	500	5,500
140,000	140,500	500	4,500
145,000	145,500	500	2,500
148,000	150,000	2,000	2,100
152,100	157,900	5,800	

Table 5-22. Comparison of EFS Behavior in Aluminum Alloy 7075 Continually and Intermittently Exposed to Electrolyte.

Type of Test	Specimen ID	Freq. (Hz)	Stress (MPa)	Cycles in air	Cycles in Solution	CIAC	% of life	Plastic current	Elastic current	Base current	Phase Factor
Continuous		0.5	200		88,000	77,000	87.3	0.04	0.038	1.19	0.5
In air then in solution	A-b43	2/0.5	230	40,000	18,300	55,000	94.3	0.07	0.05	1.3	0.48
	A-b57	4/0.5	190	200,000	110,000	291,000	93.8	0.043	0.06	2.15	0.5
	A-b80	8/0.5	200	70,000	53,800	117,000	94.5	0.06	0.07	2.25	0.55
interrupt Test	A-b59	0.5	200		138,700	130,000	93.7	0.05	0.06	1.4	0.5
	A-b82	0.5	200		135,000	120,000	88.9	0.01	0.015	0.35	0.43

All current unit = $\mu A/cm^2$

* CIAC = Crack Indication at Cycle.

Table 5-23. Electrolyte Exposure History for 7075 Al Specimen A-b82 Intermittently Subjected to EFS Testing.

Solution in at or before # of cycle	Solution out At or after # of cycle	# of Cycles in Solution	Then # of Cycles in Air
1	10,000	10,000	28,800
38,800	48,700	9,900	3,300
52,000	56,300	4,300	9,700
66,000	67,200	1,200	7,900
75,100	76,400	1,300	6,800
83,200	83,800	600	5,500
89,300	89,900	600	4,900
94,800	95,000	200	5,000
100,000	100,500	500	6,500
107,000	107,500	500	7,500
115,000	115,500	500	5,100
120,600	121,000	400	7,500
128,500	135,000	6,500	

Table 5-24. Comparison of EFS Response for 4130 Steel Exposed to Gel Electrolyte vs. Liquid Electrolyte.

Type of Test	Specimen ID	Freq. (Hz)	Stress (MPa)	Life (cycle)	CIAC	% of life	Plastic current	Elastic current	Base current	Phase Factor
In liquid		0.5	600	196,600	146,500	75	0.01	0.1	0.04	-0.3
Tested in Gel	S-54	0.5	600	80,600	56,000	69.5	0.01	0.1	0.035	-0.3
	S-52	0.5	600	120,200	86,000	71.5	0.011	0.11	0.03	-0.29
	4130-2	2.5	600	187,900	180,000			0.44		-0.32
	St210-52	5	600	141,200	130,000		0.02	0.94	0.08	-0.38

All current unit = $\mu A/cm^2$
* CIAC = Crack Indication at Cycle.

Table 5-25. Comparison of EFS Response for Ti-6Al-4V Exposed to Gel Electrolyte vs. Liquid Electrolyte.

Type of Test	Specimen ID	Freq. (Hz)	Stress (MPa)	Life (cycle)	CIAC	% of life	Plastic current	Elastic current	Base current	Phase Factor
In liquid	Ti-21	0.5	580	176,000	172,000	97.7	0.02	0.06	0.05	0.25
In gel	Ti-22	0.5	580	66,600	62,000	93.1	0.022	0.075	0.025	0.22
In gel	Ti-19	2.5	580	263,000	255,000	97.0	0.07	0.35	0.025	0.19
In gel	Ti-23	5	580	172,700	167,000	96.7	0.08	0.61	0.12	0.12

All current unit = $\mu A/cm^2$
* CIAC = Crack Indication at Cycle.

Table 5-26. EFS Response of 4130 Steel Cycled Under Strain Control or in an EFS Cell of Small Volume.

Type of Test	Specimen ID	Freq. (Hz)	Stress (MPa)	Life (cycle)	CIAC	% of life	Plastic current	Elastic current	Base current	Phase Factor
Regular		0.5	600	196,600	146,500	75	0.01	0.1	0.04	-0.3
Strain control	S-2	0.5	600	139,300	126,000	90.5	0.02	0.12	0.03	-0.28
	S-43	0.5	600	143,100	117,000	81.8	0.03	0.13	0.03	-0.28
	4130-6	0.5	600	88,000	53,000	60.2	0.02	0.16	0.06	-0.275
	S-8	0.5	600	182,000	167,000	87.9	0.01	0.13	0.007	-0.28
Small cell	4130-3	1	600	102,500	60,000	58.5	0.01	0.19	0.1	-0.32
	4130-10	0.5	600	80,800	73,000	90.3	0.01	0.11	0.35	-0.3

All current unit = $\mu A/cm^2$
* CIAC = Crack Indication at Cycle.

Table 5-27. Fatigue and EFS Response of 4130 Steel When Subjected to EFS Testing Under a Ni/NiO Driver Electrode.

Type of Test	Specimen ID	Freq. (Hz)	Stress (MPa)	Life (cycle)	CIAC	% of life	Plastic current	Elastic current	Base current	Phase Factor
Regular		0.5	600	196,600	146,500	75	0.01	0.1	0.04	-0.3
Ni/NiO	S-17	0.5	600	85,300	82,000	96.1	0.0001	0.0012	0.55	-0.44
	S-36	0.5	600	77,000	71,000	92.2	0.01	0.0125	4.5	-0.3
	S-49	0.5	600	137,700	128,000	93	0.001	0.01	0.1	-0.49

All current unit = $\mu A/cm^2$

* CIAC = Crack Indication at Cycle.

Table 5-28. EFS Response of Al 7075 When Coated with Either Aircraft Primer Plus Top Coat (T) or Primer (P).

Type of Test	Specimen ID	Freq. (Hz)	Stress (MPa)	Life (Cycle)	CIAC	% of Life	Plastic Current	Elastic Current	Base Current	Phase Factor
Regular uncoated		0.5	200	88,000	77,000	87.3	0.04	0.038	1.19	0.5
T-Coat	A-b71	0.5	200	144,500			0.0007	0.0008	0.001	0.47
T-Coat	A-b10	0.5	200	456,000	210,000	46				0.44
P-Coat	A-b58	0.5	200	142,600	100,000	70.1	0.001	0.002	0.035	-0.1
P-Coat	A-b69	2.5	200	144,000	100,000	69	0.001	0.002	0.06	-0.06
P-Coat	A-t14	5	200	70,000	50,000	71.4	0.02	0.1	0.6	-0.04
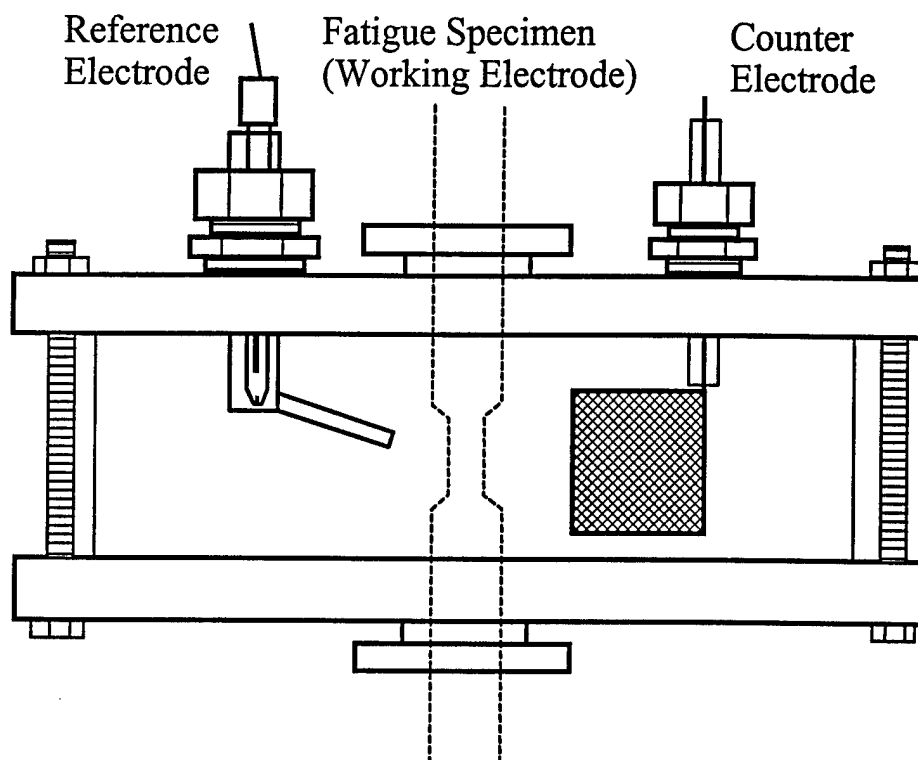
Figure 5-1. Schematic diagram of the test cell used for EFS measurements showing the relative locations of the fatigue specimen, the reference electrode, and the counter-electrode.
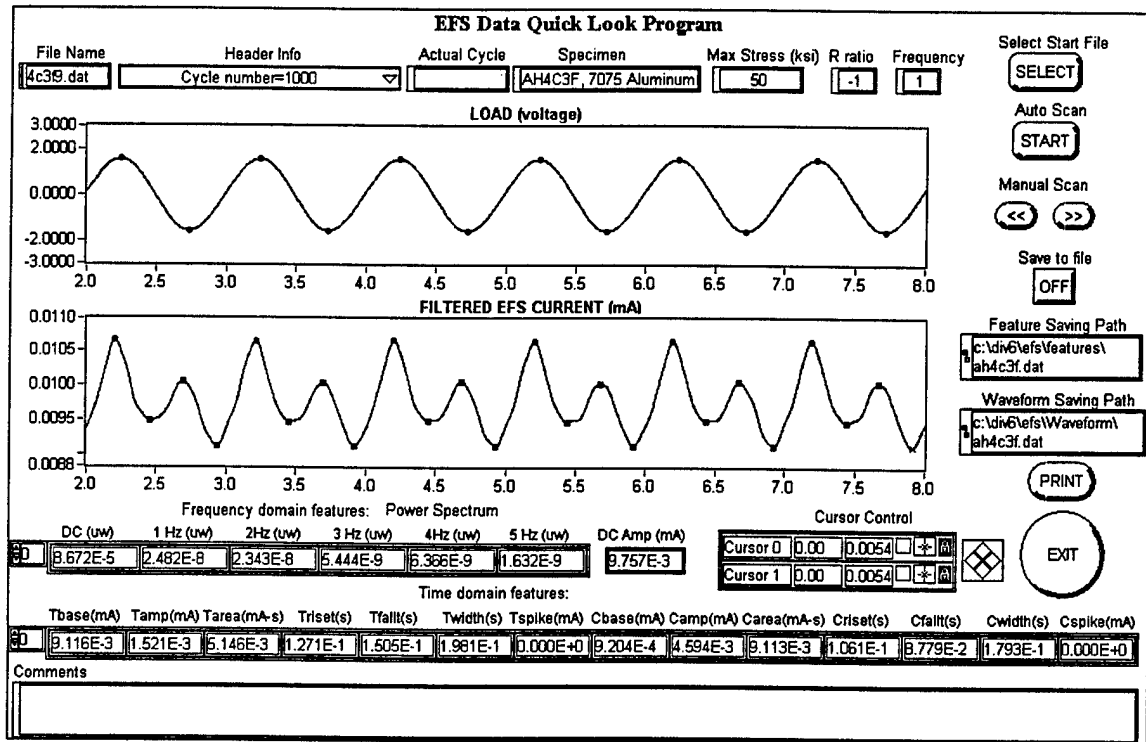
Figure 5-2. A view of the screen of the data Quick-Look program
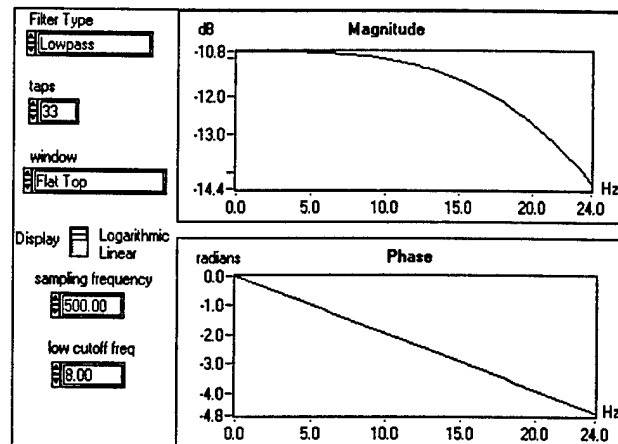
Figure 5-3. Characteristics of the digital low-pass FIR filter.

5-63
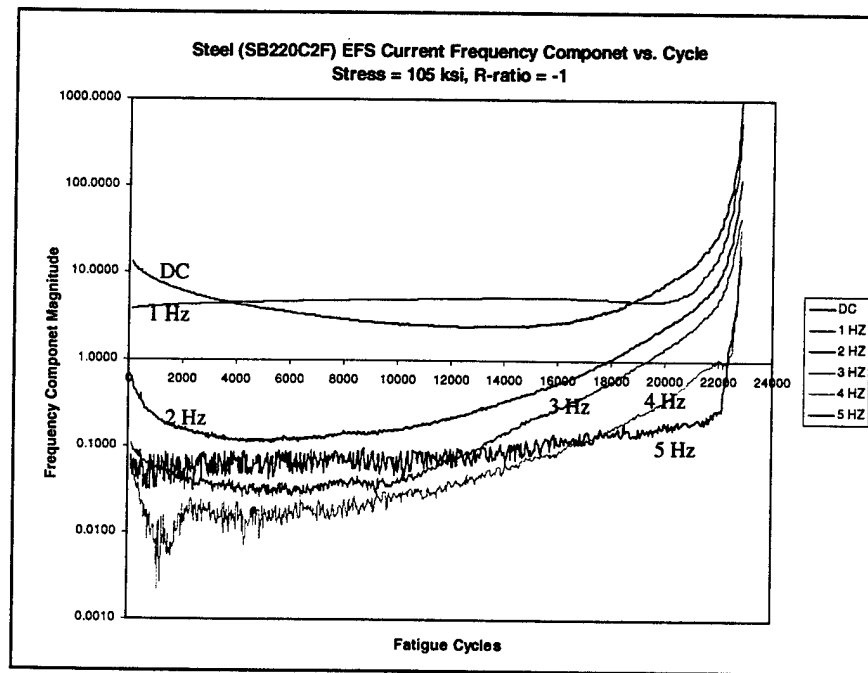
Figure 5-4. Magnitude of the frequency component of the EFS current signal as a function of the number of cycles in a fatigue test on 4130 steel.
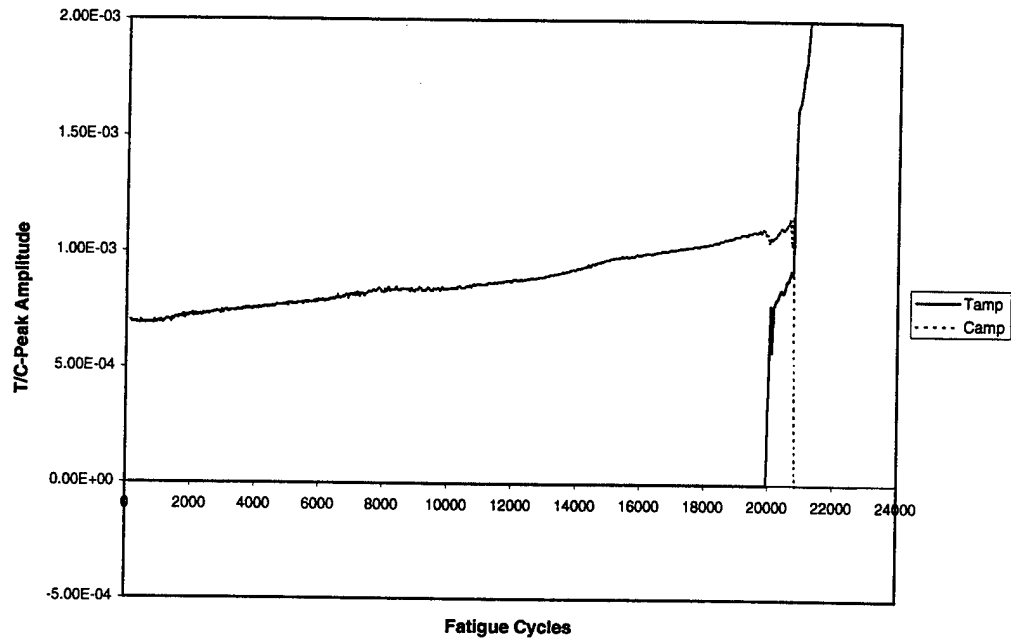
Figure 5-5. Changes in the amplitude of the T- and C-peaks during a fatigue test on 4130 steel at a maximum stress of 724 MPa and R = -1.
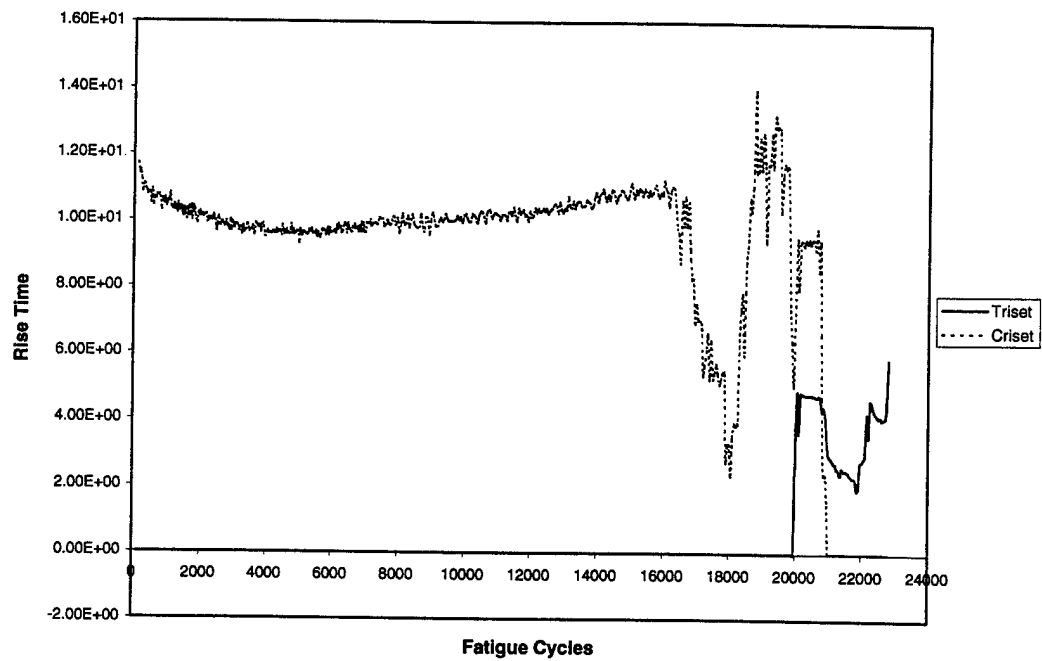
Figure 5-6. Changes in the T- and C-peaks rise-time during a fatigue test on 4130 steel at a maximum stress of 724 MPa and R = -1.

5-65
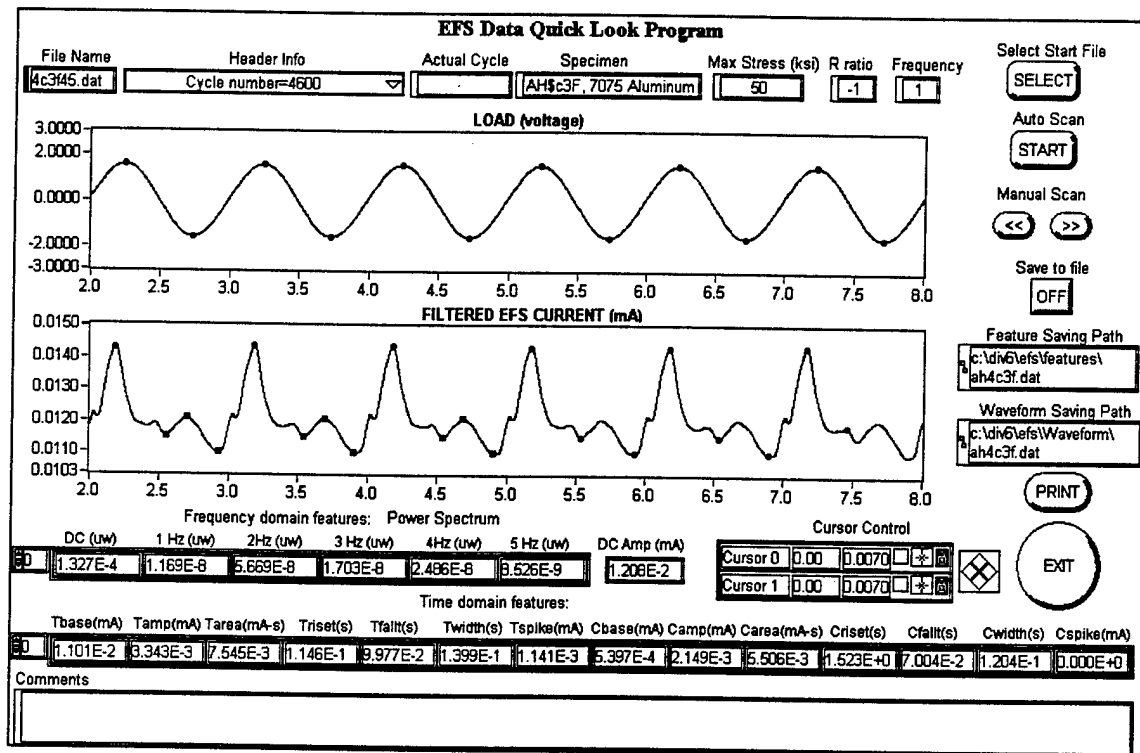
Figure 5-7. Detection of current spike in the T-peak of the EFS signal on 7075 aluminum alloy tested at a maximum stress of 345 MPa and R = -1.
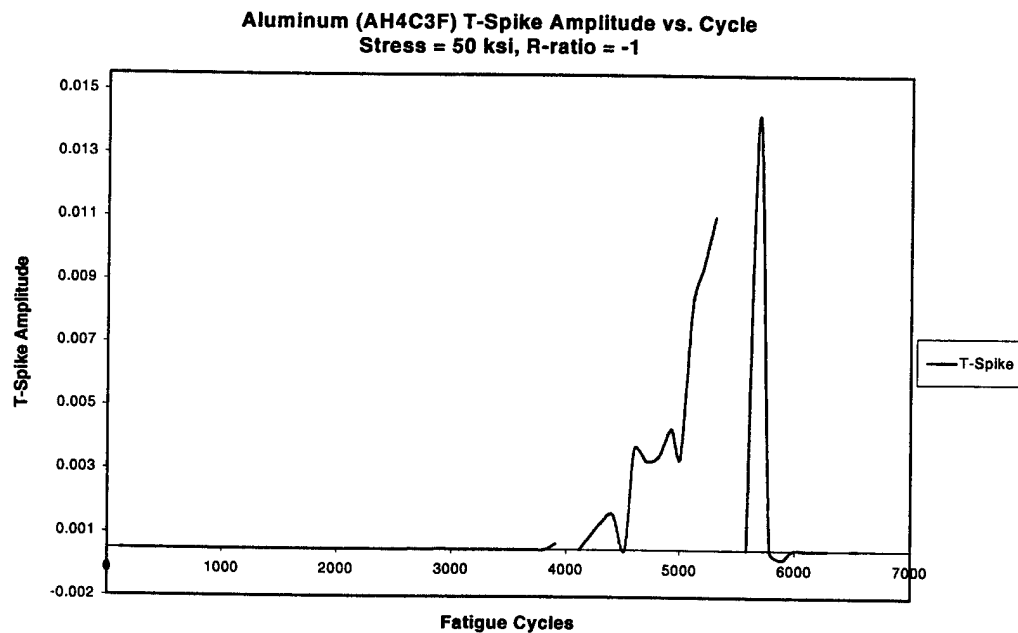
Figure 5-8. Changes in the amplitude of the T-peak spike during a fatigue test on 7075 aluminum alloy tested at a maximum stress of 345 MPa and R = -1.
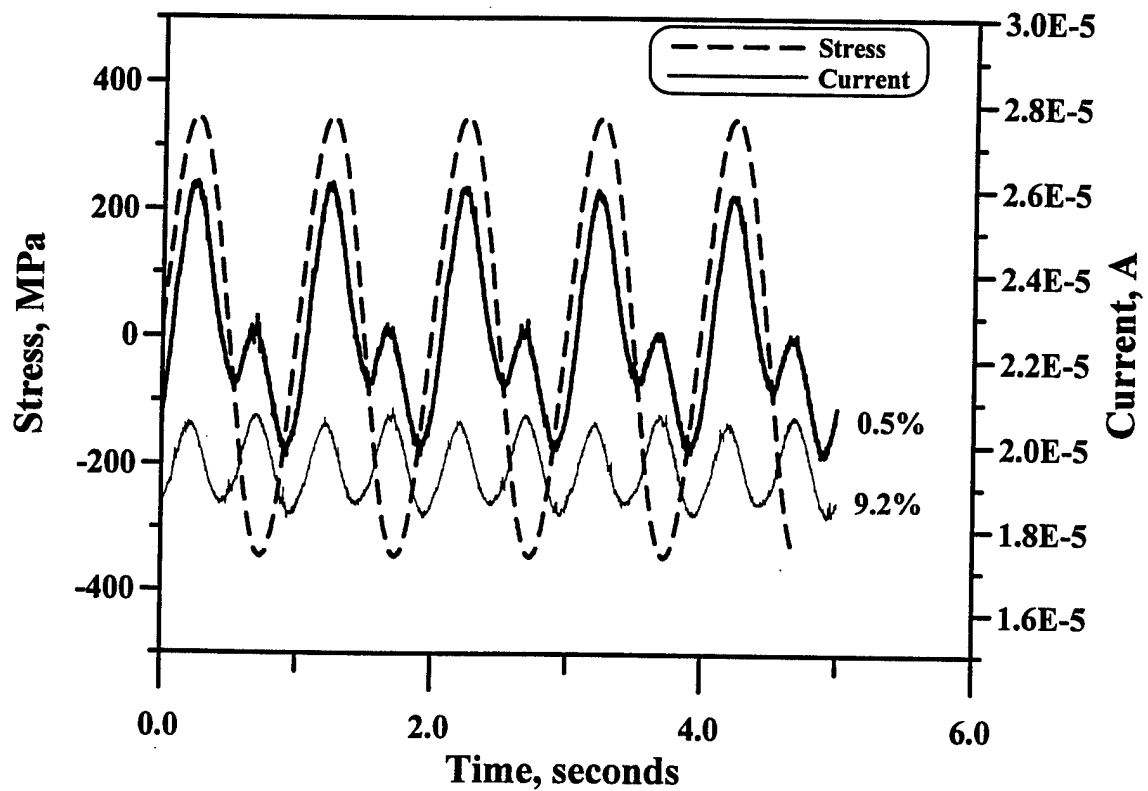
Figure 5-9a. Typical plots of the transient current and the cyclic load for 7075 Al tested at 1Hz, 345 MPa (50 ksi), R = -1, and an applied potential of 0.3 V_{SCE} obtained early in the life.

Figure 5-9b. Typical plots of the transient current and the cyclic load for 7075 Al tested at 1Hz, 345 MPa (50 ksi), R = -1, and an applied potential of 0.3 V_{SCE} obtained late in life.
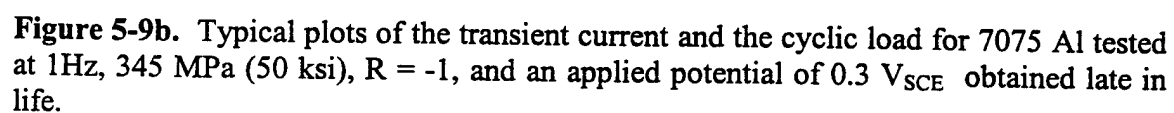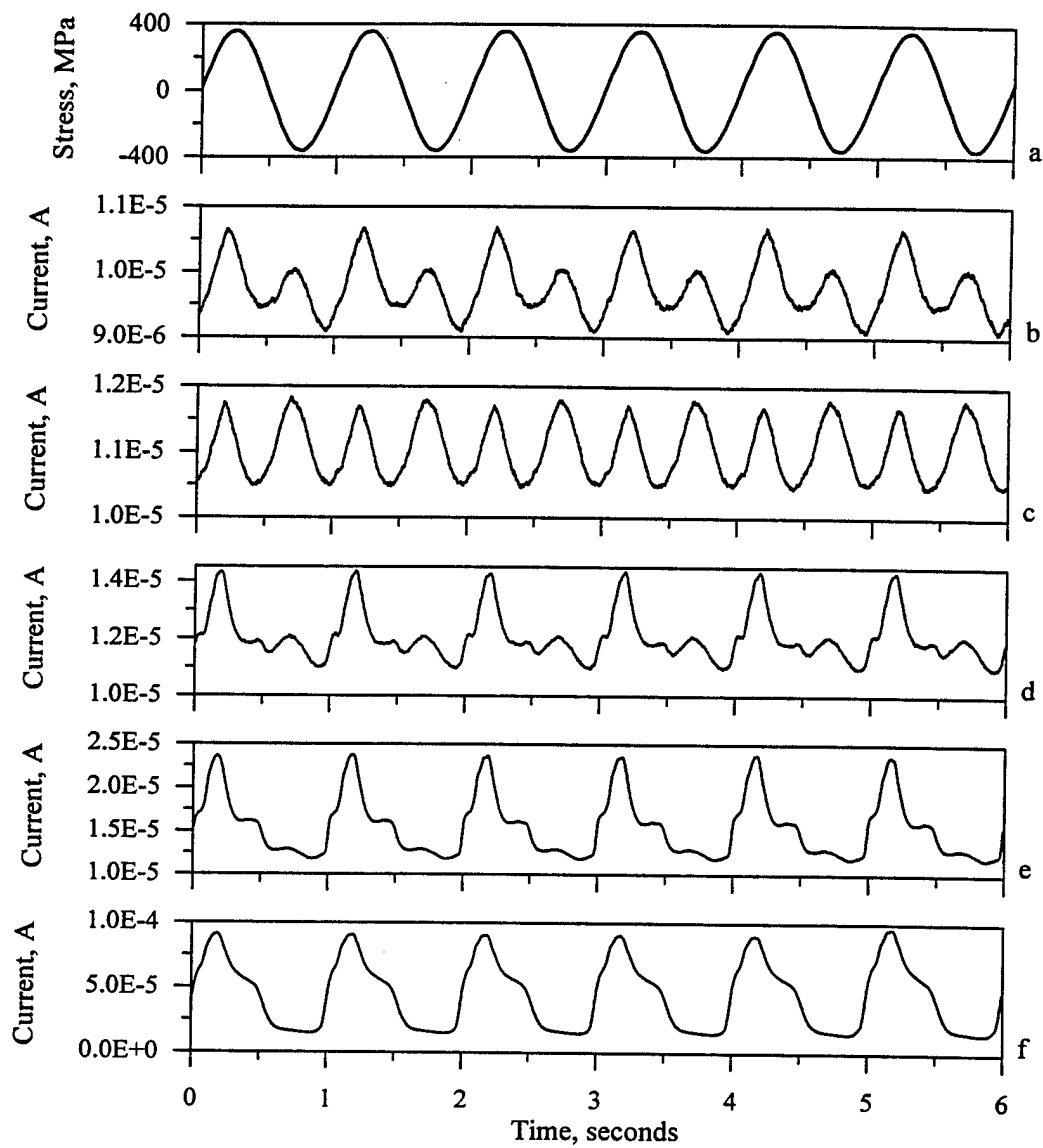
Figure 5-10. Cyclic stress (a) and filtered transient current for 7075 Al tested at 1Hz, 345 MPa (50 ksi), R = -1, and an applied potential of 0.3 V_{SCE} at various percentages of fatigue life: b) 15%; c) 32%; d) 70%; e) 85%; and f) $\approx$ 100 %.
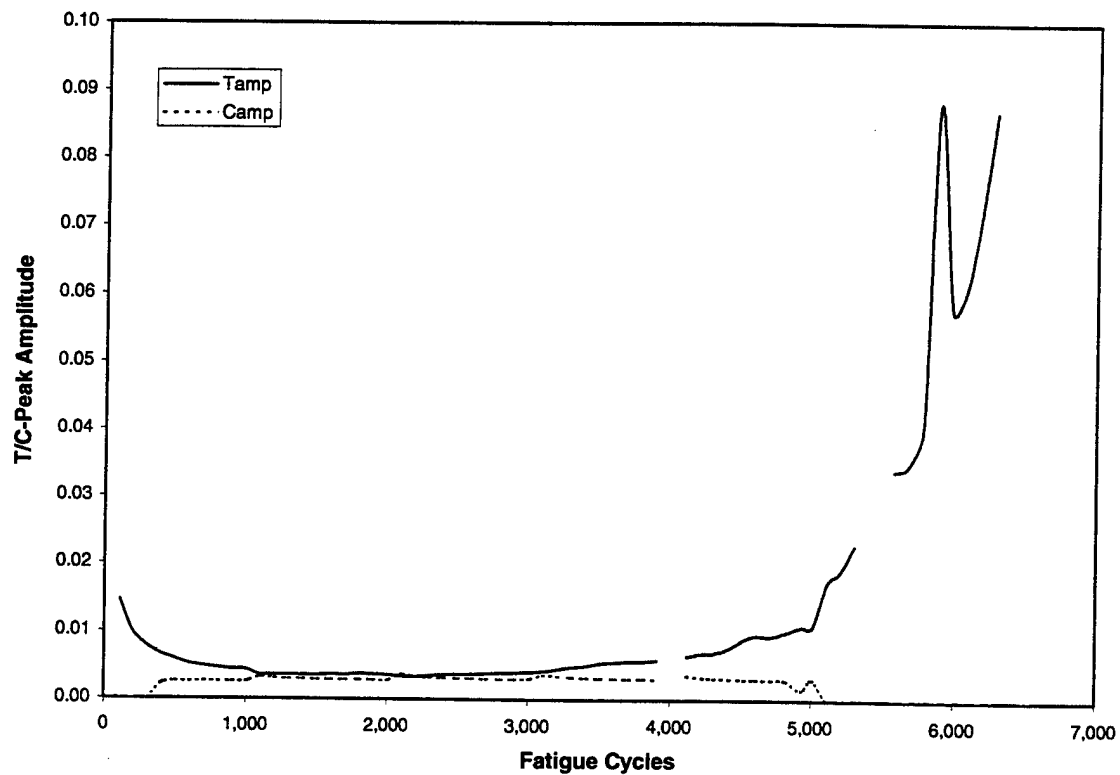
Figure 5-11. Amplitude of the EFS T- and P-peaks as a function of fatigue cycles for 7075 Al (Specimen AH4C3F) tested at 345 MPa (50 ksi), R = -1 and 1 Hz.
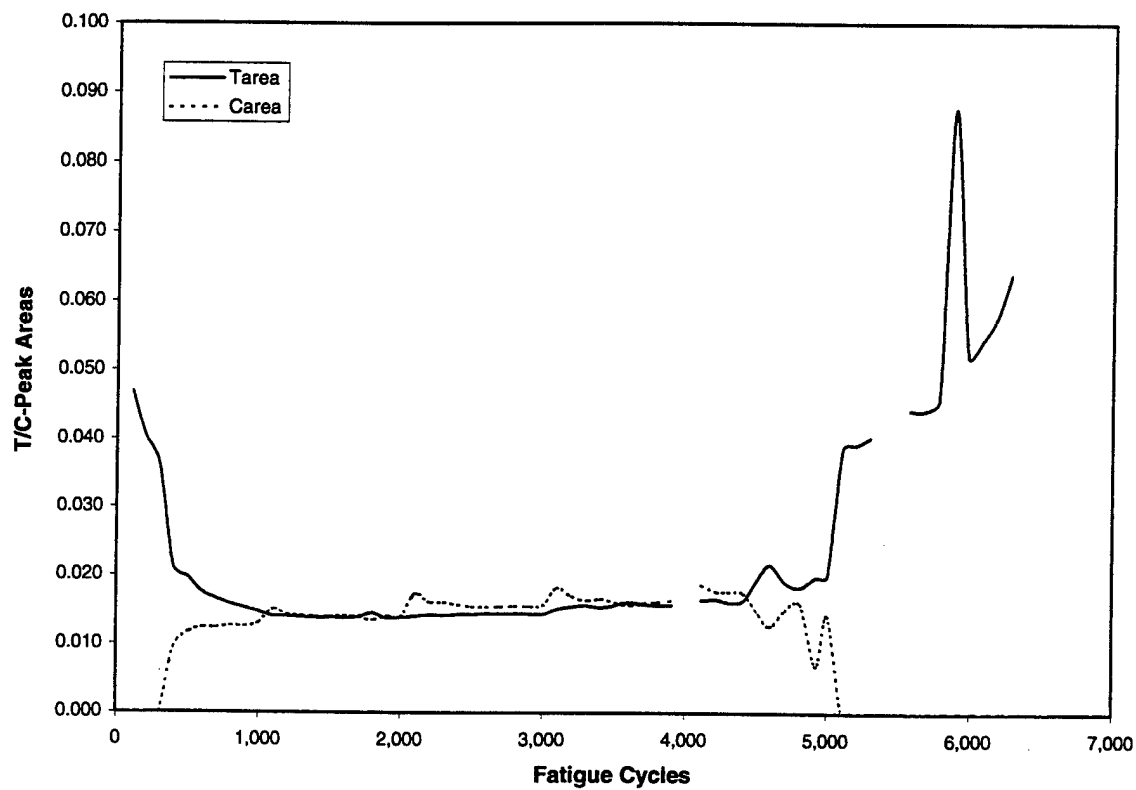
Figure 5-12. Area of the EFS T- and P-peaks as a function of fatigue cycles for 7075 Al (Specimen AH4C3F) tested at 345 MPa (50 ksi), R = -1 and 1 Hz.
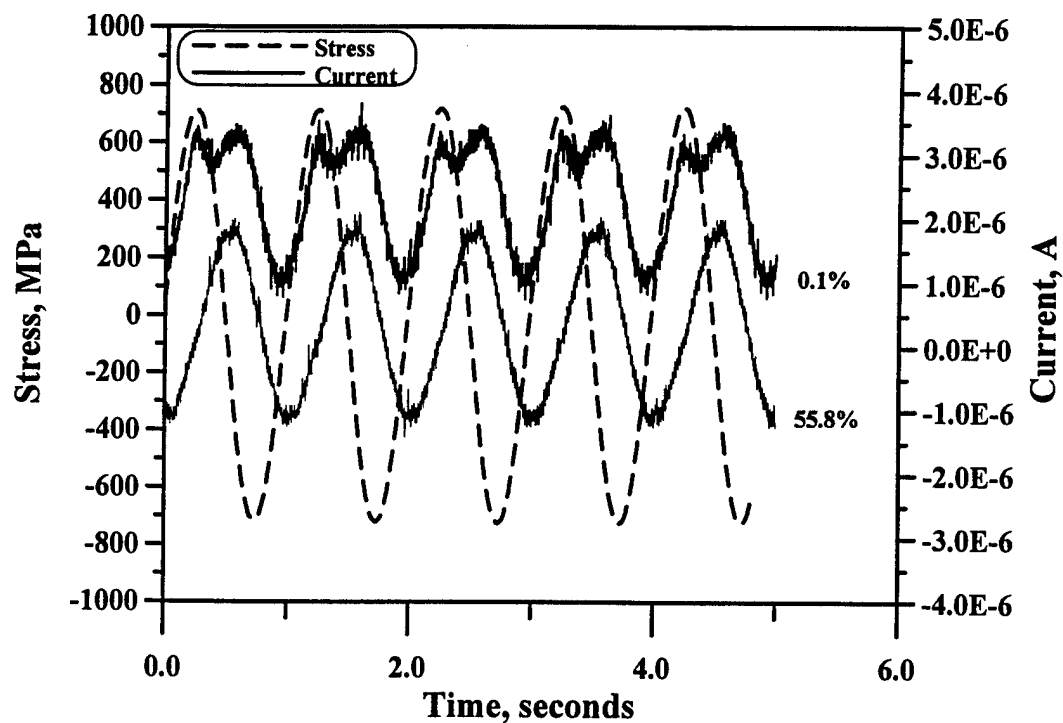
Figure 5-13a. Typical plots of the transient current and the cyclic load for 4130 steel tested at 1Hz, 724 MPa (105 ksi), R = -1, and an applied potential of 0.4 V_{SCE} at various percentages of fatigue life up to 55.8%.
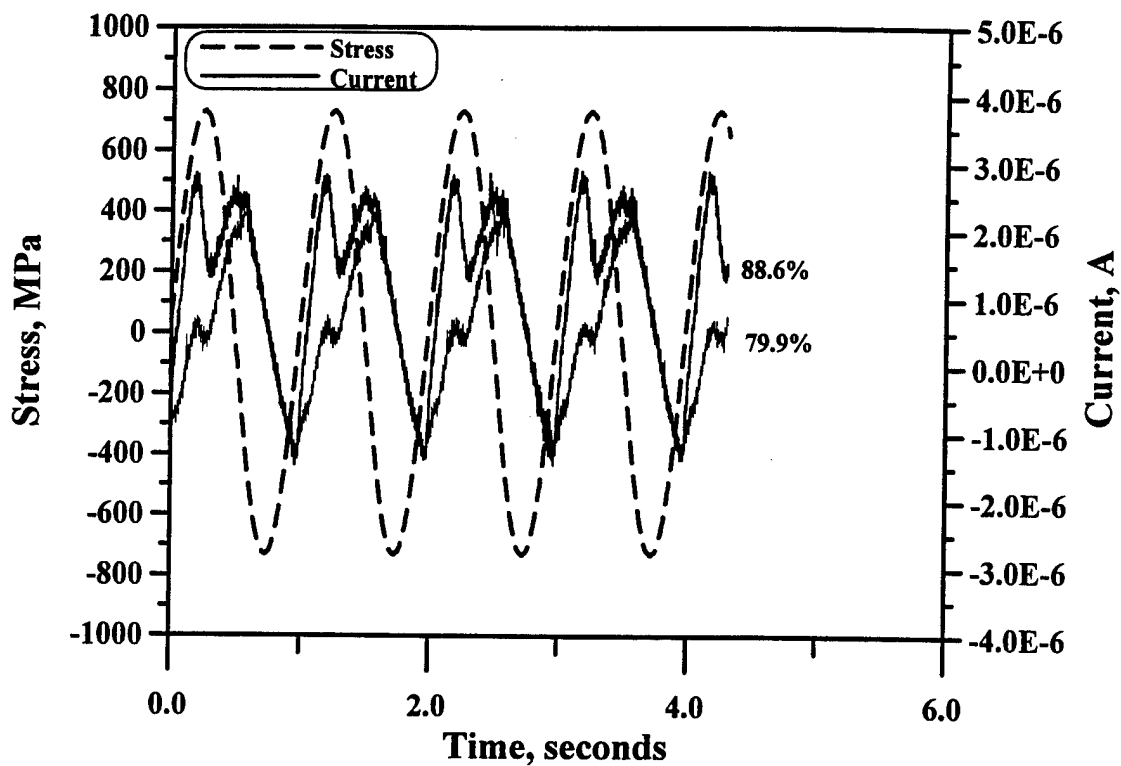
Figure 5-13b. Typical plots of the transient current and the cyclic load for 4130 steel tested at 1Hz, 724 MPa (105 ksi), R = -1, and an applied potential of 0.4 V_{SCE} at various percentages of fatigue life up to 88.6 %.
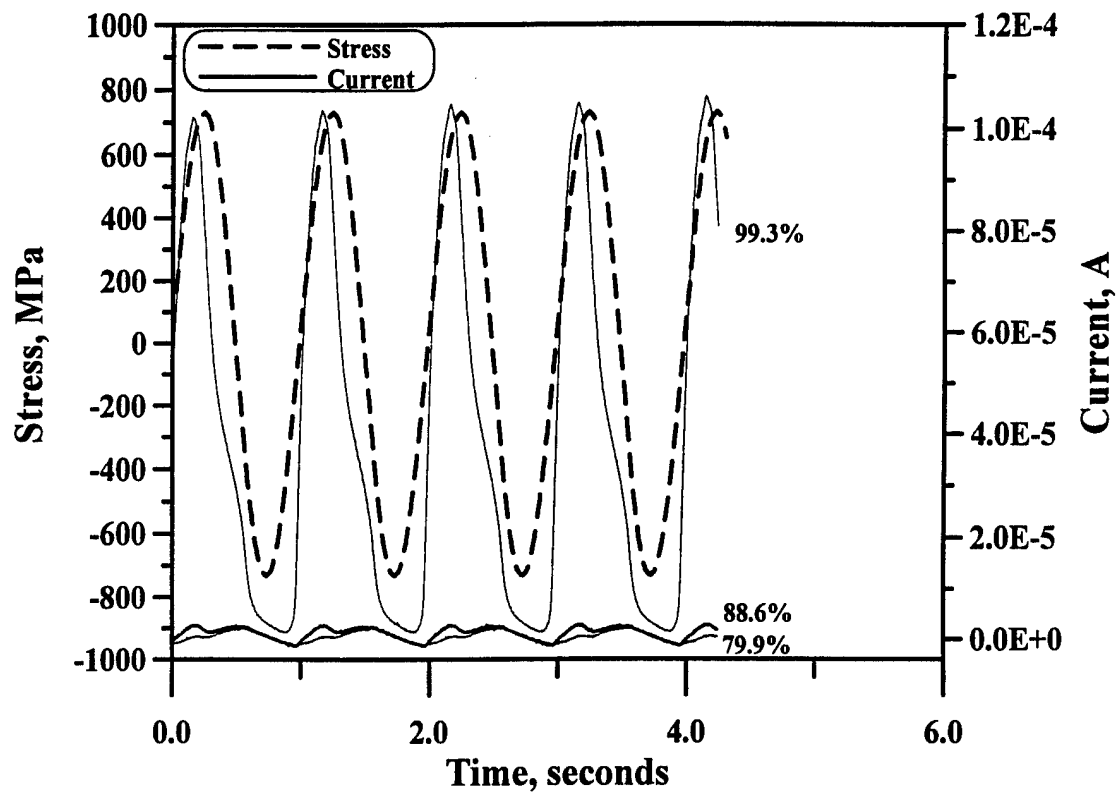
Figure 5-13c. Typical plots of the transient current and the cyclic load for 4130 steel tested at 1Hz, 724 MPa (105 ksi), R = -1, and an applied potential of 0.4 V_{SCE} , obtained late in life.
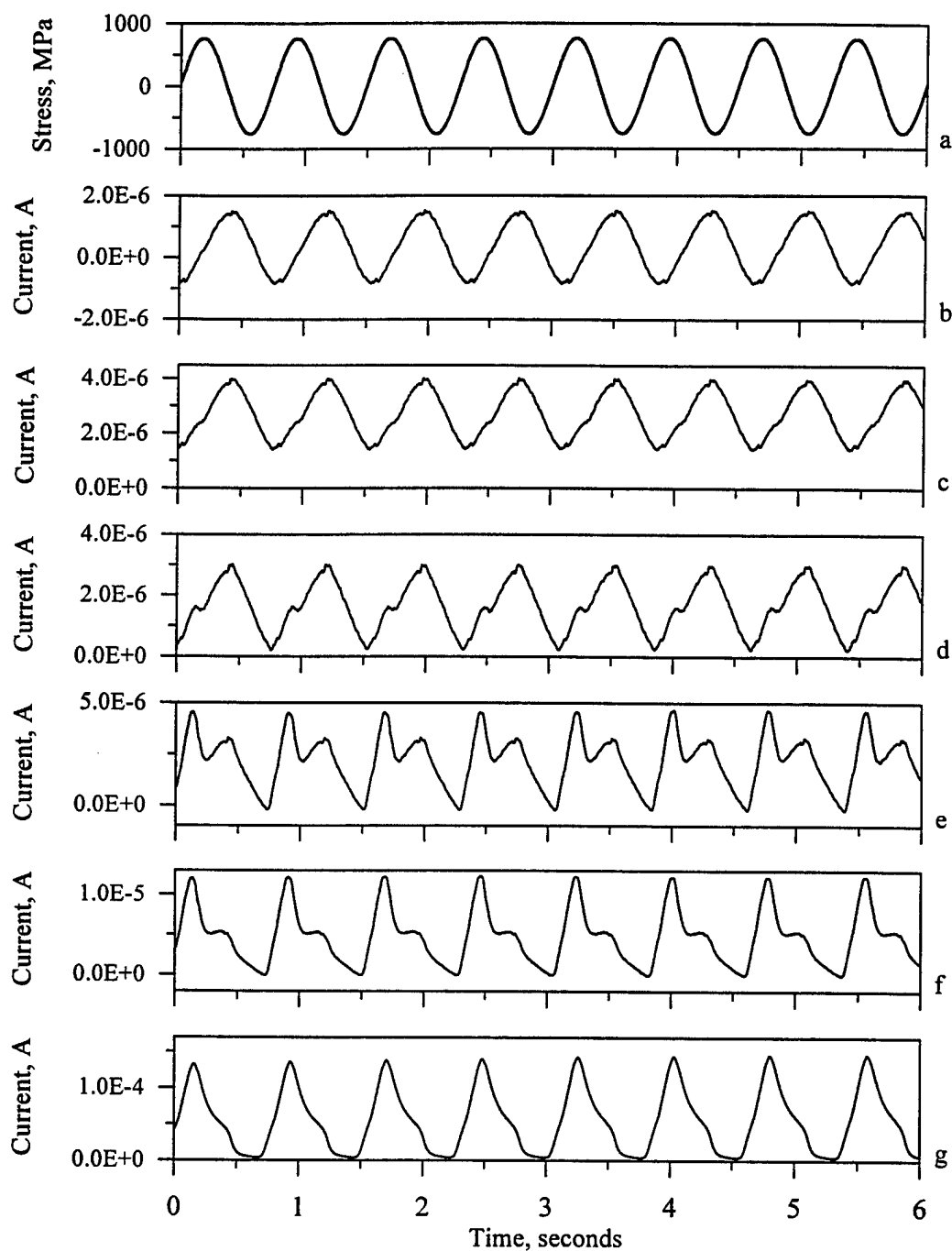
Figure 5-14. Cyclic stress (a) and filtered transient current for 4130 steel tested at 1Hz, 724 MPa (105 ksi), R = -1, and an applied potential of 0.4 V_{SCE} at various percentages of fatigue life: b) 58%; c) 72%; d) 81%; e) 94%; f) 98%; and g) ≈ 100 %.
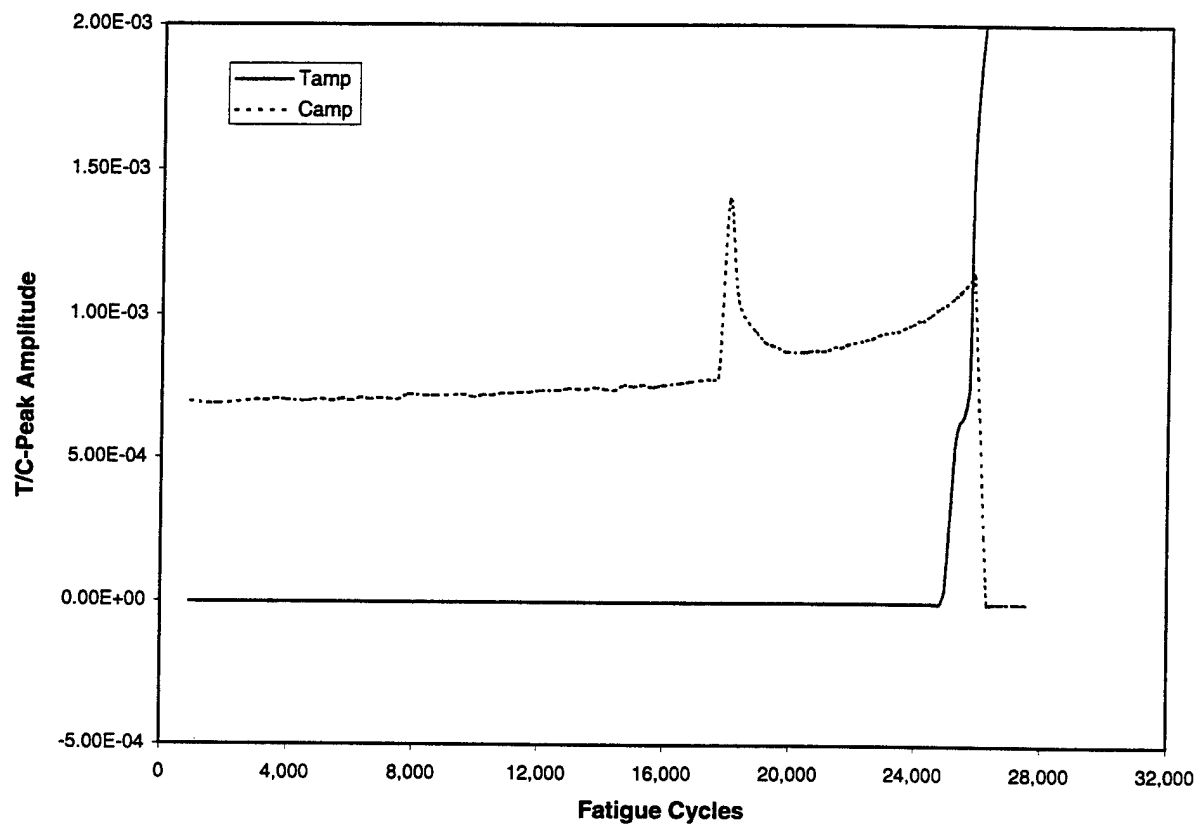
Figure 5-15. Amplitude of the EFS T- and P-peaks as a function of fatigue cycles for 4130 steel (Specimen SE335C1F) tested at 724 MPa (105 ksi), R = -1 and 1 Hz.
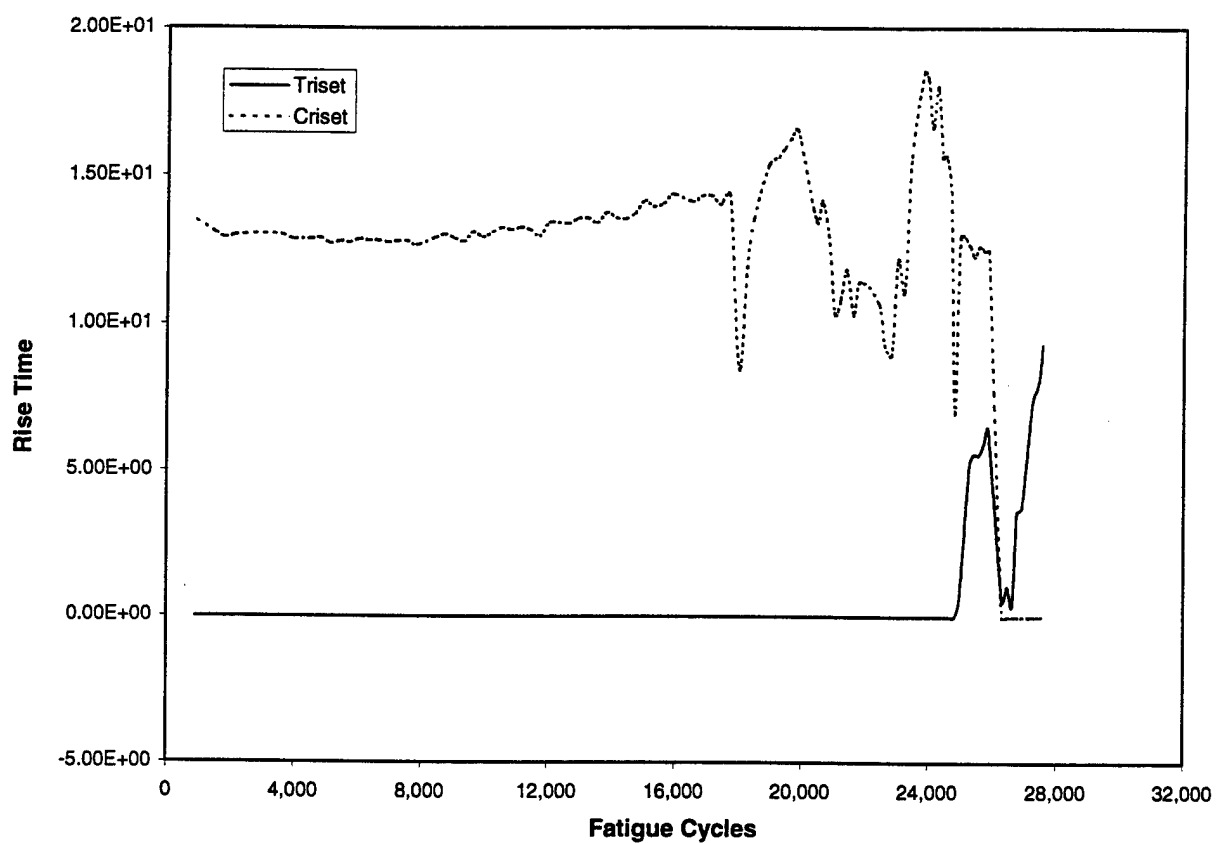
Figure 5-16. Rise time of the EFS T- and P-peaks as a function of fatigue cycles for 4130 steel (Specimen SE335C1F) tested at 724 MPa (105 ksi), R = -1 and 1 Hz.
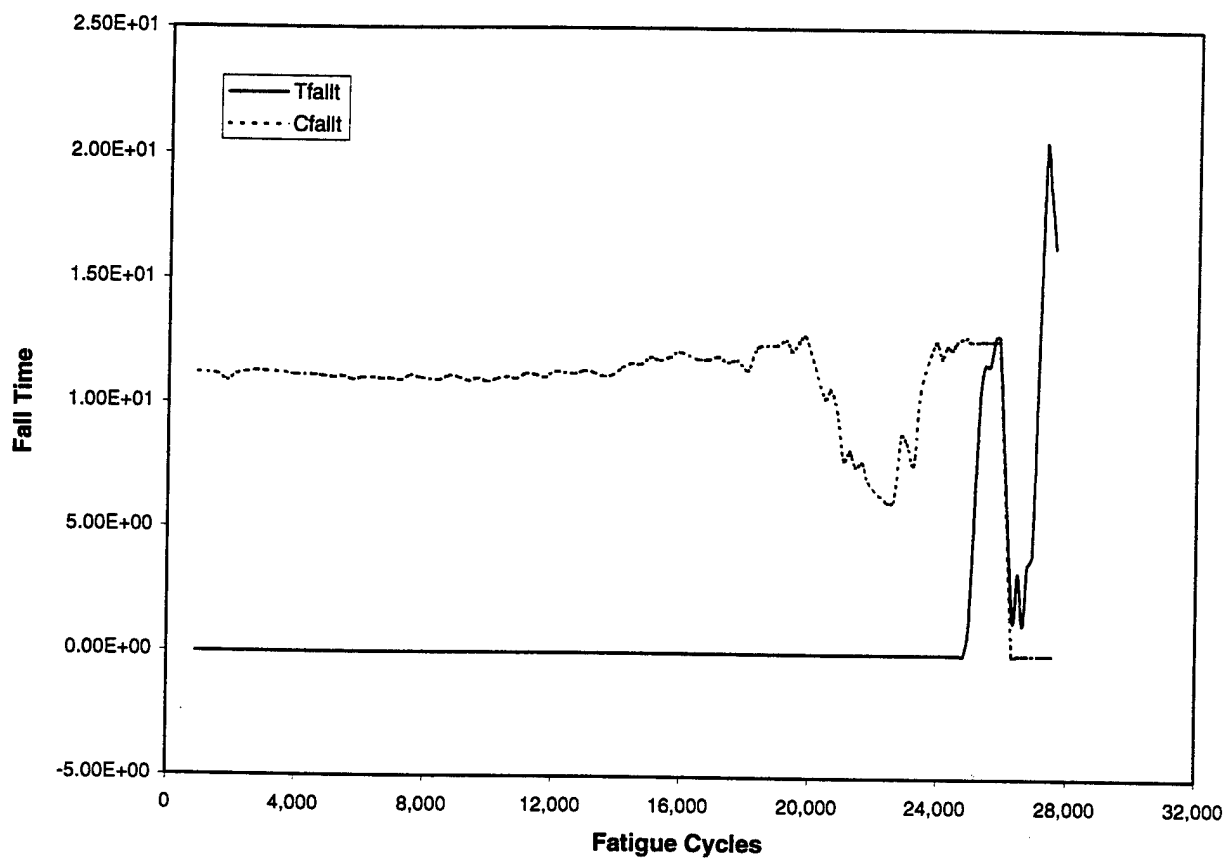
Figure 5-17. Decay or fall time of the EFS T- and P-peaks as a function of fatigue cycles for 4130 steel (Specimen SE335C1F) tested at 724 MPa (105 ksi), R = -1 and 1 Hz.
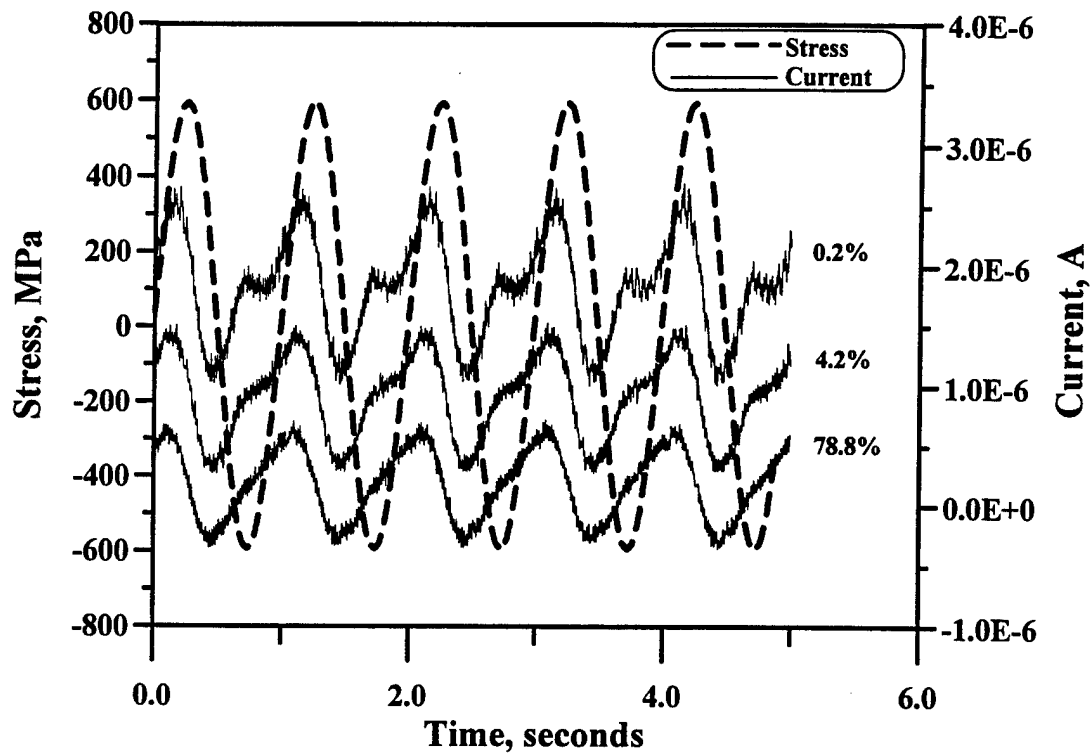
Figure 5-18a. Typical plots of the transient current and the cyclic load for Ti-6Al-4V alloy tested at 1Hz, 565 MPa (82 ksi), R = -1, and an applied potential of 0.4 V_{SCE} at various percentages of fatigue life up to 77.8%.
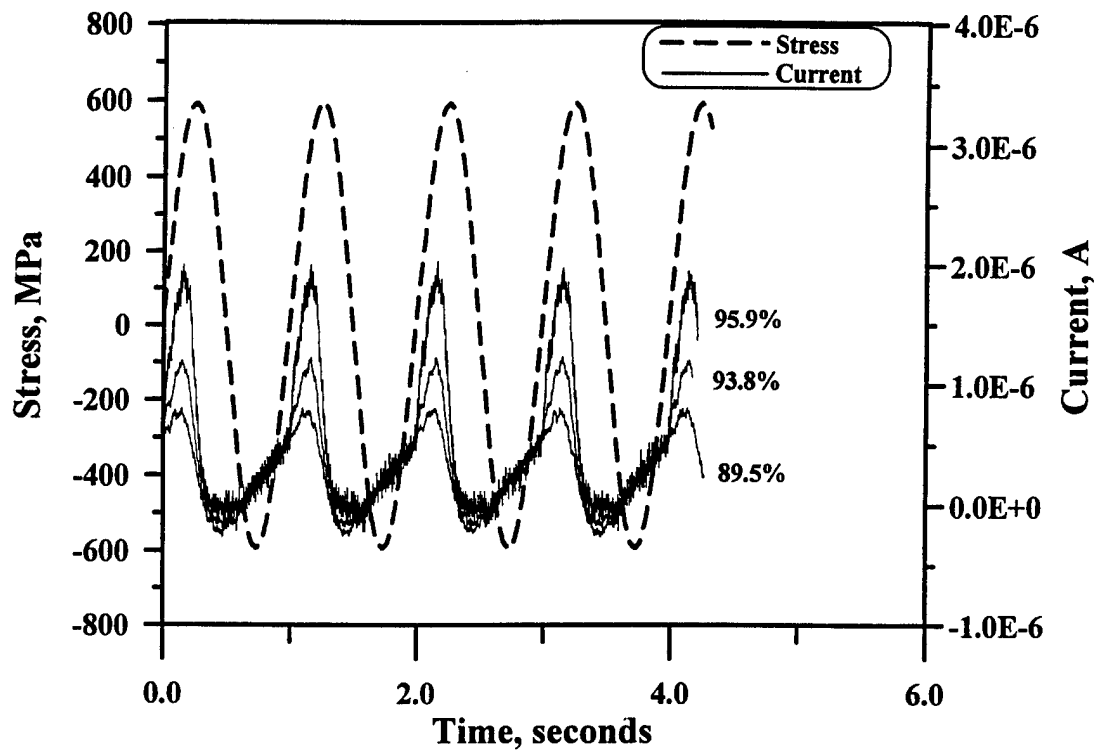
Figure 5-18b. Typical plots of the transient current and the cyclic load for Ti-6Al-4V alloy tested at 1Hz, 565 MPa (82 ksi), R = -1, and an applied potential of 0.4 V_{SCE} obtained late in life.
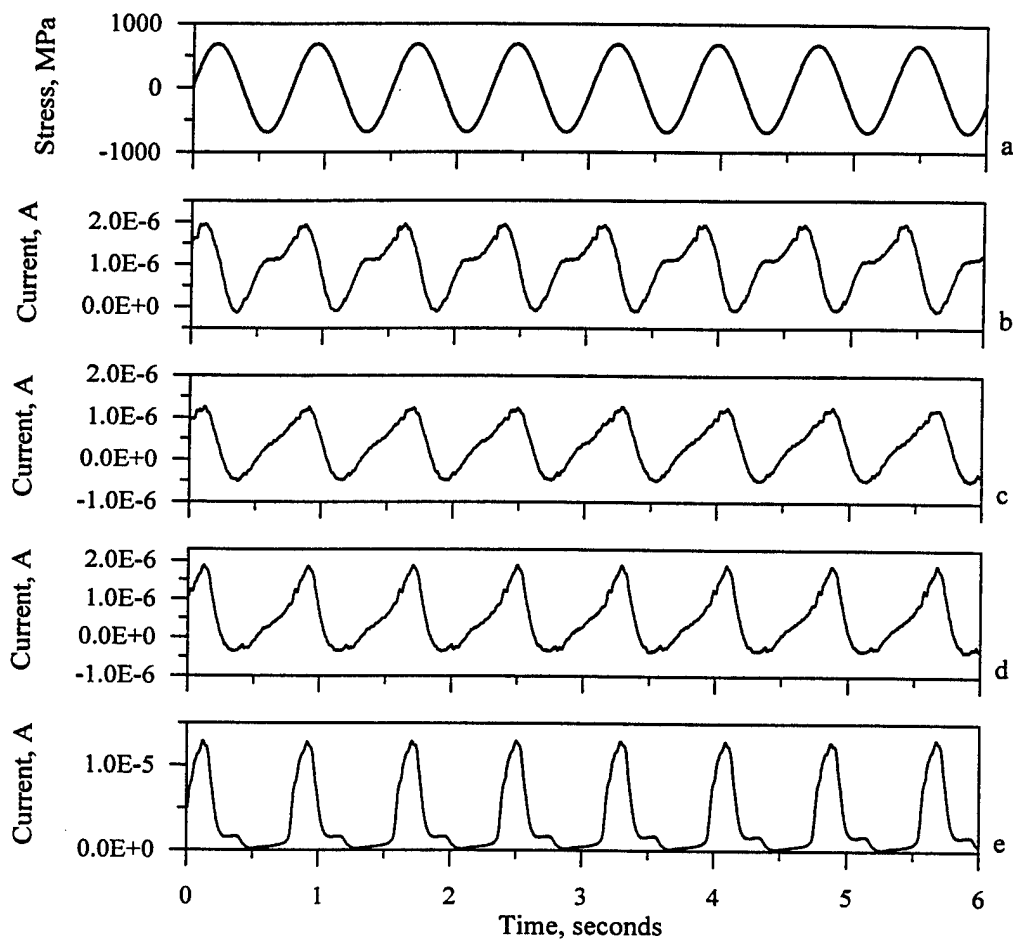
Figure 5-19. Cyclic stress (a) and filtered transient current for Ti-6Al-4V tested at 1Hz, 565 MPa (82 ksi), R = -1, and an applied potential of 0.4 V_{SCE} at various percentages of fatigue life: b) 2.5%; c) 57%; d) 80%; and e) ≈ 100 %.
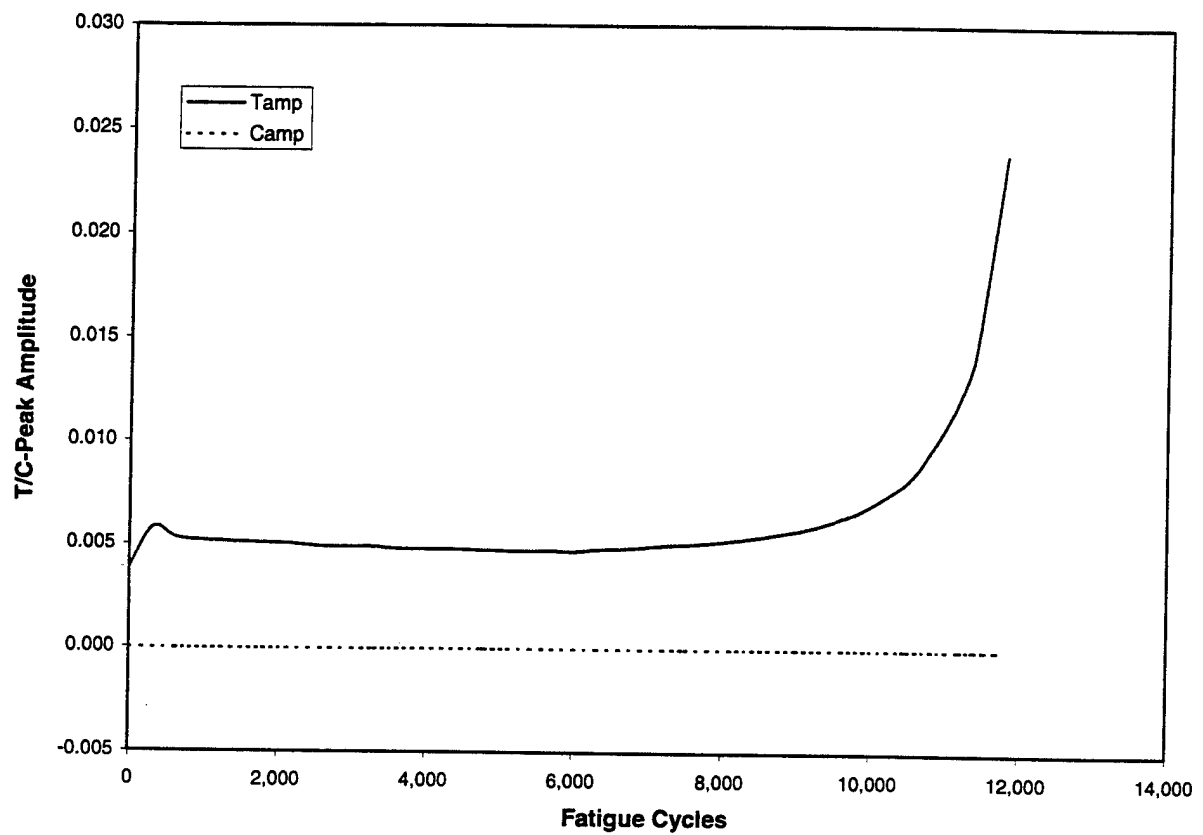
Figure 5-20. Amplitude of the EFS T- and P-peaks as a function of fatigue cycles for Ti-6Al-4V alloy (Specimen TV19CF) tested at 655 MPa (95 ksi), R = -1 and 1 Hz.
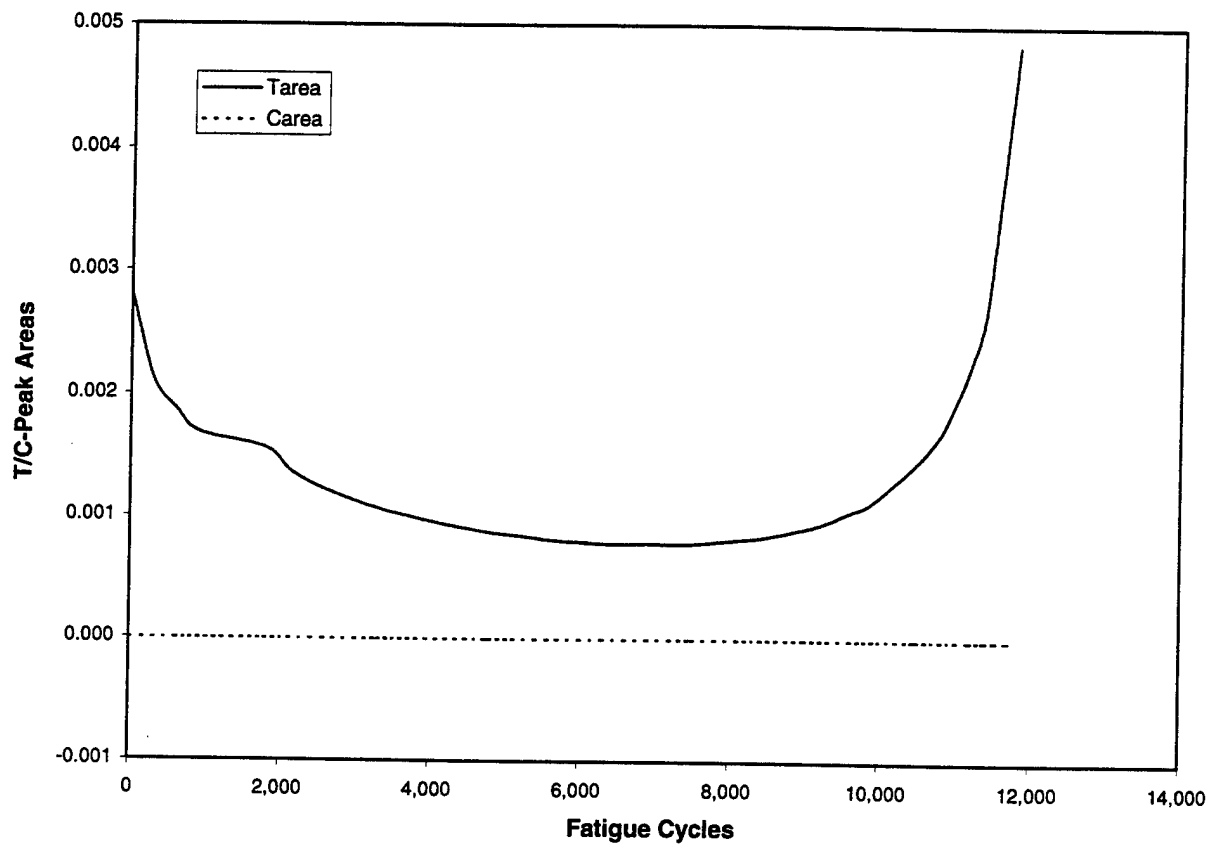
Figure 5-21. Area of the EFS T- and P-peaks as a function of fatigue cycles for Ti-6Al-4V alloy (Specimen TV19CF) tested at 655 MPa (95 ksi), R = -1 and 1 Hz.
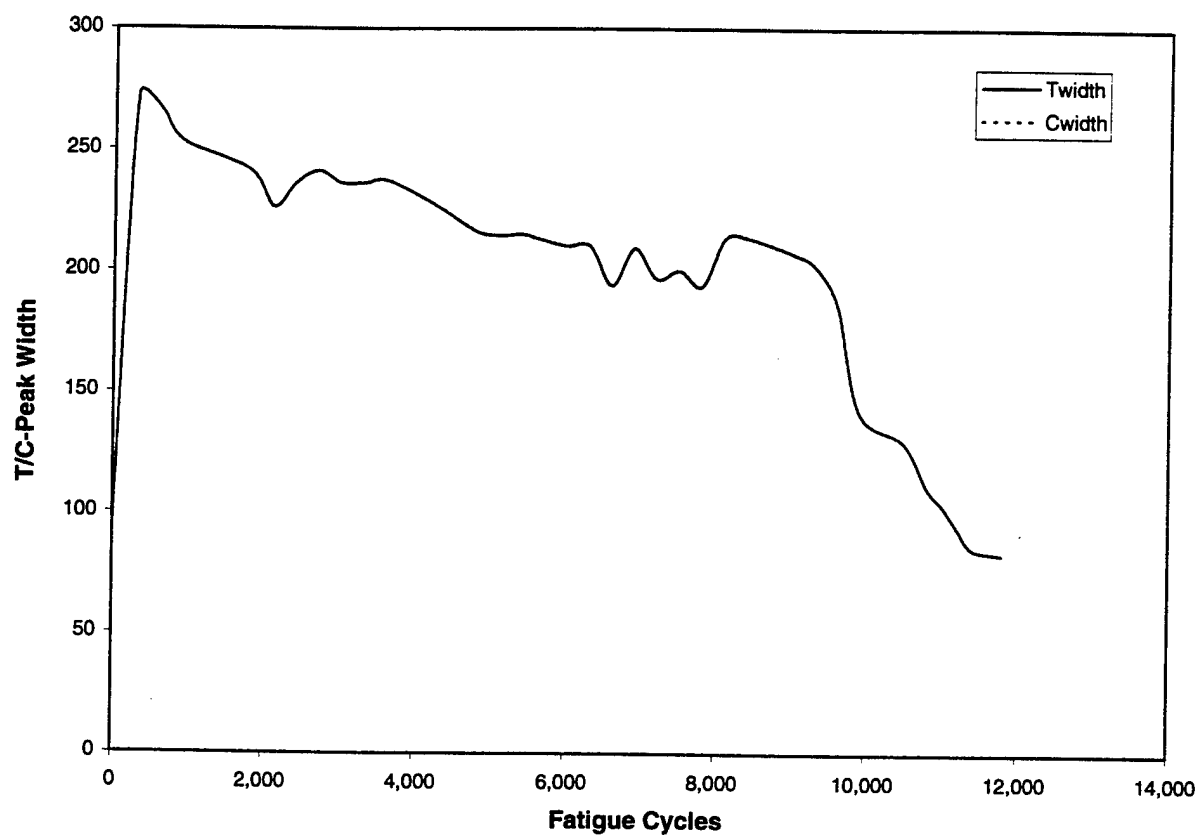
Figure 5-22. Width of the EFS T- and P-peaks as a function of fatigue cycles for Ti-6Al-4V alloy (Specimen TV19CF) tested at 655 MPa (95 ksi), R = -1 and 1 Hz.
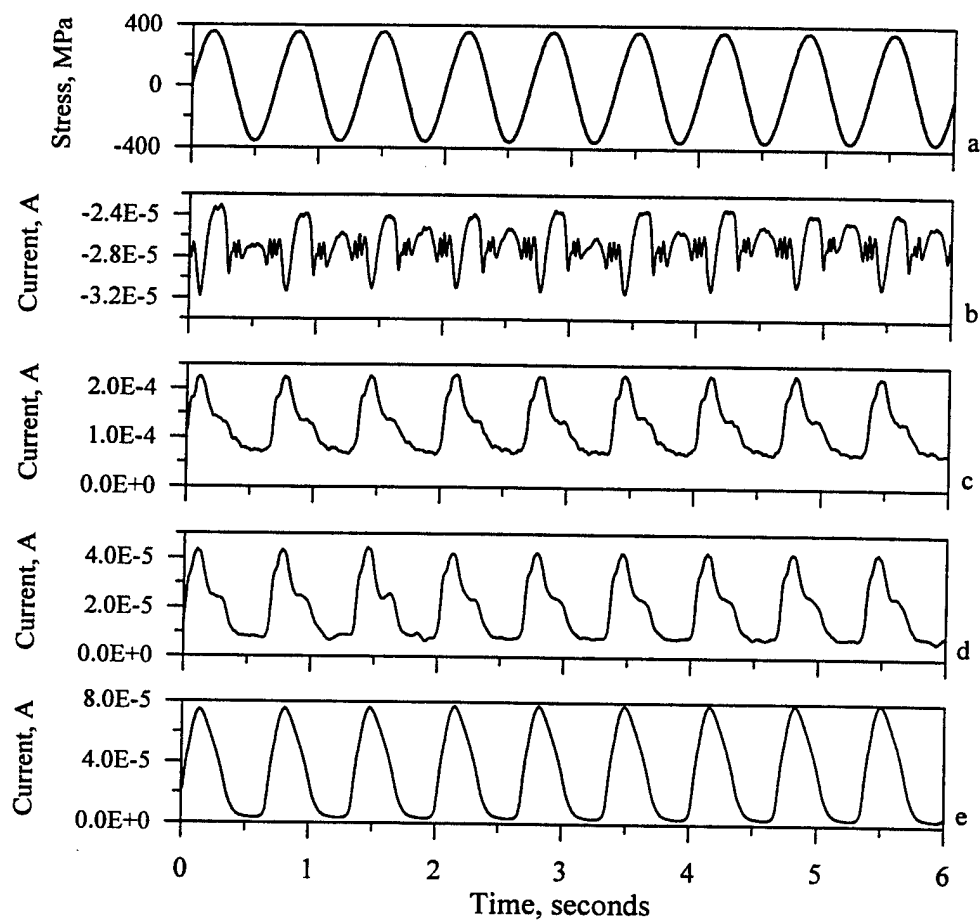
Figure 5-23. Cyclic stress (a) and filtered transient current for primer coated 7075 Al tested at 1Hz, 345 MPa (50 ksi), R = -1, and an applied potential of 0.3 V_{SCE} at various percentages of fatigue life: b) 22%; c) 79%; d) 86%; and e) ≈ 100 %.

Data Quick Look Program

File Name: af58c2af80.dat Header Info: Cycle number=12209 Actual Cycle: 12100 Comments: Max Stress (ksi): 45 R ratio: -1 Frequency: 1 Select Start File: SELECT

LOAD (Voltage)

Auto Scan: START

Manual Scan: << >>

Save to file: OFF

FILTERED EFS CURRENT (Micro Amp)

file path: c:\div6\efs\ features\

PRINT

EXIT

| Cursor 0 | 0.0000 | 6.3981 |
| Cursor 1 | 0.0000 | 6.3981 |

Average EFS Current (uA): 1.22E+1   Frequency Domain: DISPLAY   Fundamental Frequency: 5.017E+0   Mean: 5.07E+0   STD: 7.14E-2

First Five Frequency Hill Peaks

First Five Harmonics

	1st	2nd	3rd	4th	5th
Frequency (hz)	5.03E+0	1.01E+1			
Magnitude (uA)	1.44E-1	5.48E-1			

	1st	2nd	3rd	4th	5th
Frequency (hz)	5.02E+0	1.00E+1	1.51E+1	2.01E+1	2.51E+1
Magnitude (uA)	1.41E-1	4.77E-1	7.62E-3	1.65E-4	4.65E-5

Tbase(uA)	Tamp(uA)	Tarea(uA.s)	Triset(s)	Tfallt(s)	Twidth(s)	Tspike(uA)	Cbase(uA)	Camp(uA)	Carea(uA.s)	Criset(s)	Cfallt(s)	Cwidth(s)	Cspike(uA)
1.16E+1	1.36E+0	1.26E+0	3.36E-2	3.02E-2	5.19E-2	0.00E+0	1.06E+0	1.17E+0	1.16E+1	2.76E-2	2.73E-2	4.91E-2	0.00E+0

Figure 5-24. Plot of the transient current and the cyclic load for 7075 Al (Specimen AF58C2AF) tested at 1 Hz, 310 MPa (45 ksi), R = -1, and an applied potential of 0.3 V_{SCE} obtained after 12,100 cycles prior to the occurrence of the T-peak spike.

Data Quick Look Program

File Name — af58c2af88.dat

Header Info — Cycle number=13203

Actual Cycle — 13000

Comments

Max Stress (ksi) — 45   R ratio — -1   Frequency — 1

Select Start File — SELECT

Auto Scan — START

Manual Scan — « »

Save to file — OFF

LOAD (Voltage)

1.7 / 1.0 / 0.0 / -1.0 / -1.7

0.2 0.3 0.4 0.5 0.6 0.7 0.8 0.9 1.0 1.1 1.2 1.3 1.4 1.5 1.6 1.7 1.8

FILTERED EFS CURRENT (Micro Amp)

12.5 / 12.0 / 11.0 / 10.0 / 9.5

0.2 0.3 0.4 0.5 0.6 0.7 0.8 0.9 1.0 1.1 1.2 1.3 1.4 1.5 1.6 1.7 1.8

file path — c:\div6\efs\features\

PRINT

EXIT

Cursor 0 0.0000 6.0701
Cursor 1 0.0000 6.0701

Average EFS Current (uA) — 1.06E+1

Frequency Domain — DISPLAY

Fundamental Frequency — 5.017E+0

Mean — 5.04E+0   STD — 2.01E-2

First Five Frequency Hill Peaks

	1st	2nd	3rd	4th	5th
Frequency (hz)	5.02E+0	1.01E+1			
Magnitude (uA)	8.20E-1	6.39E-1			

First Five Harmonics

	1st	2nd	3rd	4th	5th
Frequency (hz)	5.02E+0	1.00E+1	1.51E+1	2.01E+1	2.51E+1
Magnitude (uA)	8.02E-1	5.57E-1	1.63E-2	1.92E-4	3.44E-5

Tbase(uA)	Tamp(uA)	Tarea(uA·s)	Triset(s)	Tfallt(s)	Twidth(s)	Tspike(uA)	Cbase(uA)	Camp(uA)	Carea(uA·s)	Criset(s)	Cfallt(s)	Cwidth(s)	Cspike(uA)
9.58E+0	2.54E+0	1.29E+0	2.92E-2	3.31E-2	5.52E-2	0.00E+0	0.00E+0	0.00E+0	0.00E+0	0.00E+0	0.00E+0	0.00E+0	0.00E+0

Figure 5-25. Plot of the transient current and the cyclic load for the same 7075 Al specimen as that in Figure 5-26 obtained at 13,100 cycles, just before the interruption of the test, showing the increases in the T-peak.

Figure 5-26. Surface crack visually detected in 7075 Al specimen. The corresponding EFS signal is shown in Figure 5-25.
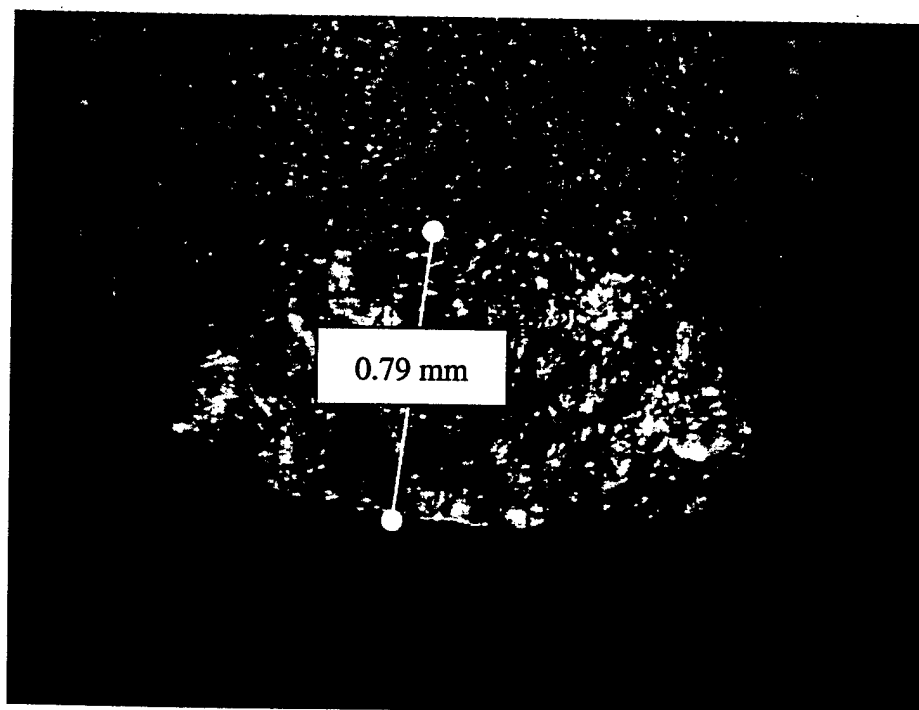
Figure 5-27. Thumbnail crack revealed by fracturing the 7075 Al specimen shown in Figure 5-26. The corresponding EFS signal is shown in Figure 5-25.

Data Quick Look Program

File Name | Header Info | Actual Cycle | Specimen | Max Stress (ksi) | R ratio | Frequency
350c3f65.dat | Cycle number=15102 | 15000 | se350c3f | 105 | -1 |

LOAD

5.000
0.000
-5.000

Select Start File

SELECT

Auto Scan

START

FILTERED CURRENT

0.005
0.002
0.000
-0.002
-0.003

0.0 0.1 0.2 0.3 0.4 0.5 0.6 0.7 0.8 0.9 1.0 1.1 1.2 1.3 1.4 1.5 1.6 1.7 1.8 1.9 2.0

Manual Scan

<< >>

Save to file

OFF

DISPLACEMENT

0.400
0.200
0.000
-0.200
-0.400

0.0 0.1 0.2 0.3 0.4 0.5 0.6 0.7 0.8 0.9 1.0 1.1 1.2 1.3 1.4 1.5 1.6 1.7 1.8 1.9 2.0

file path
c:\div6\efs\features\
12c2aF.dat

FFT at 0 to 20 Hz

| 0 | 2.3965E+0 | 3.5555E+0 | 4.1208E-1 | 6.6993E-2 | 1.0292E-1 | 6.3479E-2 |

+ Displacement - Displacement T Spike Amp

| 0.22 | -0.24 | 0.0000E+0 |

PRINT

	Tamp	Tarea	Triset	Tfall	Twidth	Camp	Carea	Crise	Cfall	Cwidth
0	0.0000E+0	0.0000E+0	0.0000E+0	0.0000E+0	0.0000E+0	6.0373E-3	1.8913E-4	1.5787E+2	1.1456E+2	2.5103E+2

EXIT

Figure 5-28. Plot of transient current (in mA) and the cyclic load for 4130 steel (Specimen SE350C3F) tested at 1Hz, 724 MPa (105 ksi), R = -1, and an applied potential of 0.4 V_{SCE} after 15,000 cycles showing emerging current spike in the rising portion of the C-peak.
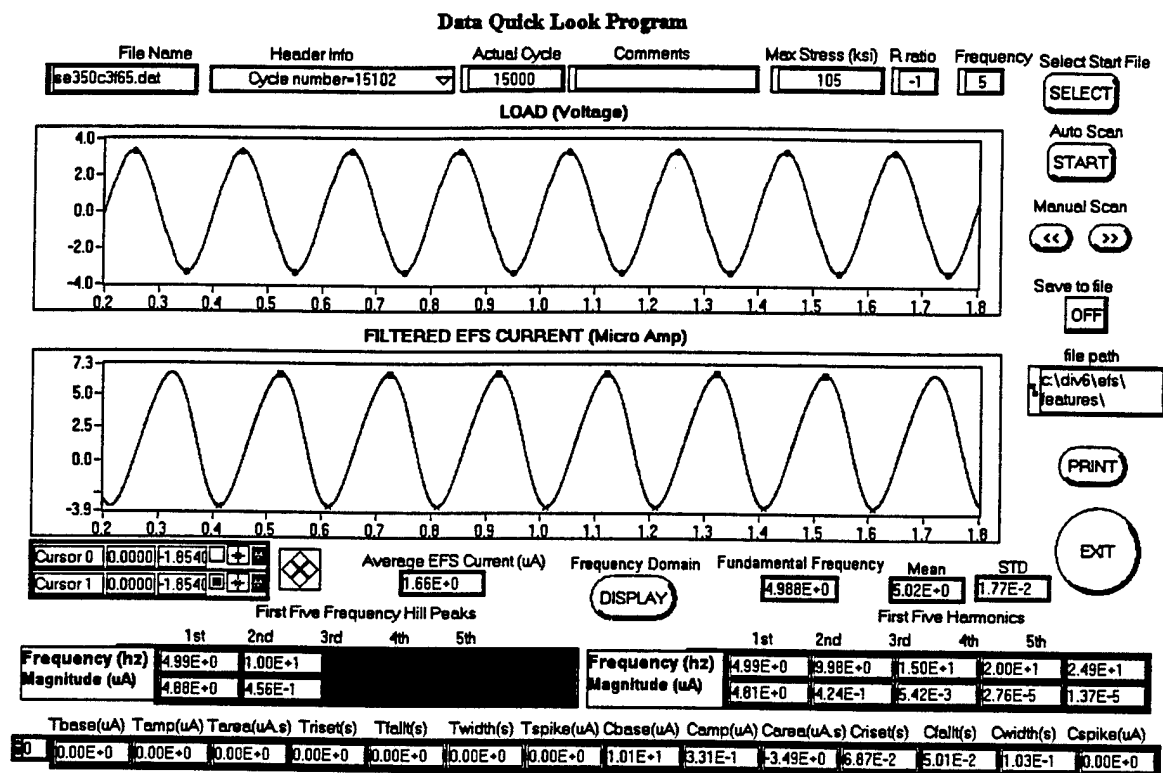
Figure 5.29. Plot of the transient current and the cyclic load for the same 4130 steel specimen as that in Figure 5-28 showing the effect of filtering on the detection of the current spike.

~75 μm

50X
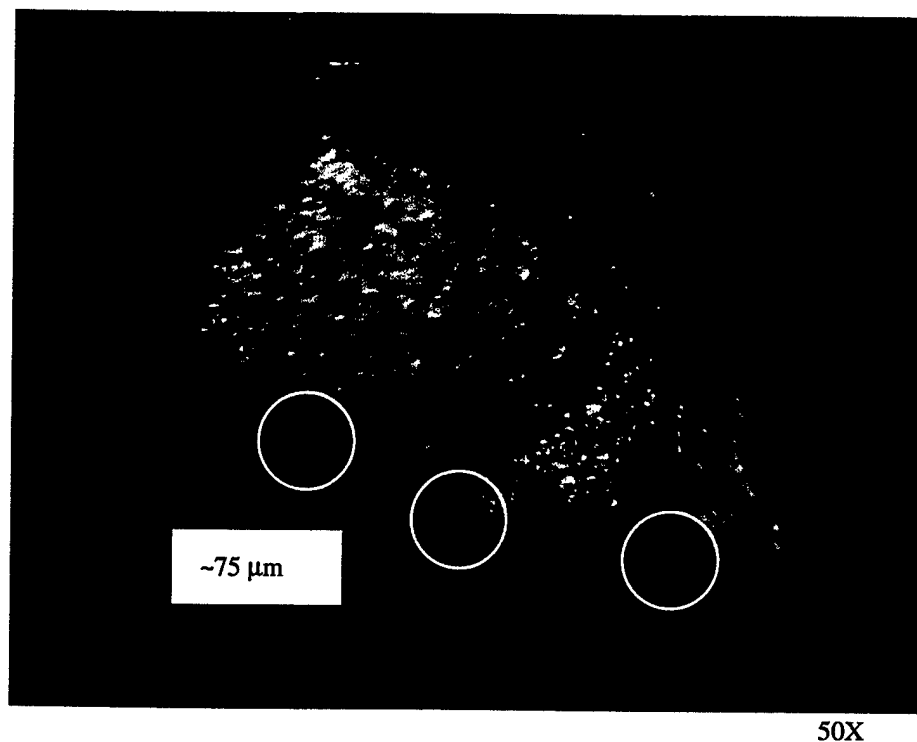
Figure 5-30. Multiple surface cracks revealed on the fracture surface of 4130 steel by heat tinting. The corresponding EFS signal is shown in Figure 5-28.
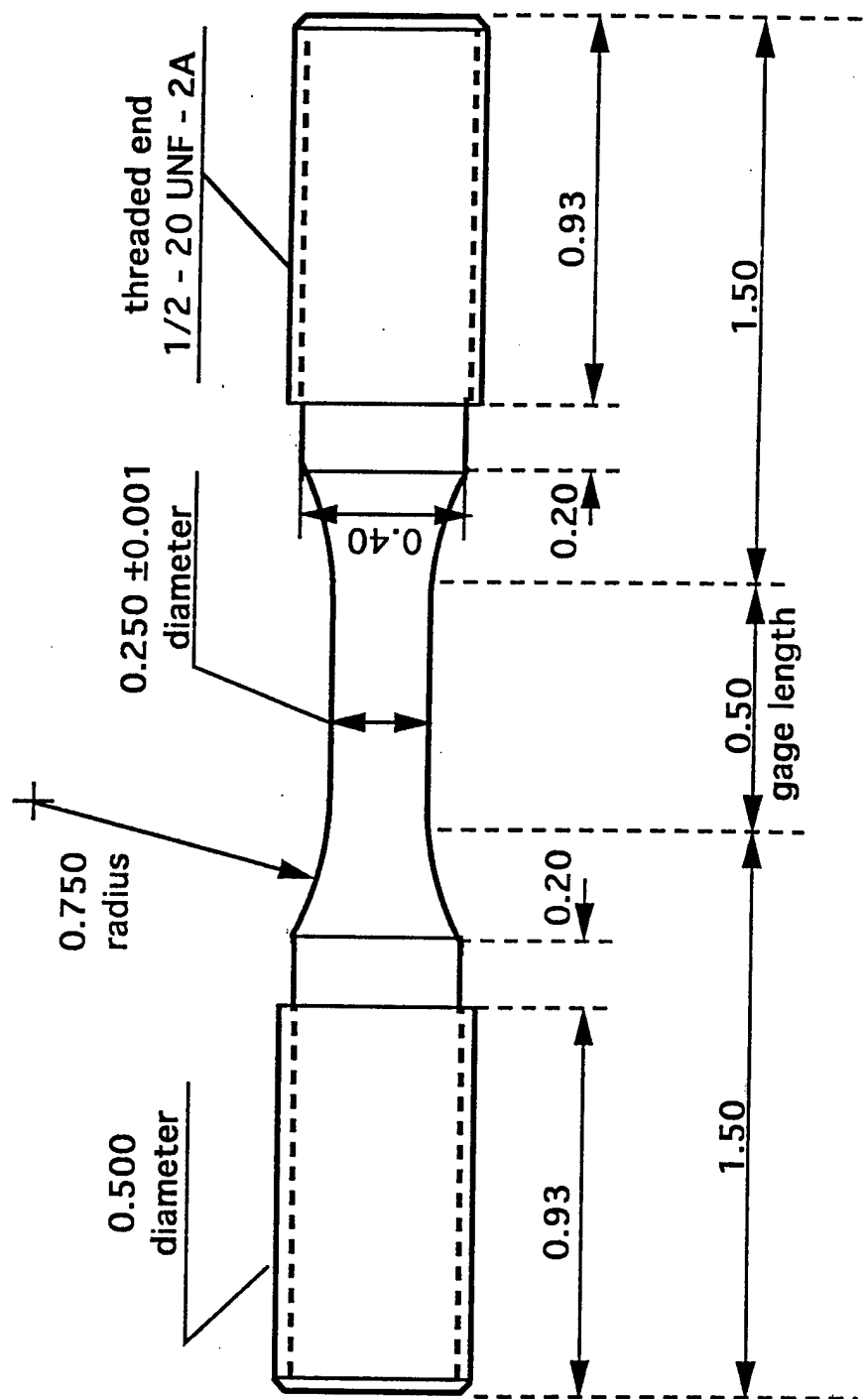
Figure 5-31. Round bar fatigue specimen design as used in the Penn tests. (All units in inches. 1 in. = 25.4 mm)
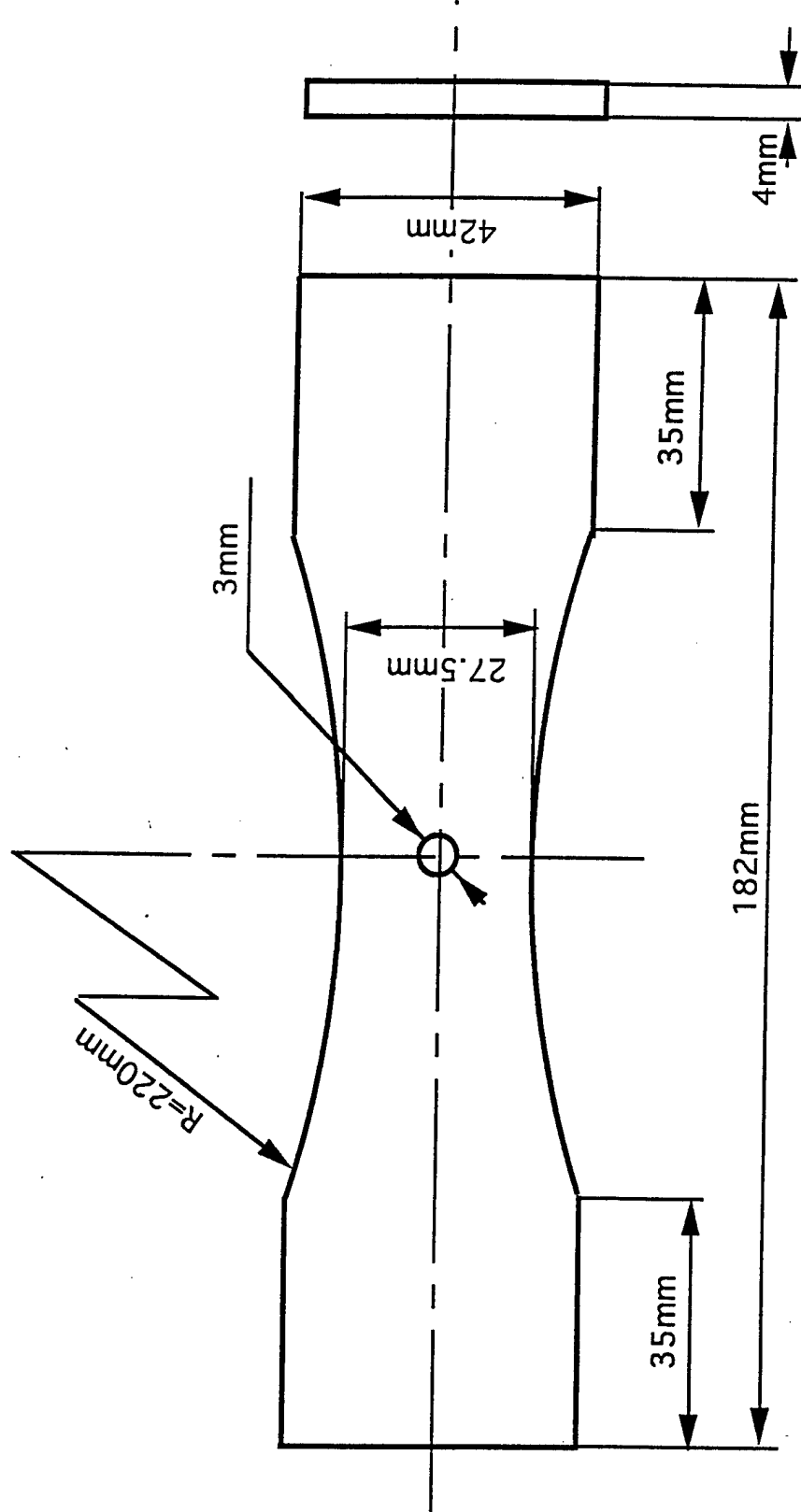
Figure 5-32. Rectangularly sectioned specimen design used in the Penn tests for testing prototype EFS cells, with and without a central hole. Hydraulic grips were employed for this design of specimen.
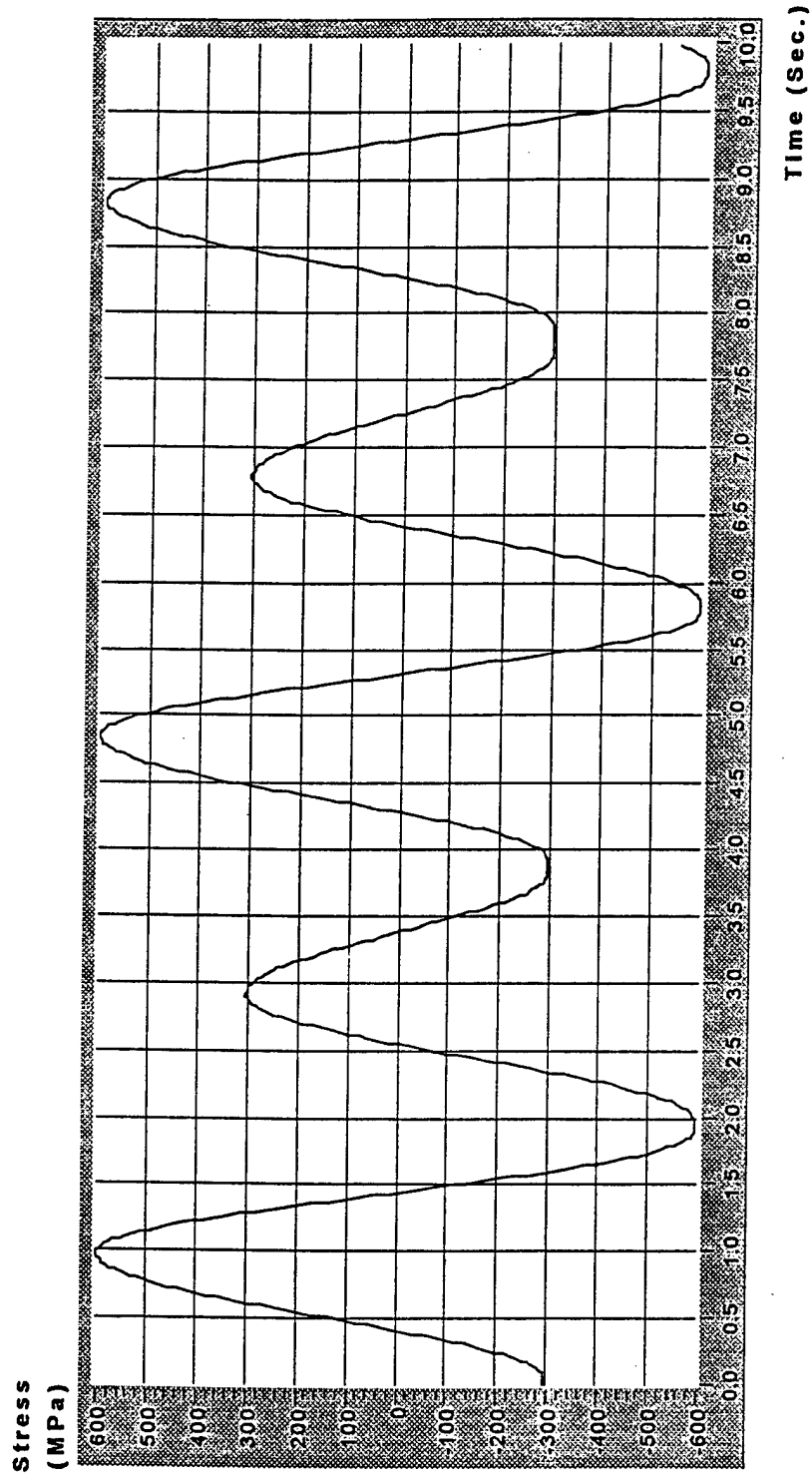
Figure 5-33. Variable loading test sequence using alternating cycles at R = -1 of 600 MPa and 300 MPa stress amplitude and of sinusoidal waveform.
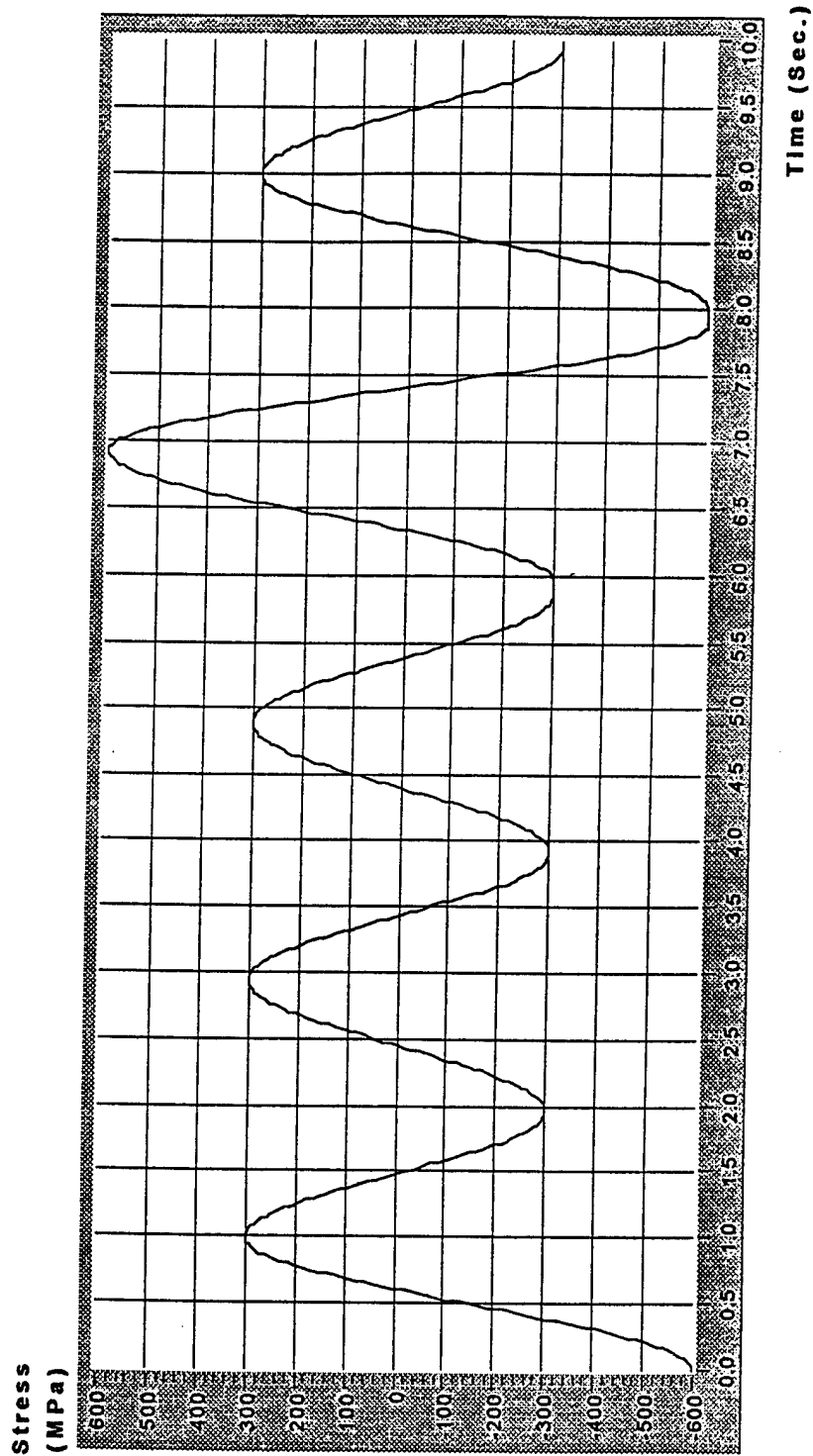
Figure 5-34. Variable loading test sequence using three cycles of 300 MPa stress amplitude followed by one cycle at 600 MPa. All cycles sinusoidal and with R = -1.
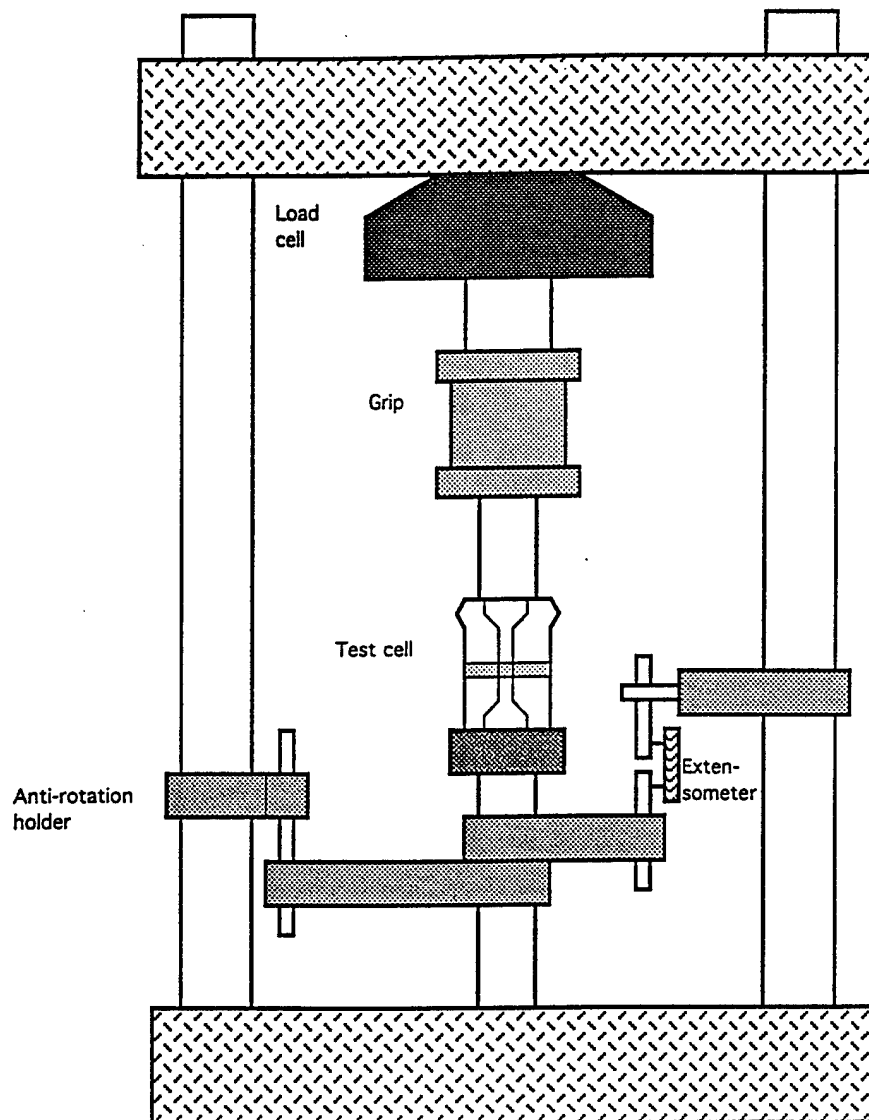
Figure 5-35. Vertical configuration of electrohydraulic test machine at Penn using a Woods metal self-aligning gripping arrangement, a round bar specimen, a cylindrical EFS cell, external extensometer, and actuator anti-rotation device. No electrical isolation was necessary with the potentiostat and data acquisition system employed for the EFS.

TEST CELL
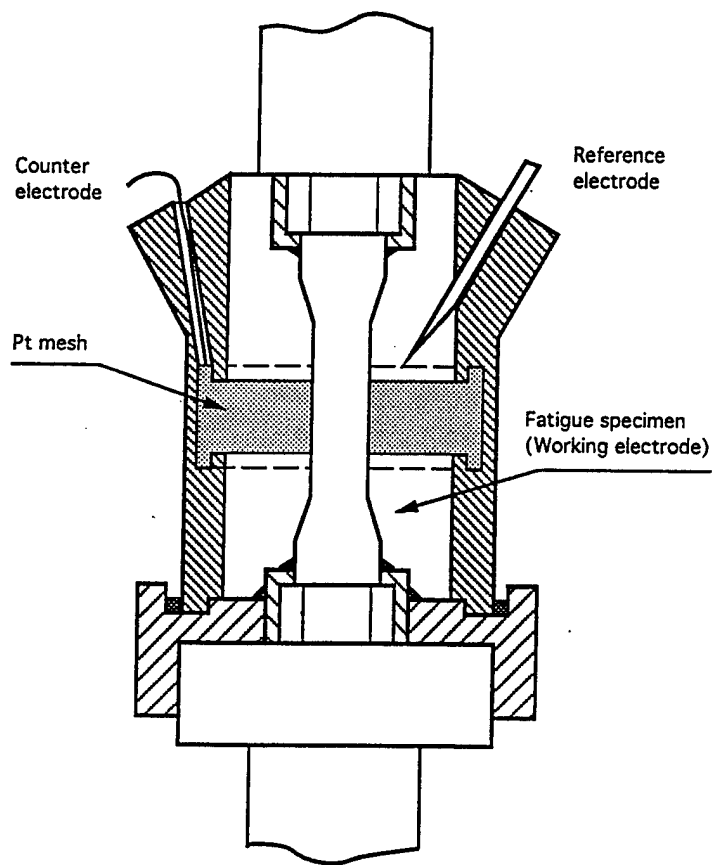
Figure 5-36. Details of EFS cell used at Penn for round bar testing in electrolyte showing systems for sealing and protecting the specimen grips. Chamber is cylindrical with all-around counter electrode.
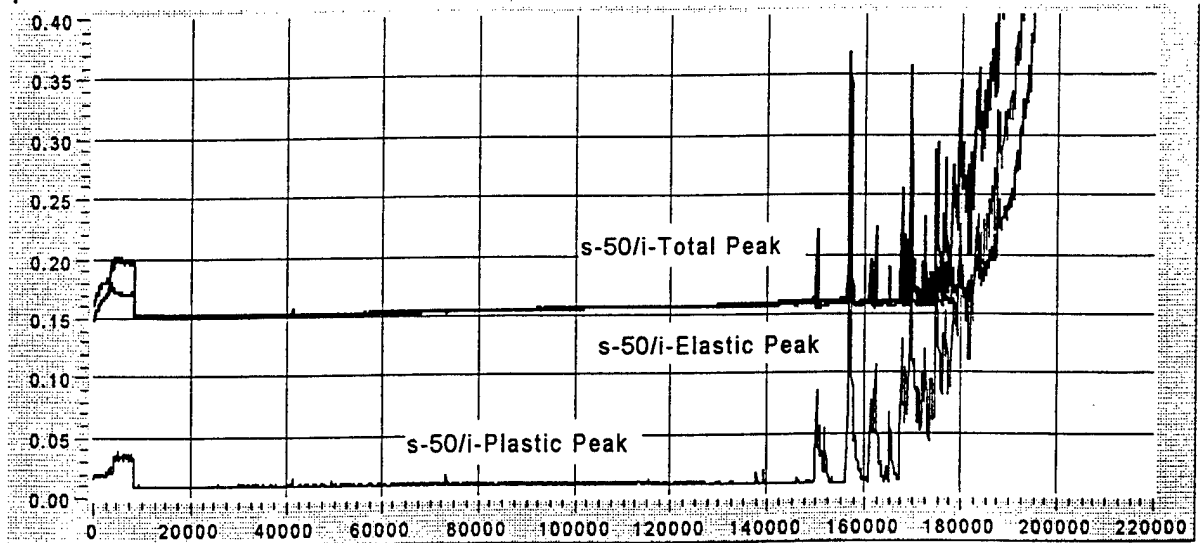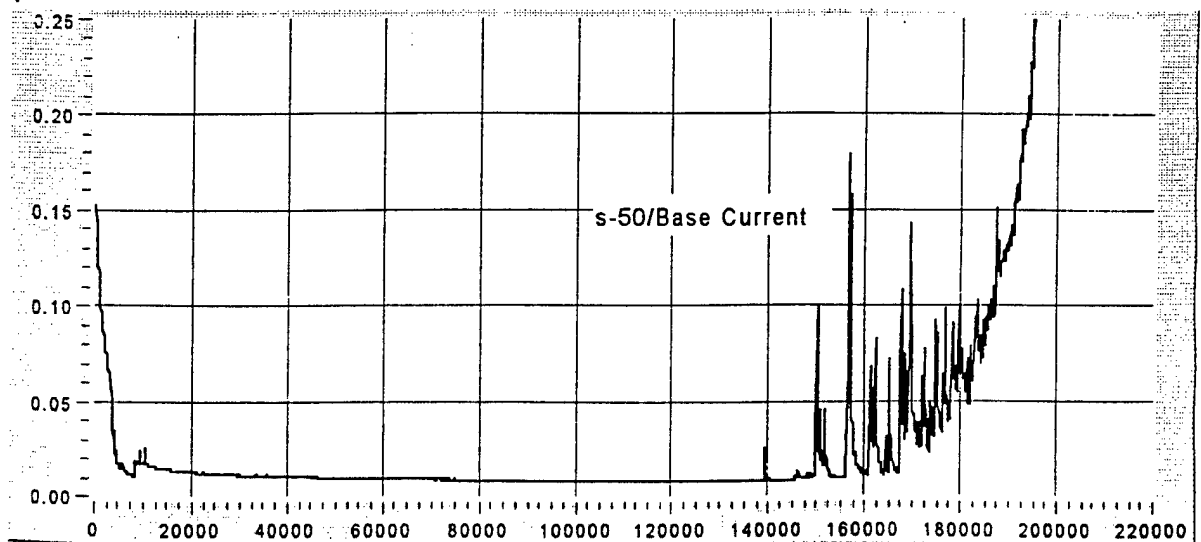
Figure 5-37. Typical plots used for presenting EFS results as a function of number of fatigue cycles or life fraction consumed, example of steel specimen S-50 cycled with a stress amplitude of 600 MPa under stress control, with a sinusoidal waveform, at a frequency of 0.5 Hz, in steel liquid electrolyte, at R = -1. This specimen failed at 209,600 cycles: a) peaks of: 1) the total EFS current, 2) that associated with elastic strain (elastic) and 3) that associated with plastic strain (plastic); b) the EFS DC base current; c) the phase shift between the elastic current and the stress signal; d) total EFS current versus time, as compared to the stress signal, at various intervals indicated by cycle number, during the life of the specimen. Note the reduction in the phase shift of the EFS peak with respect to the peak of the stress signal as life is consumed and the development of the crack peak on the tensile shoulder of the EFS waveform.

Figure 5-37 (Cont'd). Typical plots used for presenting EFS results as a function of number of fatigue cycles or life fraction consumed, example of steel specimen S-50 cycled with a stress amplitude of 600 MPa under stress control, with a sinusoidal waveform, at a frequency of 0.5 Hz, in steel liquid electrolyte, at R = -1. This specimen failed at 209,600 cycles: a) peaks of: 1) the total EFS current, 2) that associated with elastic strain (elastic) and 3) that associated with plastic strain (plastic); b) the EFS DC base current; c) the phase shift between the elastic current and the stress signal; d) total EFS current versus time, as compared to the stress signal, at various intervals indicated by cycle number, during the life of the specimen. Note the reduction in the phase shift of the EFS peak with respect to the peak of the stress signal as life is consumed and the development of the crack peak on the tensile shoulder of the EFS waveform.

Current Density

μA / c m2

0.20
0.15
0.10
0.05
0.00
-0.05
-0.10
-0.15
-0.20

0.00 0.50 1.00 1.50 2.00 2.50 3.00 3.50 4.00 4.50 5.00 5.50 6.00 6.50 7.00

150000

149900
10000

(d)

Time (Sec.)

Current Density

μA / c m2

0.35
0.30
0.25
0.20
0.15
0.10
0.05
0.00
-0.05
-0.10
-0.15
-0.20

0.00 0.50 1.00 1.50 2.00 2.50 3.00 3.50 4.00 4.50 5.00 5.50 6.00 6.50 7.00

150100

150200

150500
150800

(e)

Time (Sec.)

Figure 5-37 (Cont'd). Typical plots used for presenting EFS results as a function of number of fatigue cycles or life fraction consumed, example of steel specimen S-50 cycled with a stress amplitude of 600 MPa under stress control, with a sinusoidal waveform, at a frequency of 0.5 Hz, in steel liquid electrolyte, at R = -1.   This specimen failed at 209,600 cycles: a) peaks of: 1) the total EFS current, 2) that associated with elastic strain (elastic) and 3) that associated with plastic strain (plastic); b) the EFS DC base current;   c) the phase shift between the elastic current and the stress signal;   d) total EFS current versus time, as compared to the stress signal, at various intervals indicated by cycle number, during the life of the specimen.   Note the reduction in the phase shift of the EFS peak with respect to the peak of the stress signal as life is consumed and the development of the crack peak on the tensile shoulder of the EFS waveform.

Figure 5-38. EFS response of steel specimen S-42 during life when continually monitored by the EFS. It will be noted that the various plots in this figure (and those that follow) correspond to similar plots in Figure 5-37. Thus, in each diagram, the metal and specimen identity, along with various EFS currents, phase shifts, and waveform identities are provided. Details of the specimen fatigue conditions are given in the tables. For example, details for S-42 are provided in Table 5-11. Therefore, for brevity, captions of subsequent figures will be kept brief because the figures themselves contain the necessary information. A specific feature of this figure is (c), which shows greater detail of EFS response on an expanded cycle scale.

Figure 5-38 (Cont'd). EFS response of steel specimen S-42 during life when continually monitored by the EFS. It will be noted that the various plots in this figure (and those that follow) correspond to similar plots in Figure 5-37. Thus, in each diagram, the metal and specimen identity, along with various EFS currents, phase shifts, and waveform identities are provided. Details of the specimen fatigue conditions are given in the tables. For example, details for S-42 are provided in Table 5-11. Therefore, for brevity, captions of subsequent figures will be kept brief because the figures themselves contain the necessary information. A specific feature of this figure is (c), which shows greater detail of EFS response on an expanded cycle scale.

Phase Shift X
Period of 0.5 Hz

s-42/IO--1 (0.5 Hz)

No. of Cycles

(d)

Figure 5-38 (Cont'd).

5-103

Current Density

µA / cm2

(e)   Time (Sec.)

Current Density

µA / cm2

(f)   Time (Sec.)

Figure 5-38 (Cont'd).

Current Density
μA / c m 2

(a)

No. of Cycles

Current Density
μA / c m 2

(b)
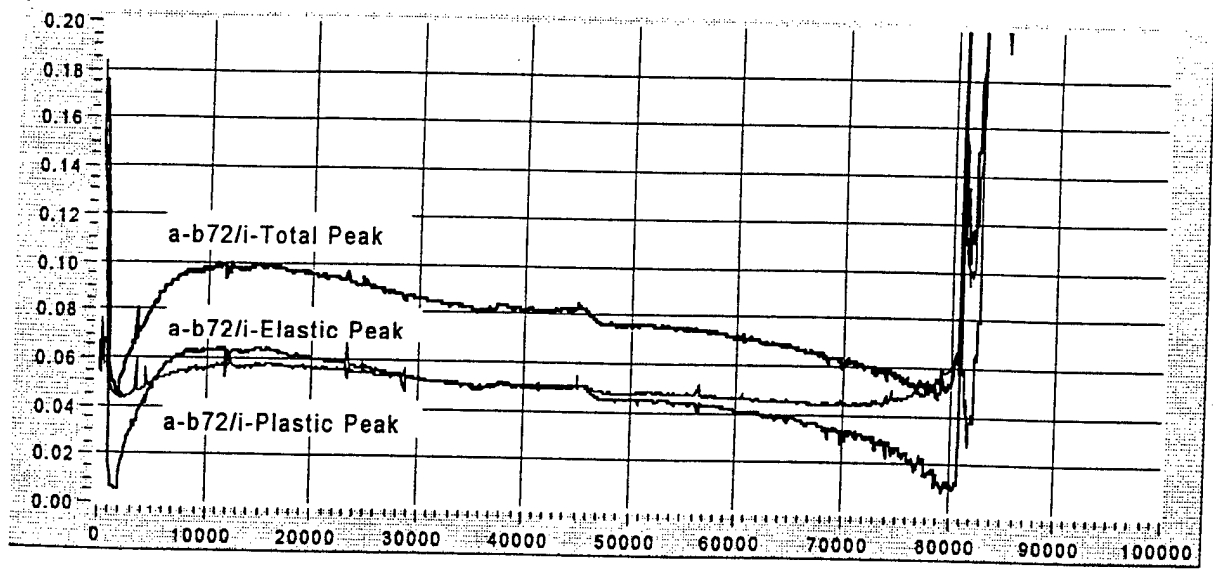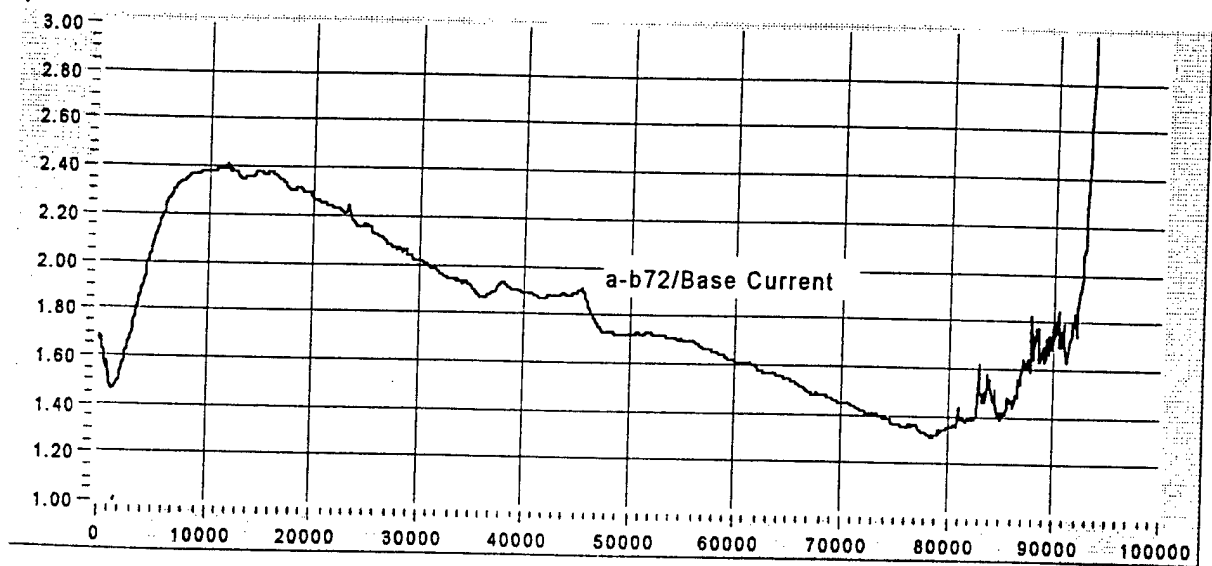
No. of Cycles

Figure 5-39. EFS response of aluminum 7075 alloy specimen A-b 72 during life when continually monitored by the EFS.
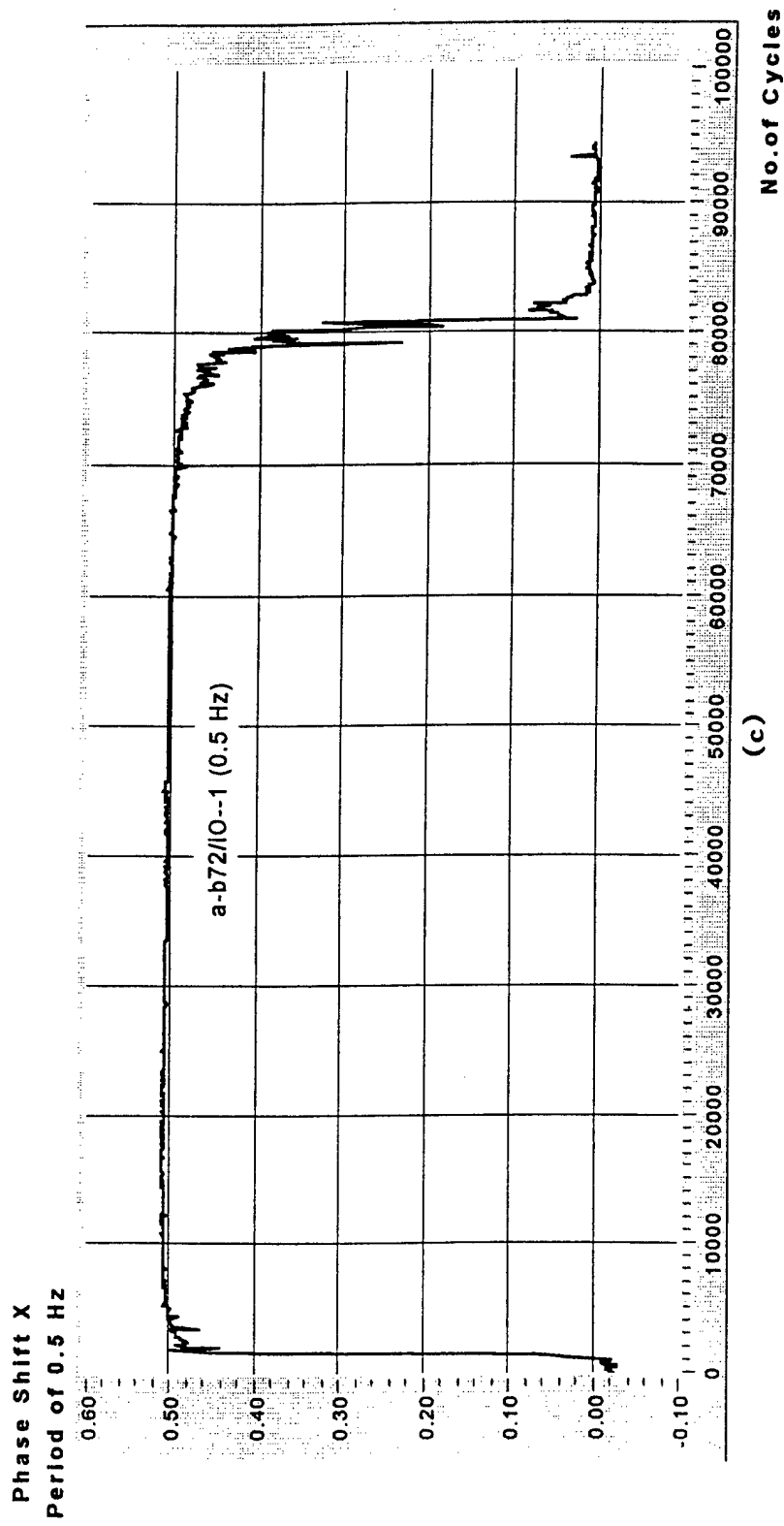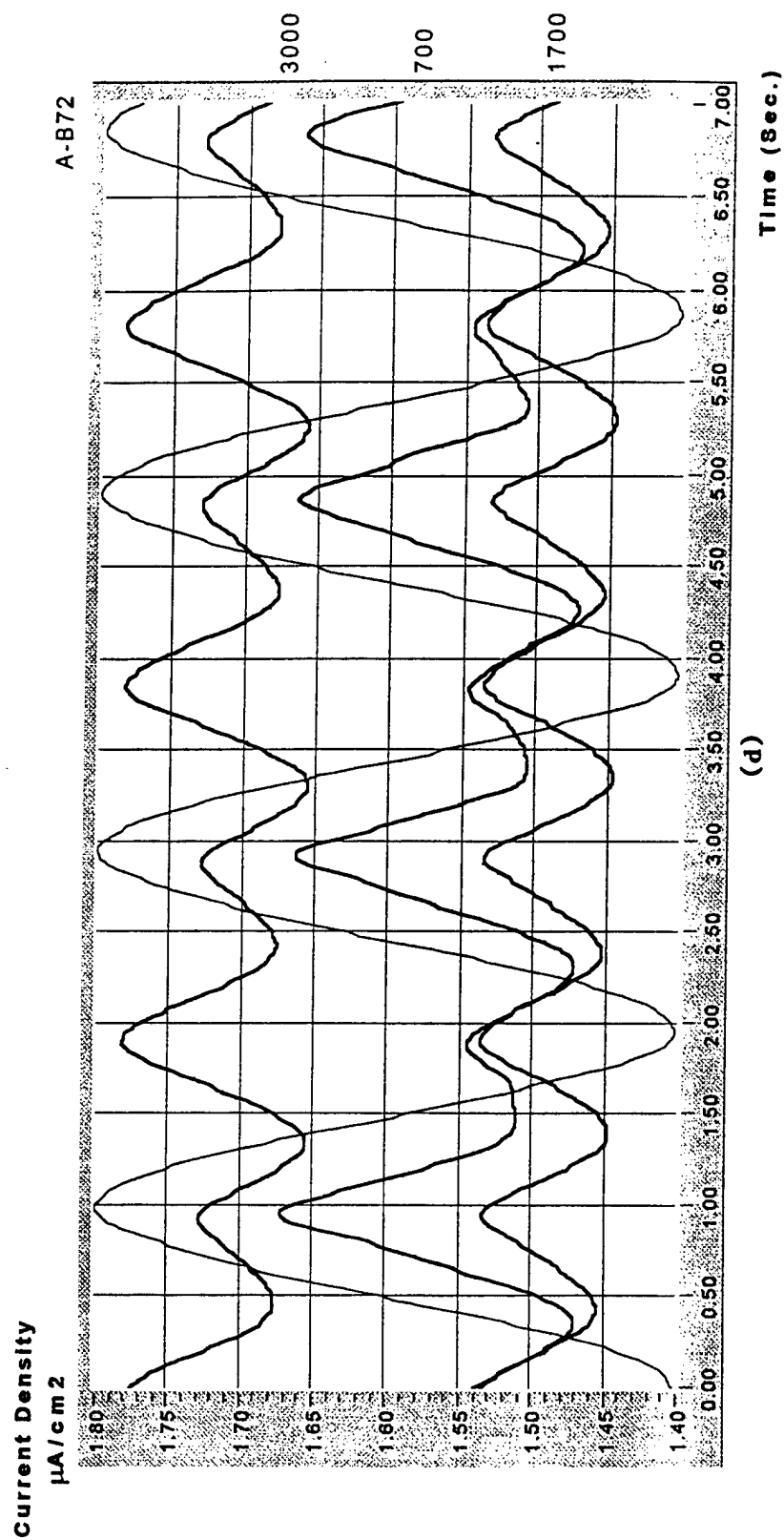
Figure 5-39 (Cont'd).

Figure 5-39 (Cont'd).

5-107
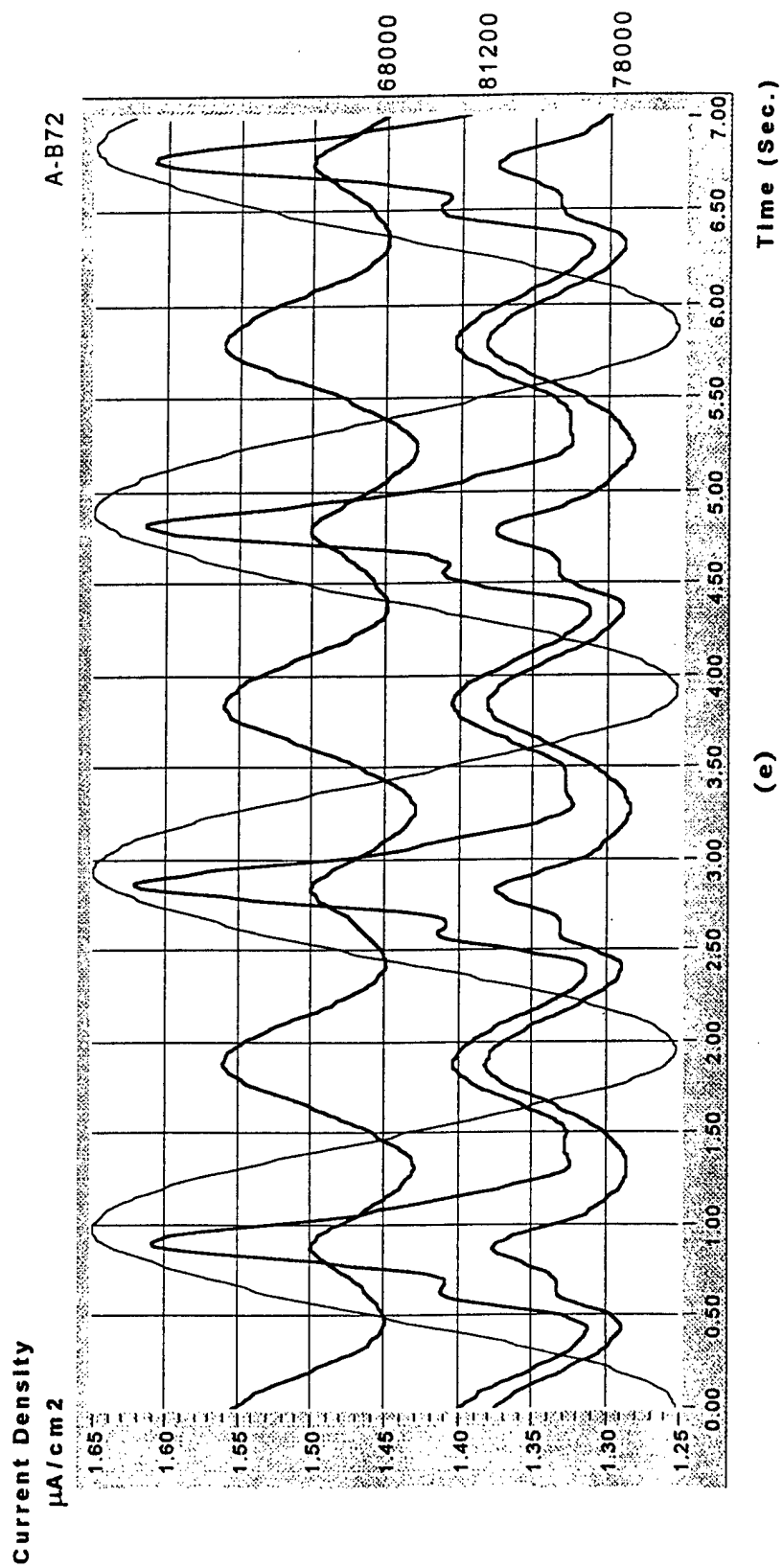
Figure 5-39 (Cont'd).

Current Density

μA / c m 2

(a)
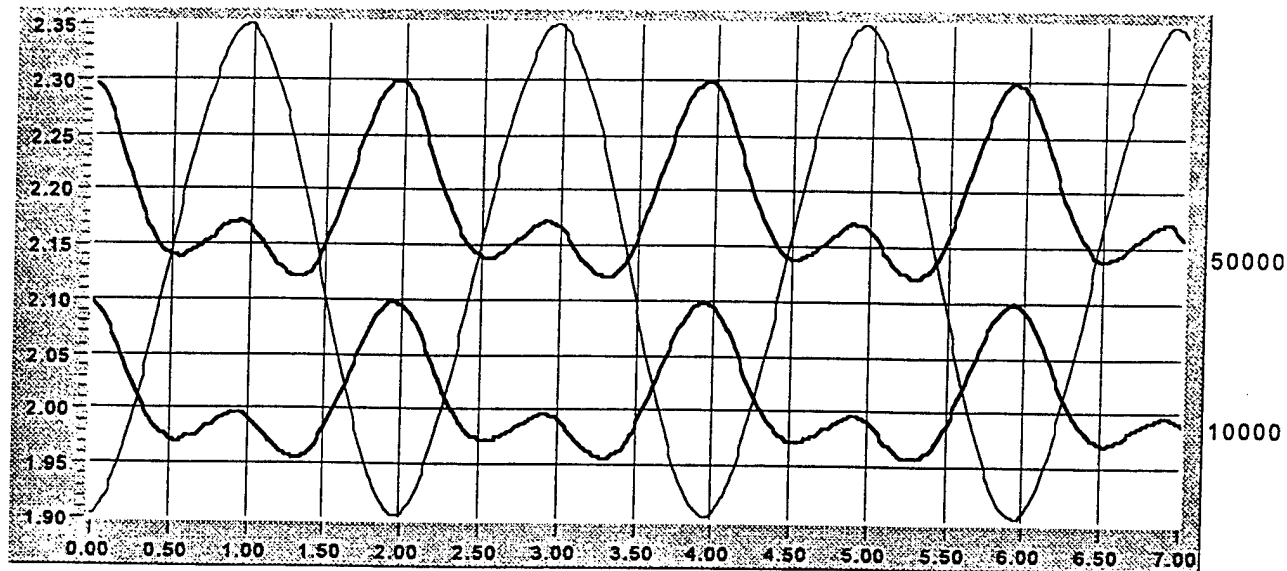
Time (Sec.)

Current Density

μA / c m 2
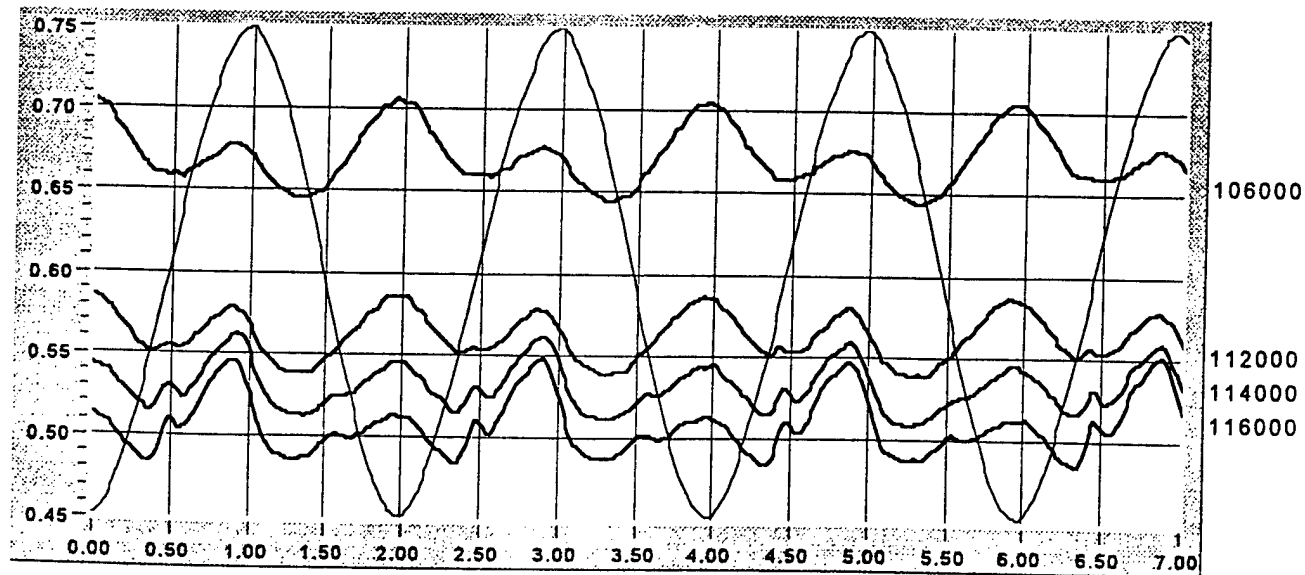
(b)

Time (Sec.)

Figure 5-40. EFS response (waveform only) of aluminum 7075 alloy specimen A-b 105 during life when continually monitored by the EFS.
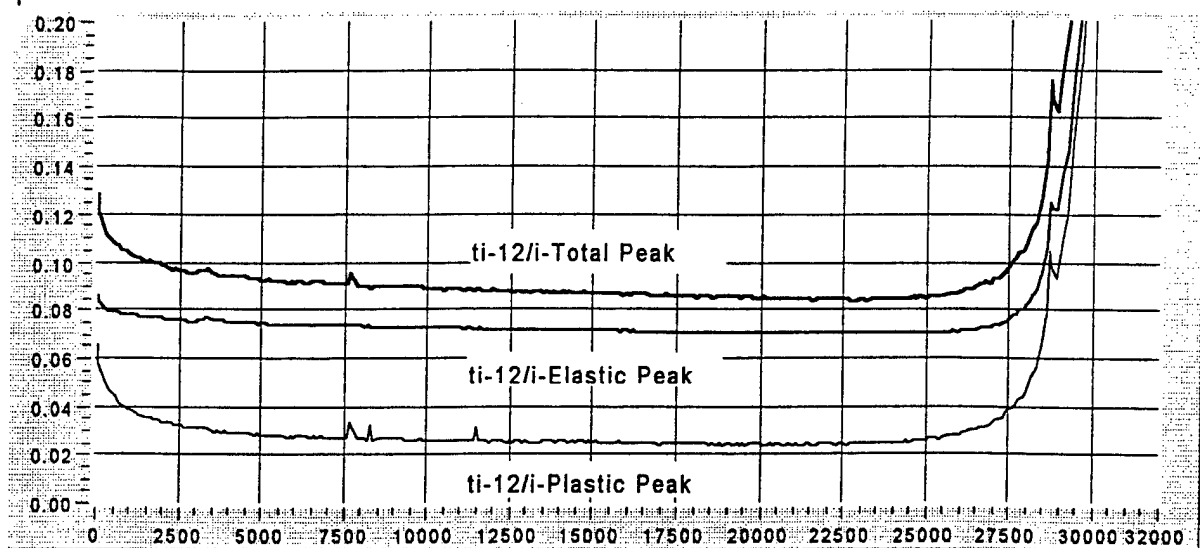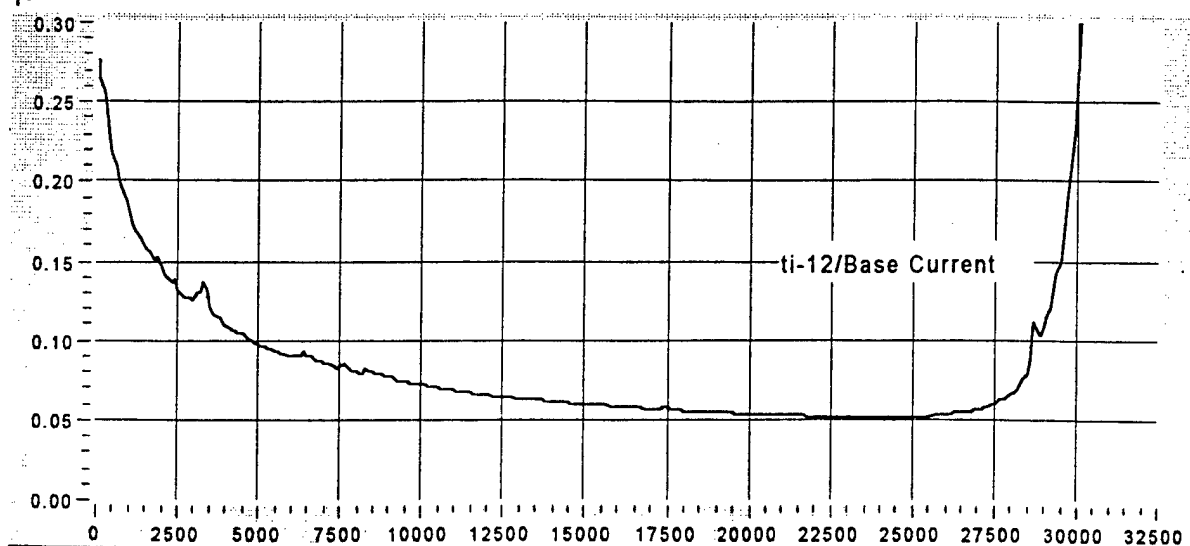
Figure 5-41. EFS response of titanium alloy specimen Ti-12 during life when continually monitored by the EFS.

Figure 5-41 (Cont'd).

5-111
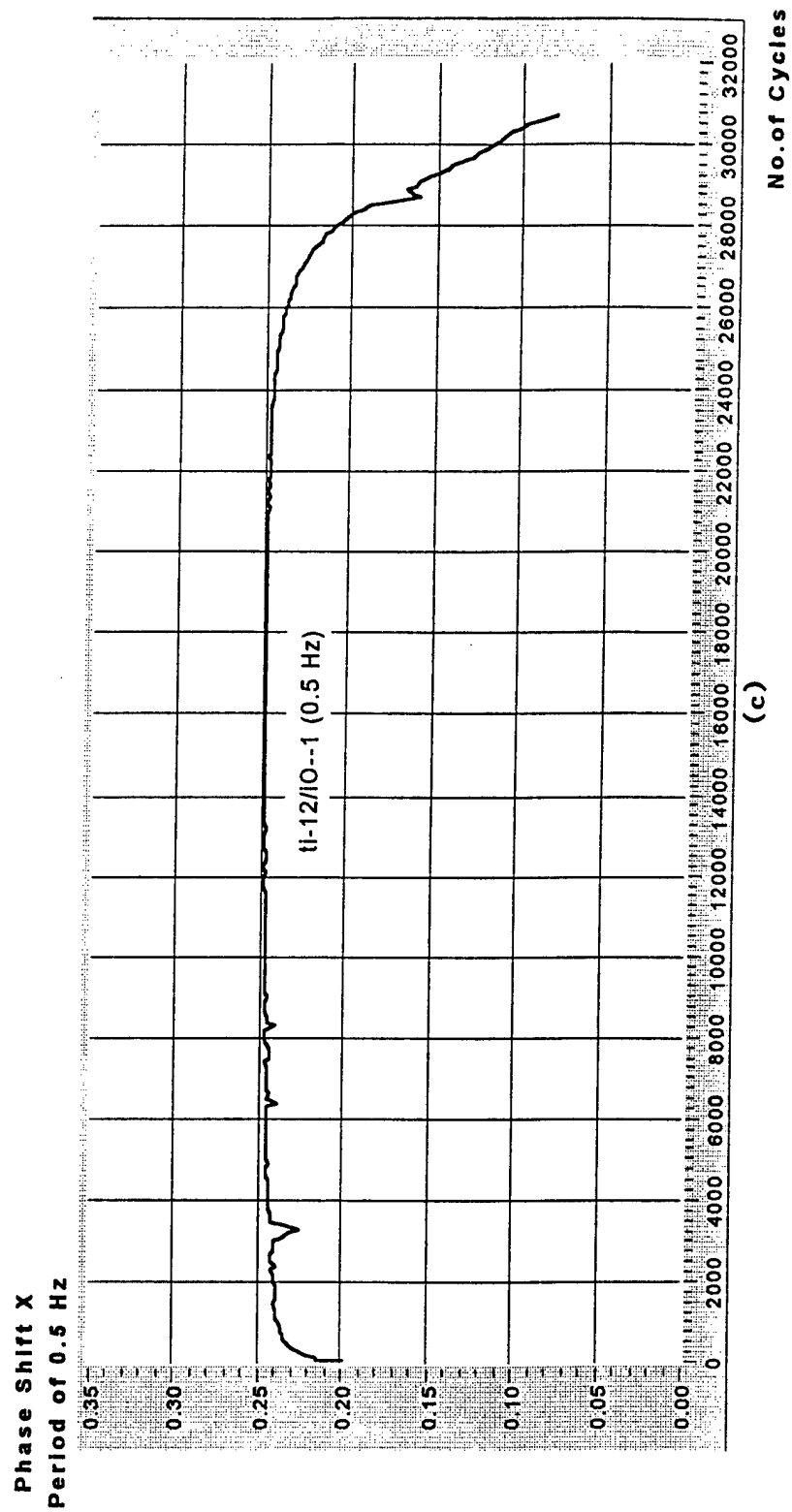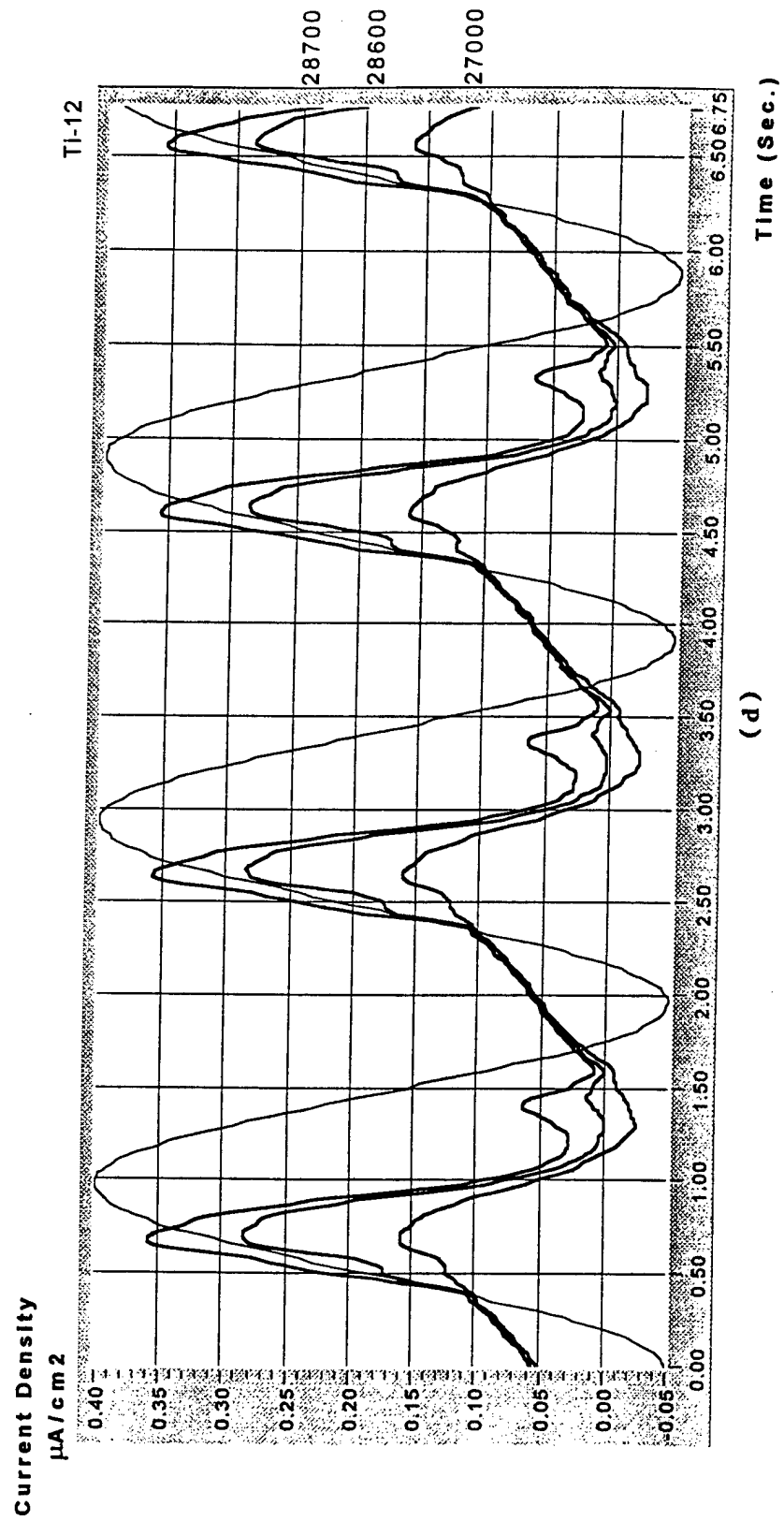
Figure 5-41 (Cont'd).
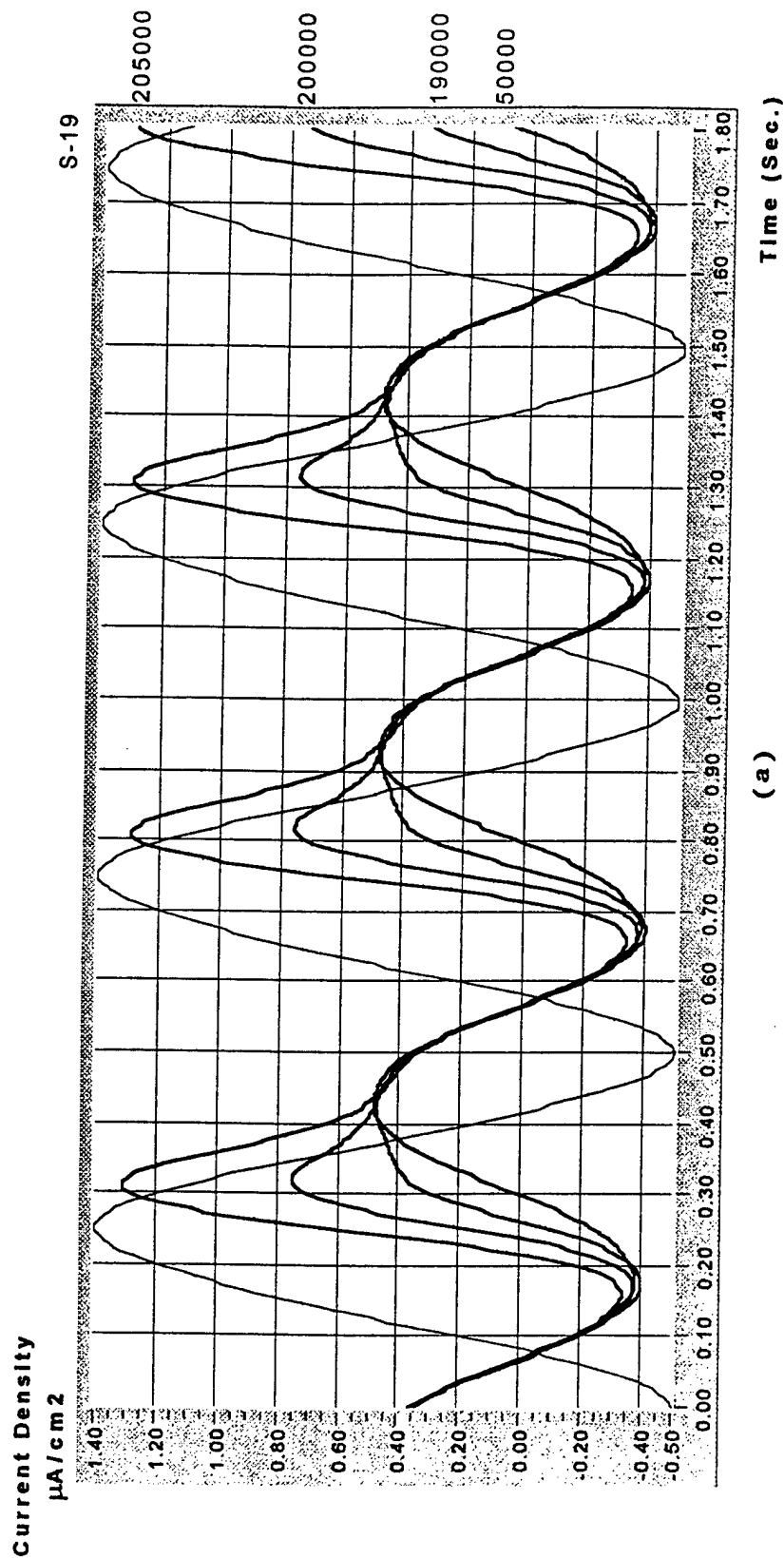
Figure 5-42. EFS current waveforms of 4130 steel in dependence on cyclic frequency recorded at various intervals during life: a) S-19 at 2 Hz; b) 4130-8 at 3.5 Hz; c) S-40 at 5 Hz.

Figure 5-42 (Cont'd). EFS current waveforms of 4130 steel in dependence on cyclic frequency recorded at various intervals during life: a) S-19 at 2 Hz; b) 4130-8 at 3.5 Hz; c) S-40 at 5 Hz.
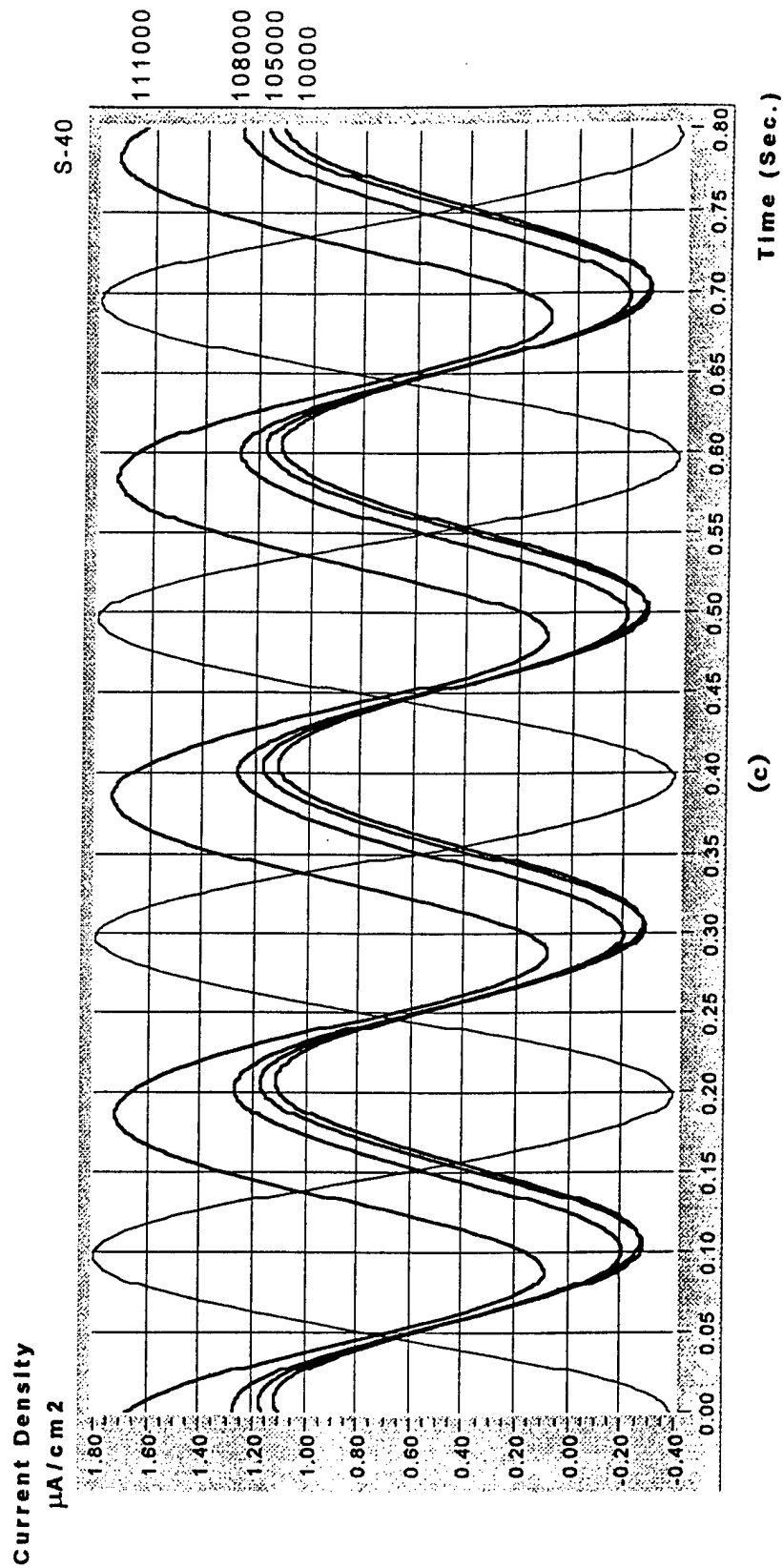
Figure 5-42 (Cont'd). EFS current waveforms of 4130 steel in dependence on cyclic frequency recorded at various intervals during life: a) S-19 at 2 Hz; b) 4130-8 at 3.5 Hz; c) S-40 at 5 Hz.
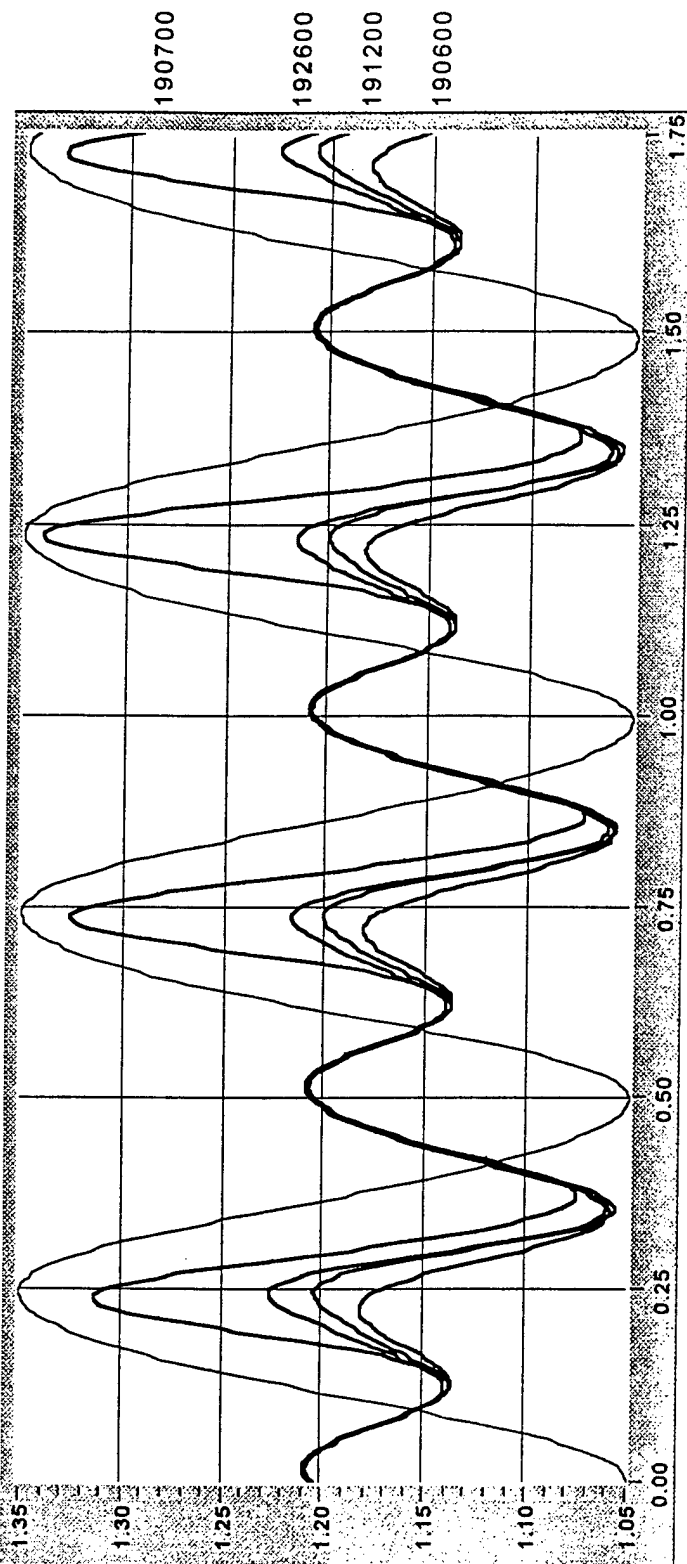
Figure 5-43. EFS current waveforms of aluminum 7075 alloy in dependence on cyclic frequency recorded at various intervals during life : a) A-t 85, 2 Hz; b) A-b 36, 3,5 Hz; c) A-b 94, 5 Hz.

Figure 5-43 (Cont'd). EFS current waveforms of aluminum 7075 alloy in dependence on cyclic frequency recorded at various intervals during life: a) A-t 85, 2 Hz; b) A-b 36, 3,5 Hz; c) A-b 94, 5 Hz.
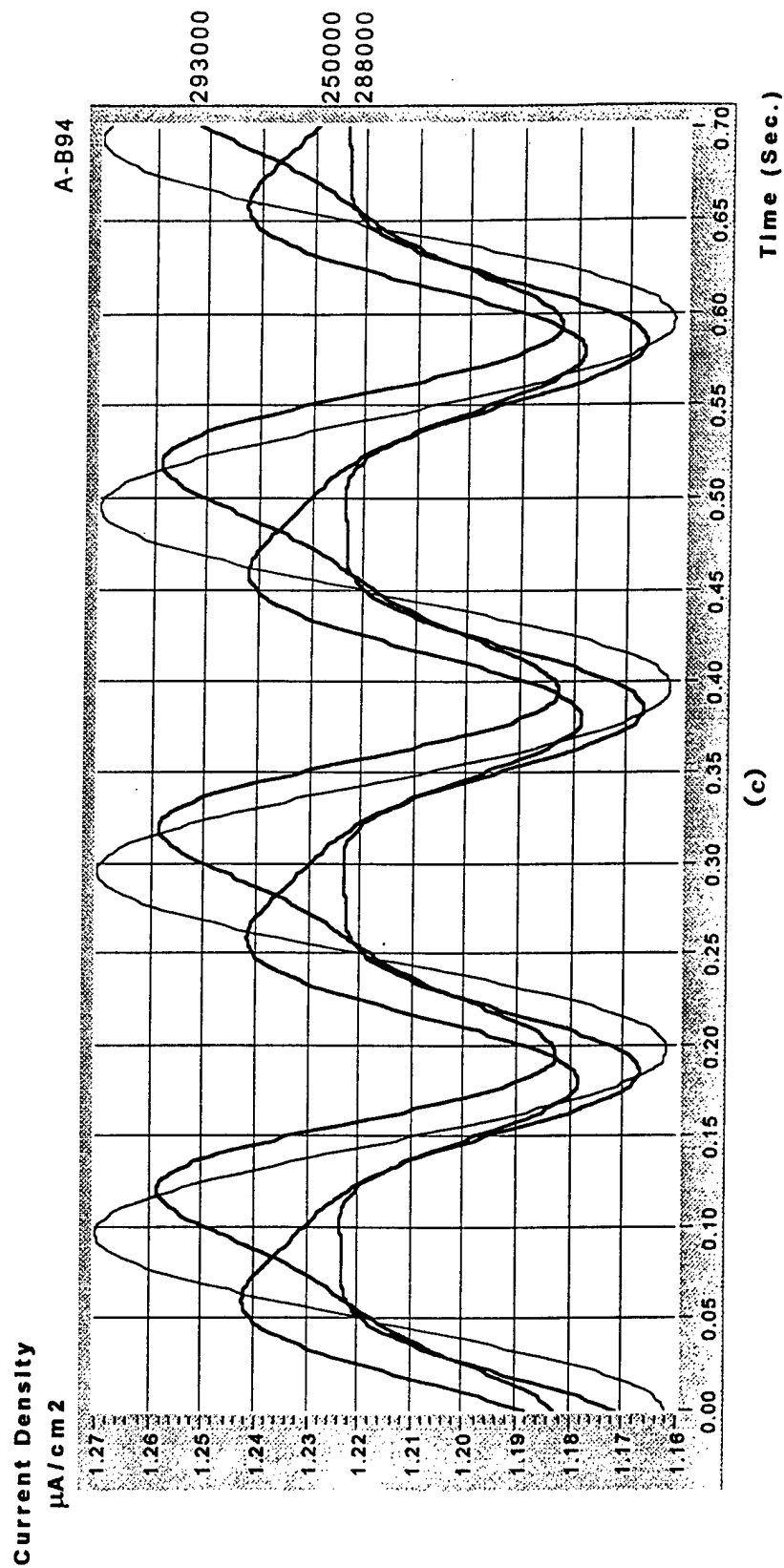
Figure 5-43 (Cont'd). EFS current waveforms of aluminum 7075 alloy in dependence on cyclic frequency recorded at various intervals during life : a) A-t 85, 2 Hz; b) A-b 36, 3,5 Hz; c) A-b 94, 5 Hz.
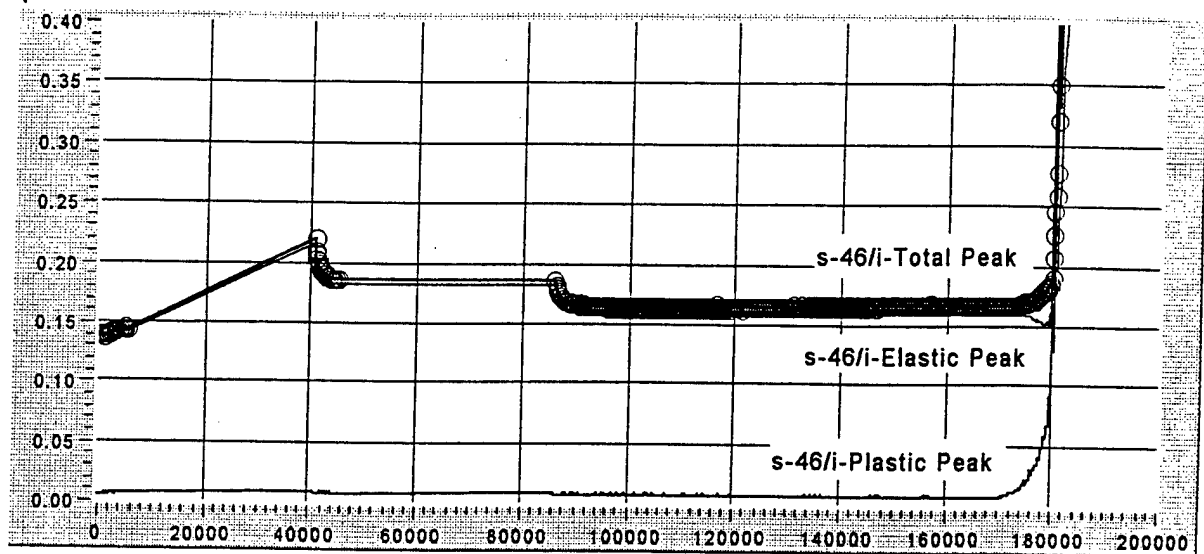
Figure 5-44. EFS response in 4130 steel specimen S-46 run partly in air and partly in electrolyte with the EFS in operation, including peak current plots and EFS waveforms. The open circle points indicate both the periods and measurements of the EFS. Straight lines joining open circle points indicate the periods of cycling in air. The organization of the individual plots is the same as that for Figures. 5–37 and 5-38.
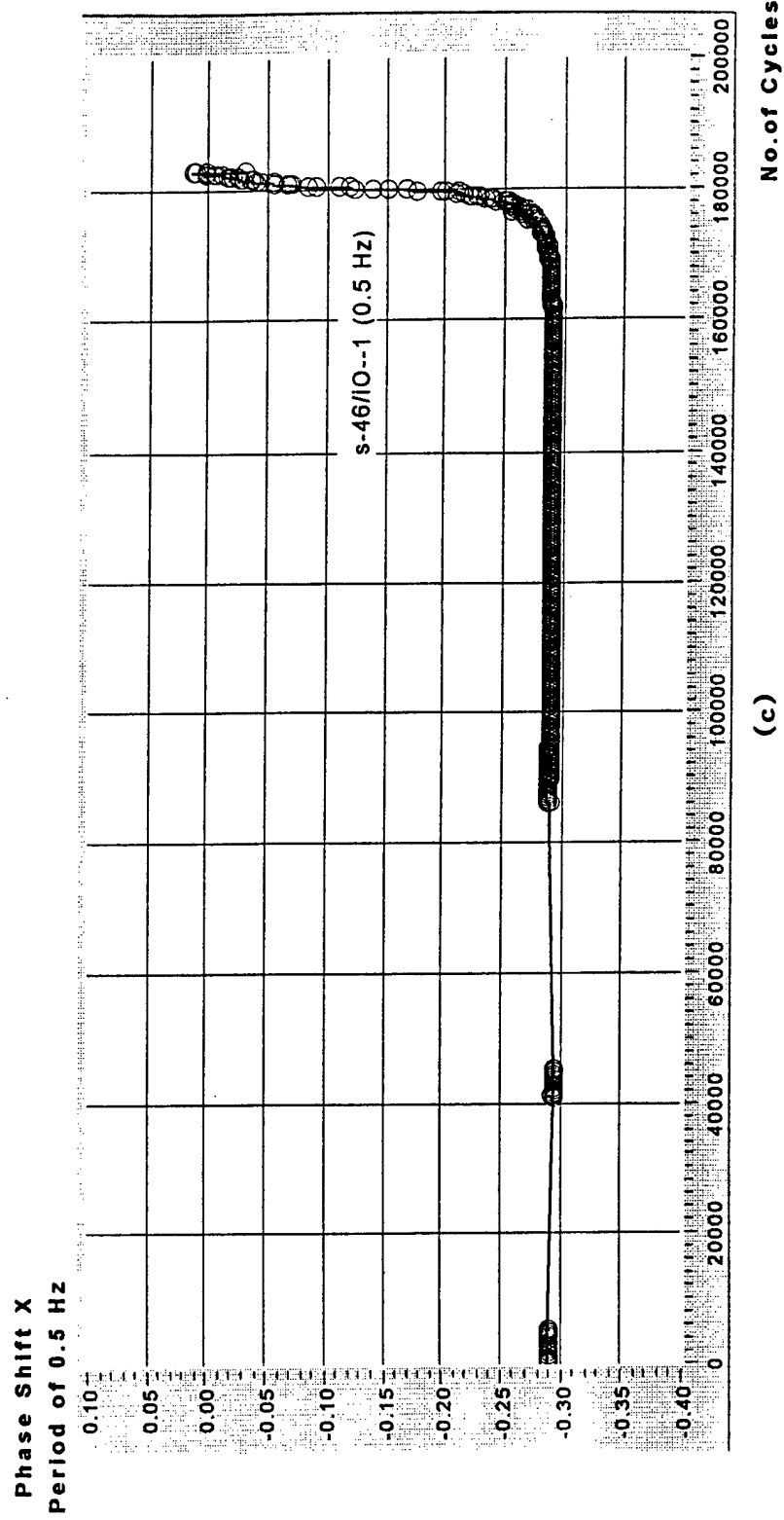
Figure 5-44 (Cont'd).

Figure 5-44 (Cont'd).

5-121
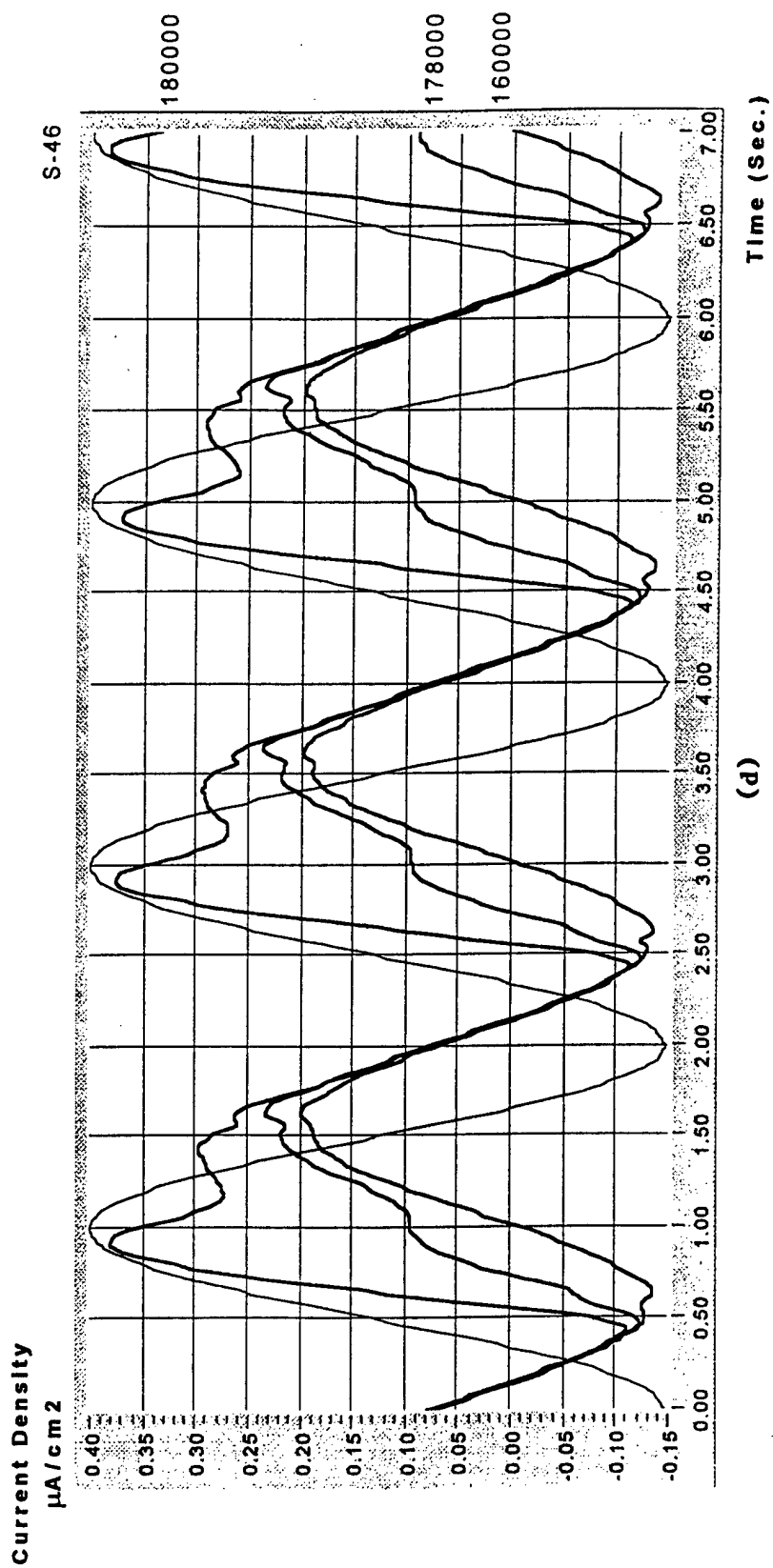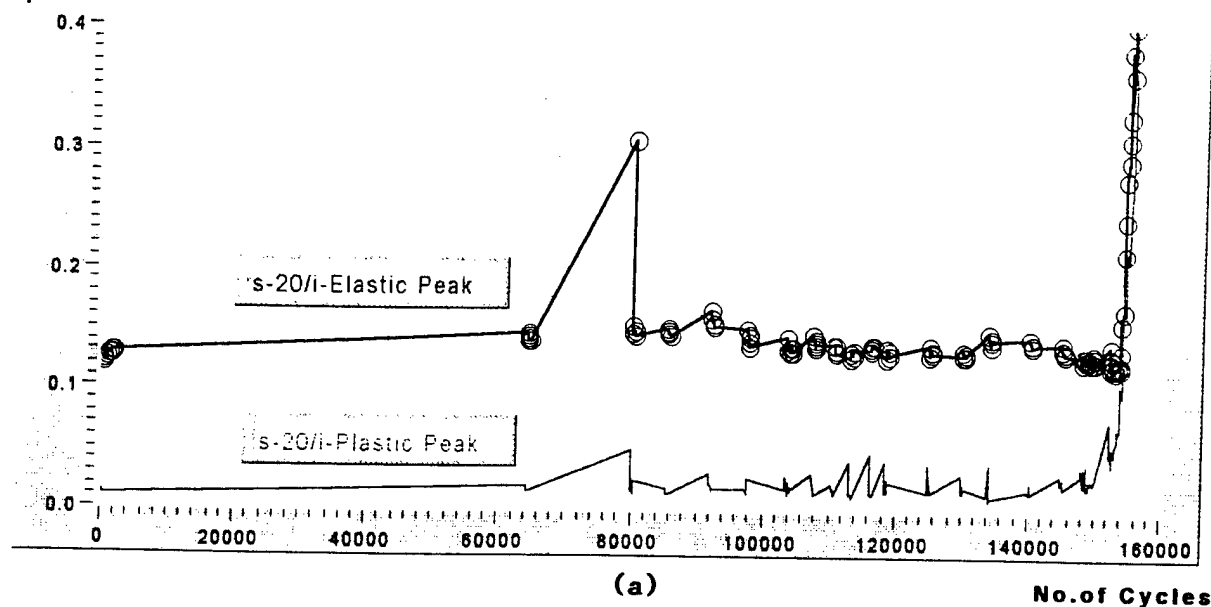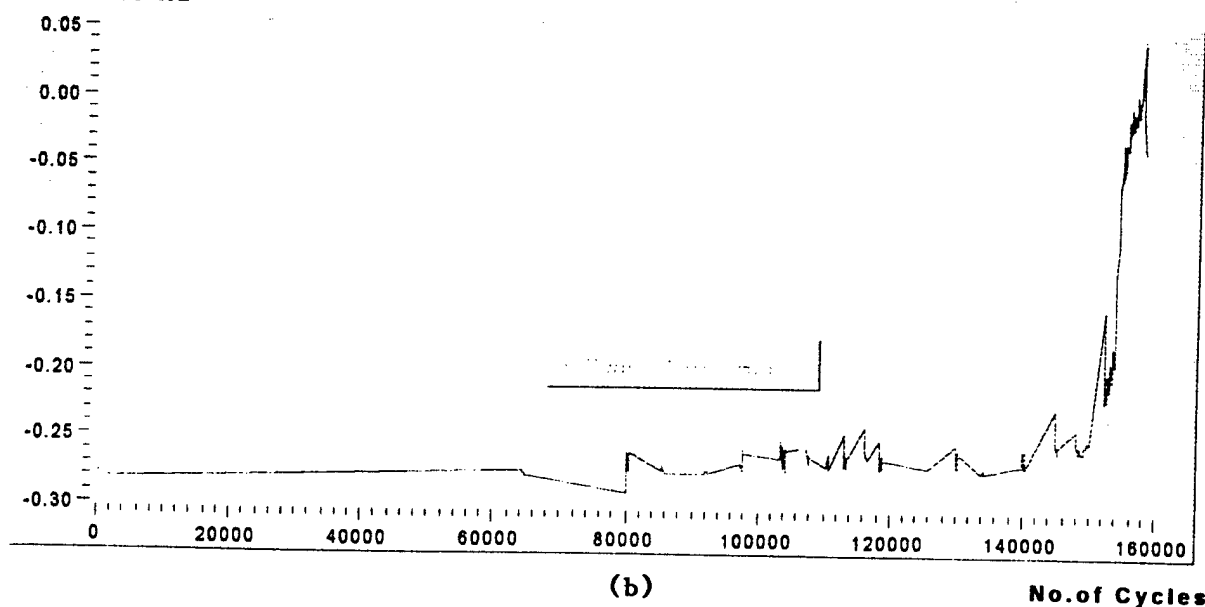
Figure 5-45. EFS response in 4130 steel specimen S-20 run partly in air and partly in electrolyte with the EFS in operation. Same convention as Figure 5-44 to indicate air/electrolyte cycle bouts. When air/electrolyte test alternations were frequent, as in this specimen in later life, the specimen was not washed and dried when the electrolyte was removed. Residual electrolyte was allowed to remain on the specimen surfaces.

Current Density
μA / c m 2

(a)

No. of Cycles

Current Density
μA / c m 2

(b)
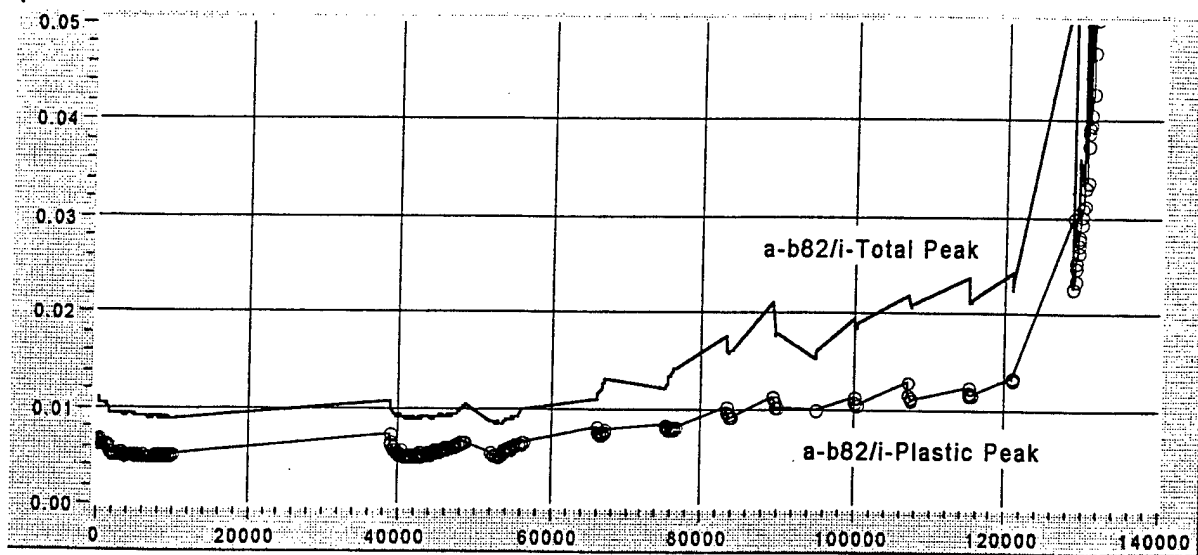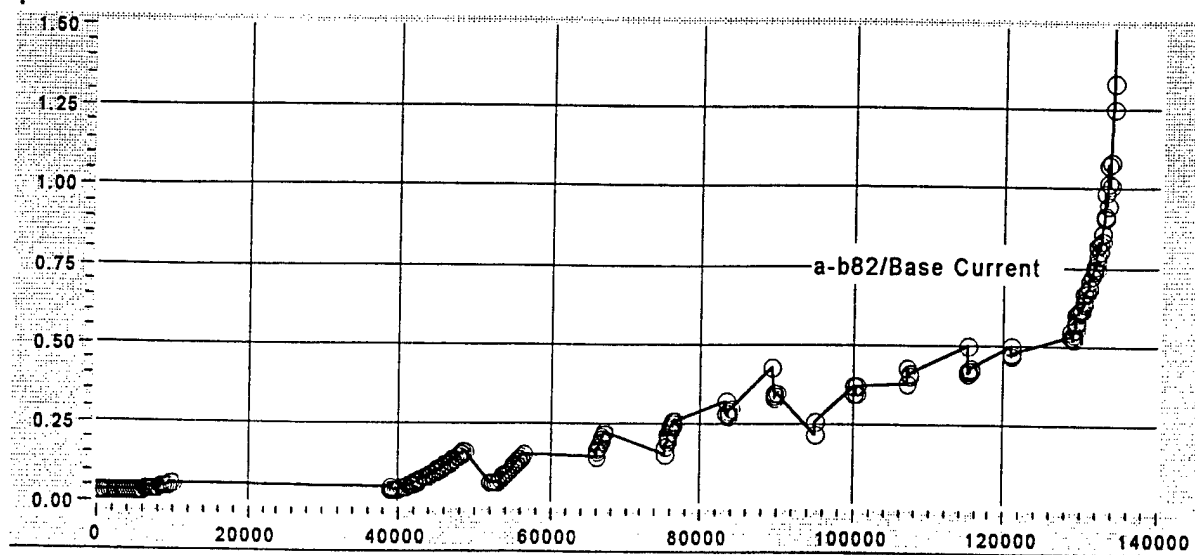
No. of Cycles

Figure 5-46. EFS response in aluminum 7075 alloy specimen A-b 82 cycled partly in air and partly in electrolyte with the EFS in operation. Same convention and washing/non-washing procedures as described in Figure 5-45.
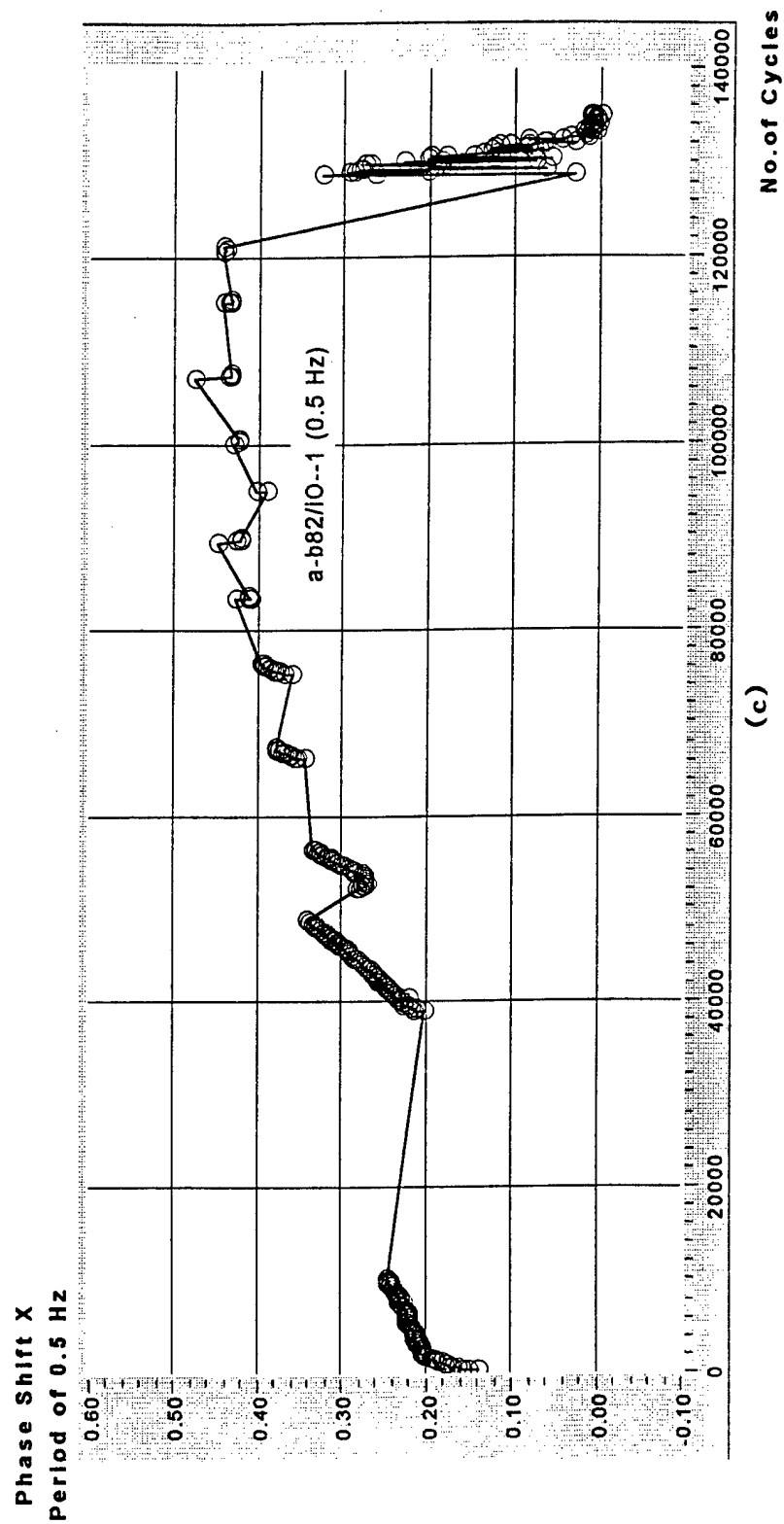
5-123

Phase Shift X
Period of 0.5 Hz

a-b82/IO--1 (0.5 Hz)

No.of Cycles

(c)

Figure 5-46 (Cont'd).

5-124

Current Density

μA / c m 2

(a)   **No.of Cycles**

Current Density

μA / c m 2
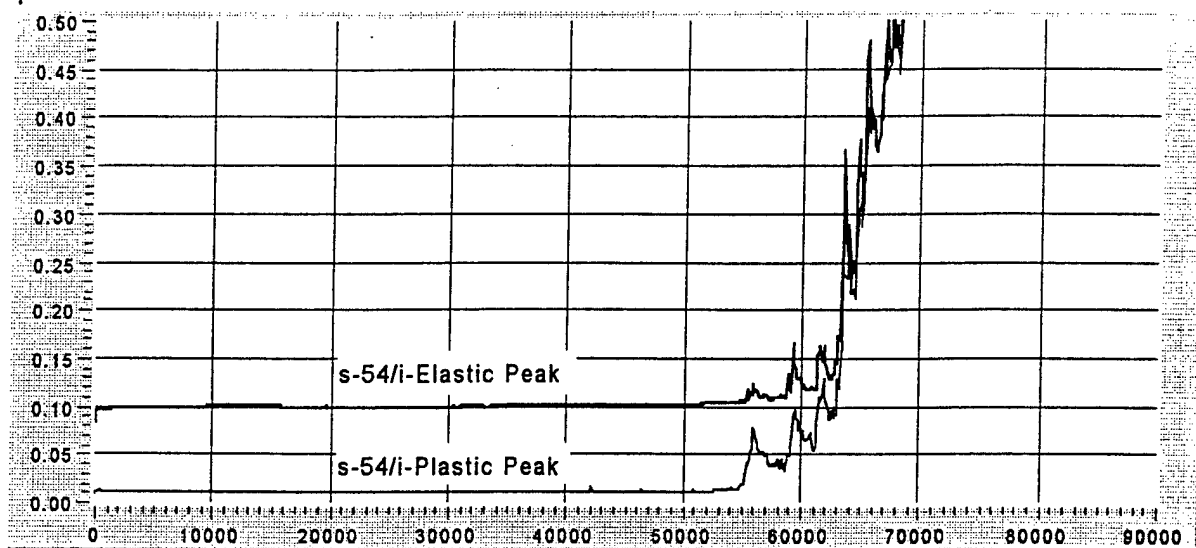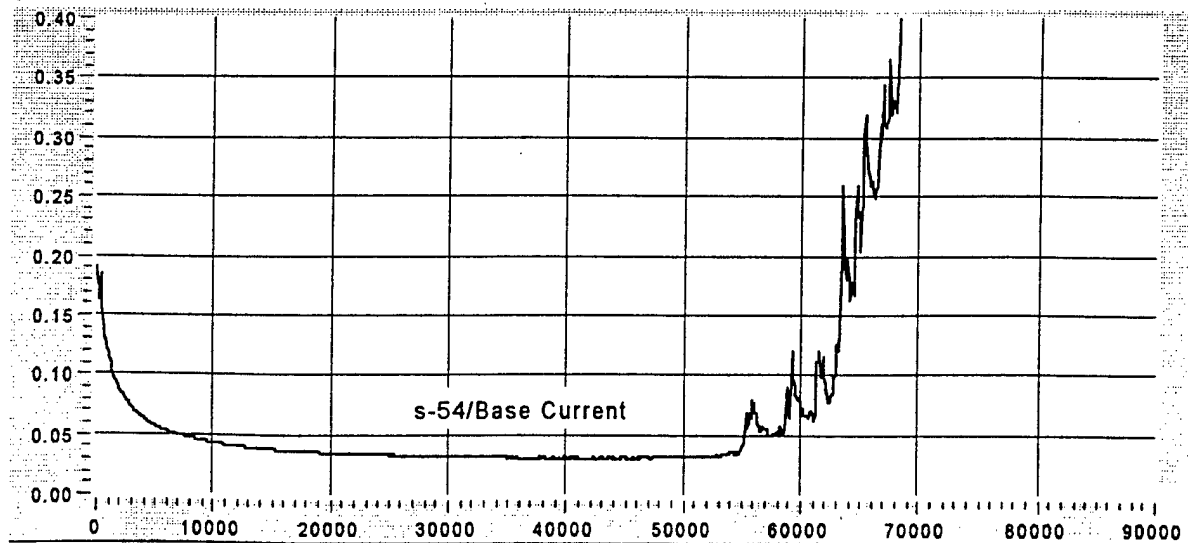
(b)   **No.of Cycles**

Figure 5-47. EFS response of 4130 steel specimen S-54 cycled continually in the gel form of the steel electrolyte indicating satisfactory EFS performance (compare with Figure 5-38 for which the results are in liquid electrolyte).
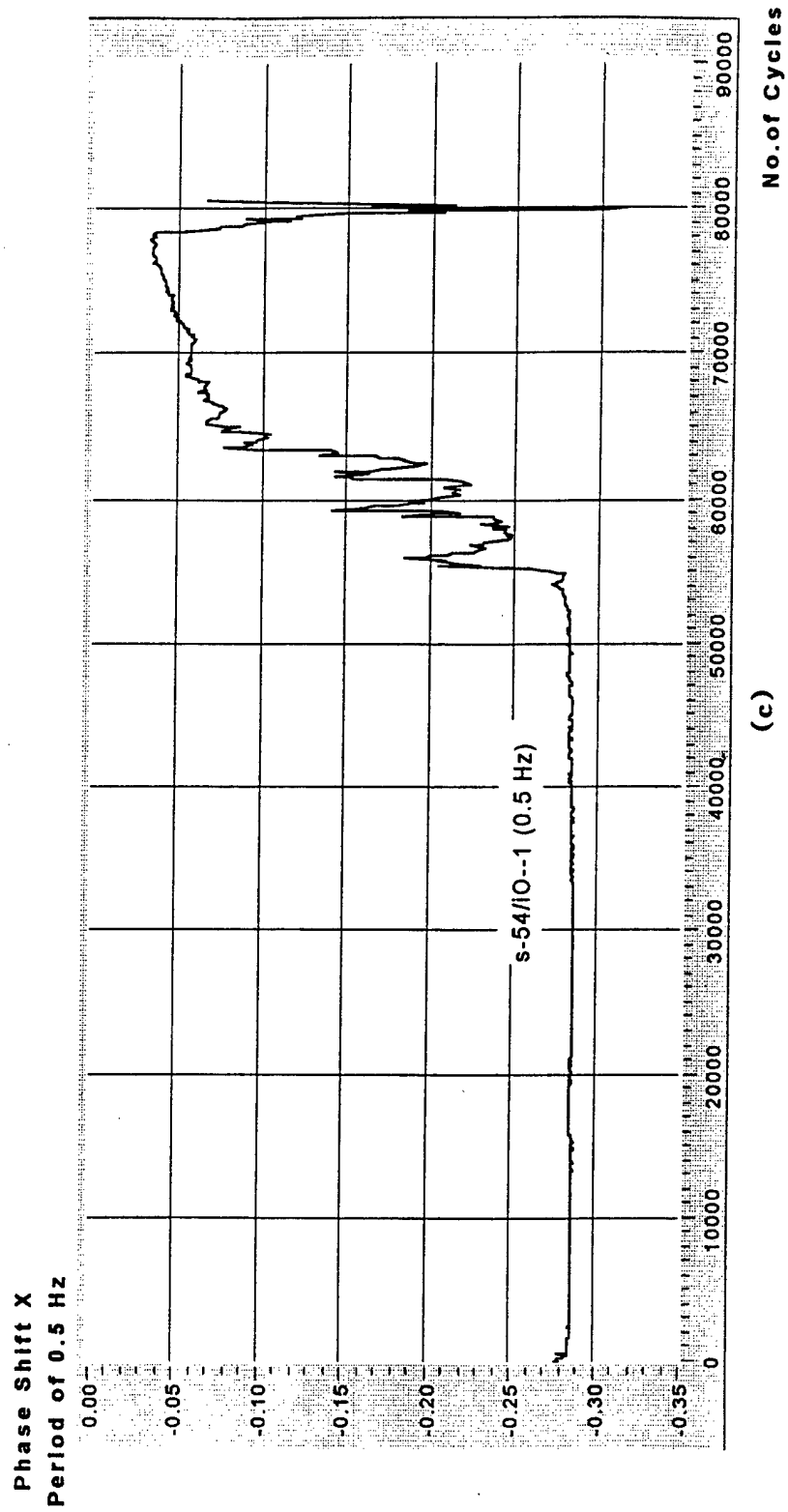
Figure 5-47 (Cont'd).

(c)

5-126

Current Density

µA / c m 2

(a)

No. of Cycles

Current Density

µA / c m 2

(b)
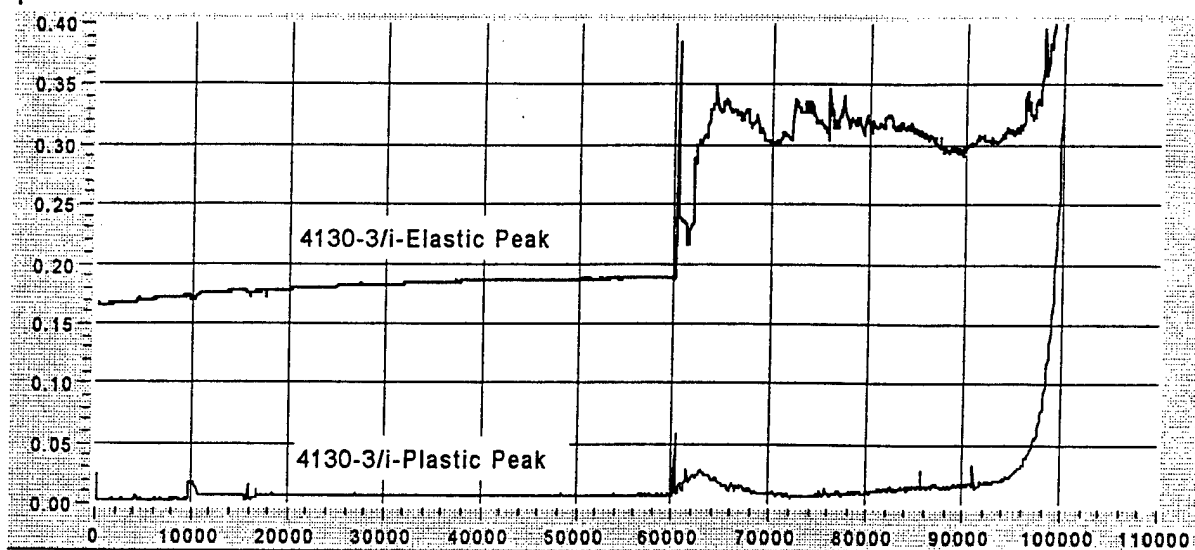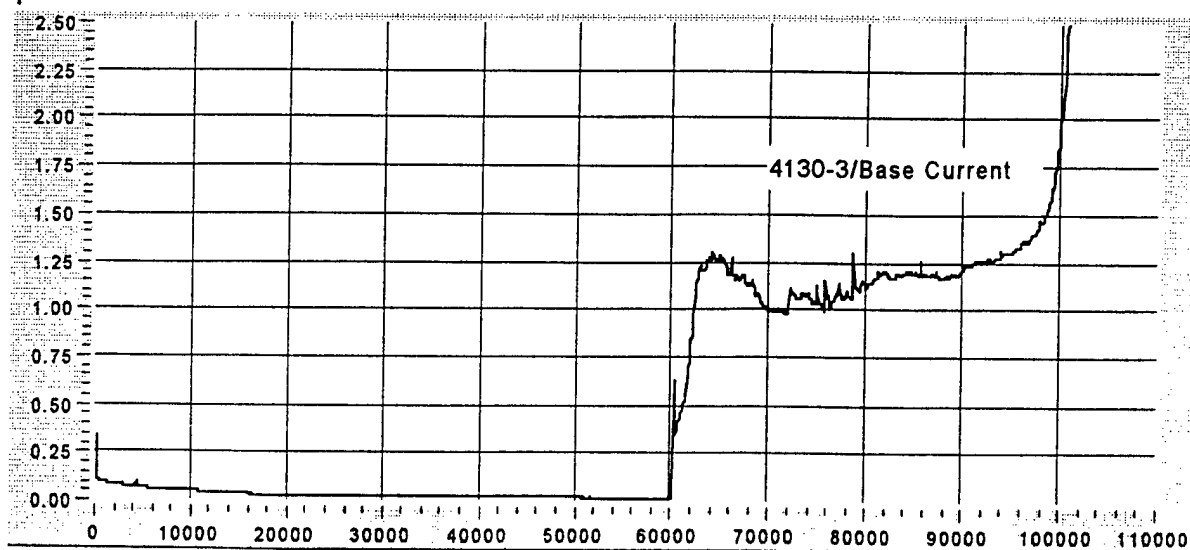
No. of Cycles

Figure 5-48. EFS response of steel specimen 4130-3 cycled at a stress amplitude of 600 MPa at 1 Hz in an EFS cell of small gel electrolyte volume (5 ml). The usual volume for the figures above was 50 ml.
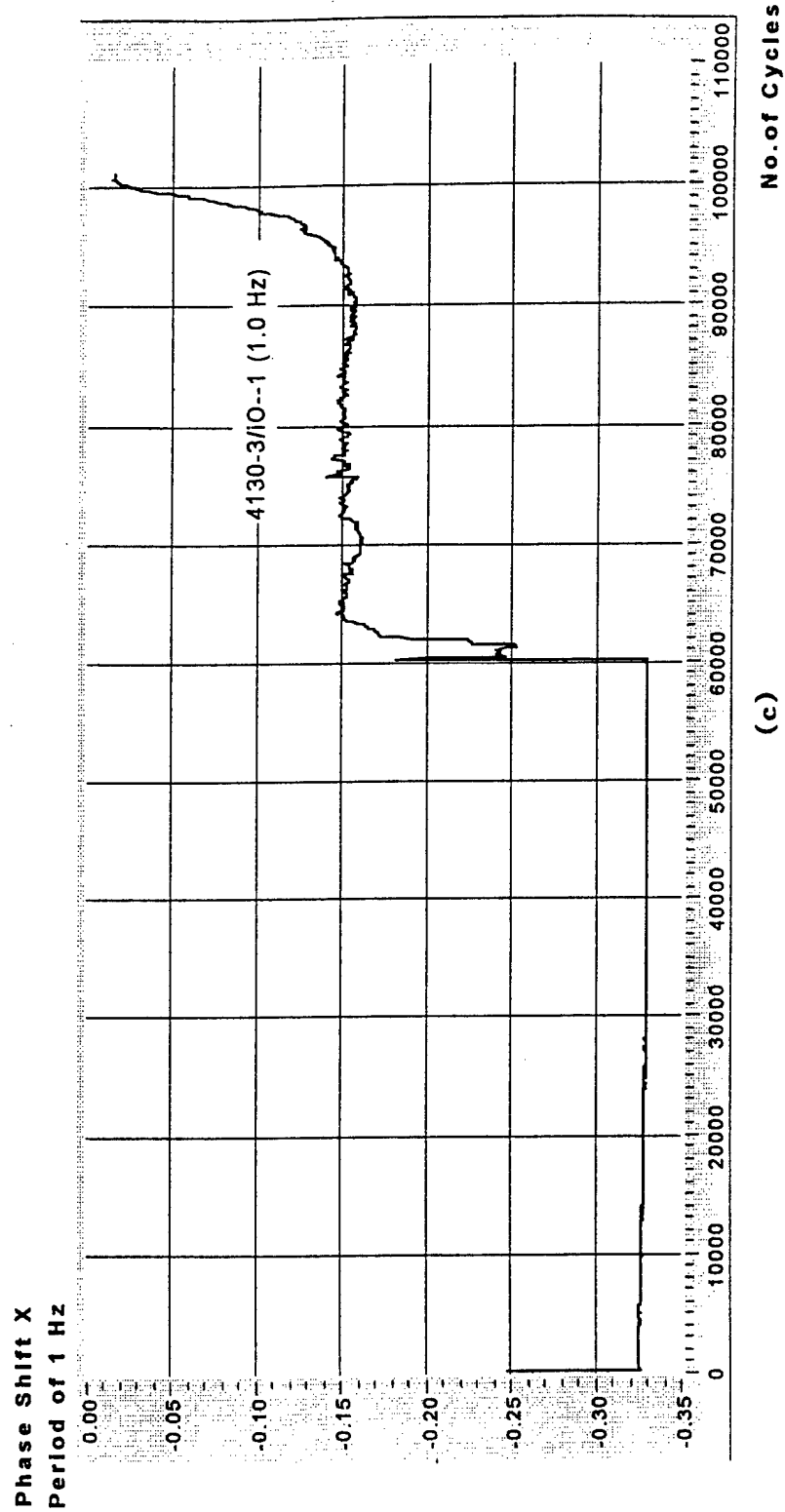
Figure 5-48 (Cont'd).
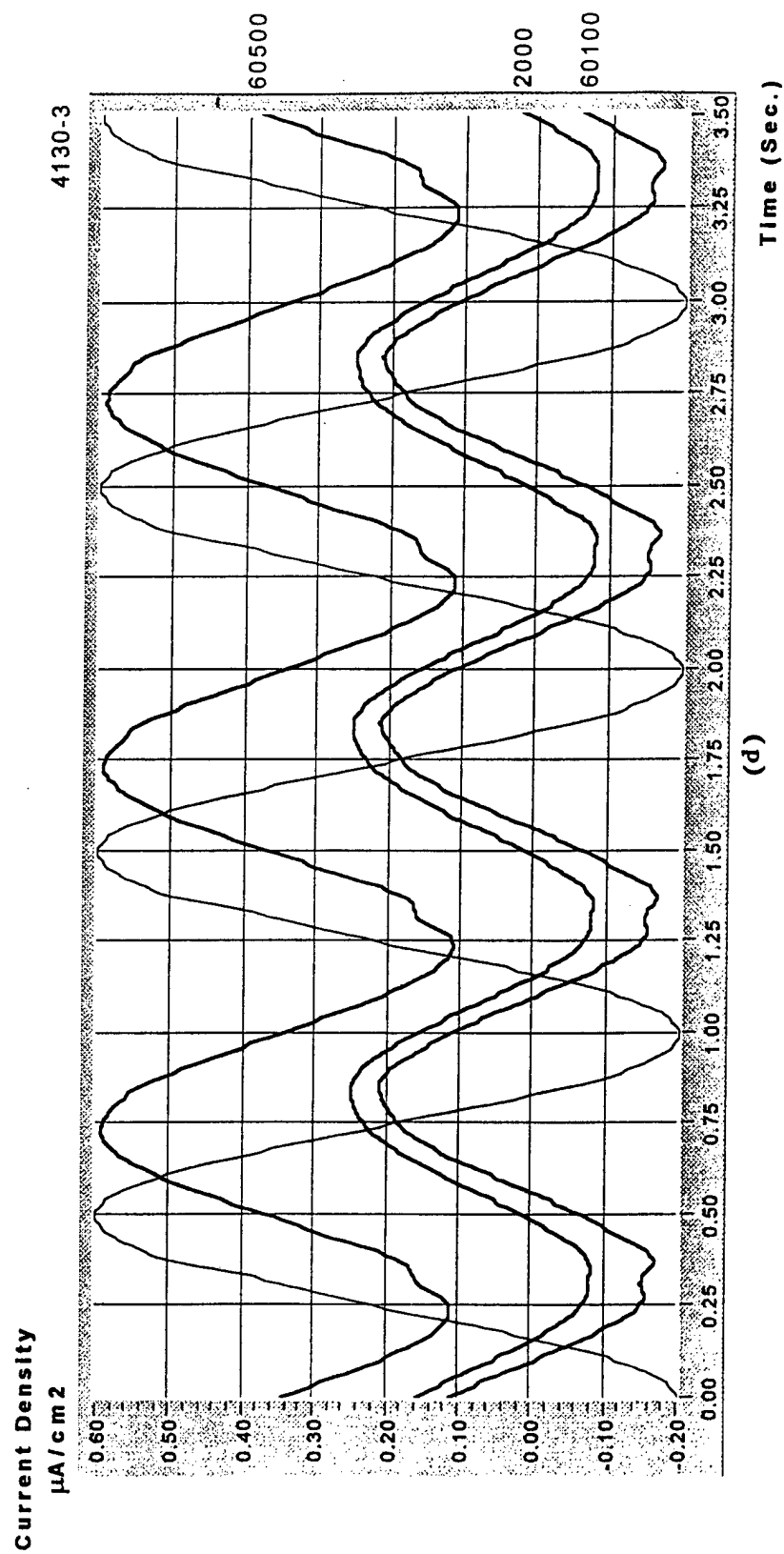
Figure 5-48 (Cont'd).

5-129
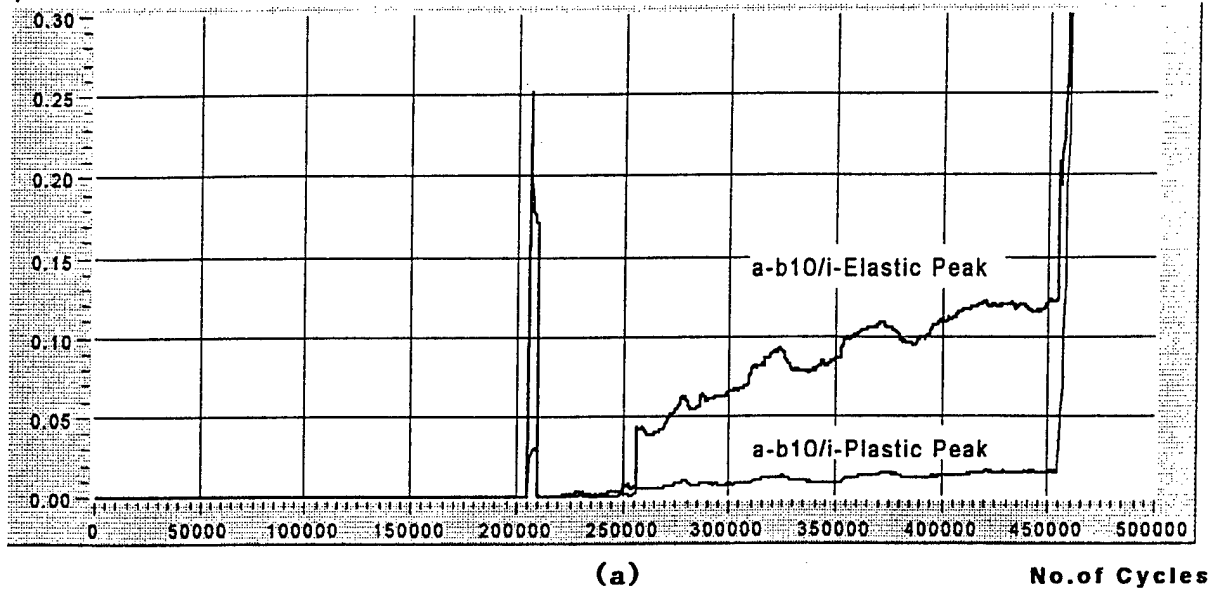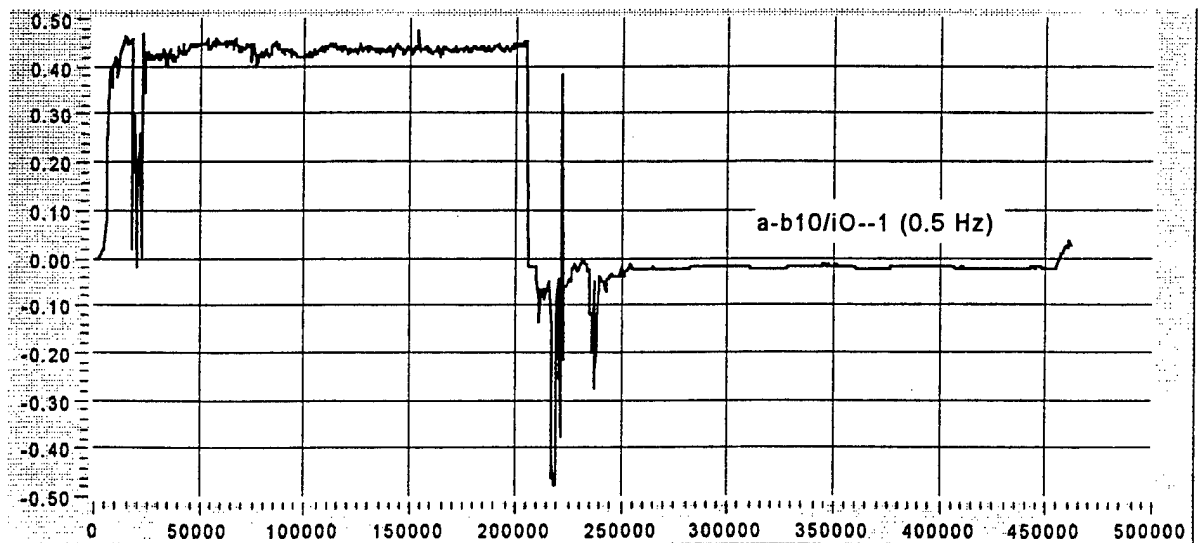
Figure 5-49. EFS response of aluminum 7075 alloy specimen A-b 10 which was coated with both military aircraft primer and top coat and which was deliberately breached with a scratch. For much of the life, very little signal could be obtained, but response later became active.
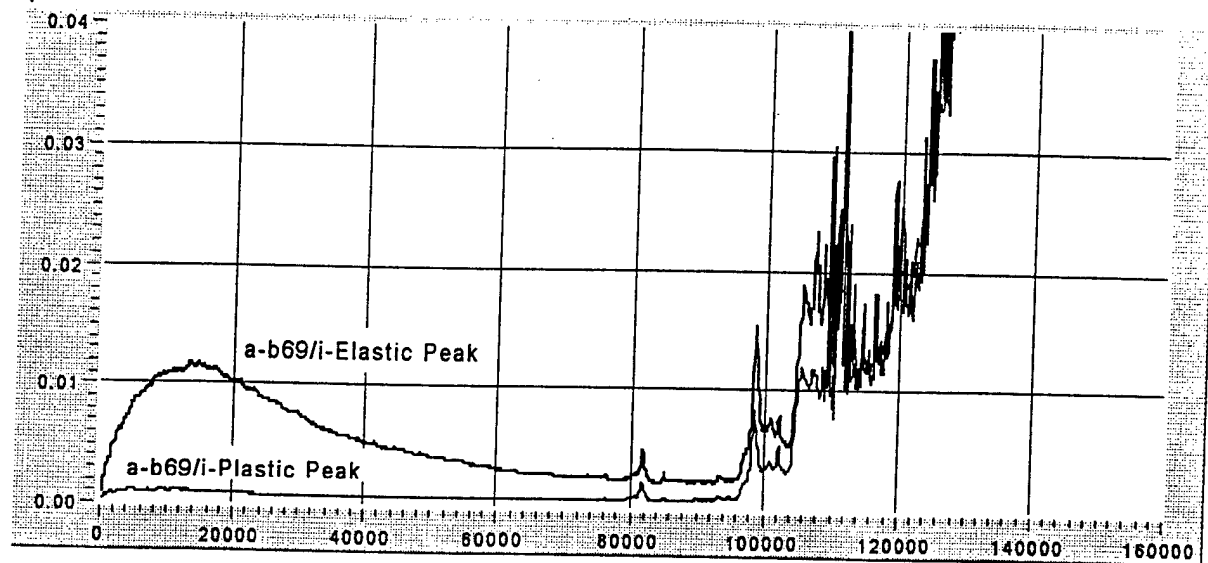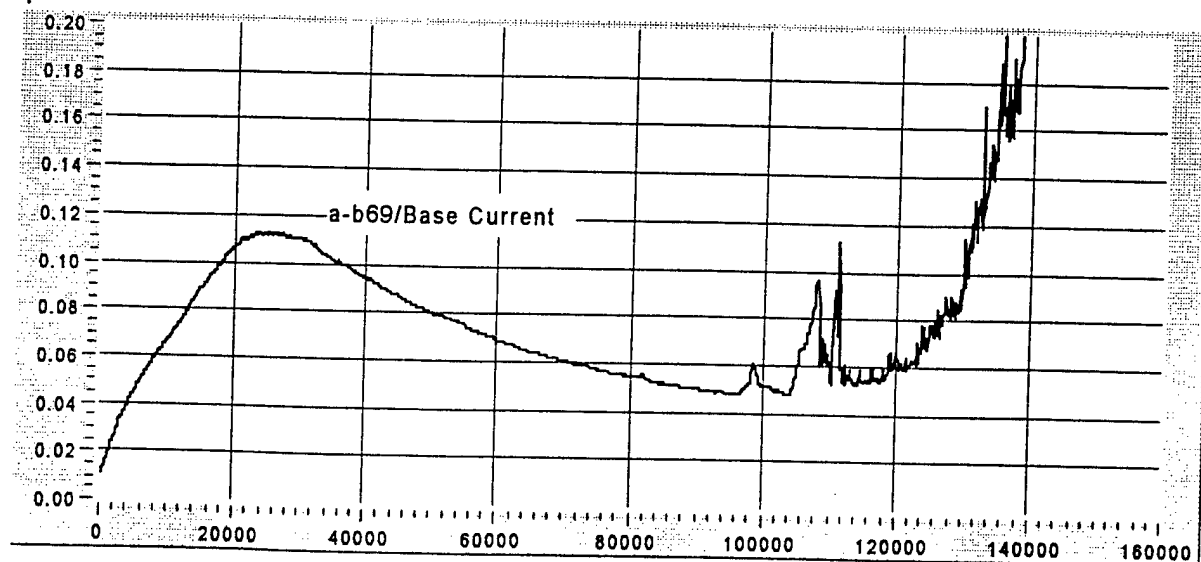
Figure 5-50. EFS response of aluminum 7075 alloy specimen A-b 69 which was coated with military aircraft primer. This porous coating allows regular EFS behavior to occur.

Phase Shift X
Period of 2.5 Hz

a-b69/IO--1 (2.5 Hz)

No.of Cycles

(c)
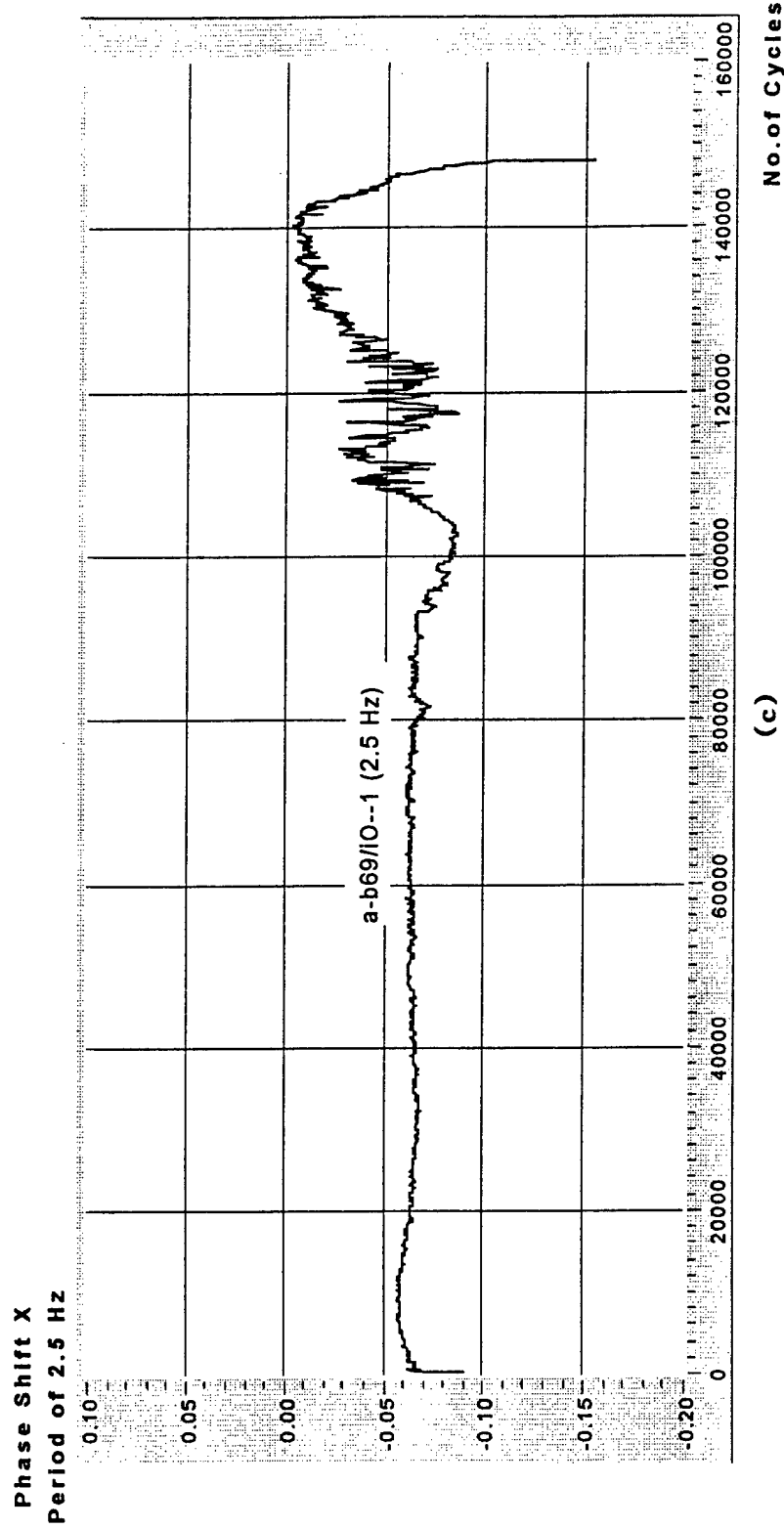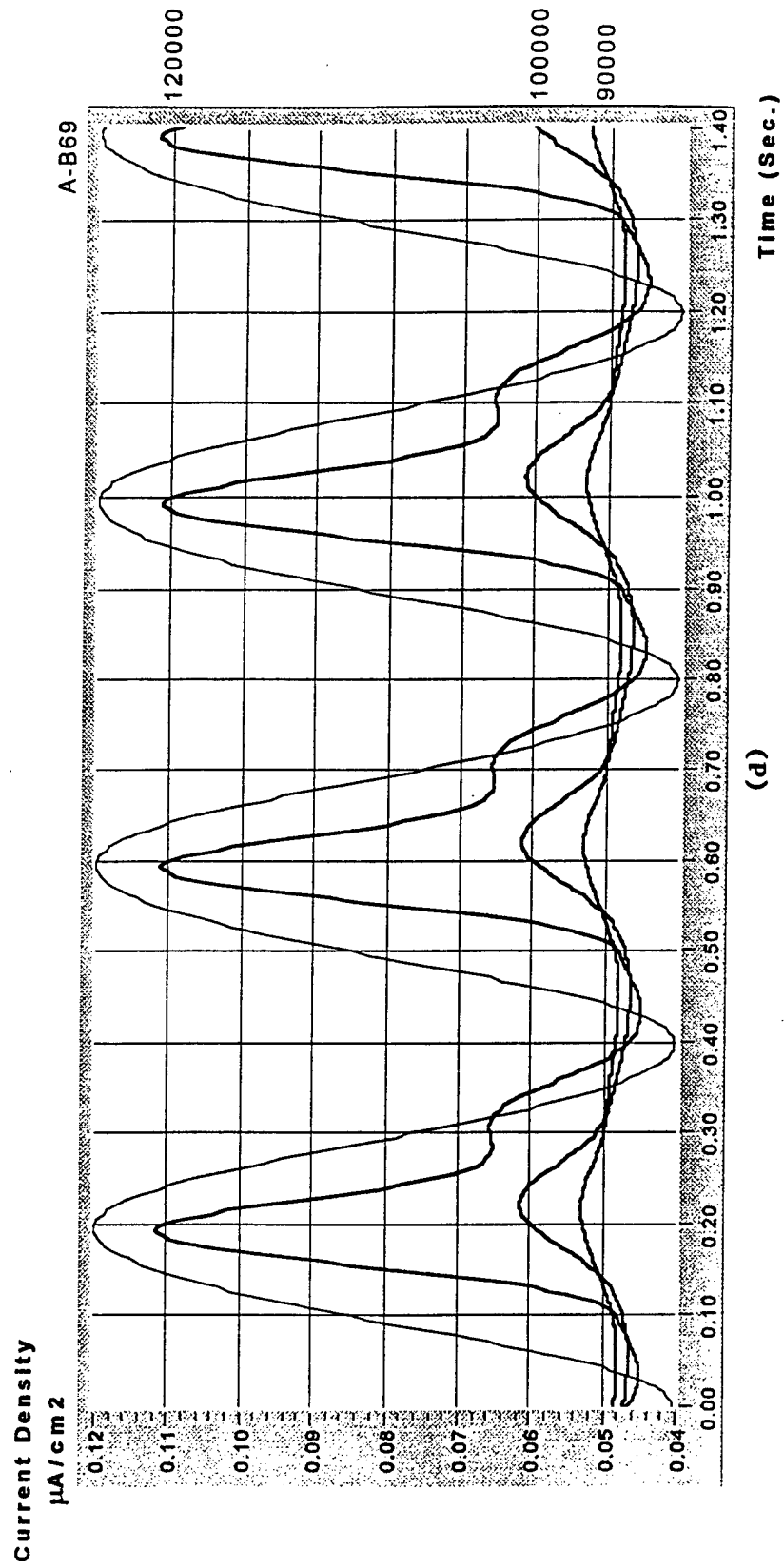
Figure 5-50 (Cont'd).

Figure 5-50 (Cont'd).
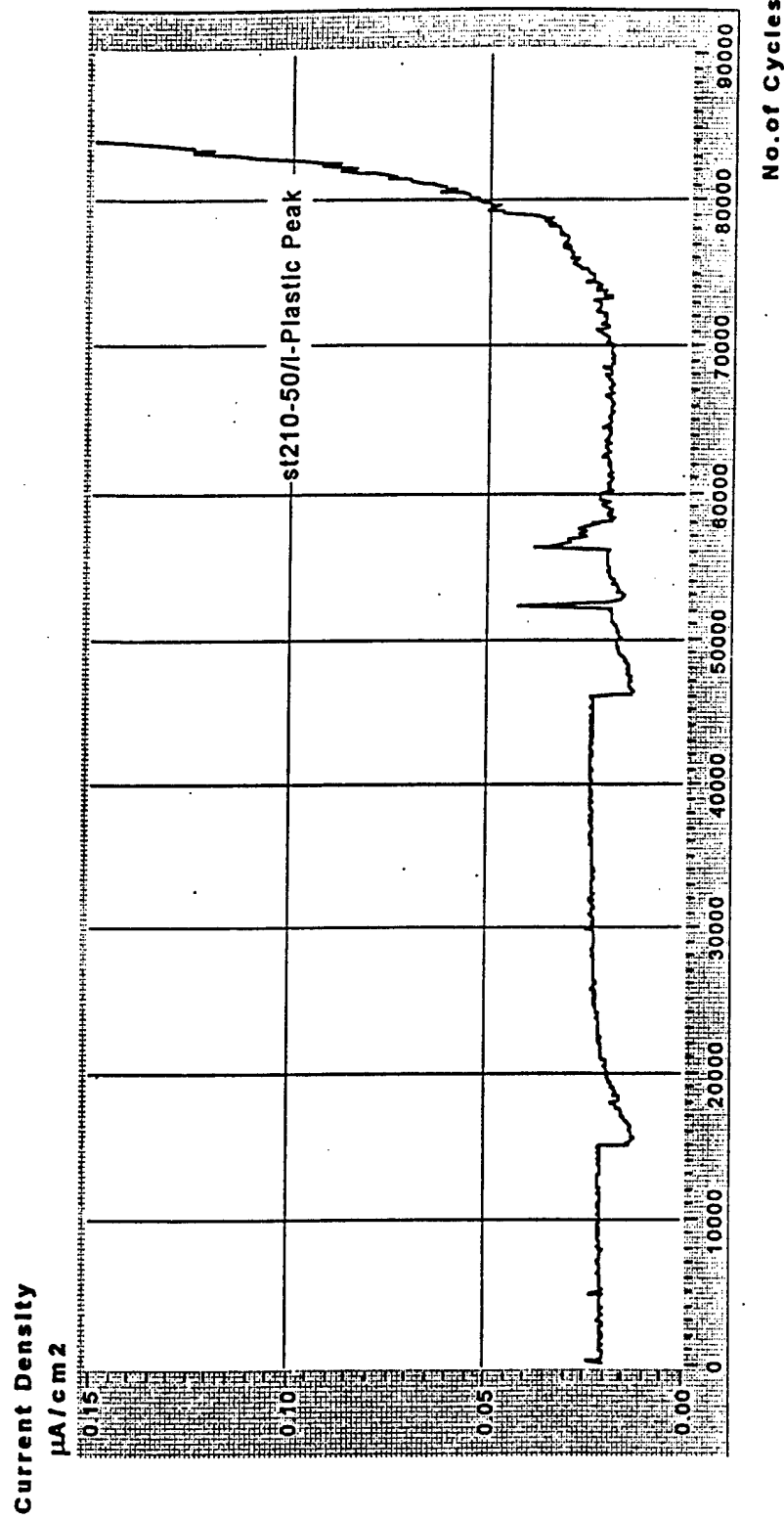
Figure 5-51. The EFS "plastic" current response in steel specimen st210-50 which was polished to a higher finish than the other steel specimens reported and was used to make a determination of crack size detectability.
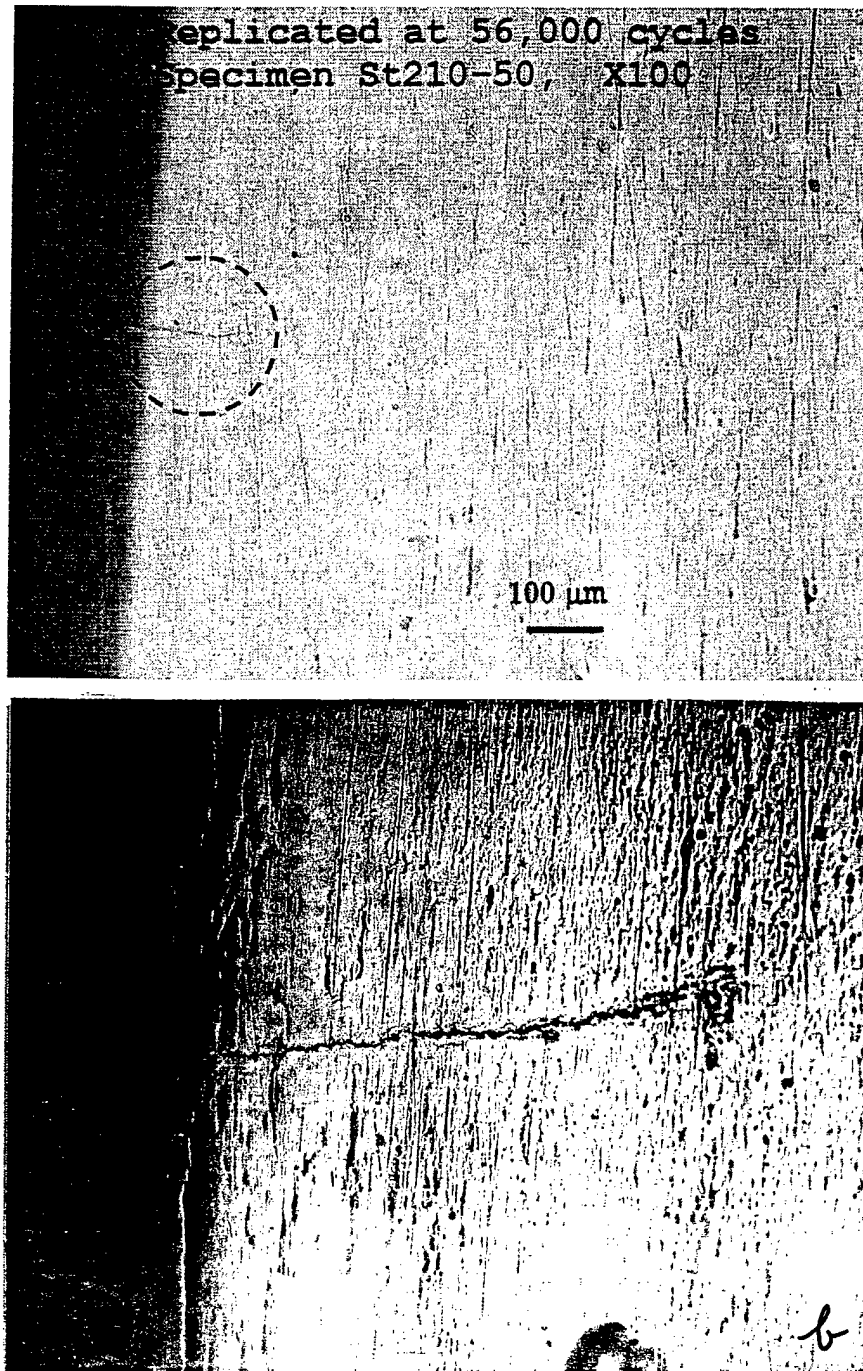
Figure 5-52. The largest cracks observed in specimen st210-50 after EFS response indicated that cracks were present (see Figure 5-51): a) 56,000 cycles, x 200; b) 84,000 cycles, x 100. The small crack visible in (a) is about 70 microns deep.
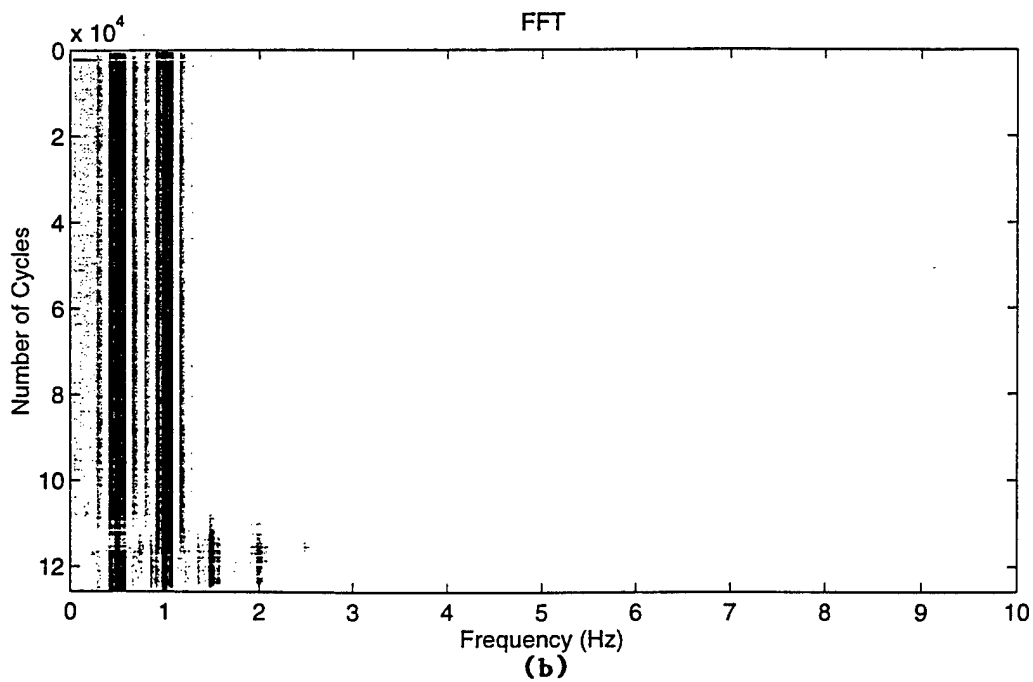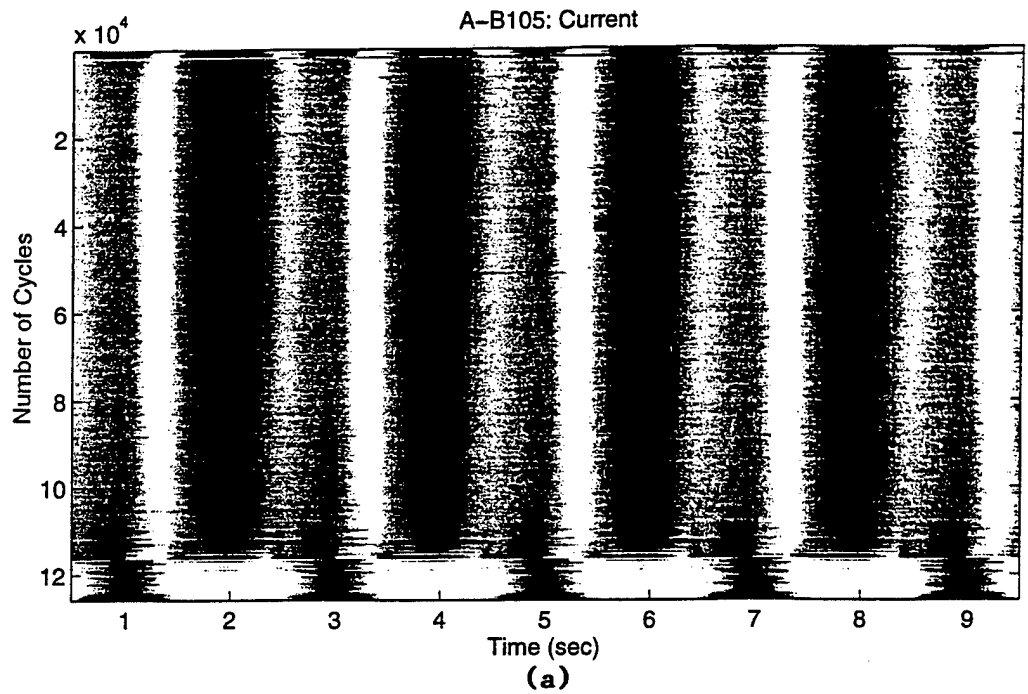
Figure 5-53. EFS current waveform map (a) displaying the fatigue damage history of 7075 aluminum specimen A-B 105 throughout its life; FFT map (b) of lifetime waveforms. The EFS response of this specimen is shown in Figure 5-40, and the fatigue conditions in Table 5-12.
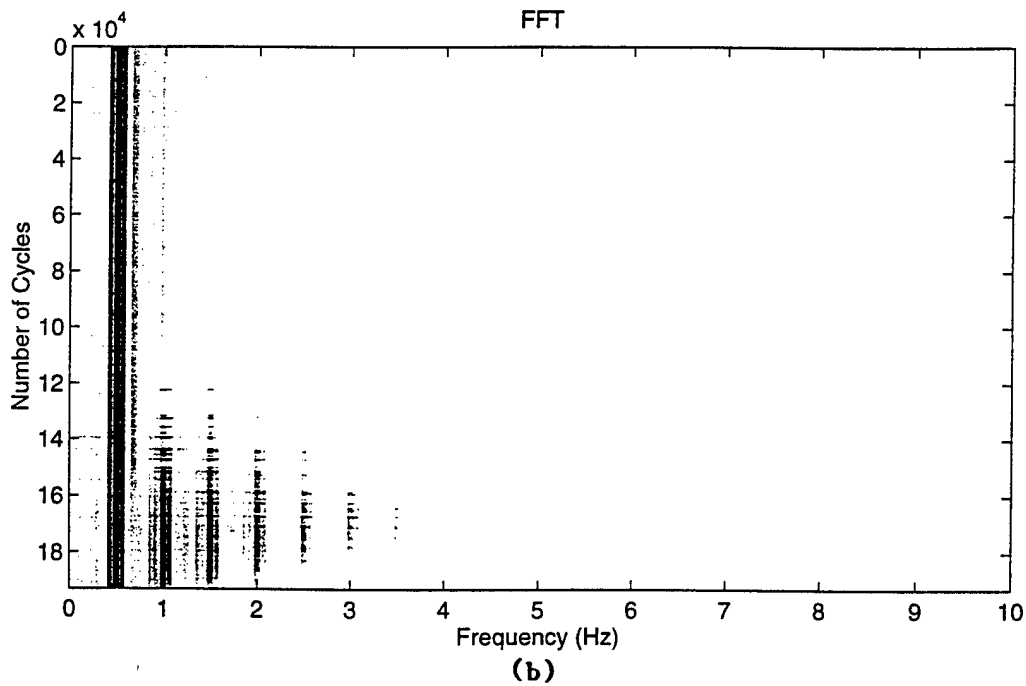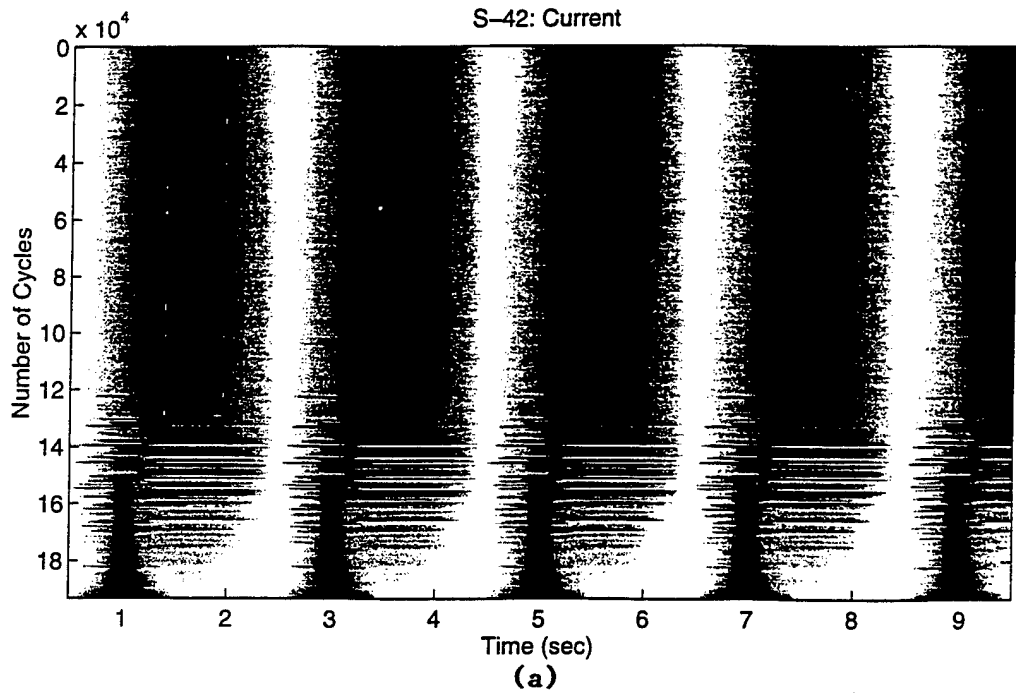
Figure 5-54. EFS current waveform map (a) displaying the fatigue damage history of 4130 steel specimen S-42 throughout its life; FFT map (b) of lifetime waveforms. The EFS response of this specimen is shown in Figure 5-38, and the fatigue conditions in Table 5-11.
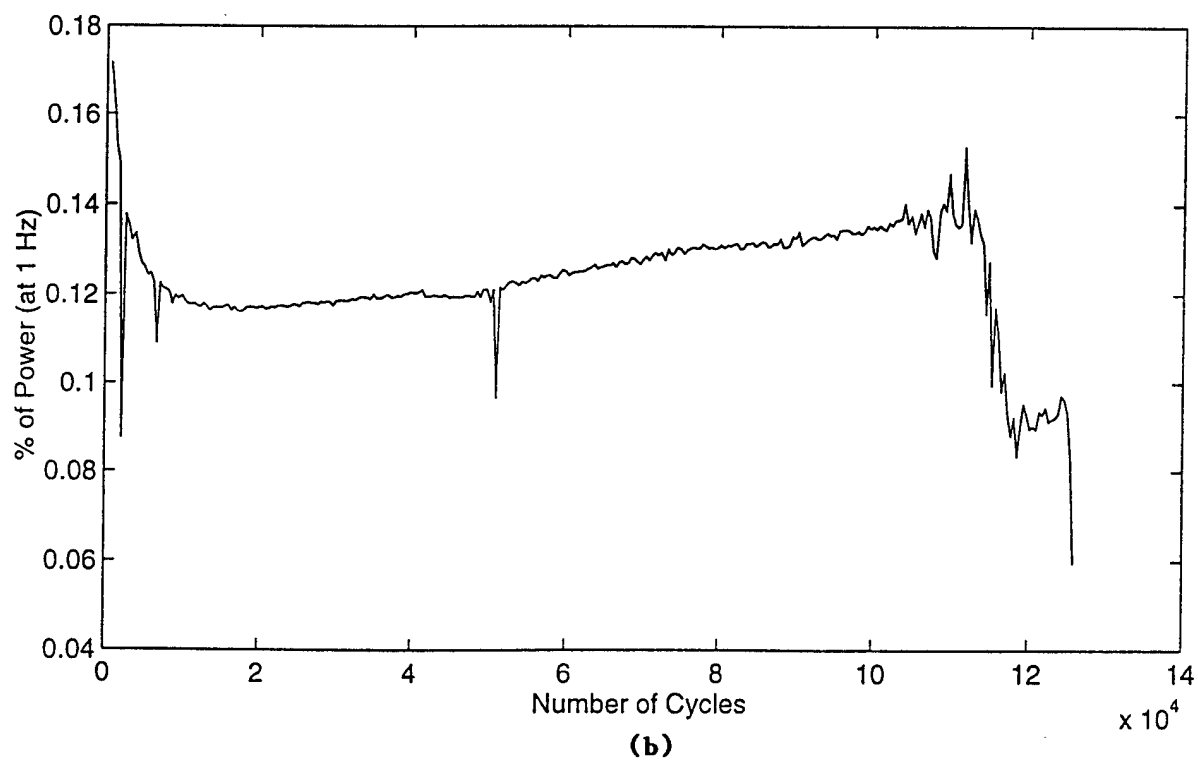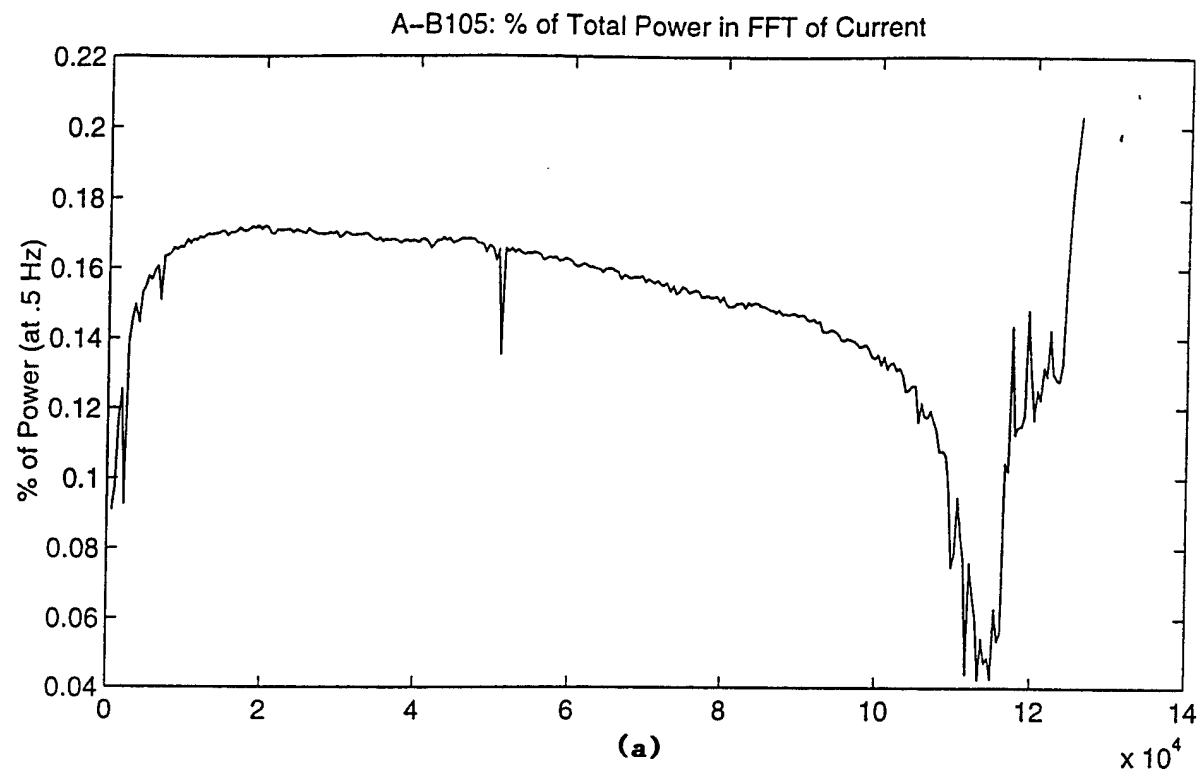
Figure 5-55. Fraction of total power in the FFT of the EFS current in aluminum 7075 specimen A-B 105 during life: (a) at 0.5 Hz; (b) at 1 Hz.
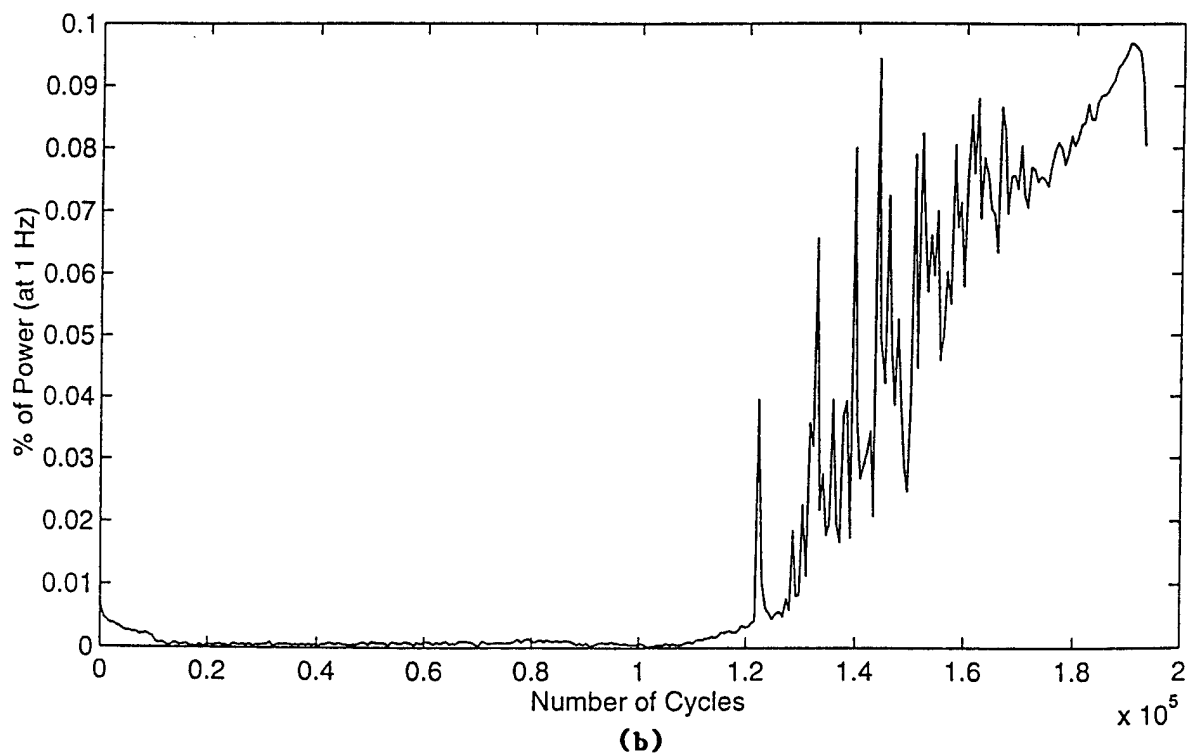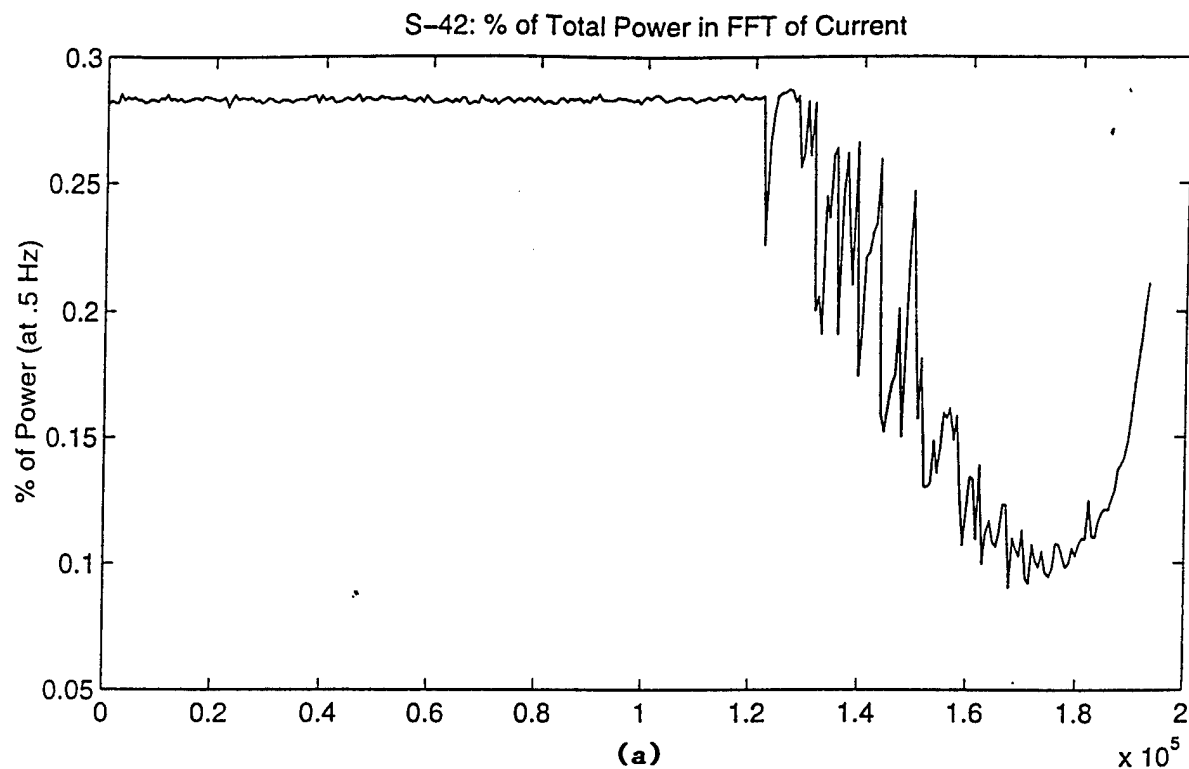
Figure 5-56. Fraction of total power in the FFT of the EFS current in 4130 steel specimen S-42 during life: (a) at 0.5 Hz; (b) at 1 Hz.
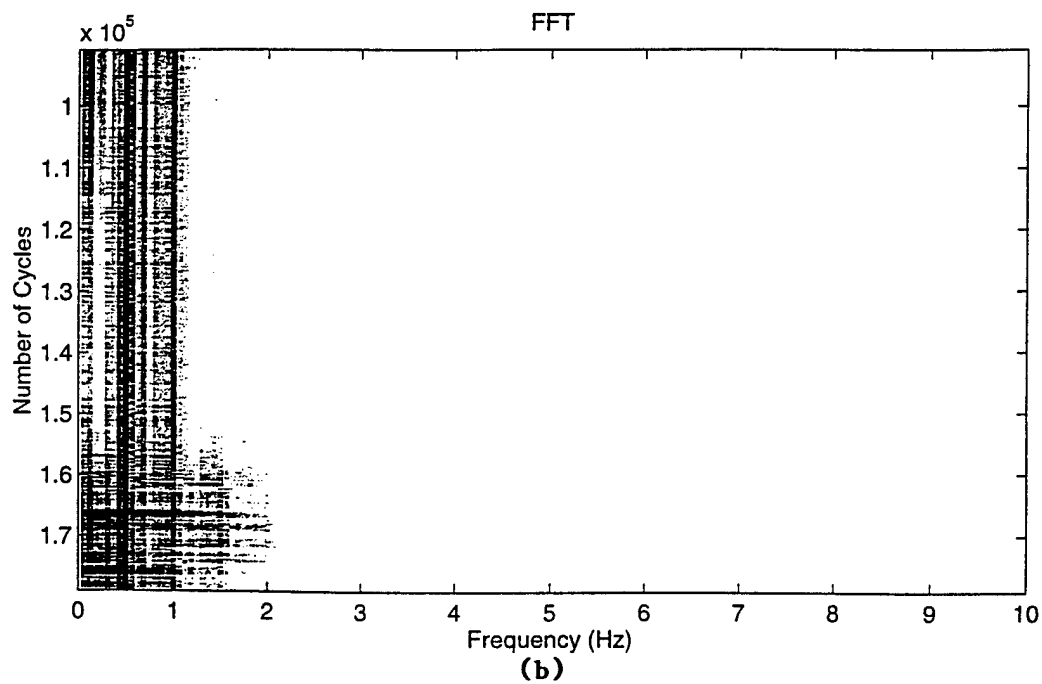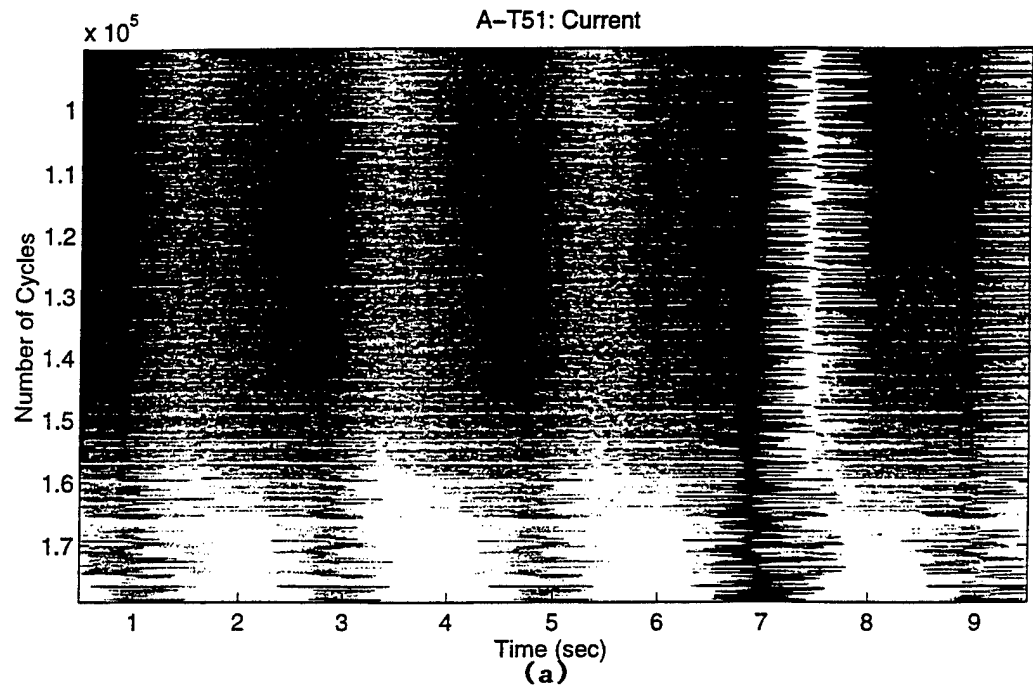
Figure 5-57. EFS waveform map (a) and FFT map (b) of aluminum 7075 specimen A-T 51 subjected to the Penn variable loading sequence of 3 low − 1 high stress cycles, described in Section 7 and shown in Figure 5-59 for exact correspondence of time scales.
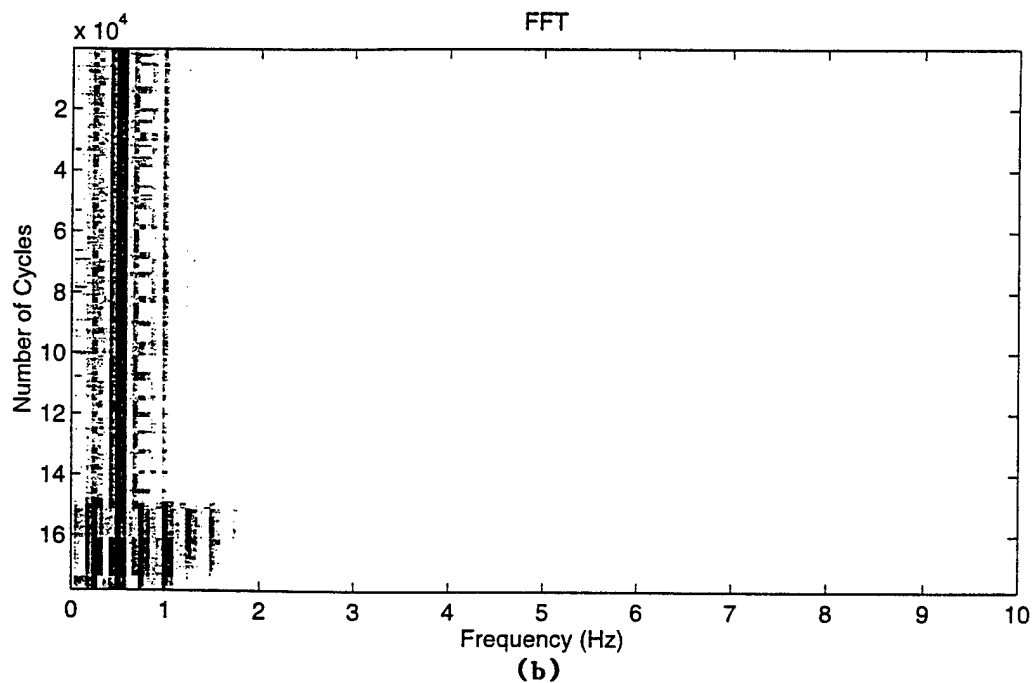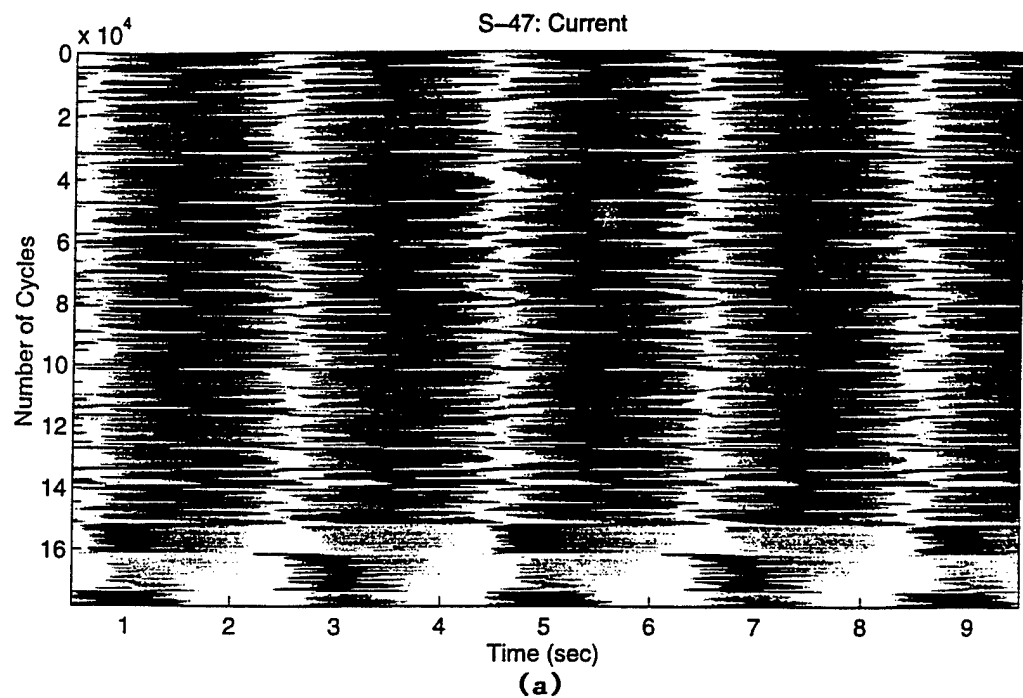
Figure 5-58. EFS waveform map (a) and FFT map (b) of 4130 steel specimen S-47 subjected to the Penn alternating high – low fatigue stress sequence described in Section 7 and shown in Figure 5-59 for exact correspondence of time scales.
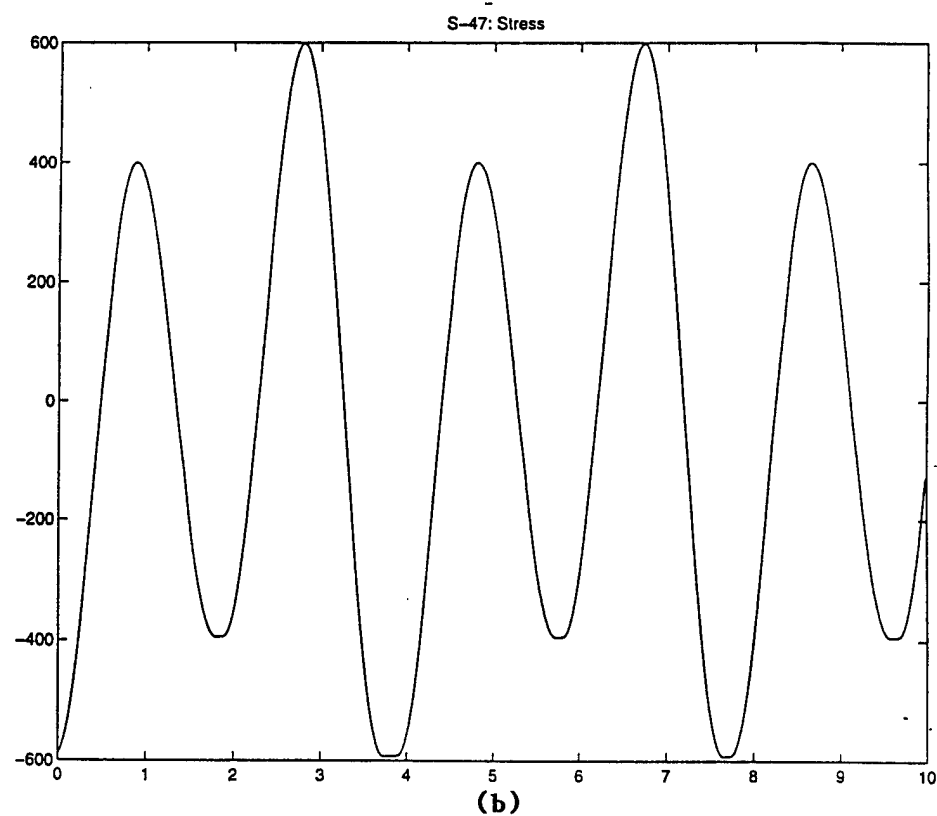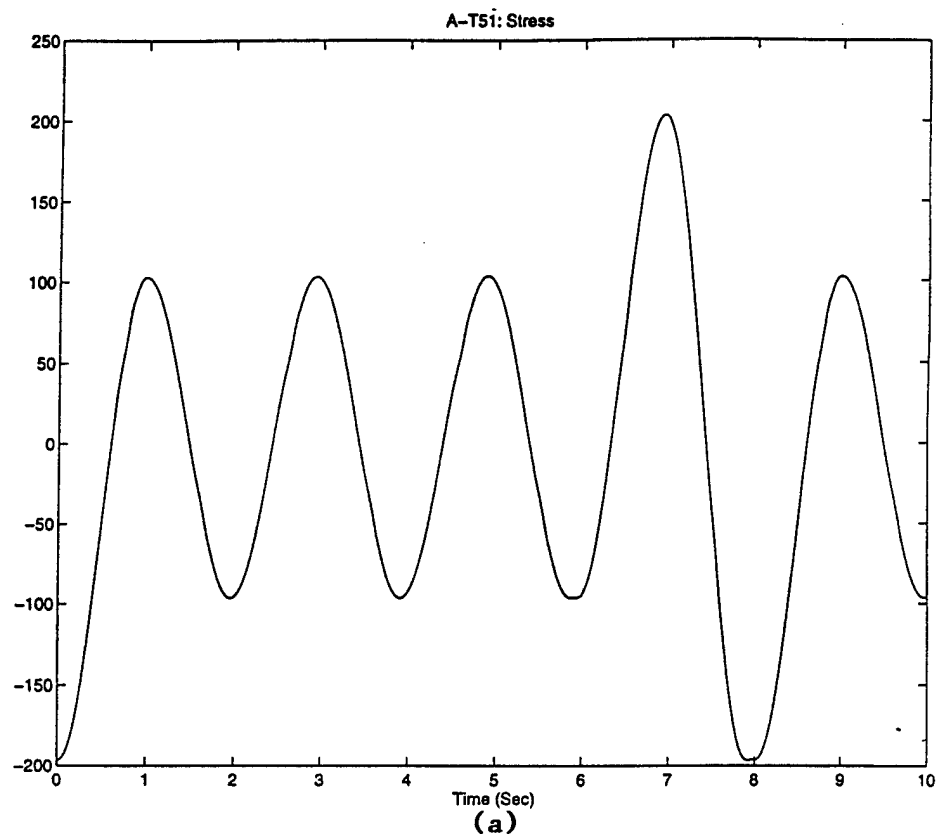
Figure 5-59. Variable loading sequences used for EFS experimentation; (a) sinusoidal 3 low – 1 high for aluminum specimen A-T 51; (b) sinusoidal alternating high – low for 4130 steel specimen S-47.
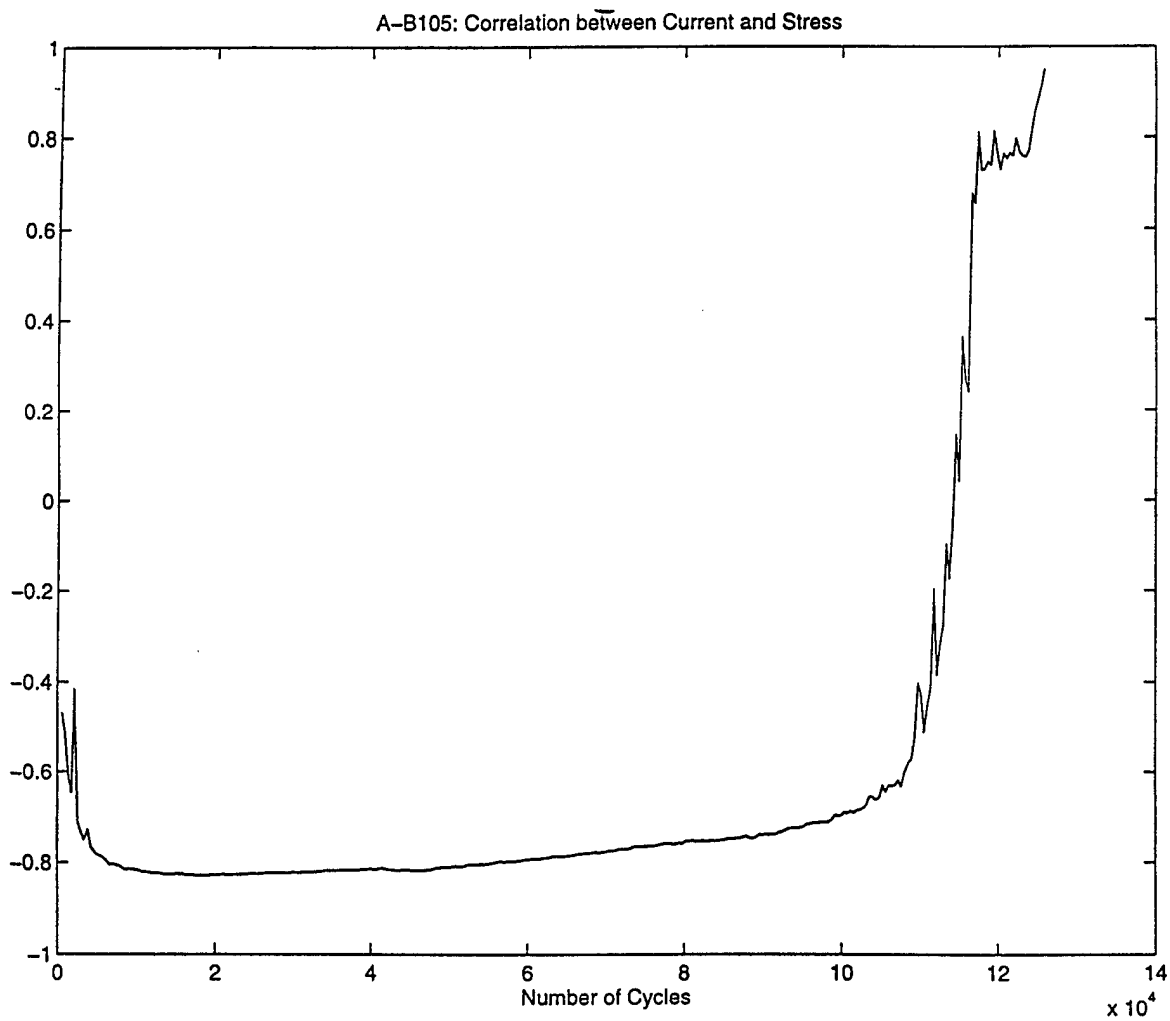
Figure 5-60. Correlation between the input stress and the EFS output signals for aluminum specimen A-b 105 during fatigue life.
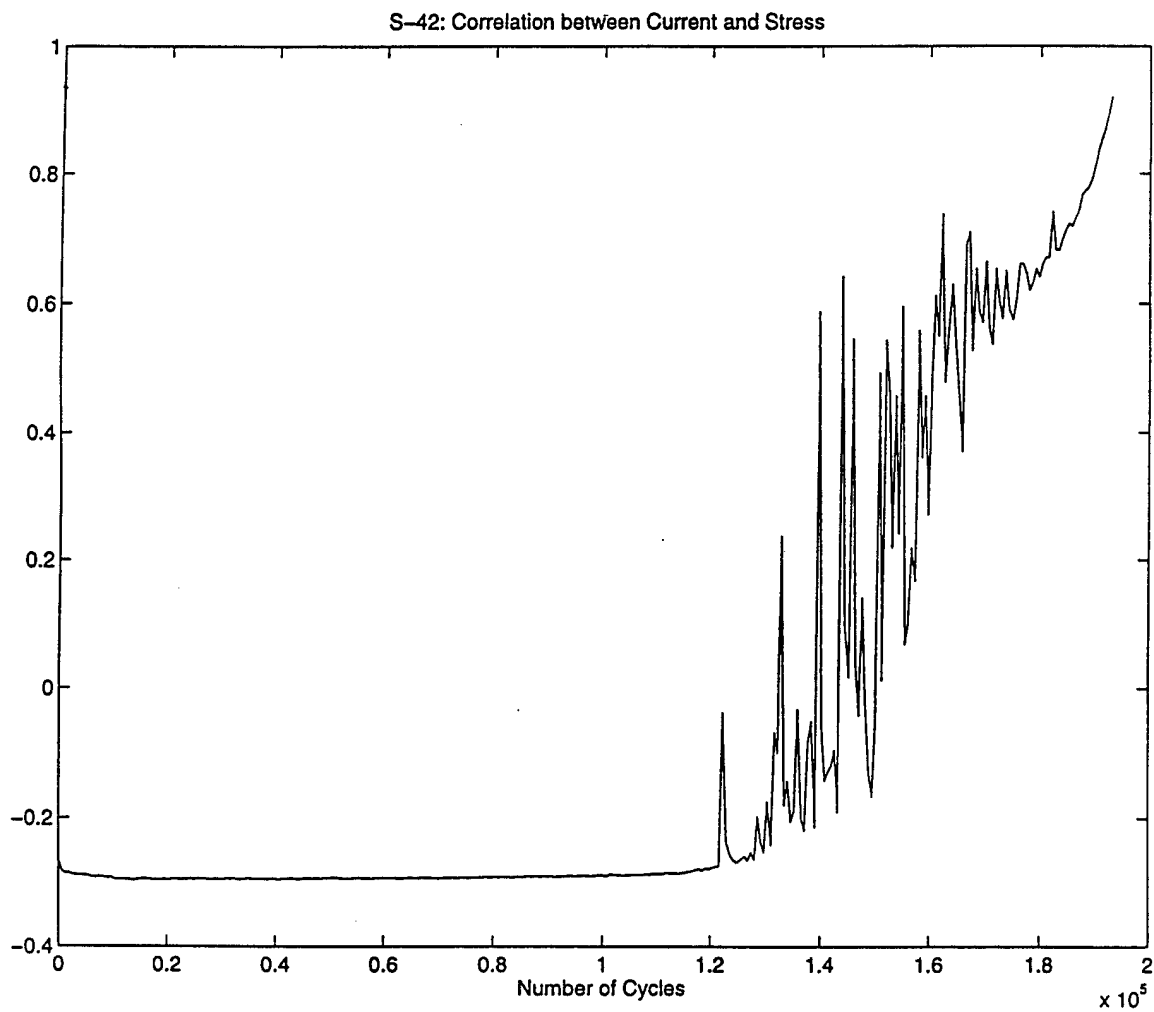
Figure 5-61. Correlation between the input stress and the EFS output signals for steel specimen S-42 during fatigue life.
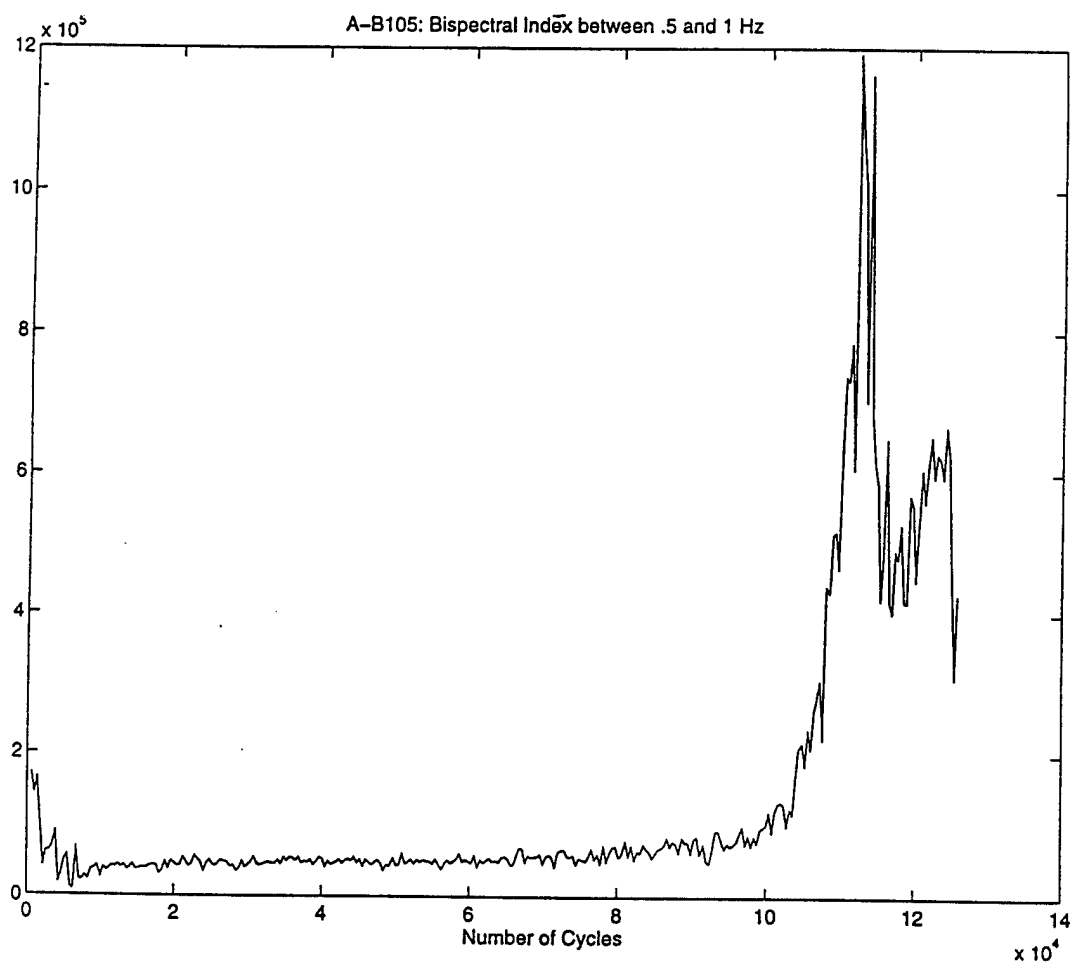
Figure 5-62. Bispectral index between the 0.5 and 1 Hz components of the EFS current of aluminum specimen A-b 105 during fatigue life.
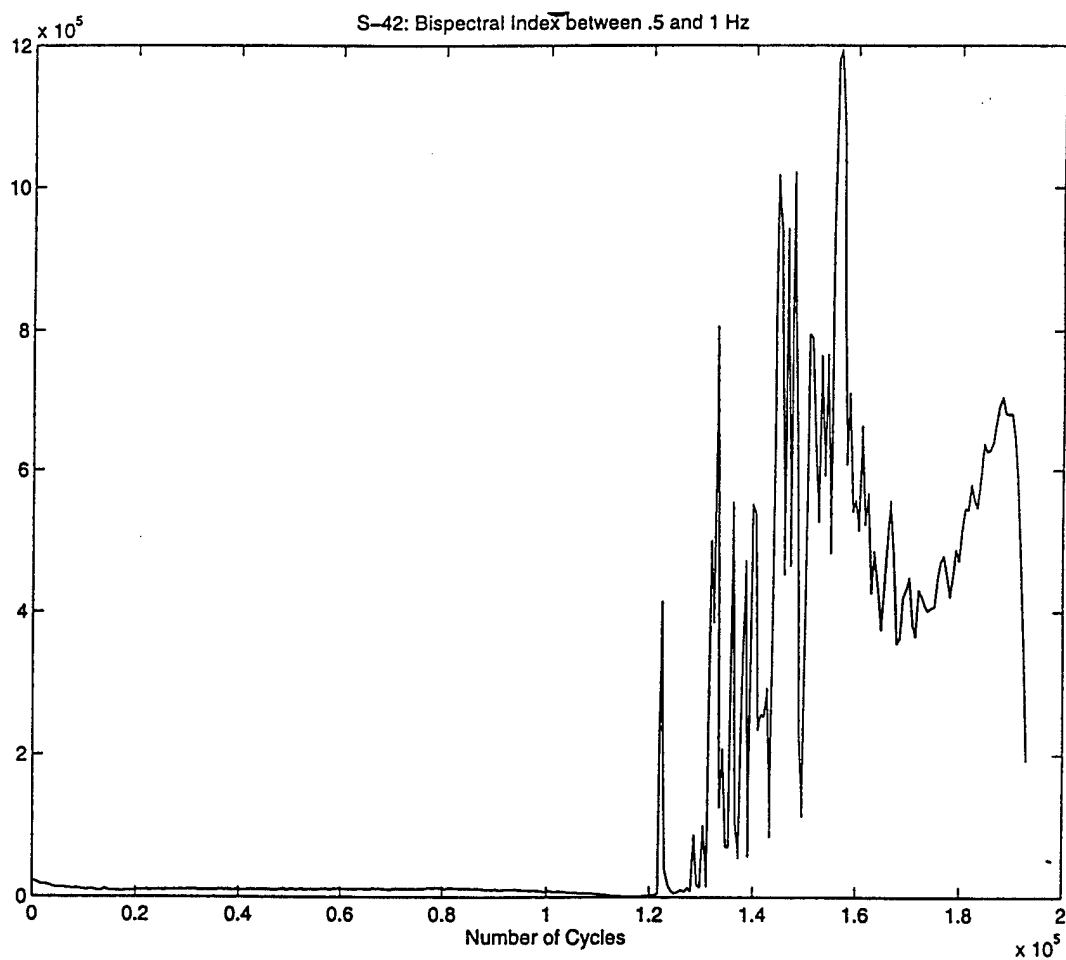
Figure 5-63. Bispectral index between the 0.5 and 1 Hz components of the EFS current of steel specimen S-42 during fatigue life.

6.0   EIS LABORATORY MEASUREMENTS

This section is devoted to the theoretical and experimental development of electrochemical impedance spectroscopy (EIS) as a prospective method of monitoring fatigue damage in aircraft alloys. The principal objective of the efforts described here was to assess how EIS can augment the analytical capabilities of the present EFS technology, particularly in the common occurrence that a measurement must be made on a coated structure.

6.1   Background and Objectives

The influence of a coating such as a primer or topcoat on the ability to measure by electrochemical means the onset and evolution of fatigue damage in a substrate alloy, as well as damage to the coating itself, was the principal issue to address in this phase of the program. In this pursuit, considerable theoretical development and experimental effort was given to exploring the attributes of other electrochemical measurement techniques that, when applied to coated surfaces, would endow significant improvements in the information content of the EFS methodology. The essential premise of these efforts is that the end-use application of the EFS methodology as an enabling sensor technology should be capable of measuring the damage state of the metallic substrate through an undisturbed coating, since the majority of fatigue critical locations on an aircraft structure involve a coated surface.

Early on, and even prior to formulating ideas for the experimental approach of this program, we became aware of the phenomenological similarities that existed between the EFS methodology and two other well established materials characterization techniques; namely, electrochemical impedance spectroscopy (EIS) and its mechanical analog electromechanical impedance spectroscopy (EMIS). In particular, EIS as conventionally employed in studies not related to fatigue damage mechanisms already had been demonstrated to be a powerful technique for gaining considerable insight into the electrochemical and transport properties of metallic substrates, as well as the dielectric properties of their complementary coatings [6.1]. Much of the work in this area today has evolved into analyzing the localized electrochemical behavior of

coated substrates as a function of various environmental exposure conditions using spatial imaging capabilities [6.2].

However, the feasibility of applying the EIS technique, not for the purpose of characterizing the electrochemical behavior of a structurally stable system but, rather, to interrogate fatigue damage incurred in a bare or coated metal substrate has not been considered heretofore, either theoretically or experimentally. The principal motivation for demonstrating feasibility lies in the notion that the EIS technique, if reduced to practice, does not require that the structure be mechanically loaded to induce an electrochemical response, which is the basis of the method. For the purpose of clarity, it is instructive to distinguish the operational aspects of EIS and EMIS, and to describe how these techniques are borne into the basic elements of EFS.

The overall goal of EIS is to measure the electrochemical response of a system to an applied frequency- and amplitude-dependent perturbation under a carefully controlled direct current (dc) polarization potential, which is applied to the system. As this is a cause-and-effect measurement, a transfer function (i.e., output over input) in terms of an impedance can be defined for the relaxation processes that are inherent to the electrochemical system. The perturbation used in EIS is a small amplitude, cyclic electric field (i.e., current or voltage) with a transfer function corresponding to a true, frequency-dependent electrical impedance ($Z(j\omega)$). Such a perturbation is useful in probing, among other processes, the charge transfer and ion mobility response of the system. In electromechanical impedance spectroscopy (EMIS) the perturbation is a cyclic, mechanical load or a mechanically-induced voltage or current fluctuation. The response of the system is measured as a cyclic current or voltage under controlled potentiostatic or galvanostatic conditions with a transfer function corresponding to frequency-dependent mechanical impedance ($Z_\sigma(j\omega)$). This sort of perturbation probes the electrochemical response of a material system to a mechanical load that causes either bulk structural changes in the material (e.g., dislocation generation, persistent slip, or crack formation or growth), changes in the structure or stability of any film or coating that may be present on the material, or interaction between the underlying material and surface film. Figure 6-1 illustrates the phenomenological relationship between the measurement themes of EMIS and EIS in terms of a common impedance metric in vector representation.

One might recognize that the EFS method principally studied in this program can be regarded as a special case of EMIS and, therefore, the experimental setup and apparatuses share common elements. The parent operational feature of EMIS is explicitly defined in the following way. The response of a system to a spectrum of perturbations from equilibrium is governed by the relaxation times τ_j (j=1,2,...,n), which define the times at which the response to the perturbation will have decayed back to equilibrium. Therefore, a great deal of useful information relevant to the mechanical relaxation of the system (for example, the microplasticity and microstructure of the substrate, and surface effects of the specimen) can be extracted by means of multi-frequency mechanical perturbation experiments (*i.e.*, the EMIS approach). Such mechanical processes, which exhibit unique and independent time constants, are reflected in the electrochemical reactivity of the material, over a spectrum of perturbations by EMIS or, to a limited extent, at a single frequency by EFS.

A principal objective of the efforts undertaken in this task was to augment the EFS methodology by coupling specific aspects of EIS and EMIS under a unifying empirical metric, that being the impedance metric. Thereby, the state of fatigue damage of aircraft alloys can be probed, including the case where such alloys are substrates underneath a surface coating. Concurrently with an assessment of fatigue damage, a further object of these efforts was to characterize the condition of the coating itself in response to fatigue loading.

6.2   EIS Theoretical Considerations

A complete derivation of a central relationship between the mechanical and electrical relaxational response of a material, a material coating, or combination thereof, and the state of fatigue damage measured in terms of a impedance transfer function constitutes an area open to much more fundamental study than could be appropriately addressed in this program. Nevertheless, a first-order effort at establishing the preliminary physical and chemical foundations through which can be ascribed a causal relationship between fatigue damage and the impedance response of a bare or coated metal substrate has been examined.

6.2.1 Electrochemical and Electromechanical Impedance

In the present approach, the state of damage of a material, which may be composed of multiple components of different materials (*e.g.*, base metal, primer, and topcoat), is characterized by measuring the electrical properties associated with each interface of every component of the material that can be derived from the impedance response of the collective system. In essence, chemical and structural changes that have occurred to each component of the system and, moreover, the sensitivity and susceptibility of such components in their present state of microstructural configuration to electrochemical processes along their respective interface, are reflected in the frequency-dependent electrical properties of the collective system. Therefore, the total impedance response of a material or structure, or that of the collective system, undergoing either mechanical or electrical perturbations, or both, can be generalized by the total impedance function as follows:

$$Z(j\omega'; j\omega'') = Z_{\sigma}(j\omega') + \sum_{n} Z_{E,n}(j\omega'') \tag{6.1}$$

Where the first term of Equation 6.1, $Z_{\sigma}(j\omega')$, is the frequency-dependent complex impedance associated with cyclic mechanical perturbations of frequency ω', *i.e.*, the electromechanical impedance (EMIS), while the second term is a linear combination of frequency-dependent complex impedance terms associated with cyclic electrical perturbations (EIS) of frequency ω'' of a material or structural system comprising n component interfaces. For example, in the case of a coated substrate, the electrolyte-coating interface and the coating-substrate interface constitute two interfacial components under the sum of Equation 6.1, which may be discriminated theoretically and experimentally. While the approach is not necessarily limited to any one model, for the specific case of simple electrochemical or dielectric interfaces having a single time constant τ, the impedance terms under the sum may behave in accordance with the single impedance arc of the Cole-Cole distribution model as given in Equation 6.2. In this model, the subscripts ∞, and 0 are used to denote the high- and low frequency limits of the impedance, respectively, and the parameter β takes into consideration non-ideal behavior of the

system, whereby individual processes are governed by a distribution of relaxation times or a distribution of activation energies [6.3].

$$Z_{E,n}(j\omega") = Z_{E,n,\infty} + \frac{Z_{E,n,0} - Z_{E,n,\infty}}{1 + (j\omega"\tau)^\beta}$$
(6.2)

The electromechanical impedance contribution to the total impedance function may be, in the broadest sense, either an impedance of current output versus cyclic mechanical load input and its corresponding phase relationship, or a true electrical impedance of mechanically-induced voltage perturbations versus current output response, as was shown in Figure 6-1. This impedance term may be monitored independently to detect the onset of fatigue damage and to relate the electromechanical response of the material to its damage state. In the absence of cyclic strain, the total impedance function reduces to a measurement of the electrical impedance (second term of Equation 6.1). This impedance characterizes the dielectric or electrochemical, interfacial behavior of the material in its existing microstructural state, as probed by electrical perturbations over an appropriate range of frequencies. In the strictest sense, measurement of electrochemical, interfacial behavior of the microstructure requires that such perturbations be assisted by an electrochemical driving force, such as a direct current (dc) bias potential.

It is important to recognize in terms of the practical implications of this approach that the mechanical perturbations applied to the system, which are relevant only to the electromechanical impedance term of Equation 6.1, may be either experimentally controlled or occur inherently within the field environment. Clearly, though, experimental control of mechanical perturbations would be ordinarily relegated to the laboratory environment rather than the field environment. In the field environment, mechanical perturbations exist as the mechanical spectrum loading of the system whose Fourier components have multiple frequencies and amplitudes that transform into a unique electromechanical impedance response (*i.e.*, EMIS). When it is not be practical or even possible to mechanically excite or gain access to a mechanically excited material, structure, or component, the important aspect of this theoretical approach is that mechanical perturbations are not needed to assess fatigue damage, since the electrochemical impedance component of Equation 6.1 only requires an appropriate spectrum of electrical perturbations. In this context,

linear independence imposed upon the mechanical and electrical impedance terms of Equation 6.1 supposes that electrochemical processes probed by means of electrical perturbations are unique and independent of those processes manifest of mechanical perturbations. In fact, their basic nature is likely to be different—mechanical perturbations probe active straining at local fatigue damage sites, and result in film rupture (depassivation) and associated refilming, whereas electrical perturbations probe the nascent electrochemical reactions, which are sensitive to the fatigue damage state, but occur following repassivation. Thus, mechanical perturbations (EFS or EMIS) are a direct measure of localized straining, whereas electrical perturbations (EIS) are a measure of changes in electrochemical reactions as some time after localized strain (*i.e.*, fatigue and damage) has developed.

6.2.2 Model for Interfacial Impedance of Fractal Surface

The basis by which the electrochemical impedance of a material is responsive to incremental changes in microstructural damage because of mechanical fatigue has been approached through analogy with fractal geometry. This notion is as yet in the preliminary states of development and its validity remains to be proven. Notwithstanding the lack of a rigorous theory, the observed phenomenon to be shown later in this report can be modeled qualitatively in the following way.

The present model relies on the notion that mechanical fatigue in a solid induces incremental changes to the microstructure as the emergence of surface irregularity, tortuosity, and connectivity. Moreover, the evolution of this microstructure can be represented within appropriate distance scales by progressive branching of a fractal geometric pattern. For instance, the fractal geometry of the Cantor bar, illustrated in Figure 6-2, is in the present context a particularly useful, albeit ideal, model of the manifestations of surface microstructure in a solid after incremental damage has occurred to an initially smooth surface. The electrochemical interface that is formed between the electrolyte and a real fractal surface of this kind gives rise to an impedance that varies precipitously toward low frequencies of the input electrical perturbation. This impedance can be modeled by means of the electrical circuit analog of the Cantor bar fractal interface (Figure 6-2), which reduces to the continued fraction of Equation 6.3 [6.4].

$$Z(j\omega) = R + \cfrac{1}{j\omega C + \cfrac{2}{aR + \cfrac{1}{j\omega C + \cfrac{2}{a^2 R + \cdots}}}} \cdots \qquad (6.3)$$

In many real electrochemical systems, the model of Equation 6.3 satisfactorily accounts for the constant phase behavior or diffusion limited processes that are observed for tortuous interfaces such as the rough surface of an electroactive material or an oxide coating. This behavior is, in fact, parameterized implicitly in the Cole-Cole distribution model (Equation 6.2) by the parameter, β.

The mathematical convenience of fractals and the physical relevance that ideal fractal geometries have in microstructure provide an initial framework on which to base a causal relationship between fatigue damage and interfacial impedance. Thereby, EIS is effected to monitor the evolution of fatigue damage of a material system (*i.e.*, coating plus substrate) by deriving the total contribution of resistive and microcapacitive behavior that develops on the surface and near surface of the material as the damage becomes increasingly fractal and as the fractal interfaces become increasingly dielectric. The sum of capacitive and resistive elements constituting all of the fractal interfaces that develop within the bulk and surface of the material are represented in the capacitance and resistance elements of the interface.

In an effort to predict the effect of incremental levels of fractal damage on the interfacial impedance of a substrate as proposed above, the model of Equation 6.3 for the Cantor bar fractal interface (Figure 6-2) is a useful vehicle for numerical simulation. The complex impedance of this model is compared in Figure 6-3 with that of an equivalent circuit model for a porous coating and its complementary substrate. Multiple branching of the Cantor bar equivalent circuit, whose impedance is defined by Equation 6.3, occurs in the element Z_d of the equivalent circuit and its effect alone is simulated for finite levels of branching (n=1, 2). Whereas, the complete circuit of the porous coating model is simulated and the parameterized constant phase element contained in Equation 6.2 ($0 < \beta < 1$) is represented by the Z_d element.

It is to be understood presently that the cumulative structure and branching of the Cantor bar fractal network used in Figure 6-3 to represent progressive states of fatigue damage is based upon a hypothetical model simulation, wherein the value of a scaling parameter was chosen arbitrarily. Therefore, the simulation is not intended to be an exact representation of what is observed experimentally for any specific type of material system at any particular distance scale. From a purely electrochemical viewpoint, the effect that a progressively fractal surface structure has on the electrochemical impedance of the interface is governed principally by different site-specific accessibilities or different reaction probabilities of the transport and electron transfer processes that partake as a consequence of the electrochemical driving force (*i.e.*, dc bias potential applied across the interface). The connectivity and tortuosity of the interface that remains because of mechanical fatigue in essence impacts the nascent reactivity of the system, both the electron transfer and diffusion processes, which can be probed by the EIS methodology. On a fundamental level, this hypothesis, which links the surface microstructure (*i.e.*, fatigue damage) of the material with the corresponding manifold of electrochemical processes, is indeed difficult to model in closed form and its validity can only be established with much more fundamental study than what is presented here.

6.3   Experimental Apparatuses and Procedures

EIS measurements were conducted during the course of the fatigue tests independently or in parallel with the EFS measurements using the three electrode experimental set-up described previously in Section 5.2. The working electrode of this generalized configuration is the material or structure to be characterized, and may be consistent with the types of materials and coatings previously mentioned. Experimental procedures were essentially similar as those described for the EFS measurements. However, most of the impedance spectra for different materials and testing conditions were obtained by interrupting the cyclic loading at specific times during the course of the fatigue tests to measure the impedance of the system over the desired range of frequencies at various levels of fatigue damage. In addition, a limited number of tests were conducted where impedance spectra were acquired simultaneously to cyclic loading of the specimens.

The apparatuses of the EIS methodology are depicted in Figure 6-4. A Solartron Model 1287 potentiostat was used in conjunction with a Solartron Model 1260 frequency response analyzer (FRA) controlled by an independent Pentium computer. In the case of electromechanical and electrochemical impedance measurements where chemical processes are not a significant contribution to the measured current response, a high gain preamplifier of the general design shown in Figure 6-4 is used in-line with the working electrode input lead of the electrochemical transducer cell. A specially designed switch permitted the potentiostat to alternatively divert its current output to the computer controlling the FRA for EIS measurements or to the computer used as data acquisition system for EFS measurements. Two complete and independent experimental set-ups (i.e., load frame, electrochemical apparatuses, and computer systems) were used in the program. A 10 mV sinusoidal voltage signal generated by the FRA was superimposed to the applied potential controlled by the potentiostat and the current response was measured through the potentiostat, using its autoscale resistor feature, to determine the impedance response as a function of frequency. A frequency range of 100 kHz to 0.03 Hz was used in most of the measurements, with the exception of the tests in which EIS measurements were obtained during cyclic loading. In this case, the lowest frequency was limited in most of the tests to 10 Hz to avoid the undesirable coupling of the electrical and mechanical signal, since the fatigue tests were conduced at frequencies ranging from 1 to 5 Hz.

For each test, prior to initiating cyclic loading of the specimen, a set of impedance scans were conducted at various times until steady state conditions were attained in order to obtain an appropriate baseline data for comparison with the evolution of the EIS measurements during the fatigue tests. The ZPlot Version 2.1 software was used as a data acquisition program for the EIS measurements and ZView for Windows Version 2.1 for analysis and plotting of the data in the form of Nyquist and Bode plots.

6.4 Development of Methodology for EIS Measurements on Bare 7075 Aluminum

6.4.3 The Case of Bare 7075 Aluminum – Open Circuit Polarization

In the following experiments, the theory and experimental methodology of EIS were used to probe the evolution of cyclic fatigue damage in bare, cylindrical fatigue specimens of aircraft

aluminum alloy (7075 Al). The specific specimen geometry and material properties are defined in Sections 2.3 and 2.4, respectively. Measurements were made on duplicate specimens using identical experimental conditions. A laboratory-scale test apparatus, consisting of a three-electrode electrochemical cell and liquid electrolyte, test specimen, and mechanical fatigue machine, was configured so that electrochemical impedance measurements could be performed without having to remove the specimen from the fatigue test machine. A three electrode electrochemical cell configuration was used in conjunction with a potentiostat and frequency response analyzer, as depicted in Figure 6-4, to measure the electrochemical impedance spectrum of the specimen at discrete intervals of the specimen's fatigue life. A fatigue machine (Model MTS, 10 kip capacity) was employed to impart progressive states of fatigue damage by subjecting the specimen to fully reversed (R = -1) sinusoidal mechanical loads (i.e., perturbations) at a peak stress of 50 ksi and frequency of 1 Hz. The specimen was mechanically fatigued under these conditions over a series of predefined number of cycles until failure was achieved. At the end of each interval in the series, wherein the specimen experienced no mechanical perturbations nor a constant load, the electrochemical impedance spectrum of the specimen was measured over discrete frequencies of small amplitude (8 - 12 mV) electrical voltage perturbations spanning 100 KHz to 50 mHz, which were centered around a DC polarization potential of 300 mV versus the reference electrode (saturated calomel electrode). This polarization potential in combination with the liquid electrolyte was determined previously in separate experiments to be well within the steady-state passive region of the aluminum alloy. The liquid electrolyte consisted of 0.3 M H_3BO_3 + 0.075 M $Na_2B_4O_7$ + 0.06 M Na_2MoO_4 in water with a final pH of 8.4.

Typical electrochemical impedance responses of 7075 aluminum alloy following progressive states of mechanical fatigue damage are shown in Figure 6-5. In this example, the specimen was subjected to the electrochemical cell's open circuit potential (OCP) during fatigue, whereas electrical voltage perturbations centered around the DC polarization potential were used to interrogate the specimen intermittently during the cessation of fatigue. The projection of the impedance response onto the complex plane clearly shows a monotonic contraction of the impedance arc as the specimen accumulates progressively greater amounts of fatigue damage. A single time-constant impedance response is observed under the present conditions leading to an

inductive response at low frequencies. Changes in the relaxational behavior of electrochemical and transport processes that occur within the specimen as fatigue damage accumulates are reflected in the spectrally resolved impedance measurements. These changes are more clearly revealed in the Debye dispersion representation of the impedance measurements as shown in Figure 6-6, which indicates that the characteristic shape and distribution of the imaginary component of the impedance measurements changes around the fundamental frequency as a function of the state of fatigue damage. This experiment demonstrates that progressive states of fatigue damage within a metallic specimen that is maintained under OCP electrochemical conditions cause characteristic changes in the electrochemical impedance spectrum of the specimen, and these changes are observed when the electrochemical impedance is measured under mechanically static conditions (*i.e.*, in the absence of fatigue cycling).

6.4.4   *The Case of Bare 7075 Aluminum – Constant Polarization*

The methods and apparatuses described above were again used to probe the evolution of cyclic fatigue damage in cylindrical fatigue specimens of 7075 aluminum alloy. However, in this experiment the specimen was subjected to a constant polarization potential of 300 mV vs. SCE during fatigue. The specimen was again intermittently interrogated during the cessation of fatigue using electrical voltage perturbations centered around the DC polarization potential.

The electrochemical impedance responses of the specimen following progressive states of fatigue damage are shown in Figure 6-7, which again shows a monotonic contraction of the complex impedance arcs as the specimen accumulates progressively greater amounts of fatigue damage. This experiment demonstrates that progressive states of fatigue damage within a metallic specimen that is maintained at a constant passive polarization potential cause characteristic changes in the electrochemical impedance spectrum of the specimen. These changes are observed when the electrochemical impedance is measured under mechanically static conditions. It should be noted, however, that the initial value of the impedance measured before cyclic loading ($\cong$ 18 kΩ) suggest that the alloy in the borate/molybdate system is not completely passive. The influence of this incomplete passivation on EIS and EFS measurements is discussed in Section 6.4.5.

6.4.5 *The Case of Bare 7075 Aluminum – EIS Measurements During Mechanical Fatigue*

The purpose of the following experiment was to determine what effects mechanical perturbations in the form of fatigue loading had on simultaneous measurement of electrochemical impedance. For this, EIS was used as in the previous case to probe the evolution of cyclic fatigue damage in a cylindrical specimen (7075 Al) using a constant polarization potential of 300 mV vs. SCE. In the present case, however, mechanical fatigue was not interrupted and, at intermittent times until failure, the specimen was concurrently subjected to the electrical perturbations of the EIS method to probe the state of damage.

Figure 6-8 shows the electrochemical impedance response of the specimen following progressive states of fatigue damage. It is evident from the measurements that the mechanical perturbations of cyclic loading couple strongly with the electrical perturbations of the EIS measurements, particularly at frequencies in resonance with the fundamental mechanical perturbation of 1 Hz. That effect intensifies with incremental fatigue damage as indicated by the unbounded fluctuations that occur in the phase-frequency plane of the impedance response (Figure 6-8b).

The observed coupling between mechanical and electrical perturbations limits the range of impedance measurements that can be reliably acquired under mechanical loading near the mechanical resonance frequency. Although the impedance arcs in the complex plane appear to have contracted at a similar rate as that observed in the previous cases, the mechanical interference in these data make accurate derivation of the impedance at the low frequency limit a difficult challenge, even with the aid of numerical fitting routines. An accurate estimate of this limit is fundamentally important to the derivation of a parameter on which to base the evolution of fatigue damage and, perhaps, alternative signal processing routines or refined measurement methods would be useful venues to explore.

6.4.6 *Modeling of EIS Response for the Case of Bare 7075 Aluminum – Implicit Damage Parameters*

This and related sections that follow demonstrate how damage parameters, readily derived from electrochemical impedance measurements, can be used to correlate implicitly the

evolution of fatigue damage during the fatigue life of the alloy system under consideration. For each case described above in Sections 6.4.1 and 6.4.2, and subsequent sections related to other alloy systems, the electrochemical impedance responses following progressive states of fatigue damage are used to demonstrate the mathematical derivation and correlation of the implicit damage parameter of interest.

In the present case of bare aluminum, a single parameter R_p is derived from the full-frequency impedance spectrum to arrive at an implicit damage parameter, which is designated symbolically as the reciprocal, $1/R_p$. The magnitude of this reciprocal resistance, or admittance, is proportional to the rate of the electrochemical process at play or, in the context of surface microstructure, a reflection of the evolution of fatigue damage.

The implicit damage parameter ($1/R_p$) was determined from each electrochemical impedance arc of the experimental data by fitting the Cole-Cole distribution model, which is mathematically defined in Equation 6.2 of Section 6.2.1, to the experimental data. In this model, the difference between the high and low limits of the impedance arc ($R_p=Z_{E,0} - Z_{E,\infty}$), the uncompensated resistance of the electrochemical cell ($R_u=Z_{E,\infty}$), the relaxational time constant τ, and the distribution factor β, constitute the fitting parameters for treatment by nonlinear regression analysis. The error associated with the parameter estimates was in most cases less than 5%. As a consequence of the regression treatment, the best-fit parameter value of R_p was used to correlate the implicit damage parameter ($1/R_p$) with the fractional fatigue life of the specimen. The results of the correlation are shown in Figure 6-9 for each of the specimen conditions described for bare aluminum in Sections 6.4.1 and 6.4.2. Also shown in this figure is the electrical circuit analog of the Cole-Cole distribution model (Equation 6.2 of Section 6.2.1) that was used to derive the value of R_p.

A convenient method of evaluating the reproducibility of these curves is illustrated in Figure 6-10. In this figure, the values of the implicit damage parameter ($1/R_p$) were for each case normalized by the corresponding value for the pre-fatigue condition ($1/R_{p0}$), thus yielding the ratio R_{p0}/R_p. The influence that the polarization conditions can bear on the sensitivity of the implicit response curves is evident. However, the multi-phasic features of these curves are

consistent in that the response profiles of R_{p0}/R_p versus incremental fatigue damage (D_f) behave as $1-exp(-\alpha D_f)$, and this increase is preceded by a level response between zero and 20% of life. This behavior, which appears to be reproducible at least within the present family of experiments, seems to suggest that the EIS methodology is capable of providing a sensitive measure of the onset of damage quite early in the fatigue life of the aluminum alloy specimen.

6.4.7 Effect of Fatigue Loading Variables on EIS Measurements of Bare 7075 Aluminum

This section concentrates on how fatigue loading variables affect the response of the EIS damage parameter as a function of incremental fatigue damage. In addition to variations in the purely mechanical variables, such as maximum and mean stresses, the effect of the electrochemical polarization potential used during cyclic loading on the sensitivity of the EIS damage parameters was explored. These variables are shown to have a significant bearing on the level to which the EIS methodology can discriminate between the progression of actual fatigue damage and what has been observed to be a time-dependent effect associated with the passivity of the surface oxide.

<u>Effect of Maximum Stress</u>

As noted above the EIS data for uncoated 7075 Aluminum alloy is accurately modeled by an equivalent circuit consisting of a Cole-Cole distributed element in parallel with the polarization resistance of the surface oxide, R_p. This resistance is preceded by another resistance, R_u, representing the uncompensated resistance of the cell, which was attributed to the ohmic resistance of the electrolyte. As noted before, the parameter $1/R_p$, which increases with the number of fatigue cycles, is a good indicator of the progression of fatigue damage.

However, as shown in Figure 6-11, the increase of this parameter, normalized with respect to the value measured before starting cyclic loading, R_{p0}/R_p, is strongly dependent on the maximum stress. For tests conducted at R = ~1, under an applied potential of 0.3 V_{SCE}, a significant monotonic increase with the percent of fatigue life is noted at 345 MPa (50 ksi), regardless of the cyclic loading frequency. The increase of the normalized $1/R_p$ is significantly

attenuated at 310 MPa (45 ksi) and not observable, except in the last 20 percent of the life, at 276 MPa (40 ksi).

It is valuable to compare these results with those corresponding to the EFS signal as summarized in Table 5-1. There is not a clear upward inflection noted in the curves for 345 MPa (50 ksi) at the same percentage of life (62 %) at which the EFS signal exhibited features characteristic of crack initiation or same significant degree of fatigue damage (see first two rows of Table 5-1). A slope change, however, appears to be detectable in the 5 Hz curve at about 60 percent life. On the other hand, both at 310 MPa (45 ksi) and 276 MPa (40 ksi) a noticeable increase in the slope is noted in Figure 6-11, approximately at the same values or even less that those indicating cracking associated features in the EFS signal (last two rows of Table 5-1).

Effect of Mean Stress

The effect of the mean stress in the EIS measurements for 7075 Al alloy was evaluated indirectly through the variation of the R ratio at a constant maximum stress. Figure 6-12 shows the effect of the stress ratio on EIS measurements conducted at 276 MPa (40ksi) and 5 Hz, under an applied potential of 0.3 V_{SCE}. It is apparent from the plots that the normalized $1/R_p$ values do not increase and even decrease with the percent of fatigue life as a result of the low maximum stress used in these tests, as discussed in the section above.

Nevertheless, a noticeable increase in the normalized $1/R_p$, which is far more pronounced and earlier for R = -1, occurs late in life. It is useful to compare the plots in Figure 6-12 with the data reported in the last rows of Table 5-2. It can be concluded that features in the EFS signal, interpreted as signs of fatigue damage or crack initiation, are detected at fatigue life percentages that are only slightly lower that the values at which the normalized $1/R_p$ exhibited upward inflections at both R= -1 and 0.05.

Effect of Polarization Potential

The applied potential is one of the most important variables affecting the response of the EIS measurements on the assessment of the progression of fatigue damage. The influence of

potential is clearly illustrated in Figure 6-13 in which the normalized $1/R_p$ is plotted as a function of the percentage of fatigue life for several specimens tested at 345 MPa (50 ksi) under various applied potentials. Whereas at 0.0 V_{SCE}, the normalized $1/R_p$ does not change with percentage of fatigue life, at higher potentials the sensitivity of the parameter increased significantly, exhibiting more than 3 times increase at 0.5 V_{SCE},

It should be noted, however, that potential changes covering a range of 500 mV do not affect the fatigue life of 7075 Al alloy. All the specimens failed in a range between 5,800 and 10,391 cycles without exhibiting any correlation with the applied potential that may lead to infer a detrimental effect of high potentials on the fatigue life, such as that generally observed when corrosion fatigue occurs. On the contrary, the specimen tested at 0.5 V_{SCE}, the highest potential applied in these tests, was the one that failed after 10,391 cycles.

Time Dependent Effects on EIS Measurements

One of the most significant challenges confronted in the application of EIS measurements for evaluating fatigue damage of bare metals is the variation of the impedance responses as the result of changes with time in the electrochemical properties of the passive films. This effect of the exposure time has been a problem confronted mainly in the case of 7075 Al alloy because stable steady state passive conditions are not attainable in the electrolyte of choice within a sufficiently short time. The relatively low values of the impedance are in agreement with relatively high passive current densities of approximately 2 to 5 $\mu A/cm^2$, as measured in very slow anodic potentiodynamic scans in the deaerated electrolyte.

Figure 6-14 shows the variation of the normalized $1/R_p$ as a function of time for a set of experimental conditions. Tests were conducted under comparable electrochemical conditions by applying a constant potential of 0.3 V_{SCE}. Within a comparable time span (the initial 150 minutes) it is apparent that prior to cycling loading the normalized $1/R_p$ exhibited only a marginal increase with respect to the specimens loaded at 276 MPa (40 ksi), although the difference increases significantly beyond this period. Only at 310 MPa (45 ksi) the increase is larger than that due merely to the time effect. Nevertheless, at longer times the increase in the

normalized $1/R_p$ is substantial in the absence of cyclic loading indicating that the alloy is not completely passive in the electrolyte currently used in the program.

These observations are extremely important because they provide an element of uncertainty, affecting the univocal determination of fatigue damage by using EIS measurements in the case of the bare 7075 Al alloy. It is difficult to have reproducible baseline data that can be used for comparison with the evolution of the impedance parameters during cyclic loading. However, the selection of other electrolytes that may confer better passivity to these types of Al alloys may help to overcome those limitations. An additional approach could be related to improving the sensitivity of the EIS measurements by conducting more localized measurements similar to those implemented in microellipsometry to measure thickness of passive films in the proximity of grain boundaries or other microstructural features [6.5].

Based upon what has been learned fortuitously through EIS measurements about the instability of the bare 7075 Al alloy in the electrolyte of choice, this problem is likely to have an impact on the interpretation of EFS measurements as well. For instance, anomalous drifts in the magnitude and occurrence of selected features, namely, the mean current amplitude, were demonstrated in Section 5.4.1.2 to manifest in the absence of cyclic loading.

6.5   Development of Methodology for EIS Measurements on Coated Materials

The development of a methodology for EIS fatigue measurements on coated 7075 aluminum is discussed separately in this section because the impedance behavior of such systems is a function of both the substrate and the dielectric properties of the coating. Consequently, model development for treatment of the impedance responses must take into consideration implicit parameters that are relevant to each component of the collective system (*i.e.*, coating and substrate).

6.5.1   The Case of Primer Coated 7075 Aluminum

As before, the same methods and apparatuses described in connection with the bare metal experiments were used to probe the evolution of fatigue damage. However, the present situation

demonstrates the evolution of fatigue damage for a cylindrical specimen of 7075 aluminum alloy that has been chemically treated to remove surface oxides and other adherends, and subsequently spray painted with a primer coating. The chemical treatment and spray coating of the specimen was conducted in accordance with standard procedures established for the maintenance of military aircraft materials of this type. The chemical composition of the primer coating used in this example conformed to military aircraft specifications MIL P 23377G Type 1 Class C, as described in Section 2.0.

Measurements were made on duplicate specimens using identical experimental conditions. Progressive states of mechanical fatigue were imparted on each specimen using fully reversed (R = -1) sinusoidal loading at a peak stress of 50 ksi and frequency of 1 Hz. A constant (DC) polarization potential of +300 mV versus the reference electrode was applied to the specimen during fatigue testing. The specimen was again interrogated intermittently, during the cessation of fatigue, using electrical voltage perturbations centered around the DC polarization potential. The results of these measurements are plotted in Figure 6-15 in the same fashion as was done in the previous cases of bare 7075 Al. In the present case, the impedance spectra change monotonically with incremental fatigue damage. However, each spectrum contains two characteristic regions (*i.e.*, time constants): one is associated with slow diffusion-limited processes that occur at the coating-substrate interface, which are realized at low frequencies; while the other, which occurs at high frequencies, is consistent with the dielectric behavior of the coating itself. The inset of Figure 6-15a further exemplifies these monotonic changes in the region of the high frequency limit.

Therefore, this experiment demonstrates that progressive states of fatigue damage within a primer coated metallic substrate, as well as damage to the coating itself, cause characteristic changes in the electrochemical impedance spectrum of the coated specimen. These changes occur independently in two regions of the frequency spectrum, which can be discriminated by the EIS methodology.

6.5.2 The Case of Primer and Top Coated 7075 Aluminum

In the present case, a cylindrical specimen of 7075 aluminum onto which were applied a primer and a topcoat, as described in Section 2, was used for the fatigue experiment. This

experiment was aimed at evaluating the ability of the EIS methodology to probe fatigue damage of the metal substrate through a highly resistive, composite coating system. Again, fully reversed (R = -1) sinusoidal loading at a peak stress of 50 ksi were used at a frequency of 1 Hz to induce incremental amounts of fatigue damage. A constant polarization potential of +300 mV versus the reference electrode was applied to the specimen during fatigue. The specimen was again interrogated intermittently, during the cessation of fatigue, using electrical voltage perturbations centered around the DC polarization potential.

As in previous EIS fatigue measurements performed on primer-coated aluminum alloy specimens, the impedance response of a specimen coated with primer and topcoat, shown in Figure 6-16, also displayed spectral dispersion with incremental fatigue. However, the changes exhibited by the spectral dispersion are not entirely monotonic and the low frequency region of the impedance spectrum is plagued by a considerable amount of noise because the impedance of the topcoat is exceedingly high ($\cong$ 10 MΩ). Given these limitations in spectral quality, the impedance spectrum in each case appears to contain at least two time constants upon close inspection. One relaxation time constant is probably related to a slow diffusion-limited process, possibly within pores or other defects of the coating, while the second is consistent with the dielectric behavior of electrolyte-coating interface.

It is important to recognize that the essential difficulty with acquiring reliable impedance measurements on a coating system of this sort, which exhibits a relatively low dielectric constant, is attributed to the configuration and measurement conditions of the experimental apparatus. Specifically, the electrochemical cell used for all fatigue experiments comprises a cell geometry, for example, the size of the counter electrode and its distance from the specimen, whose function is to transfer information about the integrated average response of the specimen, and that is best suited to systems having a low interfacial impedance. Hence, considerable improvements in EIS - fatigue measurements of coated materials should be possible with probe designs that afford more localized measurements than was possible with the immersion system used herein.

6.5.3 Modeling of EIS Response for the Case of Coated 7075 Aluminum

In the case of multicomponent systems, the damage state of each material component as a function of fatigue can be hypothetically defined and derived mathematically from the electrochemical impedance measurements. Hence, two independent damage parameters are relevant to the material system in this case: *1)* the implicit damage parameter of the coating ($1/R_{pore}$), which is related to changes in the resistance of pores (R_{pore}) and other defects within the coating; and *2)* the implicit damage parameter of the substrate ($1/R_{ct}$), which takes into consideration the charge transfer resistance (R_{ct}) and diffusion limited processes associated with the electrochemical reactivity of the substrate at the interface between the coating and substrate.

The implicit damage parameters ($1/R_{pore}$ and $1/R_{ct}$) were deconvolved from the high- and low frequency regions (*i.e.*, two time constants) of the impedance responses by fitting to the experimental measurements a model which combines the impedance response of the coating at the interface between the electrolyte and the coating, with that of the substrate at the interface between the coating and the substrate. The Cole-Cole distribution (Equation 6.2) is used here to mathematically describe the dielectric behavior of the coating, including pores and other defects within the coating that form an ensemble of dielectric interfaces. The impedance of the substrate in the interfacial region between the coating and the substrate is mathematically described by an expression that takes into consideration, in a general sense, the kinetics of charge transfer processes, and the transport (*i.e.*, diffusion) of neutral or charged chemical species; that is, the generalized Warburg impedance (see *Modeling of EIS Response for the Case of Ti-6Al-4V*, Section 6.7.2). The parameters or constants pertinent to an explicit description of the charge transfer and diffusion processes are combined into macroconstants to arrive at a generalized, hence, implicit form of the full expression. As a consequence of this parameterization in the implicit form of the model, the difference between the high and low limits of the high frequency impedance arc ($R_{pore} = Z_{E,0} - Z_{E,\infty}$), the uncompensated resistance of the electrochemical cell ($R_u = Z_{E,\infty}$), the relaxational time constant τ, the distribution factor β, and charge transfer resistance R_{ct} associated with the low-frequency, constant-phase region of the impedance, constitute the fitting parameters for treatment by nonlinear regression analysis. The best-fit parameter values of R_{pore} and R_{ct} were used to correlate the implicit damage parameter ($1/R_{pore}$) of the coating, and

the implicit fatigue damage parameter of the aluminum substrate ($1/R_{ct}$), with the fractional fatigue life of the specimen. The results of these correlations are shown in Figure 6-17 for duplicate experiments.

In contrast to the cases of bare metals, wherein the implicit damage parameters varied with incremental fatigue as an exponential rise to maximum, primer coated aluminum is shown in Figure 6-17 to produce profiles of the implicit damage parameters ($1/R_{pore}$ and $1/R_{ct}$) that can be characterized as exponential growths. This behavior is most clearly illustrated by applying the normalization technique described earlier for comparing the implicit damage profiles of replicate experiments. The results of the normalization treatment are compared in Figure 6-18 for the duplicate experiments of the present case and for each profile of the two damage parameters. Upon close inspection of these profiles, the growth behavior of the damage associated with the coating (R_{pore0}/R_{pore}) is described accurately as a biphasic exponential function of the form shown in the top panel of Figure 6-18, where the values of the rate parameters (α and β) are compared for the duplicate experiments. The latter phase (β) of this response merges with the growth of damage that has been assigned to processes encountered at the interface between the coating and the substrate by virtue of the impedance model, namely the Warburg diffusion equation (Section 6.7.2) and its implicit parameter (R_{ct}). Therefore, differentiation between the actual physical processes at play in the β-phase of the damage profile becomes ambiguous and, in this sense, the profile of R_{pore0}/R_{pore} appears effectively to capture the rate of evolution of all relevant physical processes.

This example experimentally validates the concept of the EIS methodology by demonstrating that the onset and evolution of fatigue damage within a coated material, such as aluminum alloy, is correlative with implicit damage parameters. It is further demonstrated that these parameters can be numerically derived from the electrochemical impedance response of the material as measured under mechanically static conditions (*i.e.*, without application of load to the material component).

6.5.4 Effect of Coating Quality on EIS Measurements of 7075 Aluminum

6.5.4.1 Effect of Primer Coating Quality: Examination of primer coated 7075 Al specimens using EIS revealed that in many specimens the coatings had significant defects. The existence of such defects caused the impedance spectra for specimens with poor primer coatings tend to behave more similar to bare 7075 specimens than to specimens covered with a good quality primer. As a result, impedance spectra for specimens with poor primer coatings were analyzed using the Cole-Cole model (Equation 6.2) developed for the bare specimens.

The results of EIS analyses for a 7075 Al specimen with a good primer coat are shown as a function of fatigue life in Figure 6-19. As expected, specimens with a good primer coat exhibited higher impedance values than those measured for poorly coated specimens. The value of $1/R_p$, as shown in Figure 6-19, gradually increased from values in the range of 6×10^{-7} to 7×10^{-7} ohms^{-1} during the initial 80 percent of the specimen life. Thereafter, the value of $1/R_p$ increased sharply until failure occurred at 18,828 cycles. The value of $1/R_{ct}$ was higher and, although it was clearly more variable than $1/R_p$, exhibited a noticeable increase from approximately 8×0^{-6} to 2×10^{-5} ohms^{-1} until 80 percent of the fatigue life, but thereafter remained practically constant until failure.

Figure 6-20 shows the results analyzed from the EIS scans for a specimen with defects in the primer coating. The values of both $1/R_p$ and $1/R_{ct}$ are higher than those values shown in Figure 6-19, as can be expected for specimens with coating defects. The value of $1/R_p$ monotonically increased through the initial 50 percent of the fatigue life and remained relatively constant before exhibiting an abrupt increase at 95 percent of the fatigue life. The value of $1/R_{ct}$ was practically constant at about 1.5×10^{-4} ohms^{-1} until 40 percent of fatigue life, with the exception of a peak at 10 percent that could be an anomalous data point. Above 40 percent life, $1/R_{ct}$ increased continuously but exhibited a point of inflection at about 60 percent followed by a sharp increase at 95 percent of the fatigue life, similar to that observed for $1/R_p$. It should be noted that this value is slightly higher than the percentage of life at which the EFS signal shows features characteristic of the occurrence of fatigue cracks, as discussed in Section 5.5.1.

6.5.4.2 Effect of Primer Plus Topcoat Quality: The behavior of 7075 Al alloy specimens with primer and topcoat exhibited similarities with the EIS response of specimens with primer coating alone. In addition, some of the specimens tested were also found to have coatings with defects. As with the poor primer coated cases, the EIS data for these specimens was analyzed using the Cole-Cole model selected for bare 7075 Al alloy specimens. On the other hand, specimens with good quality coatings were analyzed with the circuit model proposed for the primer coated specimens.

The results of the analyses for the 7075 Al specimens with a good quality coating are shown in Figure 6-21. Over a large percentage of the fatigue life, values of both $1/R_p$ and $1/R_{ct}$ are very low, in the order of 10^{-8} ohms^{-1} and 10^{-6} ohms^{-1}, respectively, indicating the existence of a high impedance coating without defects. At about 80 percent of the fatigue life, the value of $1/R_{ct}$ increased by more than an order of magnitude, followed by a similar increase in $1/R_p$ at 90 percent of the fatigue life. It should be noted again, that the response in terms of the impedance parameters is in agreement with the results of the EFS measurements. Also, at about 80 to 90 percent of the fatigue life distinctive features were observed in the EFS transients, as discussed in Section 5.5.1, revealing the occurrence of fatigue cracks.

The values of the impedance damage parameters calculated for specimens with poor primer and top coatings, as shown in Figure 6-22, are at least an order of magnitude higher than those observed on specimens with high quality coatings. This observation reveals that the overall impedance of the coated specimens is significantly lower, as expected from the existence of defects. The value of $1/R_p$ was found to be practically constant at about 2×10^{-6} ohms^{-1} during most of the fatigue life but increased sharply at about 90 percent. This final increase is similar to that observed in the specimen with non-defective coating (see Figure 6-21). On the contrary, after a sudden decrease as soon as cyclic loading started, $1/R_{ct}$ increased gradually over the course of the test, followed by a more pronounced increase at about 90 percent of the fatigue life, in correspondence with the final increases in $1/R_p$. Although later in the fatigue life than those observed in specimens with non-defective coatings, this response seems to indicate the development of fatigue cracks in agreement with the results obtained in the EFS measurements. Nevertheless, the overall conditions of the tests appear to be more critical to obtain good

reproducibility in the case of EIS measurements, probably due to the high sensitivity of this technique for detecting coating defects.

6.6   Development of Methodology for EIS Measurements on 4130 Steel

6.6.1   The Case of 4130 Steel

The application of EIS as a means of measuring fatigue damage also was evaluated for other aircraft alloys of importance, which include steel (4130) and titanium (Ti-6Al-4V). In the following experiments, the methods and apparatuses described previously for EIS measurements of aluminum were used again to probe the evolution of fatigue damage in cylindrical specimens of 4130 steel. Measurements were made on duplicate specimens using identical experimental conditions. Progressive states of fatigue damage were in the present case imparted on each specimen using fully reversed (R = -1) sinusoidal loading at a peak stress of 105 ksi and frequency of 1 Hz. A constant polarization potential of +400 mV vs. SCE was used throughout the fatigue test. As before, each specimen was intermittently interrogated during the cessation of fatigue using electrical voltage perturbations centered around this DC polarization potential.

A typical example of the electrochemical impedance response of 4130 steel following incremental fatigue damage is shown in Figure 6-23. The impedance behavior of this alloy was, as expected, much different than that observed for aluminum alloy, owing to the relatively fast re-passivation process that is inherent to this alloy in the borate/molybdate buffer system. In this regard, the dominant feature of the impedance response is the diffusional or constant phase contributions of the re-passivation mechanism that leads to a family of lines, rather than arcs, in the complex plane. These apparent lines appear to be arcs whose low frequency limits cannot be readily measured by the experimental apparatus.

On first examination, the family of lines as presented in the complex impedance plane of Figure 6-23 does not appear to change with incremental fatigue damage. Upon closer inspection, however, the shape of these lines can be characterized by two time constants, and spectral dispersion is evident as a monotonic decrease in the complex impedance at the low frequency

limit. Expansion of the scale at the high frequency limit (inset of top panel in Figure 6-23) is done to illustrate spectral dispersion in this region of the impedance spectrum.

6.6.2   Modeling of EIS Response for the Case of 4130 Steel

The EIS response of steel alloy to incremental fatigue was shown to contain spectral features in the complex impedance plane that were consistent with a two time-constant mechanism (see previous section). A more complex form of the simple Cole-Cole distribution model than was used for aluminum alloy is, therefore, needed to derive from the EIS spectra an implicit damage parameter (or parameters). This model must as well reflect the electrochemical processes, both the charge transfer associated with the reformation of the passive film and diffusion, hypothesized in the usual way for steel alloys of this type [6.6]. These processes contribute to the complex nature of the measured impedance response.

By convoluting the Cole-Cole distribution model for the electrolyte-substrate interface with the effects of the electrolyte-surface coating interface, the resultant equation provides better than satisfactory estimates of model parameters after deconvolution, typically less than five percent coefficient of variation. Thus, the equivalent electrical circuit model contains the passive elements defined as follows: the capacitance of electrical double layer, C_{dl}; the polarization resistance of the surface oxide, R_p; and, the constant phase element and charge transfer resistance, R_{ct}, of the Cole-Cole distribution model.

Two implicit damage parameters, $1/R_p$ and $1/R_{ct}$, can be derived from the above model, each parameter can be shown to reflect unique features of and, perhaps, sensitivity to, progressive states of fatigue damage. The evolution of these parameters with incremental fatigue damage is shown along with a diagram of the equivalent electrical circuit model in Figure 6-24. It is interesting to note that the functional form of these curves also bear a resemblance to $1-exp(-\alpha D_f)$ behavior previously noted for aluminum alloy. The onset of this functional change appears in the present case to occur earlier in the fatigue life of the steel alloy specimen than observed for aluminum alloy.

6.6.3 The Case of 4130 Steel - EIS Measurements During Mechanical Fatigue

Another challenge confronted in the application of EIS measurements for evaluating fatigue damage of aircraft materials arise from the significant differences in the repassivation kinetics observed for the various materials tested. It is well established that the kinetics of repassivation, following the mechanical breakdown of a passive film, is strongly dependent on the metal/electrolyte system [6.7, 6.8, and 6.9].

EIS measurements were conducted using 4130 steel specimens over a range of test conditions by interrupting the cyclic loading to acquire the impedance spectrum at various percentages of fatigue life. Test conditions include the variation of the maximum stress from 641 to 758 MPa (93 to 110 ksi) using an R ratio of -1 and a frequency of 1 or 5 Hz. The spectra were analyzed according to the two-time constant impedance model described in Section 6.6.2. As a typical example, the results for a specimen tested at 641 MPa (93 ksi), R = -1 and 5 Hz under an applied potential of 0.5 V_{SCE} are shown in Figure 6-25. EIS scans were obtained over a frequency range of 10^5 to 0.03 Hz after cyclic loading was temporarily interrupted. The plot shows that the values of $1/R_p$ increased from 4×10^{-4} ohms^{-1} prior to cyclic loading to about 2×10^{-3} ohms^{-1} after a few thousand cycles. After this initial increase, the value of $1/R_p$ did not change throughout the remainder of the test with the exception of a slight increase immediately prior to failure. This final increase, however, is relatively small compared to the large increase observed after initial cyclic loading. On the contrary, the value of $1/R_{ct}$ decreased from 1.3×10^{-6} ohms^{-1} prior to cyclic loading to less than 10^{-15} ohms^{-1} after a few thousand cycles and was observed to vary slightly throughout the life of the specimen. Nevertheless, the calculated values were extremely small and, therefore, the variations are not noticeable in the plot shown in Figure 6-25.

Whereas the plot of $1/R_{ct}$ did not show any distinctive feature that can be correlated with the increasing fatigue damage of the specimen, $1/R_p$ exhibited a final increase at about 96% of the fatigue life. It should be noted that features in the EFS signal associated with the occurrence of fatigue cracks, such as the current spike in the rising portion of the C-peak and the drop in the C-peak rise time, were detected at the same percentage of life (Section 5.2.3.2). These features

appeared late in life as a result of the relatively low value of the maximum stress used in this test in which the fatigue life is 130,800 cycles. Similar results were observed in all the other tests conducted on steel specimens where EIS scans were obtained after temporary interruption of the cyclic loading.

The results plotted in Figure 6-25, in particular for $1/R_{ct}$, suggest that repassivation of the 4130 steel specimen occurred rapidly. In addition, the EFS signal revealed low current transients during cyclic loading that are also a strong indication of the fast repassivation kinetics of 4130 steel in the borate/molybdate system. This strong passivity of 4130 steel in the borate/molybdate electrolyte at pH 8.4 is confirmed by the results of slow scan rate potentiodynamic polarization curves where passive current densities of around 0.1 $\mu A/cm^2$ (more than one order of magnitude lower than for 7075 Aluminum) were measured. Therefore, it was expected that EIS measurements conducted simultaneously with cyclic loading would be more sensitive to the progression of fatigue damage.

In order to examine the effect of cyclic loading on the impedance parameters, several tests were conducted where EIS scans over a frequency range of 10^5 to 10 Hz were performed at various percentages of life while cyclic loading of the specimens was done continuously. The EIS scans were analyzed using the same model as above and results obtained for one such specimen tested with a maximum stress of 724 MPa (105 ksi), R = ~1 and a frequency of 1 Hz are shown in Figure 6-26. In this test, the value of $1/R_p$ was observed to increase rapidly at the start of the test, followed by a more gradual increase until about 60 percent of the fatigue life and an almost constant value of 2.3 ohms^{-1} until failure occurred at 27,640 cycles. In contrast, the value of $1/R_{ct}$ increased slowly at the start of the test followed by a more rapid increase after about 60 percent of the fatigue life that continued until the failure of the specimen.

In these tests the values of both $1/R_p$ and $1/R_{ct}$ are at least two orders of magnitude greater than those obtained when cyclic loading was interrupted to conduct EIS measurements. This difference can be attributed to the fact that under continuous cycling at 1 Hz there is no sufficient time for the steel to be repassivated completely. Then, the surface remained relatively active in those areas of the specimen surface in which mechanical breakdown of the passive film due to

slip emergence had occurred. It should be noted, however, that the values calculated for R_p and R_{ct} using the two time constant impedance model are affected by the values of the impedance measured at low frequencies. When the lowest frequency used in the EIS measurements was increased from 0.03 Hz to 10 Hz to avoid coupling of the voltage input signal with the frequency adopted for cyclic loading, a significant decrease in both R_p and R_{ct} occurs when the impedance data is fitted to the model.

From the results discussed above it appears that EIS measurements conducted during cyclic loading show promise as a method to determine the fatigue life of the material. The technique can be useful provided it is used throughout the life of the specimen or component such that the changes in the impedance response can be followed. It should be noted, however, that subsequent tests exhibited poor reproducibility, even though the same general pattern was observed, indicating that additional work is needed to eliminate many elements of uncertainty in these measurements.

6.7   Development of Methodology for EIS Measurements on Ti-6Al-4V Alloy

6.7.1   The Case of Ti-6Al-4V Alloy

In the present case, EIS measurements were used to probe the evolution of fatigue damage within cylindrical specimens of Ti-6Al-4V alloy. Measurements were made on duplicate specimens using identical experimental conditions. Progressive states of mechanical fatigue were imparted on each specimen using fully reversed (R = -1) sinusoidal loading at a peak stress of 85 ksi and frequency of 1 Hz. A constant polarization potential of +400 mV vs. SCE was used during mechanical fatigue. Again, each specimen was intermittently interrogated during the cessation of fatigue using electrical voltage perturbations centered around this DC polarization potential.

A typical result of the impedance response is shown in Figure 6-27 at each state of incremental fatigue damage. The complex impedance is shown to change rapidly early in the life of the specimen, thereafter the diffusional component of the response dominates and the complex impedance converges to a steady-state condition. Although this convergence is monotonic with

incremental fatigue damage, spectral dispersion of the family of complex impedance curves is less evident than that observed for aluminum or steel. Expansion of the complex impedance plane at the high frequency limit (Figure 6-27a) reveals only a small degree of spectral dispersion. The lack of spectral dispersion, although subject to speculation, can be tentatively ascribed to the rapid re-passivation kinetics of the alloy. In fact, the high impedance values at low frequencies are related to this phenomenon.

Under the present experimental conditions, the nascent reactivity of the surface structure created by fatigue damage is rapidly re-passivated between the time mechanical fatigue is ceased and when the EIS measurement is initiated. The net result is a condition in which the granularity of the surface microstructure and complementary reactivity cannot be discriminated over the comparatively large distance scales at which measurements are made.

6.7.2 *Modeling of EIS Response for the Case of Ti-6Al-4V Alloy*

The EIS response of titanium alloy also can be characterized by the effect of two time constants. As speculated earlier, the nascent reactivity of the surface structure created by fatigue damage in this alloy is rapidly re-passivated between the time mechanical fatigue is ceased and when the EIS measurement is initiated. This effect makes resolving the spectral components of each time constant problematic. Nevertheless, since it is evident that the diffusional component of the EIS response dominates the spectra toward low frequencies, model calculations are in the present case based upon the generalized, finite-length Warburg impedance, which is used to describe one-dimensional diffusion of a chemical species (*i.e.*, ion or molecule) in solution, and is conventionally written as follows:

$$Z_W(j\omega) = R_D \frac{\tanh\left[(js)^\phi\right]}{(js)^\phi} \tag{6.4}$$

Where $s = l^2(\omega/D)$, l is the diffusion length of the electrode, D is the diffusion coefficient of the diffusing species, and the diffusion resistance, R_D, is determined from the low frequency limit of $Z_W(j\omega)$. The parameter, ϕ, varying as $0 \leq \phi \leq 1$ is the angle of the impedance in the

6-29

complex plane and for non-distributed, ideal diffusion is equal to 0.5 (*i.e.*, 45°). When *l* is infinitely large, the hyperbolic tangent term approaches unity, and Equation 6.4 reduces to the infinite-length Warburg impedance [6.10].

The impedance response of titanium alloy in the present experiment can best be described by combining the Warburg impedance function of Equation 6.4 with the effects of the interfacial capacitance of the electrical double layer, C_{dl}, formed at the surface of the oxide coating, and with the effects of the polarization resistance, R_p, of the surface oxide itself. This convoluted model was used to derive the implicit damage parameter, $1/R_{ct}$, concerned only with the Warburg component, since the parallel combination of C_{dl} and R_p was difficult to resolve. The evolution of $1/R_{ct}$ with incremental fatigue damage is shown in Figure 6-28 along with the complete equivalent circuit diagram of the model.

Although the estimates of model parameters were acceptable (*i.e.*, <10% coefficient of variation), a monotonic correlation between the stated damage parameter and incremental fatigue damage, as has been demonstrated for the bare aluminum and steel alloys, is not evident for titanium alloy under the present experimental conditions. The effects of the rapid re-passivation kinetics for this alloy, the cell configuration employed, and the time elapsed between the cessation of mechanical fatigue and when the EIS measurement was initiated, prohibited the EIS methodology from capturing the nascent reactivity of the induced damage state at each increment. Those effects are revealed in Figure 6-28 by noting that the values of the damage parameter are remarkably consistent in distinctly different fatigue life regimes.

The fact that the model parameter, ϕ, of Equation 6.4 deviated markedly from ideality (~0.8 vs. 0.5) is relevant to the argument that the experimental conditions and configuration of the electrochemical cell are not entirely suitable for probing the state of fatigue damage in this alloy. Over the long distance scales of the present cell configuration, the actual effects of fatigue damage on the nascent, ideal transport properties of the interface are averaged-out to the extent that the method becomes insensitive to the surface state. This averaging-out effect is further augmented by the rapid re-passivation that occurs to the surface state. Based upon these notions,

significant improvements in the EIS methodology for titanium alloy are anticipated with the advent of an electrochemical transducer specifically designed for localized measurements.

6.8   Concluding Remarks

The results of the measurements presented in this section clearly indicate that EIS can be used as a complementary technique of EFS to evaluate the progression of fatigue damage both in coated and bare materials. In the case of bare materials, the main limitation arises from the effects of the surface film in the impedance response. For the case of 7075 Al alloys, the time dependent effect, which is related to the lack of complete passivation by the initial surface prior to fatigue loading, requires a correction for these effects in order to correlate the value of the impedance parameters with the progression of fatigue damage. The simplest approach to overcome this problem appears to be a modification of the electrolyte composition. Another possibility, without changing the composition of the electrolyte, is to conduct the tests at higher anodic potentials. For example, the impedance response was shown to exhibit far more sensitivity to fatigue damage at a potential of 0.5 V_{SCE} than at lower values, as clearly illustrated in Figure 6-13.

In the case of 4130 steel, an effect opposite to that observed for 7075 Aluminum appears to be a challenge. The initial surface state is highly passive as revealed by the high value of the impedance at low frequencies, and repassivation of the surface state after incremental fatigue damage is very fast. In one case, monotonic increases in the impedance damage parameters $1/R_p$ and $1/R_{ct}$ were observed with incremental fatigue damage by acquiring EIS data at intervals during which the specimen was not under cyclic loading. However, in a second case, the acquisition of EIS data during cyclic loading was shown to increase the sensitivity of those parameters as a function of incremental fatigue damage. Unfortunately, a limited number of tests were conducted under that condition, and replicate experiments performed under the condition of interrupted cyclic loading exhibited undesired variability. This variability is likely due to the rapid repassivation of the surface microstructure of steel, under the conditions of constant polarization. More specifically, crucial information about the state of damage is lost between the time cyclic loading is ceased and when the EIS measurement is initiated.

The use of EIS measurements in the case of Ti-6Al-4V is even more difficult than that for 4130 steel because the repassivation of Ti alloys is faster that that of steel. As in the case of steel, the extremely low passive dissolution requires that measurements of the impedance be conducted at very low frequencies, typically less than 0.01 Hz. This procedure is extremely time consuming. However, modifications can be adopted, such as acquiring data at limited number of frequencies, to reduce the overall acquisition time. Alternatively, full-frequency EIS measurements based upon white-noise signal injection and fast Fourier transform (FFT) deconvolution might provide a convenient, yet unexplored, solution.

The implication of the rapid repassivation effect for steel and titanium alloys in terms of the EIS experimental method and its applicability to periodic monitoring of aircraft alloys of this sort can be generalized in the following way. The electrochemical state of the local microstructure of the system as a consequence of fatigue damage must be preserved to the extent that the nascent reactivity of the system as probed by EIS can be adequately discriminated. In that context, the electrochemical conditions of the present experiments, which include continuous exposure of the specimen to the electrolyte environment at a constant polarization potential, defeat the intent of the EIS method. That is because the electrochemical state of the microstructure is altered through rapid repassivation before it can be probed by the EIS measurement. For these alloys, therefore, a causal relationship between fatigue damage parameters and incremental fatigue damage might be better correlated under experimental conditions that closely mimic periodic inspection of a structure than the conditions used in the present case.

In summary, EIS appears as a valuable technique to follow the progress of fatigue damage in aircraft components. However, additional work needs to be done to eliminate some of problems discussed above. The technique appears to be very promising for coated 7075 Aluminum, particularly primer coated specimens. Testing of specimens with good quality coatings is necessary to build a solid database that can be used for comparison with components exhibiting coating defects.

6.9   References

6.1   Mansfeld, F., Kendig, W., and Tsai, S., "Evaluation of Corrosion Behavior of Coated Metals with AC Impedance Measurements," *Corrosion-NACE* (1982), 38(9), 478-485.

6.2   Lillard, R. S., Moran, P.J., and Isaacs, H.S., "A Novel Method for Generating Quantitative Local Electrochemical Impedance Spectroscopy," *J. Electrochem. Soc.* (1992), 139(4), 1007-1012.

6.3   Cole, K. S., and Cole, R. H., "Dispersion and Absorption in Dielectrics I. Alternating Current Characteristics," *J. Chem. Phys.* (1941), 9, 341-351.

6.4   Liu, S. H., "Fractal Model for the ac Response of a Rough Interface," *Phys. Rev. Lett.* (1985), 55(5), 529-532.

6.5   Sugimoto, K., Matsuda, S., Ogiwara, Y., and Kitamura, K., "Microscopic Ellipsometric Observation of the Change in Passive Film on 18Cr-8Ni Stainless Steel with the Initiation and Growth of Pit," *J. Electrochem. Soc.*, (1985), 132 (8), 1791-1795.

6.6   Gabrielli, C., *Identification of Electrochemical Processes by Frequency Response Analysis*, Technical Report No. 004/83, monograph, Solartron Instruments, August 1984, 59-67.

6.7   Beck, T.R., "Techniques for Studying Initial Film Formation on Newly Generated Surface of Passive Metals," *Electrochemical Techniques for Corrosion*, R. Baboian, ed. National Association of Corrosion Engineers, Houston, TX, pp. 27-34, 1978. (and listed references).

6.8   Shibata, T., and Fujimoto, S., "Straining Electrode Behavior of Pur Iron in High Temperature and High Pressure Aqueous Solution," *Trans. Japan Institute Metals* (1984), 28, 553-560.

6.9   Carranza, M.R., and Galvele, J. R., "Repassivation Kinetics in Stress Corrosion Cracking I. Type 304 Stainless Steel in Choloride Solutions," *Corrosion Sci.* (1988), 28, 233-250.

6.10   Macdonald, R. J., and Johnson, W. B., "Physical and Electrochemical Models," *Impedance Spectroscopy: Emphasizing Solid Materials and Systems*, Ed. J. Ross Macdonald, USA : John Wiley & Sons, Inc., 1987, 84-132.
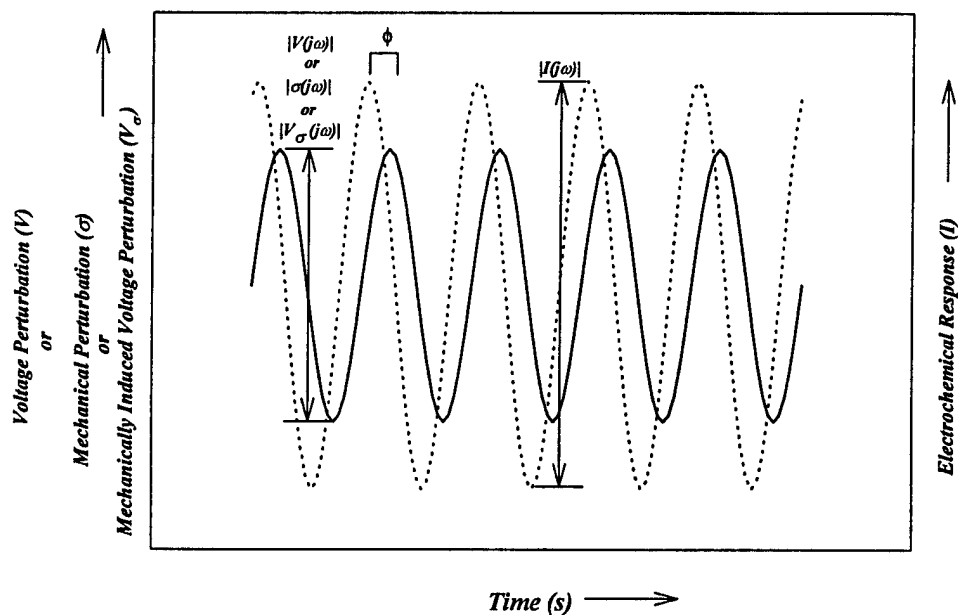
(a)
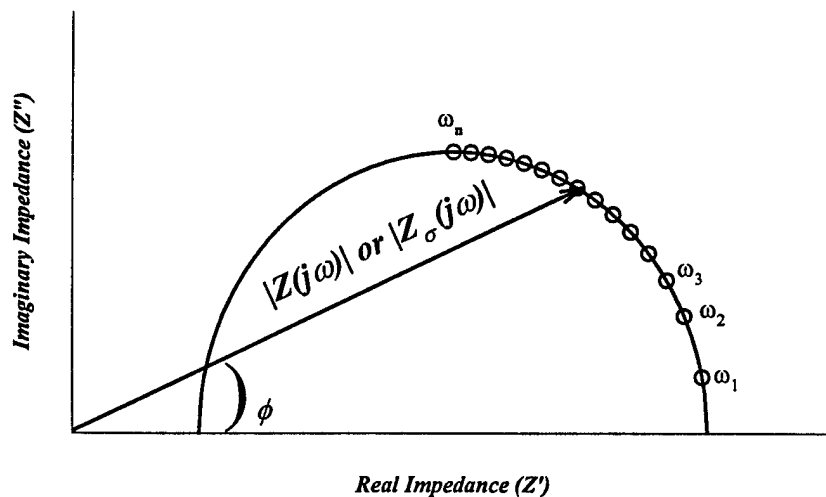
(b)

Figure 6-1. Analog signal (a) and vectorial representation (b) of the electrochemical ($Z(j\omega)$) and electromechanical (Z_σ ($j\omega$)) impedance which constitute the underlying metrics of the methodology. The angle ϕ is the phase shift between the perturbation and response of the system and the impedance arc represents an ideal interface.
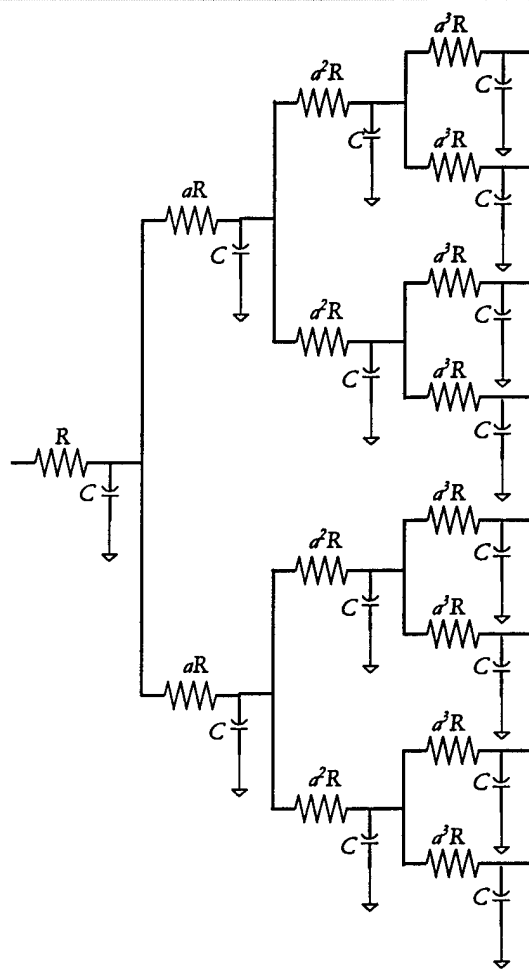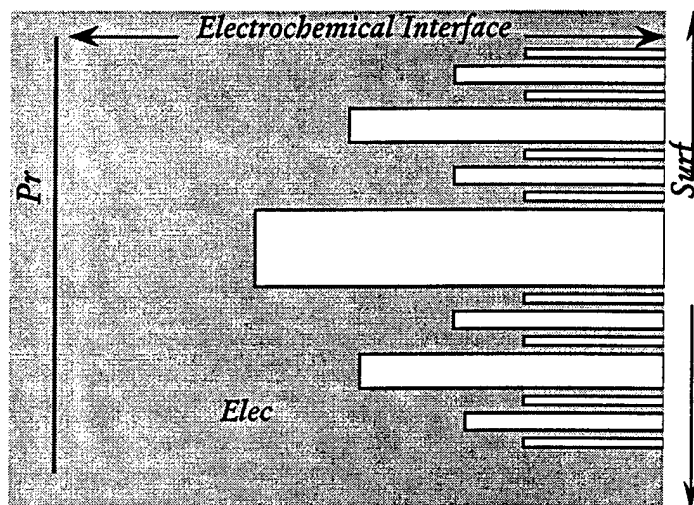
Figure 6-2. Cantor bar model of a fractal interface showing branching (n=4) of surface structure, and the equivalent electrical circuit used for numerical simulations.
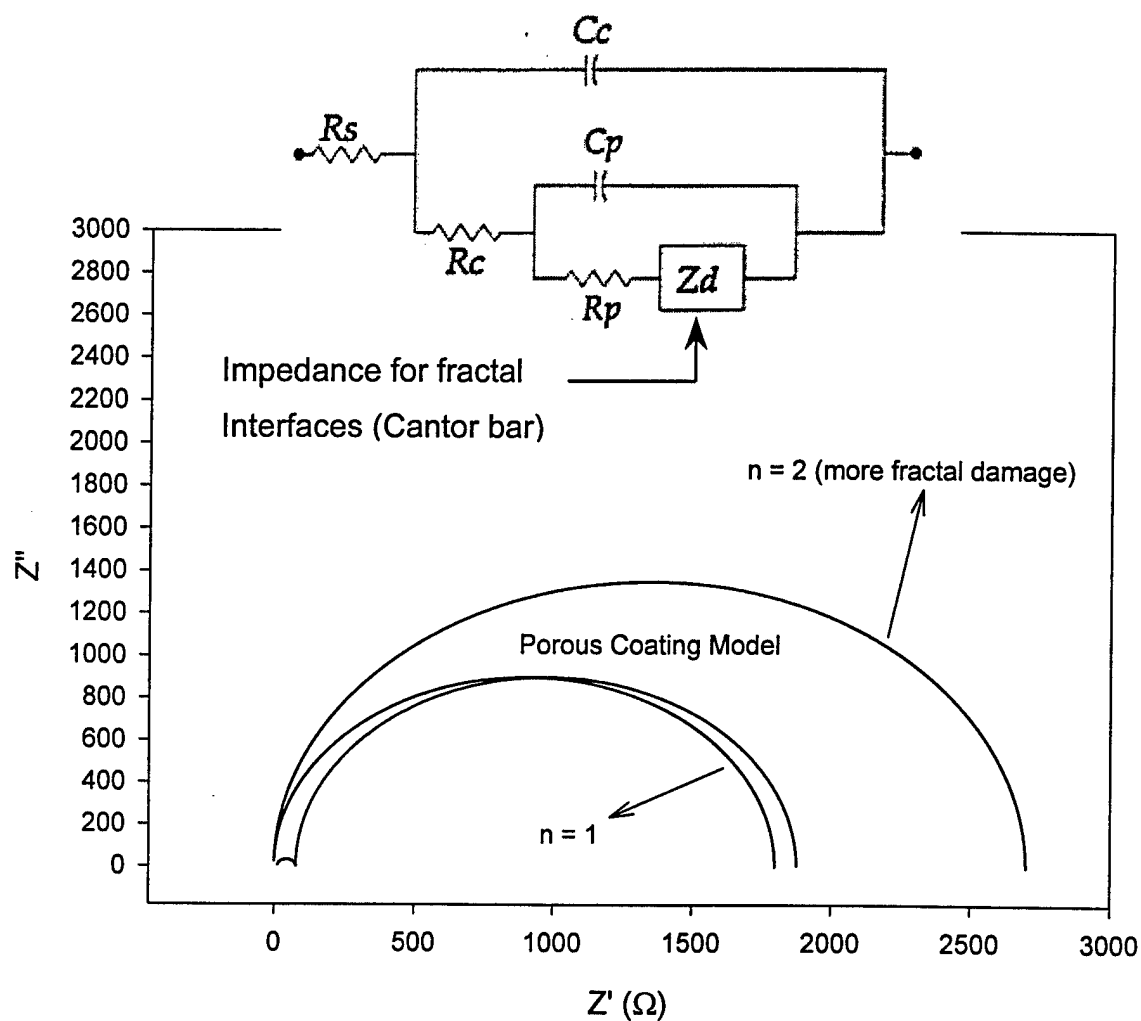
Figure 6-3. Numerical simulation of the Cantor bar fractal interface comprising the Z_d element of the circuit for discrete levels of branching (n=1,2) and arbitrary scaling. The complete circuit, which is used to model a substrate with a porous coating, also is simulated. In this case, the Z_d element is represented by the parameterized constant phase element with $0 < \beta < 1$ (Equation 6.2).
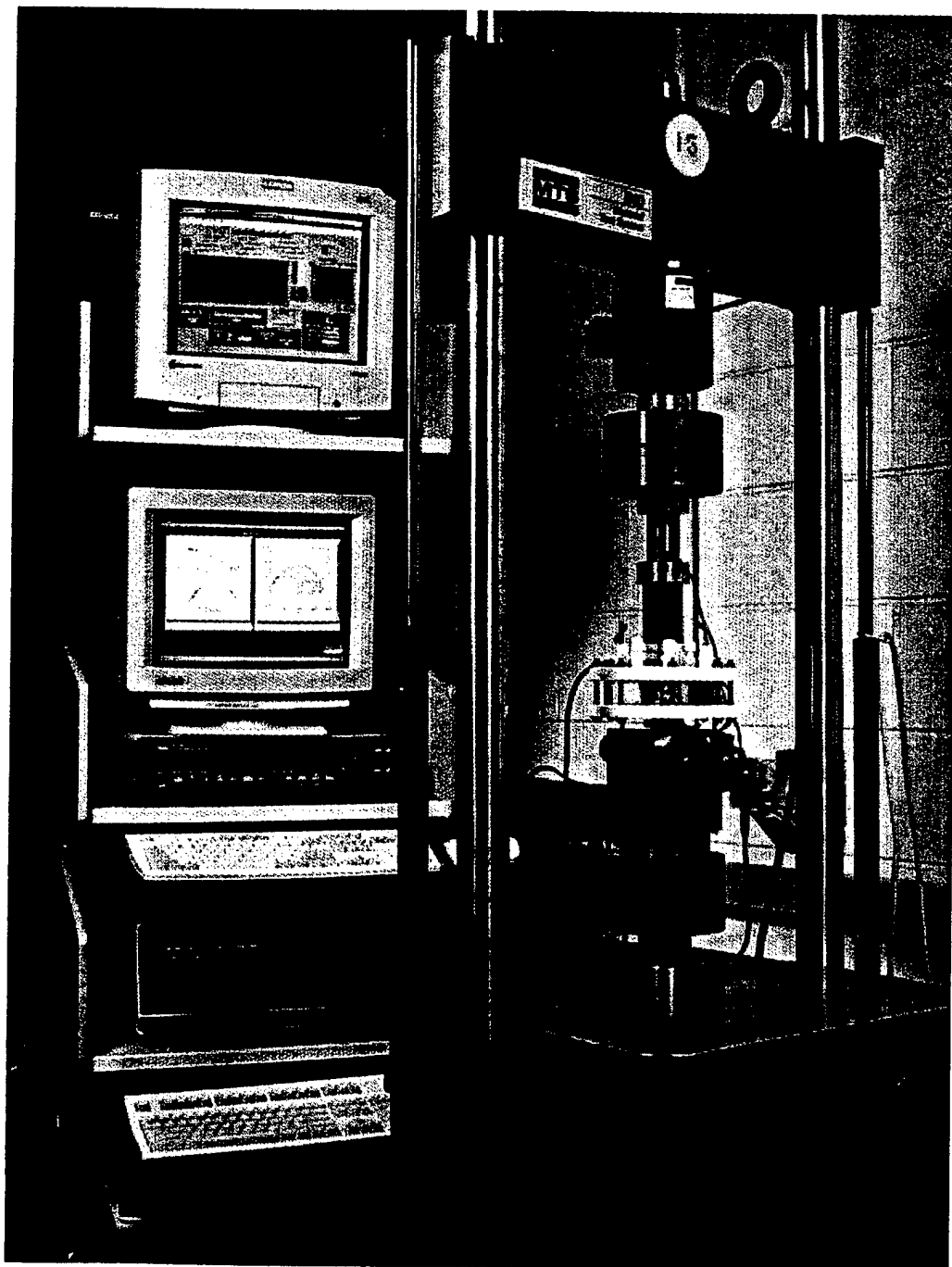
Figure 6-4. Schematic diagram showing the electrochemical instrumentation used for EFS and EIS measurements.

AJ-35C-2A-F

-Z"(Ω) vs **Z' (Ω)**

Legend:
- Pre-Fatigue
- 7% (of Life)
- 15%
- 22%
- 29%
- 44%
- 59%
- 73%
- 88%

(a)

Phase Angle (θ) / **IZI (Ω)** vs **Frequency (Hz)**

(b)

Figure 6-5. Electrochemical impedance response of aircraft aluminum alloy (7075 Al) following progressive states of mechanical fatigue damage, as indicated, for a specimen subjected to the electrochemical cell's open circuit potential (OCP) during fatigue. The specimen was interrogated intermittently, during the cessation of fatigue, with electrical voltage perturbations centered around a DC polarization potential of +300 mV vs. SCE . a) Real and imaginary projection of the impedance spectrum (Nyquist plot). b) Phase angle θ between voltage perturbations and current output, and modulus IZI versus frequency relationship of the impedance spectrum (Bode plot).

7075 Al R = -1 50 ksi 1 Hz +300 mV vs. SCE
OCP During Fatigue - EIS at Zero Load
Specimen Failure at 5463 Cycles
12-DEC-97

(a)

(b)
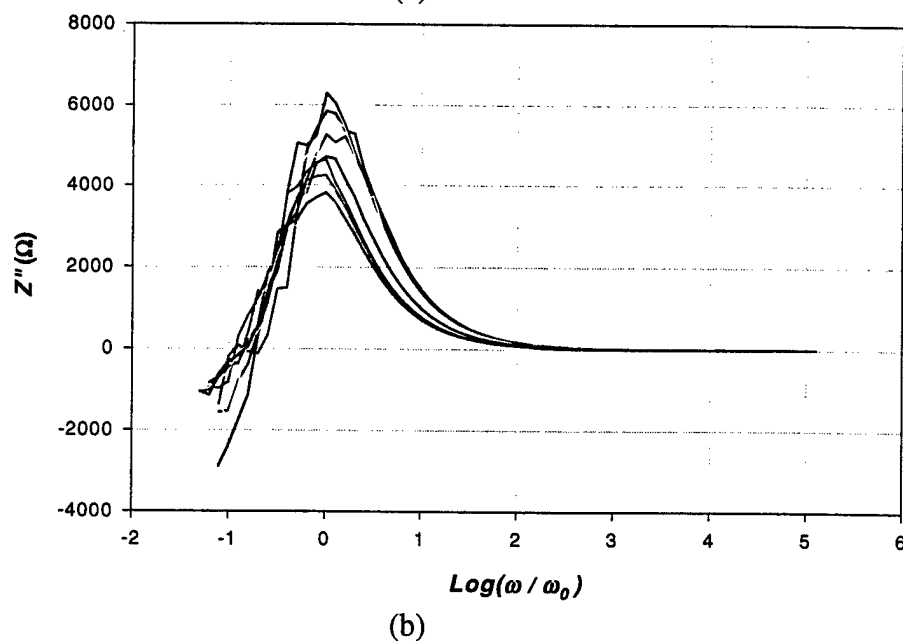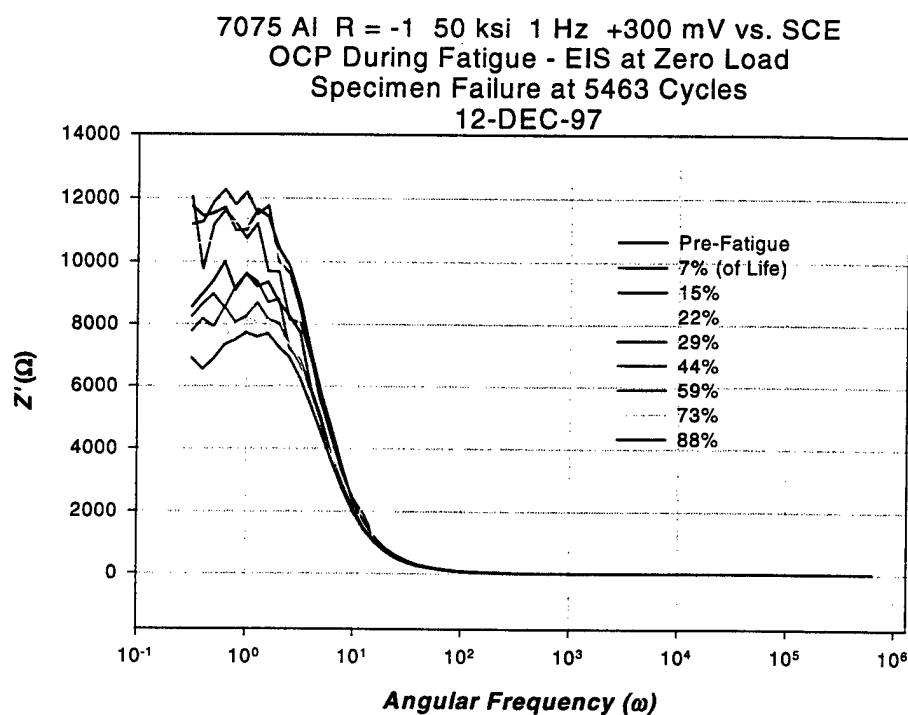
Figure 6-6. The Debye dispersion representation of the same experimental data as is shown in Figure 6-5. a) Real component of the electrochemical impedance versus angular frequency of the applied perturbations. b) Imaginary component of the electrochemical impedance versus log of the normalized angular frequency (normalized to the fundamental dispersion frequency).

7075 Al R = -1 50 ksi 1 Hz +300 mV vs. SCE
Constant Polarization - EIS at Zero Load
Specimen Failure at 5433 Cycles
31-DEC-97
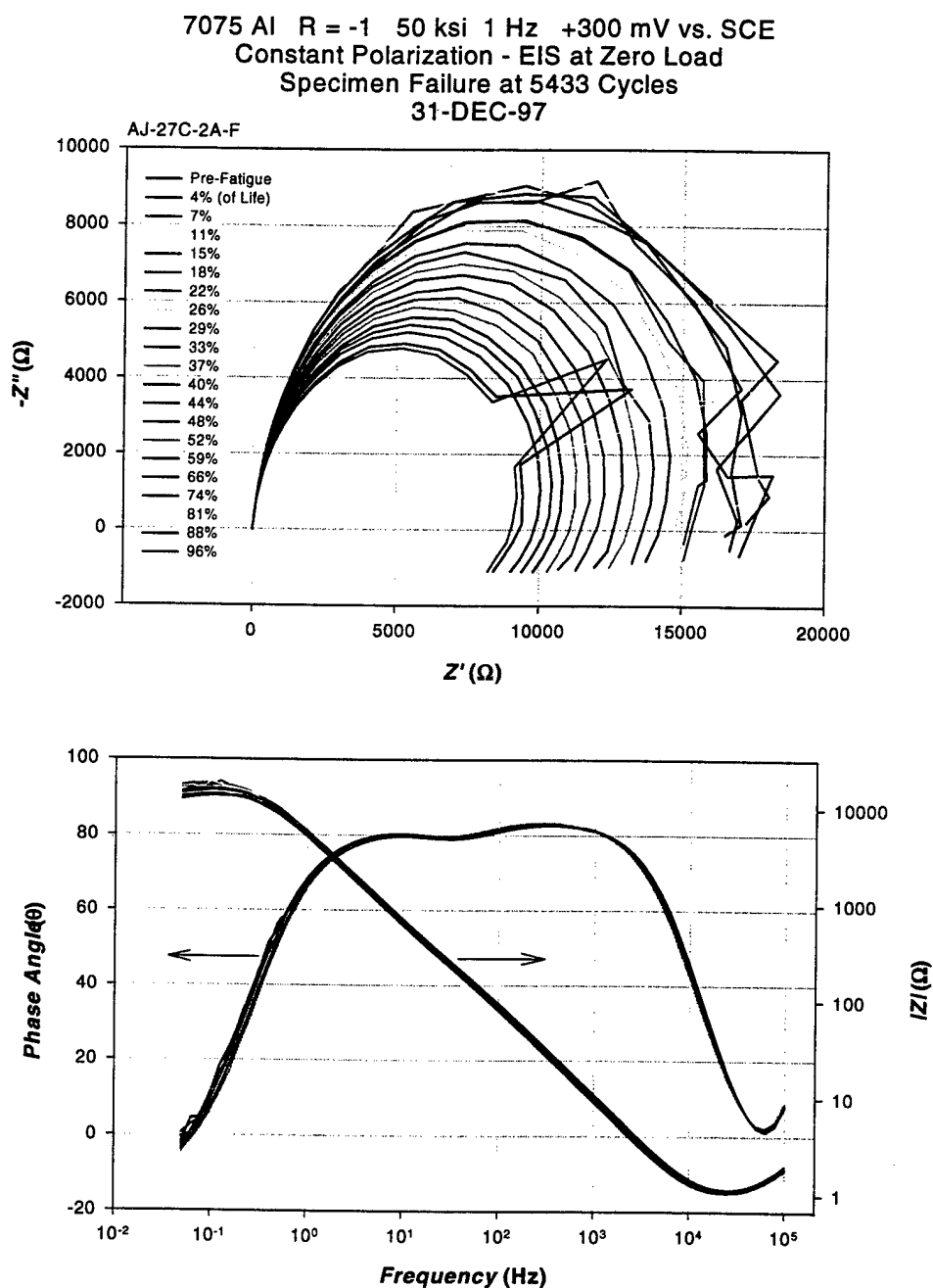
(b)

Figure 6-7. Electrochemical impedance response of aircraft aluminum alloy (7075 Al) following progressive states of mechanical fatigue damage, as indicated, for a specimen maintained at a DC polarization potential of +300 mV vs. SCE during fatigue. The specimen was interrogated intermittently, during the cessation of fatigue, with electrical voltage perturbations centered around the DC polarization potential. a) Real and imaginary projection of the impedance spectrum (Nyquist plot) b) Phase angle θ between voltage perturbations and current output, and modulus IZI versus frequency relationship of the impedance spectrum (Bode plot).

7075 Al   R = -1   50 ksi   1 Hz   +300 mV vs. SCE
Constant Polarization - EIS During Fatigue
Specimen Failure at 6725 Cycles
30-DEC-97
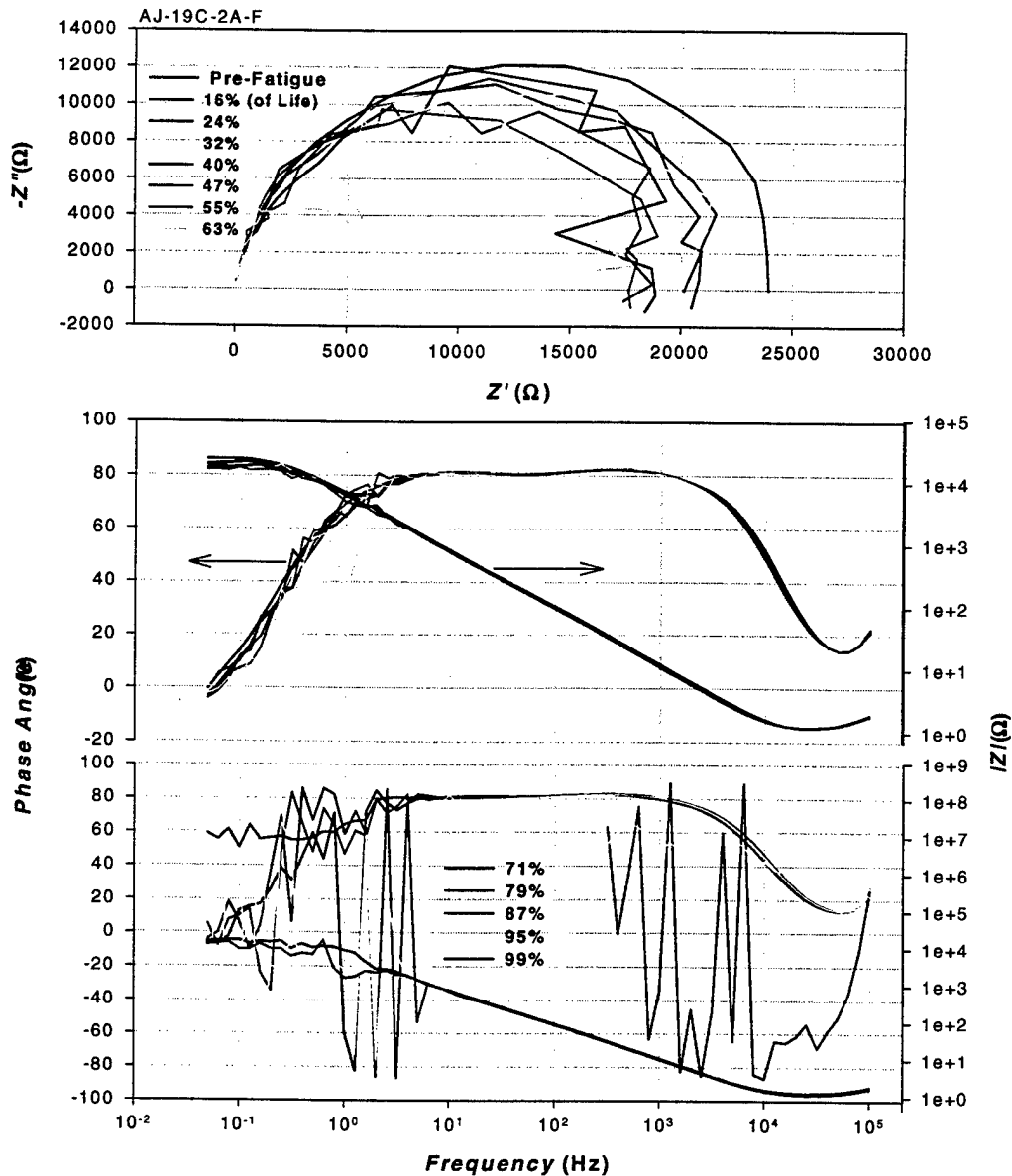
(b)

Figure 6-8. Electrochemical impedance response of aircraft aluminum alloy (7075 Al) following progressive states of mechanical fatigue damage as indicated. The specimen was interrogated intermittently, during mechanical fatigue, with electrical voltage perturbations centered around a DC polarization potential of +300 mV vs. SCE. a) Real and imaginary projection of the impedance spectrum (Nyquist plot). b) Phase angle θ between voltage perturbations and current output, and modulus |Z| versus frequency relationship of the impedance spectrum (Bode plot), showing effect of coupling between mechanical and electrical perturbations near the mechanical resonance frequency (1 Hz).

6-41
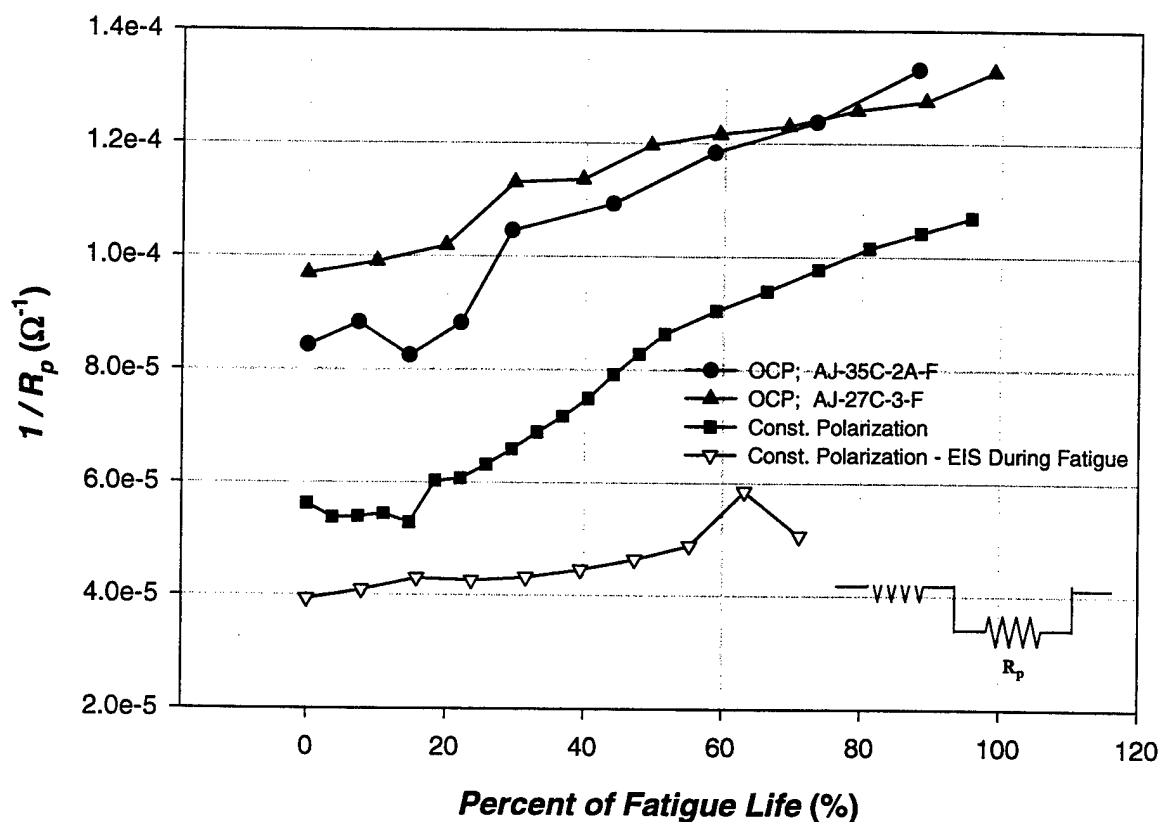
Figure 6-9. Evolution of the implicit fatigue damage parameter ($1/R_{p}$)) versus fatigue life for various experiments on aluminum alloy. The values of the implicit damage parameter for each progressive state of fatigue damage were derived from non-linear fits of the Cole-Cole distribution model to the impedance arcs of the experimental measurements. The electrical circuit analog of this model is shown.
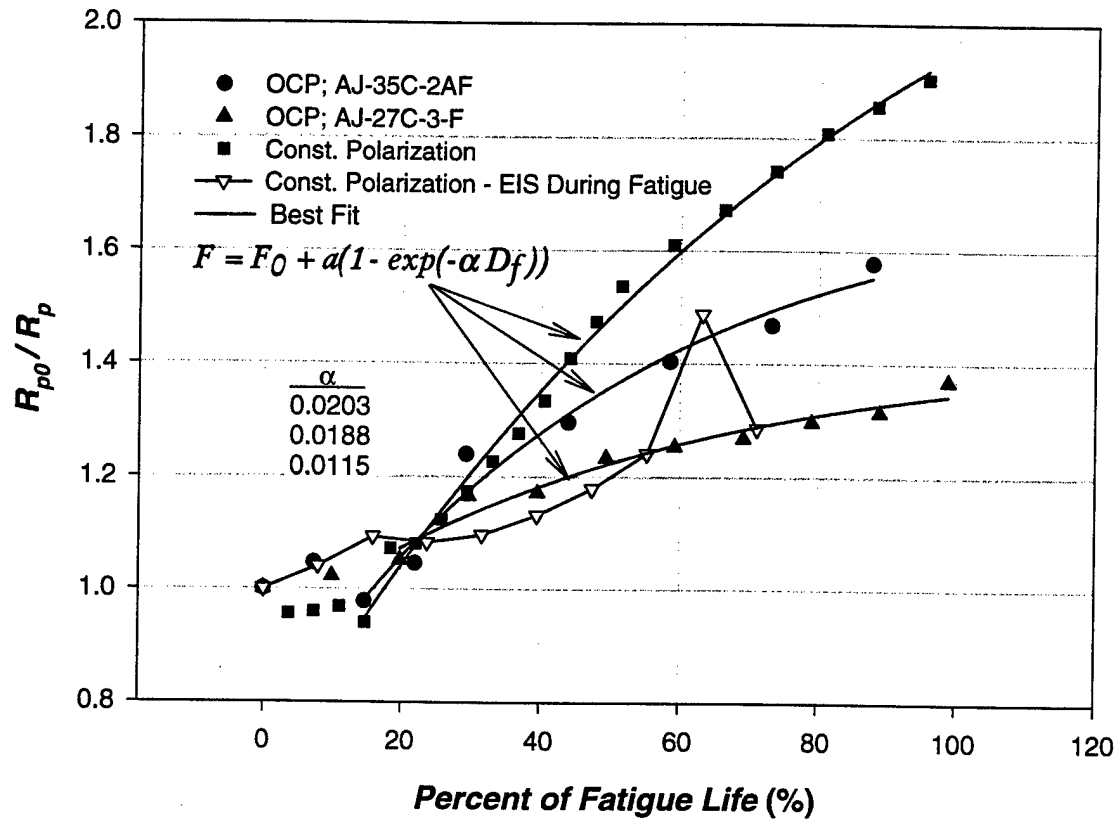
Figure 6-10. Evolution of the implicit fatigue damage parameters of Figure 6.10.1 normalized in each case to the corresponding pre-fatigue value (0%). Model function for exponential growth of implicit parameter and corresponding rate constants are shown on graph.
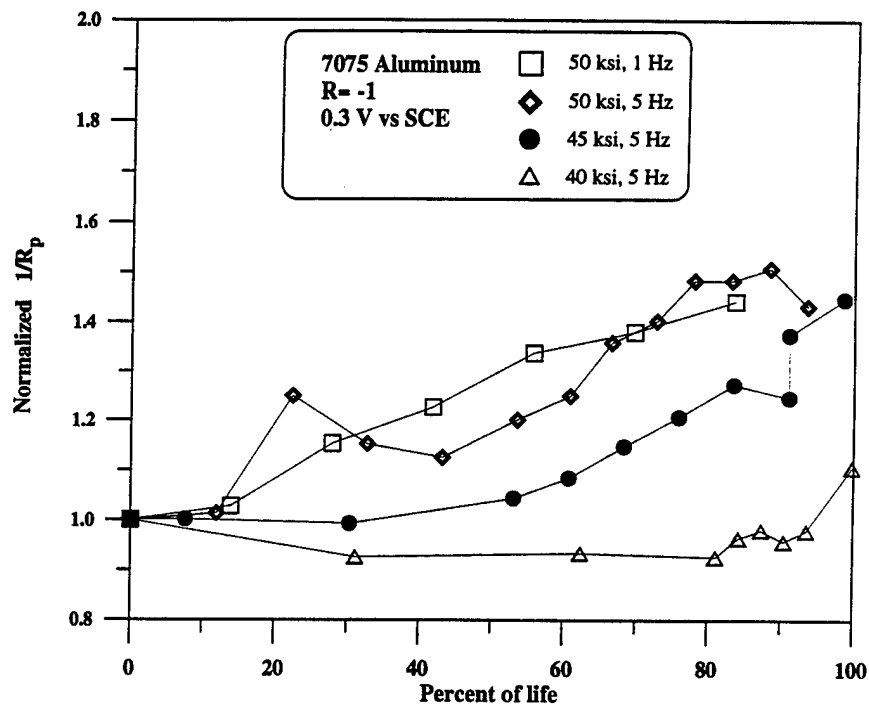
Figure 6-11. Variation of normalized fatigue damage parameter $1/R_p$ (R_{pO}/R_p) for 7075 aluminum as a function of percent of fatigue life for various values of the maximum stress.
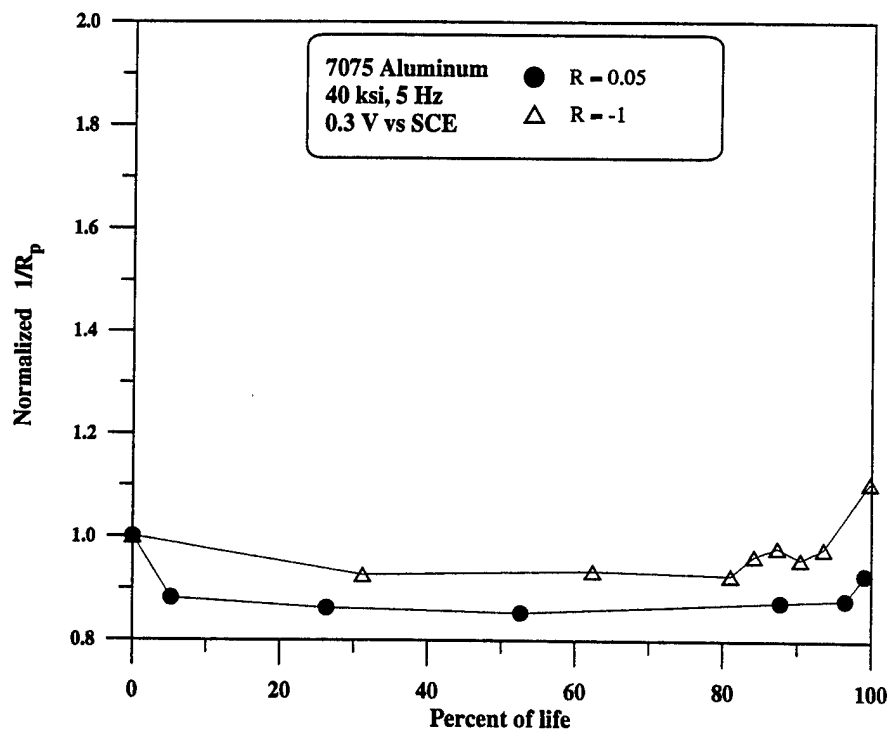
Figure 6-12. Variation of normalized fatigue damage parameter $1/R_p$ (R_{pO}/R_p) for 7075 aluminum as a function of percent of fatigue life for R = 0.05 and R = -1.
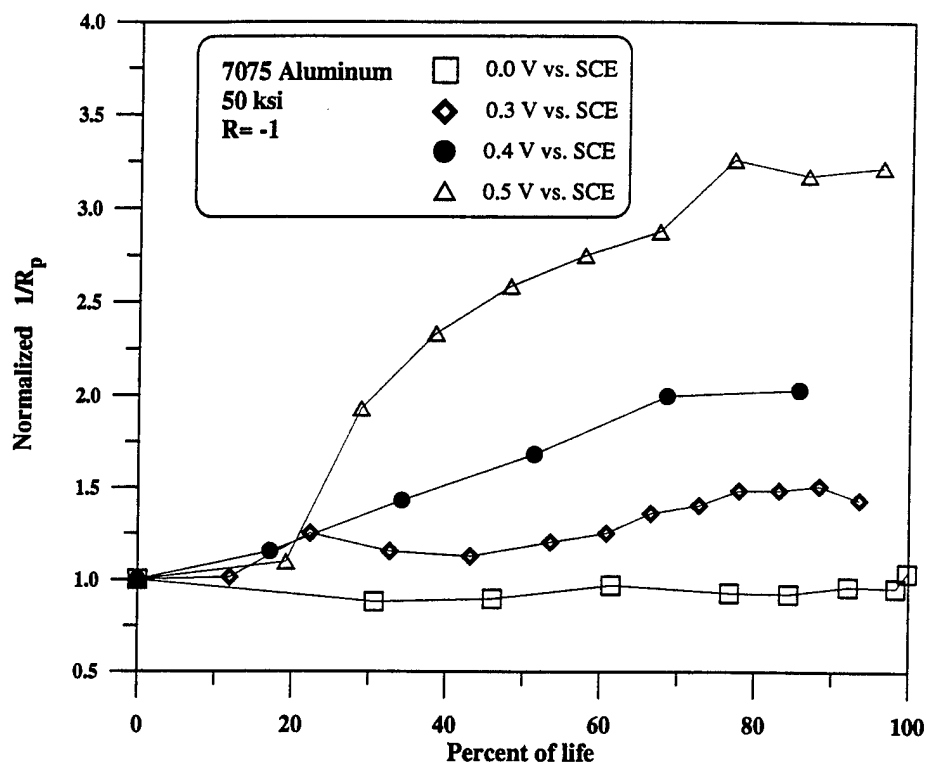
Figure 6-13. Effect of applied polarization potential on the variation of normalized fatigue damage parameter $1/R_p$ (R_{po}/R_p) for 7075 aluminum as a function of percent of fatigue life.
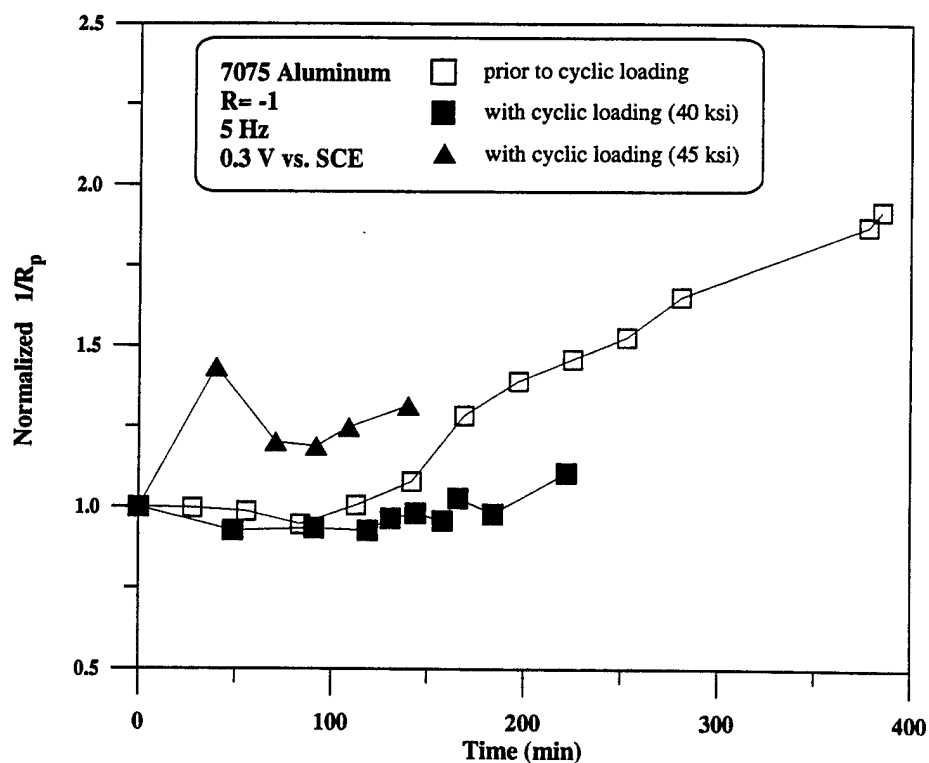
Figure 6-14. Variation of normalized fatigue damage parameter $1/R_p$ (R_{po}/R_p) for 7075 aluminum as a function of exposure time to the solution prior to cyclic loading and at different times during temporary interruption of cyclic loading.
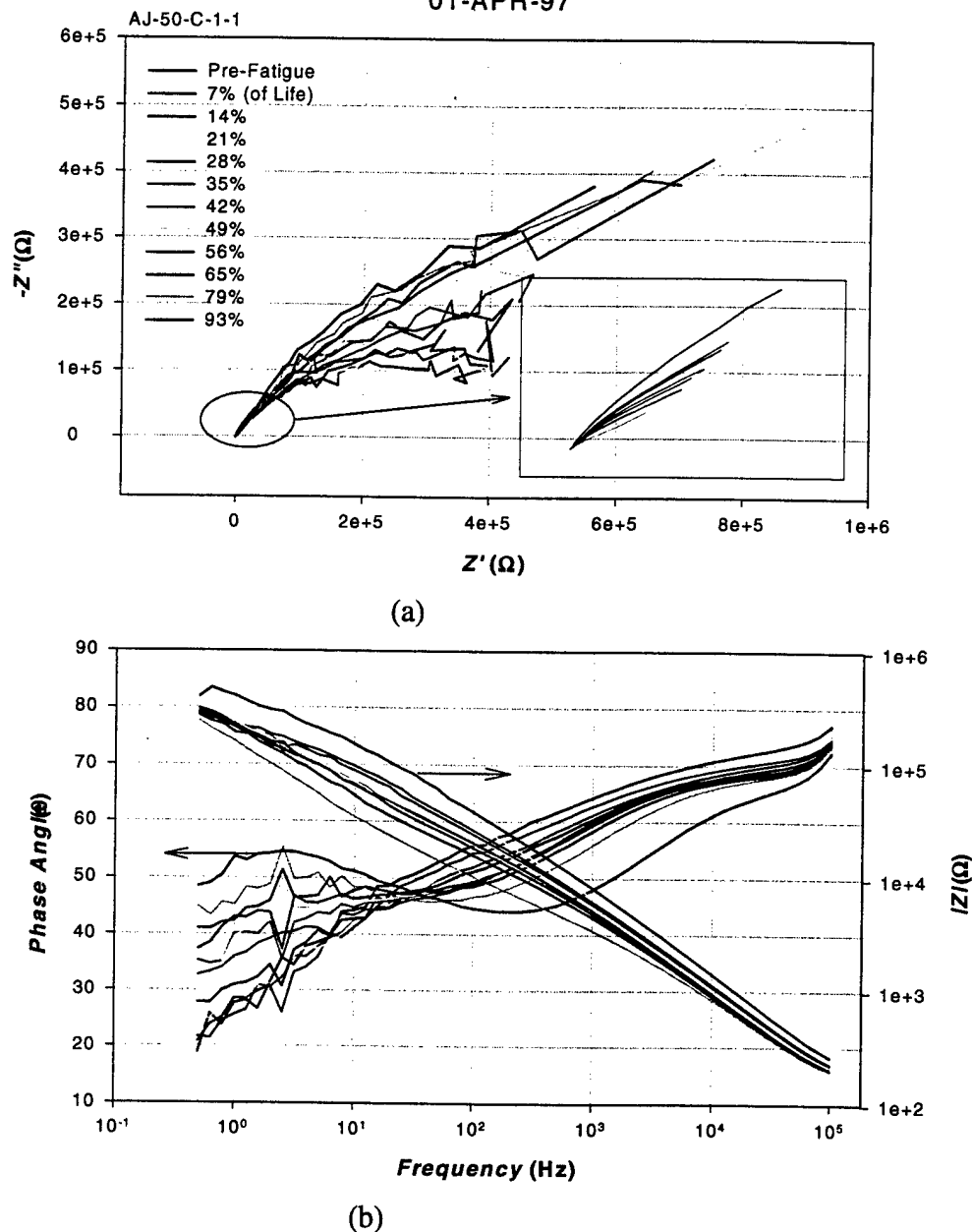
Figure 6-15. Electrochemical impedance response of primer coated aircraft aluminum alloy (7075 Al) following progressive states of mechanical fatigue damage, as indicated, for a specimen maintained at a DC polarization potential of +300 mV vs. SCE during fatigue. The coated specimen was interrogated intermittently as described previously. a) Real and imaginary projection of the impedance spectrum (Nyquist plot), showing and expansion of the high frequency limit (inset). b) Phase angle θ between voltage perturbations and current output, and modulus |Z| versus frequency relationship of the impedance spectrum (Bode plot).

Primer & Topcoat 7075 Al   R = -1   50 ksi   1 Hz   +300 mV vs. SCE
Constant Polarization - EIS at Zero Load
Specimen Failure at 9,819 Cycles
05-MAY-98
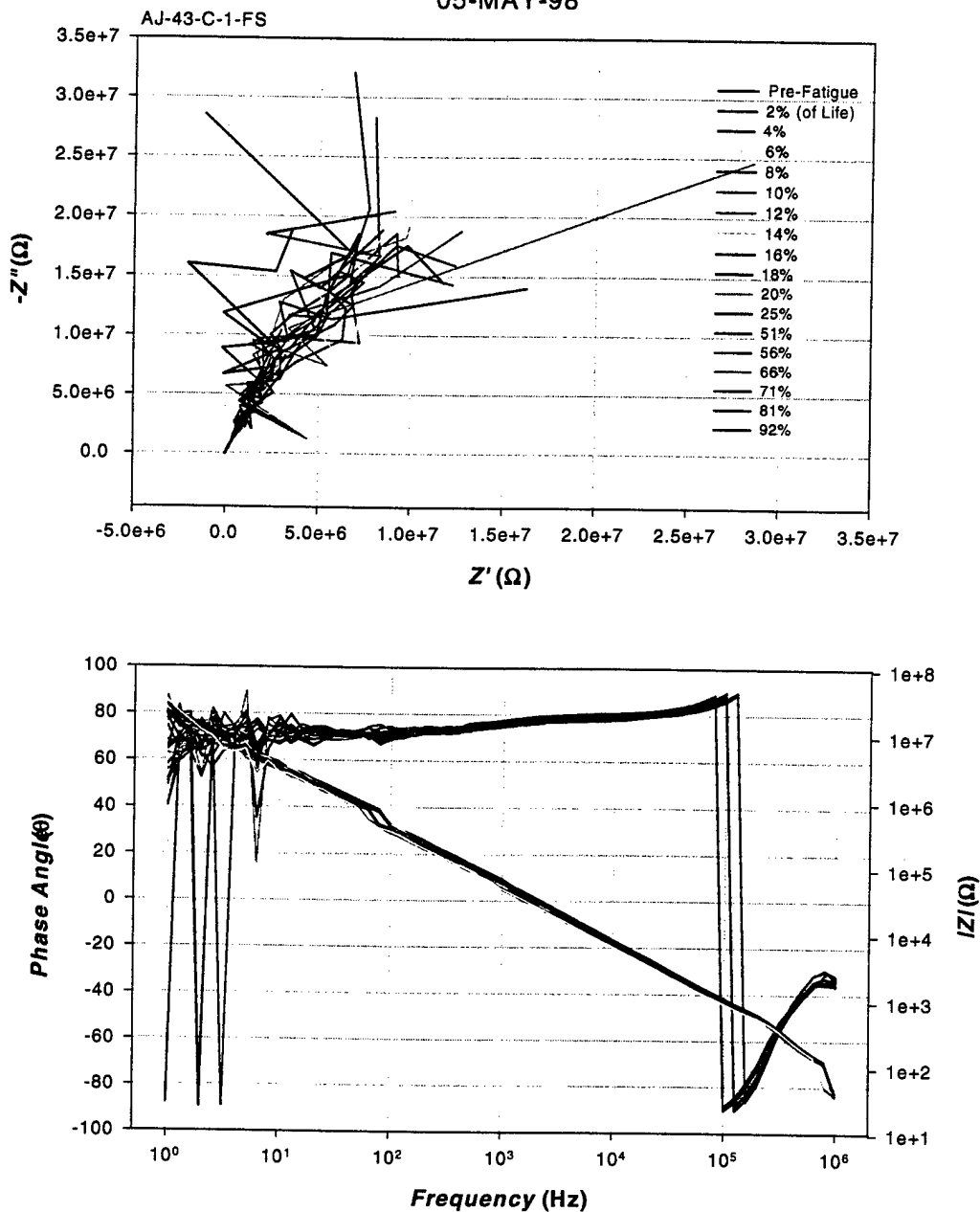
(b)

Figure 6-16. Electrochemical impedance response of coated aircraft aluminum alloy (7075 Al), primer and topcoat, following progressive states of mechanical fatigue damage, as indicated, for a specimen maintained at a DC polarization potential of +300 mV vs. SCE during fatigue. The coated specimen was interrogated intermittently as described previously. a) Real and imaginary projection of the impedance spectrum (Nyquist plot). b) Phase angle θ between voltage perturbations and current output, and modulus IZI versus frequency relationship of the impedance spectrum (Bode plot).

Primer Coated 7075 Al   R = -1   50 ksi 1 Hz   +300 mV vs. SCE
Constant Polarization - EIS at Zero Load
Specimen Failure at 11,375 and 9,836 Cycles
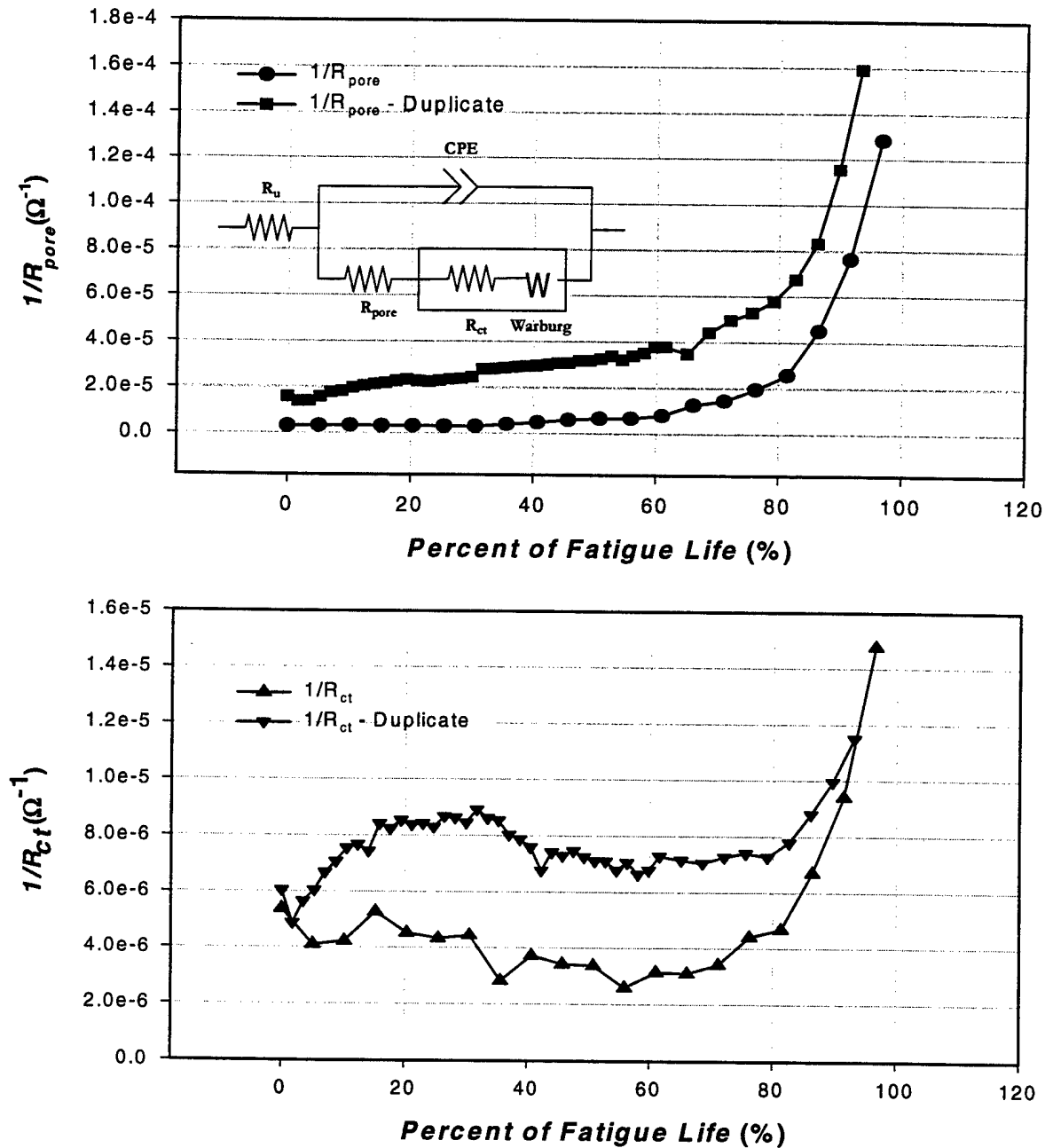
Figure 6-17. Evolution of implicit damage parameters ($1/R_{pore}$ and $1/R_{ct}$) following progressive states of fatigue damage for primer coated 7075 aluminum (duplicate experiments). The values of the implicit parameter were derived by fitting a two time-constant impedance model to the experimental data. The equivalent circuit analog of this model is shown.

Primer Coated 7075 Al   R = -1   50 ksi   1 Hz   +300 mV vs. SCE
Constant Polarization - EIS at Zero Load
Specimen Failure at 11,375 and 9,836 Cycles

$$F = a\, exp(\alpha D_f) + b\, exp(\beta D_f)$$

α	β
0.0168	0.1192
0.0130	0.1601
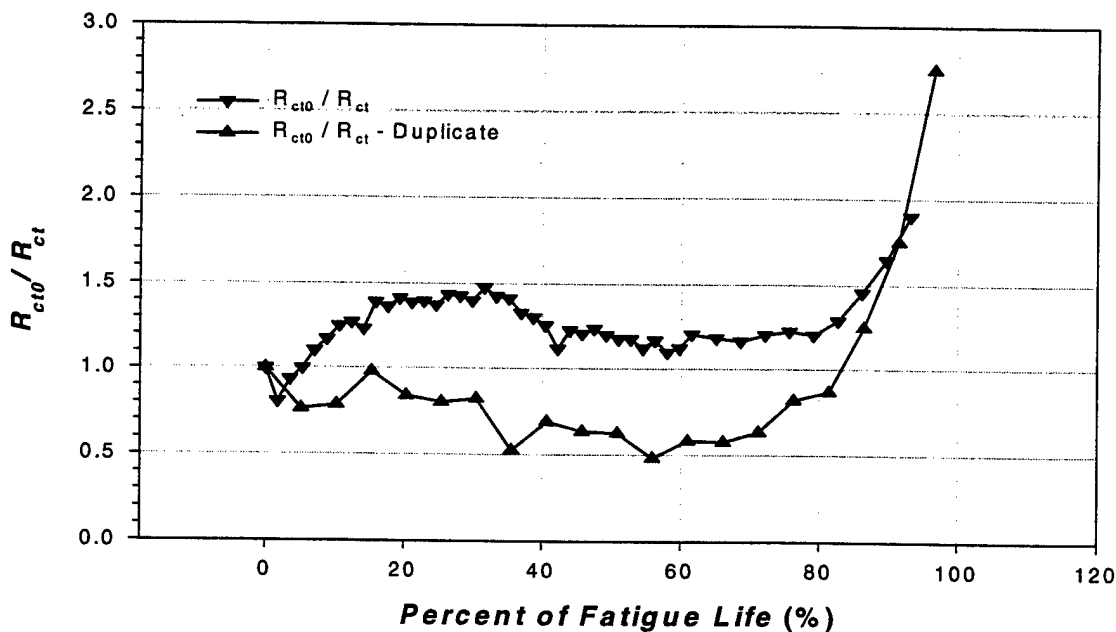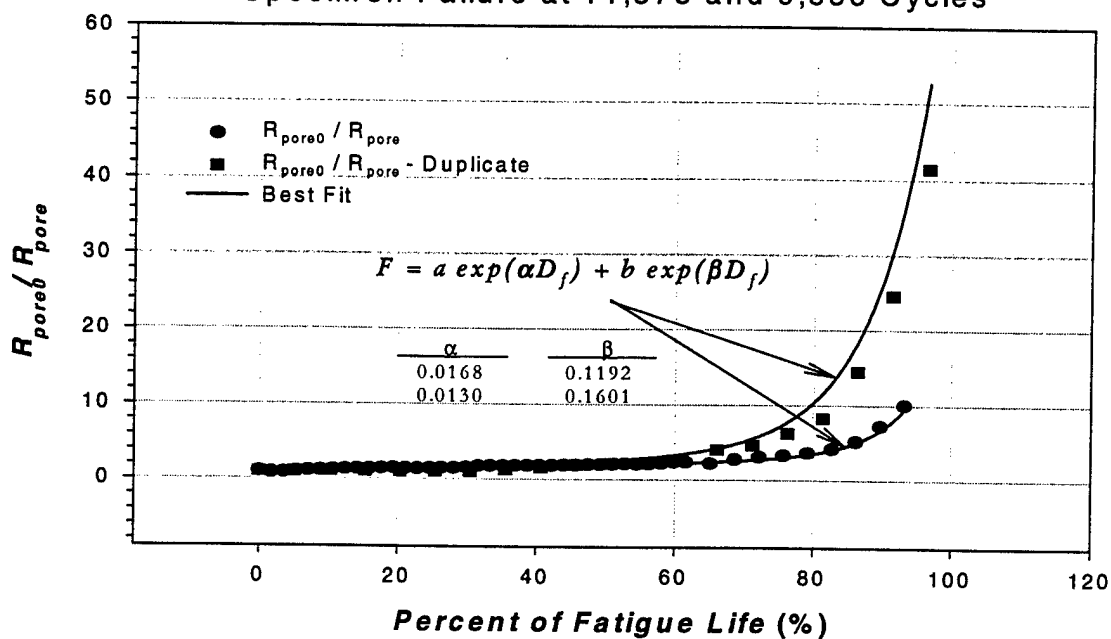
Figure 6-18. Evolution of the implicit fatigue damage parameters of Figure 6-17 normalized in each case to the corresponding pre-fatigue value (0%). Model function for biphasic exponential growth of implicit parameter and corresponding rate constants are shown in top panel.

6-49
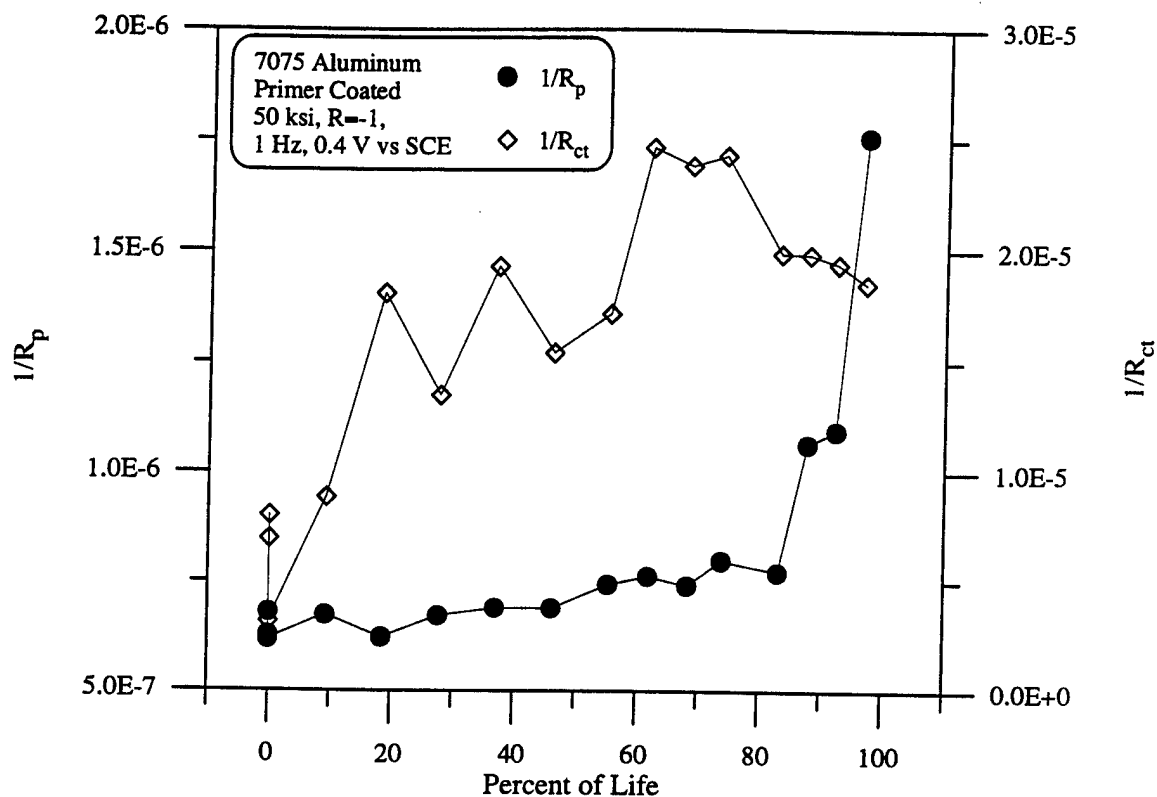
Figure 6-19. Variation of fatigue damage parameters $1/R_p$ and $1/R_{ct}$ for primer coated 7075 aluminum without coating defects as a function of percent of fatigue life.
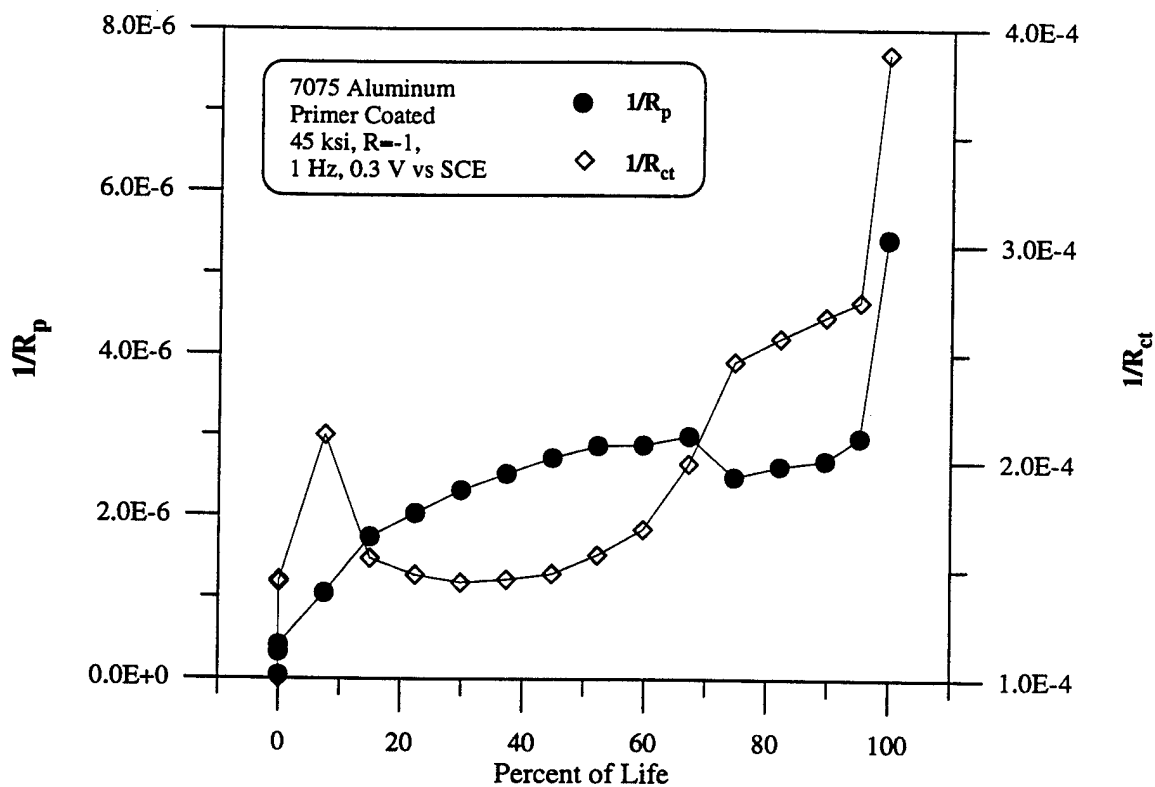
Figure 6-20. Variation of fatigue damage parameters $1/R_p$ and $1/R_{ct}$ for primer coated 7075 aluminum with coating defects as a function of percent of fatigue life.
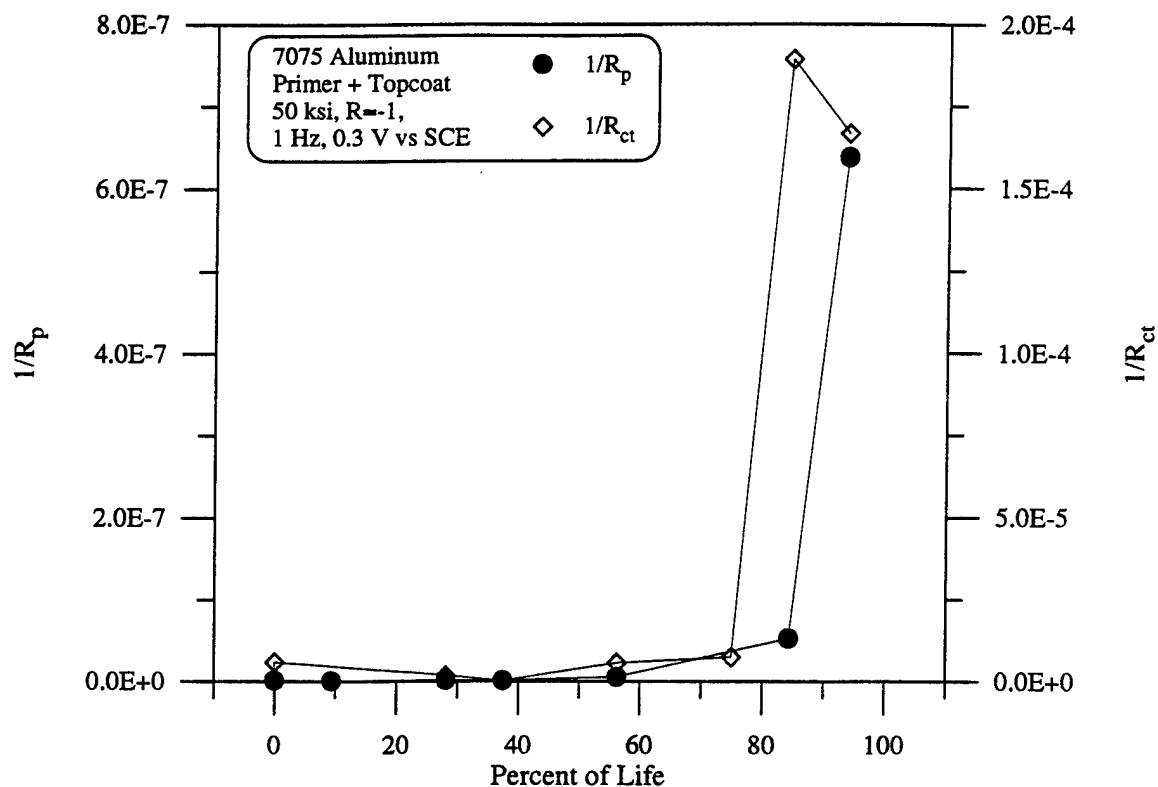
Figure 6-21. Variation of fatigue damage parameters $1/R_p$ and $1/R_{ct}$ for primer and top coated 7075 aluminum without coating defects as a function of percent of fatigue life.
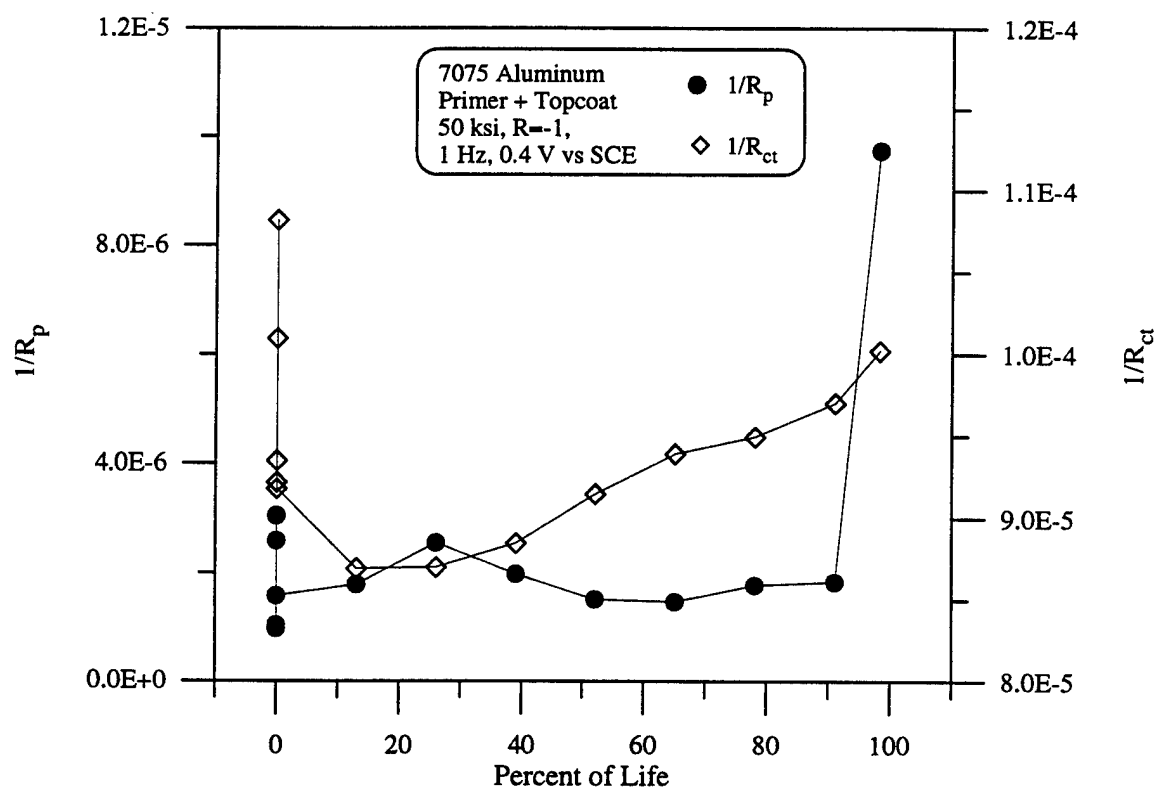
Figure 6-22. Variation of fatigue damage parameters $1/R_p$ and $1/R_{ct}$ for primer and top coated 7075 aluminum with coating defects as a function of percent of fatigue life.

Figure 6-23. Electrochemical impedance response of steel (4130) following progressive states of mechanical fatigue damage, as indicated, for a specimen maintained at a DC polarization potential of +400 mV vs. SCE during fatigue. The specimen was interrogated intermittently, during the cessation of fatigue, with electrical voltage perturbations centered around the DC polarization potential. a) Real and imaginary projection of the impedance spectrum (Nyquist plot), showing an expansion of the high frequency limit (inset). b) Phase angle θ between voltage perturbations and current output, and modulus |Z| versus frequency relationship of the impedance spectrum (Bode plot).

4130 Steel   R = -1   105 ksi   1 Hz   +400 mV vs. SCE
Constant Polarization - EIS at Zero Load
Specimen Failure at 13,735 Cycles

$F = F_0 + a(1 - exp(-\alpha D_f))$

$\alpha = 0.0487$
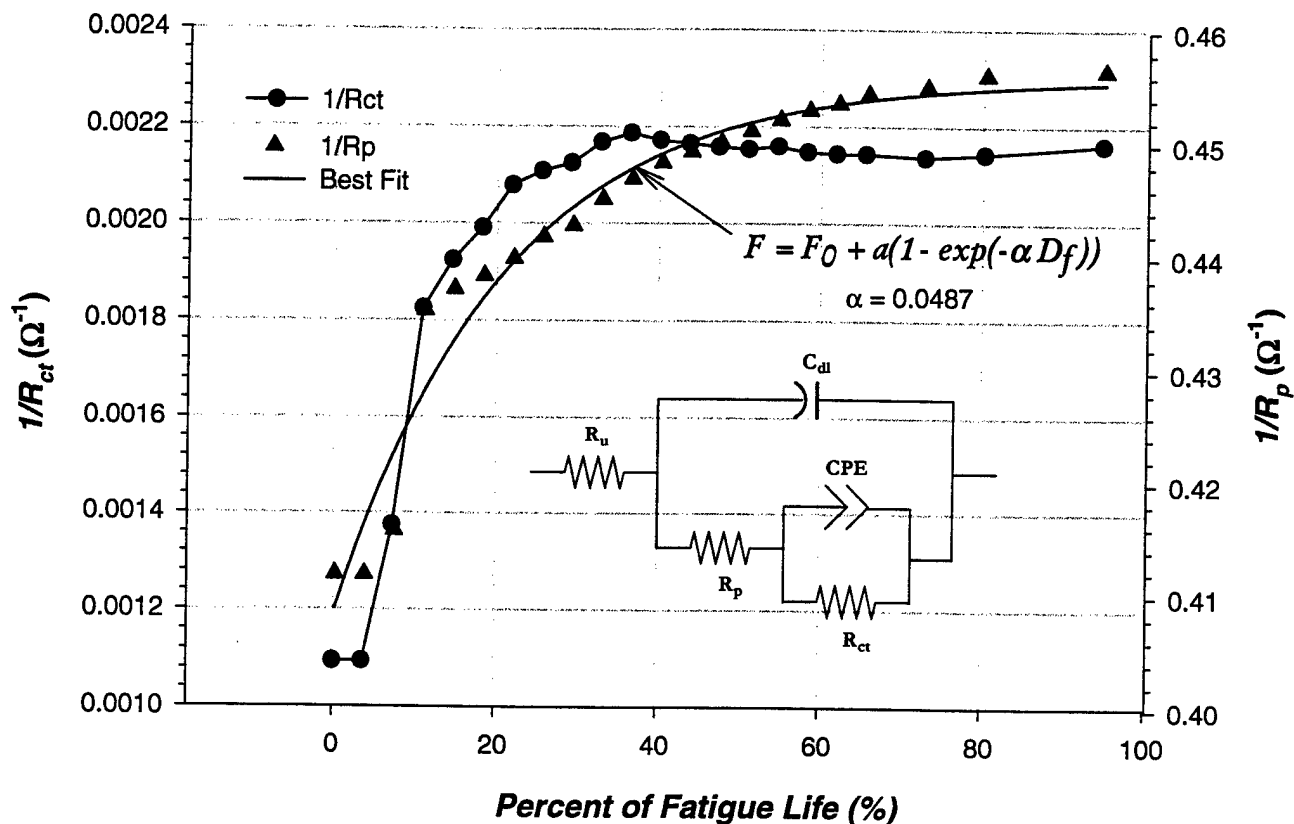
Figure 6-24. Evolution of implicit damage parameters ($1/R_p$ and $1/R_{ct}$) following progressive states of fatigue damage for steel alloy (4130). The values of the implicit parameters were derived by fitting a two time-constant impedance model to the experimental data. The equivalent circuit analog of this model is shown. Model function for exponential growth of implicit parameter and corresponding rate constant also are shown on graph.
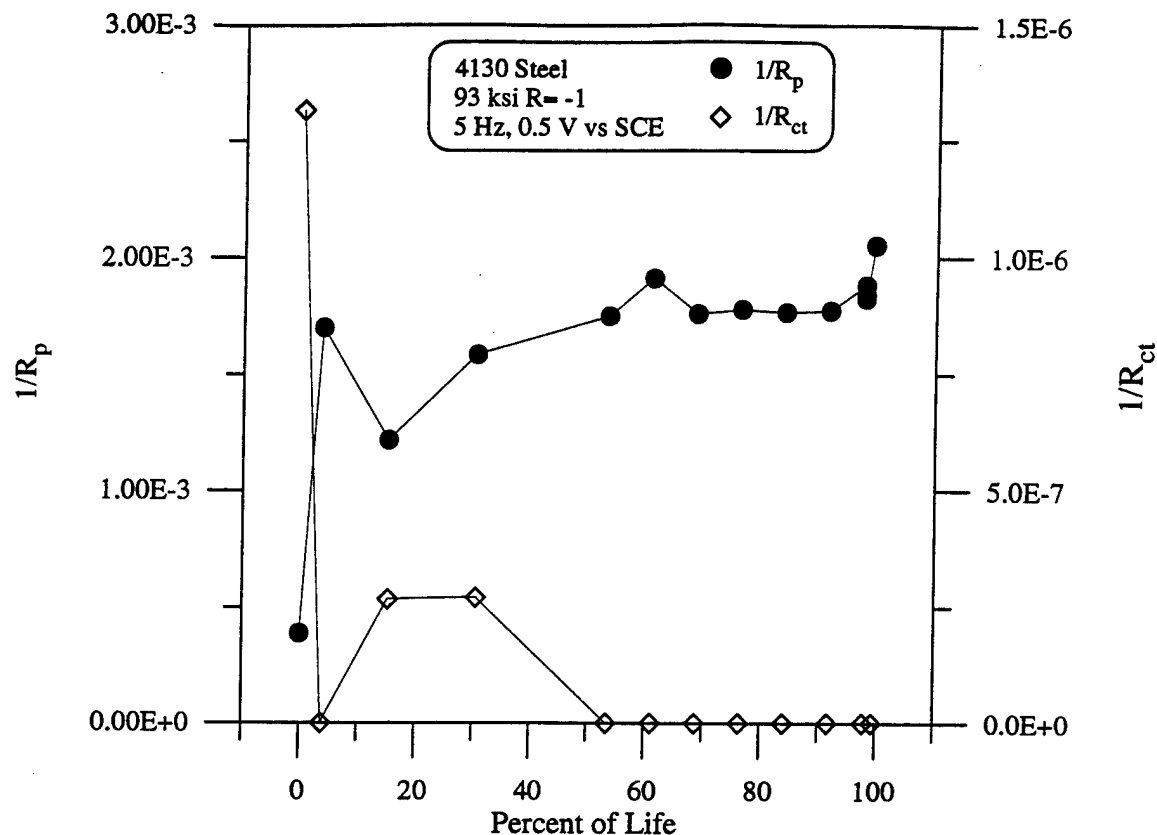
Figure 6-25. Variation of fatigue damage parameters $1/R_p$ and $1/R_{ct}$ for 4130 steel as a function of percent of fatigue life with temporary interruption of cyclic loading.
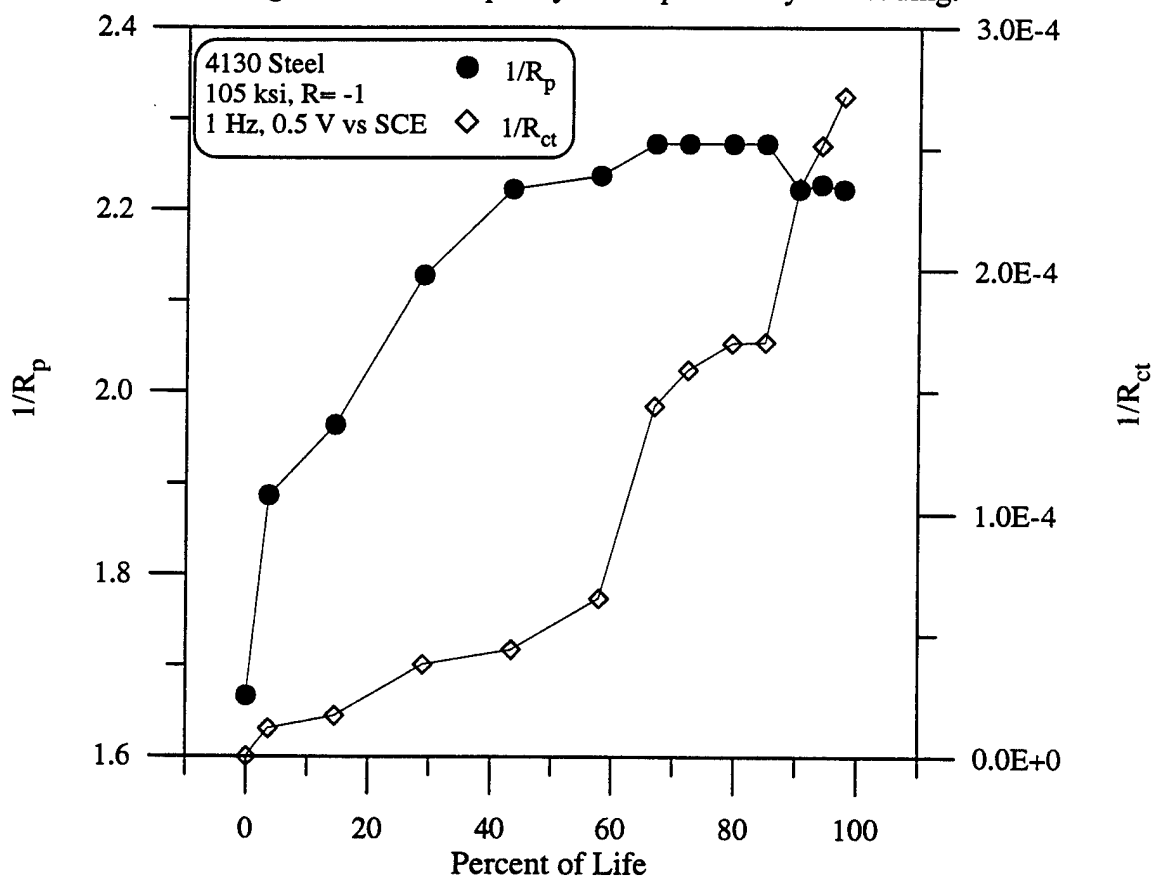
Figure 6-26. Variation of fatigue damage parameters $1/R_p$ and $1/R_{ct}$ for 4130 steel as a function of percent of fatigue life with continuous cyclic loading.

Ti64 R = -1 85 ksi 1 Hz +400 mV vs. SCE
Constant Polarization - EIS at Zero Load
Specimen Failure at 52,040 Cycles
04-FEB-98

(a)

(b)
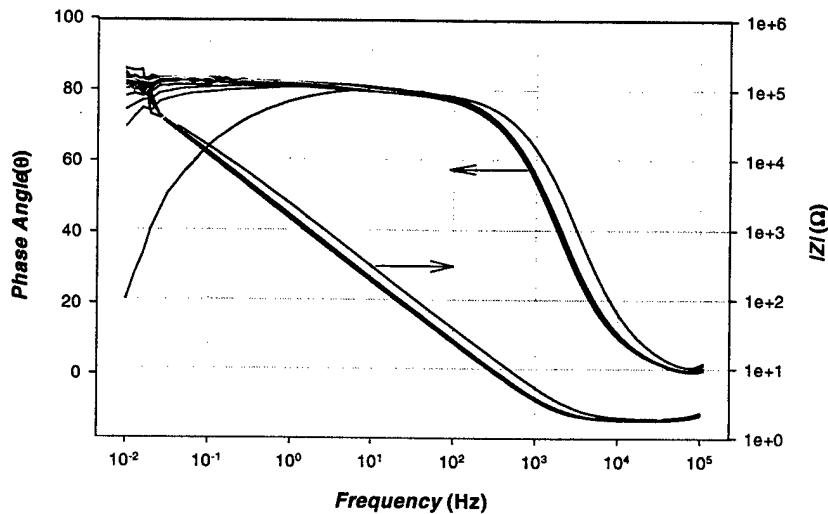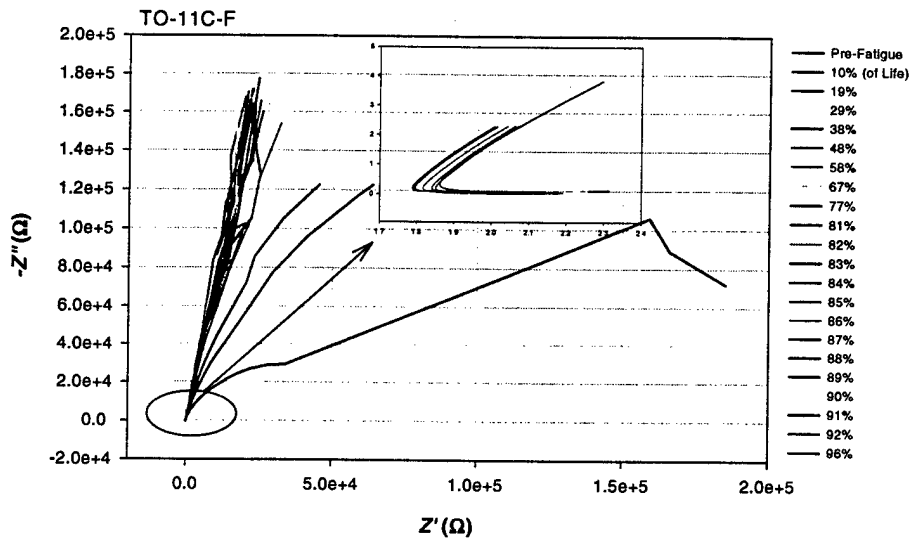
Figure 6-27. Electrochemical impedance response of titanium (Ti-6Al-4V) following progressive states of mechanical fatigue damage, as indicated, for a specimen maintained at a DC polarization potential of +400 mV vs. SCE during fatigue. The specimen was interrogated intermittently, during the cessation of fatigue, with electrical voltage perturbations centered around the DC polarization potential. a) Real and imaginary projection of the impedance spectrum (Nyquist plot), showing an expansion of the high frequency limit (inset). b) Phase angle θ between voltage perturbations and current output, and modulus $|Z|$ versus frequency relationship of the impedance spectrum (Bode plot).

Ti64 R = -1 85 ksi 1 Hz +400 mV vs SCE
Constant Polarization - EIS at Zero Load
Specimen Failure at 52.040 Cycles
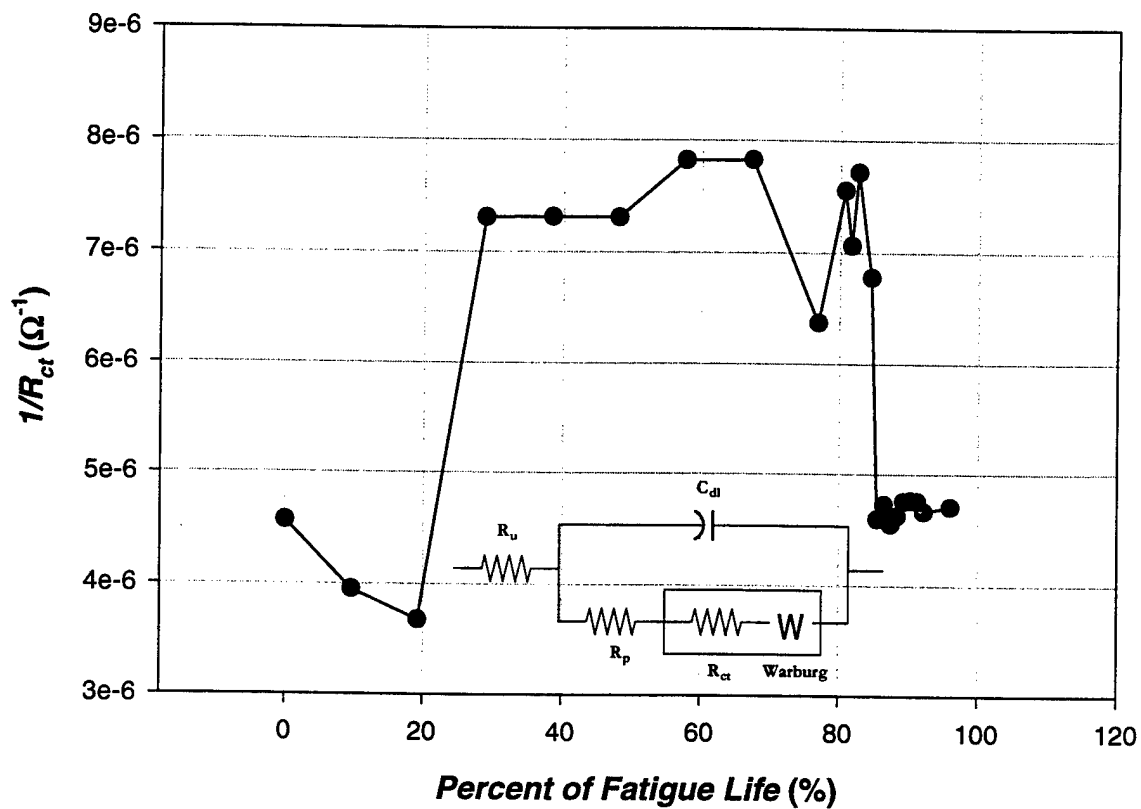
Figure 6-28. Evolution of the implicit damage parameter ($1/R_{ct}$) following progressive states of fatigue damage for titanium alloy (Ti-6Al-4V). The values of the implicit parameter were derived by fitting a two time-constant impedance model to the experimental data. The equivalent circuit analog of this model is shown.

7.0 EFS MEASUREMENTS UNDER SPECTRUM LOADING

Fatigue damage in aircraft occurs through variable amplitude, spectrum loading, and as such is an important issue to consider in the context of the EFS. Since the majority of the developmental work on EFS summarized in previous sections has considered constant amplitude fatigue cycling, the key issue is assessing EFS performance under spectrum loading in comparison to that observed under constant amplitude fatigue cycling. If differences in observed behavior exist, the challenge is to then understand, rationalize, and account for these differences when interpreting EFS current and predicting damage state.

7.1 Objective and Approach

Preceding EFS developmental work has considered constant amplitude loading. However, the typical fighter/trainer aircraft service loading is characterized by a more complex, variable amplitude (VA) loading as a consequence of aerodynamic and maneuver loading. The primary goal of this section is to determine how EFS performance is influenced by spectrum loading conditions since damage evolution in practice will occur under VA loading.

The different types of variable amplitude loading included in the testing and discussed in this section are schematically illustrated in Figure 7-1. The four types of simple spectra are designed to better understand how loading perturbations influence EFS output. The simplest spectra, classified as types A and B, are designed to understand how periodically applied loading peaks (typically quantified with an overload ratio defined as the ratio of the overload magnitude to the steady-state constant amplitude magnitude) influence EFS current. The alternating high-low sequence, type C, is a special case of the type B spectra with no interim cycles between the perturbations. The last simple spectrum, type D, differs from the other three since the periodic, variable R-ratio load perturbations cause less damage than the constant amplitude portion of the sequence since their minimum load is less. Performing this simple spectrum work is an important precursor to the complex, flight-by-flight aircraft loading also considered and shown in Figure 7-1.

Finally, another issue addressed in this section concerns the strain localization occurring on aircraft structure as a primary consequence of the methods used to fasten structural components. Damage typically occurs where stresses are highest, usually in the vicinity of some type of design detail such as a fastener hole with a localized stress concentration. Whereas much of the work detailed in the previous sections of this report has been with smooth fatigue specimens without a stress concentration, some of the tests detailed herein are performed with specimens exhibiting more realistic geometries with design characteristics consistent with typical fatigue critical locations (FCLs) on aircraft structure. Including this stress concentration in specimens subjected to actual aircraft loading is an important consideration since the root-mean-square (or average) stress in a spectrum pass is low even though peak stresses that occur infrequently may be high.

In summary, the approach utilized to investigate the influence of spectrum loading will be to first focus on more simple, repeating spectra. Given a better understanding of this type of loading, the applied spectra will then increase in complexity until the most complex, non-repeating, random cycle-by-cycle loading spectra are considered. The interpretation of behavior under this complex type of loading will be based on lessons learned from the features of the behavior derived from the simpler spectrum loading cases.

7.2   T-38 Fatigue Critical Locations and Loading Histories

During the design process of an aircraft, certain locations are identified as fatigue critical and potentially life limiting. The concept of modern damage tolerant design is to insure that fatigue cracks that occur in these locations can be detected and repaired prior to structural failure. Furthermore, other fatigue critical locations will gradually manifest themselves over time as:

a) cracks are detected during periodic inspections,

b) the loading environment changes (*e.g.*, as a consequence of avionics upgrades or modified external stores), and,

c) the mission (also termed usage) of the aircraft is modified.

Over almost 40 years of flying the T-38, a number of fatigue critical locations have been identified and tracked. These FCLs are described in Table 7-1 and illustrated in Figure 7-2 for the primary structural components of the aircraft. Although in a few cases aircraft re-designs have mitigated the influence of some FCLs, flying the aircraft for the next 40 years (the current USAF goal) requires close monitoring of some of the more critical locations and continuous engineering support using flight load recording programs and damage tolerance analysis updates to establish relevant inspection schedules [7.1].

The current fleet of T-38 aircraft are subjected to a variety of usages depending upon the specific mission of the training activity. For instance, two common usages are derived from the Specialized Undergraduate Pilot Training (SUPT) syllabus and the Introduction to Fighter Fundamentals (IFF) syllabus. Ongoing [7.2, 7.3] as well as past testing and analysis at SwRI for the USAF has shown that the most aggressive, shortest fatigue lives are observed with the IFF usage. Consequently, the IFF usage was selected for the most complex spectrum testing conducted in the current program.

Summary statistics for the IFF usage loading environment are shown in Table 7-2 for the different FCLs identified in Table 7-1. This loading environment is summarized in Table 7-3 for both aluminum and steel fatigue critical locations. The data included in Table 7-3 are important to consider when determining the character and magnitudes of the variable amplitude loading. The mean values of the maximum applied stresses are approximately 207 MPa and 483 MPa for the aluminum and steel FCLs, respectively. In general, the levels of compression applied are relatively low and on the order of 20 percent of the peak tensile loading.

7.3 Experiments Using Simple, Periodically Repeating Load Spectra

The first experiments used to understand how EFS current was influenced by variable amplitude loading conditions were undertaken using relatively simply, repeated loading blocks schematically illustrated in Figure 7-1. The results from these experiments, using the type B and type C loading at Penn and the type B and D at SwRI will be summarized in this section.

7.3.1 Behavior of Aluminum Alloy 7075

The work at Penn utilized two different loading sequences in stress control: 1) an alternating high-low sinusoidal sequence continually repeated (type C), and 2) a repeated sinusoidal sequence in which three cycles at low amplitude were followed by one cycle of higher amplitude (type B). The EFS and fatigue results of these tests are reported below:

The fatigue life behavior, EFS response, and testing details for the aluminum alloy subjected to these two variable loading sequences are listed in Table 7-4, and compared to behavior under constant amplitude, corresponding to that of the higher of the amplitudes used in the variable loading sequence. "Sequence - 1" indicates the first of the two programs listed above and "Sequence - 2" the second. As provided in the table, the ratio of the two amplitudes was about 2 and the cycles column lists a count of all cycles irrespective of amplitude. The magnitudes of the EFS currents in the tests at constant amplitude and in type C variable amplitude are comparable, but lower by an order of magnitude in type B. From these limited results in simple loading sequences, it would appear that crack detection sensitivity is not much affected by the variable loading sequence.

More details of the nature of the electrochemical/mechanical interactions can be obtained from considering the behaviors of the EFS parameters during life. These behaviors are shown in Figure 7-3a to d. Prior to crack nucleation, the current response is more erratic, consistent with the amplitude alternations, but the phase shift remains constant around 0.50 until cracking occurs, at which point the phase shift drops to zero rapidly. The waveform results seen in Figure 7-3c and d are also interesting. Note from the phase shift plot, Figure 7-3b, that the waveforms shown in c and recorded at 40,000 cycles, coincide with the point of first crack indication. Since the crack is small, its effect is also small. No crack peaks are visible and the C-peak dominates the T-peak during the cycle of higher amplitude. These two peaks are more equal at the lower amplitude.

The waveforms shown in Figure 7-3d were recorded at 45,900 cycles, after the crack was well developed, but before it was dominatingly large. The hierarchical structure of the current signal is now radically altered: 1) at the lower amplitude, the T-peak now dominates the C-peak;

2) a large crack peak is inherited at the onset of the tensile reversal in the lower amplitude from the compressive reversal of the higher amplitude; 3) a smaller crack peak is seen at the onset of the tensile reversal of the higher amplitude because it is affected by the lower amplitude preceding it; 4) crack peaks are visible in the compressive reversals of both high and low amplitudes; and 5) the T-peak of the higher amplitude is much enlarged because of the crack dependent plasticity, but the C-peak remains large because of the input from the "elastic" current. This signal is rich in features and harmonics, promising to yield a harvest for signal processing and opportunities for discriminating damage and cycles from an EFS signal in the situation where the load cycle is not recorded. Further developments of these features are shown in Figure 7-3e, recorded at 48,000 cycles when the damage had progressed still further. These results are very promising. Moreover, the prominence of the crack peaks suggest that damage will be measurable even when the loading sequence is complex.

7.3.2 Behavior of Steel and Titanium

Both the variable loading sequences (types B and C) which were used on aluminum were also explored on the subject steel and type B variable amplitude loading was also applied to titanium. The main fatigue and EFS results for these tests are shown in Table 7-5, with the high-low ratio being 2 : 1 for steel based on a high amplitude of 600 MPa, and a ratio of 2.9 : 1 for titanium based on a high amplitude of 580 MPa. Given the regularity of these programs, the EFS responded reliably with indications of damage and cracking in spite of their greater complexity than simple sinusoidal cycling. Based on the respective lives, it appears that the cycles of lower amplitude produced little or no damage in both metals. Proof of this conclusion can be derived from the EFS waveforms, as follows.

Examples of the EFS current waveforms, compared to those of the variable stress, are shown in Figure 7-4a and b for specimen S-6. As noted above for tests on steel, for the longer lives studied here, steel does not show the EFS double peak typical of the FCC metals, but rather a single peak out of phase from the stress cycle. Note that a "flat" appears in the current trace both at the transition from the low amplitude cycles to the overload cycle, and from the high amplitude cycle back again to the low. The flat coincides with the zero on the ordinate. This flat

is explained by a quirk in the MTS variable loading software, which is unable to run together smoothly cycles of different amplitude even when both are sinusoidal. Momentarily then, the strain rate drops to near zero and the EFS signal does likewise. The EFS is sensitive enough to pick up this phenomenon.

Reference to Figure 7-4a and b shows a number of interesting phenomena: 1) phase shifts occur in the mid-life region, *i.e.*, between 600,000 and 685,000 cycles, indicating damage to develop very slowly (Figure 7-4a) and most of it being caused by the cycle of large amplitude; 2) later in life, *i.e.*, Figure 7-4b, the current settles down for the cycles of lower amplitude, but the peak for the cycle of large amplitude grows significantly (note that the ordinate scale in b is double that of a). This indicates that the fatal crack is growing steadily but only during the cycle of high amplitude. There is no other technique known to these investigators which can provide information experimentally of this type when the crack is as small as it is here (the potential drop method might provide similar information for longer cracks). Post-test fractography could not do so because the crack is growing so slowly that the increments would not be discernible on the fracture surface even if they were microscopically resolvable. Note from Table 7-5 that the life for S-6 is about four times longer than that of the constant amplitude test run at 600 MPa. Three quarters of the cycles operate at low amplitude and appear not to be damaging for most of the life.

The results show that it is feasible to measure damage with the EFS in variable loading conditions, at least under relatively simple block loading sequences. Furthermore, EFS offers promise as a laboratory tool for exploring the fundamentals of fatigue behavior under variable-amplitude loading.

7.3.3 Simple Spectrum Investigations at SwRI

Testing was conducted using both steel and aluminum material in the standard cylindrical, S-N type specimen geometry described earlier. A schematic of the two types of simple spectrum loading employed is shown in Figure 7-5. This loading differed from that performed at Penn in that the loading perturbations were applied periodically with more (2000

versus 3) constant amplitude cycles linking the perturbations. Figure 7-5 also indicates the loading stress and other pertinent details regarding the shape and character of the simple spectra. In one case a periodic overload/underload stress cycle is applied whereas in the second case the maximum stress is fixed and the minimum stress is varied linearly.

The goal during these spectrum tests was to assess EFS current magnitude measurements made during the perturbation as well as compare with the current signals both before and after the variable amplitude segment. The pre- and post-perturbation behavior comparisons are important due to the differing natures of the spectra. In the case of the overload/underload spectra, the perturbation is *more severe* than the baseline constant amplitude loading. Conversely, the fixed peak, varying minimum load sequence exhibits a perturbation whose application *is less severe* than the baseline constant amplitude loading.

Typical behavior for the steel subjected to an overload/underload sequence is illustrated in Figure 7-6. Even though the overload was followed by an underload (*e.g.,* a high compressive peak), it is interesting to note in Figure 7-6(a) that the primary current variation occurs during the overload. In fact, the behavior is quite flat or unchanging during the compressive portion of the cycle. As the life of the specimen progresses, the magnitude of the peak during the overload also increases markedly. This peak amplitude magnitude was observed even at relatively short lives. This having been said, the data in Figure 7-6(a) also exhibits an initial transient (from 2000 to 8000 cycles) where the peak current magnitude actually decreases as applied cycles increased. Since 4130 steel is expected to exhibit cyclic softening, this transient is not likely to be due to a transient in the mechanical response of the material. Instead, it is believed to be due to the initial settling-in response of EFS as the electrochemical nature of the surface charges during the initial portion of the test. However, later in the life, the general trend was as indicated in Figure 7-6 with a gradual increase in magnitude as cycling progressed.

The shape of the current response during a given constant amplitude cycle also changes. After the overload, the signal tends to be flatter at the peak presumably indicative of the damage that occurred during the overload. The overload also tended to cause a mean current shift that gradually decays. This is most apparent from the early-in-life and late-in-life current plot insets

7-7

indicated in Figure 7-6(b). At 2,000 cycles (top inset) early in the life, little or no change in current signal is noted comparing the pre- and post-overload current response. However, later in life at 20,000 cycles (lower inset) the shape of the signal clearly changes and a positive DC bias is introduced that gradually decays. This might be indicative of highly localized damage that occurred at a crack growing in the specimen (since it was relatively close, within 600 cycles, to the end of the life of the specimen).

The current responses shown in Figure 7-6 also indicate the same waveform changes which were observed in the previously discussed simple spectrum tests at Penn. Specifically, the tension peak dominates the current response during the large cycles where most of the damage occurs. Furthermore, as fatigue damage evolves later in life, the tension peaks also begin to dominate the current response during the constant amplitude cycles following the overload/underload cycle. This growth of the tension peak is manifested in the phase shift which accompanies fatigue damage (presumable microcracking), as discussed in the previous section.

Two representative current traces are also shown in Figure 7-7 for similar testing performed on the 7075 aluminum. The current trace exhibits an initial transient, evident by comparing the magnitude of the current during the overload early (4000 cycles) and later (6000 cycles) in life. However, even at this point in the life, on the order of 20% of the total life, an obvious DC bias in the current is observed following the application of the overload/underload. The base current behavior in the aluminum does differ from the steel in that the tension and compression cycles each result in high signal magnitudes (hence the current signal is 2x that of the loading frequency). This is consistent with what is typically observed under constant amplitude loading conditions for the 7075 material, as reported in Section 5.

A representative current response for the steel subjected to the second type of simple spectra (fixed peak load, varying minimum load as illustrated by Type D in Figure 7-1) is shown in Figure 7-8. Although this data appears very different with a "wider" current response, this is somewhat misleading since the output of the potentiostat exhibited considerable 60 Hz noise during this particular experiment (the potentiostat broke down shortly after this test was completed). Nevertheless, the signal is sufficiently robust to make the observation that at this

point, late in life when a crack was presumably present, little difference in current response is apparent between the pre- and post-perturbation regimes. This is important since it implies that the less damaging loading perturbation in and of itself did not cause any type of current shape or magnitude changes. Current signal changes that occur purely as a result of loading changes are a potential concern with variable amplitude loading. It is clear from these results that modifications in the minimum load have little impact on current output after the perturbation. Furthermore, the amplitude of the current signals are clearly a function of the alternating load, not the peak load.

7.3.4 Current Magnitude During Simple Spectrum Tests

During the simple spectrum testing at Penn, current magnitude differences between the spectrum-loaded and constant-amplitude samples were noted. One issue that was surprising during the SwRI overload/underload tests was the magnitude of the current recorded during the overload. A plot of the peak-to-peak current magnitude is shown in Figure 7-9 before, during, and after the application of the loading perturbation on a steel sample.

Several interesting points emerge from this representation of the magnitude of the current during application of the peak overload. During the earliest portion of the life, the current magnitude changes during the tensile peak overload by a factor of 5x when compared with the pre- and post-perturbation magnitude. This magnitude initially decreases (the so-called settling-in transient) and then rapidly increases exponentially throughout the test. Furthermore, it should be noted that this increase was not confined to the latter stages when a crack would certainly have been present, the increase occurred throughout the life. By the half-life point, the magnitude difference was approximately 10x. Finally, in the later stages of the life, magnitude increases had grown to on the order of 100x.

Based on earlier constant amplitude tests, the magnitude of this overload current is greater than expected from simply changing stress level. To further complicate matters, there is also a strain rate effect manifested in the recorded data. Since the loading frequency was essentially constant, the loading rate changed during the overload with a higher effective rate of strain applied to the specimen. This increased strain rate in and of itself will lead to an increase

in current magnitude[1]. However, strain rate effects aside, it is believed that the current peaks are largely a result of damage incurred during the overload/underload sequence. As such, the data clearly illustrates the potential suitability for the EFS technology to track damage on a cycle-by-cycle basis.

7.3.5 *Overall Observations - Simple Spectrum Testing*

The results presented herein clearly illustrate the complications that occur when the applied loading sequence is variable amplitude. For instance, the observed current changes can be quite high and exceed 100x for overloads only 50% higher than the nominal applied constant amplitude cycle. Furthermore, the loading perturbations can cause biases and transient behavior in the current output that are not particularly well understood. Although these biases can sometimes decrease with time, they are often accompanied by a change in shape of the signal that often remains after a considerable number of cycles.

While the variable amplitude loading may make it difficult to interpret and assess current quantitatively, it is important to note that the subsequent current response is consistent with expectation based on an understanding of the mechanics of the loading perturbation. There was no apparent degradation in EFS response when the loading was variable amplitude. Observed signal changes were relatively consistent and largely in accordance with expectation based on constant amplitude tests. Furthermore, there did not appear to be any signal changes indicating a loss in sensitivity. The obvious implication is that regardless of how the damage is created, the EFS current response still contains useful information for assessing crack initiation and growth.

In summary, the Penn work has illustrated that the conventional techniques to assess crack formation still apply under variable amplitude cycling. As observed in the Penn testing, the tension and compression peaks change in accordance with that observed under constant amplitude loading and phase shift can be used as an effective indicator of impending failure. Moreover, the periodic variable-amplitude cycle testing performed at SwRI has demonstrated

---

[1] This effect is addressed in Section 5.2.3.6 on frequency effects. Based on data detailed in this section, a strain rate increase of 1.5x would be expected to yield a current magnitude increase on the order of 2%. The obvious implication from the data presented in Figure 7-9 is that only a small portion of the current magnitude increase could have been a direct result of a change in the loading frequency.

that: a) if transients occur, unless late in life, they decay to the steady-state value apparent in the pre-overload current signal, b) current signal shape changes consistent with the damage created during the overload are manifested in constant amplitude cycling following an overload, and c) a benign load perturbation with damage content less than the constant amplitude cycling results in no apparent post-perturbation, current signal anomalies.

In short, the four simple spectra applied provide no cause for concern in using EFS as a fatigue indicator under variable amplitude cycling. The observed behavior is relatively complex with evidence of current signal change with both loading magnitude and strain rate effects. Clearly, there is much to yet be learned regarding quantifying and interpreting the signals; but it is significant to note that no apparent unexplainable behavior was manifested during the simple variable amplitude loading.

Even though the comparative methodologies used by Penn and SwRI differ, the overall conclusion from the testing performed in each lab using four different types of simple spectra is the same. The testing performed clearly illustrates that EFS current can be interpreted and used when the specimen is subjected to variable amplitude loading. The key question that remains, however, is how does this assertion apply to the more complex type of aircraft loading typically applied during use. Hence, the focus of the next section is to further explore this issue by applying a loading history consistent with that observed in-service.

7.4   Experiments Using Complex, Aircraft Load Spectra

Whereas the previous variable amplitude testing examined relatively simple sequences, the focus of this section is use of complex, aircraft loading spectra. As before, both steel and aluminum specimens were used with loading spectra derived from relevant fatigue critical locations on the T-38 aircraft. All tests using complex, aircraft load spectra were performed at SwRI.

7.4.1   Description of Loading Spectra

The magnitude and character of the loading spectra are specific to the FCL chosen. Two representative FCLs, A-20 for the aluminum material and B-11V for the steel material, were chosen for the present tests. Although summary statistics were provided previously in Table 7-2, the histograms included in Figures 7-10 to 7-13 more fully indicate load magnitudes and R-ratios for the two selected spectra. The terminology used in these figures, namely SFH and kSFH (for later data representation), simply refer to "spectrum flight hours" and "1000 spectrum flight hours," respectively.

Comparing the two spectra is useful to understand their fundamental differences in character. First, for the aluminum material A-20 location, the histogram of stress range (Figure 7-10) tends to be evenly distributed around a mean value of 75 MPa. Conversely, for the steel material used for B-11V, the loads asymmetrically surround the mean stress of 140 MPa as observed in Figure 7-12. This implies that for the steel the load ranges tend to be smaller and more frequent than in the aluminum. Little apparent difference exists between A-20 and B-11V with regard to load ratio (Figures 7-11 and 7-13). The average load ratio is in the range of 0.30-0.35 and little compression is observed in either spectrum.

Although the data presented in Figures 7-10 and 7-12 indicated actual stress ranges, some scaling of the spectra was applied during testing. This was done to insure that the life of the specimen was in the range desired for the experiments. This procedure is consistent with common practice of scaling spectra when performing fatigue tests that apply for stress concentrators that are not present on the test specimen. In this context, scaling of the spectra is indicative of what occurs in the region of a design detail with a stress concentration. This is an important issue since virtually all fatigue critical locations occur at stress concentrations.

7.4.2   Correlation of EFS Signal with Damage State

The testing using simple spectra clearly illustrated the complexity associated with interpreting a current signal that varies as a function of both life and loading magnitude. This problem is magnified even more for the aircraft loading spectra which is randomized and has

virtually no repeating loading cycles. Hence, decoupling these influences and understanding the contributions of each is problematic given the schedule and budget allotted for this program.

One of the limitations of smooth specimen "crack initiation" testing is knowing definitively the damage state at any given time or number of cycles. When this is considered along with the fact that fatigue life can typically vary by a factor of 5-10x, correlating behavior under variable amplitude loading with constant amplitude loading is problematic since an extensive amount of testing would be required to establish empirical relationship between the two types of loading. Hence, a different approach was adopted herein to assess EFS performance under aircraft spectrum loading conditions.

This approach, where EFS signal is directly correlated with damage state, is shown schematically in Figure 7-14. When a small defect is embedded in the gage length of a fatigue crack initiation specimen, a crack grows from the defect as fatigue loading is applied. The growth of this crack, as measured by the length of the crack, is a measure of the fatigue damage state and is plotted on the ordinate in Figure 7-14. For comparison, the EFS response is quantified (peak-to-peak current amplitude) and plotted on the abscissa. A baseline series of experiments are then performed using this flawed specimen under constant amplitude conditions to generate the band of data. Similar experiments are then performed under spectrum loading so as to allow a comparison with the band of constant amplitude data. The two types of experiments are then compared (both magnitude and trend as a function of increasing damage state) and deemed similar if consistency is observed. Hence, if no fundamental differences are observed between the EFS current signal between variable amplitude and constant amplitude loading (at a given crack size), then periodic EFS measurements under constant amplitude loading could be used to assess the fatigue damage in actual aircraft subjected to variable amplitude loading. This approach was viewed as being better to assess spectrum effects since it eliminates the inherent variability associated with crack initiation experiments.

7.4.3 Description of Aircraft Spectrum Experiments

A series of eleven tests were performed using preflawed crack initiation samples. Triangular shaped notches, with a total chordal surface length and depth of 0.38 mm, were

embedded in the 5.1 mm diameter gage section of otherwise smooth, cylindrical specimens. These flaws were created using an electric discharge machining (EDM) technique so as to promote rapid crack initiation under fatigue loading. Photographs of typical specimen fracture surfaces illustrating both the initial flaw, as well as crack size and shape at failure, are shown in Figure 7-15. During testing the electrochemical environment was identical to that used in the S-N, crack initiation testing described in Sections 2 and 5.

At periodic intervals in the test, the length of the fatigue crack extending from the notch was measured using an optical method with a polycarbonate scale attached to the specimen. During crack length measurement the electrolyte was drained to a level just below the flaw so as to limit measurement errors resulting from viewing through the fluid. Testing was subsequently resumed once the electrochemical conditions in the EFS cell had reached steady-state. Furthermore, a limited number of acetate replicates were also made of the surface of the specimen to verify the accuracy and suitability of the visual measurement technique utilized.

Cracks were grown under different types of constant amplitude and variable amplitude, spectrum loading conditions depending on the material being tested with EFS data periodically recorded under fully-reversed constant amplitude loading conditions. For all tests, the load amplitude was fixed at a constant level during the period of EFS current measurements. The maximum stress for the steel and aluminum specimens during the EFS current measurements was 620 and 207 MPa, respectively. The corresponding cycle count and crack length were recorded at each of these distinct measurement points.

For cracks grown under constant amplitude loading conditions, the applied loading cycle was identical to the EFS measurement cycle. Different scaling factors were applied during the spectrum loading using the aircraft-derived IFF usage. For the aluminum material, the A-20 spectrum was scaled to a maximum peak spectrum stress of 400 MPa. For the steel material, the B-11V spectrum was scaled to a maximum peak spectrum stress of either 689 or 965 MPa.

7.4.4   Observed EFS Current Responses under Aircraft Spectrum Loading

A typical current response during spectrum tests is indicated by the inset current traces shown on the crack length versus spectrum flight hour plot in Figure 7-16. Although a crack was

continually growing during these tests, the shape of the current traces typically changed as the test progressed. This is somewhat curious since features were apparent in the current responses that during S-N tests were previously believed linked to crack initiation. Nevertheless, there was no consistent progression of current waveform throughout the tests, as in the case of smooth specimen tests reported in Section 5. For instance, the so-called compression peak would occur intermittently in the current response. However, one consistent trend was typically observed in latter stages of the tests near specimen failure. The current signal shape was characterized by either a rapid increase to the peak value or, similarly, a rapid decrease from peak to minimum current level.

As the test progressed, the current magnitude (as measured by the peak-to-peak amplitude) increased. This current increase is shown as a function of crack length in Figure 7-17 for (a) steel and (b) aluminum. Regardless of the material, a similar basic trend is evident in this data. Initially, a relatively constant current amplitude is observed until approximately a 2 mm crack at which point the current magnitude increases monotonically. The significance of Figure 7-17 is that regardless of the loading used to create the fatigue crack, the same basic trend and current magnitudes are observed. The obvious conclusion is that the EFS response is the same for both constant and variable amplitude loading and is independent of the character and type of loading applied.

Readers are cautioned to not misinterpret the so-called equivalent damage curves shown in Figure 7-17. The experiments detailed were not designed to assess EFS sensitivity to crack length. Rather, they were performed to create quantifiable damage in different manners while observing a measure of current amplitude, in this case the peak-to-peak amplitude. This amplitude measure is used for convenience and may not necessarily represent the optimum measure of EFS signal. As such, Figure 7-17 *does not* indicate in any manner or form the resolution of the EFS technology for sizing growing fatigue cracks. A systematic and more complete discussion of EFS crack detection resolution is included in Section 5.

Some slightly anomalous behavior was noted for the aluminum tests in Figure 7-17(b). During the early stages of the two spectrum tests there were significant transient holds in the test

that resulted in a biased current response marked "transient data." These transients subsequently decayed with time and further cycling. Finally, it must also be noted that the conclusion that EFS current is similar at a given damage state under either constant or variable amplitude loading was derived with a growing crack. Admittedly, crack propagation is a different phenomena than crack initiation. However, the processes are sufficiently similar to suggest that the conclusion applies to the complete failure process from initiation all the way to specimen failure due to a propagating crack. As such, these results are believed to be definitive evidence that EFS current can be used to indicate fatigue damage *regardless* of the type of loading used to create the damage.

7.4.5   Predicting EFS Current Amplitudes

The results from another related experiment can further put in context the damage state responses shown in Figure 7-17. As discussed in Section 3.5, the effects of environment (water, dye penetrant, and EFS electrolyte) on fatigue crack growth were examined in detail. One experiment was performed on 4130 steel with EFS under controlled potential conditions. The focus of this test was to demonstrate that the electrochemical EFS process did not add additional damage to the structure by increasing fatigue crack growth rate. In addition to this primary purpose, the test also secondarily provided an EFS current response over nearly an order of magnitude range of crack growth rate data.

The EFS current response is shown in Figure 7-18 for this compact tension sample cycled at an R-ratio of 0.5. Both the current amplitude (measured peak-to-peak) and mean current (DC current) exhibited a linear response with crack growth rate when plotted on a log-log scale as shown in Figure 7-18(a). These data are further shown in Figures 7-18(b) and (c) but this time plotted on a linear axis and correlated to stress intensity factor range and FCG rate, respectively. The linearity of this data is remarkable considering some of the pragmatic issues (*e.g.*, high signal to noise ratios and occasional transient behavior) associated with measuring an EFS current signal. Although at this time the mechanistic basis for the presence of this linearity is unknown, it is important to understand whether this empirical observation is truly significant or whether it is a by-product of the experimental approach used.

Given the data in Figure 7-18(b), linking EFS current amplitude to applied stress intensity factor range, the question then is whether it can be used to predict the current levels observed during the constant amplitude and spectrum testing detailed in Figure 7-17(a). Since stress intensity factor range is the variable used to relate the two tests, a K solution for a surface cracked cylindrical bar subjected to tension was extracted from reference [7.4]. The subsequent current level prediction, using ΔK to bridge the difference in specimen geometry, is shown in Figure 7-19. It can be clearly observed that this empirical prediction provides a reasonable comparison to the original data. Both current magnitude as well as trends in the magnitude with surface crack length are predicted well in view of the apparent scatter in the data recorded during the spectrum and constant amplitude tests. This agreement is especially significant considering the differences between the crack growth experiment and the S-N specimen testing which includes the following:

- long crack, compact tension specimen versus small crack, cylindrical S-N specimen,
- through crack versus surface crack,
- significantly different electrochemical setups and exposed specimen areas,
- different applied stress levels, and,
- different load ratios of R=0.5 and R=-1.

Even though these differences existed, the fact that limited empirical data (one test) is able to predict current amplitude as well as observed in Figure 7-19 is significant.

The merit of using the capability of EFS current amplitude to predict crack length might on the surface appear to be of little value in the context of the crack initiation focus of the EFS technology. However, the significance of this predictive capability is believed to lie in the understanding of the electrochemical processes that would occur with a further understanding of the basis of the observed empirical trend. To date, the actual process that the EFS current response is measuring has not been definitively shown. It is believed that future efforts to understand what current amplitude is actually measuring in a controlled crack growth experiment

will benefit EFS technology by providing important insight into the physical process yielding the observed current response.

Further study of this intriguing result will provide information that can be extended to the crack initiation process. For instance, if further testing can indicate what fatigue or fracture mechanics quantity is controlling EFS current magnitude, this would provide an invaluable tool for relating data from radically different test specimens and loading conditions. Moreover, does EFS current primarily indicate the electrochemistry and fatigue damage process in the crack or on the surface of the specimen? Knowing the answer to this question will provide a rational basis for determining required sensor positions at or near the FCL of interest and assist in determining how EFS current measured at one point remote from the FCL can be related to localized fatigue damage in the FCL. For these reasons, we believe that understanding EFS current behavior during fatigue crack growth will yield critical information that is directly applicable to applying EFS technology to the crack initiation and early growth process.

7.5   Concluding Remarks

The tests described in this portion of the report have been directed at understanding EFS current response under spectrum loading conditions. The results presented for both simple and complex aircraft loading spectra indicate that EFS current response is similar to the behavior observed during constant amplitude load cycling. The obvious implication is that regardless of the nature of the loading, the EFS current response can be used as an indicator of damage state.

The testing described herein has clearly illustrated the complexity of the current response under conditions of changing load magnitude. This was one of the primary reasons that led to quantifying EFS current magnitude as a function of damage state as described in Section 7.4.2. The key implication of this method is the similarity between the signal levels under constant and variable amplitude loading conditions. This is an important observation from the viewpoint of using EFS technology as a predictor of fatigue damage state. Furthermore the first order, engineering prediction of current magnitude level (Section 7.4.5) shows further promise for linking EFS behavior between these two critical types of loading environments. In summary, the

variable amplitude loading phase of this program has clearly demonstrated that the complexities associated with spectrum loading can probably be overcome with additional characterization work.

7.6   References

7.1   Tiffany, Charles F. (Chair), "Aging of U.S. Air Force Aircraft - Final Report," Committee on Aging of US Air Force Aircraft, National Materials Advisory Board, Commission on Engineering and Technical Systems, National Research Council, Publication NMAB-488-2, National Academy Press, Washington, DC, 1997.

7.2   "T-38 Coupon Testing," SwRI Project No. 06-1334, USAF Contract No. F41608-96-D-0108, D.O. No. 0018.

7.3   "T-38 Durability and Damage Tolerance Analysis Update," SwRI Project No. 06-7278, USAF Contract No. F41608-90-D-2060, D.O. No. 0044.

7.4   Forman, R.G., *et al.*, "Fatigue Crack Growth Computer Program NASGRO," Version 3.00, JSC-22267B, NASA Johnson Space Center, July 1996.

Table 7-1. Summary of the characteristics of different T-38 fatigue critical locations with critical crack sizes based on the IFF usage.

Aircraft Location	Description of FCLs	FCL Identification	Material (form)	Thickness* (in)	Hole* Diam (in)	Crit Crk* Length (in)
Wing	radius (root and 44% spar)	A-4, A9	7075-T7351 (plate)	0.15-0.60	N/A	0.20-0.27
	fastener holes (44% spar)	A-1, A-5, A-8a, A-10a, A-18	7075-T7351 (plate)	0.27-0.60	0.20-0.28	0.20-0.48
	fastener holes (66% spar hinge)	A-12a, A-12b	7175-T74 (forging)	0.090	0.20	0.32-0.34
	fastener holes (near WS 64.8)	A-15, A17	7075-T7351 (plate)	0.19-0.28	0.28	0.60-0.61
	fastener hole and D-panel	A-19, A-20	7075-T7351 (plate)	0.19-0.55	0.20-0.28	0.21-0.45
Fuselage	longeron details (cockpit encl.)	B-1 to B-5CEM	7075-T73511 (extr)	0.18-0.25	N/A, 0.17	0.26-2.55
	splice bolt – upper longeron	B-6	steel - MP35N	0.625 diam	N/A	0.13
	splice – upper longeron (aft)	B-7	7075-T6 (forg/plate)	0.50	N/A	0.32
	fastener holes (dorsal longeron)	B-11V, B-11H	4130 steel	0.10-0.15	0.19-0.21	0.30-0.43
	outboard main engine mount	B-14	17-4PH/13-8PH	0.340	N/A	0.24-0.33
	tail cone attach bolt	B-15	5Cr-Mo-V	0.324 diam	N/A	0.057
Empennage	radius (vertical stabilizer)	C-1	7075-T6 (plate)	0.20	N/A	N/A
	radius and holes (horiz stabilizer)	D-1, D-4	4330M (tube)	0.18-0.22	N/A, 0.63	0.15-0.70

* 1 in. = 25.4 mm

Table 7-2. Summary Statistics for T-38 FCLs Subject to the IFF Usage

Aircraft Location	FCL Identifier	Material		Applied Stress, MPa				Load Ratio (R-ratio)		
		Al	Fe	σ_{max}	σ_{min}	$\Delta\sigma_{avg}$	$\Delta\sigma_{rms}$	R_{avg}	R_{rms} (>0)	R_{rms} (<0)
Wing	A-1	✓		199.2	-48.9	62.0	67.6	0.29	0.32	0.17
	A-10a	✓		260.6	-68.9	67.6	73.1	0.28	0.31	0.23
	A-12a	✓		141.3	-25.5	38.6	41.4	0.39	0.41	0.19
	A-12b	✓		109.6	-26.9	29.0	31.7	0.32	0.35	0.19
	A-15	✓		221.3	-54.5	73.1	80.0	0.33	0.36	0.12
	A-17	✓		204.8	-42.7	60.0	65.5	0.35	0.38	0.1
	A-18	✓		213.0	-44.8	59.3	64.8	0.35	0.38	0.1
	A-19	✓		211.0	-54.5	67.6	73.1	0.26	0.3	0.21
	A-20	✓		266.8	-55.8	74.5	80.7	0.35	0.38	0.1
	A-4	✓		311.6	-77.2	101.3	110.3	0.28	0.31	0.18
	A-5	✓		239.2	-59.3	77.9	84.1	0.28	0.31	0.18
	A-8a	✓		228.2	-56.5	74.5	80.7	0.28	0.31	0.18
	A-9	✓		208.9	-55.2	51.7	55.8	0.29	0.32	0.22
Fuselage	B-11[2]		✓	492.9	-119.3	140.6	153.7	0.28	0.32	0.15
	B-14		✓	463.3	-203.4	149.6	162.7	0.31	0.36	0.33
	B-15		✓	722.5	572.2	26.2	29.0	0.96	0.96	0
	B-6		✓	1073.4	610.1	95.1	106.2	0.89	0.89	0
	B-7	✓		285.4	16.5	59.3	66.2	0.6	0.61	0
	B-1CEM	✓		227.5	19.3	20.0	33.1	0.82	0.84	0
	B-2CEM	✓		195.8	0.7	22.1	31.7	0.73	0.75	0
	B-3	✓		91.0	-2.8	17.9	20.7	0.56	0.57	0.06
	B-4CEM	✓		257.1	-6.2	31.7	42.7	0.68	0.7	0.02
	B-5	✓		297.1	44.8	55.8	62.0	0.67	0.68	0
Empennage	D-1		✓	392.3	-396.4	60.0	66.9	-0.54	0.46	21.08
	D-4		✓	57.9	0.0	5.5	6.9	0.05	0.14	0

[2] A factor of 2.75 has been applied to the baseline loading to reflect results from a material change and subsequent FE modeling of this region of the aircraft.

Table 7-3. Global Statistics for T-38 FCLs Given the IFF Usage

Material	Statistical Quantity	Applied Stress, MPa				Load Ratio (R-ratio)		
		σ_{max}	σ_{min}	$\Delta\sigma_{avg}$	$\Delta\sigma_{rms}$	R_{avg}	R_{rms} (>0)	R_{rms} (<0)
aluminum	*minimum:*	91.0	-77.2	17.9	20.7	0.26	0.3	0
	maximum:	311.6	44.8	101.3	110.3	0.82	0.84	0.23
	average:	219.2	-31.7	55.2	61.4	0.43	0.45	0.12
	std. dev.:	57.9	34.5	22.8	22.8	0.18	0.18	0.08
steel	*minimum:*	57.9	-396.4	5.5	6.9	-0.54	0.14	0.00
	maximum:	1073.4	610.1	149.6	162.7	0.96	0.96	21.08
	average:	533.6	77.2	79.3	87.6	0.33	0.52	3.59
	std. dev.:	340.6	418.5	59.3	64.1	0.56	0.33	8.57

Table 7-4. Fatigue Life Behavior and EFS Response of 7075 Aluminum Alloy Subjected to Both Forms of Penn Variable Loading Programs

Type of Test	Specimen ID	Freq. (Hz)	Stress (MPa)	Life (cycle)	CIAC	% of Life	Plastic Current	Elastic Current	Base Current	Phase Factor
Constant Amplitude		0.5	200	88,000	77,000	87.3	0.04	0.038	1.19	0.5
VA-type B	A-t51	0.5	200/100	180,000	150,000	83.3	0.004	0.005	0.1	0.3
VA-type C	A-t64	0.5	230/130	51,800	42,000	81.0	0.055	0.03	1.3	0.5

Table 7-5. Fatigue Life Behavior and EFS Response of 4130 Steel and Titanium Alloy Subjected to Both Forms of Penn Variable Loading Programs.

For 4130 Steel

Type of Test	Specimen ID	Freq. (Hz)	Stress (MPa)	Life (cycle)	CIAC	% of Life	Plastic Current	Elastic Current	Base Current	Phase Factor
Constant Amplitude		0.5	600	196,600	146,500	75.0	0.01	0.1	0.04	-0.3
VA-type C	S-47	0.5	600/300	178,500	149,000	83.5	0.02	0.135	0.2	-0.3
VA-type B	S-6	0.5	600/300	745,200	655,000	87.9	0.013	0.1	0.003	-0.29

For Titanium Alloy

Type of Test	Specimen ID	Freq. (Hz)	Stress (MPa)	Life (cycle)	CIAC	% of Life	Plastic Current	Elastic Current	Base Current	Phase Factor
Constant Amplitude	Ti-21	0.5	580	176,000	172,000	97.7	0.02	0.06	0.05	0.25
VA-type B	Ti-10	0.5	580/200	149,300	140,000	93.8	0.08	0.19	0.5	0.07

Simple Spectra

- overload **(type A)**
- overload / underload
  (type B)
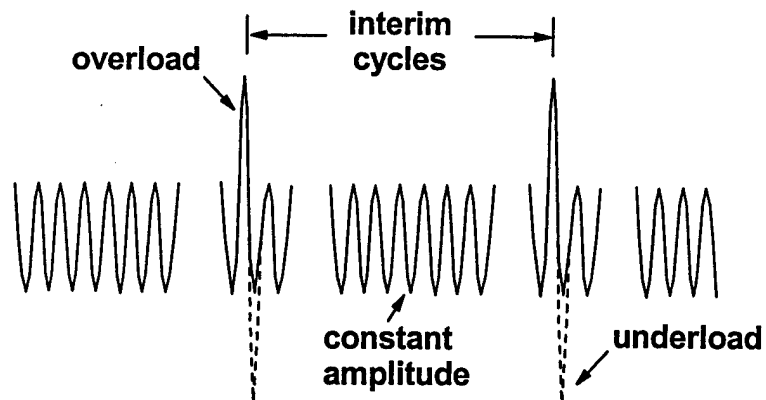
- alternating high-low
  loading **(type C)**
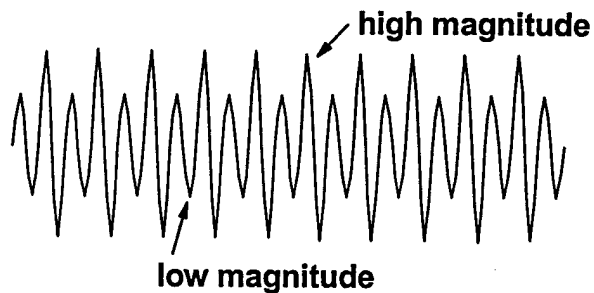
- fixed peak magnitude,
  symmetrically variable
  R-ratio **(type D)**
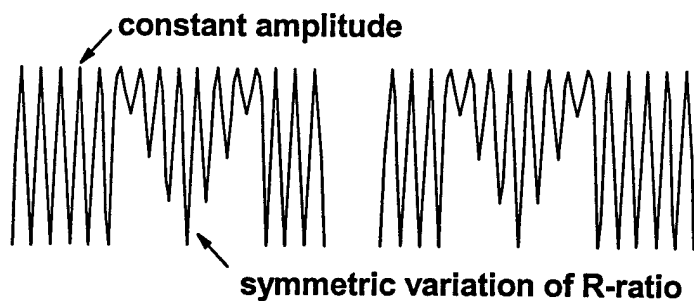
Complex Spectra

- flight-by-flight aircraft
  loading derived from
  measurements on parts
  and components subjected
  to the actual usage
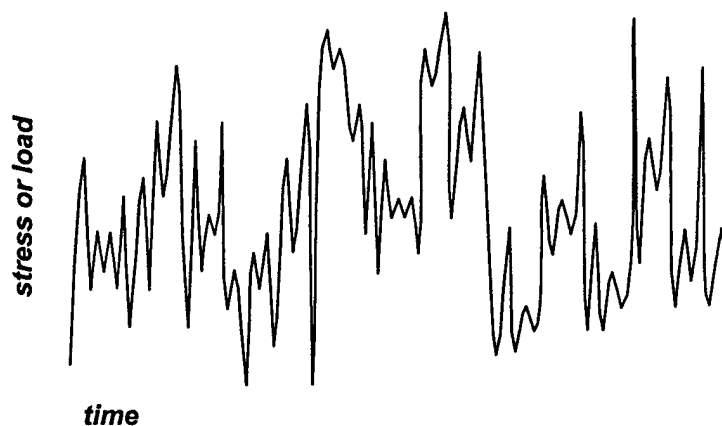
Figure 7-1. Different types of simple and complex spectra applied during testing.
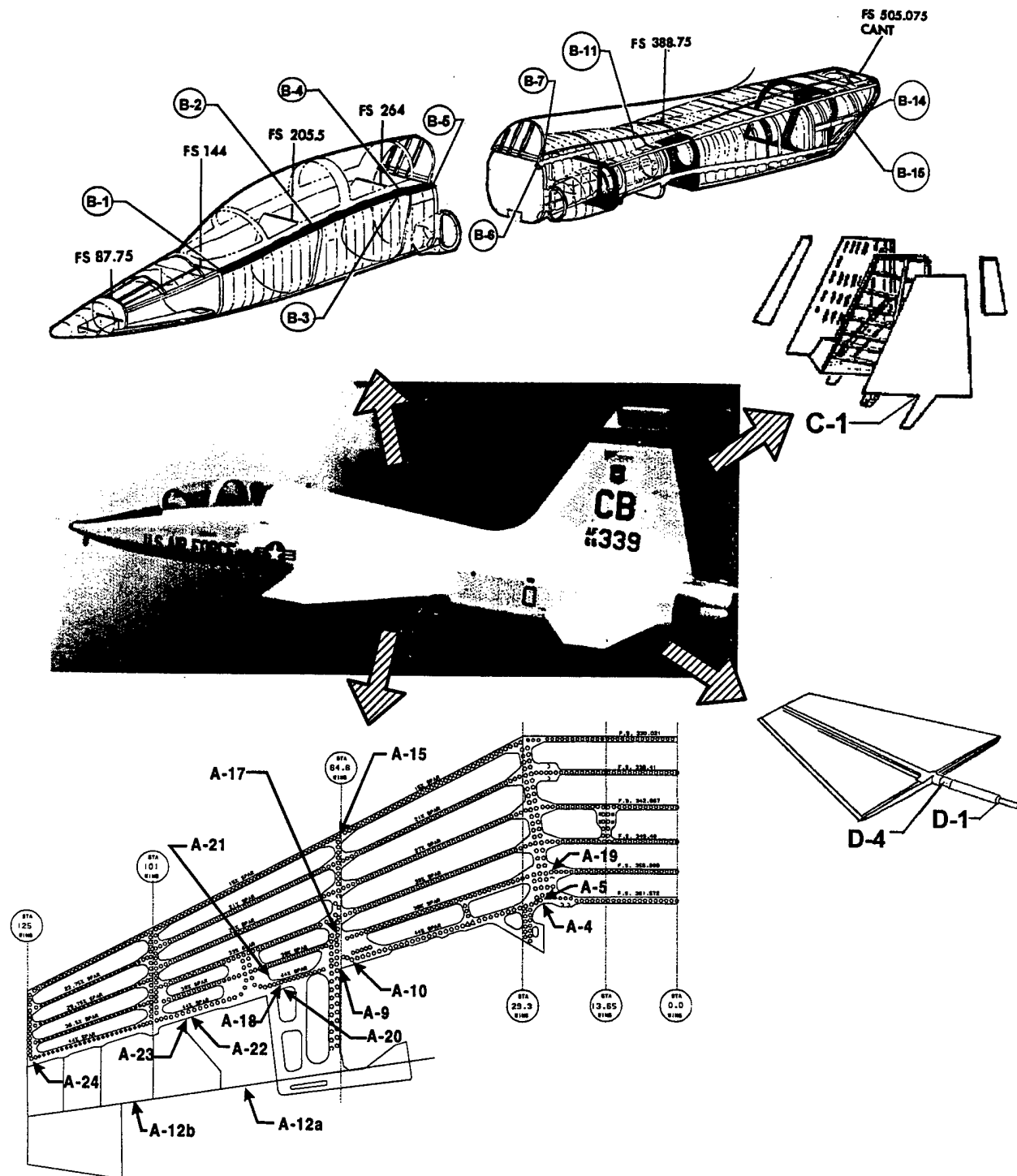
Figure 7-2. Schematic illustrating the different T-38 fatigue critical locations by aircraft area. The different aircraft areas include (clockwise from upper left) forward fuselage, center/aft fuselage, vertical tail, horizontal stabilizer and lower wing.

Current Density
µA/cm2
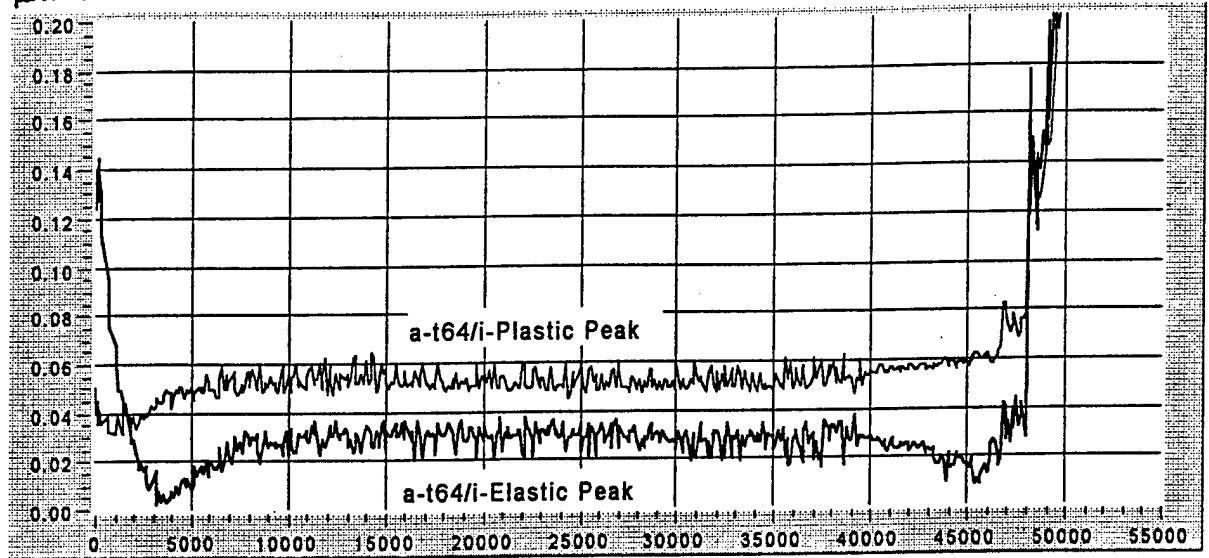
(a)   No.of Cycles

Phase Shift X
Period of 0.5 Hz
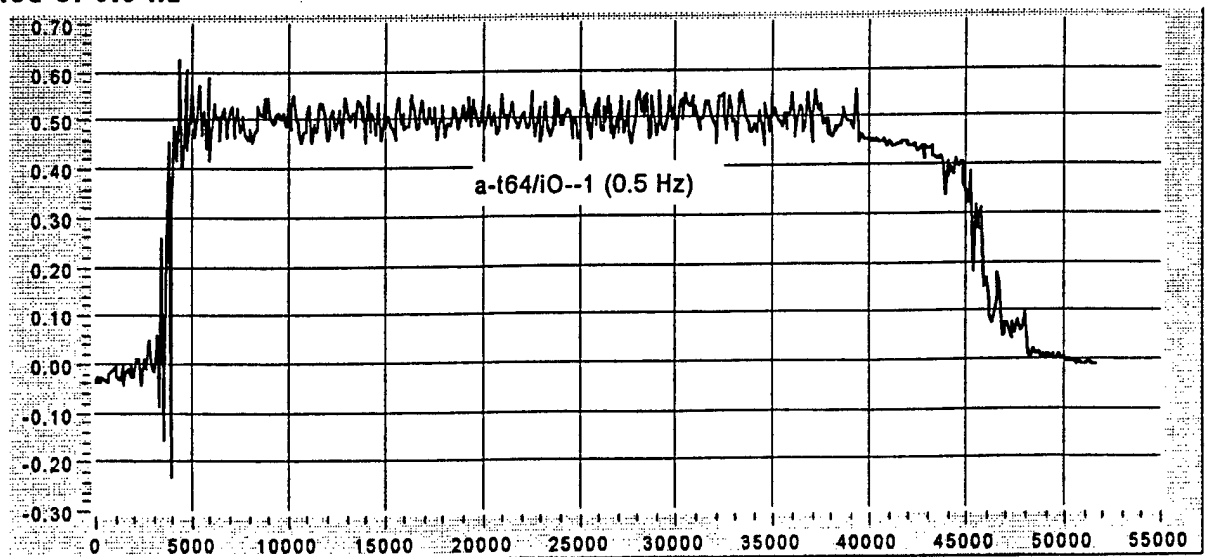
(b)   No.of Cycles

Figure 7-3. EFS response of 7075 aluminum specimen A-T 64 subjected to the type C alternating high-low variable loading program at Penn: a) current response, b) phase shift, c) load and current waveforms at 40,000 cycles, d) load and current at 45,900 cycles, and e) load and current at 48,000 cycles.

7-26

Figure 7-3 (Cont'd). FS response of 7075 aluminum specimen A-T 64 subjected to the type C alternating high-low variable loading program at Penn: a) current response, b) phase shift, c) load and current waveforms at 40,000 cycles, d) load and current at 45,900 cycles, and e) load and current at 48,000 cycles.

7-27
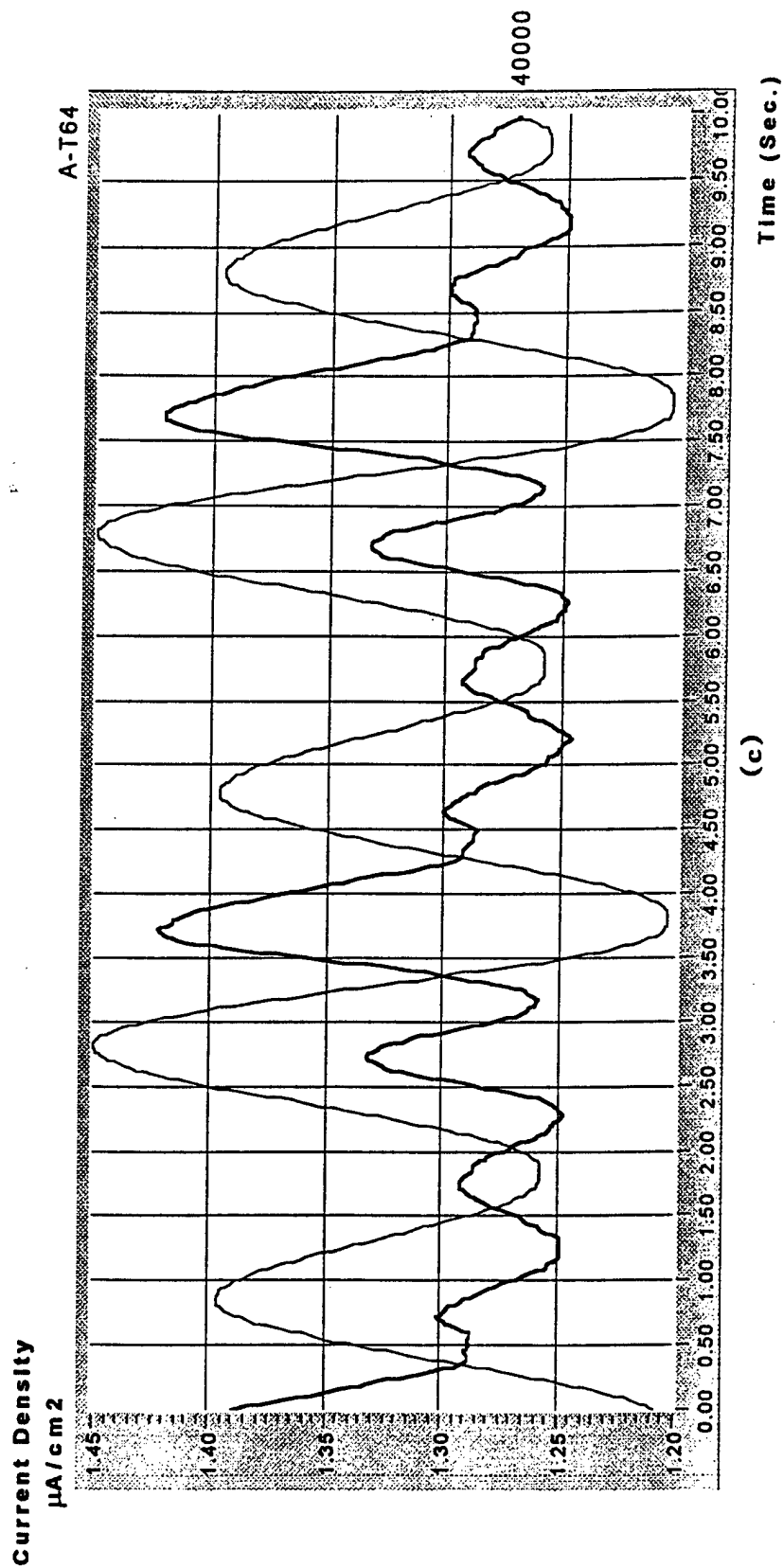
Figure 7-3 (Cont'd). FS response of 7075 aluminum specimen A-T 64 subjected to the type C alternating high-low variable loading program at Penn: a) current response, b) phase shift, c) load and current waveforms at 40,000 cycles, d) load and current at 45,900 cycles, and e) load and current at 48,000 cycles.

Figure 7-3 (Cont'd). FS response of 7075 aluminum specimen A-T 64 subjected to the type C alternating high-low variable loading program at Penn: a) current response, b) phase shift, c) load and current waveforms at 40,000 cycles, d) load and current at 45,900 cycles, and e) load and current at 48,000 cycles.

7-29

Current Density

µA / cm2   S-6

(a)   Time (Sec.)

Current Density

µA / cm2

(b)   Time (Sec.)
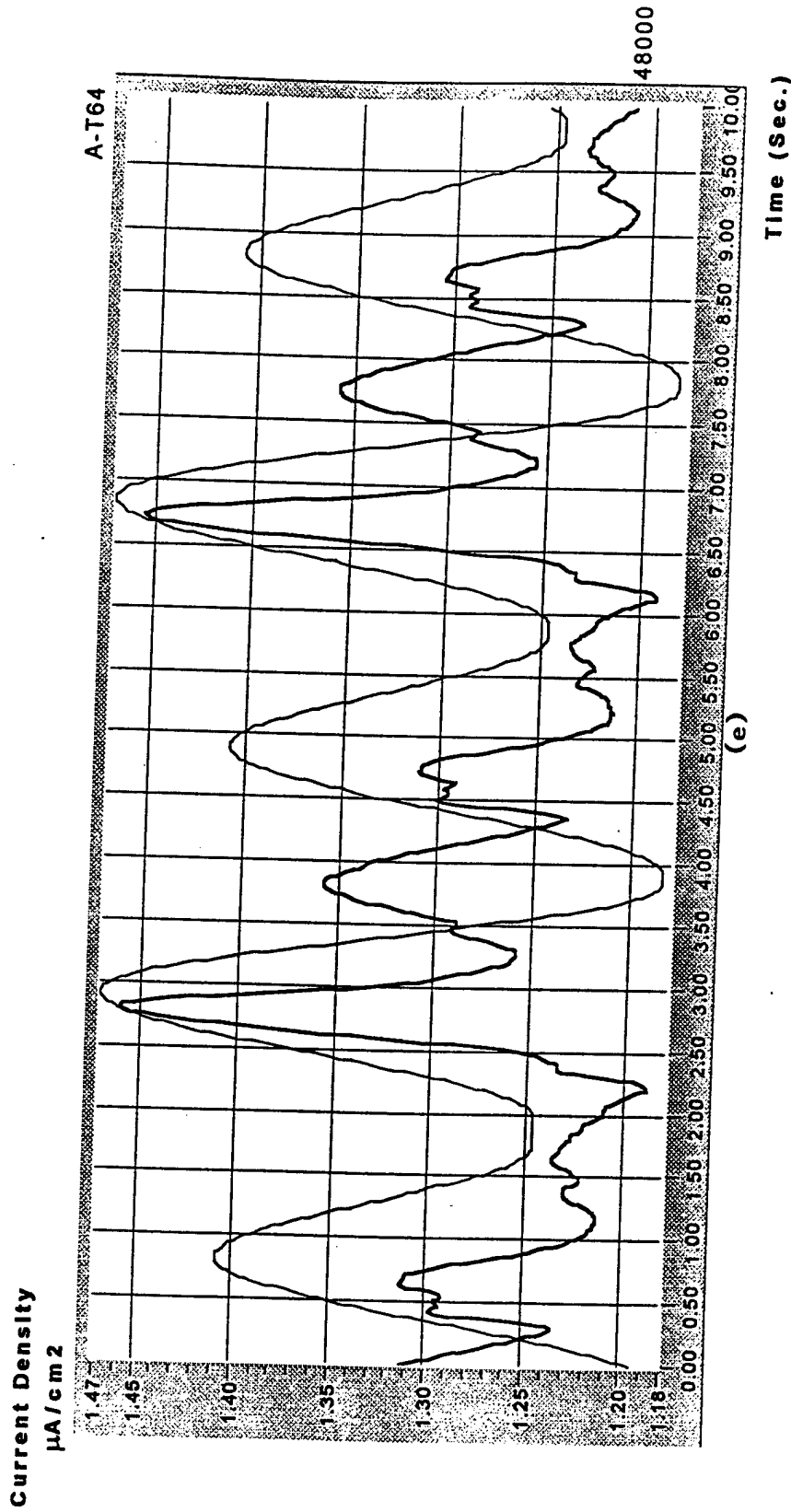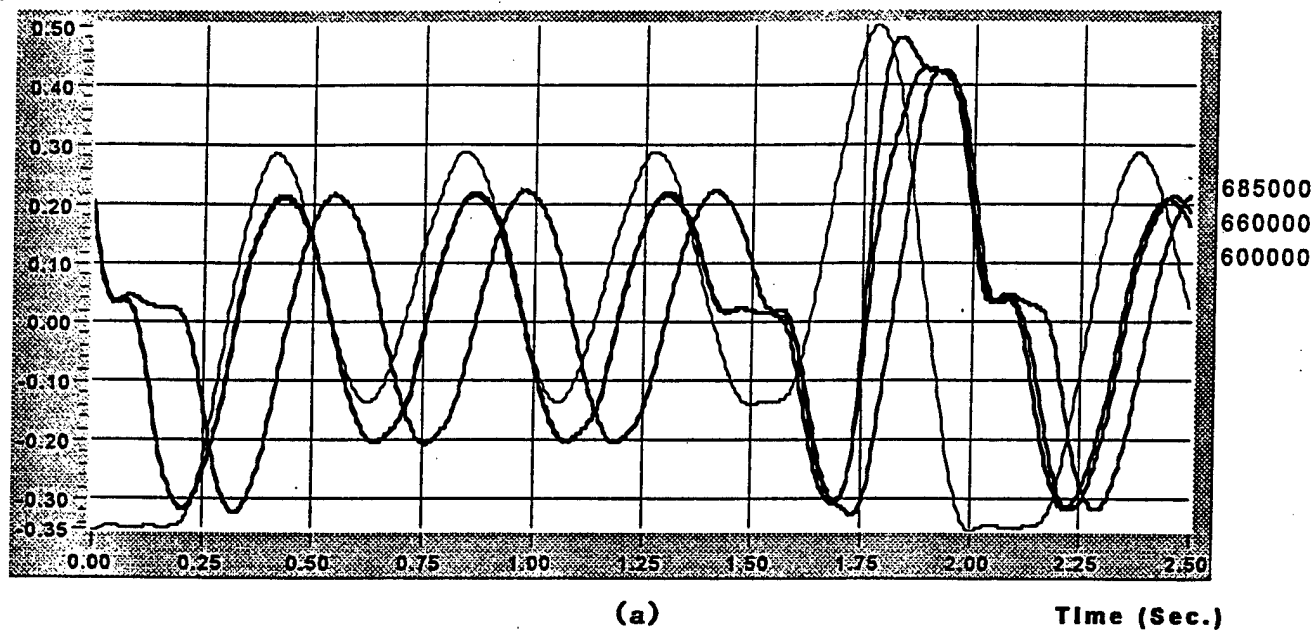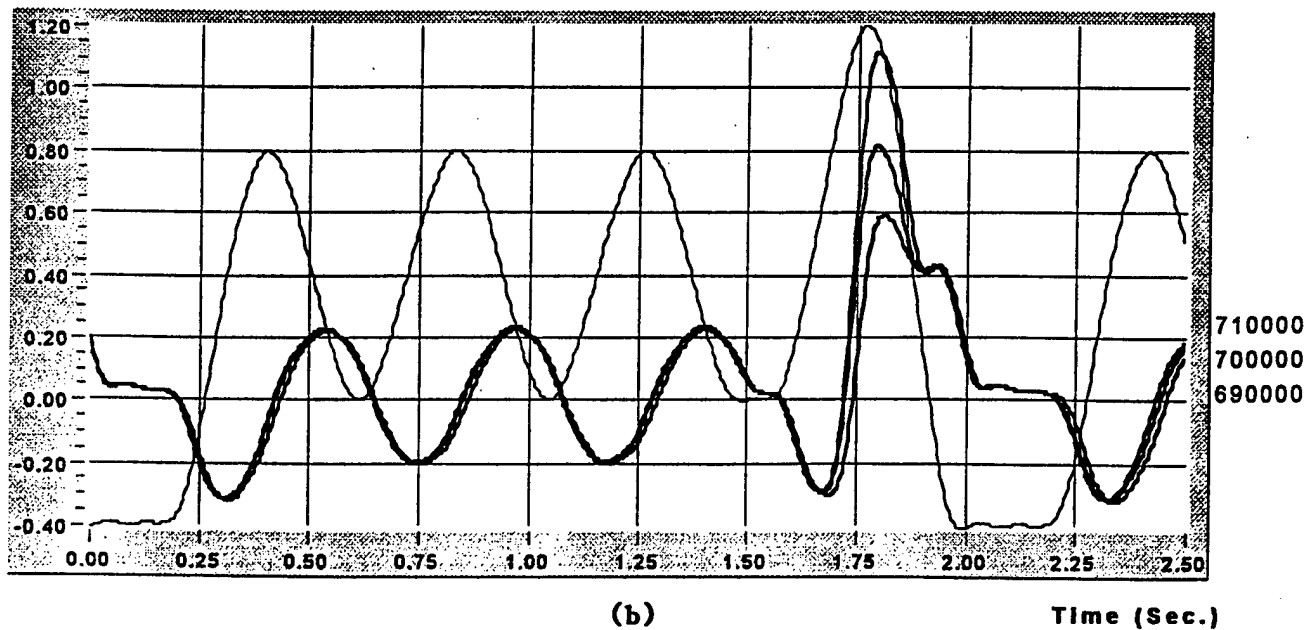
Figure 7-4. EFS waveforms of 4130 steel specimen S-6 subjected to the type B loading with 3-low/1-high cycles at Penn. a) 600,000 – 685,000 cycles and b) 690,000 – 710,000 cycles.

Laboratory: SwRI
Material: aluminum and steel
Life Regime: 10,000 cycles
Approach: load perturbations every 2000 cycles

Loading: 276 MPa, R-ratio = -1 (aluminum)
689 MPa, R-ratio = -1 (steel)

Overload: 1.5x peak load
Variable R-ratio: 0.5, 0.0, -0.5, -1.0, -0.5, 0.0, 0.5
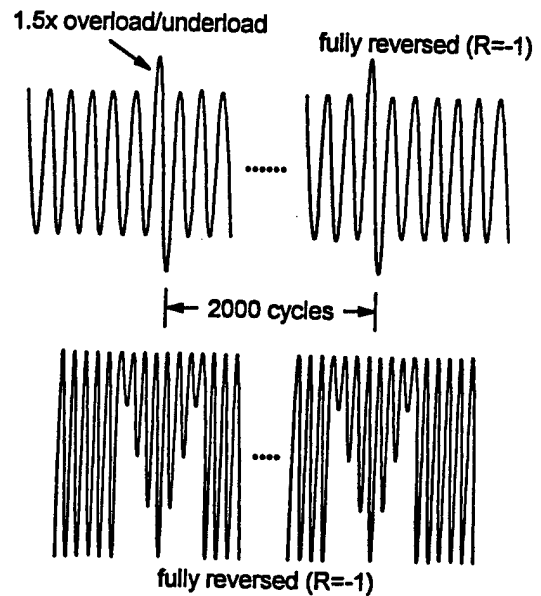
Figure 7-5. Simple spectra applied during investigations performed at SwRI.
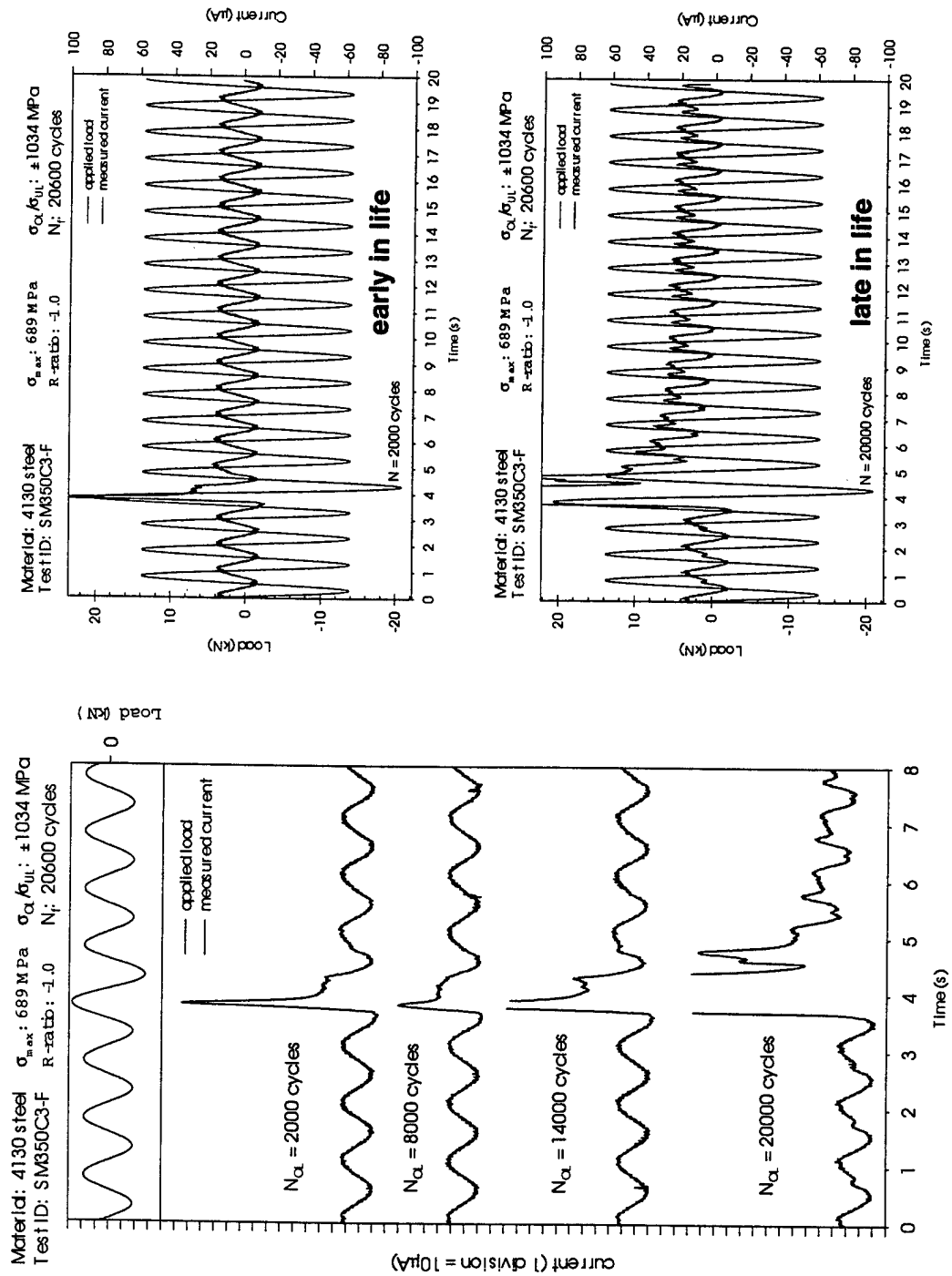
Figure 7-6. Current signal for steel specimens (a) as a function of applied cycles and (b) early and late in life. (Specimen failure occurred at 20,600 cycles.)
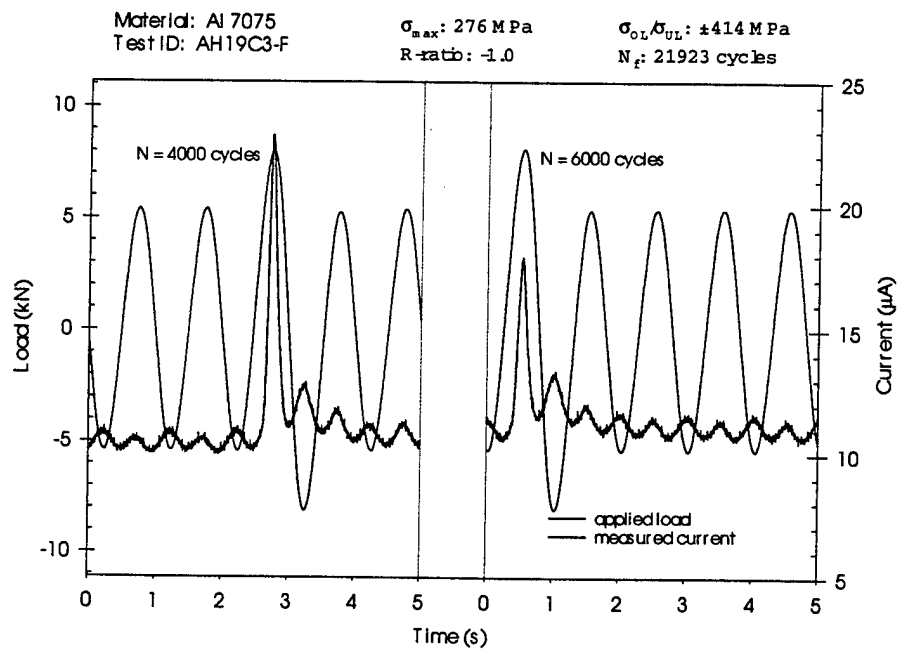
Figure 7-7. Current signal for aluminum specimens as a function of applied cycles. (Specimen failed at 21,923 cycles.)
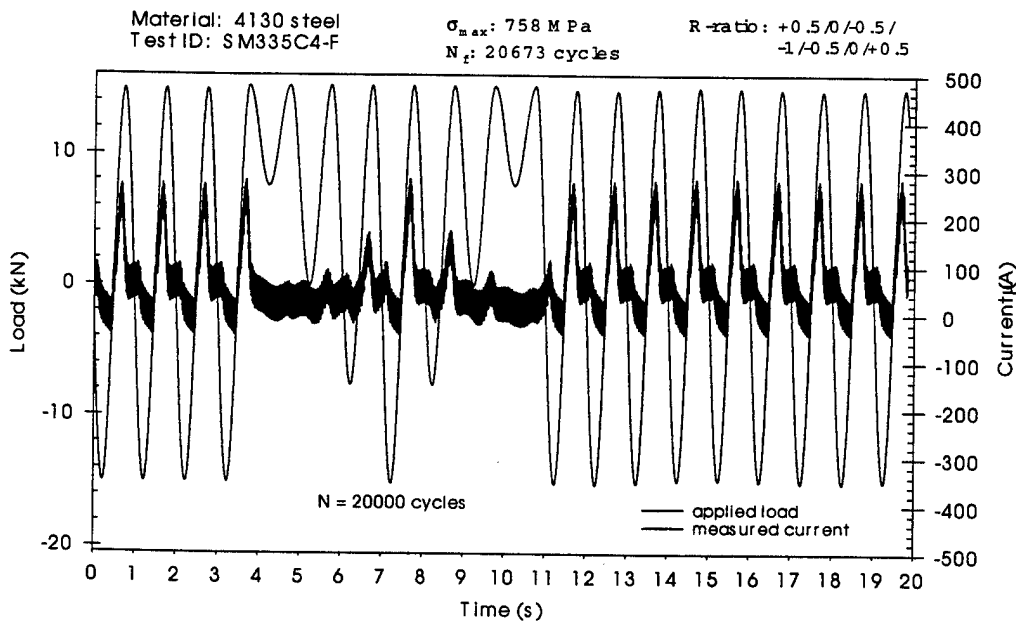
Figure 7-8. Current signal for a steel specimen with a simple R-ratio modification spectrum. (Specimen failed at 20,673 cycles.)
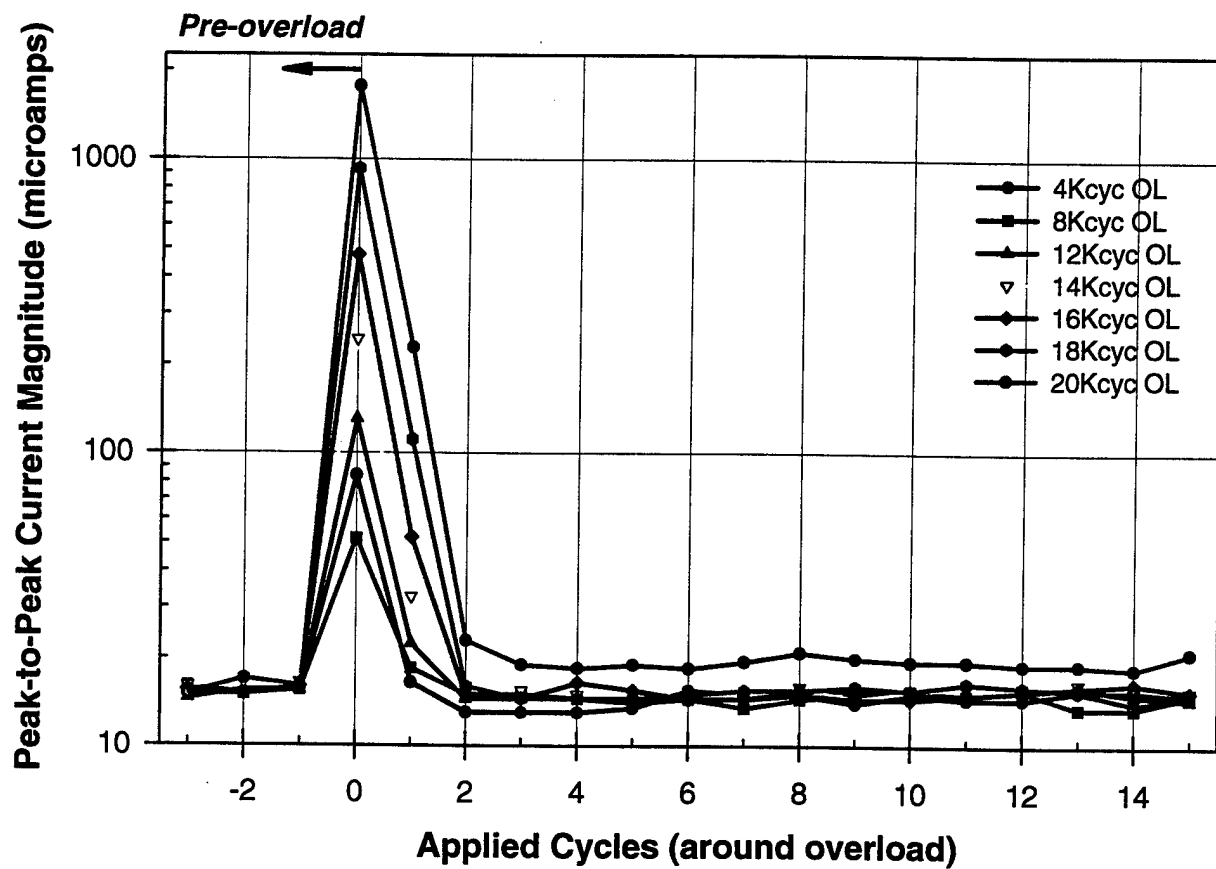
Figure 7-9. Peak current amplitude changes as a function of life for a steel specimen.
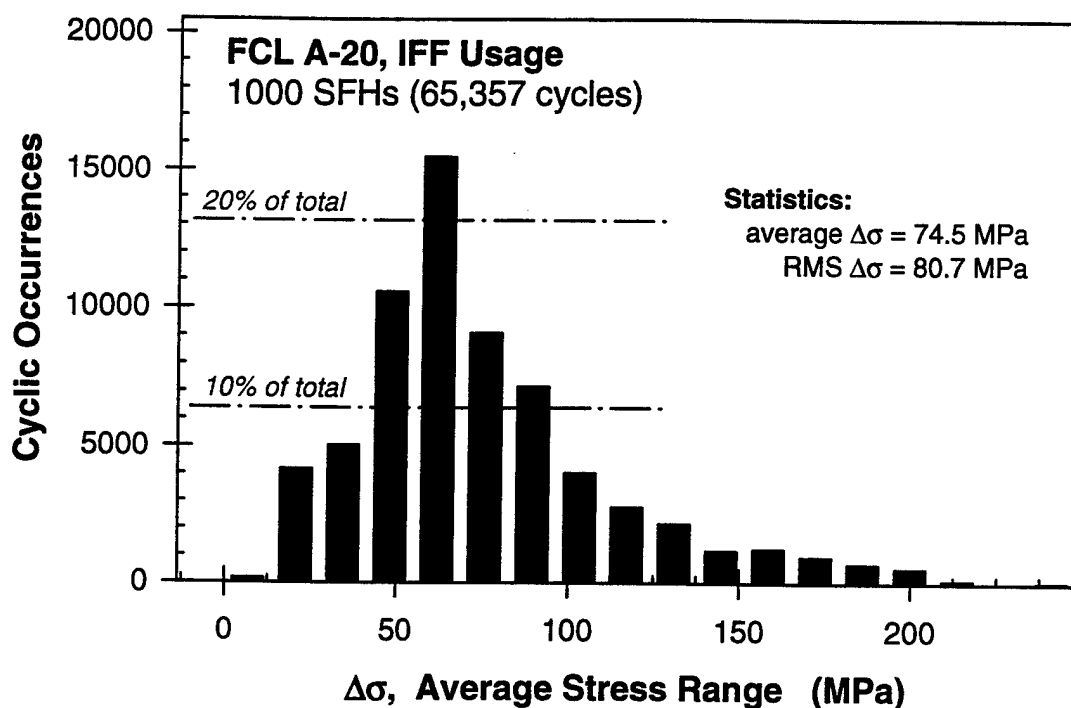
Figure 7-10. Summary of the load range characteristics of the IFF usage for FCL A-20.
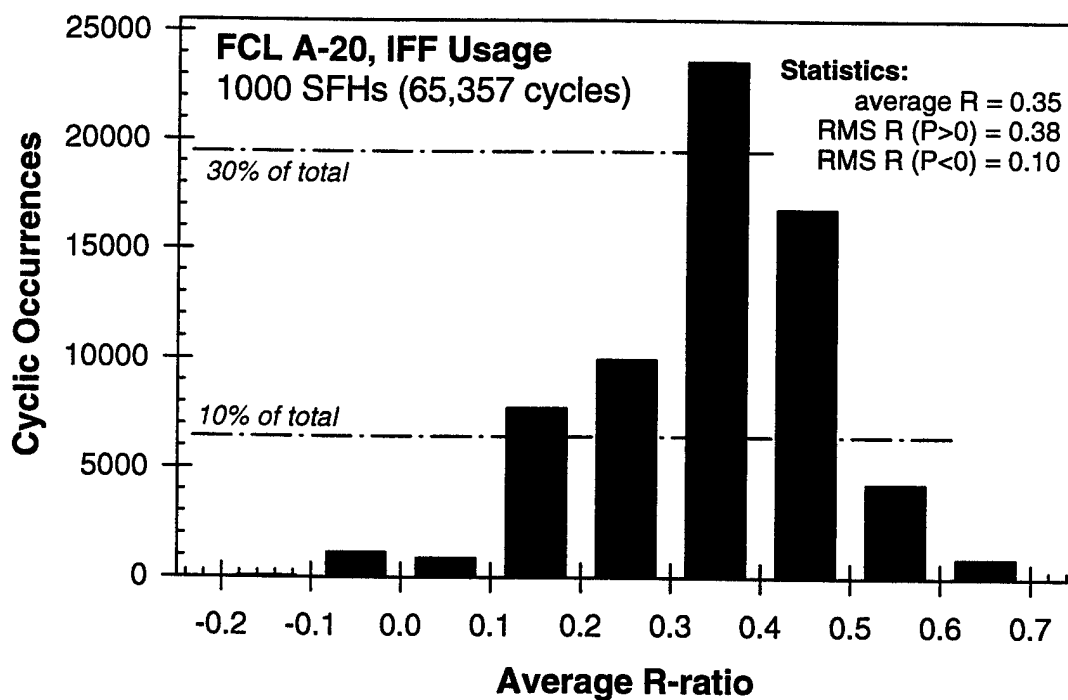
Figure 7-11. Summary of the R-ratio characteristics of the IFF usage for FCL A-20.
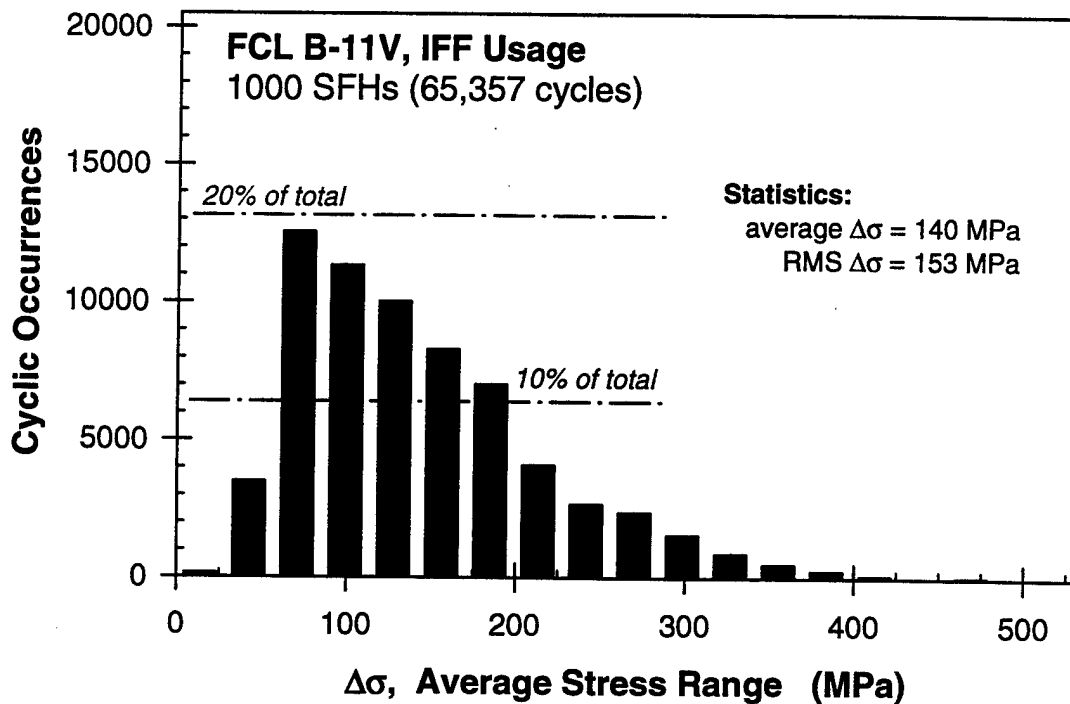
Figure 7-12. Summary of the load range characteristics of the IFF usage for FCL B-11V.
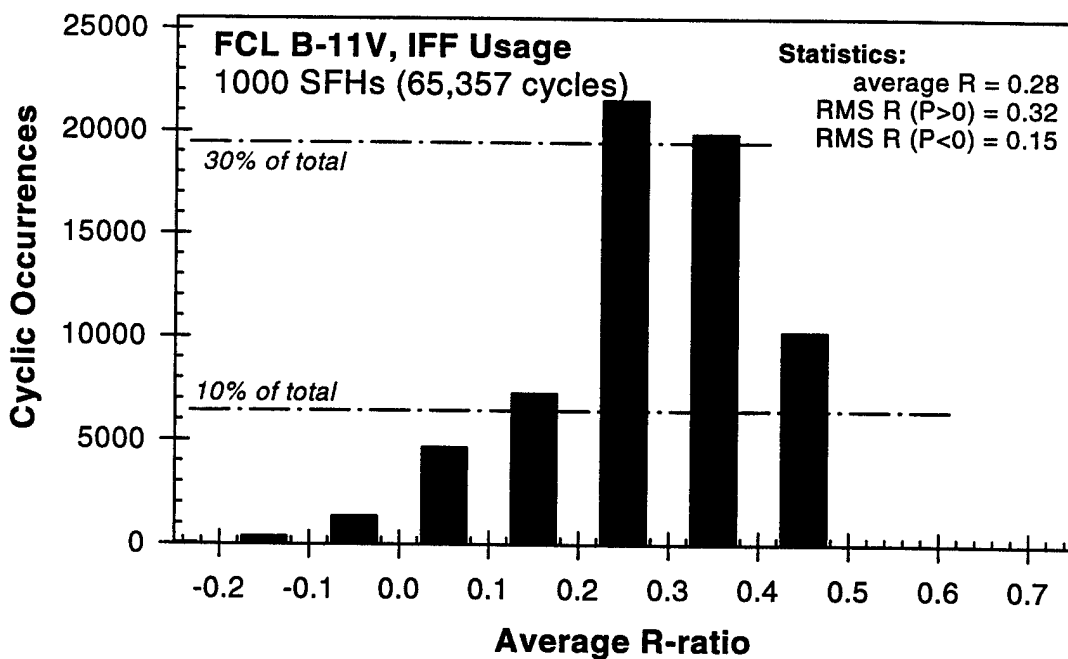
Figure 7-13. Summary of the R-ratio characteristics of the IFF usage for FCL B-11V.
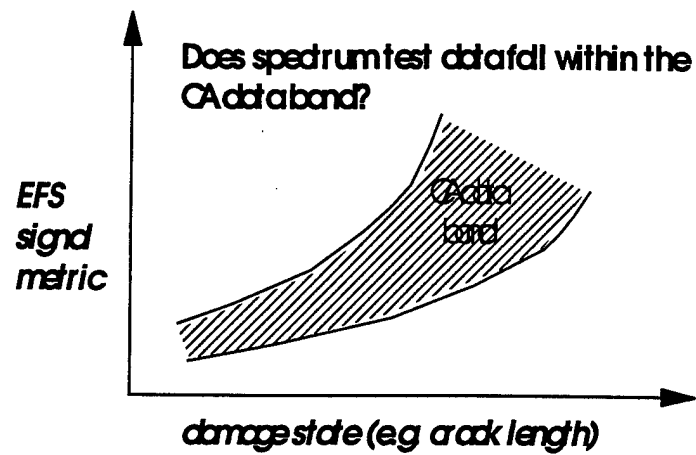
Figure 7-14. Concept of equivalent damage states for constant and variable amplitude loading.
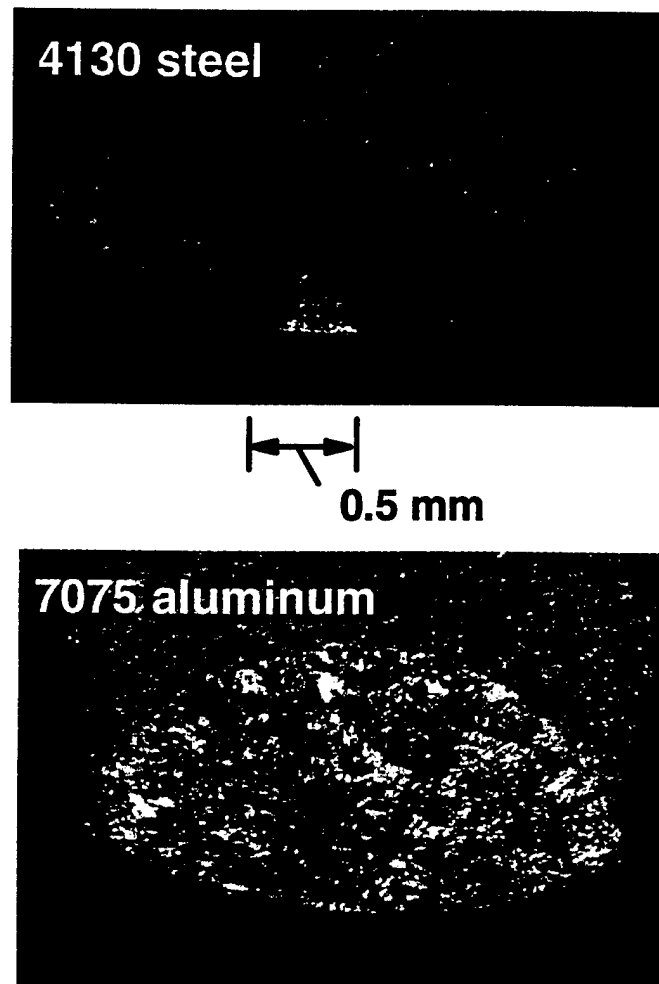
Figure 7-15. EDM starter notch and final crack shapes for steel and aluminum specimens
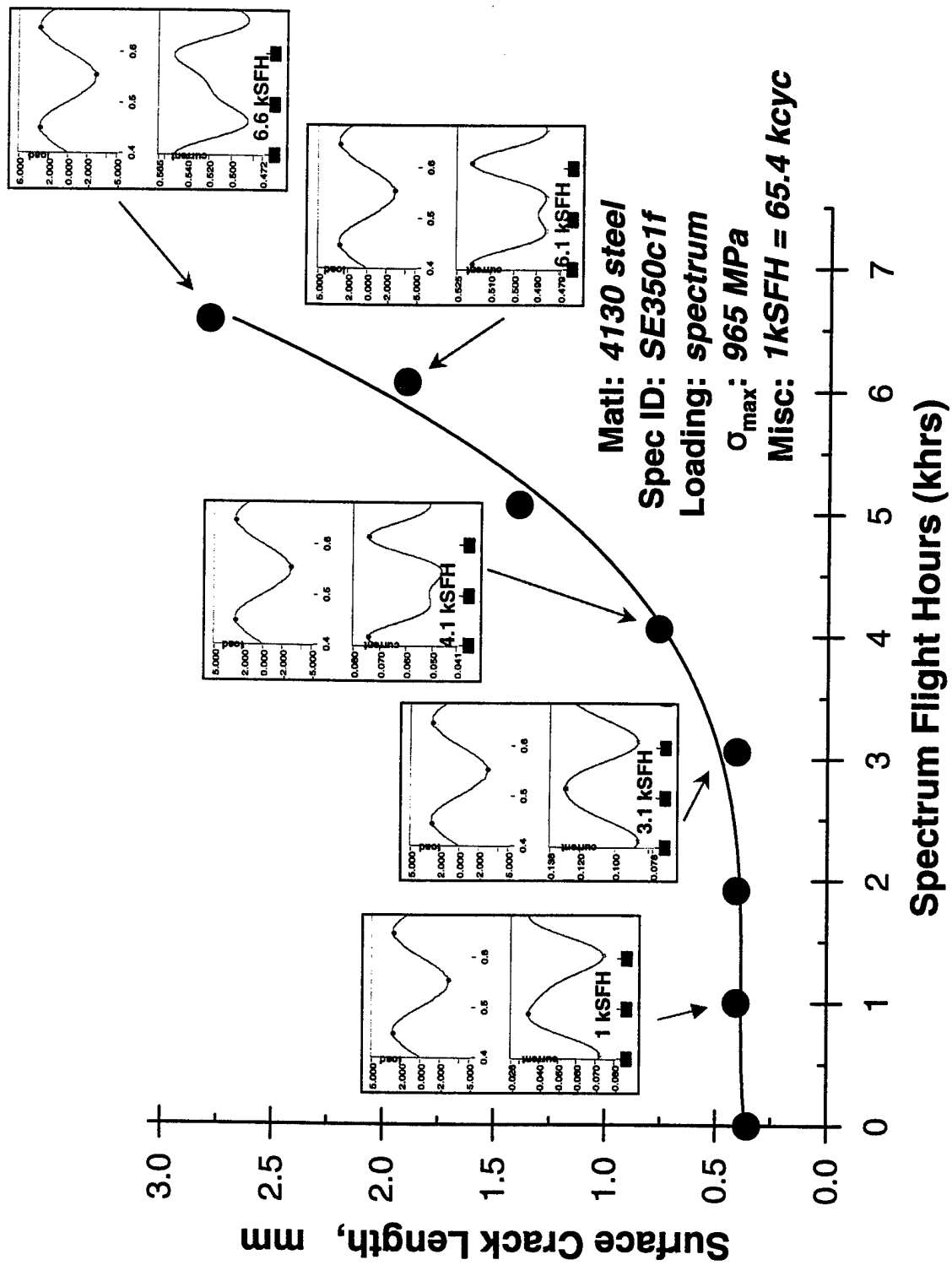
Figure 7-16. Representative EFS current response as a function of crack growth and spectrum flight hours.
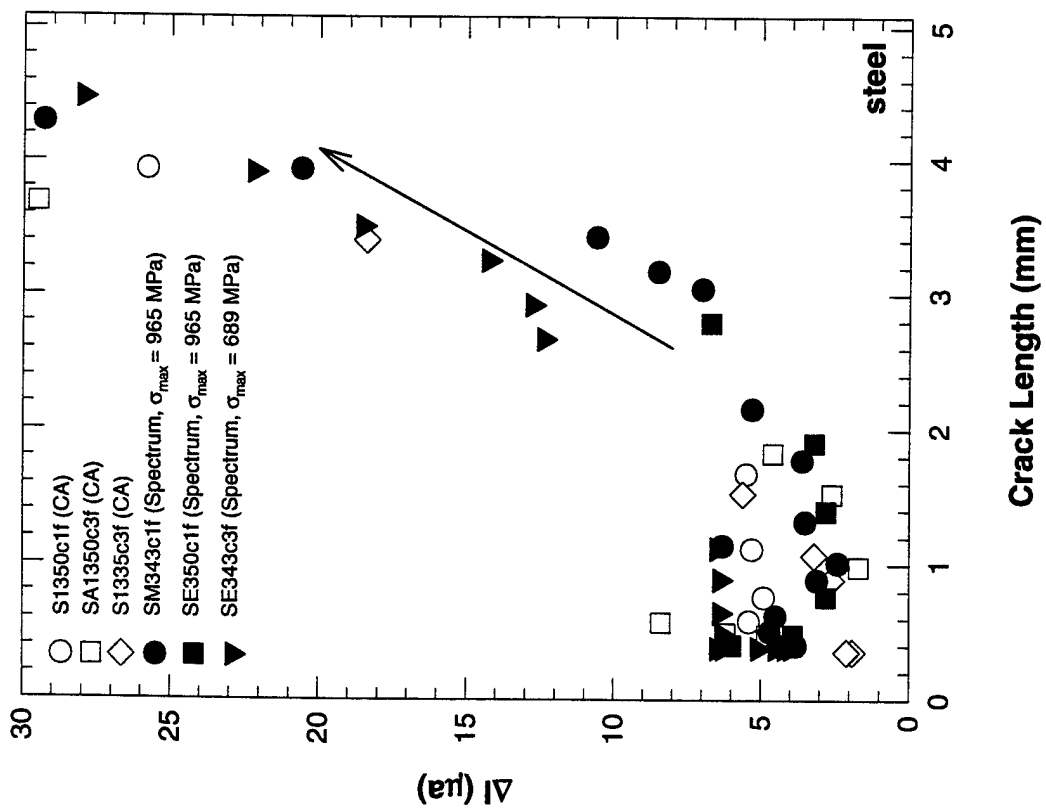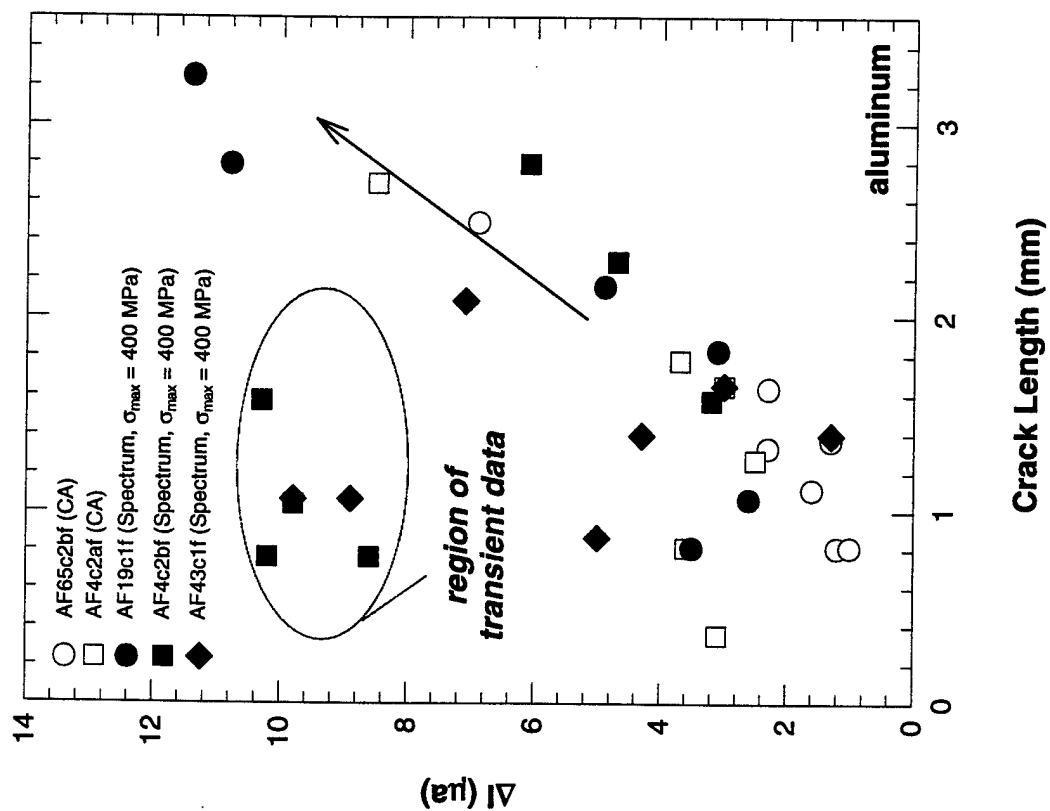
Figure 7-17. Current magnitude change with crack length for (a) steel and (b) aluminum specimens.
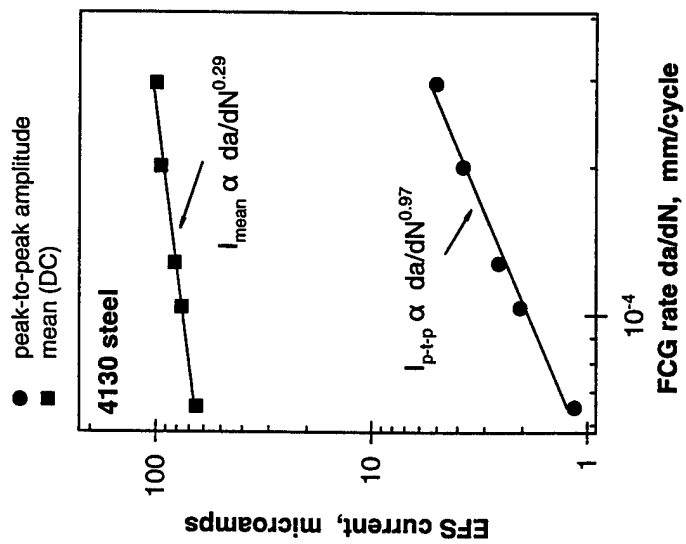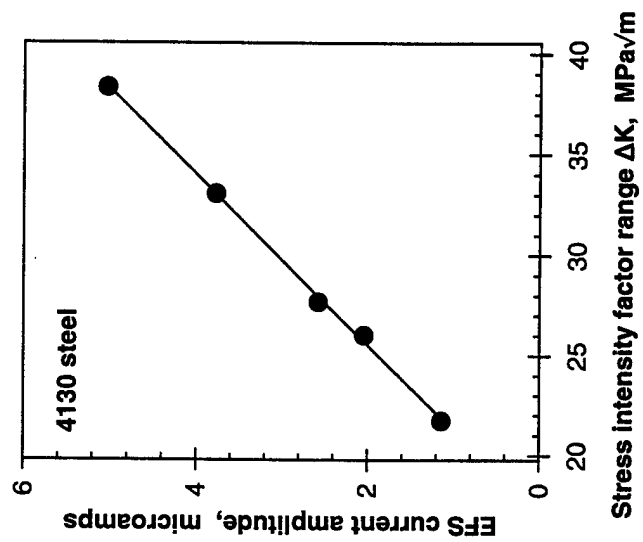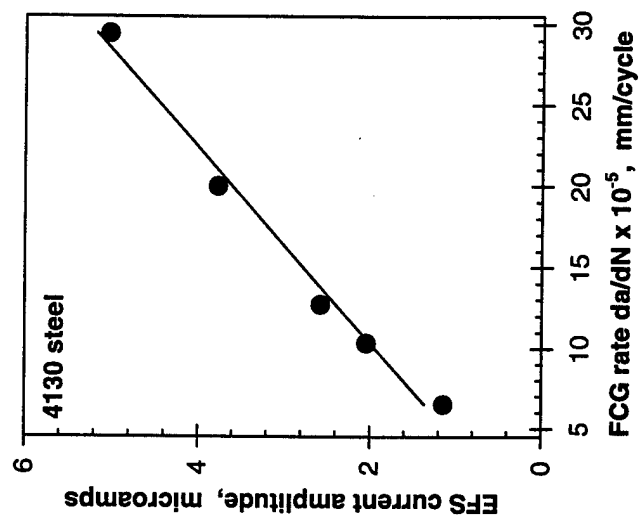
Figure 7-18. Current change observed with crack growth parameters during the FCG experiment under controlled EFS conditions shown as a function of (a) log crack growth rate, (b) applied ΔK and (c) crack growth rate.
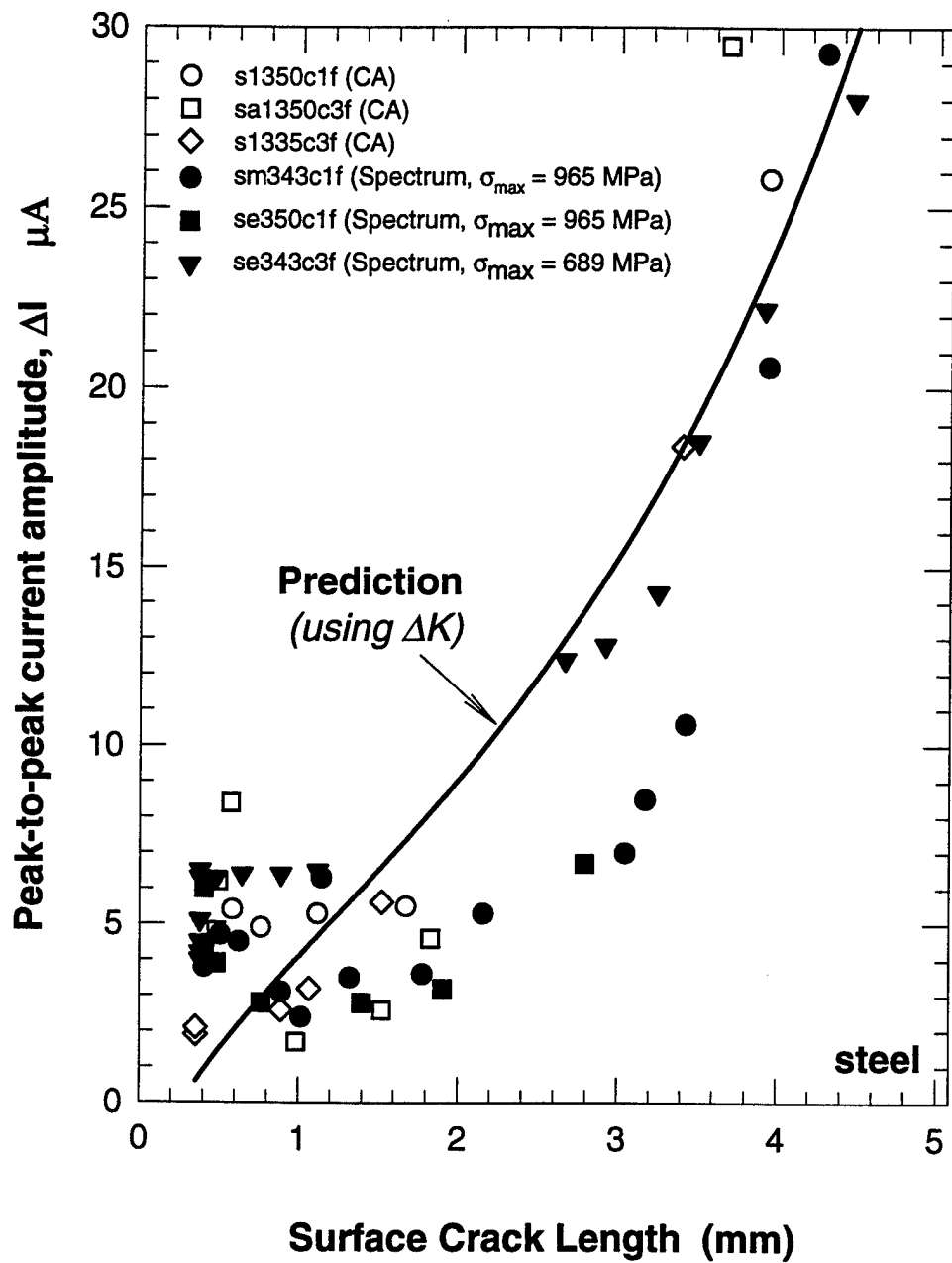
Figure 7-19. Predicted current level for constant amplitude and variable amplitude spectrum tests on surface-flawed, cylindrical specimens based on data measured during R=0.5 fatigue crack growth experiments on compact-tension specimens.

8.0 FIRST GENERATION ELECTROCHEMICAL FATIGUE SENSOR

8.1 Objective

Encouraged by the success of EFS measurements reported in the preceeding sections, it was the objective of this effort to develop a prototype electrochemical fatigue sensor that is capable of:

1) monitoring flat surfaces of limited wetted surface areas (1 - 2 sq. cm.),

2) functioning with small amounts (~5 ml.) of gelled electrolyte,

3) accommodating a two- or three-electrode system, and

4) use with any aqueous electrolytes—*i.e.*, a sensor which is rugged, yet chemically inert.

8.2 Sensor Design and Construction

The prototype EFS cell, hereafter known as the cell, was made to accommodate the flat specimen. Details and dimensions of this prototype cell are given in Figure 8-1. In the quest of maintaining a rugged and inert cell body, Teflon was chosen as the construction material. Teflon is a readily available fluorocarbon polymer exhibiting extreme chemical insensitivity, acceptable strength, and excellent machinability. Teflon is further recommended by its continued use in the chemical and electrochemical industries. The aforementioned "barnacle electrode" (see Section 4.3) is constructed of Teflon [8.1].

A cylinder of Teflon was machined to the shape and dimensions shown in Figure 8-1. This figure shows part A with a circular groove accommodating a chemically resistant, elastomeric "O" ring surrounding an inner Teflon lip which when clamped to the specimen, part B, defines an exact wetted surface area on the specimen as the working electrode (1.5 sq. cm.). Dimensions of "O" rings and machined groove widths, depths and radii are according to specifications provided in Ref. [8.2]. Part C of Figure 8-1 is a Teflon plate to which the cell is mechanically attached to the flat specimen, part B, by Nylon nuts and bolts. Non-metallic fasteners are used to avoid the development of a galvanic couple in the event of leaks in the system. This initial design is for flat specimens without center holes and will accommodate liquid electrolyte as well as gelled electrolyte.

It became apparent that flat specimens without stress concentrators would have fatigue lives that would extend well beyond a reasonable EFS testing interval. A flat steel specimen initially stressed at 600 MPa with R = 0 showed a life of 1.14 megacycles. With this in mind, the flat specimen was modified with a center hole through the thickness to provide stress concentrations at the horizontal poles of the hole's edges. These also provide focused sites for crack nucleation. Figure 8-2 shows the flat specimen with the center hole. In order for effective EFS measurements to be made on such a specimen, the entire internal cylindrical area of the hole needs to be wetted with electrolyte. This required that the back plate, part C of Figure 8-1, be modified to allow throughput of liquid or gel. Figure 8-3 depicts schematically the apparatus that allowed the generation of data shown in Table 8-1 for the small prototype cell and two flat steel specimens with center holes. From Figure 8-3, we note the back plate, part C, also contains an opening sealed by an "O" ring allowing for symmetrical wetting of the steel specimen. The prototype configuration of Figure 8-1 allows an electrolyte volume of 5.5 ml. The prototype configuration of Figure 8-3 allows a volume of electrolyte of 7.0 ml. Figure 8-4 is an isometric sketch of parts A and D of Figures 8-1 and 8-3. It should be noted that part D could have a center hole located at E (Figure 8-4) to accommodate a Luggin capillary tube. The Luggin capillary tube, filled with agar, could be extended into part A and provide the electrolytic contact for a salt bridge connection to a calomel reference electrode. Since the two electrode experiments described in Section 4 were successful, the use of the reference electrode is not necessary for effective EFS measurements. Thus, the hole and the Luggin capillary are only required, should the three-electrode system be desired.

8.3   Sensor Performance

The sensor prototype depicted in Figure 8-1 was used in conjunction with the gelled steel electrolyte to monitor EFS signals on a flat steel specimen without a hole. As previously mentioned, a flat steel specimen, initially stressed at 600 MPa with R = 0, showed a life of 1.14 megacycles. This unrealistic time to failure prompted the inclusion of a center hole in flat specimens, giving more reasonable failure times. Table 8-1 shows the results of two steel specimens with center holes exposed to the gelled electrolyte (small cell). These two specimens conform to the dimensional specifications given in Figure 8-2 and are enveloped by the prototype test apparatus shown in Figure 8-3. It should be noted that the apparatus of Figure 8-3 when used with a gelled electrolyte must allow all of the exposed metallic area (4.5 sq. cm.) to be

wetted by the electrolyte. To ensure that the total volumes of parts A, D, and C, as well as the exposed metallic surface area is filled with electrolyte, the gel is agitated just prior to injection in the chamber. The thixotropy of the gel allows a more fluid, less viscous, material to be injected upon agitation. This provides optimal cell and specimen wettability. The electrolyte then becomes more viscous (gels) in place. From Table 8-1, we note that the EFS values of elastic, plastic and base currents as well as the phase factor are in the range of viable measurements allowing percent of life predictions (appearance of the crack peak). This is discussed more fully in Section 5 of this report. These results are heartening for the use of the electronically-driven, two-electrode, gelled electrolyte, Teflon-prototype system of EFS measurements. It must be emphasized, however, that these results are preliminary and limited in number. Additional experiments are required for verification.

8.4   Sensor Performance in Relation to Stress Concentrations.

8.4.1   Objective

In many aircraft components, fatigue damage develops at inaccessible locations, either from the specific geometry of a stress concentration, such as under the head of a rivet in a lap joint, or because it is not possible to position a sensor at the exact site of the developing damage. It is necessary, therefore, to investigate the possibility of correlating measurements of damage at a less stressed region of the aircraft, which is accessible, with that which is occurring in a nearby stress concentration. This problem is termed: "the elastic/plastic problem" or "the mechanical transfer problem." To check on the feasibility of the EFS to handle this problem, preliminary experiments have been performed on flat bar specimens, rather than those with cylindrical gauge sections, because they offer flexibility in introducing stress concentrators, they can be large enough to permit remote EFS sensing, they provide the opportunity to develop practical sensors, and they represent a step towards application of the EFS. Specifically, the objective is to evaluate EFS response both at a location remote from a stress concentrator and a location close to it. A report of these experiments follows:

8.4.2   Experimental Approach

As noted above a flat bar specimen of the design shown in Figure 8-2, either with or without the hole in the center of the guage section, which provided the stress concentration when it was present, was fatigued with a practical sensor attached to the mid-region of the gauge

section. When the hole was absent, cycling the specimen with R = 0 at a stress amplitude of 600 MPa served to represent cycling at a remote location. For this condition, a simple prototype cylindrical sensor made of teflon containing 5 ml of gel sealed with an "o" ring against the flat side of the bar and retained with a screw attachment system was employed. When a hole was present in the specimen, we used the same EFS apparatus positioned over the hole with the gel forced into the hole and with the opposite side of the hole being sealed, according to the details given in Sections 8.2 and 8.3. Therefore, any damage developing inside the hole would be accessible to the EFS.

Tests were run with the Penn Instron electrohydraulic machine, Model 1331, equipped with hydraulic grips of 20,000 lbs capacity, on 4130 steel with the two electrode variant of the EFS (*i.e.*, the reference electrode was dispensed with, but the potentiostat was used for the driver potential) using the gel steel electrolyte. Data on both load and EFS response were acquired as usual with the Penn Labview system and recorded for analysis by the techniques reported in Section 5.3.2.

8.4.3   Elastic-Plastic Results

Three flat bar specimens, designated S-F 3 through 5, were tested at the conditions tabulated in Table 8-1. Note that the intention was to fatigue in the neighborhood of 600 MPa stress amplitude with R = 0, for comparison with the behavior of the cylindrical specimens fatigued at this stress amplitude. Since the EFS was being used, the frequency was kept low (0.5 to 2Hz) as indicated in Table 8-1. Tests run at such low frequency take an inordinate amount of time and therefore S-F 3, which did not contain a hole, was fatigued at progressively higher amplitudes to promote to failure. The stress of 600 MPa was too high for S-F 4 and 5 and accordingly lower stresses were used with these specimens to prevent them from breaking too quickly. The average behavior of the cylindrical specimens is also listed in Table 8-1 for comparison purposes. Note that the lives of these cylindrical specimens were considerably shorter than that of S-F 3. This is explained by the fact that those specimens were cycled at R = -1, rather than R = 0, and therefore the stress range was much greater in the round bar specimens. Also, note that the fatigue behavior of S-F 3 corresponds to pronounced "elastic" conditions, in accordance with the objective of this sub-section.

8-4

The EFS response is also listed in Table 8-1. For those specimens subjected to a variety of stresses, this table lists the results for the lowest stress used. Since the flat bar specimens were cycled at lower stress ranges, their EFS currents are also lower except for the base current, as expected, which is electrochemically determined. Note that S-F 4 was inadvertently overloaded in the opening cycles of its life, which was thereby considerably shortened. It is extremely encouraging that the EFS picked up quickly on its developing damage, as early as 11% of life, and followed it to complete fracture. This inadvertent overload also explains the rather high level of EFS current in this specimen. Whatever the history of these specimens, however, the EFS currents were experimentally accessible, demonstrating one aspect of feasibility.

More details of the EFS behavior for S-F 3 are provided in Figure 8-5, a through d, along with the details of the stressing history. The EFS parameters show their usual sensitivity to frequency and stress level. The reader is requested not to be distracted by the instabilities which became evident during the bout of cycling at 660 MPa, which were caused by a bug in the data aquisition software, later rectified. There is evidence that the damage was beginning to develop markedly around the end of the final bout of cycling. However, the specimen broke at 1,140,000 cycles at a point remote from the sensor, again happily consistent with the objective of this sub-section.

The detailed EFS behavior of S-F 4, recorded after the accidental overload cycles mentioned above, is shown in Figure 8-6(a) to (c). The overloads were shown by the EFS to have produced rapid crack initiation, the cracks were found to have been initiated in the hole, as subsequently determined by fractography, and the instabilities produced by it are clearly evident in all parts of Figure 8-6. The capacity of the EFS to read behavior in accessible stress concentrations is clearly demonstrated by this result.

For completeness, the results for S-F 5 are shown in Figure 8-7(a) and (b). This specimen was run without untoward incident and revealed the typical long drawn out fatigue behavior in a hard steel specimen cycled at low stress; namely, late life nucleation in the stress concentrator and subsequent crack propagation. (It is interesting to note that the cycles spent in crack propagation by S-F 4 and S-F 5 were about the same at 80,000 cycles, much longer than observed in round bar specimens, as discussed previously in Section 5.) The EFS current density

plot, Figure 8-7(a), indicates the onset of cracking and the large instabilities as the crack grows. These were particularly pronounced in this flat bar specimen (*i.e.*, greater than in round bar specimens): the crack was able to grow larger because there was greater volume of material in the specimen available to it. Again, the promise of the device to operate with success in actual structures is indicated by this result. Equally encouraging are the results of the waveform plots, illustrated in Figure 8-7(b). The appearance of the crack peak and the progressive phase shift as the damage develops are similar to behavior in cylindrical specimens and well pronounced in spite of the low background stress range.

The results of the above tests are considered extremely encouraging for the eventual solution of the elastic/plastic problem. For one thing, the 5 ml cell filled with the generic gel electrolyte performed satisfactorily without interuption or maintenance in spite of its small volume and the lengthy duration of the tests, that of S-F 3 taking many days. Moreover, the EFS responses were similar to those for regular tests with cylindrical specimens and accessible to the data aquisition system even though the current transients were small because the stress ranges were small. In total, the following features were reproduced:

1) the waveform shapes and responses,
2) the stress effect,
3) the effect of changes in frequency, over a limited range,
4) the phase shift behavior,
5) the response to cracking.

The physics of the EFS are such that it must receive a "suspicion" of the damage produced in an inaccessible stress concentration in order to be able to respond to it. The present results show that the EFS has the sensitivity to pick up a suspicion if it is within the sensing area but quantitative measures of what constitutes a suspicion is not yet clear. It remains to be determined during Phase 2 of the program just how well the EFS performs on the elastic/plastic problem.

8.5   Summary

From the foregoing, it is clear that a first generation prototype EFS cell has been successfully developed to meet all of the objectives of this task. Specifically, the cell is a two-electrode, electronically-driven sensor capable of accommodating liquid or gelled electrolytes, rugged, easily fabricated, and capable of accepting any EFS circuit design, capable of accommodating any flat metallic surface with a minimum width of ~ one inch, and a depth enabling its attachment to an end plate, capable of yielding effective EFS signals from a wetted surface areas of ~1.5 cm^2 to 4.5 cm^2 and an electrolyte volume (liquid or gel) of ~ 5 ml. to 7 ml., from a surface with or without stress concentrations, *e.g.*, holes, sufficiently sensitive to yield comparable EFS behavior, including crack prediction, to that of cylindrical specimens exposed to larger volumes of electrolytes, functional without causing any deleterious effects such as crevice corrosion of the wetted surface. It should be noted that the cell is also expected to be extendable to the two-electrode, self-driven system described in Section 4.

The successful development of first generation prototype cells and the results thus far obtained on steel assure their continued use in Phase 2, especially as to chemical and mechanical transference studies. These prototypes are expected to afford an easy transition to advanced cells appropriate for EFS measurements on fatigue prone aircraft components.

8.6   References

8.1   De Luccia, J., and Berman, D., "An Electrochemical Technique to Measure Diffusible Hydrogen in Metals (Barnacle Electrode)," ASTM - STP 727, (1981), p.256.

8.2   Military Specification, MIL - P - 5514 F, Design Chart 7 - 1.

Table 8-1. Stressing conditions, and fatigue and EFS response of flat bar 4130 steel specimens fitted with a prototype EFS cell.

Specimen ID	Hole at center	Freq. (Hz)	Stress (MPa)	R Ratio	Life (cycle)	Cracking at cycle	% of life	Plastic current	Elastic current	Base current	Phase factor
S-F3	No	0.5(2)	600 (640,660, 690,740)	0	1,140,000			0.004	0.045	0.056	-0.28
S-F4	Yes	0.5	460	0	140,000	15,000	11	0.01	0.025	0.065	-0.23
S-F5	Yes	0.5(2.5)	400 (440)	0	580,000	500,000	86	0.002	0.022	0.0086	-0.28
Cyclindrical		0.5	600	-1	196,600	146,500	75	0.01	0.1	0.04	-0.3

All current unit = $\mu A/cm^2$
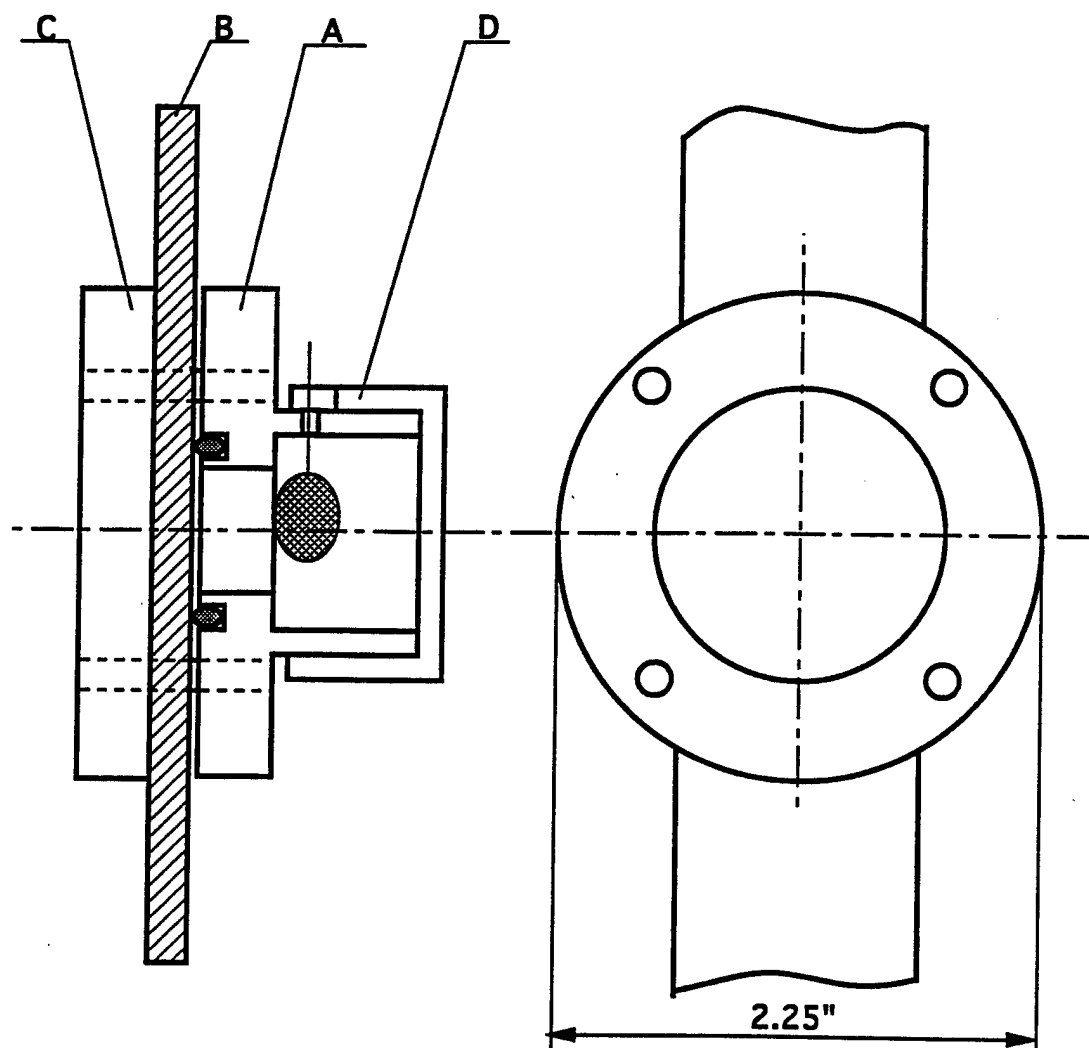
Figure 8-1. Schematic representation of an EFS cell prototype to accommodate a solid, flat specimen.
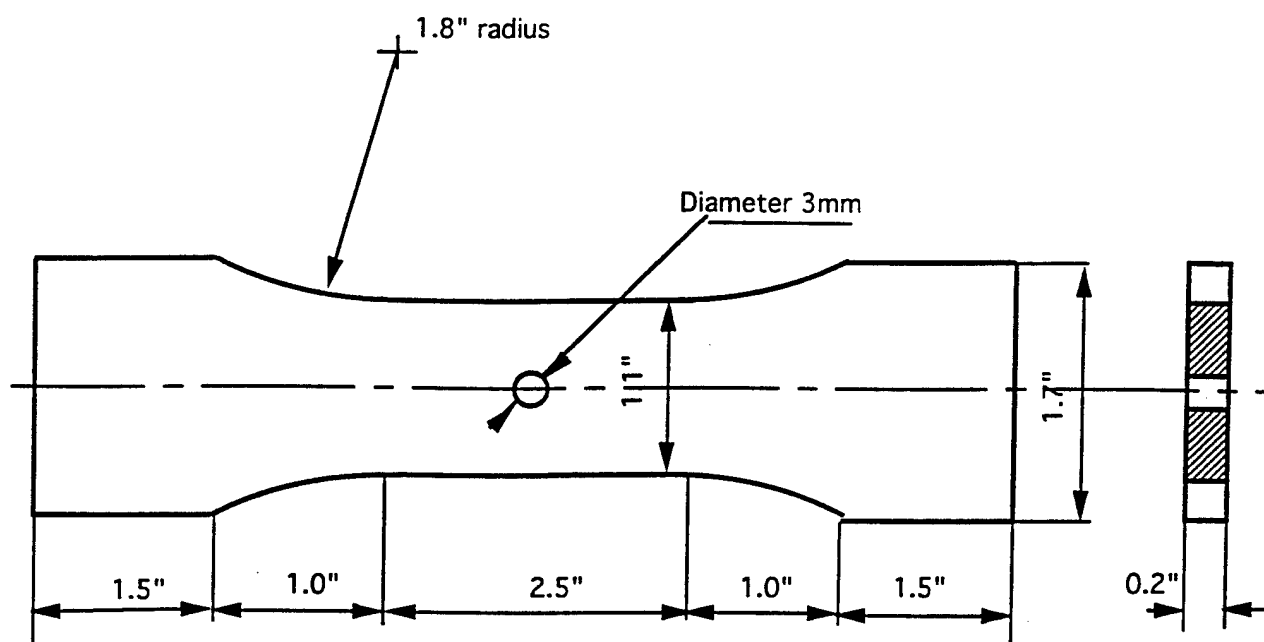
Figure 8-2. Dimensions of flat fatigue specimen with a center through hole.
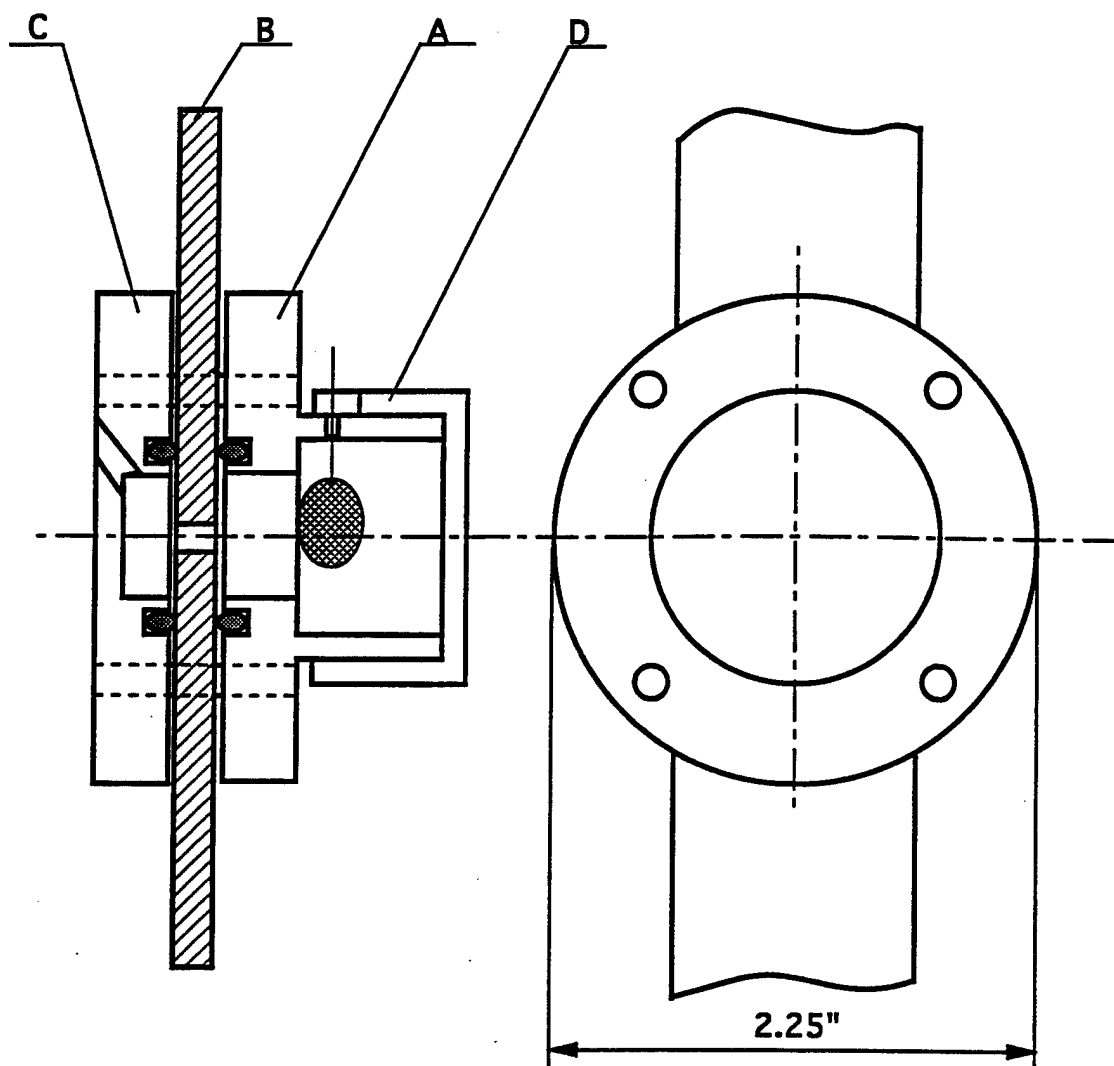
Figure 8-3. Schematic representation of an EFS prototype cell to accommodate a flat specimen with a center through hole
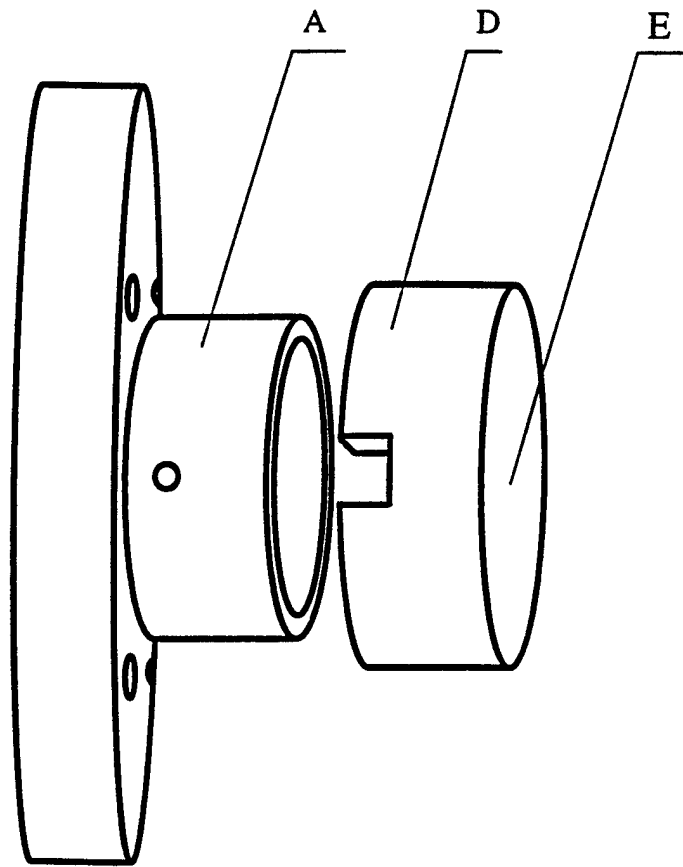
Figure 8-4. Isometric view of Parts A and D of Figures 8-1 and 8-3.
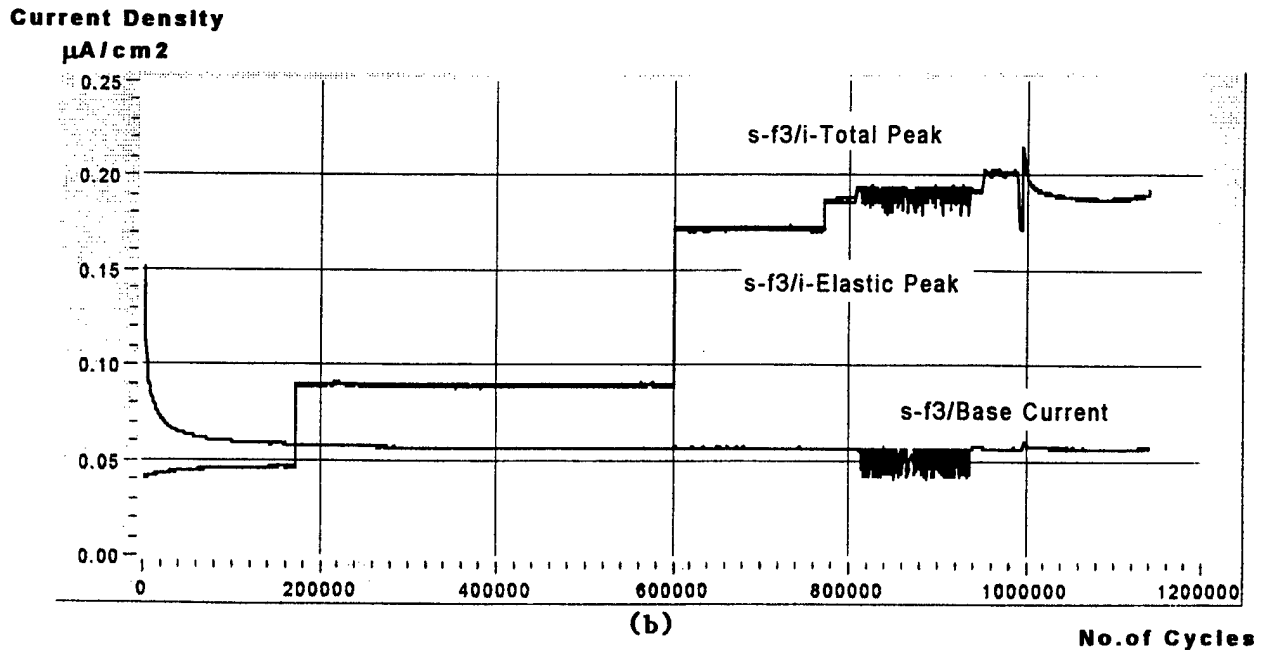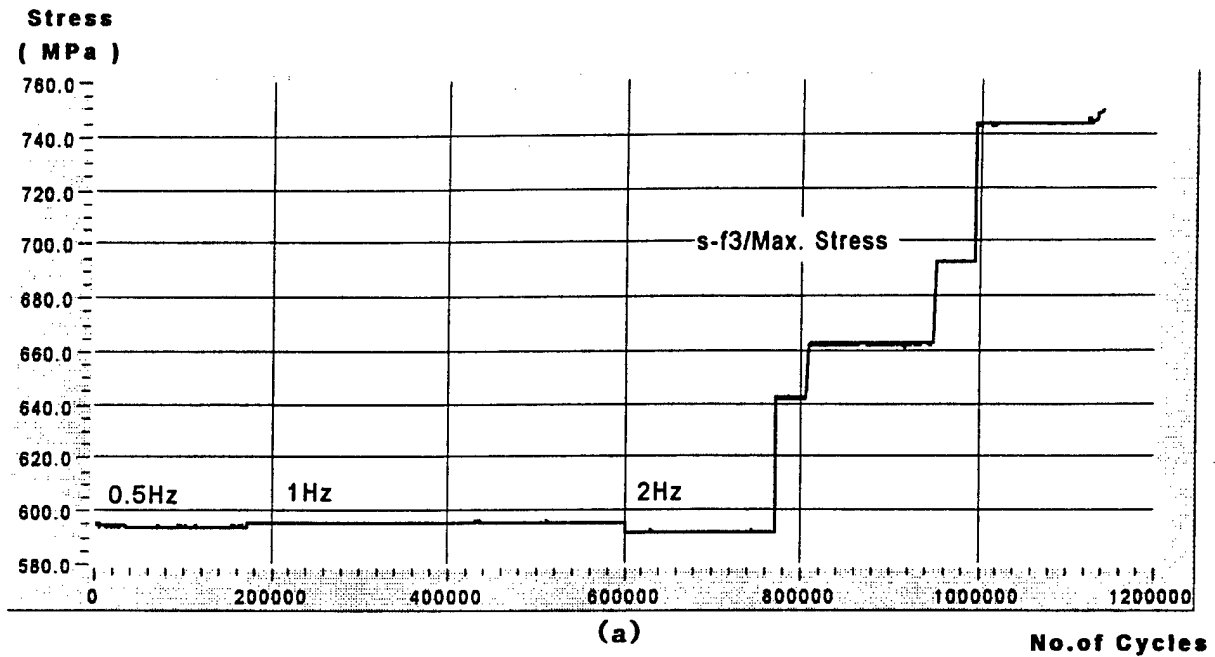
Figure 8-5. Fatigue stressing history and EFS response of 4130 steel flat bar specimen S-F3. The instabilities recorded while the specimen was being stressed at 660 MPa are not a real material phenomenon but were caused by a bug in the software.

(c)

(d)
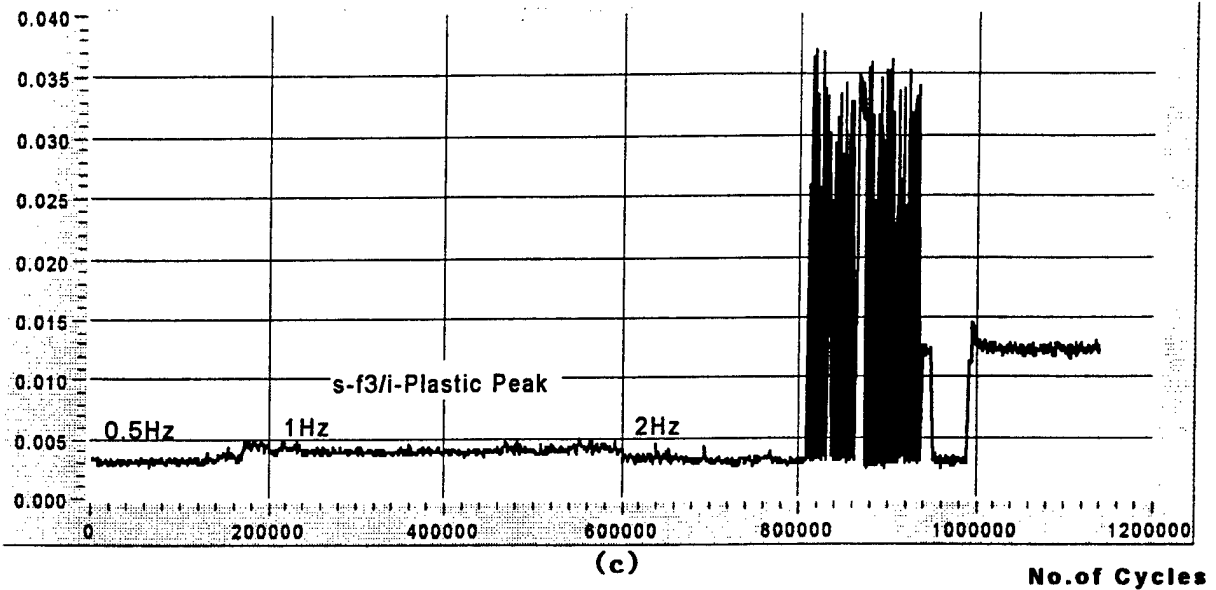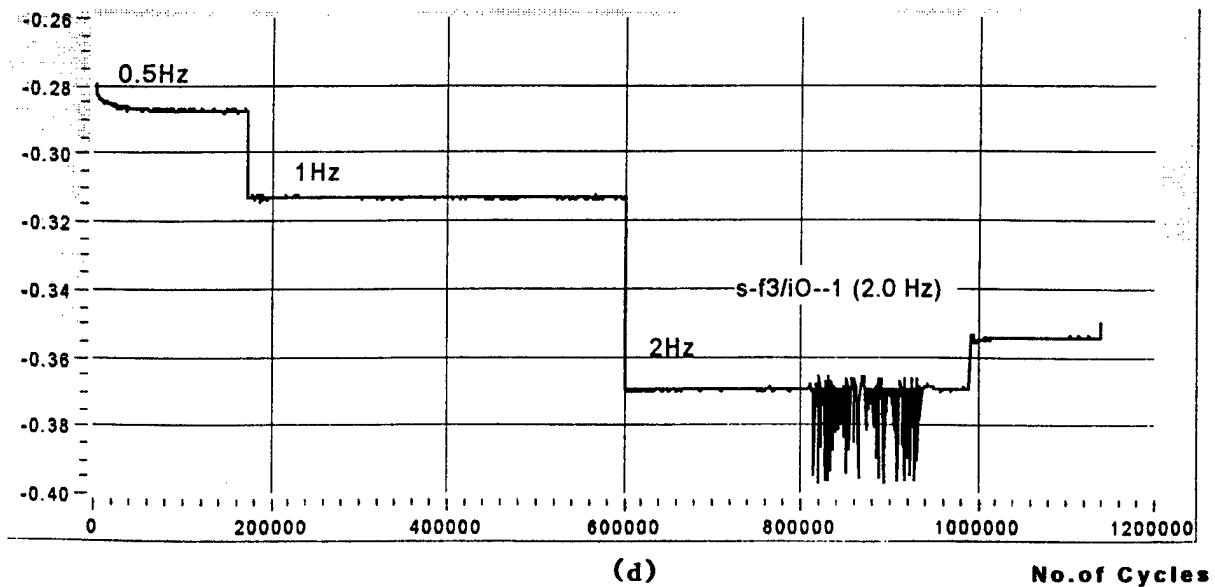
Figure 8-5 (Cont'd). Fatigue stressing history and EFS response of 4130 steel flat bar specimen S-F3. The instabilities recorded while the specimen was being stressed at 660 MPa are not a real material phenomenon but were caused by a bug in the software.
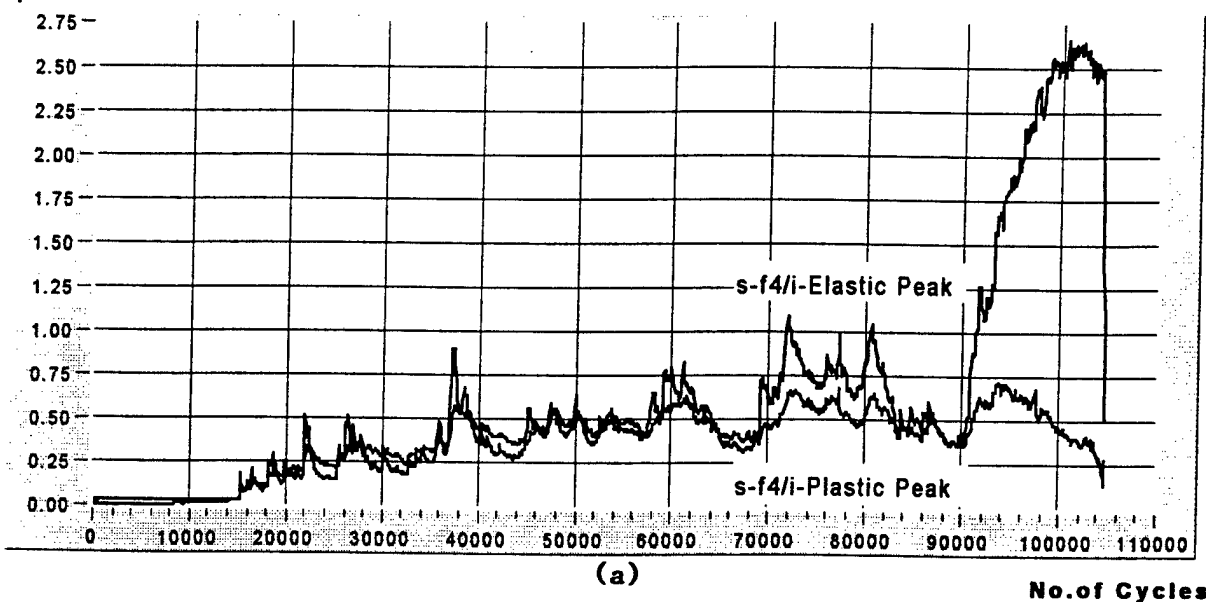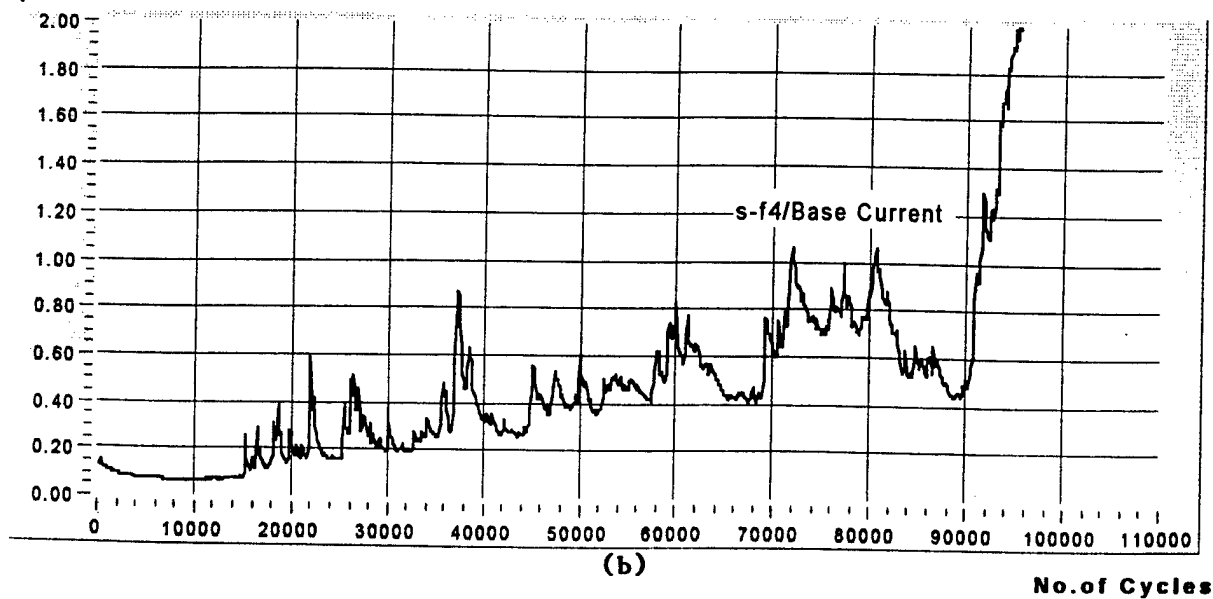
Figure 8-6. EFS response of 4130 flat bar steel specimen S-F4 cycled at 460 MPa and fitted with a prototype EFS cell.
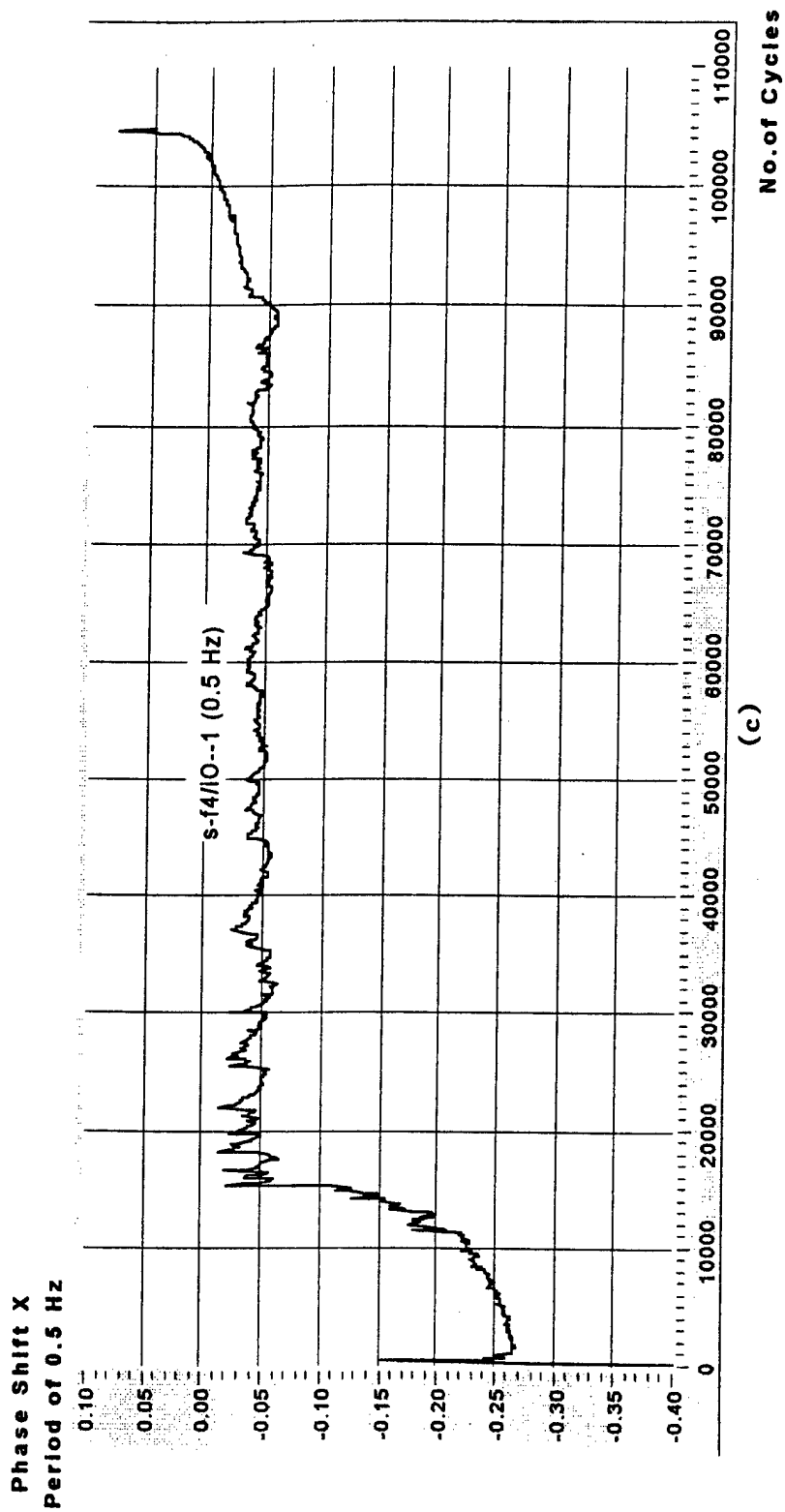
Figure 8-6 (Cont'd). EFS response of 4130 flat bar steel specimen S-F4 cycled at 460 MPa and fitted with a prototype EFS cell.
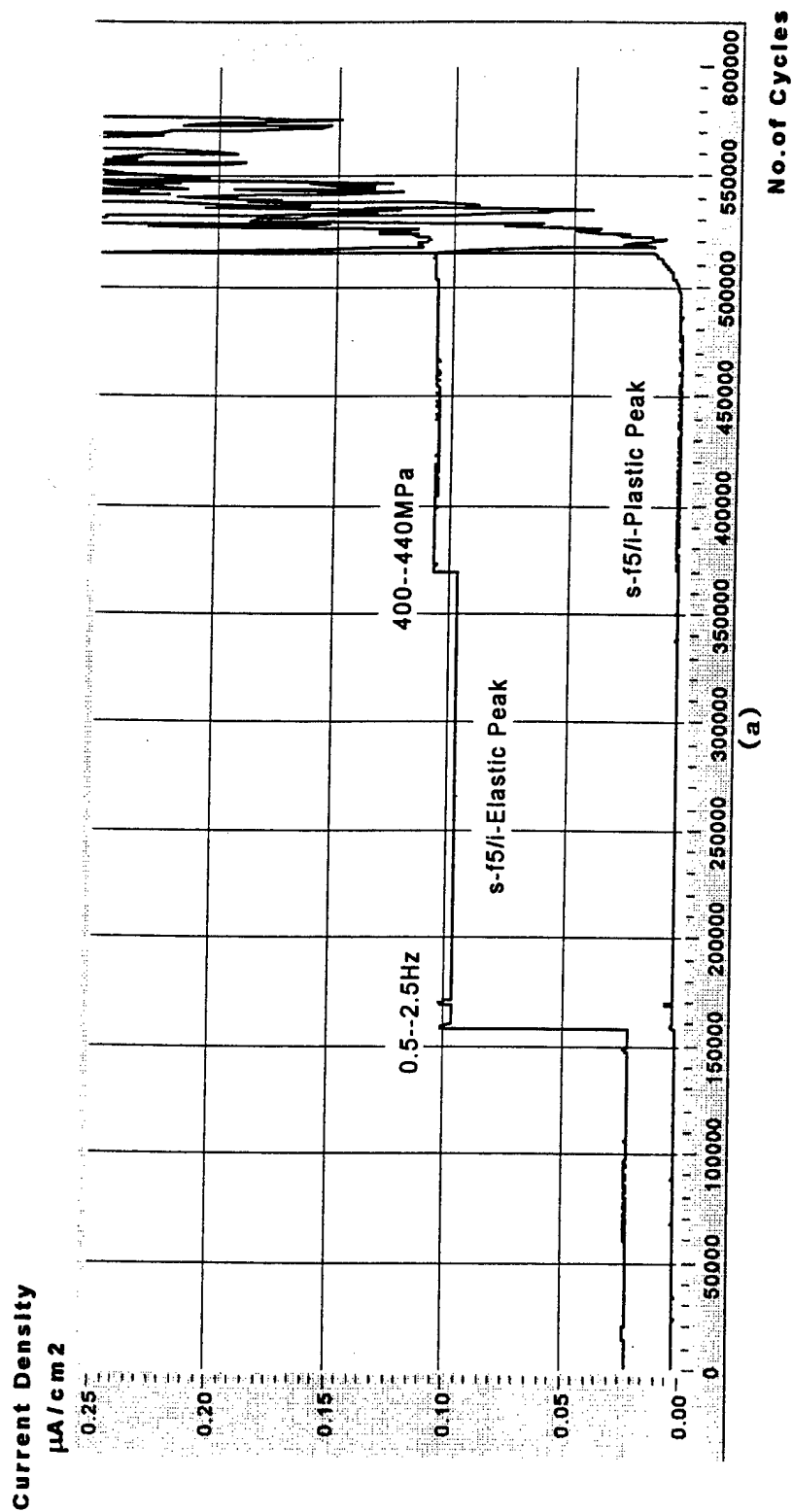
Figure 8-7. EFS response of 4130 flat bar steel specimen S-F5 fitted with a prototype EFS cell.

8-17
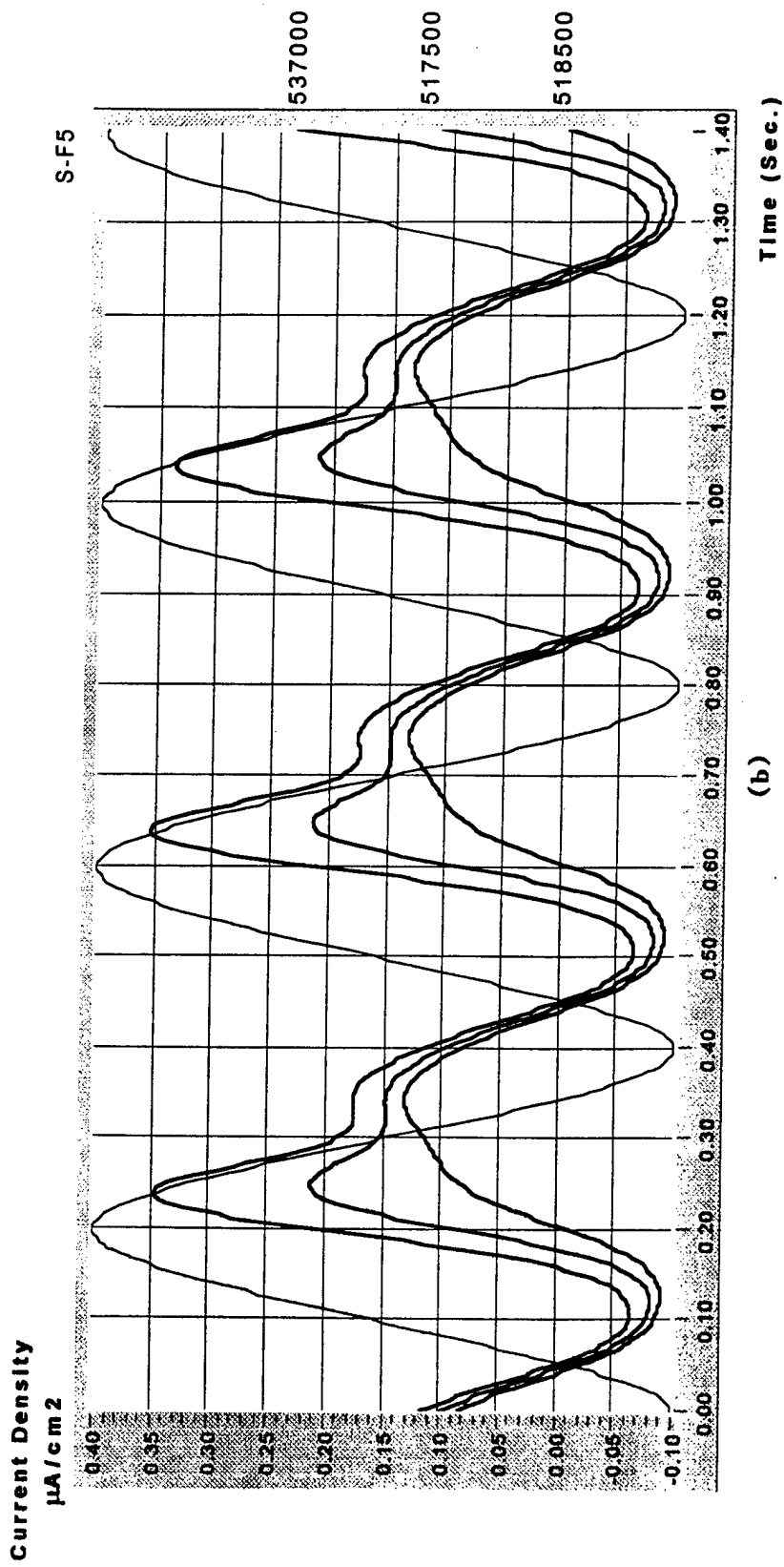
Figure 8-7 (Cont'd). EFS response of 4130 flat bar steel specimen S-F5 fitted with a prototype EFS cell.

9.0 ELECTRICAL ISOLATION OF EFS MEASUREMENTS

The objective of work summarized in this section was to assess the feasibility of electrically isolating EFS/EIS measurements on large structures such as aircraft. Stray fields will induce currents along the component being inspected (working electrode) which will split and partially go into the EFS probe. This would be problematic since the current could divide between the working electrode, counter electrode, reference electrode, and also various other leakage paths. This could shift the potential of the electrodes as well as induce stray signals into the EFS probe. This problem was approached through a combined experimental and analytical approach.

9.1 Computer Modeling of Environmental Electromagnetic Fields

Modeling (using ANSYS/EMAG finite-element code which works well at low frequencies [9.1]) shows induced currents of amps are possible and realistic in a large structure. Using computer modeling with a 10-A current located 1 m above an aluminum plate (1m x 1m x 6.4 mm), the computer model shows that the currents are not evenly distributed, are circulating, and penetrate throughout the entire plate at low frequencies of interest in the current project (*i.e.*, less than 100 Hz). Additionally, inhomogeneities will perturb these currents. Comparison of measurements with these calculations is discussed below in Section 9.4.1.

9.2 Electrical Isolation of EFS Laboratory Measurements at Penn

In early EFS-development work, an electrically isolated system was used; that is, the specimen was electrically isolated from the electro-hydraulic testing machine by means of insulated grips, both because it was found essential to do so in order to obtain valid measurements of the transient current (the effect of grounding the specimen to the machine was to produce erratic signals) as much as to avoid interference from stray currents. Clearly, to make EFS measurements on a "real" structure, isolation might not be feasible. Therefore it was desired: 1) to modify the potentiostat system to circumvent the need for isolation and 2) to eliminate stray current effects, which might be significant in a structure as large as an aircraft, by separating them from the EFS signal. This work was divided between Penn and SwRI with Penn

dealing with problem (1) and SwRI with problem (2). The following describes Penn's research with respect to this isolation problem (1).

One aspect of the electrical isolation problem is the modification of a key instrument of the EFS—the potentiostat. Most of the commercially available potentiostats are built in such a way that they are suited for a wide-range of traditional electrochemical experimentation. In such tests, a small piece of specimen (the working electrode) is typically placed in a beaker, and interacts with the rest of the world through the internal circuit of the potentiostat. Within this circuit, the working electrode is connected to a point called virtual ground. In other words, the working electrode is not really grounded. On the other hand, the current output is ground referenced. While such an arrangement is satisfactory for a traditional electrochemical test, it created a problem for the application of the EFS, because a grounded working electrode can be expected to interfere with the current measurement circuit to form a ground loop.

For most EFS applications, the component under investigation, (the working electrode), can be expected to be somehow connected to another object, especially the earth ground. In such a case, as found when we grounded our specimen in our early work, the transient current signal will be disturbed.

The first attempt to solve the problem was to modify the external connections of the commercial potentiostat in such a way that the working electrode was grounded, in the meantime, keeping the output signal floating. This floating signal was passed through a signal conditioning box, and then connected to the data acquisition board in differential mode. While the ground loop problem was thus solved, other problems arose from such an arrangement. These problems include the ease of interference with the current signal due to its floating nature and the complicated signal conditioning circuit, and resulting unpredictable phase shifts.

Finally, after experimenting with several commercial potentiostats, we gave up on modifying them, (in part because of their noisy circuits) and decided to build our own potentiostat to solve these problems. The new potentiostat was built in such a way that the working electrode and the output signals have the same grounding point. Other measures were also taken to improve the performance of the potentiostat, which include using a battery for a

clean control potential, a set of sampling resistors for small current measurement, and a built-in filter with cutoff frequencies of 5, 10, and 25 Hz, respectively. It has been demonstrated in subsequent experiments that this potentiostat works very satisfactorily for EFS tests.

In order not to be constrained to using a three-electrode system, we further modified the in-house potentiostat to include a two-electrode measurement circuit. Now the potentiostat can work in three modes by means of a switch operated from the front panel: 1) the traditional three-electrode mode as before; 2) the two-electrode mode without a reference electrode; and 3) the two-electrode mode with a reference electrode included in the circuit for monitoring the applied voltage.

Penn is planning to apply for a patent covering these potentiostat improvements. Circuit details will be provided in the disclosure statement as it is prepared in due course.

9.3 Background Noise Measurements During Laboratory Experiments at SwRI

9.3.1 Electrical Measurements During EFS Testing

Electrical measurements were conducted at SwRI on an EFS cell during data taking with the standard Solartron SI 1287 Electrochemical Interface. For these measurements the EFS cell was set up in the standard way. The test sample was 4130 steel exposed to the generic EFS electrolyte and the polarization potential was 0.4 V_{SCE}. The mechanical load was administered using Material Test System (MTS) Model 810, #15. The load was measured with a standard load cell, MTS Model 661.21A-02. In addition to this standard setup, a Hewlett Packard Dynamic Signal Analyzer (DSA) model 3562A was connected directly across the counter electrode (CE) and working electrode (WE). (The second reference electrode connection (RE2) was shorted to the WE connection. The "LO" connection was coupled to ground on the back of the unit; however, no additional grounding wire was used to connect to a grounding stake.) The DSA has very high input impedance (1M-Ohm), and therefore does not perturb the EFS measurement. The DSA and supporting laptop computer were powered from an uninterruptable power supply (UPS) which was unplugged from wall outlet to ensure that no ground loops were extraneously introduced. The mechanical modulation (loading) frequency was nominally 1 Hz,

which was generated from an MTS 458.20 micro-console, which is routinely used to drive the MTS system. A schematic overview of this set-up is provided in Figure 9-1.

Typical data are shown in Figure 9-2 through Figure 9-4. Figures 9-2 and 9-3 show the data with the work piece electrically isolated from the MTS machine. (This was done using non-conducting spacers.) Note the very rich harmonic structure with 1-Hz-frequency spacing. This signal is a combination of standard EFS signal and any other synchronous electrical noise, which may be generated by the MTS equipment. The low-pass filter used in the Solartron SI 1287 Electrochemical Interface has a nominal cut-off frequency at 10 Hz; therefore, these additional frequency components will definitely influence the signal shape and analysis. The spectrum was further investigated to determine the source of the harmonics with the MTS machine operating, but with one grip on the sample not tightened. This is discussed further below.

Figure 9-4 shows data from the same test cell, but with the sample non-isolated. This is important because in a "real world" application, the work piece will probably be grounded. This was done by electrically connecting the working electrode to the upper part of the MTS machine. Note that the 1 Hz signal is still present, as well as a rich assortment of harmonics. (The DSA was connected between the working electrode and counter electrode on the EFS cell.) Note the very good noise floor for this instrumentation, as can be seen from the data off resonance from noise spikes.

To further investigate the noise characteristics in the laboratory setting during EFS measurements, additional data were taken with a setup similar to that described above. The details were different in the following way: MTS model 810, #17 was used in conjunction with a HP 35670A Dynamic Signal Analyzer. During some of the tests the load cell was disconnected and the displacement monitor was used instead. This was done so that the grip could be physically disconnected from the EFS work piece, to confirm that the EFS signal would disappear. When the grip was disconnected, the EFS signal did in fact disappear. However, since the noise floor in this setup was slightly higher than in the previous measurements, it was not proven for certain that all the higher harmonics were from the EFS signal alone, *i.e.*, some of them could have been from the MTS drive unit or the load cell. During these tests it was observed that under certain conditions, strong 8 Hz and 75 Hz signals were sometimes present.

These signals were present when the UPS was plugged into the wall outlet, but when the UPS was unplugged and operated in the stand-alone mode, they disappeared. Therefore, they were probably from other mechanical tests going on in the same laboratory.

9.3.2 Grounded Work Piece Measurements with Solartron SI 1287 Electrochemical Interface

Since the "real world" application of this technology will probably require the work piece to be grounded, an effort was made to operate the Solartron SI 1287 Electrochemical Interface unit with a grounded work piece. According to the manual, it should be possible to obtain data with a grounded working electrode. The manual additionally states, however, that it is not advisable to ground the WE with the 2, 20, or 200 microamp ranges selected [9.2]. (Note these ranges are of interest in the present experiments.) Because the data of interest is in the frequency range 1-5 Hz (and harmonics) the 60-Hz noise component is the most troublesome. Several techniques were used to isolate the noise. The Solartron SI 1287 has output monitors on the back of the unit to monitor the current and voltage signals; these can be monitored with an oscilloscope. The current output was monitored as various grounding connections were utilized. This oscilloscope was isolated from ground loops using a Topaz Ultra-isolator model 91892-11; however, this was later found to be unnecessary.

The dominant 60-Hz noise component was present even if the MTS control unit and hydraulics were turned off and disconnected from the wall plug. Additionally, the supporting computers and frequency response analyzer (FRA) were also found not to be a major 60-Hz noise source in the EFS current data. (For some of these experiments, the EFS cell was replaced with a 25 K-Ohm resistor.) In some cases, the geometrical setup of the lab contributes to the 60-Hz component; for instance, noise was picked up from the computer monitors if the lead wires were too close.

A major contribution to the 60-Hz noise that interferes with the EFS signal is introduced when there is a path directly into the first amplifier in the electrochemical interface, i.e., the current-to-voltage converter. Therefore, if the work piece is grounded and is simply connected to the working electrode connection on the Solartron SI 1287 Electrochemical Interface Unit, a direct path to the first amplifier is present, which leads to increased 60-Hz noise.

The following arrangement was determined to be of interest for the present measurements (see Figure 9-5) which simulate a "real world" application. This is the "two electrode" configuration, but could be modified for the "three electrode" configuration, if necessary:

1. Work piece is grounded to electrical ground.
2. Work piece in the EFS cell is connected to the "CE" connection on the Solartron.
3. Counter electrode in the EFS cell is connected to the "WE" connection on Solartron. (Note: the concept here is that the Solartron is measuring current flow between the WE and CE connections.)
4. Reference electrode connection "RE1" is connected to "CE". (Note: in this configuration the sign convention for the polarization voltage has to be reversed from that of the normal operation.)
5. Reference electrode connection "RE2" is connected to "WE".
6. "LO" jumper on the Solartron unit is left floating.

This situation gives comparable signal-to-noise ratios as those of the so-called "isolated" work piece measurements, in which the work piece is connected to the WE, the counter electrode is connected to CE, and the "LO" connection is jumped to ground.

9.3.3 Summary and Discussion of Laboratory Noise Measurements

A Dynamic Signal Analyzer (DSA) was used across an operating EFS cell to determine noise characteristics. Significant harmonic content exists which is from the EFS signal, and possibly very minor contributions from the mechanical and electrical noise from the MTS.

There is an EFS signal present with a grounded-work-piece setup when using the Solartron SI 1287. The grounded-work-piece configuration is important, since that will probably be the way that a practical "real world" instrument is configured.

The harmonic content of these signals below 10 Hz compare very well to those calculated by Fourier analysis of the time-domain signal recorded from the Solartron instrumentation. This means that real-time spectral analysis could also be used to process the EFS data.

9.4　Background Noise Measurements on Large Structures in the Lab

9.4.1　*Measurements on Large Aluminum Plate*

Electrical noise measurements were conducted on a large aluminum plate, isolated from ground on a wooden support. These measurements are difficult to do properly because of the electromagnetic pickup, ground loops, and variable surface resistance. Experimental details are described in the following paragraphs.

A probe was fabricated for these experiments. It has two spring-loaded electrodes, 1-inch apart in a Teflon housing. For the experiments described here, it was electrically isolated using a Sony/Tek model 6909 Optical Isolator which was battery powered (SmartUPS model 1400). Current measurements (of the injected currents) were done using a Fluke clip-on current transformer Model 801-600. Frequency response measurements were conducted using a Hewlett-Packard Model 89410A or a Hewlett Packard Model 3562A Dynamic Signal Analyzer (DSA). Injection currents were implemented using a drive frequency typically 23 Hz from the spectrum analyzer output and amplified with a McIntosh Model 2300 power amplifier.

Typical data are shown in Figure 9-6, which displays signal in dB(v-rms) (*i.e.*, decibels referenced to 1-volt rms) as a function of frequency. For this experiment, 3.8 A was injected at 23 Hz into the plate. The resulting spectrum was obtained with the probe electrodes in the direction of the expected induced currents. Note the 60-Hz pickup, which is typical for almost any experiment. In this case the magnitude of the 23-Hz injected signal is almost the same as the extraneous 60-Hz pickup.

The aluminum plate was connected with a clip lead to an electrical conduit within the laboratory. A large noise spike that appeared at 50 Hz was from some electrical apparatus within the building. In this case, the 23-Hz injected signal decreased since some of it can find another path to ground, further away from the probe, so that it was not as readily detected.

The aluminum plate was connected directly to the building ground. In this case, the injected signal was much smaller than the 60-Hz pickup, presumably because there was a good path to ground for the injected current to follow.

Results validate the computer simulations (see Section 9.1) in that the currents were non-uniform and the direction of the probe alignment was very important, thus indicating the directionality of the currents.

9.4.2 *Measurements in the Power Engineering Research Facility*

Measurements were also conducted in the Power Engineering Research Facility (PERF) located at SwRI. These measurements simulate measurements on large structures, such as airplanes. In this facility, the electrical grounding and noise characteristics have been very well characterized. Additionally, it contains a large shielded enclosure (Faraday room) which can be used to simulate an aircraft, in both the grounded and ungrounded mode.

The PERF Parent Room (PR) is a 11 x 25 x 14-ft electrical enclosure (Faraday Cage) made out of 3/8-inch-thick stainless steel. The Parent Room is located within a larger laboratory area, with approximately 25 x 45 x 17-ft dimensions. Inside it is a smaller enclosure called the shielded enclosure (SE) which is approximately 8 x 8 x 8 ft. These enclosures are electrically isolated from the building, but can be connected to the building ground through large braided cables. For these measurements the paint was taken off from two different patches on the Parent Room, so that good electrical contact could be made with the probes. (Probes have been previously described in Section 9.4.1; briefly, they have spring-loaded electrodes, 1 in. apart.) Two probes were positioned approximately 1.5 in. apart with perpendicular directions from the probe electrodes. The signals were isolated using a Sony/Tek model 6909 Optical Isolator which was battery powered (SmartUPS Model 1400), and subsequently analyzed using a Hewlett Packard Dynamic Signal Analyzer (DSA) Model 3562A.

Data were digitally recorded, and later graphed using standard methods. Five test configurations were used, ranging from the parent room being completely electrically isolated, to that of the parent room being connected to the building and a motor-generator set running inside the parent room. A typical data set (C5-100m.prn) is shown in Figure 9-7.

For this large structure, no significant differences were found for the 60-Hz (and other frequency) pickup encountered from the various test configurations. That is, the 60-Hz pickup was very similar to that found previously using the large (1 m^2) aluminum plate discussed in

Section 9.4.1. Additionally, during the more advanced test configurations, the motor-generator running inside the parent room did not significantly increase the noise generated and detected on the outside surface. This was expected based on standard electromagnetic field theory.

9.4.3 Summary and Discussion of Measurements on Large Structures

Measurements were done on large structure in the PERF (Power Engineering Research Facility), simulating an airplane. It appears that with a grounded structure, the amount of 60 Hz pickup is comparable to that from a large (1 m²) plate.

9.5 Background Noise Measurements on T-38A Aircraft

Background noise measurements on aircraft were conducted utilizing T-38A's located at Randolph AFB, TX in collaboration with the Air Education and Training Command (AETC) 12th Maintenance Squadron. An initial visit to the facility was made in July 1998 [9.4], with subsequent measurements conducted in August. Aircraft are located in open-air hangars for scheduled and non-scheduled maintenance. Aircraft are normally grounded to a grounding electrode in the floor of the hangar, but can be ungrounded if necessary. A photograph of the aircraft in the hangar at Randolph AFB is shown in Figure 9-8.

On August 6, 1998, measurements were conducted on T-38A tail number RA 68/143 located in Hangar 4 at Randolph AFB. A Hewlett Packard 35670A Dynamic Signal Analyzer (DSA) powered with a SmartUPS model 1400 was used for the data accumulation. Various measurements were made utilizing the Teflon probe (previously described in Section 9.4.1), and standard-voltmeter point probes, as shown in Figure 9-9. Measurements were taken on painted and unpainted sections, with and without the UPS plugged into the wall outlet. Measurements were also taken with the aircraft connected and disconnected from the standard grounding electrode in the floor of the hangar. Typical data are shown in Figure 9-10.

It appears from these measurements that the aircraft hangar environment may not be as electrically noisy (at low frequency) as the laboratory environment at SwRI, except for intermittent noise at 2.5, 40, 80 Hz and RF. A summary and comparison of these measurements is provided in Table 9-1 in Section 9.7.

9-9

9.6   Methods to Improve Signal-to-Noise Ratio

Based on the above information, a variety of methods for improving the signal-to-noise ratio during EFS measurements are recommended:

1. RF shielding will probably be necessary due to intermittent RF noise, which may be modulated at low frequencies (refer to intermittent noise mentioned above, observed during data taking).

2. Establish a single-point ground.

3. If special electronic hardware is designed, standard techniques should be utilized such as differential input to reject common-mode noise.

4. If UPS (*i.e.*, batteries) are used as a power source, unplug from wall outlet during data taking.

5. Care must be taken to not pick up unwanted 60-Hz noise from computer monitors and nearby transformers due to being physically close to them.

6. Investigate the effects of the polarization feedback loop on the electronics. This is used to stabilize the polarization voltage; however, it may have influence on the measurements if not properly designed.

9.7   Concluding Remarks

Table 9-1 below summarizes observed 60-Hz noise, which is expected to be the most troublesome component, because of its high intensity and low frequency nature. Occasionally, intermittent RF (radiofrequency) noise was present in the laboratory, as well as aircraft hangar situations, so that RF shielding should also be considered for future field instruments. Additionally, unexplained low-frequency noise (in addition to the ubiquitous 60-Hz component) was observed at 2.5 Hz, 40, and 80 Hz (in the aircraft hangar) as well as 8 Hz, and 75 Hz (in the

laboratory) which indicates some data averaging will be necessary for the field instrument. These quoted frequencies are only given as examples, they are not expected to be unique. It appears that large structures can be used to simulate the aircraft hangar environment for testing purposes. From the work described above it can be seen that there are several methods to measure EFS signals (time or frequency domain), increase the signal-to-noise ratio, and configure the electrode arrangement for practical measurements in the field environment.

The most encouraging result from this work is that measurements of background noise levels in aircraft hangars were found to be equivalent to, or less than, noise measured during EFS measurements in a typical mechanical testing laboratory. Thus, the successful measurements of EFS current in the microampere range in the laboratory which are documented in this report demonstrate the feasibility of EFS measurements on aircraft hangars.

9.8   References

9.1   ANSYS/EMAG computer code by ANSYS, Inc. for doing finite-element electromagnetic calculations.

9.2   *Solartron SI 1287 Electrochemical Interface User Guide* [Solartron a division of Solartron Group Ltd, Hampshire, UK] 1996, Section 3.1, page 2.6.

9.3   *The Fundamentals of Signal Analysis*, Hewlett Packard Application Note 243, 1994 Hewlett-Packard Co. (5952-8898E); also located at the World Wide Web site http://www.tmo.hp.com/tmo/Notes/pdf/5952-8898E.pdf.

9.4   Point of contact was CMSgt Tony Hicks, AETC/LDMTS, 210/652-3130.

Table 9-1. Summary of Typical 60-Hz Noise Measurements

Configuration	60 Hz Noise Figure Note: referenced to 1-volt rms	Reference Spectrum	Comments
Al Plate (1 x 1 m)	-105 dB	EFS1R.PRN	Plate isolated
Al Plate	-95 dB	EFS3R.PRN	Plate connected to building steel
PERF (14 x 25 x 11 ft)	-105 dB	C5-100M.PRN	PERF connected to building steel
EFS Cell	-93 dB	ISOA1.PRN	Isolated work piece
EFS Cell	-93 dB	TRAC6	Isolated work piece
EFS Cell	-20 dB	TRAC13	Pickup electrodes not connected
EFS Cell	-82 dB	TRAC30	Non-isolated work piece
T-38A	-126 dB	TALON9.DAT	Aircraft grounded Under wing on bare screws, 3" apart
T-38A	-117 dB	TALON4.DAT	Aircraft ungrounded Aft of canopy
T-38A	-118 dB	TALON3.DAT	Aircraft grounded Aft of canopy
T-38A	-44 dB	TALON6.DAT	On paint (non-penetrating) 3" apart
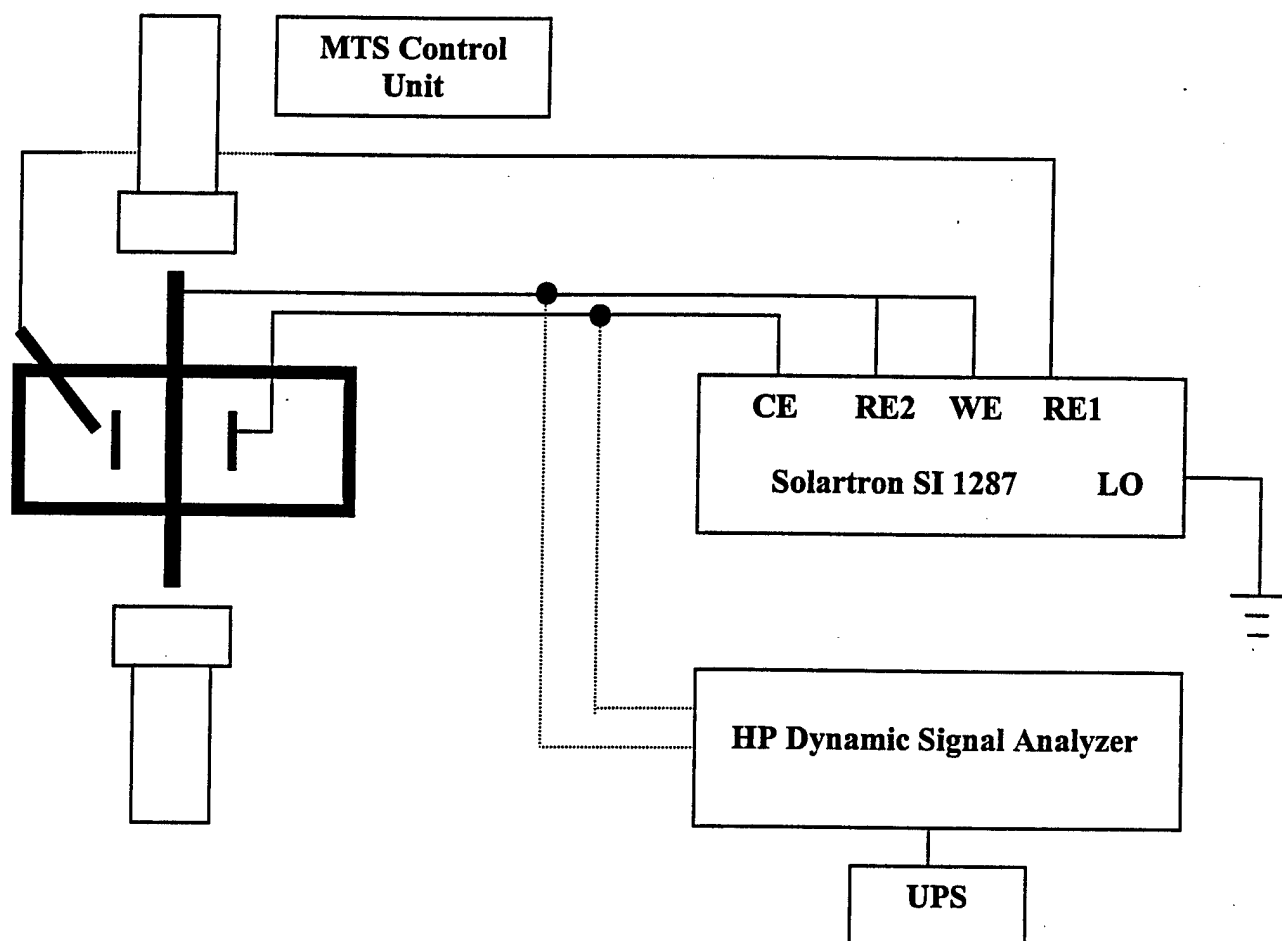
Figure 9-1. EFS Set-up With Digital Signal Analyzer (DSA)

EFS Isolated Specimen
ISOA1.PRN Col. 1 (3/23/98)

EFSFREQ1.WB1
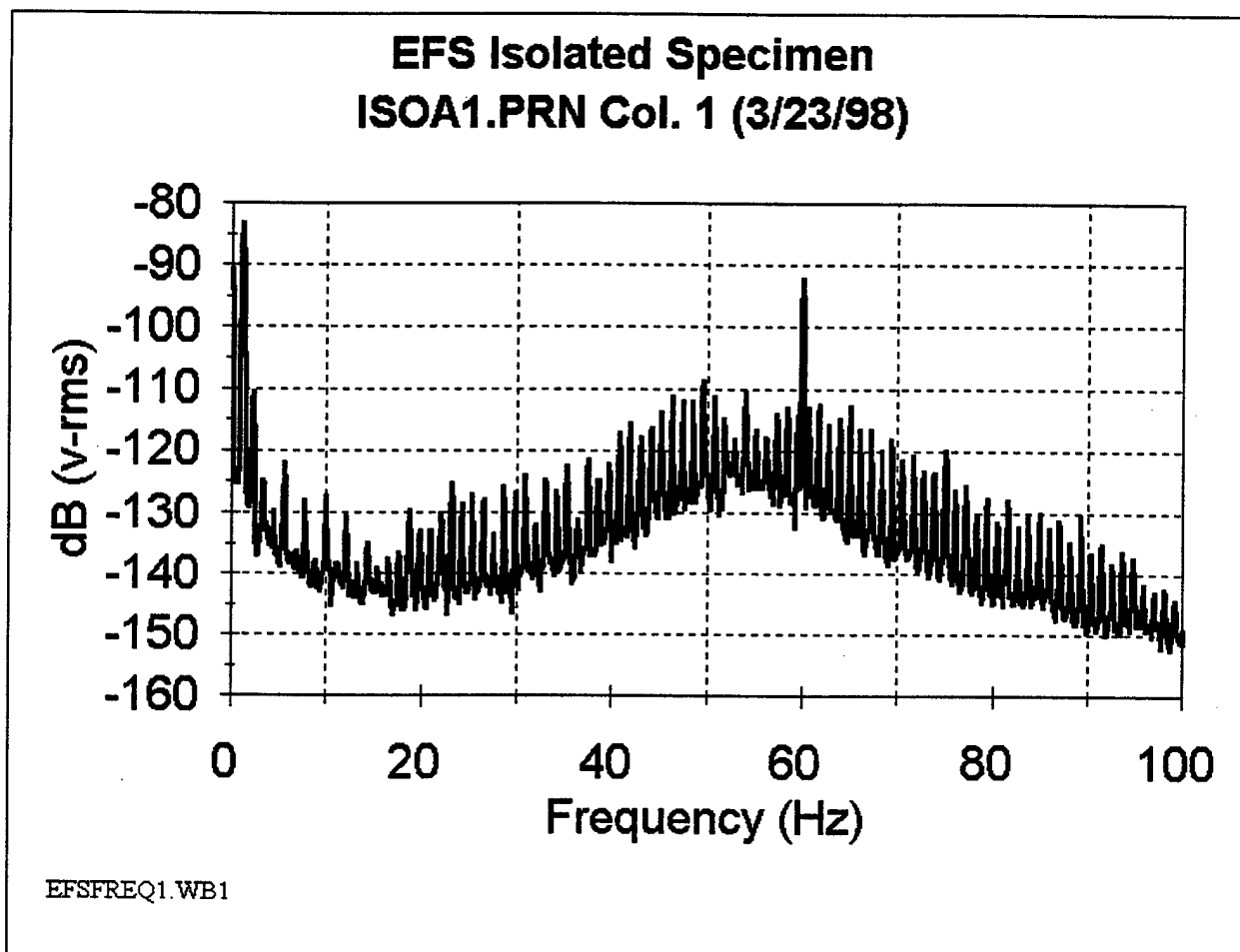
Figure 9-2. Electrical spectrum taken across EFS cell during operation: Isolated Work Piece

EFS Isolated Specimen
ISOA2.PRN Col. 1 (3/23/98)

EFSFREQ1.WB1
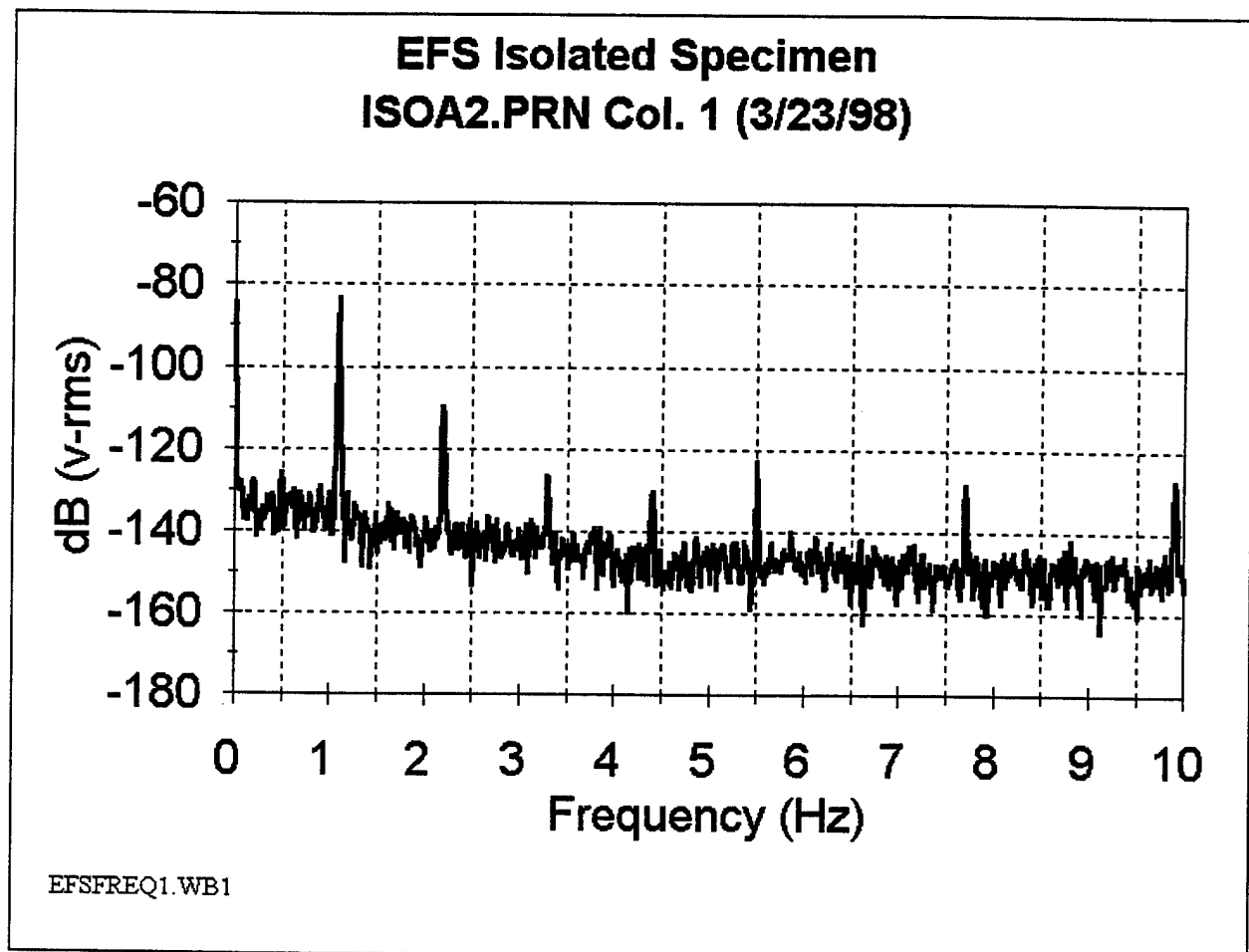
Figure 9-3. Electrical spectrum taken across EFS cell during operation: Isolated Work

EFS Non-Isolated Specimen
NONISOA2.PRN Col. 1 (3/23/98)

EFSFREQ1.WB1
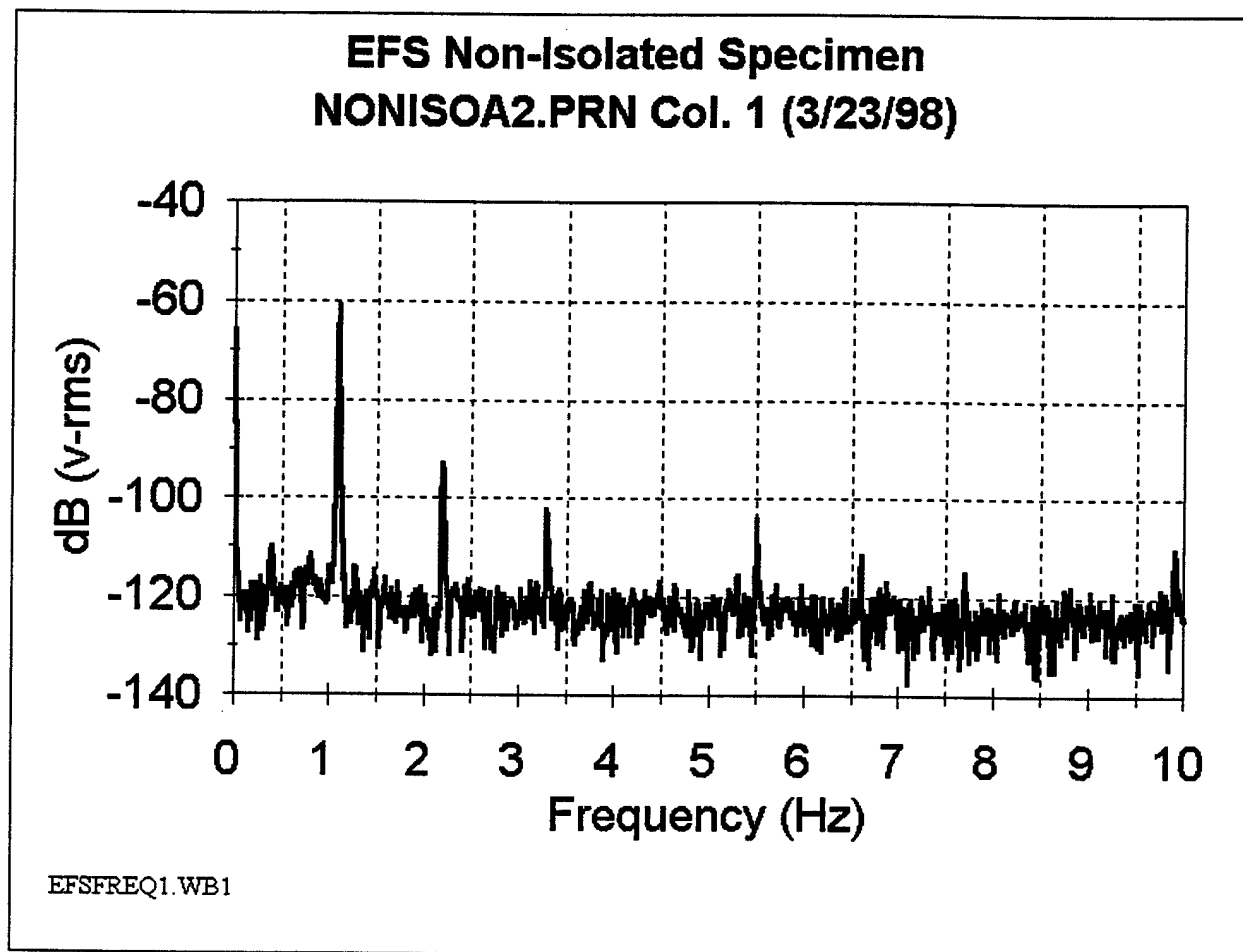
Figure 9-4. Electrical spectrum taken across EFS cell during operation: Non-Isolated Work Piece
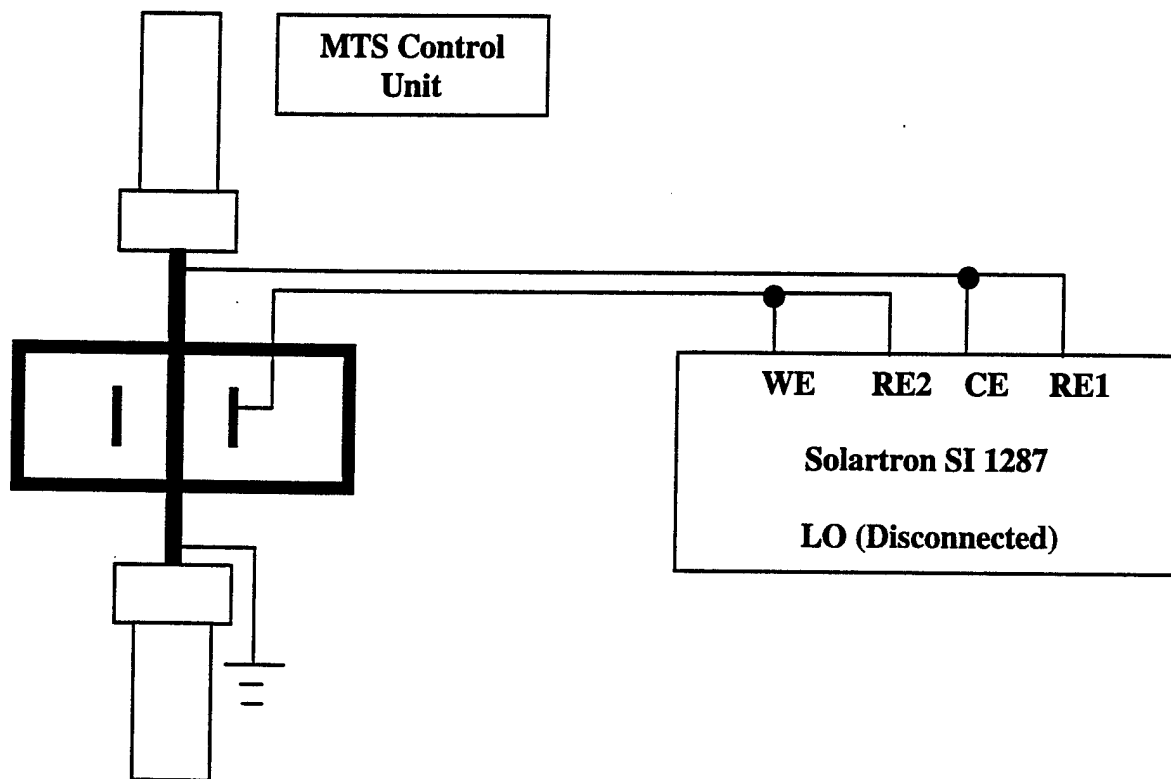
Figure 9-5. EFS two-electrode set-up with grounded work piece.
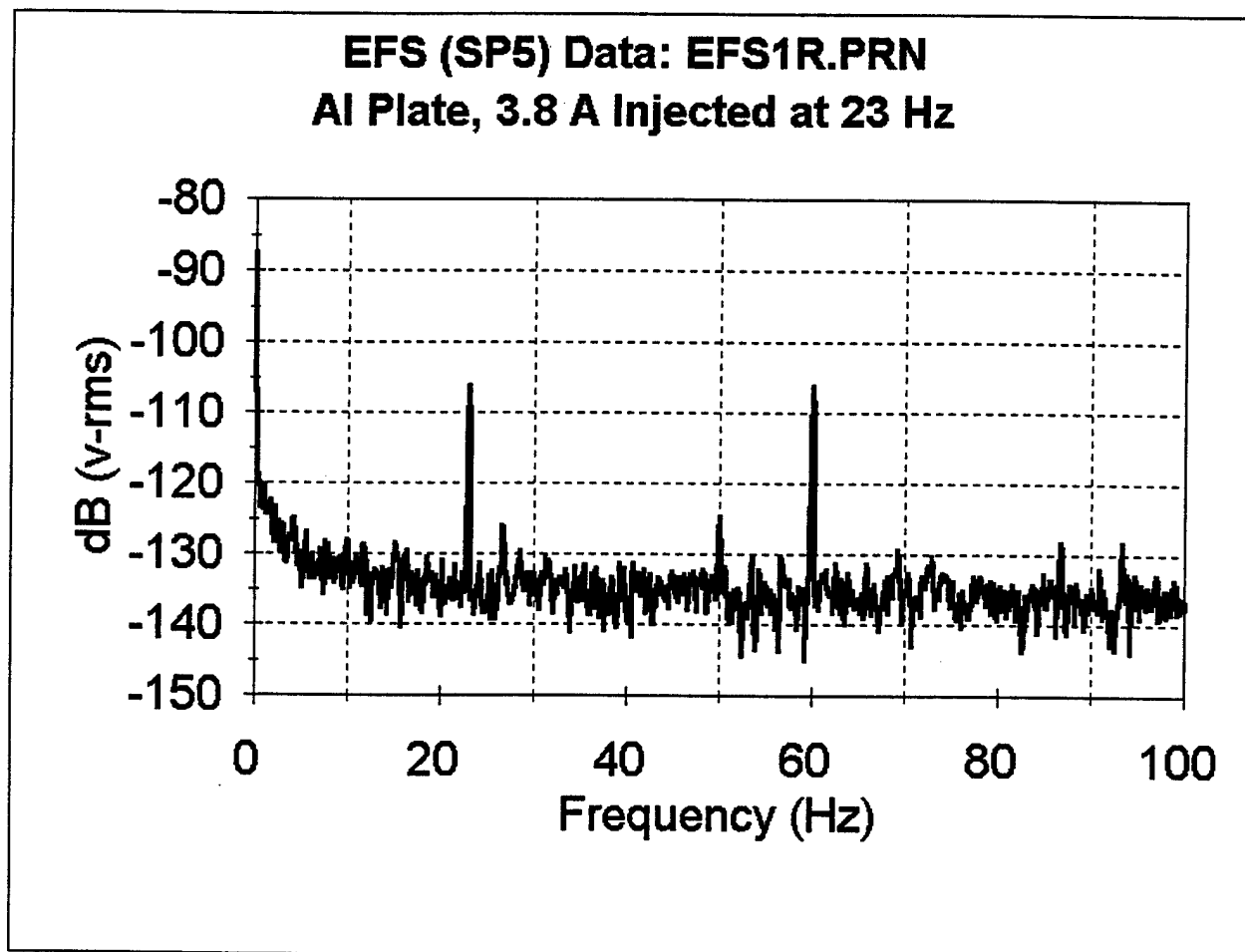
Figure 9-6. Electrical spectrum taken from large aluminum plate. (Current injected into plate is 3.3 Amps at 23 Hz.)
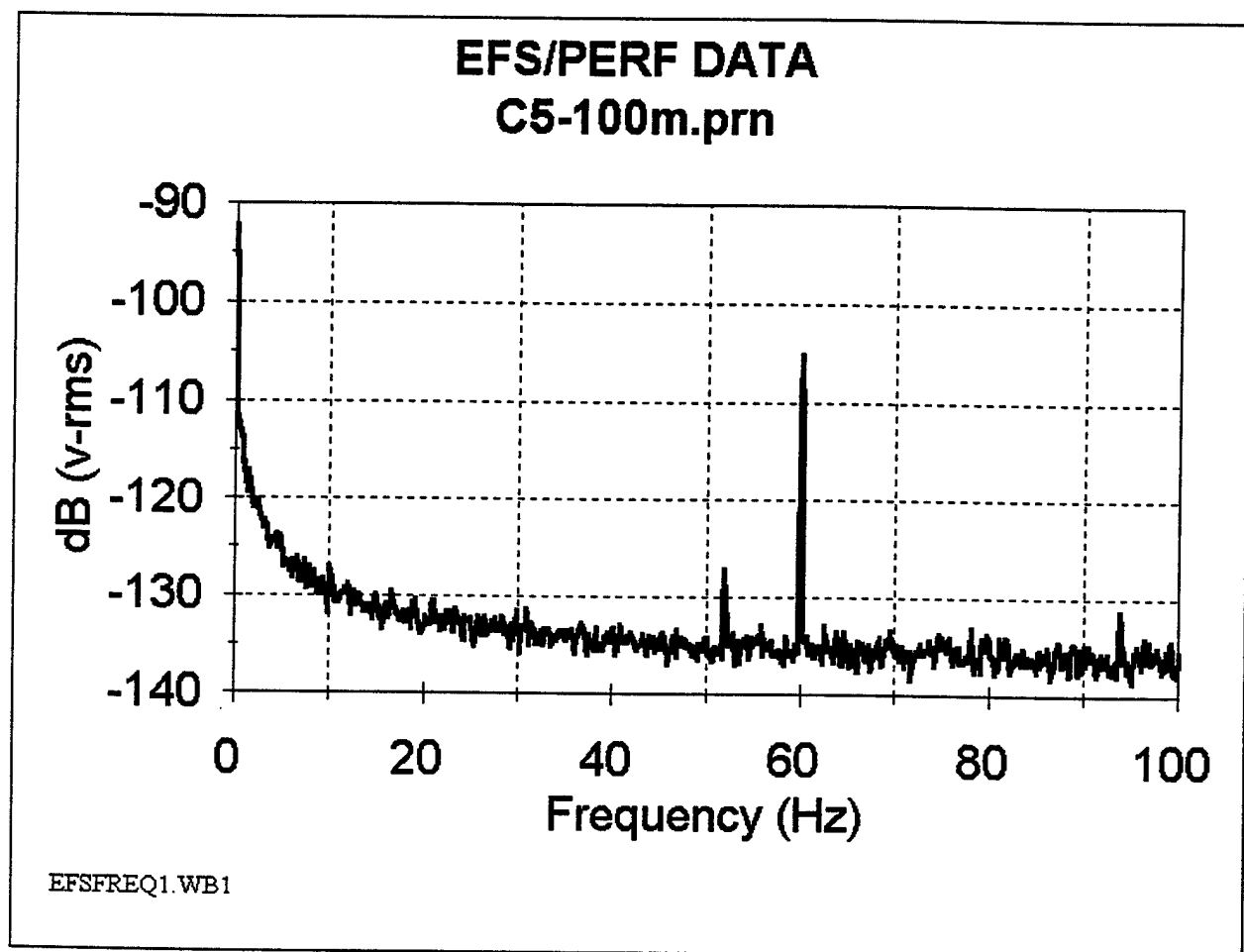
Figure 9-7. Electrical spectrum of noise from large structure. (For this data the structure was connected to building steel and a motor was running inside the large structure; datafile: C5-100M.PRN.)
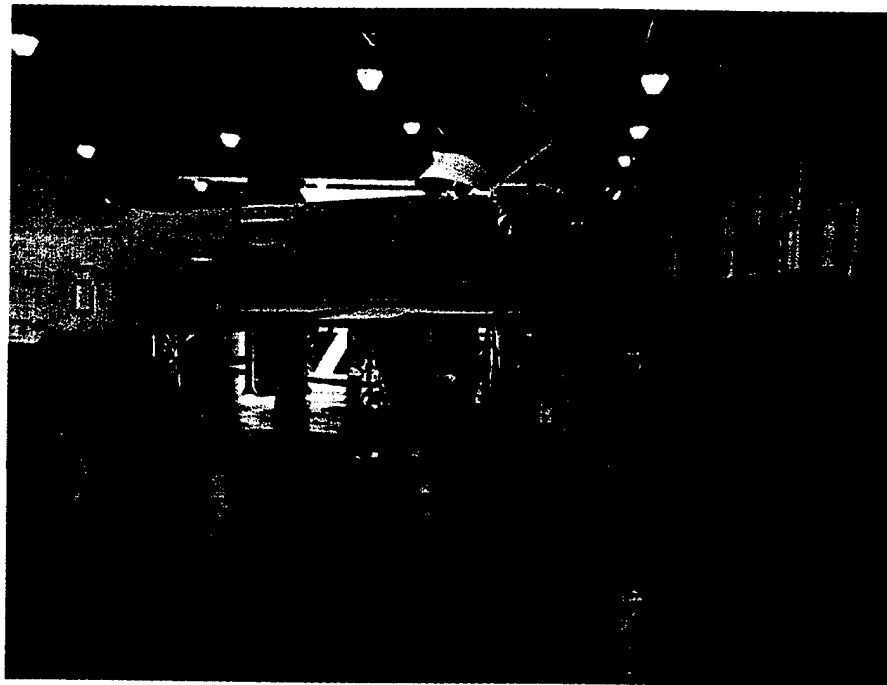
Figure 9-8. Photograph of T-38A aircraft in Hangar 4, Randolph AFB, TX.
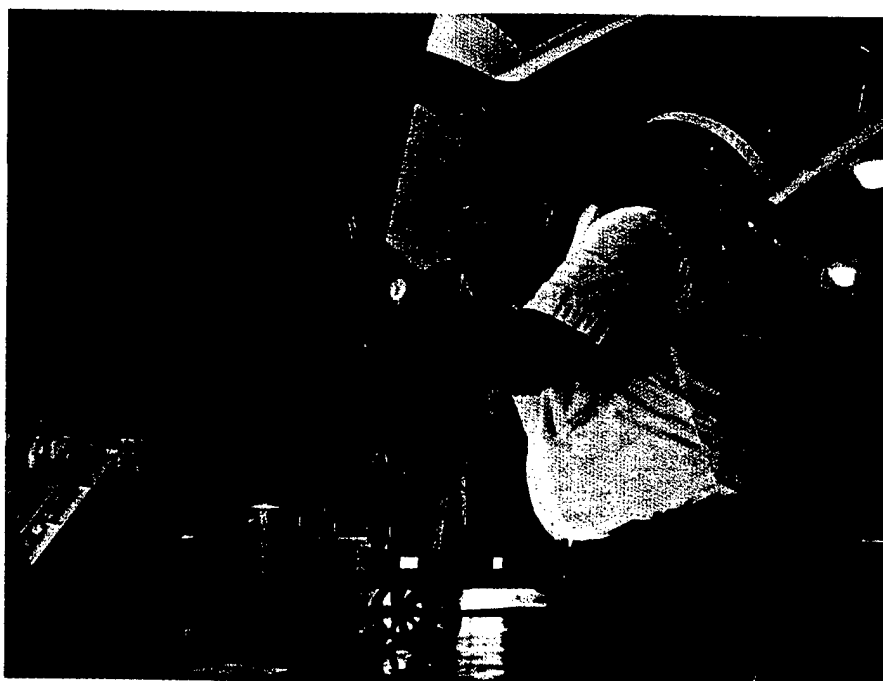
Figure 9-9. Photograph taken during measurements on T-38A aircraft.

◇ X:60 Hz   Y:-128.409 dBV
□ X:39.375 Hz   Y:-141.256 dBV
✕ X:2.5 Hz   Y:-132.361 dBV
Pwr Spec 1   TALON9.DAT
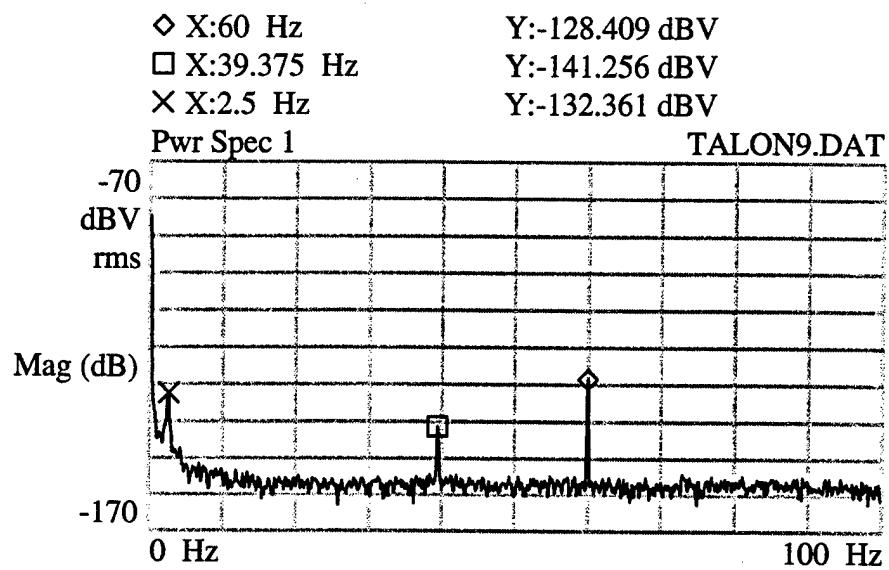
Figure 9-10. Electrical spectrum taken on T-38A. (This data was taken on exposed screws on the underside of the right wing, with electrodes 3 inches apart. Note: the spike at 2.5 Hz was intermittent.)

10.0 ECONOMIC ASSESSMENT

The economic feasibility of applying the Electrochemical Fatigue Sensor (EFS) for fatigue damage assessment in military aircraft in general, and the T-38 wing in particular, was assessed. The economic evaluation focussed on three elements: 1) the producibility of an EFS for specific application to fatigue damage assessment of military aircraft materials and structures, as compared to the producibility of currently available technological devices for fatigue damage assessment; 2) the affordability of the production of an EFS, as compared to currently available devices for fatigue damage assessment; and 3) a cost versus benefit analysis of the usability and supportability of the EFS sensor for application to military aircraft materials and structures, as compared to the cost versus benefits of currently available devices for fatigue damage assessment.

Producibility and affordability are easily estimated, since the materials, processes and technologies required to build an EFS instrument are well understood. The cost benefit analysis is far more complex due to the various ways in which the EFS could be used as an element of the overall USAF Aircraft Structural Integrity Program. EFS technology can be used to supplement or possibly replace some conventional non-destructive inspection testing (NDT) and allow cost savings by more cost-effective repairs or maintenance.

The approach to perform the cost-benefit analysis was to select one area (the inner wing) on the T-38A aircraft, for which there are extensive test data, and estimate the cost of implementing an EFS measurement program. An estimate was made of potential cost savings which would accrue if the EFS data could be used to perform more cost-effective repairs. These data provide the basis for a quantitative cost benefit analysis.

As the EFS technology matures in future phases of development, a better understanding of cost benefits can be realized. More sophisticated methods such as Northwestern University's methodology for economic assessment [10.1], can be employed to quantify benefits on a much broader scale.

10.1 Producibility

10.1.1 Introduction

The producibility of an EFS instrument was examined to assure that the materials, processes, personnel skills and facilities are available for the production of a sufficient number of instruments to allow them to be introduced in a realistic implementation scenario. In making the producibility assessment, a conceptual EFS instrument was postulated based on the current laboratory device which uses a liquid electrolyte, common electrode materials and state-of-the-art electronics. The producibility of this device was compared to the producibility of currently available devices used for fatigue damage assessment.

10.1.2 EFS Producibility

In summary, the fabrication of an EFS instrument for widespread use is straightforward once the baseline configuration has been selected. Furthermore, a high production rate is feasible.

The EFS is a device intended to evaluate the state of fatigue damage in a structure. It consists of a standard three electrode electrochemical cell in which the structure is one of the electrodes. A reference electrode and a counter electrode, immersed in an electrolyte which is also in contact with the structure of interest, make up the sensing device. Only the region of the structure being evaluated for fatigue damage is in contact with the electrolyte. The cell is excited by a potentiostat, and the structure is usually chosen as the anode. The potential applied to the cell is selected to passivate the surface of the structure and not to adversely influence the fatigue behavior of the structure in contact with the electrolyte. In the absence of stress, a constant current will flow in the cell.

If cyclic loading is applied to the structure equipped with an EFS, the cell current will fluctuate also in complex relation to the load cycle. Microplasticity occurring in the structure by action of fatigue can strongly influence the transient behavior of the cell current. Moreover, the development of fatigue damage also produces characteristic transient current behavior. In particular, when microcracks are present, microplastic effects associated with their stress concentrations produce extra current spikes in the transient current, indicating their presence at

10-2

very small crack sizes. Signal analysis of the cell current thus provides qualitative and quantitative indications of the fatigue damage.

In order to evaluate fatigue damage with the EFS, a simple container has to be prepared, adaptable to the geometry of the structure and sufficient to contain electrolyte and electrodes, typically a calomel electrode for the reference electrode and a platinum mesh for the counter electrode. A good fit of the cell with the structure is necessary to bring the electrolyte into full contact with the fatigue critical location in the structure. It is usually most practical to use a gel electrolyte. The chemicals and materials needed are inexpensive and readily available. A method has to be devised to attach the cell to the structure, *e.g.*, by straps or adhesive, and an "O" ring seal will typically be used to avoid leakage of the electrolyte. Development work has shown that a simple two electrode systems can be effective in utilizing the EFS. It may even be possible to eliminate the potentiostat by using a driver electrode system, such as Ni/NiO, with respect to the structure.

For data acquisition, the cell current is input to a PC and analyzed using commercially available software. To date, Labview has been employed for this purpose, including the generation of specialized programs within Labview to analyze the data. Much of the development work has been performed with standard, commercially available potentiostats produced for electrochemical research and technology. It is our experience that most of these instruments are too electrically noisy to be optimally useful for the EFS, in which the currents are small and the variations complex. Better results have been obtained by constructing ad hoc potentiostats better adaptable to the EFS and without the multiplicity of features found on commercial potentiostats, and offered to deal with various electrochemical measurements. The components needed to construct these in-house potentiostats cost $300 - 500. Given the low price of small, high powered computers, the total cost of an EFS system should not exceed $7000, including software sensors, frames, and one computer per inspection site. Miniaturized potentiostats could be produced for a few dollars each after an outlay of about $30,000.

Setting up the EFS for application is simple in theory and practice. The cell is first attached to the structure, and the electrodes are connected to both the potentiostat and the data acquisition system. The electrolyte is injected into the cell, and EFS readings can be recorded

immediately, provided the structure is under load. Depending on the material and the surface condition of the structure, a "settling-in" period may be necessary for the cell interface conditions to become established for optimal EFS response. After testing has been completed, careful cleaning of the surface in contact with the EFS will be necessary to avoid the potential for subsequent environmental effects on the fatigue behavior. Care must be used in application of the EFS (for example, air pockets left in the gel electrolyte can cause corrosive effects of the structure) and personnel will have to be thoroughly trained. The analytical software used to the present has involved special methods for presenting the measurements, as well as Fourier analysis of the transient current. The appearance of higher harmonics at higher fatigue life fractions can be associated with developments in the fatigue damage. For commercial testing in which the load spectra can be expected to be more complex, more sophisticated signal processing will be necessary. Given the great advances in such processing, no special difficulties are anticipated in data analysis.

10.1.3 Current NDT Instrument Producibility

By definition, current NDT instruments can be produced and are produced in sufficient numbers to be used within the NDT arena. For purposes of comparison, we have summarized in Table 10-1 some qualitative producibility issues for the NDT technologies which perform similar tests.

10.2 Affordability

10.2.1 Introduction

The affordability of an EFS instrument was estimated in terms of a conceptual EFS instrument based on the current laboratory device which uses a liquid electrolyte, common electrode materials and state-of-the-art electronics. The affordability of this device was compared to the affordability of currently available devices used for fatigue damage assessment.

10.2.2 EFS Affordability

The affordability of the EFS instrument was assessed by estimating the cost of the instrument described in Section 10.1.2. The estimated production cost of a single instrument is $250.00 including the sensing unit, enclosure, and mounting.

In summary, the cost of postulated production EFS instruments is quite reasonable compared to other NDT technologies. These production cost estimates are subject to revision as the technology matures, but we believe the estimates we have made are conservative.

10.2.3 Current NDT Instrument Affordability

The cost of NDT instruments varies considerably with function as discussed in Appendix CC. For information purposes, Table 10-2 summarizes relevant instrument costs and related operations costs.

Defects detected and the size of a crack which can be detected are dependent on many factors, including material composition, material thickness, transducers/probes/film used, skill of the operator/interpreter, depth of the flaw, etc. For the purpose of this analysis, manufacturers and users of the equipment types listed were polled and asked, for inspection of aluminum aircraft skins under optimum conditions, which of the following sizes is typically the smallest crack which the equipment can reliably detect (see Table 10-2): precrack conditions, <0.010", 0.010 - 0.025", 0.025 - 0.050", or >0.050". Equipment which can only find cracks greater than 0.050 inch is not included, since durability size flaws are smaller than 0.050 inch.

Labor costs in Table 10-2 are indicated for three functions: setup, data recording, and data analysis and are rated as high/medium/low [h, m, l].

10.3 Cost Benefit Analysis

10.3.1 Introduction

Efforts to assess the economic benefits which could be derived from the use of EFS technology in military aircraft maintenance have been focussed on a well characterized element

of the widely used T-38A aircraft. At this early stage of EFS technology development the potential benefits are not well understood since the full range and mode of potential applications is still being explored. Therefore the approach has been to select a single application and quantify potential cost savings for that single application.

When the development of the EFS is complete, the role of EFS applications within the Aircraft Structural Integrity Program [ASIP] will be definable. At present, fatigue prediction of durability has little scope within ASIP. It is believed that the apparently unique ability of the EFS to indicate fatigue condition without prior instrumentation will add a new synthesis of durability to ASIP which would complement the (linear elastic fracture mechanics) damage tolerance crack growth methodology.

Cost savings in our T-38A wing section example are generated on the likelihood that EFS technology will allow more cost effective repairs than current inspection methods allow. The postulated scenario is that EFS inspections, which are better able to predict small cracks, will allow less expensive repairs to be made. This is possible, for example, if EFS inspections indicate the high probability of the presence of a small crack which would propagate into a large (expensive repair) crack with safety implications prior to the next scheduled damage tolerance inspection. Thus, an early low cost repair (*e.g.*, re-worked hole) could be done instead of an expensive repair (*e.g.*, replaced skin section) later. By focussing on the well-characterized T-38A wing, we can provide a first conservative quantitative assessment of the economic benefit, which can be refined and widened in scope in the future as the technology and its true applicability become better understood.

10.3.2 Usability/Supportability

The EFS is believed implicitly to be usable and supportable. That is, the EFS is in principle a simple, usable device. After development it will be straightforward to apply it to aircraft in service, locating it near but not necessarily coincident with fatigue critical areas of local stress concentration. Its supportability is inherent in its periodic application. In this detail, it is similar to conventional nondestructive inspection. It offers advantages in supportability over

continuous recording of flight loads history as required by counting accelerometers and similar devices.

10.3.3 Quantitative Cost Analysis

Cost analysis involved 6 fatigue critical locations of the T-38A inner wing section. This analysis included only those aircraft operating in three major roles, as discussed below. A simple basing scheme was considered, *i.e.*, the total number of aircraft were equally distributed over the required number of bases. The life cycle cost (LCC) span is five years. The current Air Force base labor cost of $31.93/hour was used to compute labor costs. This analysis did not attempt to show the cost benefit of reduced downtime, improved safety margins, enhanced testing integrity or the value of mission readiness.

The first step in the analysis approach was to determine the type of data required to estimate the costs of both (existing and EFS) testing methods. In the case of the existing NDT procedure, the data primarily consisted of labor cost to perform the test procedure since all significant investment cost has already been expended. The only exception was the recurring cost of replacement eddy current probes. Investment costs, including program management and initial training, and labor costs were included for the EFS system. EFS installation was considered to take place at base level and to extend over a period of two years.

For this analysis, data were available for aircraft systems operating in three major roles: Student Undergraduate Pilot Training (SUPT), Introduction to Flying Fundamentals (IFF), and Euro NATO Joint Pilot Training (ENJPT). Technical Order (T.O.) 1T-38A-6 (Nondestructive Inspection Manual) was used to determine the number of wing fastener holes in the inspection areas and the number of flight hours required before initial and recurring inspections were necessitated; the initial and recurring hours extracted from this T.O. are those shown in the ENJJPT data table in Appendix DD. Technical Order 1T-38A-36 (NDI Procedures) was reviewed to obtain a better understanding of nondestructive inspection step-by-step procedures for performing Rotoscan Eddy Current fastener hole inspections. Work Cards were reviewed to determine the frequency of recurring inspections. Data were also obtained through responses to two questionnaires developed to obtain input for the Life Cycle Cost Model used for this analysis. The data were further broken out for six fatigue critical location (FCL) inspection zone

areas (an illustration of inspection zones Area 1 through Area 6 is presented in Appendix DD) by aircraft major role. Input data to the quantitative cost analysis are summarized in Table 10-3.

For modeling purposes, the three aircraft usage roles were each modeled as individual systems while the FCL zone areas were treated as subsystems. Cost reports were generated for each system for both the NDT and EFS methods. Data were obtained from responses to two separately developed questionnaires. One questionnaire was sent to Headquarters AETC, NDI Directorate, for distribution to Training Bases performing NDI testing on T-38A aircraft participating in the type of training for the three major roles being modeled. The second questionnaire was sent to individuals developing the EFS. Copies of the EFS and NDI questionnaires are located at Appendix DD. Responses to the questionnaires were tabulated and the tables generated from the questionnaires, T.O. 1T-38A-6, and Southwest Research Institute DADTA analysis are also located at Appendix DD.

10.3.4 Estimating Methodology

The cost benefit analysis (CBA) was performed with the Joint Operating and Support Technology Evaluation (JOSTE) Life Cycle Cost (LCC) model which was originally developed to estimate advanced technologies for the Joint Strike Fighter (JSF). The model was obtained from the LCC Office of the Aeronautical Systems Center, (ASC/SYA), Wright Patterson AFB, OH. The JOSTE model is used extensively for cost benefit analyses involving modifications of Air Force and Navy aircraft comparing new technologies. JOSTE is an accounting model which covers acquisition, deployment and operating costs at the system subsystem and component levels. A summary of the results of the comparative cost analysis is provided in Table 10-4.

The costs estimated for inspections using EFS technology is approximately 23% of the NDI costs and this 5 year estimate includes $2,724,854 for acquisition and installation of new equipment. After the equipment is purchased, on-going inspections would be reduced to less than $140,000/yr or approximately 5% of the mean NDI cost. These extrapolations of EFS implementation costs will be used in the next section to estimate cost savings which could accrue by using EFS to perform timely, cost effective repairs.

10.3.5 *Quantitative Benefits Analysis*

Potential cost savings can be realized by using EFS technology to plan and schedule cost effective airframe repairs. While current NDT testing is used for the scheduling of repairs to maintain safety, more cost effective repairs would be possible using the EFS capability to predict (probabilistically) smaller cracks. By predicting cracks that can be repaired inexpensively, substantial cost savings can be realized, *e.g.*, reworking a hole versus replacing a skin section.

The application of EFS technology is estimated to increase the cost avoidance benefit accruing from NDT alone by 15%. This estimate is based on the following reasoning: The cost of the current NDT is accepted because the impact of structural failures and loss of aircraft would be incomparably greater.

As basis for an estimate, consider that the replacement value of the T-38 fleet exceeds $5 billion dollars. As an extreme lower bound, consider that the value of preventing losses (which the damage tolerance inspections do) is 1% of the total value of the fleet, or $50M annually. And again simply assume that in 15% of the cases, an accurate predictor of durability size flaws will permit timing for more economical repair. The cost savings forecast from the application of EFS technology for the T-38A aircraft is therefore forecast to be 0.15 X $50M = $7.5M per year. After subtracting the yearly EFS inspection costs, the total cost savings for the T-38A are forecast to be ~ $7.2 million/year.

10.4 Summary and Conclusion

A preliminary economic assessment of the application of the EFS to military aircraft airframes has been conducted. We have examined the producibility and affordability of the instrument and found it to be both producible and affordable, especially compared to other NDT technologies. The costs of the EFS instrument are projected to be quite low, but analyses (including software) are expected to be more sophisticated than for some NDI techniques.

Potential cost saving resulting from the application of EFS technology has been extrapolated for the T-38A aircraft for which a considerable data base is available. The assumption was employed that the EFS sensor could be used to increase the savings realized by

current NDT methodologies by 15%. After accounting for the costs of performing the EFS measurements, annual repair cost savings for the T-38A are estimated at ~$7.2M per year.

10.5 References

10.1 Vanessa J. Brechling, "A Methodology for the Economic Assessment of Nondestructive Evaluation Techniques Used in Aircraft Inspection.". DOT/FAA/AR-95/101, dated November 1995

Table 10-1. Current NDT Instrument Producibility

Technology	Comment
Acoustic Emission	-off the shelf -mostly lacking automated interpretation
X-Ray Computed Tomography	-small mobile devices not widely available
Advanced Electromagnetic	-off the shelf -mostly lacking automated interpretation
Advanced Visual Inspection	-off the shelf -includes imaging software
Laser Ultrasonic Inspection System (LUIS)	-very elaborate system -few available
Dye Penetrant	-off the shelf -widely available -commonly used and understood

Table 10-2. NDT Instrument and Operation Costs

Equip-ment	Capital Equip't	Cost of Probes	Cost of Expendables	Labor Time/Level	Labor Costs*	Produ-cibility	Avail-ability	Defects Detectable	Comments
EFS	$8-15 K	Low	Low	Low/med	m,l,l	Good	in devel-opment	Precrack damage, crack initiation & early propagation	Lengthens intervals between inspections
Acoustic Emission	$30-40 K	Low	Low	High/high	m,l,l	OTS	OTS/custom	Precrack damage, crack initiation & early propagation	
X-ray (2) Computed Tomography	$1-2.5 M	Included	can be very high	Low/high	h,h,h	LAB	limited	Cracks (0.025 – 0.050")	OSHA regs, source, storage, size limitations, access to 2 sides, energy, maintenance
Compton (2) X-ray backscatter	Varies	Included	can be very high	Low/high	h,m,m	LAB	limited	Cracks (0.025 – 0.050")	OSHA regs, source, storage, coating removal not necessary, energy, maintenance
Reverse (2) Geom. X-rays	varies	Included	can be very high	Low/high	h,m,m	LAB	limited	Cracks (0.025 – 0.050")	OSHA regs, source, storage, energy, maintenance
Advanced Electromagnetics	$10-250K	included	Low	High/high	m,m,m	OTS	OTS	local strain, cracks, (<0.010")	Coating removal not necessary
Advanced Visual Inspection	$25-100 K	low	Low	Low/med	m,m,l	OTS	OTS	surface flaws, through-cracks (0.025 - 0.050")	
Advanced Ultrasonics	$50-250 K	low	Low	High/high	m,m,m	OTS	OTS	fatigue damage, crack initiation & propagation (<0.010")	
Laser Ultrasonic Inspection System (L.U.I.S.)	$1-3 M	included	included in labor rate	High/high	h,m,m	LAB	Limited	fatigue damage, crack initiation & propagation (precrack conditions)	Parts must be removed from aircraft, size limitations
Dye Penetrant	$0	NA	very low	High/low	m,m,l	Excellent OTS	OTS	cracks, porosity (0.010-0.025")	Must have clean, depainted structure flaws must be open to surface

* Labor costs for Setup/Data Recording/Data Analysis; h = high, m = medium, and l = low

Table 10-3. Summary of Input Data to Quantitative Cost Analysis

Data Type:

Aircraft Type: T-38A		Current	EFS
Test Sensors/AC		N/A	20
Acquisition Cost/Sensor		N/A	$250
Installation Kit Cost/AC		N/A	$10
Installation Time/AC		N/A	1 Hr
Sensor Remove/Replace/Failure		N/A	2.5 Hrs
Ancillary Equip			
Multiplex Recorder/Site		N/A	1
Cost/Recorder		N/A	$5000
Recorder Life (yrs)		N/A	10
AC Qty			
SUPT		300	300
IFF		88	88
ENJJPT		94	94
Annual Flying Hours/Acft			
SUPT		348	348
IFF		312	312
ENJJPT		420	420
Number Holes Inspected/Yr			
SUPT		30900	30900
IFF		50072	50072
ENJJPT		9588	9588
Number of Annual Recurring Inspections/FCL Zone Area			
SUPT			
	FCL Area 1	30	32
	FCL Area 2	10	17
	FCL Area 3	39	22
	FCL Area 4	8	10
	FCL Area 5	10	6
	FCL Area 6	6	15
IFF			
	FCL Area 1	165	32
	FCL Area 2	65	17
	FCL Area 3	232	22
	FCL Area 4	40	10
	FCL Area 5	56	6
	FCL Area 6	11	15
ENJJPT			
	FCL Area 1	32	32
	FCL Area 2	17	17
	FCL Area 3	22	22
	FCL Area 4	10	10
	FCL Area 5	6	6
	FCL Area 6	15	15

Table 10-3. Summary of Input Data to Quantitative Cost Analysis (Cont'd)

Hours per Annual Recurring Inspection/FCL Zone Area (Best Case /Worse Case

SUPT			
	FCL Area 1	2490/4980	420
	FCL Area 2	90/1580	238
	FCL Area 3	3354/6708	308
	FCL Area 4	368/736	120
	FCL Area 5	560/1120	84
	FCL Area 6	53/105	180
IFF			
	FCL Area 1	13118/26235	420
	FCL Area 2	5135/10270	238
	FCL Area 3	19953/39905	308
	FCL Area 4	1840/3680	120
	FCL Area 5	3136/6272	84
	FCL Area 6	96/193	180
ENJJPT			
	FCL Area 1	2656/5312	420
	FCL Area 2	1343/2686	238
	FCL Area 3	1892/3784	308
	FCL Area 4	460/920	120
	FCL Area 5	336/672	84
	FCL Area 6	131/262	180

Table 10-4. Summary of the Comparative Cost Analysis

Cost Item		NDT (Worst Case)	NDT (Best Case)	NDT (Mean)	EFS
SUPT					
	Acquisition	0	0	0	$ 1,560,000
	O&S	$ 2,324,089	$1,162,045	$ 1,743,067	$ 220,083
IFF					
	Acquisition	0	0	0	$ 457,600
	O&S	$14,009,432	$7,004,716	$10,507,074	$ 220,071
ENJJPT					
	Acquisition	0	0	0	$ 488,800
	O&S	$ 2,177,721	$1,088,860	$ 1,633,290	$ 218,454
Installation		0	0	0	$ 15,395
Multiplex Recorder ($5000 ea)		0	0	0	$ 15,000
Probes (95/yr @ $125 ea		$ 59,375	$ 59,375	$ 59,375	0
TOTAL		$18,570,617	$9,314,996	$13,942,806	$ 3,195,403
Maintenance Labor Hours		579,563	289,782	434,672	14,465

11.0 DISCUSSION

Engineering materials derive their general corrosion resistance from the presence of stable oxide films that serve to protect the surfaces of these materials from reactions with the environment. During cyclic loading, the fatigue process causes strains to become localized — initially at the microscopic scale on the order of the material grain size. These localized strains eventually cause the material's protective oxide film to rupture either at grains with the weakest orientations, or at microstructural defects such as second phase particles. This mechanical depassivation process exposes fresh and highly reactive metal surface that readily reacts causing metal dissolution. Provided the surface is in the passive regime, the damaged film is rapidly repaired. Metal dissolution is accompanied, almost immediately, by film repair (i.e., repassivation). The current measured by EFS is due to the almost simultaneous dissolution and film repair reactions. Thus, the EFS measurement is inextricably related to what is in effect a corrosion reaction.

Consequently, the selection of an optimum EFS electrolyte required careful consideration to achieve a balance between being sufficiently benign to preclude degradation of the materials and structures under inspection, while at the same time being sufficiently reactive to provide a measurable EFS response. Based on the battery of polarization tests, corrosion tests, corrosion-fatigue tests, and EFS measurements performed in the present program, this balance has been successfully achieved with the selected electrolyte—a borate buffer with the addition of molybdate. All materials exhibited excellent resistance to general corrosion, combined with the absence of pitting or crevice corrosion when exposed to the EFS electrolyte for time intervals that were long compared to those likely to be encountered during periodic inspections. Furthermore, both S-N and fracture mechanics (fatigue crack growth rate) testing indicated that the aircraft materials exposed to the EFS electrolyte exhibit results which were indistinguishable from those in laboratory air, and were in many cases better than those obtained in water or liquid dye penetrant—two environments to which aircraft are commonly exposed. In regard to the latter observations, the addition of molybdate to the electrolyte serves as an inhibitor to localized corrosive effects and in this regard may actually be beneficial to the durability of aircraft components.

The fact that a common electrolyte was demonstrated to be effective for EFS measurements on all three aircraft alloys examined represents a significant simplification to further development and application of the technology in the laboratory, as well as to eventual application of EFS to aircraft inspections. Moreover, the fact that EFS measurements were successfully demonstrated on the three prototypical aircraft alloys, with widely differing compositions and microstructures, suggests that EFS measurements can be made on virtually all structural alloys used in aircraft. This is perhaps not too surprising in view of the fundamental nature of the EFS response—that is, film rupture and repair, a phenomenon common to all passivating materials.

Systematic changes in the EFS response were observed throughout the fatigue life for all three alloys examined. Moreover, the rich information content of the measured current waveforms provided the opportunity to employ data processing to extract several cyclic response features that correlate with the evolving fatigue damage. In the time domain, the most useful of these features were the magnitude of the current amplitude, and the emergence of "crack" peaks in the current waveforms. In addition, analysis in the frequency domain was also found to be informative. Specifically, because of the systematic relationships between the load (or strain) waveform and the current waveform, Fast Fourier Transform (FFT) spectrum analysis was employed to distinguish between current contributions associated with elastic and plastic straining—each of which appears to be fundamentally different. The separation of the "plastic" current enabled the phase relationship between the plastic current and straining to be defined in terms of a phase shift factor which was demonstrated to be associated with the onset of measurable fatigue damage. Although the work at SwRI emphasized the time-domain analysis and the work at Penn emphasized the frequency-domain analysis, both approaches were found to be enlightening and in fact complementary. For example, since changes in the phase shift factor were caused by the emergence and eventual dominance of the plastic current, this feature was consistent with the observed increase in the current magnitude.

Ideally, one would like to employ EFS to accurately assess the state of fatigue damage, and thus the residual life, over the entire range of fatigue lives that might be applicable to various

aircraft components. However, the present results on smooth fatigue specimens showed that the ability of EFS to detect the onset of fatigue damage is highly dependent on the life regime. Specifically, at short lives and high strains, EFS detects fatigue damage relatively early in life and can track the evolving damage throughout most of the life. However, at long lives and low strains, fatigue damage in smooth specimens is either non-existent, or subtle, for most of the fatigue life; consequently, EFS can only detect damage relatively late in life. Nevertheless, it should be recognized that this result is consistent with current knowledge of the actual fatigue damage process in smooth specimens, rather than an intrinsic limitation of EFS.

Specifically, the fraction of life at which EFS (or any other inspection technique) is capable of detecting fatigue damage is dependent on the nature of the specimen or component geometry, as well as the loading mode. For the smooth cylindrical fatigue specimens employed in the present program, the region of subcritical crack growth is relatively short since the crack driving force increases relatively rapidly in this uniformly stressed specimen tested under load control. In contrast, fatigue cracks in aircraft components initiate at notches that have steeply decreasing stress gradients. This situation favors early crack initiation due to the concentrated stresses at the notch surface and is followed by substantial subcritical crack growth as the crack driving forces remain relatively constant as the crack grows away from the notch. Thus, in effect the crack driving force in most aircraft components is less steep than that in the cylindrical fatigue specimen. Consequently, there is greater opportunity to detect microcracking and monitor subsequent subcritical crack growth.

In view of the above situation, it is informative to consider the minimum crack size that EFS is capable of detecting. Interrupted fatigue tests in the present program have shown that cracks as small as 70-75 μm could be detected with EFS. This represents an improvement on presently available inspection techniques. Moreover, this size is believed to be an upper-bound estimate on the ability of EFS to detect cracks. Specifically, the above size was not limited by the sensitivity of EFS, but rather by the experimental difficulties in optically finding and resolving microcracks while attempting to verify the EFS indication. It is believed that a number of factors could decrease the EFS-detectable crack size, not the least of which is optimization of test specimen geometry and surface condition to improve the probability of optically finding and

resolving smaller microcracks. The minimum EFS-detectable crack size is also expected to decrease as EFS utilizes smaller sensors to acquire localized measurements.

Previous studies on lower-strength austenitic stainless steel have indicated that EFS is capable of detecting fatigue damage prior to crack initiation [11.1-11.2]. This early detection of damage is associated with the fact that this soft material exhibits substantially more deformation prior to the development of microcracks. In contrast, the higher strength aircraft materials examined in the present program tend to initiate microcracks at preexisting microstructural defects, such as second-phase particles, and this process occurs with considerably less prior deformation. Thus, there is less opportunity to detect fatigue damage prior to microcrack initiation in the aircraft alloys, although this may still be achievable as sensor sizes decrease and more local measurements become possible with EFS.

The present results obtained with EFS under variable amplitude loading are encouraging, but by no means complete. Results obtained with simple loading histories comprised of periodic overloads and/or underloads demonstrated that EFS features characteristic of fatigue damage under constant amplitude loading could also be resolved under variable amplitude loading. These results also demonstrated that damage evolution during variable amplitude loading could be tracked on a cycle-by-cycle basis. EFS results obtained under actual T-38 spectra corresponding to fatigue critical locations (FCLs) in the wing and fuselage demonstrated an equivalence to those obtained under constant amplitude loading when compared at a given damage state (*i.e.*, crack size). These results demonstrate that the EFS response measures the fatigue damage state, independent of the prior history of loading. The uniqueness of a fatigue damage state means that periodic EFS measurements obtained under simple constant amplitude loading could be used to assess fatigue damage generated under more complex aircraft loading spectra. However, as discussed below, this approach may have economic limitations.

Although the above EFS results under variable amplitude loading are encouraging, they do not provide a solution to all variable amplitude issues encountered in-service. Specifically, a methodology for the on-line interpretation of the EFS responses under actual aircraft spectrum loading is not yet available. A more complete solution to the interpretation of EFS under

variable amplitude loading would be needed before EFS could be used as an in-flight monitor of fatigue damage. This mode of EFS application is attractive for a number of reasons. Firstly, continuous monitoring of damage would provide a more robust assessment of fatigue damage evolution than would the periodic "snapshots" of damage that are obtainable from conventional (periodic) inspections. Secondly, this approach would obviate the need for application of loading while the aircraft is on the ground. Even in a depot setting, the application of fatigue loading would be a complex and challenging operation. Although simple loading modes might be feasible, these may not properly stimulate the complex multiaxial loading modes experienced at most FCLs in flight. Further, while the application of complex loading modes are achievable in full-scale aircraft testing, these probably are not economically feasible for periodic inspections.

One of the attractive features of EIS is that it can be used without the need to load the structure. This feature results from the fact that measurements occur in response to electrical perturbation, as opposed to mechanical (loading) perturbations as required by EFS. In this regard, the EIS measurements on bare 7075 aluminum alloy are encouraging. Specifically, a metric was formulated in terms of $1/R_p$ that was found to detect fatigue damage as early as 20% of the total fatigue life, for short lives where cracking develops early in life. This metric was also found to track damage (cracking) throughout the remainder of fatigue life thereby providing a means of quantifying the evolution of fatigue damage. However, at longer fatigue lives in smooth specimens, EIS is similar to EFS in that damage is not detected until considerably later in life, since crack initiation occurs relatively late in life in this regime of stress/life.

However, in contrast to the above encouraging EIS results on aluminum alloy, EIS results on 4130 steel and Ti-6Al-4V were found to be more problematic because of the more rapid repassivation kinetics in these alloys, compared to the aluminum alloy. These results serve to highlight the fundamental difference between EFS and EIS. Namely, EFS measures the depassivation/repassivation reaction that occur during active straining, whereas EIS measures the influence of prior fatigue loading on the nascent surface reactivity. Thus, the EIS measurement is a less direct response to fatigue damage.

Although EIS is highly sensitive to the chemical state of the surface, this feature provides both advantages and disadvantages to the potential application of this technique as a fatigue sensor. The advantage is that it can provide information on the overall condition of coatings that may be present. For example, the difference between a high-quality coating and a defective coating was found to be readily apparent in the EIS response. Incomplete passivation and associated time-dependent changes in the surface condition are also readily apparent with EIS. On the other hand, the potential disadvantage of EIS sensitivity to surface chemistry is that the measurements will likely be highly sensitive to chemical contaminants that might be present on the surface. Although any such effect would likely be readily apparent in the EIS measurement, methods would need to be developed to appropriately adjust the calibration between EIS response and extent of fatigue damage for such effects. The problem of chemical contamination will also influence the application of EFS. Although the effect might be less significant in the case of EFS, it might also be less obvious in the response, and thus potentially more difficult to compensate for in the calibration.

EIS measurements detected the presence of incomplete passivation in the aluminum alloy exposed to Electrolyte 8. These results were partially responsible for the switch to the generic electrolyte (Electrolyte 7). Because of the measured incomplete passivation in the aluminum alloy, EIS measurements were eventually performed over a range of applied potential. Unlike EFS, the EIS measurements were found to be influenced by applied potential in the range of 0.3 to 0.5 V vs. SCE and the sensitivity of the EIS measurements to fatigue damage increased with increasing potential. Unfortunately, this dependence was not discovered until most of the EIS measurements in the present program had already been completed. Thus, the overall performance of EIS was negatively influenced by the fact that the electrolyte and measurement potential were optimized for EFS measurements, rather than EIS measurements.

Apart from the above differences, the performance of EIS and EFS were found to be similar in certain respects. For example, both methods exhibited similar difficulties at very long lives where, as discussed previously, the progression of fatigue damage was highly non-linear. Both methods also exhibited similar success with primer-coated material, but had difficulties

with primer plus top-coated material because of the non-conductive nature of this coating that constitutes a barrier to the passage of current.

The successful formulation of a gel form of the generic electrolyte, combined with the initial success of the self-polarizing Ni/NiO electrode, demonstrates the feasibility of developing relatively simple and robust sensors that will facilitate further EFS laboratory development and field application. In addition to their simplicity, these sensors will enable measurements to be made on a localized level. Such localized measurements will enable specimens to be tested that better simulate actual fatigue critical locations on aircraft. As mentioned previously, localized measurements also have the potential to improve the sensitivity of both EFS and EIS. Most of the measurements in the present program were made in bulk liquid electrolytes using uniformly-stressed specimens with a large surface area; thus, results represented an integrated average over a significant area—most of which was passivated. Although local measurements may result in smaller current responses, the proportion of fatigue-damaged area will increase, and this is expected to result in greater measurement sensitivity.

Electrochemical measurements are traditionally made with the working electrode (specimen) electrically isolated. This configuration facilitates a wide variety of laboratory corrosion studies to be performed, as well as eliminates the pick-up of noise through ground loops. For these reasons most modern potentiostats are designed to operate with electrically isolated working electrodes, particularly when low current measurements are required as in the case of EFS. Consequently, early EFS measurements [11.1-11.2], as well as some of those in the present program, were made with electrically isolated working electrodes (*i.e.*, fatigue specimens). However, this mode of operation is impractical for actual measurements on aircraft since it would be difficult, if not impossible, to electrically isolate the entire aircraft. Fortunately, the work at Penn has demonstrated that high-quality EFS measurements can be obtained in the laboratory with relatively simple, special-purpose potentiostats in which the working electrode and output signal have a common ground. This demonstration represents an important step in transitioning EFS measurements from small coupons in the laboratory to aircraft in a hangar.

Because of the small currents measured in both EFS and EIS, it was also necessary to demonstrate the feasibility of making these measurements in the electromagnetic noise environment of a typical hangar. This was accomplished by SwRI's background noise characterizations performed on T-38 aircraft in a hangar at Randolph AFB in San Antonio. These measurements showed that the hangar environment actually exhibited less electrical noise (for the problematic 60 Hz regime) than that which was typical of the mechanical testing laboratories in which the EFS/EIS development efforts were conducted. Consequently, the fact that these low current (μA) measurements were successfully made throughout the present program in the mechanical testing laboratories at both Penn and SwRI demonstrates the feasibility of performing such measurements in the hangar environment.

In summary, many of the technical hurdles associated with the application of EFS to the assessment of fatigue damage in aircraft (previously identified in Section 1) have been overcome. Briefly, the present program has demonstrated the following:

1. The phenomenon underlying EFS occurs in high strength aircraft alloys.

2. EFS measurements can be made with electrolytes that are benign to aircraft materials.

3. EFS signals change in a characteristic manner that tracks fatigue damage.

4. EFS can detect fatigue microcracking in the size range of 70-75 μm, and improvements on this minimum detectable crack size are believed to be possible.

5. EIS can also be used to systematically track fatigue damage in high strength aluminum alloys.

6. Although EIS is a less mature technology than EFS, it has potential for sensing fatigue damage without having to mechanically load the aircraft.

7. Both EFS and EIS can measure fatigue damage on primer-coated aircraft alloys, although measurements on surfaces with both primer and topcoats are presently problematic—at least for topcoats without defects or flaws, which are electrically insulating.

8. EFS measurements can be made with small sensors having as little as 5 ml of electrolyte and 1.5 cm^2 surface contact areas, and smaller, simpler sensors can be developed.

9. EFS measurements are feasible in the typical electromagnetic noise environments of aircraft hangars.

A more detailed summary of key results and conclusions is provided in Section 12. Remaining technical challenges for application of EFS technology to assessment of fatigue damage in aircraft are discussed below.

The remaining technical challenges to further development of EFS and EIS are inextricably related to the envisioned mode of application of these technologies. Thus, a brief discussion of these potential application modes is a useful prelude to further discussions. The following four distinct modes of EFS application are envisioned:

Mode 1:   Laboratory tool for characterizing and understanding the evolution of fatigue damage in aerospace alloys tested in well-controlled laboratory experiments.

Mode 2:   Tool for monitoring fatigue damage evolution in full-scale testing—either of critical components or the entire aircraft.

Mode 3:   Fatigue sensor for periodic in-service inspection of aircraft components during overhaul.

Mode 4:   In-flight fatigue sensor for continuous or periodic monitoring of fatigue damage evolution at fatigue critical locations in aircraft.

Naturally, the technical challenges increase significantly upon transitioning to higher modes of application—this is particularly true of transitioning from Modes 1 and 2 to Modes 3 and 4. As discussed below, Modes 3 and 4 each have their own unique technical challenges.

Presently, EFS technology is sufficiently mature for Mode 1 application. In particular, the demonstrated ability of EFS to detect fatigue damage on a cycle-by-cycle basis during the simple spectra with overloads and underloads would be applicable to fundamental studies of load interactions during variable amplitude loading. Although potential drop methods have been employed in similar fashion, they are limited to relatively large crack sizes compared to EFS. This limitation is due to the fact that potential drop measurements are very sensitive to lead placement, particularly for small cracks. Accurate lead placement is typically not possible when studying naturally initiated microcracks because of the uncertainty in the precise location in

which the crack will initiate. EFS would also be a valuable tool for basic studies of the behavior of small fatigue cracks, which are important to developing improved design methods for high cycle fatigue. The ability of EFS to detect microcracks of 70 μm (or perhaps smaller) could greatly improve testing efficiency during such high cycle fatigue tests.

The EFS technology is close to the point where it can be employed in Mode 2 applications involving full-scale fatigue testing of components or aircraft. Presently, EFS application in these areas would be limited to fatigue critical locations where the sensor would have direct access to the fatigue initiation site. However, as discussed below, future developments could extend EFS to less accessible fatigue critical locations. The successful demonstration of small probes to facilitate local EFS measurements represents a significant advance for Mode 1 application to laboratory studies, as well as Mode 2 application to full-scale testing.

There are presently five remaining technical challenges that must be overcome in order for EFS to be employed in Mode 3 and 4 applications. Each of these is briefly outlined and discussed below.

The first challenge is to fully quantify the relationships between EFS response and evolving fatigue damage. Although systematic changes in EFS waveform and amplitude occur throughout the fatigue life, quantitative relations having the fidelity needed for run/retirement/repair decisions are not yet in hand. The primary challenge in this regard is developing methods to either eliminate or account for the settling-in transients that occur at the beginning of testing, as well as following test interruptions. Both types of settling-in transients are believed to be associated with time-dependent changes in the electrochemical nature of the surface film and/or electrolyte. Since these settling-in transients are characterized by decreases in current response with time, the subsequent increases which occur with evolving fatigue damage result in an overall response that is not single-valued. This phenomenon is tolerable in the case where continuous monitoring is performed (Mode 4) since the settling-in transients are readily identifiable in these instances and signal processing could likely be developed to deal with them. However, the lack of a single-valued function between EFS signal and fatigue

damage is considerably more problematical for periodic (Mode 3) inspection. In the latter case, only brief "snapshots" of the EFS response would be available thereby precluding ready identification of trends in the current transients.

It is interesting to consider whether or not the presence of coatings would minimize or eliminate the above settling-in transient. This might be the case if the electrochemical nature of the primed or painted surfaces were more consistent than that of the bare surface for which most, if not all, of the settling-in transient have been observed. Presently insufficient data are available to determine if coatings could mitigate the settling-in effects.

This leads to the second technical challenge, namely a more extensive characterization of the ability of EFS to assess the state of fatigue damage of coated surfaces. Success with both EFS and EIS has been demonstrated with primed surfaces that are applicable to fatigue critical locations on interior aircraft structure. However, painted surfaces have proven to be problematic. Of course coatings could always be removed locally; however, this would represent added expense, and thus methods need to be developed to avoid this, if possible. Additional EFS and EIS developmental efforts on coatings are needed, including examination of aged coatings for which measurements might be considerably easier due to the presence of cracks and other defects in the coating. EIS has demonstrated success in this area including the ability to detect the quality of coatings. This is consistent with the fact that EIS was originally developed to study surfaces including coated surfaces, and thus this application of the technology is relatively mature, compared to its application to the assessment of fatigue damage.

The third technical challenge involves the development of methods to effectively load the aircraft to stimulate the EFS measurements, or alternatively to devise methods to preclude the need to load the aircraft in order to obtain measurements. In this regard, application Modes 3 and 4 differ substantially. Specifically, EFS is ideally suited to Mode 4 applications since the actual in-flight aircraft loading can be used to stimulate the EFS measurement. In contrast, EFS is not nearly as well suited to periodic inspections of aircraft on the ground (Mode 3) since loading the aircraft in the hangar is not likely to be feasible for both technical and economic reasons. Properly loading all of the fatigue critical locations in the complex, multiaxial manner

that they experience in-flight is not a simple task. Although such loading is accomplished in full-scale aircraft tests, such an approach is clearly not feasible for periodic inspections at depots. Application of the EFS as a continuous in-flight monitor (Mode 4) has the advantage that it provides the precise multiaxial loading typical of most fatigue critical locations. However, the associated technical challenge is to properly interpret signals arising from these complex, multiaxial spectra. Although the variable amplitude loading work performed in the present program provides a foundation for resolving this issue, the fully-developed methodology needed for proper interpretation of the EFS signal under actual aircraft spectra is not yet available. In the event that this problem proves to be intractable, an alternative approach might be to perform periodic flight tests involving specifically designed aircraft maneuvers to stimulate the EFS with well-defined and simpler loading (i.e., more nearly constant amplitude). A second alternative would be to fully develop the EIS technique thereby eliminating the need to load the aircraft. EIS measurements would be best suited for periodic inspections at the depot (Mode 3) where they could be performed using electrical stimulation. In view of the confounding interactions between the electrical and mechanical (loading) perturbations—that is, the EIS-EMIS interactions reported in Section 6—there would appear to be no advantage to applying EIS to in-flight measurements (Mode 4).

In order for EFS to achieve widespread use as an inspection tool, it must be applicable to most fatigue critical locations on aircraft. This requirement leads to the fourth remaining technical challenge. Specifically, methods need to be developed to enable EFS information to be acquired at inaccessible locations—that is, at a convenient measurement location somewhat removed from the actual surface where fatigue damage (specifically, a microcrack) nucleates. A prime example of such an inaccessible location is a fastener-filled hole. Since fatigue microcracks tend to nucleate at the interior surface of the hole, the fastener prevents ready access to the surface where cracks nucleate. Although measurements at such locations are problematical for all inspection techniques, they are particularly challenging for EFS because of its dependence on film rupture and electrochemical reactions that primarily occur at the nucleation site.

It may be possible to detect microcracking in such inaccessible locations by positioning the sensor at an adjacent surface in order to detect the crack-tip stress field that is projected ahead of a growing crack. Such an EFS response might also be complemented by an increase in the net-section (ligament) stress adjacent to the fatigue critical location. Using these remote measurements, it may be possible to develop mechanical transfer functions (e.g., using fracture mechanics principles) to relate the remotely sensed damage to the fatigue damage at the inaccessible site. It may also be possible to detect cracking at the nucleation site within the hole if ingress of electrolyte to this local site occurs. This would be possible if the fastener were inserted dry and if the exterior paint were cracked around the rivet head—a situation that often occurs on aircraft. All of the above avenues need to be explored in developing methods to treat this aspect of the problem.

Most of the EFS measurements in the present program have been conducted under well-controlled electrochemical conditions. The electrochemical conditions encountered on aircraft in service are not likely to be as well controlled. Developing methods to enable EFS measurements to be made under these more complex electrochemical conditions represent the fifth technical challenge to development of EFS as an inspection tool. The practical situation that needs to be considered is the case in which depassivation can occur by purely chemical means in occluded regions of aircraft—specifically, within the crevices that abound in the built-up structure of aircraft. Examples of such behavior were observed during testing in the present program. EFS measurements were in several instances confounded by the presence of local corrosion in the fatigue specimen. In one case, this occurred in a crevice produced by an aged o-ring seal, and in another case this occurred due to pitting produced by chloride impurities which had leaked from the reference electrode. In both instances, the molybdate inhibitor performed effectively and precipitated at these regions to mitigate the local corrosion—nevertheless, the local corrosion associated molybdate precipitation reactions affected the EFS measurements. The background electrochemical noise associated with such reactions cause significant currents to be generated and these make the relatively small EFS current both difficult to resolve and erratic in nature. EFS and EIS measurements under these practical conditions need to be explored. However, it is relevant to note that successful EFS measurements were made for propagating cracks (see Section 7). These observations are encouraging since the electrochemical conditions within

cracks are expected to be similar to those within crevices. Although these measurements on cracked specimens did not exhibit all of the waveform features characteristic of tests on smooth specimens, the measured current amplitudes were found to correlate with crack size.

11.1 REFERENCES

11.1 Li, Y.F., Farrington, G.C., and Laird, C., "Cyclic Response-Electrochemical Interaction in Mono and Polycrystalline AISI 316L Stainless Steel in H_2SO_4 Solution, Part I," *Acta Metall. Mater.*, 41 (1993) 693-708.

11.2 Li, Y.F., Farrington, G.C., and Laird, C., "Cyclic Response-Electrochemical Interaction in Mono and Polycrystalline AISI 316L Stainless Steel in H_2SO_4 Solution, Part II," *Acta Metall. Mater.*, 41 (1993) 709-721.

11.3 Li, Y.F., Farrington, G.C., and Laird, C., "Cyclic Response-Electrochemical Interaction in Mono and Polycrystalline AISI 316L Stainless Steel in H_2SO_4 Solution, Part III," *Acta Metall. Mater.*, 41 (1993) 723-37.

12.0 SUMMARY AND CONCLUSIONS

Baseline Properties (Section 2)

1. Microstructures and mechanical properties of the three materials examined in this study—7075-T73511, quenched and tempered 4130 steel, and Ti-6Al-4V—were selected to be typical of alloys used in military aircraft in general and the T-38 aircraft in particular.

2. The S-N fatigue properties of these materials in the intermediate cycle regime (10^3 to 10^6 cycles) were consistent with those reported in the literature and in MIL Handbook 5. Moreover, the S-N data generated at Penn and at SwRI were found to be in agreement within the typical data scatter for such tests (10X on life) and no systematic bias was found between the two laboratories, thereby facilitating inter laboratory comparison of results.

Electrolyte Optimization (Section 3)

3. Based on thermodynamic considerations (Pourbaix diagrams) combined with kinetic measurements (potentiodynamic polarization scans), several electrolytes were identified in which the aircraft alloys exhibited the required corrosion resistance and passivity in the unstrained state while, at the same time, exhibited adequate mechanical depassivation at localized straining caused by fatigue loading to produce measurable EFS current responses. These electrolytes are based on the borate buffer system with the addition of molybdate as an inhibitor and are identified as 7 and 8 in Table 3-1. Electrolyte 7 (pH = 8.4) was shown to be optimal for 4130 steel and for Ti-6Al-4V, while Electrolyte 8 (pH = 6.9) was initially identified as being optimal for 7075-T73511.

4. 4130 steel and Ti-6Al-4V exposed to liquid Electrolyte 7 and 7075-T73511 exposed to liquid Electrolyte 8 were found to exhibit "excellent" resistance to general corrosion (corrosion rate less than 0.02 mm/yr.), as well as no evidence of either pitting corrosion or crevice corrosion.

5. Electrolyte 7 was demonstrated to form a stable gel when combined with Laponite, whereas the formation of a stable gel with Electrolyte 8 was found to be problematic due to its lower pH (6.9 vs 8.4).

6. Based on the ability of Electrolyte 7 to form a stable gel, as well as its ability to promote a more stable passive film in the aluminum alloy under cyclic loading, this electrolyte was ultimately recommended for use with all three aircraft alloys. The composition of this generic EFS electrolyte is as follows:

$$0.3M \ H_3BO_3 + 0.075 \ Na_2B_4O_7*10H_2O + 0.06M \ Na_2MoO_4 \quad (pH=8.4)$$
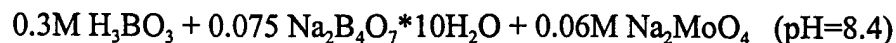
The identification of this generic EFS gel electrolyte is significant in that it will simplify continuing EFS developmental work in the laboratory, as well as possible future applications of EFS to aircraft in the field.

7. Various candidate EFS electrolytes, including the generic EFS electrolyte, have been shown to have no measurable effect on the S-N fatigue response of the three aircraft alloys compared to a baseline laboratory air environment. Moreover, the measured fatigue lives in the generic EFS electrolyte were found to be longer than those measured in water—an environment to which aircraft are commonly exposed while in service.

8. Fatigue crack growth rates in 4130 steel exposed to the generic EFS liquid electrolyte and cycled at a frequency of 0.5 Hz were found to be identical to those in laboratory air and two-to-three times slower than those in distilled water or liquid dye penetrant.

9. Fatigue crack growth rates in 7075-T73511 exposed to the generic EFS electrolyte and cycled at a loading frequency of 0.5 Hz were identical to those in laboratory air, while at 0.05 Hz the rates were nearly indistinguishable (within 10%) from those in laboratory air and about 20% slower than those in liquid dye penetrant.

10. Based on the above results (3 through 9), it can be concluded that a generic EFS electrolyte has been developed that is not detrimental to aircraft materials or structures and, as indicated below in conclusions 13 through 17, is capable of producing measurable and informative EFS current responses.

Electrode Optimization (Section 4)

11. The concept of greatly simplifying the EFS measurement by using a Ni/NiO electrode to sense the EFS current response while also maintaining a constant potential has been demonstrated in several experiments. This two-electrode system eliminates the need for a separate reference electrode, as well as the need for an electronic potentiostat to maintain a fixed potential.

12. The feasibility of employing a two-electrode system driven by a potentiostat for EFS application has been established. Initial success has also been achieved with a self-polarizing, two-electrode (Ni/NiO) system. However, further development work is needed to demonstrate that the self-polarizing system has the capacity to supply the current required when aircraft components are subjected to cyclic straining. (However, since the potentiostatically driven, three-electrode system presently provides the highest fidelity EFS measurements, this system was used in most of the EFS measurements in the present program and is the basis for the associated conclusions given below, unless otherwise noted.)

EFS Results on Uncoated Materials (Section 5)

13. The onset and evolution of fatigue damage in all three aircraft alloys corresponds to distinct changes in the EFS current signals throughout the fatigue life; these changes are qualitatively consistent and reproducible, although their details are specific to each alloy type.

14. A variety of relatively simple signal processing parameters have been developed to assist in identifying the onset and evolution of fatigue damage from the measured EFS current signals. Since details of the EFS signal are dependent on alloy, the optimum signal processing parameter to detect fatigue damage also depends on alloy type.

15. The onset of EFS-detectable fatigue damage in the relatively high-strength alloys examined herein appears to correlate with the occurrence of fatigue microcracking. The percentage of fatigue life at which microcracks are detected is dependent on the life regime—that is, at short lives the onset of fatigue microcracking is detected earlier in life, while at longer fatigue lives the detection of fatigue microcracking occurs later in life. These results are consistent with well-known physical trends in fatigue damage accumulation—specifically, that microcracks occur early in the life of smooth specimens with short lives, and very late in the life of smooth specimens with long lives.

16. Changes in applied potential within the passive regime of the various alloys do not affect the measured current amplitudes and other features of the EFS signal (this differs from the EIS response to the applied potential—see Conclusion 27).

17. Interrupted tests on 4130 steel specimens at both Penn and SwRI revealed that the earliest EFS indications of fatigue damage correspond to microcracks of about 70 to 75 μm in length. Although similar interrupted tests on 7075 aluminum have not been successful to the same degree, preliminary evidence suggests this is due primarily to difficulty in visually verify the presence of such small microcracks, and not due to limitations in EFS ability to detect microcracking in this alloy.

18. Cyclic frequency appears to alter the magnitude of the EFS signal, albeit not in a very consistent manner because the effect was found to be alloy dependent. Although the onset and evolution of fatigue damage could be detected over the range of frequencies measured (1 Hz to 5Hz), this dependence will complicate the interpretation of EFS signals under the variable amplitude and variable frequency loading experienced on aircraft. (See additional conclusions below on variable amplitude loading).

19. Intermittent EFS measurements during fatigue testing have been demonstrated to sense the development of fatigue damage effectively. However, "settling-in" current transients have been observed on reapplication of the sensor, which appear to be due to changes in the surface condition. Since these "settling-in" transients compromise efficient application of the sensor for periodic inspections, methods need to be devised to minimize, or eliminate, this phenomenon.

EFS Results on Coated Material (Section 5)

20.   Fatigue damage can be detected with EFS in 7075 aluminum specimens with a primer coating, although the onset of detectable fatigue damage (i.e., microcracking) is delayed somewhat compared to that of uncoated specimens, when tested under otherwise identical conditions. Nevertheless, once damage is detected, features of the EFS signal at a given percentage of life are similar in coated and uncoated specimens.

21.   The total fatigue lives of primer-coated and uncoated specimens were found to be the same, within the overall scatter observed in fatigue testing. When combined with the above results, this fact suggests that the onset of fatigue microcracking in primer coated and uncoated specimens actually occur at similar percentages of life; however, the delayed EFS indication of cracking in the coated specimens seems to correspond to the additional cycles needed to enlarge the microcracks in the substrate to a size at which they can penetrate the ductile coating and be detected.

22.   EFS results on specimens with primer and top coats appear to be highly variable. This is believed to be due to the fact that high-quality top coats offer an impermeable barrier to the EFS signal, while those top coats that contain inherent defects enable EFS signals to be transmitted through the coating.

EIS Results (Section 6)

23.   The possibility of using Electrochemical Impedance Spectroscopy (EIS) to complement EFS as a fatigue sensor was explored with the motivation of a) providing an improved assessment of the fatigue damage state in coated components, and b) eliminating the need to mechanically load the specimen or structure in order to perform the measurement. Because the sensitivity of the EIS measurements is highly specific to the chemical state of the surface being interrogated, the results are highly specific to the alloy composition and coating condition; thus, results and conclusions provided below are broken down by alloy type and surface condition (coated versus uncoated).

EIS on Uncoated Aluminum Alloy

24.   EIS measurements on bare 7075 Al can be quantified in terms of a fatigue damage parameter ($1/R_p$). At short lives (<10,000 cycles) this parameter exhibits initial signs of fatigue damage at about 20% of the fatigue life and thereafter increases monotonically with increasing fatigue damage (as characterized by fractional fatigue life).

25.   EIS measurements in terms of $1/R_p$ on bare 7075 Al show reasonable reproducibility and can be used to forecast fatigue life within a factor of two; such reproducibility is on the order of the observed scatter in measured fatigue life at shorter lives and is likely dominated by the stochastic nature of the crack initiation process.

26.   Coupling of EIS and EMIS occurs when electrical perturbation frequencies approach the mechanical perturbation frequency (i.e., fatigue loading frequency). Although this

coupling confounds interpretation of the EIS fatigue damage parameter ($1/R_p$), this is not viewed as a serious disadvantage since the primary utility of EIS would be as a periodic in-service inspection tool, rather than a continuous monitoring tool, and in this mode EIS would not be required to operate under mechanical loading.

27. The sensitivity of EIS measurements is strongly dependent on the applied potential under which measurements are made. The applied potential used for most of the measurements in the present work (0.3 V vs SCE) was initially optimized for EFS response, and was subsequently discovered to be less than ideal for EIS measurements. The sensitivity of EIS measurements can be increased by a factor of three if the potential is increased from 0.3 V to 0.5 V vs SCE. This increase in potential does not affect the fatigue life.

28. EIS measurements suggest that 7075 Al is not completely passive in the originally selected electrolyte. This incomplete passivation gives rise to time-dependent changes in the surface condition of 7075 Al which can confound the interpretation of both EFS and EIS data. Thus, further optimization of the electrolyte or a passivation treatment prior to conducting measurements would be beneficial to both EFS and EIS, but particularly the latter.

EIS on Coated Aluminum Alloy

29. EIS measurements on both primer-coated and primer plus top-coated 7075 Al specimens revealed that the fatigue damage parameter $1/R_p$ increases exponentially with increasing fatigue damage, as indicated by fractional fatigue life. Marked increases in $1/R_p$ occur at 80 to 90% of the total fatigue life of coated specimens. This onset of clearly detectable fatigue damage in coated 7075 Al is similar for both EFS and EIS measurements and likely occurs when the coating becomes cracked by the underlying fatigue cracking in the metal substrate.

30. EIS measurements also provide a method for assessing the coating quality. Specifically, 7075 aluminum alloy specimens with inherent coating imperfections exhibit at least an order of magnitude lower background impedance, and correspondingly higher $1/R_p$ values, than specimens with high-quality coatings.

EIS on Bare Steel and Titanium

31. EIS measurements on 4340 and on Ti-6Al-4V are hampered by the rapid repassivation kinetics of these materials, combined with the remote nature of the present measurements, which provide an integrated average of the response over the highly passivated specimen surface. The relative success of EFS under these same material conditions highlights the fundamental differences in the two techniques. Specifically, EFS relies on mechanical depassivation via active fatigue loading (straining) to produce the measured current transients, whereas EIS relies on inherent changes in the nascent electrochemical reactivity of the fatigue-damaged surfaces subsequent to fatigue loading.

32. Although EIS measurements under fatigue loading overcome some of the above limitations, it is unclear what advantage this approach would provide over the simpler EFS measurements.

EFS Under Variable Amplitude Loading (Section 7)

33. EFS measurements on smooth specimens subjected to simple variable amplitude loading, consisting of periodic overloads and underloads, exhibit current-waveform features that are identical to those observed in constant amplitude loading. Moreover, these features (amplitude increases, emergence of crack peaks, and phase shifts) can be used to detect the onset of microcracking and track the evolution of fatigue damage on a cycle-by-cycle basis.

34. EFS measurements conducted under spectrum loading revealed that variations in the EFS current response primarily result from changes in loading amplitude and are relatively insensitive to changes in mean load, thereby simplifying interpretation of the measured current response signal.

35. The magnitudes of EFS current signals measured during constant amplitude loading and during simulated aircraft spectrum loading were found to be similar for a given fatigue damage state—as characterized by crack size. These results imply that the EFS response is primarily dependent on the actual damage state, and not on the prior history of loading; consequently, periodic EFS measurements on aircraft, e.g., obtained under simple constant-amplitude loading, could (in theory) be used to assess the state of fatigue damage in an aircraft.

36. Understanding and interpreting the EFS signal response under variable amplitude loading is critical to successful application of EFS as an in-flight monitor of fatigue damage. Although the present results are encouraging, additional work is needed to develop quantitative metrics required for assessing fatigue damage under the complex loading spectra experienced by aircraft in flight, including the effect of cyclic frequency.

37. For a growing macrocrack in a compact-tension specimen, a linear relationship was found between the EFS current amplitude (or range) and ΔK. Using fracture mechanics analysis, this relationship was used to predict the EFS current versus crack length relationship measured under both constant and variable amplitude loading of cylindrical specimens containing small surface cracks. These results suggest a possible method for transferring EFS current response versus crack size from one geometry to another—a feature that could prove to be useful in quantitatively calibrating EFS measurements on complex geometries such as those that occur on aircraft.

EFS Prototype Sensor (Section 8)

38. A first-generation prototype sensor has been developed that contains as little as 5 ml of the gelled generic electrolyte wetting a flat surface area of 1.5 cm^2. This sensor utilized a two-electrode system connected to a potentiostat to maintain a constant potential at the

surface being interrogated. However, the use of a self-polarizing, two-electrode system (e.g., Ni/NiO) is also feasible, and consequently would further simplify and ruggedize the sensor.

39.   The performance of the prototype sensor has been demonstrated on flat steel specimens containing a central hole to provide a stress concentration. Local EFS measurements with the prototype sensor reproduced the current response features previously obtained on cylindrical specimens immersed in liquid electrolyte, including the systematic changes in waveform and phase shifts associated with the formation of microcracking. These results also exhibited the same dependence on applied stress and cyclic frequency that has been previously noted for the cylindrical specimens exposed to liquid electrolyte.

Electrical Isolation (Section 9)

40.   Measurements of background electrical noise on large aluminum structures, including aircraft in hangars, were found to be equivalent to, or less noisy than, those measured during EFS experiments in a typical mechanical testing laboratory. Thus, the successful demonstration of EFS current measurements in the microampere range in the laboratory suggests that similar measurements can be accomplished on aircraft in hangars.

41.   In view of the low frequency of typical EFS measurements, the predominant sources of noise were 60-Hz noise from nearby instrumentation such as transformers and computer terminals, as well as intermittent radio frequency (RF) noise.

42.   The potentiostat designed and built at Penn has clearly demonstrated the advantage of using an EFS system with the working electrode (specimen or component to be inspected) and the output signal of the potentiostat connected to a common electrical ground.

43.   Combining the above approach with methods to improve the signal-to-noise ratio, such as RF shielding, and optimization of the physical configuration of the set-up and EFS probe, should enable practical EFS measurements to be made in the field environment.

Economic Assessment (Section 10)

44.   The producibility and affordability of the EFS is estimated to be favorable in relation to other NDI technologies. Specifically, the cost of the EFS sensors and instrumentation is projected to be quite low. However the analysis software is expected to be more sophisticated than for some NDI techniques.

45.   The application of EFS technology to inspection of the T-38A aircraft is projected to increase the savings realized by present non-destructive inspection technologies by 15%, giving a projected savings of $7.2 million/year.

13.0 RECOMMENDATIONS

Based on the technical discussion in Section 11, as well as the summary of results and conclusions in Section 12, the following recommendations for future development and application of electrochemical fatigue sensor technology are made:

1. The feasibility of a Ni/NiO, self-polarizing two-electrode system has been demonstrated. In view of the potential of such a system to simplify and ruggedize the EFS probe, additional effort is warranted to fully develop this concept so that measurements are as consistent and reliable as those obtainable with a three-electrode system and electronic potentiostat.

2. Additional experiments are needed to better define the smallest crack size that can be reliably detected with EFS on the various aircraft materials. Present attempts have been limited by the ability to visually detect the presence of small microcracks once the EFS has provided a crack indication. Experiments designed to overcome this limitation should utilize a geometry that localizes the crack initiation region, as well as a surface preparation (such as electropolishing) which maximizes the chance of optically finding surface microcracks.

3. Although consistent trends have been demonstrated between EFS current response and fatigue microcrack nucleation and growth, there is a need to develop these trends into fully quantifiable relationships that can be used to assess the state of fatigue damage with the reliability needed to make run/repair/retire decisions on aircraft components. A primary technical challenge to achieving this goal is to develop methods to either eliminate or compensate for the settling-in transients that often occur on initial application, or periodic reapplication, of the EFS probe due to time-dependent changes in the nature of the surface film, particularly on aluminum alloys. Such work also needs to be done in the presence of coatings that are likely to influence the underlying time-dependent changes in the surface condition.

4. Utilizing the EFS technology as an in-service monitor of evolving fatigue damage has a number of distinct advantages—for example, the structure would be self-loaded in a manner consistent with the evolving fatigue damage, and continuous measurements would result in more rigorous and reliable fatigue assessments. However, in order to apply the EFS as an in-service monitor, a more complete understanding and quantification of fatigue damage accumulation under complex, aircraft spectrum loading needs to be developed, including methods to account for frequency (i.e., strain-rate) effects.

5. Widespread application of EFS will require it to be suitable for most, if not all, of the known fatigue critical location on aircraft. Such widespread application will require the EFS to provide information relevant to inaccessible sites where the sensor cannot be

placed in direct contact with the surface on which fatigue damage nucleates. Such information can conceivably be acquired by sensing cracks indirectly through their attendant crack-tip plasticity, or by remotely sensing expected increases in net section stress as the crack grows. The development of a solution to this problem will likely require a coordinated experimental-analytical approach.

6. With the present level of development of prototype sensors that enable localized measurements of evolving fatigue damage, the EFS technology is sufficiently mature to be applied as a laboratory tool. For example, its demonstrated ability to monitor fatigue damage on a cycle-by-cycle basis could provide a valuable tool for fundamental study of load interaction effects and for the development of improved models to predict fatigue crack growth under variable amplitude loading. Also, the demonstrated ability of EFS to detect 75 μm surface cracks in 4130 steel could be exploited to characterize the early growth of microcracks in turbine blade materials—information of likely importance to the formulation of improved methods to design against high cycle fatigue in gas turbine engines.

7. Although the present work has demonstrated the benign nature of the EFS electrolyte, practical application of the sensor will likely require measurements to be made in situations where more aggressive service environments may be present. In particular, this can occur where chlorides or other contaminants can cause chemical depassivation within crevices and other occluded regions that are common at fatigue critical locations on aircraft. Thus, the capability of EFS/EIS to assess fatigue damage in the presence of background electrochemical "noise" from such localized corrosion needs to be systematically examined.

8. Widespread application of EFS to the periodic assessment of fatigue damage in aircraft may be practically limited by the need to load the structure in order to activate the EFS response. Mechanical loading may not always be technically or economically feasible, particularly if complex loading modes are required to properly activate specific fatigue critical locations. (Of course, the previously mentioned application of EFS as an in-service monitor remains as an alternative—in which case the problems associated with signal interpretation under spectrum loading will need to be resolved.) The EIS technology represents another alternative. Although EIS measurements are widely used to study chemical breakdown of passivity in coated specimens in the absence of cyclic deformation, the application of this technology to the assessment of fatigue damage is relatively new and will require time and resources to mature. Nevertheless, EIS has two potential advantages: a) eliminating the need to load the structure by applying electrical perturbations rather than mechanical perturbations, and b) providing supplemental information to assess the state of the coating—*i.e.*, porosity, corrosion under the coating, cracking due to aging, or lack of adherence.

APPENDIX AA

BASELINE MATERIAL PROPERTIES

This appendix summarizes data associated with Section 2 concerning the baseline material properties. The contents include:

- Description of the specimen numbering methodology,
- Listing of the tensile test data for all three materials (all data included), and,
- Tabulation of the smooth specimen fatigue tests performed on all three materials.

SPECIMEN NUMBERING METHODOLOGY

Due to the fact that testing will take place at both Penn and SwRI, it is important to adopt a standard methodology for numbering specimens that can be used to identify the pedigree and source of the specimens.

1. Material Identification

Three materials are involved in this program. These include alloys of aluminum, steel and titanium. All received products are cut into a number of pieces to facilitate handling and allow ease of transfer between laboratories. The steel is being cut-up so as to not result in warpage of the long bars during heat treatment. The aluminum and titanium will not be further subdivided from the original received material.

The raw material has been identified using the identification scheme shown below:

aluminum: 14 bars (each 6-ft long), ID'ed as A, B, C, ... N bar

titanium: 24 bars (each 50-inch) long, ID'ed as A, B, C, ... X bar

steel: bar A - subdivided into 4-15.5" segments (A1 to A4) plus 10" piece(A5)
        bar B - subdivided into 4-15.5" segments (B1 to B4) plus 10" piece(B5)
        bar C - subdivided into 4-15.5" segments (C1 to C4) plus 10" piece(C5)
        bar D - subdivided into 4-15.5" segments (D1 to D4) plus 10" piece(D5)
        bar E to N - subdivided into 3-24" segments (E1 to E3 thru N1 to N3)

The 4130 steel was sent out this week and thermally treated (all material will be heat treated at the same time and in the same lot). The aluminum and titanium material were received in the heat treated condition required.

2. Specimen Identification

Since we will be performing a large number of experimental evaluations during this program at both Penn and SwRI, it is useful to use a consistent specimen identification scheme to minimize confusion. As such, for the sake of documentation, the following unified convention is proposed. The specimen ID is designed so as to specifically track the position of the specimen in the raw supplied stock.

Proposed Specimen ID $\rightarrow$ *UVV - WWXY - ZZ...*

where: *U* identifies material type: A = aluminum
                                     S = steel
                                     T = titanium

VV identifies bar/block ID (described above)

WW denotes long axis position of the gage of the specimen
           (in inches) relative to an identified reference end of the bar

X illustrates thickness position ID: T = toward top surface
                                    C = centrally positioned
                                    B = toward bottom surface

Y identifies width position of the gage of the specimen (in
           inches) relative to an identified reference side of the bar

ZZ denotes any other desired or required identifier. This could be
           indicative of type of test, type of specimen, ID of lab or
           researcher, subtask work is performed in or any other.

Consider the following examples:

AA - $52B2$ - $F \rightarrow$ aluminum specimen from bar $\underline{A}$, located $\underline{52}$ inches from the end of the bar, excised from the bottom lower segment of the thickness and $\underline{2}$ inches from the outside reference edge of the extrusion (the specimen is for fatigue testing).

$SA4$ - $4C3$ - $T \rightarrow$ steel specimen from bar $\underline{A4}$, located $\underline{4}$ inches from the end of the bar, excised from the center of the thickness and $\underline{3}$ inches from the outside reference edge of the bar (the specimen is for tensile testing).

      The primary advantage with using a numbering scheme like the above is that we have tracked a variable that potentially may, at a later date, prove important to know. While there are several approaches that could be used to track position, this one is relatively straightforward and easy to apply. Every effort was made to use this method when numbering and machining specimens.

TENSILE PROPERTIES FOR THE MATERIALS

Upon receipt of the material, tensile testing was performed on all materials to establish the baseline strength levels. These data are shown below and referenced to available standard data (if possible).

Table AA-1. Tensile properties for the aluminum material as a function of length and width.

Material	Specimen ID's	YS, MPa	TS, MPa	% Elong	% RA	E, GPa
Aluminum	*AA-72C-1-TM*	445	512	15.0	34.5	66.2
(7075-T73511)	*AA-72C-2A-TM*	441	513	15.0	37.7	65.5
	AA-72C-2B-TM	443	514	15.0	35.1	66.2
	AA-72C-3-TM	443	514	15.0	35.1	66.2
	AN-72C-1-TM	444	515	15.7	37.7	67.6
	AN-72C-2A-TM	441	514	14.3	34.1	65.5
	AN-72C-2B-TM	439	513	14.3	36.0	66.2
	AN-72C-3-TM	442	514	13.6	30.3	65.5
	AG-72T-1-TM	439	513	13.6	31.3	66.9
	AG-72T-2A-TM	448	517	13.6	32.8	66.9
	AG-72T-2B-TM	447	514	14.3	35.8	65.5
	AG-72T-3-TM	453	522	15.0	32.8	66.2
	AG-72B-1-TM	445	515	13.6	33.3	68.9
	AG-72B-2A-TM	441	511	14.3	32.5	67.6
	AG-72B-2B-TM	445	513	13.6	30.8	68.9
	AG-72B-3-TM	444	515	14.3	35.9	68.3
	Average	**444**	**514**	**14.4**	**34.1**	**66.7**
	Standard Deviation	3.60	2.47	0.7	2.3	1.19
	Mil Hndbk 5G (B-basis)	434	503	8.0	-	71.7

B - basis: 90 percent of population equals or exceeds limits with a confidence interval of 95%

Table AA-2. Tensile properties for the steel material as a function of length and width.

Material	Specimen ID's	YS, MPa	TS, MPa	% Elong	% RA	E, GPa
Steel	*SN1-6C-1-TM*	1046	1098	19.3	65.4	202
(4130)	*SN1-6C-2-TM*	1040	1102	18.6	61.3	202
	SN1-6C-3-TM	1035	1100	20.0	61.9	202
	SN1-6C-4-TM	1043	1102	17.9	61.8	208
	SH1-6C-1-TM	978	1049	17.9	63.5	201
	SH1-6C-2-TM	1002	1074	17.9	61.2	201
	SH1-6C-3-TM	1020	1091	18.6	61.9	206
	SH1-6C-4-TM	1011	1075	18.6	63.4	207
	SE2-30C-1-TM	1029	1095	17.9	60.0	203
	SE2-30C-2-TM	1040	1108	20.0	63.4	202
	SE2-30C-3-TM	1040	1102	17.9	62.1	201
	SE2-30C-4-TM	1054	1118	19.3	63.7	201
	Average	**1028**	**1093**	**18.7**	**62.5**	**203**
	Standard Deviation	21.70	18.44	0.8	1.5	2.40
	Mil Hndbk 5G (S-basis)	944	1069	8.5	-	200

S - basis: Minimum values (industry standard) interpolated from handbook values.

Table AA-3. Tensile properties for the heat treated titanium material as a function of length.

Material	Specimen ID's	YS, MPa	TS, MPa	% Elong	% RA	E, GPa
Ti-6-4	*TA-33C-TM*	902	958	17.9	53.8	105
(aged)	*TA-39C-TM*	904	963	18.6	51.3	104
	TA-45C-TM	887	956	19.3	51.2	108
	TL-33C-TM	894	958	18.6	52.0	112
	TL-39C-TM	881	959	18.6	50.7	108
	TL-45C-TM	900	956	17.9	52.2	106
	TT-33C-TM	889	956	12.5	53.9	105
	TT-39C-TM	881	957	13.0	52.0	108
	TT-45C-TM	898	967	17.1	50.5	108
	Average	**893**	**959**	**17.1**	**52.0**	**107**
	Standard Deviation	8.80	3.79	2.5	1.2	2.37

SMOOTH SPECIMEN FATIGUE TESTS

The following three tables provide a listing of the smooth specimen fatigue tests performed during this program.

Table AA-4. Tabulation of the smooth specimen fatigue tests performed on the aluminum material at both Penn and SwRI.

Lab	Spec Ident	Coating	Environment	Specimen Area (mm^2)	Freq (Hz)	R-ratio	Cycles to Failure	Maximum Stress (MPa)	Failure Location	Miscellaneous Comments
Penn	A-t99	Uncoated	Lab Air	31.4	20	-1	178200	200	Gage	Soak in soln for 164 hr
Penn	A-t90	Uncoated	EFS Solution	31.4	0.5	-1	72300	230	Gage	
Penn	A-t88	Uncoated	Water	31.4	0.5	-1	24350	230	Gage	
Penn	A-t87	Uncoated	EFS Solution	31.8	0.5	-1	64200	200	Gage	
Penn	A-t85	Uncoated	EFS Solution	31.7	2	-1	210200	200	Gage	
Penn	A-t78	Uncoated	EFS Solution	31.6	0.5	-1	65600	200	Gage	
Penn	A-T77	Uncoated	Lab Air	31.5	4	-1	178900	210	Gage	New chamber
Penn	A-t75	Uncoated	EFS Solution	31.6	0.5	-1	53700	250	Gage	
Penn	A-T74	Uncoated	EFS Solution	31.6	5	-1	>114500	200	Gage	Search small-crack + unknown cyc
Penn	A-t73	Uncoated	EFS Solution	31.2	0.5	-1	671200	150	Gage	Test filter
Penn	A-T65	Uncoated	Lab Air	31.6	0.5	-1	25952	250	Gage	
Penn	A-t64	Uncoated	EFS Solution	31.7	0.5	-1	51800	?230	Gage	Variable-1 small peak @ 131 MPa
Penn	A-t62	Uncoated	Water	31.2	8	-1	100000	150	Gage	
Penn	A-t61	Uncoated	EFS Solution	31.6	0.5	-1	>117950	200	Gage	Test stopped?
Penn	A-t51	Uncoated	EFS Solution	31.5	0.5	-1	180000	200	Gage	variable-3 small peak @ 100 MPa
Penn	A-T43	Uncoated	Lab Air	31.5	20	-1	111300	200	Gage	
Penn	A-t41	Uncoated	EFS / Lab Air	31.3	0.5 - 20	-1	77099	179-200	Gage	4000 cyc in air @ 20Hz Smax 200 MP
Penn	A-t40	Uncoated	EFS Solution	31.4	0.5	-1	107200	180	Gage	
Penn	A-t39	Uncoated	EFS Solution	31.5	0.5	-1	70000	200	Gage	
Penn	A-T38	Uncoated	Lab Air	31.5	3 - 5	-1	957800	190	Gage	3-5 Hz
Penn	A-t30	Uncoated	steelgel	31.6	0.5	-1	179400	200	Gage	
Penn	A-T28	Uncoated	Lab Air	31.5	8	-1	120000	220	Gage	
Penn	A-t25	Uncoated	EFS Solution	31.5	0.5	-1	53412	230	Gage	
Penn	A-T18	Uncoated	Lab Air	31.7	0.5	-1	80600	250	Gage	
Penn	A-T17	Uncoated	Lab Air	31.6	0.5	-1	26238	250	Gage	
Penn	A-t16	Uncoated	EFS Solution	31.6	0.5	-1	40149	250	Gage	
Penn	A-t100	Uncoated	EFS Solution	31.3	0.5	-1	160800	180	Gage	
Penn	A-b94	Uncoated	EFS Solution	31.4	5	-1	314800	200	Gage	
Penn	A-b93-2	Uncoated	EFS Solution	31.6	0.5	-1	108000	200	Gage	
Penn	A-b93	Uncoated	EFS Solution	31.6	0.5	-1	108000	200	Gage	long passivation

Table AA-4. *continued*

Lab	Spec Ident	Coating	Environment	Specimen Area (mm^2)	Freq (Hz)	R-ratio	Cycles to Failure	Maximum Stress (MPa)	Failure Location	Miscellaneous Comments
Penn	A-b91	Uncoated	EFS Solution	31.4	0.5	-1	39500	230	Gage	
Penn	A-b9	Uncoated	EFS Solution	31.6	.5/2.5	-1	1636000	150	Gage	*Try new Pstat*
Penn	A-b84	Uncoated	EFS Solution	31.3	0.5	-1	240000	170	Gage	
Penn	A-b83	Uncoated	EFS Solution	31.6	0.5	-1	64600	230	Gage	
Penn	A-b82	Uncoated	EFS Solution	31.5	0.5	-1	>135000	200	Gage	*Interrupt test*
Penn	A-b80	Uncoated	EFS / Lab Air	31.6	0.5 - 8	-1	123800	200	Gage	*53800 cyc in EFS solution @ .5 Hz*
Penn	A-b72	Uncoated	EFS Solution	31.3	0.5	-1	96400	200	Gage	*New P-stat*
Penn	A-b71	Coated	EFS Solution	31.4	0.5	-1	144500	200	Gage	*Coat-White*
Penn	A-b7	Uncoated	steelgel	31.6	5	-1	166800	200	Gage	
Penn	A-B69	Coated	EFS Solution	31.6	2.5	-1	50000	200	Gage	*Coat-Green*
Penn	A-b68	Uncoated	Lab Air	31.0	20	-1	328000	200	Gage	*1000 cyc in EFS solution*
Penn	A-b67	Uncoated	steelgel	31.4	2.5	-1	251500	200	Gage	
Penn	A-b60	Uncoated	steelgel	31.0	0.5	-1	167000	200	Gage	
Penn	A-b59	Uncoated	EFS Solution	31.5	0.5	-1	>138700	200	Gage	*Interrupt test*
Penn	A-b58	Coated	EFS Solution	31.7	0.5	-1	142600	200	Gage	*Coat-Green*
Penn	A-b57	Uncoated	EFS / Lab Air	31.3	0.5 - 4	-1	310000	190	Gage	*110000 cyc in EFS solution @ .5 Hz*
Penn	A-B47	Uncoated	Lab Air	31.5	20	-1	248000	200	Thread	
Penn	A-b45	Uncoated	EFS Solution	31.4	2.5	-1	571800	180	Gage	
Penn	A-b43	Uncoated	EFS / Lab Air	31.4	0.5 - 2	-1	58300	230	Gage	*18300 cyc in EFS solution @ .5Hz*
Penn	AB38T5	Uncoated	Lab Air	31.1	0.5	-1	22386	300	Gage	
Penn	AB38T4	Uncoated	Lab Air	31.7	0.5	-1	80000	230	Gage	
Penn	AB38T3	Uncoated	Lab Air	31.1	0.5	-1	3500	380	Gage	
Penn	AB38T2	Uncoated	Lab Air	31.7	0.5	-1	540000	195	Gage	
Penn	AB38B5	Uncoated	Lab Air	31.6	0.5	-1	540372	190	Gage	
Penn	AB38B3	Uncoated	Lab Air	31.6	0.5	-1	43077	270	Gage	
Penn	AB38B2	Uncoated	Lab Air	31.7	0.5	-1	6600	340	Gage	
Penn	AB38B1	Uncoated	Lab Air	31.7	0.5	-1	601900	210	Gage	
Penn	A-b36	Uncoated	EFS Solution	31.3	3.5	-1	123400	200	Gage	*New grips*
Penn	A-b33	Uncoated	EFS Solution	31.3	0.5	-1	131700	160	Gage	

AA-8

Lab	Spec Ident	Coating	Environ-ment	Specimen Area (mm^2)	Freq (Hz)	R-ratio	Cycles to Failure	Maximum Stress (MPa)	Failure Location	Miscellaneous Comments
Penn	A-b31	Uncoated	EFS Solution	31.7	2.5	-1	747200	180	Gage	?
Penn	A-b23	Uncoated	EFS Solution	31.4	0.5	-1	88600	200	Gage	
Penn	A-b22	Uncoated	EFS Solution	31.6	0.5	-1	222700	200	Gage	
Penn	A-B21	Uncoated	Lab Air	31.2	3	-1	138400	190	Gage	
Penn	AB19	Uncoated	Lab Air	31.5	4	-1	1823300	190	Gage	
Penn	A-b12	Uncoated	EFS Solution	31.4	0.5	-1	1700	200	Stop	
Penn	A-B11	Uncoated	Lab Air	31.7	8	-1	236000	200	Gage	
Penn	A-b108	Uncoated	EFS Solution	31.7		-1	789400	200	Gage	*Unkown cycles in air; freq?*
Penn	A-b105	Uncoated	EFS Solution	31.4	0.5	-1	125800	200	Gage	
Penn	A-b103	Uncoated	Lab Air	31.5	20	-1	124200	200	Gage	*Soak in soln for 146 hr*
Penn	A-b10	Coated	EFS Solution	31.7	0.5	-1	461700	200	Gage	*Coat-White*
SwRI	AC12C1F	Uncoated	Lab Air	31.4	3	0.05	73436	345	Gage/Rad	
SwRI	AC12C2AF	Uncoated	Lab Air	31.7	3	0.05	>251546	303	Grip	
SwRI	AC12C2BF	Uncoated	Lab Air	31.4	20	0.05	>373399	310	Grip	
SwRI	AC12C3F	Uncoated	EFS Solution	31.7	1	-1	>162630	221	Grip	
SwRI	AC19C1F	Uncoated	Lab Air	31.7	3	0.05	>175274	345	Grip	
SwRI	AC19C2AF	Uncoated	Lab Air	31.7	3	0.05	14457	379	Gage	
SwRI	AC19C2BF	Uncoated	EFS Solution	31.9	1	0.05	5581	448	Gage	
SwRI	AC19C3F	Uncoated	EFS Solution	31.9	1	-1	10397	345	Gage	
SwRI	AC27C1F	Uncoated	Lab Air	31.9	5	0.05	>102954	379	Grip	
SwRI	AC27C2AF	Uncoated	Lab Air	31.9	20	0.05	70680	379	Gage/Rad	
SwRI	AC27C2BF	Uncoated	Lab Air	31.9	10	0.05	>365427	310	Grip	
SwRI	AC27C3F	Uncoated	EFS Solution	31.9	1	0.05	6077	448	Gage	
SwRI	AC35C1F	Uncoated	Lab Air	31.9	20	0.05	>57790	379	Grip	
SwRI	AC35C2AF	Uncoated	Lab Air	31.9	20	0.05	>62653	379	Grip	
SwRI	AC35C2BF	Uncoated	EFS Solution	31.7	1	0.05	9202	448	Gage	
SwRI	AC35C3F	Uncoated	EFS Solution	31.7	1	0.05	14719	448	Gage/Rad	
SwRI	AC43C1F	Uncoated	Lab Air	31.7			0	379		*Overloaded*
SwRI	AC43C2AF	Uncoated	Lab Air	31.7	20	0.05	43954	379	Gage/Rad	
SwRI	AC43C2BF	Uncoated	EFS Solution	31.7	1	0.05	24201	448	Gage	

Table AA-4. continued

Lab	Spec Ident	Coating	Environ-ment	Specimen Area (mm^2)	Freq (Hz)	R-ratio	Cycles to Failure	Maximum Stress (MPa)	Failure Location	Miscellaneous Comments
SwRI	AC43C3F	Uncoated	EFS Solution	31.7	1	0.5	31181	448	Gage	Specimen removed
SwRI	AC4C1F	Uncoated	Lab Air	31.7	3	0.05	>524540	276	Grip	
SwRI	AC4C2AF	Uncoated	Lab Air	31.7	3	0.05	>119592	345	Grip	
SwRI	AC4C2BF	Uncoated	Lab Air	31.4	20	0.05	>1183864	310	Grip	
SwRI	AC4C3F	Uncoated	EFS Solution	31.7	1	0.05	8713	448	Gage/Rad	
SwRI	AC50C1F	Uncoated	Lab Air	31.7	10	0.05	82265	414	Grip	
SwRI	AC50C2AF	Uncoated	Lab Air	31.7	10	0.05	8762	448	Gage	
SwRI	AC50C2BF	Uncoated	EFS Solution	31.7	1	0.05	30264	448	Gage	
SwRI	AC50C3F	Uncoated	EFS Solution	31.9	N/A	-1	4334	345	Gage	Frequency not known
SwRI	AC58C1F	Uncoated	Lab Air	31.7	10	0.05	50606	414	Gage	
SwRI	AC58C2AF	Uncoated	Lab Air	31.7	10	0.05	10774	448	Gage	
SwRI	AC58C2BF	Uncoated	EFS Solution	31.8	1	0.05	8604	448	Gage	
SwRI	AC58C3F	Uncoated	EFS Solution	31.7	1	-1	11387	345	Gage/Rad	
SwRI	AC65C1F	Uncoated	Lab Air	31.7	10	0.05	12832	448	Gage	
SwRI	AC65C2AF	Uncoated	EFS Solution	31.7	1	0.05	8804	448	Gage	
SwRI	AC65C2BF	Uncoated	EFS Solution	31.7	1	0.05	7600	448	Gage	
SwRI	AC65C3F	Uncoated	EFS Solution	20.2	10	0.05	418069	276	Gage	
SwRI	AF12C2BF	Uncoated	EFS Solution		5	0.5	416310	276	Gage	
SwRI	AF19C3F	Uncoated	EFS Solution		5	-1	6500	310	Gage	Specimen removed
SwRI	AF27C2AF	Uncoated	EFS Solution		5	0.05	56995	276	Gage	
SwRI	AF27C2BF	Uncoated	EFS Solution		1	-1	157	448	Gage	
SwRI	AF35C2AF	Uncoated	EFS Solution		5	-1	30283	276	Gage	
SwRI	AF35C2BF	Uncoated	EFS Solution		1	-1	10160	345	Gage	
SwRI	AF35C3F	Uncoated	EFS Solution		1	-1	8345	310	Gage	Specimen removed
SwRI	AF43C2AF	Uncoated	EFS Solution		5	-1	32067	276	Gage	
SwRI	AF4C3F	Uncoated	EFS Solution		5	-1	13186	310	Gage	
SwRI	AF50C1F	Uncoated	EFS Solution		1	-1	7202	345	Gage	
SwRI	AF50C2AF	Uncoated	EFS Solution		1	-1	15933	310	Gage	
SwRI	AF50C3F	Uncoated	EFS Solution		5	0.05	44639	345	Gage	
SwRI	AF58C1F	Uncoated	EFS Solution		1	-1	8699	345	Gage	Steel solution
SwRI	AF58C2AF	Uncoated	EFS Solution		1	-1	13000	310	Gage	Specimen removed
SwRI	AF58C2BF	Uncoated	EFS Solution		5	-1	54176	241	Gage	

Table AA–4. *continued*

Lab	Spec Ident	Coating	Environ-ment	Specimen Area (mm^2)	Freq (Hz)	R-ratio	Cycles to Failure	Maximum Stress (MPa)	Failure Location	Miscellaneous Comments
SwRI	AF65C2AF	Uncoated	EFS Solution		5	-1	9623	345	Gage	
SwRI	AF65C3F	Uncoated	EFS Solution		1	-1	14622	310	Gage	
SwRI	AH12C2AF	Uncoated	EFS Solution	19.7	1	-1	9836	345	Gage	
SwRI	AH12C2AF	Uncoated	EFS Solution	19.7	1	-1	10391	345	Gage	
SwRI	AH12C2BF	Coated	EFS Solution	19.5	5	-1	109798	241	Gage	*Primer+Topcoat*
SwRI	AH12C3F	Uncoated	EFS Solution	19.5	1	-1	49252	276	Gage	
SwRI	AH19C2AF	Coated	EFS Solution	20.3	1	-1	12383	345	Gage	*Primer+Topcoat*
SwRI	AH19C2BF	Coated	EFS Solution	20.3	1	-1	7680	345	Gage	*Primer+Topcoat*
SwRI	AH19C3F	Uncoated	EFS Solution	19.7	1	-1	>22115	276	Gage	*60ksi OL @ 2000 cycs*
SwRI	AH27C1F	Coated	EFS Solution	20.2	1	-1	10828	345	Gage	*Primer*
SwRI	AH27C2AF	Coated	EFS Solution	19.3	5	-1	66817	241	Gage	*Primer*
SwRI	AH27C2BF	Coated	EFS Solution	20.3	5	-1	67331	276	Gage	*Primer*
SwRI	AH35C2AF	Coated	EFS Solution	20.3	1	-1	10672	345	Gage	*Primer+Topcoat*
SwRI	AH35C2BF	Coated	EFS Solution	20.3	1	-1	26788	310	Gage	*Primer+Topcoat*
SwRI	AH35C3F	Uncoated	EFS Solution	20.2	1	-1	6511	345	Gage	
SwRI	AH43C2BF	Coated	EFS Solution	19.7	5	0.5	1275000	276	Gage	*Primer+Topcoat*
SwRI	AH43C3F	Uncoated	Lab Air	20.1	3	-1	6294	345	Gage	
SwRI	AH43C3F	Uncoated	EFS Solution	20.1	3	-1	6294	345	Gage	
SwRI	AH4C1F	Uncoated	Lab Air	20.3			524540	276	Gage	*R-ratio &Frequency (?)*
SwRI	AH4C2AF	Coated	EFS Solution	20.3	5	-1	22200	276	Gage	*Primer+Topcoat*
SwRI	AH4C2BF	Coated	EFS Solution	20.1	5	0.05	172214	276	Gage	*Primer+Topcoat*
SwRI	AH4C3F	Uncoated	EFS Solution	20.3	1	-1	7178	345	Gage	
SwRI	AH4C3F	Uncoated	EFS Solution	20.3	1	-1	7178	345	Gage	
SwRI	AH502BF	Uncoated	EFS Solution	20.3	1	-1	6140	345	Gage	
SwRI	AH50C1F	Uncoated	EFS Solution	20.1	1	-1	29828	310	Gage	
SwRI	AH50C2AF	Coated	EFS Solution	20.1	5	-1	8725	345	Gage	
SwRI	AH58C2BF	Coated	EFS Solution	20.3	5	0.05	92918	276	Gage	*Primer*
SwRI	AH58C3F	Coated	EFS Solution	20.1	1	-1	11161	345	Gage	*Primer*
SwRI	AH65C1F	Uncoated	EFS Solution	20.3	1	-1	5836	345	Gage	*Primer*
SwRI	AH65C2AF	Uncoated	EFS Solution	20.3	1	-1	6706	345	Gage	
SwRI	AH65C2BF	Uncoated	EFS Solution	20.3	1	-1	8818	345	Gage	
SwRI	AJ12C1F	Uncoated	Lab Air	20.2	20	0.05	68791	310	Gage	

Table AA-4. *continued*

Lab	Spec Ident	Coating	Environ-ment	Specimen Area (mm^2)	Freq (Hz)	R-ratio	Cycles to Failure	Maximum Stress (MPa)	Failure Location	Miscellaneous Comments
SwRI	AJ12C2AF	Uncoated	EFS Solution	20.2	1	0.05	44819	276	Gage	
SwRI	AJ12C2BF	Uncoated	EFS Solution	20.2	1	0.05	409423	221	Gage	
SwRI	AJ12C3F	Uncoated	EFS Solution	20.3	10	0.05	348936	221	Gage	
SwRI	AJ19C1F	Uncoated	EFS Solution	20.2	1	0.05	310804	159	Gage	
SwRI	AJ19C2AF	Uncoated	EFS Solution	20.1	1	0.05	6725	345	Gage	
SwRI	AJ19C2BF	Uncoated	EFS Solution	20.2	1	0.05	50500	386	Gage	
SwRI	AJ19C3F	Uncoated	Lab Air	20.2	20	0.05	86410	276	Gage	
SwRI	AJ27C1F	Uncoated	EFS Solution	20.2	1	0.5	294491	276	Gage	
SwRI	AJ27C2AF	Uncoated	EFS Solution	20.4	1	-1	5433	345	Gage	
SwRI	AJ27C2BF	Uncoated	EFS Solution	20.2	1	-1	345877	159	Gage	
SwRI	AJ27C3F	Uncoated	EFS Solution	20.1	1	-1	4047	345	Gage	
SwRI	AJ35C2AF	Uncoated	EFS Solution	20.2	1	-1	5463	345	Gage	
SwRI	AJ35C2BF	Uncoated	EFS Solution	20.2	10	0.5	57076	345	Gage	
SwRI	AJ35C3F	Uncoated	EFS Solution	31.7	1	0.05	7814	448	Gage	
SwRI	AJ43C1FS	Uncoated	EFS Solution	20.1	1	-1	9819	345	Gage	
SwRI	AJ43C2FS	Uncoated	EFS Solution	19.9	1	-1	7319	345	Gage	
SwRI	AJ43C3FS	Uncoated	EFS Solution	19.2	10	-1	4172835	159	Gage	
SwRI	AJ4C1F	Uncoated	Lab Air	20.1	20	0.05	40509	310	Gage	Environment (?)
SwRI	AJ4C2AF	Uncoated	EFS Solution	20.2	20	0.05	196792	276	Gage	
SwRI	AJ4C2BF	Uncoated	EFS Solution	20.2	10	-1	72158	186	Gage	
SwRI	AJ4C3F	Uncoated	EFS Solution	20.2	10	-1	~2293490	138	Gage	Smax from 138 to 152 MPa
SwRI	AJ50C1FS	Uncoated	EFS Solution	19.2	1	-1	11375	345	Gage	
SwRI	AJ50C2FS	Uncoated	EFS Solution	19.9	1	-1	9836	345	Gage	
SwRI	AJ50C3FS	Uncoated	EFS Solution	19.7	5	-1	935505	159-221	Gage	Smax from 159 to 221 MPa

Table AA-5. Tabulation of the smooth specimen fatigue tests performed on the steel material at both Penn and SwRI.

Lab	Spec Ident	Coating	Environment	Specimen Area (mm^2)	Freq (Hz)	R-ratio	Cycles to Failure	Maximum Stress (MPa)	Failure Location	Miscellaneous Comments
Penn	4130-10	Uncoated	EFS Solution	24.3	0.5	-1	780800	600	Gage	*Small-Cell test*
Penn	4130-2	Uncoated	Gel	24.5	2.5	-1	187900	600	Gage	
Penn	4130-3	Uncoated	EFS Solution	24.4	1	-1	?102500	600	Gage	*Strain-control test*
Penn	4130-4	Uncoated	EFS Solution	24.5	1.5	-1	>10,900	600	Gage	*Search small-crack*
Penn	4130-5	Uncoated	EFS Solution	24.4	0.5	-1	24700	700	Gage	
Penn	4130-6	Uncoated	EFS Solution	24.4	0.5	-1	289000	600	Gage	*Strain control test*
Penn	4130-7	Uncoated	EFS Solution	24.4		-1	?143300	600	Gage	*Search small-crack*
Penn	4130-8	Uncoated	EFS Solution	23.6	3.5	-1	55700	600	stop	
Penn	4130-9	Uncoated	EFS Solution	24.4	0.5	-1	?59,200*	600	Gage	*Search small-crack*
Penn	J2-24-1	Uncoated	Lab Air	30.9	0.5	-1	99588	615	Gage	
Penn	J2-24-2	Uncoated	Lab Air	31.0	0.5	-1	25533	710	Gage	
Penn	J2-24-3	Uncoated	Lab Air	30.9	0.5	-1	10233	750	Gage	
Penn	J2-24-4	Uncoated	Lab Air	31.2	0.5	-1	547110	550	Gage	
Penn	J2-24-5	Uncoated	Lab Air	30.7	0.5	-1	124000	600	Gage	
Penn	J2-24-6	Uncoated	Lab Air	31.0	0.5	-1	26200	700	Gage	
Penn	J2-24-8	Uncoated	Lab Air	30.8	0.5	-1	314150	570	Gage	
Penn	S-1	Uncoated	EFS Solution	31.8	0.5	-1	205150	600	Gage	
Penn	S-12	Uncoated	Lab Air	31.8	0.5	-1	144481	600	Gage	
Penn	S-13	Uncoated	Lab Air	31.7	1	-1	>418566	560	Thread	
Penn	S-14	Uncoated	EFS Solution	31.8	0.5	-1	45000	600	Teflon	
Penn	S-15	Uncoated	Lab Air	31.8	8	-1	>275000	560	Thread	
Penn	S-16	Uncoated	EFS Solution	31.6	0.5	-1	780,000	600	Gage	*Search small-crack*
Penn	S-17	Uncoated	EFS Solution	31.8	0.5	-1	85300	600	Gage	*Ni/NiO electrode*
Penn	S-18	Uncoated	EFS/Lab Air	31.8	8	-1	152500	600	Gage	*82500 cyc @ .5 Hz in EFS soln*
Penn	S-19	Uncoated	EFS Solution	31.7	2	-1	216100	600	Gage	
Penn	S-2	Uncoated	EFS Solution	31.7	0.5	-1	?139300	600	Gage	*Strain-control test*
Penn	S-20	Uncoated	EFS Solution	31.6	0.5	-1	>157900	600	Gage	*Interrupt test*
Penn	S-21	Uncoated	EFS Solution	31.8	0.5	-1	136600	600	Gage	
Penn	S-22	Uncoated	Lab Air	31.7	0.5	-1	83333	650	Gage	
Penn	S-23	Uncoated	Lab Air	31.8	0.5	-1	101720	620	Gage	

Table AA-5. *continued*

Lab	Spec Ident	Coating	Environ-ment	Specimen Area (mm^2)	Freq (Hz)	R-ratio	Cycles to Failure	Maximum Stress (MPa)	Failure Location	Miscellaneous Comments
Penn	S-25	Uncoated	EFS Solution	31.8	0.5	-1	259800	600	Gage	
Penn	S-27	Uncoated	EFS Solution	31.8	0.5	-1	112800	600	Gage	
Penn	S-28	Uncoated	Lab Air	31.7	0.5	-1	>1690000	535	Thread	
Penn	S-3	Uncoated	Lab Air	31.8	0.5	-1	30700	650	Gage	
Penn	S-30	Uncoated	Lab Air	31.7	8	-1	11670000	520	Gage	
Penn	S-33	Uncoated	Lab Air	31.8	0.5	-1	353000	550	Gage	
Penn	S-35	Uncoated	EFS Solution	31.8	0.5	-1	341100	600	Gage	
Penn	S-36	Uncoated	EFS Solution	31.8	0.5	-1	77000	600	Gage	Ni/NiO electrode
Penn	S-38	Uncoated	Water	31.7	8	-1	48000	550	Gage	
Penn	S-39	Uncoated	EFS Solution	31.8	0.5	-1	262000	570	Gage	
Penn	S-390	Uncoated	EFS Solution	31.8	0.5	-1	262000	570	Gage	Current-control test
Penn	S-4	Uncoated	Lab Air	31.8	0.5	-1	37660	600	Gage	
Penn	S-4b	Uncoated	EFS Solution	31.8	0.5	-1	37660	600	Edge	
Penn	S-40a	Uncoated	EFS Solution	22.6	5	-1	116000	600	Gage	
Penn	S-41	Uncoated	EFS Solution	31.8	0.5	-1	>531800	550	Gage	plus more cycles
Penn	S-42	Uncoated	EFS Solution	31.9	0.5	-1	193800	600	Gage	
Penn	S-43	Uncoated	EFS Solution	31.6	0.5	-1	?143100	600	Gage	Strain-control test
Penn	S-44	Uncoated	Lab Air	31.5	8	-1	1673240	540	Gage	
Penn	S-46	Uncoated	Water	31.8	0.5	-1	?	600	Gage	
Penn	S-46c	Uncoated	EFS Solution	31.2	0.5	-1	>182800	600	Gage	Interrupt test
Penn	S-47	Uncoated	EFS Solution	31.8	0.5	-1	178500	?600	Gage	Variable-1 small peak @ 307 MPa
Penn	S-48	Uncoated	Water	31.7	0.5	-1	>27100	600	Gage	Test stopped
Penn	S-49	Uncoated	EFS Solution	31.6	0.5	-1	137700	600	Gage	Ni/NiO electrode
Penn	S-5	Uncoated	Lab Air	31.8	0.5	-1	13747	700	Gage	
Penn	S-50	Uncoated	EFS Solution	31.7	0.5	-1	209600	600	Gage	
Penn	S-52	Uncoated	Gel	31.8	0.5	-1	120200	600	Gage	
Penn	S-53	Uncoated	EFS Solution	31.8	0.5	-1	123400	600	Teflon	
Penn	S-54	Uncoated	Gel	31.8	0.5	-1	80600	600	Gage	
Penn	S-6	Uncoated	EFS Solution	31.7	0.5	-1	745200	?600	Gage	Variable-3 small peak @ 307 MPa 0.5-1 Hz
Penn	S-7	Uncoated	Lab Air	31.8	0.5	-1	>422500	535	Thread	

Table AA-5. *continued*

Lab	Spec Ident	Coating	Environment	Specimen Area (mm^2)	Freq (Hz)	R-ratio	Cycles to Failure	Maximum Stress (MPa)	Failure Location	Miscellaneous Comments
Penn	S-8	Uncoated	EFS Solution	31.8	0.5	-1	?183800	600	Gage	*Strain control test*
Penn	S-9	Uncoated	EFS Solution	31.7	0.5	-1	108900*	600	Gage	
Penn	ST210-50	Uncoated	EFS Solution	12.4	0.5		>85,600	600	Gage	*Square section,Search crack*
Penn	St210-52	Uncoated	Gel	24.6	5	-1	141200	600	Gage	
SwRI	SA112C1F	Uncoated	Lab Air	31.7	5	0.05	>3000000	758	Gage	*Runout*
SwRI	SA112C2F	Uncoated	Lab Air	31.8	10	0.05	78925	1034	Gage/Rad	
SwRI	SA112C3F	Uncoated	Lab Air	31.8	10	0.05	186505	896	Gage/Rad	
SwRI	SA112C4F	Uncoated	Lab Air	31.7	2	0.05	15163	1103	Gage/Rad	
SwRI	SA14C1F	Uncoated	Lab Air	31.8	5	0.05	>578197	862	Grip	
SwRI	SA14C2F	Uncoated	Lab Air	31.9	3	0.05	>3000000	620		*Runout*
SwRI	SA14C3F	Uncoated	Lab Air	31.9	15	0.05	>18700000	896		*Runout*
SwRI	SA14C4F	Uncoated	Lab Air	31.9	2	0.05	13009	1103	Gage/Rad	
SwRI	SB220C1F	Uncoated	EFS Solution	31.7	10	0.05	>784589	896	Grip	
SwRI	SB220C2F	Uncoated	Lab Air	31.8	1	-1	22833	724	Gage	
SwRI	SB220C3F	Uncoated	Lab Air	31.9	7.5	0.05	219580	965	Gage/Rad	
SwRI	SB220C4F	Uncoated	EFS Solution	31.9	1	0.05	45142	1034	Gage	
SwRI	SB228C1F	Uncoated	Lab Air	31.9	10	0.05	>235990	965	Grip	
SwRI	SB228C2F	Uncoated	Lab Air	31.8	10	0.05	31817	965	Gage/Rad	
SwRI	SB335C1F	Uncoated	Lab Air	31.8	10	0.05	143105	965	Gage/Rad	
SwRI	SB335C2F	Uncoated	Lab Air	31.7	10	0.05	49348	1034	Gage	
SwRI	SB343C1F	Uncoated	Lab Air	31.7	10	0.05	36331	1034	Gage	
SwRI	SB343C2F	Uncoated	Lab Air	31.8	10	0.05	313200	896	Gage/Rad	
SwRI	SB343C3F	Uncoated	EFS Solution	31.9	5	0.05	30286	1034	Gage	
SwRI	SC220C1F	Uncoated	EFS Solution	20.3	1	-1	7499	724	Gage	
SwRI	SC220C2F	Uncoated	EFS Solution	20.3	1	-1	116231	586	Gage	
SwRI	SC220C3F	Uncoated	Lab Air	20.3	1	0.05	396	1103	Gage	
SwRI	SC220C4F	Uncoated	EFS Solution	20.3	10	0.05	1088945	896-931	Gage	*Smax from 896 to 931 MPa*
SwRI	SC228C1F	Uncoated	EFS Solution	20.2	1	0.05	140211	951	Gage	
SwRI	SC228C2F	Uncoated	EFS Solution	20.3	1	-1	7092	758	Gage	
SwRI	SC228C3F	Uncoated	EFS Solution	20.3	10	0.05	109447	600	Gage	

Table AA-5. *continued*

Lab	Spec Ident	Coating	Environ- ment	Specimen Area (mm^2)	Freq (Hz)	R-ratio	Cycles to Failure	Maximum Stress (MPa)	Failure Location	Miscellaneous Comments
SwRI	SC228C4F	Uncoated	EFS Solution	20.3	10	0.5	2777500	1034-1069	Gage	Smax from 1034 to 1069 MPa
SwRI	SC451C1F	Uncoated	EFS Solution	20.3	5	0.05	540759	862-1000	Gage	Smax from 862 to 1000 MPa
SwRI	SC451C2F	Uncoated	EFS Solution	20.3	1	-1	104221	600	Gage	
SwRI	SC451C3F	Uncoated	EFS Solution	20.3	10	-1	2678424	552-620	Gage	Smax from 552 to 620 MPa
SwRI	SC451C4F	Uncoated	EFS Solution	20.3	1	-1	82017	607	Gage	
SwRI	SC459C1F	Uncoated	Lab Air	20.3	20	0.05	6496033	896-1000	Gage	Smax from 896 to 1000 MPa
SwRI	SC459C2F	Uncoated	Lab Air	20.3	2	0.05	2268	1103	Gage	
SwRI	SC459C3F	Uncoated	EFS Solution	20.3	1	-1	117464	600	Gage	
SwRI	SC459C4F	Uncoated	Lab Air	20.3	1	0.05	1105225	931-951	Gage	Smax from 931 to 951 MPa
SwRI	SD112C2F	Uncoated	EFS Solution	20.3	1	-1	2275	724	Gage	
SwRI	SD14C1F	Uncoated	EFS Solution	20.3	1	0.05	12065	724	Gage	
SwRI	SD14C2F	Uncoated	EFS Solution	31.7	1	-1	15828	724	Gage	
SwRI	SD14C3F	Uncoated	EFS Solution	20.3	1	0.05	123455	965	Gage	
SwRI	SD14C4F	Uncoated	EFS Solution	20.3	1	-1	13735	724	Gage	
SwRI	SE335C1F	Uncoated	EFS Solution	20.3	1	-1	27641	724	Gage	
SwRI	SE343C1F	Uncoated	EFS Solution	20.3	1	-1	14325	724	Gage	
SwRI	SE343C2F	Uncoated	EFS Solution	20.3	5	-1	>23000	724	Gage	Removed
SwRI	SE350C3F	Uncoated	EFS Solution	20.1	5	-1	>15000	724	Gage	Removed
SwRI	SI335C4F	Uncoated	EFS Solution	20.1	5	-1	93452	655	Gage	
SwRI	SI343C3F	Uncoated	EFS Solution	19.7	5	-1	23426	724	Gage	
SwRI	SM335C1F	Uncoated	EFS Solution	20.1	1	-1	21804	724	Gage	
SwRI	SM335C4F	Uncoated	EFS Solution	19.9	1	-1	20673	758	Gage	
SwRI	SM350C1F	Uncoated	EFS Solution	19.7	5	-1	130791	641	Gage	
SwRI	SM350C2F	Uncoated	EFS Solution	20.1	1	-1	20600	1034	Gage	
SwRI	SM350C3F	Uncoated	EFS Solution	20.3	1	-1	20600	689-1034	Gage	Smax from 689 to 1034 MPa
SwRI	SM350C4F	Uncoated	EFS Solution	20.0	1	-1	28741	724	Gage	

Table AA-6. Tabulation of the smooth specimen fatigue tests performed on the titanium material at both Penn and SwRI.

Lab	Spec Ident	Coating	Environment	Specimen Area (mm^2)	Freq (Hz)	R-ratio	Cycles to Failure	Maximum Stress (MPa)	Failure Location	Miscellaneous Comments
Penn	Ti-11	Uncoated	Gel	23.6	0.5	-1	>1395000	?579	Gage	*Variable-3 small peak @ 200 MPa*
Penn	Ti-12	Uncoated	Steel Solution	24.4	0.5	-1	31300	620	Gage	
Penn	Ti-14	Uncoated	Lab Air	23.5	10	-1	83760	560	Gage	
Penn	Ti-16	Uncoated	Lab Air	24.5	10	-1	135600	580	Gage	
Penn	Ti-18-1	Uncoated	Steel Solution	24.4	0.5 - 2	-1	1500000	580	Gage	*.5-2Hz*
Penn	Ti-19	Uncoated	Gel	24.5	2.5	-1	263000	580	Gage	
Penn	Ti-21	Uncoated	Steel Solution	24.5	0.5	-1	>176000	580	Thread	
Penn	Ti-22	Uncoated	Gel	24.6	0.5	-1	66600	580	Gage	
Penn	Ti-23	Uncoated	Gel	24.6	5	-1	172700	580	Gage	
Penn	Ti-4	Uncoated	Lab Air	24.4	10 - 20	-1	1514000	500	Gage	*10-20 Hz*
Penn	Ti-7	Uncoated	Lab Air	24.4	0.5	-1	6390	750	Gage	
Penn	Ti-9	Uncoated	Lab Air	24.4	10	-1	23420	620	Gage	
SwRI	TA11CF	Uncoated	Lab Air	31.9	1	0.05	5015	896	Gage	
SwRI	TA19CF	Uncoated	Lab Air	31.7	20	0.05	>880534	793	Grip	
SwRI	TA4CF	Uncoated	Lab Air	31.7	5	0.05	22641	827	Gage/Rad	
SwRI	TE11CF	Uncoated	Lab Air	31.9	10	0.05	48580	827	Gage/Rad	
SwRI	TE19CF	Uncoated	Lab Air	31.7	1	0.05	6168	896	Gage	
SwRI	TE26CF	Uncoated	Lab Air	31.7	5	0.05	12800	862	Gage	
SwRI	TE34CF	Uncoated	Lab Air	31.7	10	0.05	39419	827	Gage/Rad	
SwRI	TE41CF	Uncoated	Lab Air	31.7	1	0.05	6076	896	Gage	
SwRI	TE4CF	Uncoated	Lab Air	31.8	20	0.05	>4689941	689	Grip	
SwRI	TH19CF	Uncoated	EFS Solution	31.8	1	-1	5936	876	Gage	
SwRI	TO11CF	Uncoated	EFS Solution	31.7	1	-1	52040	586	Gage	
SwRI	TO26CF	Uncoated	EFS Solution	31.7	1	-1	47464	586	Gage	
SwRI	TO41CF	Uncoated	EFS Solution	31.7	1	-1	18683	655	Gage	
SwRI	TO4CF	Uncoated	EFS Solution	31.7	1	-1	13644	655	Gage	
SwRI	TT19CF	Uncoated	Lab Air	20.2	10	0.05	>3500000	689	Gage	*Runout*
SwRI	TU11CF	Uncoated	Lab Air	20.3	10	0.05	64061	758	Gage	
SwRI	TU19CF	Uncoated	Lab Air	20.3	10	0.05	56139	738	Gage	
SwRI	TU26CF	Uncoated	Lab Air	20.2	10	0.05	39601	717	Gage	

Table AA-6. *continued*

Lab	Spec Ident	Coating	Environment	Specimen Area (mm^2)	Freq (Hz)	R-ratio	Cycles to Failure	Maximum Stress (MPa)	Failure Location	Miscellaneous Comments
SwRI	TU34CF	Uncoated	Lab Air	20.3	10	0.05	>3360000	717	Gage	*Runout*
SwRI	TU41CF	Uncoated	Lab Air	20.3	10	0.05	>3000000	717	Gage	*Runout*
SwRI	TU4CF	Uncoated	Lab Air	20.3	10	0.05	28898	793	Gage	
SwRI	TV11CF	Uncoated	EFS Solution	20.3	1	0.05	46900	565	Gage	
SwRI	TV19CF	Uncoated	EFS Solution	20.3	1	-1	11888	655	Gauge	
SwRI	TV4CF	Uncoated	EFS Solution	20.3	10	0.05	69404	738	Gage	
SwRI	TW19CF	Uncoated	EFS Solution	20.3	5	-1	17843	655	Gauge	
SwRI	TW34CF	Uncoated	EFS Solution	20.2	5	-1	30114	586	Gauge	
SwRI	TW41CF	Uncoated	EFS Solution	20.2	1	-1	14847	655	Gage	
SwRI	TX11CF	Uncoated	EFS Solution	20.3	10	-1	43453	586	Gage	
SwRI	TX19CF	Uncoated	EFS Solution	20.3	10	0.5	24481	896	Gage	
SwRI	TX26CF	Uncoated	EFS Solution	20.2	10	0.5	148079	841	Gage	
SwRI	TX34CF	Uncoated	EFS Solution	20.2	10	0.05	1700000	717-758	Gage	*Smax from 717 to 758 MPa*
SwRI	TX41CF	Uncoated	EFS Solution	20.2	10	0.05	7500000	676-772	Gage	*Smax from 676 to 772 MPa*
SwRI	TX4CF	Uncoated	EFS Solution	20.3	10	0.05	32758	717	Gage	

APPENDIX BB

STATISTICAL ASPECTS IN COMPARING THE FATIGUE LIVES OF T-38 METALS CYCLED IN DIFFERENT ENVIRONMENTS

STATISTICAL ASPECTS IN COMPARING THE FATIGUE LIVES OF T-38 METALS CYCLED IN DIFFERENT ENVIRONMENTS

Introduction.

One issue concerning the application of the EFS is whether or not exposure to the EFS electrolyte produces an adverse environmental effect on the life of the specimen/structure. For this reason, careful comparisons have been made of the lives of specimens fatigued in laboratory air, electrolyte continuously or intermittently applied, or in water. Fatiguing in water usually produces such a strong effect that there can be little equivocation concerning a corrosion fatigue effect. Fortunately, the electrolytes chosen for EFS testing have been so benign that it is difficult to determine whether or not there is an environmental effect. Only in 7075 aluminum at the longest lives explored here has a possible adverse effect been observed, and that has been explained by contamination from the reference electrode. The purpose of this appendix is to inquire whether we can prove under project budget constraints that the EFS electrolyte causes no environmental effect.

The Statistical Problem

When a number of fatigue specimens is cycled to failure, under as similar as possible conditions of stress, frequency, surface preparation and all the other factors that affect fatigue behavior, a distribution of lives is observed - the familiar phenomenon of fatigue scatter. Likewise, the application of different environments, with or without intervention with the EFS, will give different populations of fatigue lives. If only a few specimens are used to gather the data, it may not be possible to determine whether or not the populations are different because of fatigue scatter. It is a general rule of statistics that the scatter in the results increases as the square root of the number of specimens used to obtain the results, but no one knows whether or not this is also true of fatigue, even for tests conducted at a single constant stress or strain amplitude.

If an S/N curve is obtained by using many specimens, including duplicate tests at different stress levels, random scatter at each level tends to be mutually correcting. The fatigue behavior can then be described by scatter bands drawn to embrace the results. An investigator

may choose to perform a regression analysis or to draw a best fit line to the results to describe the S/N behavior, but no tool is available to provide an estimate of the accuracy of the S/N curve.

Definition of the fatigue life is difficult in the regime of finite life. Most engineering structures are intended to be used at levels either at the transition from finite life to infinite life or at significantly lower levels to account for factors of ignorance or "safety". The rise of the field of fracture mechanics was produced in part as a response to this deterministic problem. Determining an effect of environment in these regimes becomes even more difficult because the life distribution will include specimens with lives that extend beyond the regime of practical testing periods. In the following we address the question as to whether the results obtained here in comparing fatigue behavior during exposure to the EFS or to other environments can be discriminated with a high measure of confidence in the case where the environmental effect appears to be small.

Population Comparison - Theoretical Considerations

Suppose that we are interested in comparing fatigue behavior in air against that in EFS electrolyte and further suppose that we are comparing behavior at a stress level where we expect a probability of fracture of 10%. It the differences in population are small and the uncertainty of discriminating them is large (the hoped-for result), it is appropriate to choose a stress or strain level with a small probability of fracture. In theory one could test many specimens to establish the population distributions for the conditions being compared and use the statistical tool of the binomial distribution to make a judgment concerning the results. The binomial distribution is not regarded as optimum for present purposes but is sufficient for the numbers considered here. If we were able to sample many specimens out of the respective populations, we would discover that the possible practical probabilities will depend on the size of the sample and will appear as shown in Table 1 for a 95% confidence level.

Consider that we might choose to break 20 specimens each for air and for the EFS, at a stress level where the expected probability of fracture is 10%. According to Table 1, we would expect between 0 and 6 fractures, the remainder being run-outs. If for example five specimens broke in air and three in EFS electrolyte, then their distributions might belong to a single population and there is no basis for distinguishing them. However, their populations could well be different. Let us then suppose that one of the conditions has a theoretical probability of

fracture of p% rather than 10% at the stress level chosen for making the comparison. Table 2 provides information about how the ranges of probability and ranges of broken specimen numbers depend on p, for a sample size of 20 specimens. Table 2 shows that the possibly different probabilities of fracture cannot be distinguished over wide ranges. For example, if 6 specimens were to break, they could apply to populations from p = 10% to p = 50%. Probability differences from 10% to 60% could be distinguished, however, because the range of broken specimens at p = 60% is 7 - 16. It would require a stroke of luck to make discriminations between lesser probability differences. For example, if 15 specimens were to break at p = 50%, or 11 were to break at p = 30%, then one could make a discrimination versus a population for which p = 10%. Of course, it is difficult to justify a new technology on the basis of luck. It is necessary to recall that even a sample size of 20 is well beyond the time and budget resources of most fatigue investigations, including the present one. The discrimination problem becomes even more difficult at smaller sample sizes.

Is there a solution to this difficulty? For example, is anything to be gained by attempting a discrimination at higher stress, where the expected probability of fracture is 50%, say? Table 3 shows the practical probabilities and their dependence on sample size for such a probability at the 95% confidence level. Examination of the figures in Table 3 shows that the discrimination problem becomes even more difficult for this situation, because the range of fractured specimen numbers increases. This is one reason why the different distributions of rather similar fatigue results appear even more similar at high stress levels in the finite life region. In actual practice, the interesting probabilities of fracture are those close to 0%

Conclusion.

At various stages of the present investigation, comparisons have been made between the fatigue properties of the various metals, and judgment have been offered. Since the results in air and in EFS electrolyte are so similar, claims of differences, if any, have been made tentatively. It is indeed encouraging that the results are so similar that discriminating them is a difficult problem. Even in that case, that of aluminum alloy at the lowest stresses and longest lives investigated (Figure 3.12), where "engineering judgment" might propose that specimens exposed to the EFS continuously have shorter lives than those broken in air, it is uncertain that the populations are different. For the still lower stresses that will apply in service, it would take

at least 70 specimens for each condition, i.e., tests in air versus tests in EFS electrolyte, to unambiguously distinguish two different populations with 10% and 30% theoretical probability of fracture. Experimentation at this level of effort is beyond the means of the program. A more economical approach is to employ the fracture mechanics tests reported in Chapter 3 in which the EFS electrolyte is shown to be quite benign. Moreover, in most of the comparisons made, the specimen has been exposed to the electrolyte throughout life. The EFS will be rarely employed in such a fashion. Periodic testing is a much more likely application of the EFS. It seems conservative to conclude that no significant adverse environmental effect need be anticipated in the application of the EFS, especially if current clean-up procedures (1) are used after testing to remove electrolyte residues.

Reference

1)   TECH. MANUAL NAVAIR 01 - 1A - 509 T.O. 1-1-691 TMi-1500-344-23, 1 January 1992 (Section 9-7.1)

APPENDIX CC

COMPARISON OF METHODS FOR
NONDESTRUCTIVE INSPECTION AND EVALUATION

FOR DURABILITY SIZE FATIGUE DAMAGE

INCLUDING THE TENSIODYNE
ELECTRO CHEMICAL FATIGUE SENSOR

CURRENTLY UNDER DEVELOPMENT

PREPARED FOR
TENSIODYNE SCIENTIFIC CORPORATION

BY

KAREN I. MILLER

NATIONAL HYDROGEN ASSOCIATION
1800 M STREET NW   SUITE 300 NORTH
WASHINGTON D.C.   20036

JANUARY 1998

EFS ECONOMIC ASSESSMENT - FINAL REPORT

1.0 SCOPE

1.1 Purpose. The purpose of this task is to provide economic data of the Electrochemical Fatigue Sensor (EFS) in comparison to existing methods of aging aircraft inspection, in support of Contract # F41608-96-D-0108-0010. The purpose of this overall program is to acquire services to improve the United States Air Force's (USAF) capability to perform durability assessments of military aircraft, including both airframes and engines, through the application of the EFS to specific military aircraft alloys. –

This task provides assistance for gathering economic data for the EFS compared to existing methods of aging aircraft inspection, as described in the matrix provided.

1.2   Application. In order to determine the degree of cost savings to the USAF, an economic comparison of the EFS with existing methods of aging aircraft inspection is necessary, as described in the matrix provided. NDE methods to be used for comparison include acoustic emission, various X-ray techniques, advanced electromagnetics, visual inspection techniques, advanced ultrasonics, and dye penetrant, where applicable.

2.0   DELIVERABLES

This report completes the requirement for the deliverable under contract to deliver assistance in obtaining economic data in order to facilitate a comparison of certain aspects of this evaluation with existing methods of aging aircraft inspection.

2.1   Methodology. In order to fill out the matrix provided, the contractor researched a variety of nondestructive evaluation (NDE) equipment. This was accomplished through research in books and journals published by the American Society for Nondestructive Testing (ASNT), attendance at the ASNT 1997 Fall Conference and Quality Testing Show, as well as numerous discussions in person and by telephone with individuals who use, manufacture, or distribute NDE equipment.

2.2   Cost Analysis. Costs of testing are made up of several factors, including labor costs, costs of test materials (supplies), operating costs, and fixed costs. These costs vary by several hundred percent for any NDE test, depending on factors such as quantity and frequency of testing, parts handling, automation, sensitivity, tolerance, accuracy, and the caliber of the test personnel required.

The optimum interval between nondestructive tests for damage in-service varies with the conditions of service and with the types of discontinuities. This period should be short enough so that discontinuities not detected at the preceding inspection do not have time to propagate to failure between inspections. In the case of aircraft, there are natural locations or periods of time at which inspection can be made most economically.

The use of an inspection method which provides the earliest warning of potential fatigue damage can allow for the most economical scheduling for repair.

2.3   Results. The Attached EFS Comparison Matrix evaluates cost factors and inspection attributes for a variety of NDE equipment, as defined in the Statement of Work (SOW). I added columns to clarify information which is pertinent to this investigation but not previously depicted in the matrix provided with the SOW. An explanation of the data columns is as follows:

Equipment: The type of NDE equipment evaluated
Capital Equipment: The cost to purchase the capital equipment required for the
        NDE method.
Cost of Probes: Actual probe, or EFS cell, or acoustic emission microphone, etc.
Cost of Expendables: Supplies which are not reused, such as penetrant,
        developer, film, etc.
Labor Time/Level: The relative amount of time and average caliber of the test
        personnel required.
Labor Costs: As defined in original tasking.
Producibility: Indication of the ease to produce this equipment. LAB indicates
        this equipment can exist only in a specialized laboratory. OTS indicates
        the equipment is produced and available off-the-shelf.
Availability: Indication of the degree of availability.
Defects Detected: Types of indications which this equipment is primarily
        designed to detect.
Comments: Notes on particular advantages or disadvantages of the equipment.

Particular factors considered advantageous for the purpose of cost comparison include equipment costs, the reduction of aircraft downtime, and ease of inspection with respect to personnel. For most of the equipment analyzed, the capital equipment costs varied significantly for the same equipment in direct correlation to the ease of use. Many NDE equipment vendors were on hand at the 1997 ASNT Fall Conference and Quality Testing Show to demonstrate a variety of packaging systems which helped to analyze or interpret basic output from NDE data. See attached listing of exhibitors. These packaging systems produce a variety of options for the user, however, they render a straightforward cost comparison rather difficult. For example, in the case of electromagnetic techniques or ultrasonics, a customer can purchase the basic equipment which produces a blip on a CRT screen, which must be calibrated and interpreted by a higher caliber inspector. As an alternative, a variety of packages are available which convert that blip to a graphical mapping display which can indicate areas of variance in a preferred color scheme for easier identification and interpretation, allowing inspections to be performed by a lower caliber inspector. Therefore, the equipment cost should be considered with respect to the labor considerations when evaluating NDE equipment costs. With regard to the EFS, the capital equipment costs are estimated assuming a fully commercialized product.

Aircraft downtime can be reduced by faster inspection techniques, reduction of ancillary requirements such as aircraft coating removal (which also reduces pollution prevention costs), or lengthened intervals between aircraft inspections. The EFS has the potential to more accurately determine the optimum interval between inspections.

Through this analysis, the contractor determined that the EFS, when fully developed, will fill an need in the NDE market by detecting fatigue life damage, improving fatigue life predictions needed to avoid possible catastrophic failure, and aiding in cost effective inspection, maintenance and repair.

3.0   SUMMARY

The different types of NDE equipment are designed to meet a variety of unique objectives. Mechanical-optical techniques can help determine color, crack, dimensions, film thickness, gaging, reflectivity, strain distribution and magnitude, surface finish, surface flaws, and through-cracks. Penetrating radiation methods help determine in-plane bond separation, cracks, density and chemistry variations, elemental distribution, foreign objects, inclusions, microporosity, misalignment, missing parts, segregation, service degradation, shrinkage, thickness, and voids. Ultrasonics are used to determine crack size, debonds, grain size, thickness, misalignment, and mechanical properties. There are few types of NDE equipment which can detect fatigue life damage, with no baseline (pre-fatigued) data required.

The EFS will allow the user to measure fatigue damage before the creation of cracks large enough to be reliably detected by NDE methods presently employed. Properly calibrated, such a technology will provide earlier warning and assure the ability to schedule economical repairs before the damage is large enough to require elaborate structural rebuilding. This also reduces the chance of catastrophic failure.

Economic Assessment

Subphase 10

<u>Aim</u>:   Scope usage lab application of EFS versus other technologies.

<u>Focus</u>
1.   Producibility - availability and producibility of materials and devices.

2.   Affordability - cost of materials, labor, capital equipment, and expendables.

<u>Approach</u>
Characterization of USAF components
Lab simulation
Cost of materials
Feasibility

<u>Discussion</u>
Should not your economics assessment involve a cost benefit analysis?

What do you get for your money?

The nice thing about the EFS is you get something whether or not you have a crack.

<u>Matrix</u>

	Capital Equipment	Cost of Probes (3)	Cost of Expendables	Labor Costs (5) , (1)		Producibility	Availability
EFS	8k to 15k	Few 100$	Cheap	a) m, c, c	b) 1c	No problem	No problem (6)
Acoustic Emission	(7) 30-40 k	Few 100's	Cheap	a) m, c, c	b) 1c	Exists	Available
X-ray (2) Computed Tomography	Vast	Part of Capital Equipment	High Energy & Building Maintenance	a) ?	b) 2h	Exists	Limited Access
Compton (2) X-ray Bach Scatter	Vast	Part of Capital Equipment	High Energy & Building Maintenance	a) ?	b) 2h	Exists	Limited Access
Reverse (2) Geom. X-rays	Vast	Part of Capital Equipment	High Energy & Building Maintenance	a) ?	b) 2h	Exists	Limited Access
Advanced Electro-magnetics	10 – 21k	Part of Capital Equipment	Cheap	a) m, m, m	b) 1h	Exists	No problem
Coherent Optics	Vast	Part of Capital Equipment	Cheap	a) m, m, m	b) 1h	Exists	No problem
Advanced							

				a) m, m, c b) 1h	Exists	No problem
Visual Inspection	Cheap	Cheap	0	a) m, m, c b) 1h	Exists	No problem
Infrared Tomography	High (4)	Part of Capital Equipment	Cheap	a) ? b) 1h	Exists	Limited Access
Advanced Ultrasonics	High (4)	Cheap	Cheap	a) m, m, m b) 1m	Exists	Regular Ultrasonics Available & Cheap
Dye Penetrant	– 0	$50.00	0	a) m, m, c b) 1c	Exists	Available

Notes

1. These costs involve two aspects:
   a. Having labor actually perform the tests.
   b. Getting the equipment / aircraft to the testing or vice versa.
2. Not really a lab device, consists of labs in themselves for macro pieces of equipment, such as aircraft.
3. By "probe", I mean the EFS cell or the acoustic emission microphone, etc.
4. By "high", I mean I am not sure because it depends on how fancy the computerization.
5. Labor cost involve:
   a. setting up
   b. recording measurements
   c. analyzing data
   Under (a) (see Note 1) we have these categories.
   Under (b), we have two categories:
   1. The equipment is mobile and goes to the part, so is included in setting up.
   2. We have to fly the A/c to the lab (as in Sacramento).
   For example, for the EFS, setting up would be time consuming, recording would be automatic and analyzing data would be computerized.
   We have three categories: h (high), m (moderate), and c (cheap). For EFS, setting up is moderate, the other two are cheap.
6. Capital equipment costs for EFS are low. All we need, for a lab project, is a potentiostat, not a very fancy one, and a computer for recording data assuming we already have a machine for fatiguing the specimen. Gamry's potentiostats, which seem quite suitable, could be purchased for less than 10k, and a satisfactory computer might be 2.5k. Cells are very cheap and easy to machine in local jobbing shops. The same equipment could be used in the field if 110 volts are available. A chip to do the job in an isolated, independent EFS, would be cheap but the tooling costs to make the first one would run from 30 – 50k.
7. This was the cost of our lab acoustic emission apparatus, which is a good one.

Monolithic Structures Comparison Matrix

Equipment	Capital Equipment	Cost of Probes (3)	Cost of Expendables	Labor Time/Level	Labor Costs ($), (l)	Producibility	Availability	Defects Detected/ (Crack Sizes)*	Comments
EFS	$8-15 K	low	low	low/med	a) m,c,c b) 1c	good	in development	fatigue damage, crack initiation & propagation (precrack conditions)	lengthens intervals between inspections
Acoustic Emission	$30-40 K	low	low	high/high	a) m,c,c b) 1c	OTS	OTS/custom	fatigue damage, crack initiation & propagation (precrack conditions)	
X-ray (2) Computed Tomography	$1-2.5 M	included	can be very high	low/high	a) ? b) 2h	LAB	limited	bond separation, cracks, voids, foreign objects, misalignment (0.025 - 0.050")	OSHA regs, source, storage, size limitations, access to 2 sides, energy, maintenance
Compton (2) X-ray backscatter	varies	included	can be very high	low/high	a) ? b) 2h	LAB	limited	bond separation, cracks, voids, foreign objects, misalignment (0.025 - 0.050")	OSHA regs, source, storage, coating removal not necessary, energy, maintenance
Reverse (2) Geom. X-rays	varies	included	can be very high	low/high	a) ? b) 2h	LAB	limited	bond separation, cracks, voids, foreign objects, misalignment (0.025 - 0.050")	OSHA regs, source, storage, energy, maintenance
Advanced Electromagnetics	$10-250K	included	low	high/high	a) m,m,m b) 1h	OTS	OTS	local strain, hardness, composition, cracks, corrosion, voids, matls.ID (<0.010")	coating removal not necessary

Advanced Visual Inspection	$25-100 K	low	low	low/med	a) m,m,? b) 1h	OTS	OTS	surface flaws, through-cracks (0.025 - 0.050")	
Advanced Ultrasonics	$50-250 K	low	low	high/high	a) m,m,m b) 1m	OTS	OTS	fatigue damage, crack initiation & propagation (<0.010")	
Laser Ultrasonic Inspection System (L.U.I.S.)	$1-3 M	included	included in labor rate	high/high	$95/hr labor rate	LAB	limited	fatigue damage, crack initiation & propagation (precrack conditions)	parts must be removed from aircraft, size limitations
Dye Penetrant	$0	NA	very low	high/low	a) m,m,c b) 1c	Excellent OTS	OTS	cracks, porosity (0.010-0.025")	must have clean, depainted structure flaws must be open to surface

* defects detected and the size of a crack which can be detected are dependent on many factors, including material composition, material thickness, transducers/probes/film used, skill of the operator/interpreter, depth of the flaw, etc. For the purpose of this analysis, manufacturers and users of the equipment types listed were polled, and asked, for aluminum aircraft skins, under optimum conditions, which of the following sizes is the typically the smallest crack which the equipment can accurately detect: precrack conditions, <0.010", 0.010 - 0.025", 0.025 - 0.050", or >0.050". If the equipment could only find cracks >0.050", that equipment was removed from the matrix as not being competitive.

APPENDIX DD

COST BENEFIT ANALYSIS

STRUCTURAL EVALUATION FOR
DURABILITY SIZE FATIGUE DAMAGE

IN FATIGUE CRITICAL LOCATIONS OF THE
T-38 AIRCRAFT INNER WING LOWER SURFACE

USING THE TENSIODYNE
ELECTRO CHEMICAL FATIGUE SENSOR

CURRENTLY UNDER DEVELOPMENT

PREPARED FOR
TENSIODYNE SCIENTIFIC CORPORATION

BY

LAURENT J. J. LEGAULT
1311 TALON RIDGE COURT
DAYTON OH 45440

APRIL 1998

COST BENEFIT ANALYSIS FOR T-38A STRUCTURAL TESTING

Background: The current non-destructive testing methods are limited since they only indicate whether a structural flaw has reached a critical point where replacement is eminent. These methods give no indication of how much stress the structure has endured or if the problem will continue to grow after the aircraft has been returned to service. The newer Electrochemical Fatigue Sensor provides the capability to determine when a structure has reached its limit and also how much stress the component has already endured. The EFS can provide a real time indication of the remaining life of a structure or component.

Objective: The objective of this CBA is to compare the costs of current NDI (nondestructive inspection) testing procedures with the more reliable EFS testing approach.

Ground Rules: This analysis included only those aircraft operating in the roles identified as SUPT, IFF and ENJJPT. A simple basing scheme was considered, i.e., the total number of aircraft were equally distributed over the required number of bases. The life cycle cost (LCC) span is five years. Current Air Force base labor cost of $31.93/hour was used to compute labor costs. This analysis did not attempt to show the cost effect of reduced downtime, improved safety margins or enhanced testing integrity.

Approach: The first step in the analysis approach was to determine the type data required to estimate the costs of both testing methods. In the case of the existing NDI testing procedure, the data primarily consisted of labor cost to perform the test procedures since all significant investment cost has already been expended. The only exception was the recurring cost of replacement Eddy Current probes. Investment costs, including program management and initial training, and labor costs were included for the EFS system. EFS installation was considered to take place at base level and extend over a period of two years.

Data Collection: For this analysis, data were available for aircraft systems operating in three major roles: Student Undergraduate Pilot Training (SUPT), Introduction to Flying Fundamentals (IFF), and Euro NATO Joint Pilot Training (ENJJPT). Technical Order (T.O.) 1T-38A-6 (Nondestructive Inspection Manual) was used to determine the number of -29 Wing fastener holes in the inspection areas and the number of flight hours required before initial and recurring inspections were necessitated; the initial and recurring hours extracted from this T.O. are those shown in the ENJJPT data table in Appendix C. T.O. 1T-38A-36 (NDI Procedures) was reviewed to obtain a better understanding of Nondestructive Inspection step-by-step procedures for performing Rotoscan inspections and Eddy Current fastener hole inspections. Work Cards were reviewed to determine the frequency of recurring inspections. Data were also obtained through responses to two questionnaires developed to obtain input for the Life Cycle Cost

Model used for this analysis. The data were further broken out for six failure critical location (FCL) inspection zone areas (a color illustration of inspection zones Area 1 through Area 6 is presented in Appendix A) by aircraft major role.

For modeling purposes, the major roles were each modeled as individual systems while the FCL zone areas were treated as subsystems. Cost reports were generated for each system for both the NDI and EFS methods. Data were obtained from responses to two separately developed questionnaires. One questionnaire was sent to Headquarters AETC, NDI Directorate, for distribution to Training Bases performing NDI testing on T-38A aircraft performing the type of training for the three major roles being modeled. The second questionnaire was sent to individuals developing the EFS. Copies of the EFS and NDI questionnaires are located at Appendix B. Responses to the questionnaires were tabulated and the tables generated from the questionnaires, T.O. 1T-38A-6, and Southwest Research Institute DADTA analysis are located at Appendix C.

Data Type:

Aircraft Type: T-38A	Current	EFS
Test Sensors/AC	N/A	20
Acquisition Cost/Sensor	N/A	$50
Installation Kit Cost/AC	N/A	$10
Installation Time/AC	N/A	1 Hr
Sensor Remove/Replace/Failure	N/A	2.5 Hrs
Ancillary Equip		
Multiplex Recorder/Site	N/A	1
Cost/Recorder	N/A	$5000
Recorder Life (yrs)	N/A	10
AC Qty		
SUPT	300	300
IFF	88	88
ENJJPT	94	94
Annual Flying Hours/Acft		
SUPT	348	348
IFF	312	312
ENJJPT	420	420
Number Holes Inspected/Yr		
SUPT	30900	30900
IFF	50072	50072
ENJJPT	9588	9588
Number of Annual Recurring Inspections/FCL Zone Area		
SUPT		
FCL Area 1	30	32
FCL Area 2	10	17

FCL Area 3	39	22
FCL Area 4	8	10
FCL Area 5	10	6
FCL Area 6	6	15

IFF

FCL Area 1	165	32
FCL Area 2	65	17
FCL Area 3	232	22
FCL Area 4	40	10
FCL Area 5	56	6
FCL Area 6	11	15

ENJJPT

FCL Area 1	32	32
FCL Area 2	17	17
FCL Area 3	22	22
FCL Area 4	10	10
FCL Area 5	6	6
FCL Area 6	15	15

Hours per Annual Recurring Inspection/FCL Zone Area (Best Case/Worse Case)

SUPT

FCL Area 1	2490/4980	420
FCL Area 2	790/1580	238
FCL Area 3	3354/6708	308
FCL Area 4	368/736	120
FCL Area 5	560/1120	84
FCL Area 6	53/105	180

IFF

FCL Area 1	13118/26235	420
FCL Area 2	5135/10270	238
FCL Area 3	19953/39905	308
FCL Area 4	1840/3680	120
FCL Area 5	3136/6272	84
FCL Area 6	96/193	180

ENJJPT

FCL Area 1	2656/5312	420
FCL Area 2	1343/2686	238
FCL Area 3	1892/3784	308
FCL Area 4	460/920	120
FCL Area 5	336/672	84
FCL Area 6	131/262	180

Estimating Methodology

The cost benefit analysis (CBA) was performed with the Joint Operating and Support Technology Evaluation (JOSTE) Life Cycle Cost (LCC) Model. JOSTE was developed to estimate advanced technologies for the Joint Strike Fighter (JSF). The Model was obtained from the LCC office of the Aeronautical Systems Center, (ASC/ SYA), Wright Patterson AFB, OH. The JOSTE model is used extensively for cost benefit analyses involving modifications of Air Force and Navy aircraft comparing new technologies. JOSTE is an accounting model which covers acquisition, deployment and operating costs at the system, subsystem and component levels. The JOSTE reports can be found at Appendix D.

STUDY RESULTS

T-38A CBA
for
Current and Enhanced Testing Methods
(5 Years)

Cost Item	NDI (Worst Case)	NDI (Best Case)	EFS
SUPT			
Acquisition	0	0	$ 375,900
O&S	$ 2,324,089	$1,162,045	$ 220,083
IFF			
Acquisition	0	0	$ 110,600
O&S	$14,009,432	$7,004,716	$ 220,071
ENJJPT			
Acquisition	0	0	$ 119,050
O&S	$ 2,177,721	$1,088,860	$ 218,454
Installation	0	0	$ 15,395
Multiplex Recorder ($5000 ea)	0	0	$ 15,000
Probes (95/yr @ $125 ea)	$ 59,375	$ 59,375	0
TOTAL	$18,570,617	$9,314,996	$1,294,553
Maintenance Labor Hours	579,563	289,782	14,465

APPENDIX A

T.O 1T-38A-6 INSPECTION AREAS

T.O.1T-38A-6 Fastener Hole Inspection Zones

Area 1
Area 2
Area 3
Area 4
Area 5
Area 6
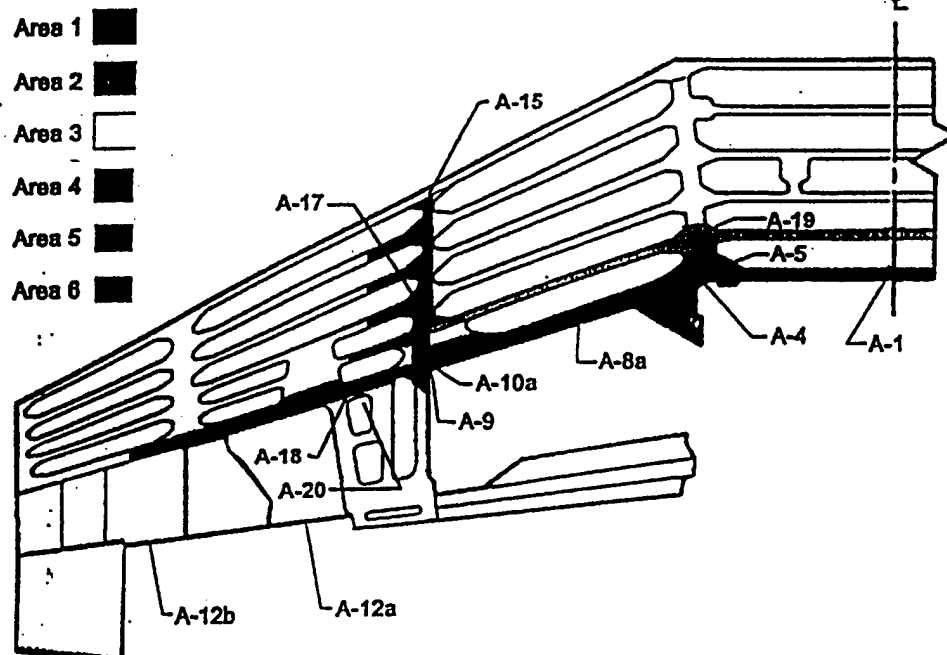
NOTE: A-1, A-2, etc., are Fatigue Critical Locations

T.O. 1T-38A-6 INSPECTION AREAS

APPENDIX B

QUESTIONNAIRES

Laurent J.J. Legault
c/o Research & Technology Resources, Ltd.
4141 Col Glenn Hwy., Suite 180
Beavercreek, OH 45431

February 27, 1998

Dr.

Dear Sir:

I am working for Matech on the project to replace T-38A aircraft nondestructive inspection (NDI) with the Electrochemical Fatigue Sensor (EFS). The EFS provides an advanced capability that indicates when a structure has reached its operational limits. The purpose of my task is to develop a cost benefit analysis. This analysis requires me to obtain cost relevant data pertaining to the EFS for compilation and input to a life cycle cost model to project costs over a five year timeframe. To derive a life cycle cost (LCC) model estimate of the EFS certain economic analysis input data are required. The questions below are designed to generate this modeling data.

In order for me to meet program deadlines, I would appreciate it if you would please provide answers to the following questions as soon as possible, but not later than one week from the date you receive this request.

1. How many EFS are going to be placed in Fatigue Critical Location (FCL) zone area one of the wing?
2. How many EFS are going to be placed in Fatigue Critical Location (FCL) zone area two of the wing?
3. How many EFS are going to be placed in Fatigue Critical Location (FCL) zone area three of the wing?
4. How many EFS are going to be placed in Fatigue Critical Location (FCL) zone area four of the wing?
5. How many EFS are going to be placed in Fatigue Critical Location (FCL) zone area five of the wing?
6. How many EFS are going to be placed in Fatigue Critical Location (FCL) zone area six of the wing?
7. What is the cost of each EFS?
8. What is the expected life of an EFS in years?
9. What is the expected labor cost to install each EFS?
10. What equipment is required to install the EFS?
11. What material (s) is (are) required for EFS installation?
12. How long does installation take (in minutes or hours)?
13. When the EFS fails, how long does it take to remove and replace it?
14. Does an access panel require opening or removal before an EFS can be installed, removed, or have information downloaded?
15. If the answer to question 9 is yes—how much time is required to open panel? How much time is required to remove a panel, if this is necessary? If the answer to question 9 is no skip this question and go on to question 11.
16. What are the estimated costs for training personnel to intall and remove EFS?
17. What is the repair concept for the EFS (i.e., remove/replace and discard, remove/replace and repair, etc.)?
18. If the EFS is to be repaired what repair parts and spares are required?
19. What is the cost of each repair part/spare?
20. What support or test equipment is required to test each EFS to ensure operability prior to installation on the aircraft?
21. What kind of downloading (monitoring) device is to be used to extract information residing in the EFS?
22. What is the cost of the EFS downloading (monitoring) device?

23. What is the expected life of the downloading device in years?
24. How many downloading devices are required?
25. How long does it take to download readings of each EFS (in minutes)?
26. What equipment is required besides the EFS and downloading device (e.g., Personal Computer)?
27. What is the reliability of the EFS (i.e., mean time between failure—MTBF)?
28. What is the MTBF of the downloading device?
29. What support equipment is required to test and repair the downloading device?
30. What is the cost of this support equipment?

Thank you in advance for your assistance in this effort. If you have any questions please call me at (937) 427-7525 or FAX questions to me at (937) 427-2781.

Regards,

Larry Legault

Laurent J.J. Legault
c/o Research & Technology Resources, Ltd.
4141 Col Glenn Hwy., Suite 180
Beavercreek, OH 45431

February 27, 1998

Mr. Barry Pittman
Headquarters AETC
Randolph AFB, TX 78150-4440

FAX (210) 652-2234

Dear Mr. Pittman,

I am working for Matech on the program for <u>Application of Electrochemical Fatigue Sensor for Improved Durability Assessment of Military Aircraft</u> (Contract Number F41608-96-D-0108). The purpose of my task is to conduct a life cycle cost (LCC) analysis pertaining to the cost of performing Nondestructive Inspections (NDI) (limited to Rotoscan and Eddy Current methodologies) on T-38A aircraft.

The LCC analysis exclusively addresses the T-38A wing area. Specifically, the scope pertains only Fatigue Critical Locations (FCLs)—areas one through six. This analysis requires me to obtain cost relevant data pertaining to Rotoscan and Eddy Current NDI for compilation and input to a life cycle cost model to project costs over a five year timeframe. To derive a life cycle cost (LCC) model estimate of these two NDI methodologies certain economic analysis input data are required. The questions below are designed to generate this modeling data.

In order for me to meet program deadlines, I would appreciate it if you would please provide answers to the following questions as soon as possible. If you can respond by March 4, that will assist me a great deal.

1. What specific equipment is required to perform Ultrasonic (Rotoscan) inspection of the wing? Please list.
2. How often does this Ultrasonic equipment need repair during a one year time frame?
3. How many spare Rotoscanners do you have on hand?
4. How many aircraft wings do you inspect in a one year time frame?
5. What support/test equipment is required for repair of the Rotoscan inspection equipment? Please list
6. How many labor hours are expended repairing Rotoscan inspection equipment per year?
7. What is the material cost per year for repairs?
8. What quantity of each piece of support/test equipment is required to support Rotoscan?
9. If you know the cost of support/test equipment, please provide.
10. What equipment is required to perform Eddy Current inspection of the boltholes of a wing? Please list.
11. How often does this Eddy Current equipment need repair during a one year time frame?
12. How many labor hours are expended repairing Eddy Current inspection devices per year?
13. What is the material cost per year for repairs?
14. How many spare Eddy Current Inspection devices do you have on hand?
15. How many bolt holes do you scan (per wing) in a one year time frame?
16. What support/test equipment is required for repair of Eddy Current inspection equipment? Please list.
17. What quantity of each piece of support/test equipment is required to support Eddy Current?

18. If you know the cost of this support/test equipment, please provide.

19. Do you repair Eddy Current probes?

20. How many new probes do you purchase per year?

21. What is the average cost of a probe?

Thank you in advance for your assistance in this effort. If you have any questions please call me at (937) 427-2575 or FAX questions to me at (937) 427-2781.

Regards,

Larry Legault

CY: Mr. Bob Bernstein, CEO, Matech

APPENDIX C

COMPILED QUESTIONNAIRE DATA

EFS QUESTIONNAIRE AND RESPONSES

1. How many EFS are going to be placed in Fatigue Critical Location (FCL) zone area one of the wing? 2 EFS PER SIDE: TOTAL 4
2. How many EFS are going to be placed in Fatigue Critical Location (FCL) zone area two of the wing? 2 EFS PER SIDE: TOTAL 4
3. How many EFS are going to be placed in Fatigue Critical Location (FCL) zone area three of the wing? 2 EFS PER SIDE: TOTAL 4
4. How many EFS are going to be placed in Fatigue Critical Location (FCL) zone area four of the wing? 1 EFS PER SIDE: TOTAL 2
5. How many EFS are going to be placed in Fatigue Critical Location (FCL) zone area five of the wing? 2 EFS PER SIDE: TOTAL 4
6. How many EFS are going to be placed in Fatigue Critical Location (FCL) zone area six of the wing? 1 EFS PER SIDE: TOTAL 2
7. What is the cost of each EFS? $ 50
8. What is the expected life of an EFS in years? FIVE YEARS
9. What is the expected labor cost to install each EFS? USE LABOR RATE IN JOSTE MODEL
10. What equipment is required to install the EFS? CLEANING PAD AND SOLUTION
11. What material (s) is (are) required for EFS installation? VELCRO, WIRE CLIPS
12. How long does installation take (in minutes or hours)? ONE HOUR
13. When the EFS fails, how long does it take to remove and replace it? TWO HOURS
14. Does an access panel require opening or removal before an EFS can be installed, removed, or have information downloaded? YES, THERE ARE A COUPLE PER SIDE
15. If the answer to question 9 is yes—how much time is required to open panel? How much time is required to remove a panel, if this is necessary? If the answer to question 9 is no skip this question and go on to question 11. APPROXIMATELY 15 MINUTES PER PANEL (WORK CARD)
16. What are the estimated costs for training personnel to intall and remove EFS? ONE HOUR
17. What is the repair concept for the EFS (i.e., remove/replace and discard, remove/replace and repair, etc.)? REMOVE, REPLACE AND REPAIR
18. If the EFS is to be repaired what repair parts and spares are required? VELCRO, SEALANT, ADHESIVE (APPROX. $10 PER KIT)
19. What is the cost of each repair part/spare? ($10 PER REPAIR KIT/$50 PER EFS SPARE)
20. What support or test equipment is required to test each EFS to ensure operability prior to installation on the aircraft? NONE REQUIRED
21. What kind of downloading (monitoring) device is to be used to extract information residing in the EFS? MULTIPLEX RECORDER
22. What is the cost of the EFS downloading (monitoring) device? $5,000
23. What is the expected life of the downloading device in years? TEN YEARS
24. How many downloading devices are required? ONE PER BASE
25. How long does it take to download readings of each EFS (in minutes)? ONE HOUR
26. What equipment is required besides the EFS and downloading device (e.g., Personal Computer)? PERSONAL COMPUTER
27. What is the reliability of the EFS (i.e., mean time between failure—MTBF)? 0 FAILURES
28. What is the MTBF of the downloading device? ABOUT 20,000 OPERATING HOURS
29. What support equipment is required to test and repair the downloading device? NONE
30. What is the cost of this support equipment? $ 0

NOTE: A PC IS REQUIRED TO READ THE DATA DOWNLOADED TO THE MULTIPLEX RECORDER. THIS PC WOULD BE CONSIDERED CAPITAL EQUIPMENT.

T-38A LIFE CYCLE COST INFORMATION

RESPONSES FROM THREE PILOT TRAINING BASES.	TRAINING BASE 1	TRAINING BASE 2	TRAINING BASE 3
1. What specific equipment is required to perform Ultrasonic (Rotoscan) inspection of the wing? Please list.	a	a	a
2. How often does this Ultrasonic equipment need repair during a one year time frame?	2 Times/ YEAR for vcr; 2 TIMES/YEAR sched maint scanner	1 TIME/YEAR on equipment (rubber boots break or leak)	1 VHS VCR RECORDER REPLACED IN 1994; 1 EPOCH 2002 REPAIRED AUG 1993
3. How many spare Rotoscanners do you have on hand?	0 ??? SEE 8 BELOW	0	0
4. How many aircraft wings do you inspect in a one year time frame?	208 WINGS	100 ACFT W/EACH WING INSPECTED 3 TIMES (300 WINGS)	ALL FASTENERS ARE SCANNED AT DIFFERENT OPERATING HRS, BUT NEVER ALL TOGETHER; AREA 1-6, A WAG WOULD BE ABOUT 20 EACH.
5. What support/test equipment is required for repair of the Rotoscan inspection equipment? Please list	MULTIMETER & SOLDERING IRON	TRANSDUCERS & CABLES	
6. How many labor hours are expended repairing Rotoscan inspection equipment per year?	40-50 HRS *	80 HRS	UNKNOWN
7. What is the material cost per year for repairs?	$ 2,000 **	$ 800 ***	PREVENTIVE MAINT=15 HRS INCLUDE SOFTWARE $109
8. What quantity of each piece of support/test equipment is required to support Rotoscan?	UT UNIT, VCR, MONITOR, & SCANNER–2 IN USE ; 1 SPARE:: STANDARDS AND SPLARS UNITS–2 EA.	TRANDUCER–5; CABLES–40; LEGS–12; BOOTS–40	UNKNOWN
9. If you know the cost of support/test equipment, please provide.	ROTOSCAN SET UP=$11,530 EA; SPLARS=$10,000 EA.; SCANNER ASSY=$1,236 EA.; STANDARDS=$4,063 EA.		N/A

T-38A LIFE CYCLE COST INFORMATION

	AUTOMATIC SCANNER	19 II, UH-1B	FT 100 OR 19EII
10. What equipment is required to perform Eddy Current inspection of the boltholes of a wing? Please list.			
11. How often does this Eddy Current equipment need repair during a one year time frame?	2 times/year for sched maint scanner	0	0 FAILURES TO DATE
12. How many labor hours are expended repairing Eddy Current inspection devices per year?	20 hours	0	N/A
13. What is the material cost per year for repairs?	about $150	0	N/A
14. How many spare Eddy Current Inspection devices do you have on hand?	0	0	0
15. How many bolt holes do you scan (per wing) in a one year time frame?	2-3 per wing for fcl 1,2,3,4,5	60	EST. 25
16. What support/test equipment is required for repair of Eddy Current inspection equipment? Please list.	MULTIMETER & SOLDERING IRON	NONE	UNKNOWN
17. What quantity of each piece of support/test equipment is required to support Eddy Current?	1 ea.	0	N/A
18. If you know the cost of this support/test equipment, please provide.	about $200	N/A	N/A
19. Do you repair Eddy Current probes?	NO	NONE	NO
20. How many new probes do you purchase per year?	40-50	40	5
21. What is the average cost of a probe?	$150	$85	$200

Page 2

C-4

T-38A LIFE CYCLE COST INFORMATION

22. How many hours does it take to rotoscan each of the following Fatigue Critical Locations?			
FCL zone area 1	4-8 Hrs	4-8 Hrs	4-8 Hrs
FCL zone area 2	4-8 Hrs	4-8 Hrs	4-8 Hrs
FCL zone area 3	4-8 Hrs	4-8 Hrs	4-8 Hrs
FCL zone area 4	3-6 Hrs	3-6 Hrs	3-6 Hrs
FCL zone area 5	3-6 Hrs	3-6 Hrs	3-6 Hrs
FCL zone area 6	1-1.5 Hrs	1-1.5 Hrs	1-1.5 Hrs
23. How long does it take to Eddy Current inspect a bolt hole?	.5-1 Hr	.5-1 Hr	.5-1 Hr
a) EPOC 2002 PANAMERICS UT (ULTRASONIC) UNIT, VCR RECORDER, MONITOR, ROTO SCANNER ASSY, AND UT STANDARDS. ALSO, CENTERING DEVICES, CABLES, EXTENSION CORDS, TRANSDUCER, PUSH CART, & RUBBER BOOTS (SOUND COUPLING).			
* DOES NOT INCLUDE MAINTENANCE ON SPLARS BECAUSE BASES ARE NOT USING THEM			
** COST IS MOSTLY FOR VCR C			
*** COST IS MAINLY FOR RUBBER BOOTS, VCR MONITORS, AND ROTOSCANNER LEGS			
**** RESPONSES FOR EACH LOCATION WERE PROVIDED BY SMSGT BARRY PITTMAN (HQAETC) WHO RECEIVED THE VERBAL RESPONSES FROM THE THREE BASES.			

SUPT NDI HOURS

	1	2	3	4	5	6	7	8	9	10	11	12	13	14
	Area	No. Holes	FCL	SUPT Initial Inspection (Hrs)	No SUPT Recurring Inspection (Hrs)	No. SUPT Recurring Insp/Yr	No Hrs per Rotoscan Inspection (Worst Case)	Rotoscan Inspection Hrs (col 6 x col 7)	No Hrs Per Eddy Current Hole Inspection	Current Hole Inspection Hours (Worst Case) (col 2 x col 9) col 6 x col 9	per Rotoscan Inspection (Best Case)	Rotoscan Inspection Hrs (col 6 x col 11)	No Hrs Per Eddy Current Hole Inspection	Current Hole Inspection Hours (Best Case) col 2 x col 13 col 6 x col 13
	1	158	A-5	4432	1867	30	8	240	1	4740	4	120	0.5	2370
	2	150	A-19	10698	5041	10	8	80	1	1500	4	40	0.5	750
	3	164	A-15	1735	1459	39	8	312	1	6396	4	156	0.5	3198
	4	86	A-18	5521	3543	8	6	48	1	688	3	24	0.5	344
	5	106	A-17	4537	3546	10	6	60	1	1060	3	30	0.5	530
	6	16	A-10A	4827	858	6	1.5	9	1	96	1	6	0.5	48

SUPT
Flying Hrs/Yr
348

No. Hole Inspections per Acft/Yr = 103
No Acft in SUPT = 300
SUPT Hole Inpsections/Yr = 30900

Total T-38 acft in SUPT, IFF and ENJJPT usages = 482
Total fastener hole inspections per year = 90560

Notes: (1) SUPT and IFF Initial and Recurring Inpspection times are taken from Southwest Research Institute's current DADTA analysis.
(2) ENJJPT Initial and Recurring Inspection times are taken from T.O. 1T-38A-6, February 1997.

IFF NDI HOURS

1	2	3	4	5	6	7	8	9	10	11	12	13	14
Area	No. Holes	FCL	IFF Initial Inspection (Hrs)	No IFF Recurring Inspection (Hrs)	No. IFF Recurring Insp/Yr	No Hrs per Rotoscan Inspection (Worst Case)	Rotoscan Inspection Hrs (col 6 x col 7)	No Hrs Per Eddy Current Hole Inspection	Current Hole Inspection Hours (Worst Case) (col 2 x col 6 x col 9)	per Rotoscan Inspection (Best Case)	Rotoscan Inspection Hrs (col 6 x col 11)	No Hrs Per Eddy Current Hole Inspection	Current Hole Inspection Hours (Best Case) col 2 x col 6 x col 13
1	158	A-5	677	300	165	8	1320	1	26070	4	660	0.5	13035
2	150	A-19	1543	722	65	8	520	1	9750	4	260	0.5	4875
3	164	A-15	261	221	232	8	1856	1	38048	4	928	0.5	19024
4	86	A-18	1006	677	40	6	240	1	3440	3	120	0.5	1720
5	106	A-17	737	594	56	6	336	1	5936	3	168	0.5	2968
6	16	A-10A	1978	472	11	1.5	16.5	1	176	1	11	0.5	88

IFF

Flying Hrs/Yr   312

No. Hole Inspections per Acft/Yr = 569

No Acft in IFF = 88

IFF Hole Inpsections/Yr = 50072

Total T-38 acft in SUPT, IFF and ENJJPT usages = 482

Total fastener hole inspections per year = 90560

Notes: (1) SUPT and IFF Initial and Recurring Inpspection times are taken from Southwest Research Institute's current DADTA analysis.

(2) ENJJPT Initial and Recurring Inspection times are taken from T.O. 1T-38A-6, February 1997.

ENJJPT NDI HOURS

1	2	3	4	5	6	7	8	9	10	11	12	13	14
Area	No. Holes	FCL	ENJJPT Initial Inspection (Hrs)	No ENJJPT Recurring Inspection (Hrs)	No. ENJJPT Recurring Inspp/Yr.	No Hrs per Rotoscan Inspection (Worst Case)	Rotoscan Inspection Hrs (col 6 x col 7)	No Hrs Per Eddy Current Hole Inspection	Current Hole Inspection Hours (Worst Case) (col 2 x col 6 x col 9)	per Rotoscan Inspection (Best Case)	Rotoscan Inspection Hrs (col 6 x col 11)	No Hrs Per Eddy Current Hole Inspection	Current Hole Inspection Hours (Best Case) col 2 x col 6 x col 13
1	158	A-5	4500	2100	32	8	256	1	5056	4	128	0.5	2528
2	150	A-19	19800	3600	17	8	136	1	2550	4	68	0.5	1275
3	164	A-15	4950	3150	22	8	176	1	3608	4	88	0.5	1804
4	86	A-18	6300	3600	10	6	60	1	860	3	30	0.5	430
5	106	A-17	8100	7200	6	6	36	1	636	3	18	0.5	318
6	16	A-10A	6300	450	15	1.5	22.5	1	240	1	15	0.5	120

ENJJPT Flying Hrs/Yr 348

No. Hole Inspections per Acft/Yr = 102

No Acft in ENJJPT = 94

ENJJPT Hole Inpsections/Yr = 9588

Total T-38 acft in SUPT, IFF and ENJJPT usages = 482

Total fastener hole inspections per year = 90560

Notes:
(1) SUPT and IFF Initial and Recurring Inpspection times are taken from Southwest Research Institute's current DADTA analysis.
(2) ENJJPT Initial and Recurring Inspection times are taken from T.O. 1T-38A-6, February 1997.

APPENDIX D

JOSTE REPORTS

JOSTE Report - Apr 17, 1998
EFS/SUPT Cost Analysis

Totals:

SubSystem O&S Costs:	$220,083
Component O&S Costs:	$0
Other O&S Costs:	$0
Total O&S Costs:	$220,083
Acquisition Costs:	$375,900
Total Costs:	$595,983
Total Manhour Requirements:	6,891 Hours

Acquisition Costs:

PME Acquisition:	$300,000
Support Equipment Production:	$0
Subsystem Pipeline Spares:	$900
Component Pipeline Spares:	$0
Warranty:	$0
Technical Data:	$3,000
System Engineering Project Management (SEPM):	$45,000
Initial Training:	$3,000
Engineering Change Orders:	$24,000
Interim Contractor Support (ICS):	$0
Item Entry:	$0
PME Hardware Development:	$0
PME Software Development:	$0
SE Hardware Development:	$0
SE Software Development:	$0
Whole Engine Spares:	$0

Subsystem Operation & Support:

Repair Cost at Base Flight Line:	$0
Repair Cost at Base Intermediate:	$220,083
Repair Cost at Depot:	$0
Reparable Spares Division (RSD) Cost:	$0
Replenishment Spares:	$0
Software Maintenance:	$0
SE Maintenance:	$0
Contractor Logistics Support (CLS):	$0
Manhours Required at Base Flight Line:	0 Hours
Manhours Required at Base Flight Intermediate:	6,891 Hours
Manhours Required at Depot:	0 Hours
Manhours Required for Contractor Logistics Support:	0 Hours

Component Operation & Support:

Repair Cost at Base Intermediate:	$0
Repair Cost at Depot:	$0
Reparable Spares Division (RSD) Cost:	$0

JOSTE Report - Apr 17, 1998
EFS/IFF Cost Analysis

Totals:

SubSystem O&S Costs:	$220,071
Component O&S Costs:	$0
Other O&S Costs:	$0
Total O&S Costs:	$220,071
Acquisition Costs:	$110,600
Total Costs:	$330,671
Total Manhour Requirements:	6,890 Hours

Acquisition Costs:

PME Acquisition:	$88,000
Support Equipment Production:	$0
Subsystem Pipeline Spares:	$600
Component Pipeline Spares:	$0
Warranty:	$0
Technical Data:	$880
System Engineering Project Management (SEPM):	$13,200
Initial Training:	$880
Engineering Change Orders:	$7,040
Interim Contractor Support (ICS):	$0
Item Entry:	$0
PME Hardware Development:	$0
PME Software Development:	$0
SE Hardware Development:	$0
SE Software Development:	$0
Whole Engine Spares:	$0

Subsystem Operation & Support:

Repair Cost at Base Flight Line:	$220,071
Repair Cost at Base Intermediate:	$0
Repair Cost at Depot:	$0
Reparable Spares Division (RSD) Cost:	$0
Replenishment Spares:	$0
Software Maintenance:	$0
SE Maintenance:	$0
Contractor Logistics Support (CLS):	$0
Manhours Required at Base Flight Line:	0 Hours
Manhours Required at Base Flight Intermediate:	6,890 Hours
Manhours Required at Depot:	0 Hours
Manhours Required for Contractor Logistics Support:	0 Hours

Component Operation & Support:

Repair Cost at Base Intermediate:	$0
Repair Cost at Depot:	$0
Reparable Spares Division (RSD) Cost:	$0

JOSTE Report - Apr 17, 1998
EFS/ENJJPT Cost Analysis

Totals:

SubSystem O&S Costs:	$218,454
Component O&S Costs:	$0
Other O&S Costs:	$0
Total O&S Costs:	$218,454
Acquisition Costs:	$119,050
Total Costs:	$337,504
Total Manhour Requirements:	6,840 Hours

Acquisition Costs:

PME Acquisition:	$94,000
Support Equipment Production:	$0
Subsystem Pipeline Spares:	$1,550
Component Pipeline Spares:	$0
Warranty:	$0
Technical Data:	$940
System Engineering Project Management (SEPM):	$14,100
Initial Training:	$940
Engineering Change Orders:	$7,520
Interim Contractor Support (ICS):	$0
Item Entry:	$0
PME Hardware Development:	$0
PME Software Development:	$0
SE Hardware Development:	$0
SE Software Development:	$0
Whole Engine Spares:	$0

Subsystem Operation & Support:

Repair Cost at Base Flight Line:	$0
Repair Cost at Base Intermediate:	$218,454
Repair Cost at Depot:	$0
Reparable Spares Division (RSD) Cost:	$0
Replenishment Spares:	$0
Software Maintenance:	$0
SE Maintenance:	$0
Contractor Logistics Support (CLS):	$0
Manhours Required at Base Flight Line:	0 Hours
Manhours Required at Base Flight Intermediate:	6,840 Hours
Manhours Required at Depot:	0 Hours
Manhours Required for Contractor Logistics Support:	0 Hours

Component Operation & Support:

Repair Cost at Base Intermediate:	$0
Repair Cost at Depot:	$0
Reparable Spares Division (RSD) Cost:	$0

JOSTE Report - Apr 16, 1998
NDI/SUPT Cost Analysis

Totals:

SubSystem O&S Costs:	$2,324,089
Component O&S Costs:	$0
Other O&S Costs:	$0
Total O&S Costs:	$2,324,089
Acquisition Costs:	$0
Total Costs:	$2,324,089
Total Manhour Requirements:	72,764 Hours

Acquisition Costs:

PME Acquisition:	$0
Support Equipment Production:	$0
Subsystem Pipeline Spares:	$0
Component Pipeline Spares:	$0
Warranty:	$0
Technical Data:	$0
System Engineering Project Management (SEPM):	$0
Initial Training:	$0
Engineering Change Orders:	$0
Interim Contractor Support (ICS):	$0
Item Entry:	$0
PME Hardware Development:	$0
PME Software Development:	$0
SE Hardware Development:	$0
SE Software Development:	$0
Whole Engine Spares:	$0

Subsystem Operation & Support:

Repair Cost at Base Flight Line:	$0
Repair Cost at Base Flight Intermediate:	$2,324,089
Repair Cost at Depot:	$0
Reparable Spares Division (RSD) Cost:	$0
Replenishment Spares:	$0
Software Maintenance:	$0
SE Maintenance:	$0
Contractor Logistics Support (CLS):	$0
Manhours Required at Base Flight Line:	0 Hours
Manhours Required at Base Flight Intermediate:	72,764 Hours
Manhours Required at Depot:	0 Hours
Manhours Required for Contractor Logistics Support:	0 Hours

Component Operation & Support:

Repair Cost at Base Intermediate:	$0
Repair Cost at Depot:	$0
Reparable Spares Division (RSD) Cost:	$0

JOSTE Report - Apr 16, 1998
NDI/IFF Cost Analysis

Totals:

SubSystem O&S Costs:	$14,009,432
Component O&S Costs:	$0
Other O&S Costs:	$0
Total O&S Costs:	$14,009,432
Acquisition Costs:	$0
Total Costs:	$14,009,432
Total Manhour Requirements:	438,617 Hours

Acquisition Costs:

PME Acquisition:	$0
Support Equipment Production:	$0
Subsystem Pipeline Spares:	$0
Component Pipeline Spares:	$0
Warranty:	$0
Technical Data:	$0
System Engineering Project Management (SEPM):	$0
Initial Training:	$0
Engineering Change Orders:	$0
Interim Contractor Support (ICS):	$0
Item Entry:	$0
PME Hardware Development:	$0
PME Software Development:	$0
SE Hardware Development:	$0
SE Software Development:	$0
Whole Engine Spares:	$0

Subsystem Operation & Support:

Repair Cost at Base Flight Line:	$14,009,432
Repair Cost at Base Intermediate:	$0
Repair Cost at Depot:	$0
Reparable Spares Division (RSD) Cost:	$0
Replenishment Spares:	$0
Software Maintenance:	$0
SE Maintenance:	$0
Contractor Logistics Support (CLS):	$0
Manhours Required at Base Flight Line:	0 Hours
Manhours Required at Base Flight Intermediate:	438,617 Hours
Manhours Required at Depot:	0 Hours
Manhours Required for Contractor Logistics Support:	0 Hours

Component Operation & Support:

Repair Cost at Base Intermediate:	$0
Repair Cost at Depot:	$0
Reparable Spares Division (RSD) Cost:	$0

JOSTE Report -- Apr 16, 1998
NDI/ENJJPT Cost Analysis

Totals:

SubSystem O&S Costs:	$2,177,721
Component O&S Costs:	$0
Other O&S Costs:	$0
Total O&S Costs:	$2,177,721
Acquisition Costs:	$0
Total Costs:	$2,177,721
Total Manhour Requirements:	68,182 Hours

Acquisition Costs:

PME Acquisition:	$0
Support Equipment Production:	$0
Subsystem Pipeline Spares:	$0
Component Pipeline Spares:	$0
Warranty:	$0
Technical Data:	$0
System Engineering Project Management (SEPM):	$0
Initial Training:	$0
Engineering Change Orders:	$0
Interim Contractor Support (ICS):	$0
Item Entry:	$0
PME Hardware Development:	$0
PME Software Development:	$0
SE Hardware Development:	$0
SE Software Development:	$0
Whole Engine Spares:	$0

Subsystem Operation & Support:

Repair Cost at Base Flight Line:	$0
Repair Cost at Base Intermediate:	$0
Repair Cost at Depot:	$2,177,721
Reparable Spares Division (RSD) Cost:	$0
Replenishment Spares:	$0
Software Maintenance:	$0
SE Maintenance:	$0
Contractor Logistics Support (CLS):	$0
Manhours Required at Base Flight Line:	0 Hours
Manhours Required at Base Flight Intermediate:	68,182 Hours
Manhours Required at Depot:	0 Hours
Manhours Required for Contractor Logistics Support:	0 Hours

Component Operation & Support:

Repair Cost at Base Intermediate:	$0
Repair Cost at Depot:	$0
Reparable Spares Division (RSD) Cost:	...